TEXTURAL, CHEMICAL AND AGE VARIATION IN MONAZITES OF THE PALEOPROTEROZOIC LONGSTAFF BLUFF FORMATION, CENTRAL BAFFIN ISLAND, NUNAVUT

by

Simon Gagné

Submitted in partial fulfilment of the requirements
for the degree of Master of Science
at
Dalhousie University
Halifax, Nova Scotia
June 2004

DALHOUSIE UNIVERSITY

DEPARTMENT OF EARTH SCIENCES

The undersigned hereby certify that they have read and recommend to the Faculty of Graduate Studies for acceptance a thesis entitled "TEXTURAL, CHEMICAL AND AGE VARIATION IN MONAZITES OF THE PALEOPROTEROZOIC LONGSTAFF BLUFF FORMATION, CENTRAL BAFFIN ISAND, NUNAVUT" by Simon Gagné in partial fulfillment of the requirements for the degree of Master of Science.

Dated: June 01, 2004

Supervisor:

External Examiner:

Readers:

DALHOUSIE UNIVERSITY

AUTHOR: Simon Gagné DATE: June 01, 2004

TITLE: TEXTURAL, CHEMICAL AND AGE VARIATION IN MONAZITES OF THE PALEOPROTEROZOIC LONGSTAFF BLUFF FORMATION, CENTRAL BAFFIN ISLAND, NUNAVUT.

DEPARTMENT OR SCHOOL: Department of Earth Sciences

DEGREE: MSc CONVOCATION: October YEAR: 2004

Distribution License

DalSpace requires agreement to this non-exclusive distribution license before your item can appear on DalSpace.

NON-EXCLUSIVE DISTRIBUTION LICENSE

You (the author(s) or copyright owner) grant to Dalhousie University the non-exclusive right to reproduce and distribute your submission worldwide in any medium.

You agree that Dalhousie University may, without changing the content, reformat the submission for the purpose of preservation.

You also agree that Dalhousie University may keep more than one copy of this submission for purposes of security, back-up and preservation.

You agree that the submission is your original work, and that you have the right to grant the rights contained in this license. You also agree that your submission does not, to the best of your knowledge, infringe upon anyone's copyright.

If the submission contains material for which you do not hold copyright, you agree that you have obtained the unrestricted permission of the copyright owner to grant Dalhousie University the rights required by this license, and that such third-party owned material is clearly identified and acknowledged within the text or content of the submission.

If the submission is based upon work that has been sponsored or supported by an agency or organization other than Dalhousie University, you assert that you have fulfilled any right of review or other obligations required by such contract or agreement.

Dalhousie University will clearly identify your name(s) as the author(s) or owner(s) of the submission, and will not make any alteration to the content of the files that you have submitted.

If you have questions regarding this license please contact the repository manager at dalspace@dal.ca.

Grant the distribution license by signing and dating below.

______________________________	______________________________
Name of signatory	Date

TABLE OF CONTENTS

LIST OF FIGURES

LIST OF TABLES

ABSTRACT

Textural and chemical characterization and U-Th-Pb chemical dating were carried out on monazite from upper greenschist to granulite facies rocks of the Paleoproterozoic (ca. 1.92-1.90 Ga) Longstaff Bluff Formation (LBF) using an electron microprobe (EMP).

In the LBF, monazite appears early in the prograde metamorphic sequence. Upper greenschist rocks contain small but widespread metamorphic monazite. The abundance and size of LBF monazite constantly increase with metamorphic grade. The transition from the Sil-Kfs zone to the migmatite zone coincides with a significant increase in size and abundance of monazite. Chemical zoning is generally weak in low- to medium-grade samples. Monazites from migmatitic samples are the most abundant and they are commonly zoned in U, Th and Y.

Chemical data show that metamorphic grade has a strong influence on monazite composition. HREE, Ca, Si, Th, U, and Y increase with metamorphic grade, while LREE abundance decreases. The spread in values of element content at higher grade suggests that factors other than metamorphic grade also control monazite composition. Sharp changes in monazite composition are observed at the transition from the Sil-Kfs zone to the migmatite zone, notably a steep increase in Y content. Highly resorbed garnet is reported from this transition.

Electron microprobe U-Th-Pb chemical dating of monazite allowed recognition of 6 different age populations within the LBF monazites. Results correlate very well with available U-Pb isotopic ages. Detrital grains were identified. Episodes of metamorphic monazite growth were dated at ca. 1880 Ma (E_1), 1850 Ma (E_2), 1830 Ma (E_3), 1800 Ma (E_4) and 1770 Ma (E_5). Chemical age data suggest the existence of a northward younging age gradient for E_2 and E_3 events, which are mainly recorded in the southernmost transects. E_4 is synchronously recorded throughout the field area and E_5 is mainly recorded in the northern part of the study area. Constraints from petrological setting and chemical mapping of monazite grains were used to interpret the ages.

The significance of E_1 is not clear, although it is similar in age with the emplacement of granite at 1897+7/-4 Ma and ca.1877-1874 Ma monazite ages obtained from by TIMS analysis. E_2 likely corresponds to development of an S1 fabric and predates growth of cordierite. E_3 is pre- to syn-garnet growth. Petrological an chemical information of E_4 monazite grains suggest that this event correspond to partial melting of the LBF and that, locally, older monazite grains were partially recrystallized during this event. E_5 monazite grains are syn- to post- development of an S2 fabric in the low-grade samples.

ACKNOWLEDGEMENTS

This thesis would not have been possible without the support and participation of many people.

First, my foremost thanks go to my supervisor, Becky Jamieson, for her generous support. Also, her guidance and constructive comments greatly improved the thesis.

The other members of my supervising committee, Peter Reynolds and Barrie Clarke, are also thanked for their generous support and their comments.

I would also like to thank especially Bob Mackay for its patience and its expertise on microprobe analysis who greatly contributed to the success of this project. Its was always a great pleasure to work him.

Je voudrais remercier particulièrement remercier Dr. Marc St-Onge, Dr. David Corrigan and Dr. David Scott de la Commission Géologique du Canada qui m'ont donné l'opportunité de travailler avec eux sur l'île de Baffin, qui ont généreusement partagé leur enthousiasme pour le travail de terrain et la géologie, ainsi que pour leur camaraderie.

Thank you very much to the fieldcrew of summers 2000-2002 for their friendship and company.

Many thanks also to all the graduate students at Dalhousie who made the duration of this thesis a wonderful experience.

Je aussi remercier ma famille et mes amis qui m'ont toujours supporté et encouragé à poursuivre mes objectifs et mes études.

Finally, I would like to thank my partner who unconditionally supported me and encouraged me even through the tougher moments. Thank you very much Sharon for being there.

1. Introduction

Over the past decade, interest in monazite as a metamorphic mineral and a chronometer has significantly increased, because this is a prevalent accessory mineral in metapelites and it has a very reliable isotopic system. Additionally, numerous recent studies (e.g., Terry et al., 2000; Spear and Pyle, 2002; Wing et al., 2003) show that growth of metamorphic monazite and its relationships with other mineral phases allow retrieval of important information on the metamorphic history of the rock. One of the most promising fields of investigation is the application of *in situ* chemical dating of monazite using the U-Th-Pb system by electron microprobe (EMP). This technique preserves the petrological setting of analysed grains and allows the geochronological information to be related to petrological and geochemical data.

The details of monazite behaviour under various metamorphic conditions are still not fully understood. This lack of information represents a fundamental obstacle in the interpretation of chemical and isotopic ages obtained from monazite. Consequently, important research efforts (e.g., Foster et al., 2002; Pyle and Spear, 2003a) have been put into understanding the relationship of monazite with other accessory and rock forming minerals involved in metamorphic reactions, documenting chemical changes with changing metamorphic grade, and investigating the nature of the chemical zoning. Important progress has been made over the last decade; however, we are only starting to understand the complexity of the chemical interaction between monazite and other mineral phases during metamorphism. All this information is required to understand the significance of monazite chemical ages obtained by EMP *in situ* dating.

The Geological Survey of Canada (GSC) and the Canada-Nunavut Geoscience Office (C-NGO) led a three-year collaborative project (2000-2002) in the central part of Baffin Island, which covers a large section of the northern margin of the Trans-Hudson Orogen. The project area encompasses the metasediments of the Foxe Fold Belt and associated plutonic rocks, which are flanked to north by the Archean Rae craton and by the Paleoproterozoic Cumberland Batholith to the south. This area had only been mapped on a reconnaissance scale in the past. The GSC/C-NGO joint mapping project aimed to obtain a transect across the orogen in order to better understand the geometry and distribution of the various rock units, and the nature of the contacts with the Archean basement, ultimately to acquire a better knowledge of the geological evolution of this area. The Foxe Fold Belt includes a thick package of turbidites, the Longstaff Bluff Formation (LBF), that shows a range of metamorphic grade from upper greenschist facies to granulite facies. These metasedimentary rocks contain minor but widespread pelitic material that recorded a prograde metamorphic sequence, which makes it an ideal candidate to study the chemical and textural variation of monazite through progressive metamorphism.

The metamorphic isograds in the central Baffin area of the Foxe Fold Belt form an east-west elongated trough (Dubach and Carmichael, 2003). In the centre sits the lowest grade area with metamorphic grade increasing outward in every direction. The LBF occupies most of the surface and is an ideal tracer for the isograds due to its pelitic layers. The origin of the metamorphism in the LBF is not fully understood. The timing of metamorphism is poorly documented in this area and links with the metamorphic evolution of the metapelites (e.g. porphyroblast growth, mineral reactions) are lacking. It was previously suggested that the area first experienced an episode of contact metamorphism caused by the emplacement of the Cumberland Batholith and related megacrystic monzogranite plutons to the south of the study area (Corrigan et al., 2001). Then, a later phase of regional metamorphism due to tectonic thickening of the crust locally overprinted the contact metamorphism. However, new U-Pb data (Wodicka et al., 2002) on the timing of the megacrystic monzogranite emplacement and the migmatisation event revealed that the previous interpretations are inadequate because the monzogranite located in the south of the area is older than the Cumberland Batholith and available ages for the LBF indicate that regional metamorphism is not related to the emplacement of this monzogranites. Recent work (Allan and Pattison, 2003; Dubach and Carmichael, 2003; Wodicka et al., 2003) also reveals that the LBF metamorphic history is relatively complex and comprises multiple events.

The purpose of this study was to:

1. acquire geochemical and textural data from LBF monazite and to relate this information to the metamorphic history,
2. acquire geochronological information on monazite growth history using EMP chemical dating,
3. compare new data with existing geochronological and metamorphic information,
4. and interpret the significance of the data acquired from LBF monazite in terms of the metamorphic history

To achieve these objectives a comprehensive EMP study of LBF monazite grains from various petrological settings and metamorphic grades was carried out. Information on textures, petrological setting and chemical zoning of monazite grains was obtained using back-scattered electron (BSE) images and X-ray maps, information on major and minor element content was provided by EMP spot analyses, and geochronological information was obtained from EMP analyses of selected monazite grains. Mineral assemblages of samples analysed in this study were examined; however, a detailed petrological study of the metamorphic mineral assemblages and phases equilibrium of LBF rocks, and characterisation of the P-T conditions are part of an ongoing Ph.D. study (K. Dubach, Queen's University) and were not addressed in this study. Because the emphasis was put on the characterisation of textural, chemical and age variation of LBF monazite, other mineral phases were not examined in detail and the nature of reactions involving monazite has not been specifically addressed.

In Chapter 2, the thesis first provides background information on the regional geology of the central Baffin area including a description of the main lithological units, information on the regional distribution of the main metamorphic zones and P-T data, and a brief summary of the regional structural geology. Chapter 3 presents the sample locations with a more detailed description of the different mineral assemblages. It also synthesises observations on LBF monazite textures and distribution. A discussion on the significance of these observations completes the chapter. Chapter 4 is more technical and provides basic information on electron microprobe quantitative analysis and specifications for monazite analysis. This chapter also describes briefly the various procedures used and discusses some of the analytical issues (e.g., analytical settings, sources of errors). The first part of Chapter 5 addresses the chemical zoning of LBF monazite; whereas the second part presents and discusses results of the variation in chemical content of monazite from different metamorphic grades. Chapter 6 presents the results of the chemical dating of LBF monazite and discusses the statistical treatment of the age data. Chapter 7 discusses the significance of the monazite chemical ages for constraining the LBF metamorphic history.

2. Regional Geology

2.1 Trans-Hudson Orogen

The Paleoproterozoic was a period of very active tectonic processes. Major collisional events from 2.0-1.8 Ga resulted in the assembly of Laurentia (Hoffman, 1988). The 1.9 -1.8 Ga Trans-Hudson Orogen (THO), one of the Paleoproterozoic orogens, involved the collision of three Archean continental blocks. The Hearne and Rae cratons to the north collided with the Superior craton to the south. The THO is a collage of island arcs, sedimentary basins, and oceanic plateaux forming the internal zone, and reworked Archean continental crust and associated cover sequences which form the external zones (Fig.2.1; Corrigan et al., 2002). The THO orogen stretches from the central U.S. through Saskatchewan, Manitoba, Hudson Bay, and Greenland, and reaches its maximum width in Baffin Island and northern Quebec. This section consists of the Cape Smith Belt (St-Onge et al., 2001e; St-Onge et al., 2002) in northern Quebec, which forms the southern margin of the orogen; the centre is occupied by the large Paleoproterozoic Cumberland Batholith (Jackson and Taylor, 1972; Jackson et al., 1990; Scott, 1997) and the northern margin is known as the Foxe Fold Belt. The latter was the area chosen by the Geological Survey of Canada and the Canada-Nunavut Geoscience Office to complete a joint mapping project to the scale of 1:100 000 across the northern margin of the THO in Baffin Island.

2.2 Geology of the central Baffin Area

The GSC/C-NGO mapping project area stretches between 68°N and 70°N latitude and 70°W to 76°W longitude (Fig.2.1), which corresponds to the area of maps NTS 37A, 37D and the western halves of 27B and 27C. The Rae craton is exposed in the north and in basement-cored domes in the south-east. This Archean crustal block forms the basement of the project area and is mainly made up of quartzofeldspathic gneisses intruded by foliated monzonitic plutons. Structurally above the basement, the Piling Group (PG), a thick sedimentary sequence of Paleoproterozoic age is divided into two sections: the Lower Piling Group (LPG) comprises a basal quartzite (Dewar Lakes Fm) overlain by a platformal carbonate sequence (Flint Lake Fm) on top of which

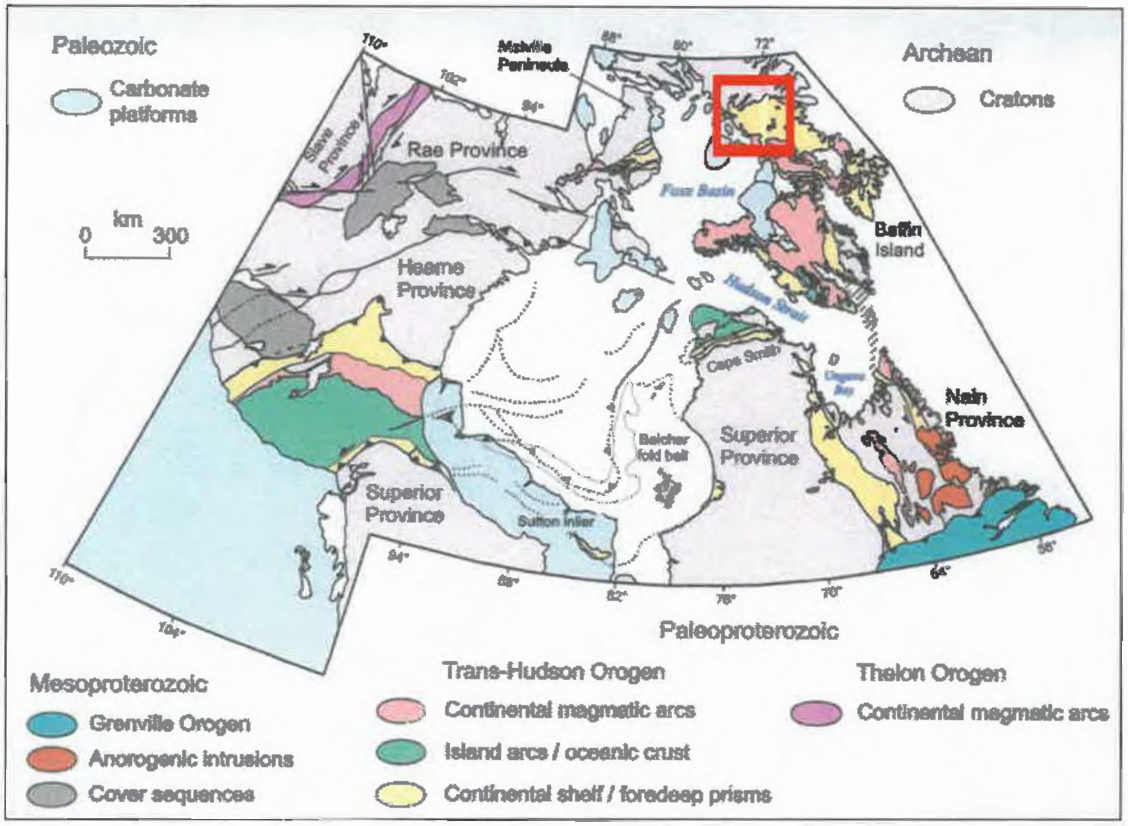

Figure 2.1 : Regional distribution and geology of Trans-Hudson Orogen in the Hudson Bay and Baffin Island area. The red box represents the area mapped through the GSC/C-NGO collaborative project (from St-Onge et al., 2001b). Samples for this study were collected in the south-east part of the mapped area.

conformably sits a unit of sulphidic schist and iron-formation (Astarte River Fm). In the south, a unit of mafic volcanics and sedimentary rocks (Bravo Lake Fm), tectonically sitting on turbidites of the Upper Piling Group, was shown to have been initially deposited at the same stratigraphic level as the Flint Lake Formation (Scott et al., 2002).

Stratigraphically above the LPG is the Upper Piling Group. A thick unit of metaturbidites constitutes the Longstaff Bluff Fm (LBF) that blankets the whole central part of the project area. Finally, the southern part exposes Rae craton basement intruded by different granitic suites. There are granodioritic plutons, white monzogranitic intrusions and pegmatitic veins and dykes of syenogranite containing Grt-Bt-Ms±Tur. This study focuses more specifically on the south-east corner of the area mapped during the 2000 field season of the GSC/C-NGO mapping project (Fig.2.2). Two geological maps at the scale 1:100 000 (St-Onge et al., 2001a, 2001c) cover the area where the samples have been taken. A more precise location of the samples is given in Chapter 3.

2.3 Description of the lithological units from the project area

This section provides a more exhaustive description of each lithological unit encountered in the project area (Fig.2.2) in order to give the regional geological context. However, the emphasis is on the PG and more specifically on the LBF. The units are described in stratigraphic order starting with the oldest.

2.3.1 Archean:

Archean rocks outcrop mainly in the northern portion of the field area, north of Flint Lake (Fig.2.2), and in basement-cored domes in the south-east of the project area where conjugate folding formed dome-and-basin structures. The Archean basement consists of orthogneiss with enclaves of the Mary River Group (Section 2.3.1.2) and both are intruded by plutonic rocks also of Archean age (Corrigan et al., 2001).

2.3.1.1 Archean orthogneiss:

The composition of the Archean orthogneiss (2.83-2.82 Ga; Wodicka et al., 2002) varies from biotite ± hornblende granodioritic to biotite ± hornblende monzogranitic layers with rare biotite ± hornblende tonalitic layers (Scott et al., 2002). The gneisses are generally well-banded and the thickness of individual layers varies from a few centimetres to metres.

2.3.1.2 Mary River Group:

The Mary River Group (Jackson, 1969; Jackson and Berman, 2000) is a package of siliciclastic and mafic volcanic rocks found within the orthogneiss in the northern exposures of the Rae Craton. These are correlative with the Prince Albert Group along strike on the Melville Peninsula. The siliciclastic rocks are the most abundant lithology of the Mary River Group. The most common facies of siliciclastic rocks is a brown-weathered psammite to semipelite with local beds of pelite (Scott et al., 2003). This

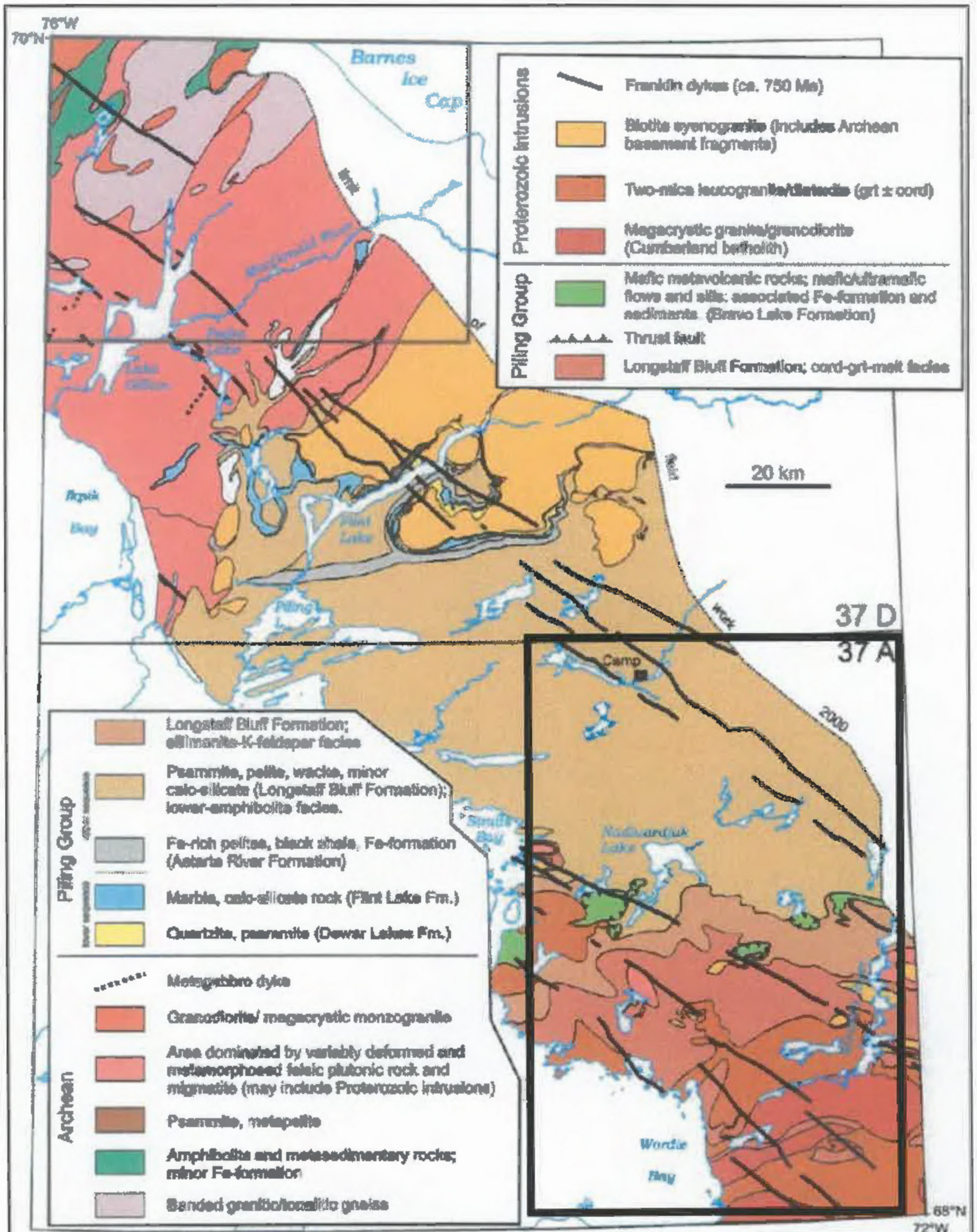

Figure 2.2 : Regional geological map of central Baffin Island (St-Onge et al., 2001b). There is a progressive increase in metamorphic grade from the campsite toward the south as highlighted by the distribution of the mineral zones in the LBF. The black box in the southern half of the map highlights the limits of the study area (transect locations in Figure 3.1).

characteristic weathering colour (caused by the presence of accessory pyrite in the sedimentary rocks) and the typical knotted texture in the more pelitic beds, formed by sillimanite aggregates, distinguishes these sedimentary rocks from the Paleoproterozoic ones.

Locally, mafic volcanic rocks are associated with the siliciclastic rocks. The volcanic rocks are generally massive to moderately foliated and characterised by hornblende ± biotite with rarely preserved clinopyroxene.

2.3.1.3 Granite intrusions:

The Archean basement also includes a variety of plutonic rocks that truncate the gneissic banding of the orthogneiss. The intrusive rocks are generally weakly to moderately foliated and vary in composition from rare syenogranite to biotite-monzogranite with local tonalite. Similar bodies in the nearby Eqe Bay area yielded Archean ages (Bethune and Scammell, 1997). Such intrusions sometimes form the basement of large areas of Paleoproterozoic sedimentary cover or basement-cored domes. For instance, the basement in the Flint Lake area (Fig. 2.2) is formed by moderately foliated Archean monzogranite (2.73-2.70 Ga; Wodicka et al., 2002). Paleoproterozoic granite also intruded the basement. The distinction between the two granites is very difficult in the field (Corrigan et al., 2001).

2.3.2 Proterozoic:

The Proterozoic rocks of the area can be divided into three main groups: 1) the PG with its sequence of metasedimentary and minor metavolcanic rocks; 2) a variety of intrusive bodies ranging from syn- to post-tectonic; 3) local diabase dykes from the Franklin swarm.

2.3.2.1 Piling Group (PG):

The PG is part of a belt of Paleoproterozoic sedimentary rocks that extends from the Melville Peninsula, where it is correlated with the Penrhyn Group (Henderson, 1983), through central Baffin Island, to the west coast of Greenland, where it is correlated with the Karrat Group (Taylor, 1982). The stratigraphic nomenclature of the PG was proposed by Morgan and his collaborators (Morgan, 1983; Tippett, 1984). The PG is divided into a Lower sequence and an Upper sequence. The Lower sequence represents a passive margin succession showing deepening of the water. At the base, there are quartzites typical of the Dewar Lakes Formation marking the oldest continental deposition on the Rae craton in this area. Above it is a sequence of carbonates called the Flint Lake Formation. Towards the south, the mafic volcanic rocks of the Bravo Lake Formation overlie the Dewar Lakes quartzites. The carbonates give way to the black sulphidic shales of the Astarte River Formation in the south. Locally the Astarte River Formation is found stratigraphically above the Bravo Lake Formation. A thin sequence of quartzites interpreted as Dewar Lakes Formation is commonly found below the volcanic rocks. The Bravo Lake Formation, structurally above the LBF, is separated from it by a thrust fault inferred to have formed early in the THO history. The Upper sequence comprises mainly the thick package of turbidites of the LBF which is interpreted as a foredeep basin environment. This unit is by far the most abundant of the PG and blankets the whole central zone of the project area.

2.3.2.1.1 <u>Dewar Lakes Formation:</u>

The basal contact of the Dewar Lakes Formation with the Archean basement was observed in numerous locations. It consistently truncates structures and lithological features of the gneissic basement, but is also conformable with overlying sedimentary rocks (Scott et al., 2003). This unit is mainly composed of quartzites and feldspathic quartzites with local layers of more psammitic or pelitic material (Scott et al., 2002a). A three-member subdivision was proposed by Scott et al. (2003) based on mapping. The lower member is composed of thin layers of pink-weathering quartzite rich in muscovite. The middle member consists of medium to thick quartzite beds with low mica content but abundant sillimanite. The upper member is composed of thinly bedded quartzitic to psammitic material with more pelitic layers. The overall thickness of the Dewar Lakes Formation varies highly throughout the field area from tens to hundreds of metres.

2.3.2.1.2 Flint Lake Formation:

The dolostone, marble, and calc-silicate units of the Flint Lake Formation are thought to represent the carbonate shelf of the passive margin of the Rae Craton (Scott et al., 2002). The abundance of carbonate material generally diminishes toward the south, so that the Flint Lake Formation is only found in the northern part of the area. The distribution of the Flint Lake Formation supports the idea of a south-facing continental margin. Individual layers have a thickness varying from few centimetres to a couple of decimetres. The overall thickness of the carbonate unit is estimated to be between 500-1000m. The Flint Lake Formation likely formed a narrow belt parallel to the edge of the Rae craton.

2.3.2.1.3 Astarte River Formation:

This formation is typically composed of black graphitic semipelites and pelites with minor sulphide-facies iron formation. The presence of sulphides gives a characteristic rusty colour to weathered outcrops. Pyrite is the dominant sulphide with local pyrrhotite. Sulphides are found in seams or disseminated. The Astarte River Formation conformably overlies the Flint Lake Formation and indicates deeper water conditions. Unlike the carbonates, the sulphidic shales stretch further south and also locally overlie the Bravo Lake Formation.

2.3.2.1.4 Bravo Lake Formation:

The Bravo Lake Formation comprises mafic and ultramafic flows and sills and associated metasedimentary rocks (Stacey and Pattison, 2003). These rocks occur along a narrow corridor at the latitude of Nadluarjuk Lake, extending from Straits Bay to the eastern limit of the mapping area (Fig. 2.2). The volcanic rocks exhibit a variety of textures including abundant pillows. Preliminary data on the Bravo Lake Formation geochemistry suggest that these rocks likely represent volcanism in a rift environment (Modeland, 2003).

2.3.2.1.5 Longstaff Bluff Formation (LBF):

The LBF is composed of a relatively homogenous succession of psammite and semipelite beds with minor pelitic components. Locally, the relative abundance of pelites varies. The thickness of the layers ranges from a few centimetres up to ca.2 m. Within the lowest metamorphic grade rocks in the centre of the belt, primary grain size is preserved and sedimentological structures such as cross-bedding and laminations can be observed locally. Graded bedding is common. Data from throughout the field area indicate that the turbidites are generally in an upright position and are tightly to isoclinally folded. The turbidites cover the whole central area and the contact with underlying units is sharp rather than a progressive transition. Neodymium isotopic analysis indicates that these rocks have a distinctly younger provenance than the ones from the Dewar Lakes Formation (Johns, 2002). The Longstaff Bluff Formation is interpreted to have originated as molasse deposited in a foredeep basin fed by erosion from orogenic uplift (Scott et al., 2003). The total stratigraphic thickness of the Longstaff Bluff Formation has been estimated at 3-5 km based on a structural cross-section (Berniolles, pers. comm.).

The mineralogy of the Longstaff Bluff Formation varies depending on the metamorphic grade. The Longstaff Bluff Formation turbidites sit in the centre of the sedimentary belt. The metamorphic grade is at the lowest in the central area and increases outward towards the north and south. A detailed description of the metamorphic grade and its distribution is given in section 2.4 and Chapter 3.

2.3.2.2 Granitic intrusions:

The project area includes a variety of granitic rocks. At least four compositionally different plutonic rocks have been observed in the project area. Paleoproterozoic intrusions cover large areas in the Lake Gillian region as well as in the Flint Lake region (Fig. 2.2). The area south of Flint Lake exposes an Archean culmination cut by Paleoproterozoic intrusions. Further south lies a large area predominantly covered by turbidites from the Longstaff Bluff Formation. At the latitude of Nadluarjuk Lake, granitic intrusions reappear and further south they become the predominant lithological unit. However, there are four varieties of plutonic rocks in the south. Based on field relations, the rocks are described from oldest to youngest:

2.3.2.2.1 Biotite±muscovite±allanite syeno- to monzogranite

Paleoproterozoic plutons intruded the northern margin of the Foxe Fold Belt. Their composition varies from syeno- to monzogranite. Biotite is widespread with common muscovite and local allanite. The intrusions are syn- to post- tectonic and the intensity of deformation ranges from massive to strongly foliated granites. Locally, enclaves of orthogneiss (basement) and metasedimentary rocks (Piling Group) are found.

2.3.2.2.2 K-feldspar megacrystic monzogranite

To the south, abundant granodioritic and monzogranitic rocks with K-feldspar megacrysts contain biotite ± hornblende ± garnet and metasedimentary enclaves correlated with the Piling Group. Field observations, compositional similarity and location close to known exposures of the Cumberland Batholith suggested that these rocks represent its northernmost exposure. However, new U-Pb data revealed an age of 1897+7/-4 Ma (Chapter 6; Wodicka et al., 2003) that these rocks are significantly older than the Cumberland Batholith magmatic event dated at 1870-1850 Ma (Wodicka and Scott, 1997; Scott, 1999). (The Cumberland Batholith is a pre- to syn-orogenic plutonic complex ranging from medium- to coarse-grained granodioritic to monzogranitic hornblende ± biotite ± garnet-bearing rocks. It commonly contains enclaves of migmatitic metasedimentary rocks. These rocks have not been positively identified in the project area, although some of the southernmost plutons may belong to the Cumberland suite.)

2.3.2.2.3 Garnet-biotite±cordierite±muscovite white monzogranite

Bodies of large massive white monzogranite are found cutting through the older granites (2.3.2.2.1 and 2.3.2.2.2 described above). These generally contain Grt-Bt± Crd±Ms. The granite varies from medium-grained to pegmatitic and forms plutons and dykes. Field relations such as the southward increase in metamorphic grade, the abundant migmatites, and outcrop observations of thin leucosome veinlets converging to form larger veins and dykes of granitic composition suggest that the granite results from the partial melting of the PG metasedimentary rocks.

2.3.2.2.4 Biotite-muscovite±garnet±tourmaline syenogranite pegmatite

The youngest intrusive rocks are Bt-Ms±Grt±Tur-bearing pegmatitic syenogranite veins locally forming small intrusive bodies, such as sills and locally dykes cutting through the sedimentary rocks.

2.3.2.3 Franklin dykes:

Large gabbroic dykes are found throughout the field area. These dykes are fresh and unaffected by Paleoproterozoic deformation or metamorphism. They consistently trend north-west and are part of the Franklin swarm (723 +2/-4 Ma; Heaman et al., 1992). The width of the dykes varies from a few metres to hundreds of metres and they may reach tens of kilometres in length.

2.3.3 Palaeozoic:

Flat-lying carbonates and minor siliciclastic rocks are found to the west of the field area in the islands of Foxe Basin. These rocks are Ordovician in age.

2.4 Metamorphism

The earliest metamorphic event that affected the project area occurred during the Archean. A zircon fraction from a biotite monzogranite taken from a layered tonalite-monzogranite-diorite gneiss in the Dewar Lakes area (Fig. 2.2) gave an age of 2673 Ma distinctly younger than the crystallisation age of 2827+8/-7Ma (Wodicka et al., 2002). The 2673 Ma age is interpreted as a metamorphic age (Wodicka et al., 2002). Based on mineral assemblages found in basement mafic rocks (Hb-Pl±Grt) and in the rocks of the Mary River Group (Bt-Sil-Grt±melt), the P-T conditions are estimated to have reached middle- to upper-amphibolite facies conditions during Archean metamorphism (Corrigan et al., 2001).

The whole Piling Group was affected by metamorphism ranging from greenschist to granulite facies. Greenschist facies rocks occupy the central part of the area and grade increases both northward and southward. To the north, the sedimentary rocks reach upper amphibolite facies (Bt+Kfs+Pl+Sil) and in the south they reach granulite facies (Crd+Grt+Kfs+melt) conditions with abundant leucosome (Corrigan et al., 2001). This study focuses on the LBF metaturbidites that display a progressive southward increase in metamorphic grade.

The metapelites and semipelites of the LBF show a systematic variation in mineralogy with increasing metamorphism. Chlorite zone is present in the central part of the area, with Bt±Ms at slightly higher grade. With increasing metamorphic grade Crd±And enter the mineral assemblage followed by Sil+Kfs at higher grade. The mineral assemblage changes to Sil+Kfs+melt and ultimately leads to Crd+Grt+Kfs+melt indicating granulite facies conditions (Scott et al., 2002). Metamorphic isograds are deformed by late D_{3P} cross-folds which suggests that metamorphic peak conditions occurred at an early stage of the deformation history (Dubach and Carmichael, 2003). Evidence for multiple metamorphic episodes was reported by Allan and Pattison (2003). P-T conditions in the Longstaff Bluff Formation metasediments varied from <550°C at 3 kbar for the biotite zone (central area) to a maximum of 800-900°C at 7 kbar in the Grt+Crd+Kfs+melt zone south of Transect 5 (K. Dubach, pers. comm.). Table 2.1 illustrates the P-T conditions estimated for each of the five sampled transects. Data were kindly provided by K. Dubach (Ph.D. in progress, Queen's University).

Table 2.1: P-T conditions along sampled transects.

Transect	Metamorphic zone	Temperature (°C)	Pressure (kbar)
1	Bt+Ms	<550°	3 or less
2	Bt+Crd±And	550-600°	3-4
3	Bt+Sil+Kfs	>660°	>4
4	Bt+Sil = Grt+Crd+Kfs	660-700°	5.6-6.2
5	Grt+Crd+Kfs+melt	700-780°	4.8-6.4

2.5 Structural geology

The area was affected by multiple deformation events. Archean deformation was largely obscured by the Trans-Hudson orogeny, but is preserved by the gneissosity and the strong foliation present in the Archean basement rocks.

The Paleoproterozoic rocks recorded at least four major deformation events (St-Onge et al., 2001c). Tight intrafolial isoclinal folds (Scott et al., 2002) define the earliest Paleoproterozoic event D_{1P} (Corrigan et al., 2001). The folds are north-verging and best preserved in the Dewar Lakes Formation siliciclastic rocks. Thin-skinned deformation characterises D_{1P}. The tectonic imbrication of Piling Group units north of Flint Lake and the thrusting of Bravo Lake Formation rocks onto LBF turbidites in the southern part of the area are interpreted to have taken place during D_{1P} (Corrigan et al., 2001; Scott et al., 2003). In the low- to medium-grade LBF samples, micas generally have a preferred orientation, although later generations may be randomly oriented. The dominant fabric is a strongly developed schistosity in the more pelitic beds. The main schistosity (S1) in the rocks of the study area generally strikes E-W. This fabric is interpreted to have developed during the early thin-skinned deformation event D_{1P} (Corrigan et al., 2001).

The second deformation event D_{2P} is essentially coaxial with the previous event and resulted in the steepening of the earlier folds (Berniolles, 2002). This event was characterised by east-northeast trending folds that affected both the supracrustal rocks of the PG and the Archean basement (Corrigan et al., 2001; Scott et al., 2002). Thick-skinned deformation associated with this event locally resulted in thrusting of Archean basement rocks on top of PG supracrustal rocks. D_{2P} folds are typically upright, tight to isoclinal, shallow plunging and north vergent (Scott et al., 2002).

A penetrative cleavage consistently clockwise with D_{2P} and D_{1P} fabrics is commonly observed in the LBF metasedimentary rocks. Field observations suggest that this is the result of an upright folding event with an axial plane slightly clockwise to D_{2P} folds (Berniolles, 2002). It is not clear yet if this clockwise cleavage represents a late pulse of D_{2P} or if it marks a distinct episode of deformation. This clockwise cleavage is common in the study area and is referred here as S2.

The third main deformation event (D_{3P}) is an orogen perpendicular folding event marked by gentle folds orthogonal to D_{1P} and D_{2P} (Corrigan, 2003). In the south, it produced a dome-and-basin pattern evident from the Bravo Lake Fm klippe. Locally, crenulations corresponding to D_{3P} can be observed on D_{2P} planar surfaces.

2.6 Summary

In summary, the central Baffin area consists of an Archean basement, the Rae craton, overlain by a thick sequence of Paleoproterozoic metasedimentary rocks, namely the Piling Group (PG), which includes, from bottom to top, a basal quartzite, a carbonate shelf sequence in the north replaced by volcano-sedimentary rocks in the south, a unit of sulphidic shale, and a thick package of turbidites. The LBF turbidites constitute by far the most extensive unit of the PG and they blanket a large surface in the centre of the map area. Both the PG metasedimentary rocks and the Archean basement are intruded by a variety of Paleoproterozoic granitic rocks.

The LBF metasedimentary rocks display a range in metamorphic grade from upper greenschist facies in the centre of the map area to upper amphibolite facies in the north and granulite facies in the south. At least three main deformation episodes were recorded in the LBF metasedimentary rocks.

The EMP chemical dating of LBF monazite aimed to provide information on the timing of monazite growth and to use the petrological information of the grains to better constrain the metamorphic and tectonic history of the area. The next chapter presents texture and distribution of monazite in the LBF metasedimentary rocks.

3. Distribution, textures and mineral assemblages of monazite in the Longstaff Bluff Formation metapelites

3.1 Introduction

This chapter provides a description of the various monazite settings and textures within the different metamorphic grades of the LBF in the study area. Variations in the accompanying mineral assemblages are also examined. Textures and setting of monazite grains provide important information on the growth history, which is essential in order to interpret properly ages obtained from monazite grains. Information on monazite was retrieved from back-scattered electron (BSE) images and element X-ray maps obtained with an electron microprobe, and thin section description.

In the first sections, essential background on monazite occurrence and behaviour through progressive metamorphic grade is given. Then description of monazite textures and distribution in each transect are presented along with detailed petrological and mineralogical descriptions.

3.2 Background

Monazite, (Ce, La, Th) PO_4, is a monoclinic phosphate of light rare earth elements (LREE) bearing Th (up to 3-15%) and U (1-3%) in significant amounts. It includes little or no Pb at the time of crystallisation (Parrish, 1990). Monazite has been found to form by igneous crystallisation and metamorphic reactions, but also occurs as a hydrothermal mineral (Vielreicher et al., 2003).

3.2.1 Natural occurrence

Monazite forms in a variety of geological settings from igneous to sedimentary and metamorphic environments. Monazite is most common in pelitic metasedimentary rocks and peraluminous granites (Spear and Pyle, 2002). Metamorphic monazite is commonly reported from metapelites of lower amphibolite facies and higher grade (Overstreet, 1967; Parrish, 1990; Smith and Barreiro, 1990). It has recently been identified in greenschist facies rocks (Wing et al., 2003) and even in prehnite-pumpellyite facies rocks (Rasmussen et al., 2001). Monazite is a mechanically resistant mineral and is commonly found as a detrital mineral in sediments. Some studies have shown that monazite can also form as a diagenetic mineral (Milodowski and Zalasiewicz, 1991; Evans et al., 2002).

3.2.2 Characteristics and optical properties

Monazite appears as a high relief mineral in plane-polarised light due to its high index of refraction, 1.777-1.849 (Nesse, 2000). Under crossed polars monazite exhibits very high birefringence, on the order of 0.45-0.52. It is a positive biaxial mineral with a $2V_z$ angle varying from 5-20°. It is colourless to faint yellow and is not pleochroic. Occurrences of monazite with a greenish tint are also reported. Magmatic and high-grade metamorphic monazite commonly display a euhedral habit. Medium- and low-grade monazite generally has a granular or anhedral habit. Monazite included in mica or cordierite, and locally K-feldspars, generally presents a dark-coloured halo caused by radiation damage in the structure of the host mineral.

Zircon, allanite, epidote, and xenotime can look similar to monazite in thin section. Distinguishing features of monazite are its colour and its habit. Monazite is generally colourless to yellowish, whereas zircon is darker, and titanite and allanite are generally brown. Epidote is commonly more greenish, but may be yellowish. Monazite generally exhibits a granular habit, but is commonly euhedral in high-grade metamorphic and magmatic rocks and may then be confused with zircon that also generally shows a prismatic habit. Euhedral titanite is less of a problem because of its distinct crystal shape. Finally, monazite typically displays a radioactive halo, due to its high Th and U content, when hosted in cordierite and micas. Zircon, xenotime, and allanite also display a halo when hosted in micas, but rarely when included in cordierite or K-feldspar. Damage to the host mineral can be so extensive that a "moat" of alteration product can form around the monazite crystal. This is commonly observed in cordierite (this study).

3.2.3 Related phosphate phases: apatite and xenotime

It is important to consider other phosphates present in the rock as they play a major role in the PO_4 budget and, in some cases, in the sequestration of REEs and Y. There are many phosphate minerals but only two, apatite and xenotime, are commonly found in metamorphic rocks along with monazite.

3.2.3.1 Apatite

Apatite, $Ca_5(PO_4)_3(F,Cl,OH)$, is a very common accessory mineral in many igneous rocks, in some sedimentary rocks and in most metamorphic rocks. Metamorphic rocks varying from pelitic, to carbonate, mafic and even ultramafic composition have been described as apatite-bearing. Studies have also reported apatite in samples covering the whole range of P-T conditions. Spear et al. (2002) suggested that apatite genesis is not controlled by its stability relative to other phosphates, but rather the availability of essential ingredients (P, Ca, and F).

Apatite is the most common phosphate mineral, with fluor-apatite being the dominant compositional variant. Apatite incorporates only minor amount of REEs, Th, U, and Y but because its modal abundance is high relative to monazite, apatite may play a significant role in the budget of these elements. Consequently, apatite can be involved in reactions with monazite, either as a reactant or as a product (e.g., Bingen et al., 1996; Broska and Siman, 1998).

3.2.3.2 Xenotime

Xenotime, $(Y,HREE)PO_4$, is an anhydrous phosphate with an APO_4 structure. Unlike monazite, xenotime contains only very little LREEs , Th, and U. In most xenotime, Y cations fill as much as 75 % of the A-site. HREEs (mainly Yb, Er, Dy, Gd, and Lu; listed in decreasing order of abundance) generally occupy the remaining sites. Because xenotime contain only traces of LREEs, its presence in the mineral assemblage will not likely affect the stability range of monazite. Xenotime is a major sink for Y and HREEs, and its presence or absence in the mineral assemblage exerts an influence on the chemical composition of monazite (Pyle et al., 2001). Partitioning of Y and HREEs between xenotime and monazite has been demonstrated to be temperature-sensitive (Pyle et al., 2001) and can be used as a thermometer.

3.2.4 Non-phosphate minerals containing elements common with monazite: allanite, epidote, and garnet

There are a few other minerals which need to be examined for their potential relationship with monazite as they share common elements. These minerals contain variable amounts of REEs or Y, Th, U, and so influence the budget for these elements and their availability at the time of monazite crystallisation.

3.2.4.1 Allanite

Allanite, (Ca, Mn, Ce, La, Y, Th)$_2$(Fe^{2+}, Fe^{3+}, Ti)(Al, Fe^{3+})$_2$O.OH[Si_2O_7OH), is a member of the epidote group and is also called orthite. Allanite is a common accessory phase in granite, pegmatite, gneiss and metapelite of appropriate composition. Like monazite, allanite hosts large amounts of LREEs, Y and Th in its structure. It is generally more common in Ca-rich rocks, which can also form monazite if the P-T conditions and rock composition are adequate. Previous studies reported partially resorbed monazite enveloped by an apatite-allanite-epidote corona as well as monazite formed after allanite (Bingen et al., 1996; Finger et al., 1998; Wing et al., 2003).

3.2.4.2 Epidote

Epidote, $Ca_2(Al_2Fe^{3+})Si_3O_{12}(OH)$, is a common primary, secondary and metamorphic mineral. Replacement of monazite by epidote through alteration processes has been observed and monazite surrounded by an apatite-allanite-epidote corona was identified (Finger et al., 1998).

3.2.4.3 Garnet

Garnet, (Ca, Mg, Fe^{2+}, Mn)(Al, $Fe^{3+}Cr^{3+}$)Si_3O_{12}, is commonly found in peraluminous granite and in most medium- to high-grade metamorphic rocks. The presence of garnet in the rock does not have any effect on the stability of monazite, but it has an influence on the Y and HREE content of both monazite and xenotime (Pyle et al., 2001). Garnet also preserves older monazites by shielding the included grains from reactions taking place in the matrix (Montel et al., 2000).

3.2.5 Metamorphism and monazite-forming reactions

Understanding the paragenesis of metamorphic monazite and monazite-forming reactions is essential to make an accurate interpretation of its geochemical signature, its growth history and the significance of ages obtained from monazite dating.

As a first question, one may naturally wonder where the components necessary to form metamorphic monazite originate. The REEs were possibly released from the weathering of major mineral phases such as feldspars, which contain minor amounts of these elements. The REEs are trapped within clay minerals, transported and deposited (McLennan, 1989) with the sediments that will later be metamorphosed. Accordingly, McLennan (1989) documented significant amounts of REEs in shales. Rasmussen (Rasmussen, 1996; Rasmussen et al., 1998) also suggested that authigenic precipitation of REE-phosphate minerals may be an important process in the sequestration of REEs and PO_4 in marine shales. Hence, all the necessary ingredients to form monazite during diagenesis or metamorphism are likely already present in shales. This could explain why monazite is most common in metapelitic rocks.

The second question is: when does monazite grow, or what reactions control growth and breakdown of monazite? The nature of monazite-forming reactions during metamorphism and the range of monazite stability are not completely understood. Many previous studies have reported the first appearance of metamorphic monazite in amphibolite facies rocks (Overstreet, 1967; Smith and Barreiro, 1990; Kingsbury et al., 1993; Bingen et al., 1996). Other studies also revealed that in rocks of appropriate composition monazite may form at greenschist facies (Franz et al., 1996; Rasmussen et al., 2001; Wing et al., 2003). The main precursors identified for monazite are allanite and apatite (Bingen et al., 1996; Wing et al., 2003).

3.3 Isograds and metamorphic zones in the study area

The samples were collected along five transects representing the main metamorphic zones of the study area (Fig. 3.1). The location of the transects was chosen in order to represent the progressive southward increase in metamorphic grade. The transects cross the three main metamorphic isograds of the study area. Isograds were determined based on the first appearance of key metamorphic minerals in the field (St-Onge et al., 2001d; Dubach and Carmichael, 2003). All samples were collected from pelitic and semipelitic horizons in the LBF to reduce variability related to protolith composition.

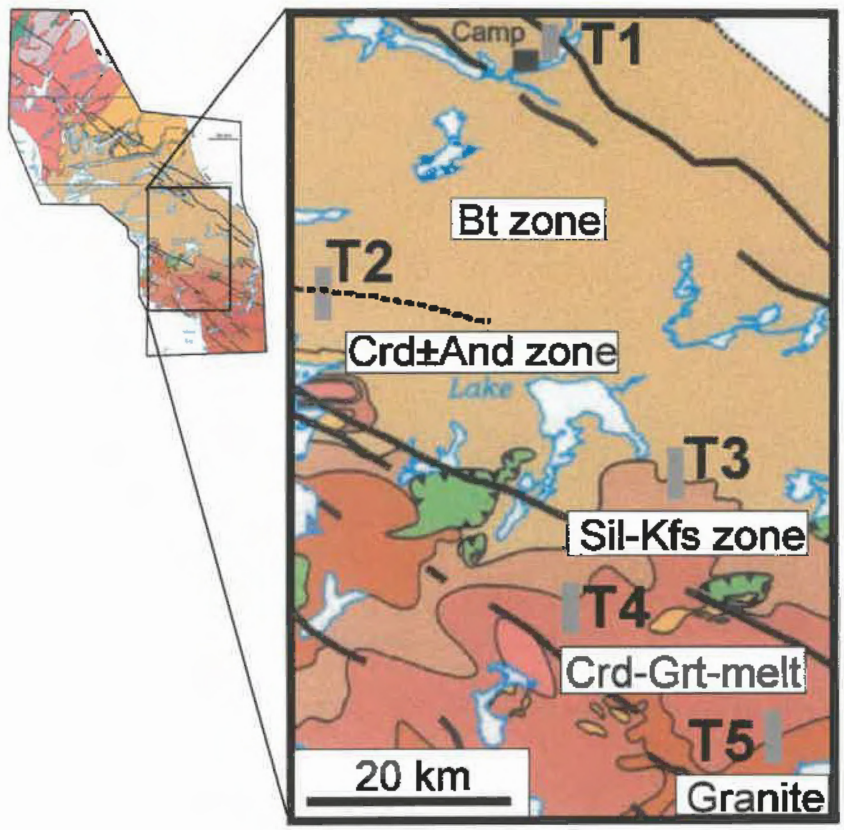

Figure 3.1: Area mapped during the summer 2000 by the GSC/C-NGO Geoscientific Joint Project (inset map on the left; after St-Onge et al., 2001c). The study focussed on samples collected along five short transects: T1, T2, T3, T4, and T5. Each of the transects represents a different mineral assemblage or crosses a metamorphic isograd. The main mineral assemblages are displayed in white boxes. See Figure 2.2 for legend.

Transect 1 sits in the middle of the biotite zone, the lowest grade sampled. Transects 2, 3 and 4 cross mineral isograds with increasing metamorphic grade (Fig. 3.1).

Transect 5 is at the boundary between migmatitic metasediments, varying from metatexites to diatexites, and leucogranite intrusions inferred to be locally derived from the partial melting of the metasediments (Corrigan et al., 2001). Transects are generally 2-3 km in length and 7-10 samples were collected within each. Samples were generally chosen from the most pelitic beds, where chances to identify monazite are best.

The next sections describe each isograd in more detail. Observations made on textural variation and distribution of monazite, related REE and phosphate minerals, and mineral assemblages are also systematically reported. Appendix 4 provides a detailed description of all thin sections used for this study.

3.3.1 Biotite zone (Transects 1-2):

The biotite zone is the lowest metamorphic grade sampled in this study. The mineral assemblage consists of Bt-Ms-Qtz-Pl, where biotite is the most abundant mica. Quartz is the dominant mineral in the matrix. The rocks in Transect 1 (T1) are LBF turbidites with psammite beds varying from 30cm to 1m thick and pelitic layers from 5-15 cm. Locally, sedimentary structures such as cross-beds are preserved.

In thin section, biotite zone samples are fine-grained with a well-developed schistosity and cleavage in the most pelitic beds. Psammitic layers display an equigranular quartz matrix with local plagioclase. Some quartz grains are still fairly rounded and preserve a detrital shape, but most show triple junctions with undulatory extinction, and interlock with other grains. Local segregation of coarser quartz-rich material is common. Micas are small and generally show a preferred orientation along one of the identified fabrics.

In this metamorphic zone, monazite is found in the most pelitic layers; psammitic and semipelitic samples contain little or no monazite. Monazite in biotite grade metapelites is fairly small, generally 10–30 μm in diameter. Monazite is generally associated with micas (biotite and muscovite), as inclusions or along grain boundaries (Fig. 2.3). Locally, monazite is also present in the matrix with quartz and feldspar. The grains are generally anhedral or granular. Monazite growing along grain boundaries is commonly elongated, indicating syn- or post-metamorphic growth relative to the micas. Few inclusions are present in these monazite grains. In thin section, monazite is difficult to find. Dark halos in biotite commonly correspond to monazite grains, although similar features also form around zircon inclusions.

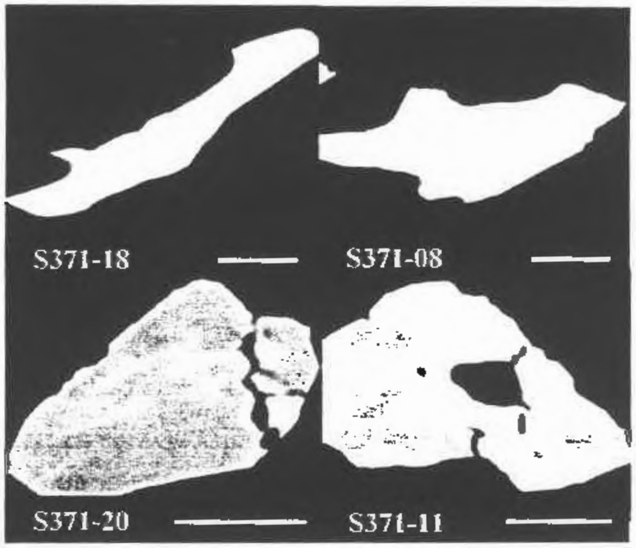

Figure 3.2: Back-scattered electron images of monazite grains from S371, a sample collected from the biotite zone. The grains show typical habit of biotite zone monazites. White bars in the lower right of each image are 10 μm long. Biotite zone monazite grains are generally anhedral, commonly elongated or parallel to mineral fabric. Some grains are possibly coalescent such as S371-11.

Other phosphate minerals coexist with monazite in the biotite zone of the LBF. Apatite is abundant and commonly shows a euhedral prismatic habit. Apatite is generally found in the matrix, but also locally occurs along mica grain boundaries and rarely as inclusions within biotite or muscovite. No sign of resorption was observed. The modal abundance of apatite is at least an order of magnitude greater than monazite. Xenotime was also found in the pelites, but is much less abundant than monazite, about an order of magnitude less common. This agrees with observation from others (Pyle and Spear 2003a). Xenotime is fairly small, generally less than 15-20 μm in diameter (Fig. 3.4). It is often found in clusters of anhedral grains that may show resorption on the edges. Monazite is closely associated with both euhedral prismatic apatite grains and partially resorbed xenotime grains, but was not found in direct contact with either.

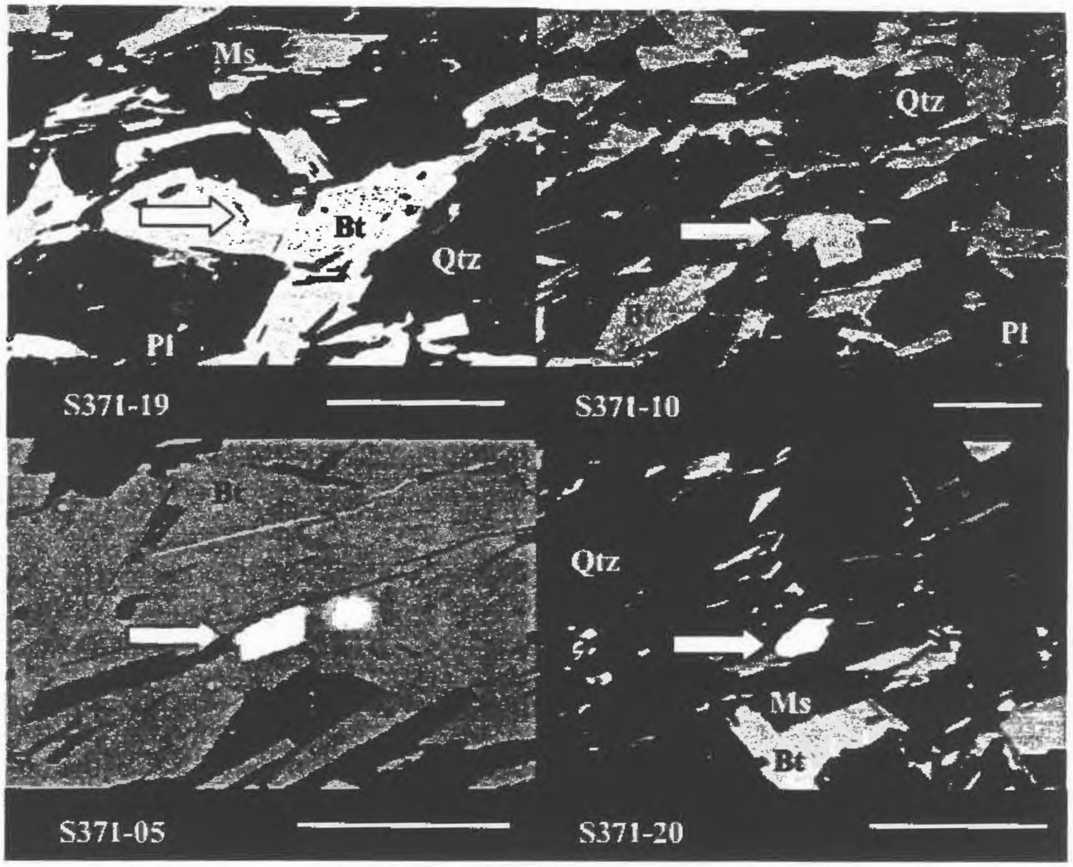

Figure 3.3 : BSE images of monazite (bright mineral shown by arrow) from the biotite zone. The images show typical petrological setting and relationship to the rock mineral fabric. In the biotite zone, monazite is typically associated with micas, particularly biotite, and is commonly elongated parallel to one of the fabrics. Scale bars = 100 μm.

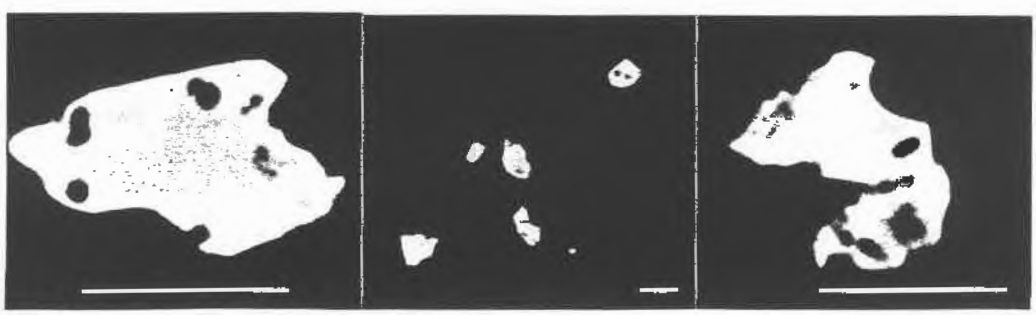

Figure 3.4: BSE images of xenotime in the biotite zone. The xenotime grains are fairly small and commonly show embayments. Scale bars = 10 μm.

3.3.2 Cordierite-Andalusite zone (transects 2-3)

This metamorphic zone is defined by an assemblage of Bt-Ms-Crd-Pl±And in metapelites. Samples generally have alternating psammitic and pelitic layers. Schistosity is well developed and cleavage moderately to weakly developed. Pelitic beds show a typical spotted texture caused by cordierite porphyroblasts. Cordierite rims are moderately to completely altered to muscovite, but most cordierite preserves a fresh core. The cordierite crystals contain inclusion trails oblique to the main matrix fabric and the S1-parallel micas are wrapped around the cordierite porphyroblasts. Andalusite was observed in the field, but samples analysed for this study did not contain any. The micas are significantly larger and the quartz matrix is coarser than in the biotite zone (Appendix 4). Abundant anhedral to euhedral biotite with numerous inclusions and weak pleochroism is present in these rocks. Muscovite is generally parallel to the main fabric. A few large muscovite crystals oblique to the main schistosity were identified and are likely late relative to the fabric development.

Monazite is common in the Crd-And zone. The grain size is still fairly small (< 40μm), but slightly larger than in the biotite zone (Fig. 3.5). The grains are anhedral with few inclusions and show no signs of resorption on the grain boundaries. Monazite is preferentially located along the grain boundaries of micas and included in biotite. Cordierite porphyroblasts also locally contain monazite inclusions (Fig. 3.6). Grains located in the matrix are locally euhedral.

Figure 3.5: BSE images showing typical habit of Crd-And zone monazite. Scale bars = 10 μm.

In this metamorphic zone, apatite is fairly abundant (at least one order of magnitude more than monazite) and shows prismatic and euhedral habit. Apatite is ubiquitous within the quartz-feldspar matrix and the micaceous layers, but is rare within the biotite and cordierite porphyroblasts.

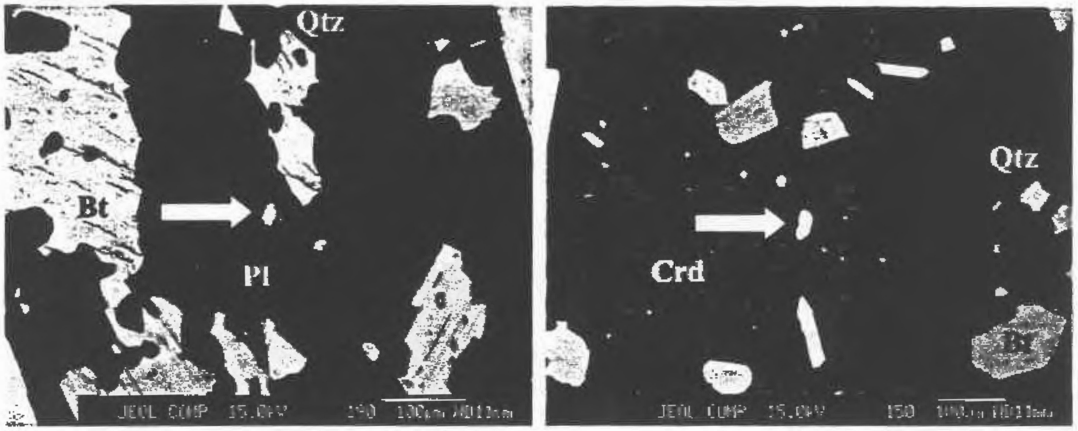

Figure 3.6: BSE images showing monazite grains (bright mineral shown by arrow) in typical setting for the Crd-And zone. Scale bars = 100 μm.

Xenotime is also found in this metamorphic zone. The grains are smaller and seem more resorbed. The modal abundance of xenotime has decreased significantly compared to the biotite zone.

3.3.3 Sillimanite-K-feldspar zone (transects 3-4)

This metamorphic zone is marked by the appearance of sillimanite which is formed by two reactions (Dubach and Carmichael, 2003). With increasing temperature andalusite is transformed into sillimanite by the reaction And = Sil. Sillimanite can also form by the breakdown of muscovite through the dehydration reaction Ms + Ab + Qtz = Sil + Kfs + H_2O. Rocks from the Sil-Kfs zone rarely contain any cordierite indicating that cordierite is consumed near the second sillimanite isograd. One of the possible cordierite-consuming reactions is Ms + Crd = Sil + Bt+ Qtz + liq. Samples near the first sillimanite isograd display abundant fibrolite clusters.

Figure 3.7: BSE images showing typical habit for monazite grains from the Sil-Kfs zone. Grains S375-02 and S378-07 are located in the matrix. Monazite S378-08 is located in a fibrolite cluster. Scale bars = 10 μm.

In this zone, monazite shows a variety of textures (Fig. 3.7). Locally, monazite is present close to, or in contact with, clusters of sillimanite (fibrolite) and these grains typically show resorbed grain boundaries (Fig. 3.8 and 3.7). Grains located in the matrix and included in micas do not show any sign of resorption. The fibrolite-bearing samples represent the first sillimanite isograd. At the second sillimanite isograd (muscovite-out), most monazite grains seem stable with no sign of resorption. In the Sil-Kfs zone, monazite grains are larger (20-80 μm). Few inclusions are present and zoning is distinct in some samples. Xenotime is very scarce and highly resorbed. Apatite modal abundance decreased slightly and the size of the grains increased relative to lower grade. Apatite habit and textures are similar as at lower grade.

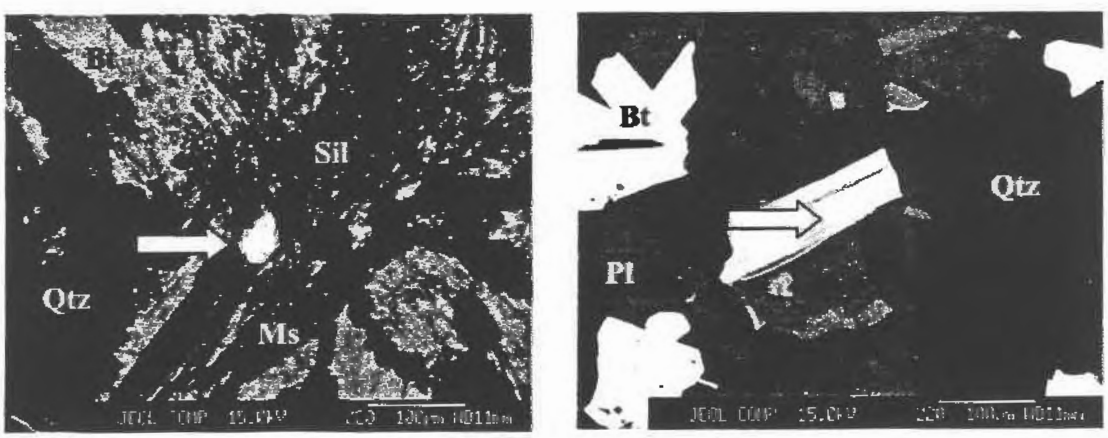

Figure 3.8: BSE images showing typical petrological setting for monazite (shown by arrow) from the sillimanite-K-feldspar zone. Grain on the left is located in a fibrolite cluster. Grain on the right is included in a biotite crystal. Scale bars = 100 μm.

3.3.4 Migmatite zone (transects 4-5)

The mineral assemblage in this metamorphic zone is characterised by Bt-Crd-Kfs-Pl-Qtz-Sil±Grt. Near the isograd, the rocks are incipient migmatites with minor leucosome. Further south, the abundance of granitic leucosome significantly increases and large leucogranite bodies are found in the southernmost transect. There is a wide variety of textures in the migmatitic rocks ranging from metasedimentary rocks with local veinlets of leucosome, to metasedimentary rocks with abundant veins and pockets of leucosome, to predominantly granitic rocks with enclaves of metasedimentary rocks. Cordierite, K-feldspar, garnet and melt are produced by the biotite dehydration reactions Bt + Sil = Crd + Kfs + Grt + melt or Bt + Sil = Crd + Kfs + melt.

Monazite is abundant in the melanosome of migmatitic samples where it is commonly included in Bt, Crd and Grt, but is much less abundant in leucosome veins. Locally, small leucosome veins contain very little monazite, whereas larger granitic bodies contain abundant monazite, both inherited and magmatic (Section 3.4).

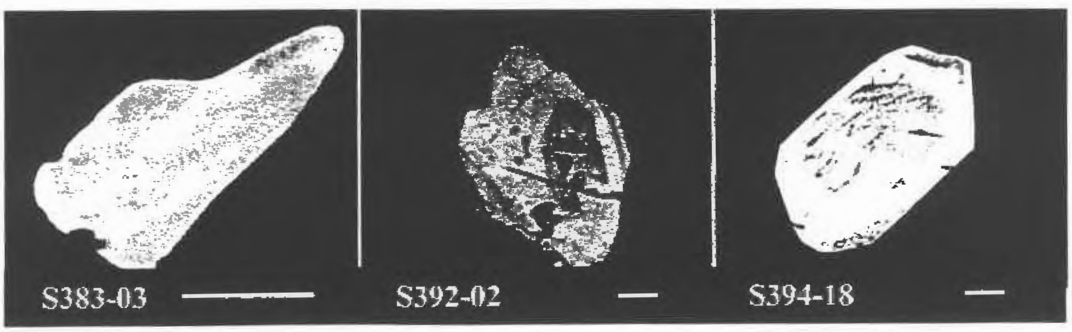

Figure 3.9: BSE images showing typical monazite habit from the migmatite zone. Monazite is much larger than at lower metamorphic grade and zoning is readily visible on the BSE image. Grain S383-03 is included in a garnet porphyroblast. Monazite S392-02 is included in biotite and S394-18 is located in the leucosome. Scale bars = 10 µm.

Monazite is generally quite large, 50-200 µm, and is commonly subhedral to euhedral (Fig. 3.9). Most monazite grains display zoning visible in BSE images. Zoning can be concentric, with variable amount of rims, or patchy. A variety of textures is observed at high grade, which likely results from a complex metamorphic history that combines migmatisation and inheritance from earlier monazite-forming events. For instance, sample S397, a syenogranite derived from partial melting of the metasedimentary rocks, contains monazite with patchy zoning and a euhedral shape more typical of magmatic origin (Chapter 6; S397-01) However, subhedral, rounded monazite grains inherited from an earlier event revealed by in-situ chemical dating (Chapter 6; S397-02) are also present.

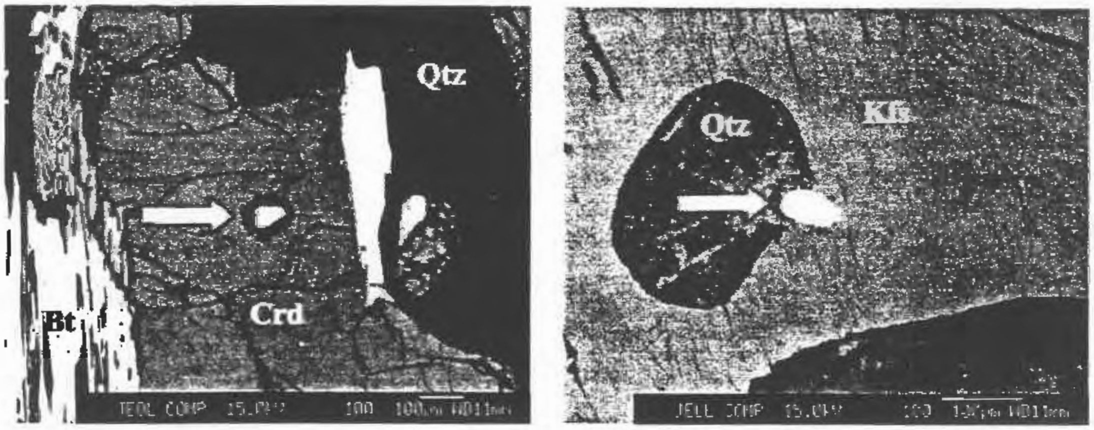

Figure 3.10: BSE images showing typical petrological setting for monazite from the migmatite zone. Grain on the left is included in a cordierite. Grain on the right is located at the boundary between a quartz and K-feldspar crystals. White bars are 100 μm.

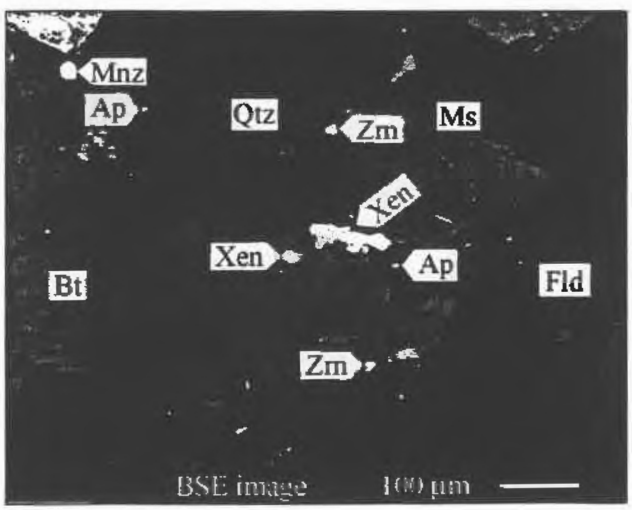

Figure 3.11: Back-scattered electron image of sample S371 with Bt-Ms-Qtz-Pl as the main metamorphic mineral assemblage and Ap-Mnz-Op-Xen-Zrn as the accessory minerals (Fld = feldspar of unidentified composition; Op = Opaque minerals; Xen = xenotime). Xenotime grains are xenoblastic with a very irregular grain boundary. Monazite grains are anhedral and more granular. Apatite is subhedral to euhedral and zircon is granular varying from anhedral to subhedral.

Apatite is abundant in the migmatite zone and commonly displays a euhedral habit. A few rare euhedral xenotime crystals were identified in the leucosome suggesting that xenotime crystallised from the melt. Xenotime grains are prismatic and fairly large, 100-300 μm.

3.4 Monazite distribution in the LBF

Monazite occurs in every metamorphic grade of the LBF metasedimentary rocks from upper greenschist to granulite facies (previous sections). The presence of monazite at grades as low as greenschist facies contrasts with previous studies (Overstreet, 1967; Smith and Barreiro, 1990; Kingsbury et al., 1993) that observed the introduction of monazite in the mineral assemblage only from lower amphibolite facies conditions (staurolite-in or Al_2SiO_5-in isograd) and above, while it confirms more recent studies documenting the presence of metamorphic monazite at lower grade (Franz et al., 1996; Pyle et al., 2001; Rasmussen et al., 2001; Wing et al., 2003).

A recent study from Wing et al. (2003) and a review from Spear and Pyle (2002) highlight the determining role that bulk composition plays in controlling the range of monazite stability during prograde metamorphism. The same studies also demonstrate that rocks with low Ca and Al content allow first appearance of monazite to occur at greenschist facies conditions. In other instances (Suzuki et al., 1991; Hawkins and Bowring, 1999; Rubatto et al., 2001), monazite identified in low-grade metasedimentary rocks was interpreted as detrital in origin. In the LBF, monazite grains identified in the lowest grade sample (S371), a Bt-Ms-Qtz metasedimentary rock displaying millimetre-thick layers of semipelitic and psammitic material, are generally interpreted as metamorphic in origin. The identification of monazite grains that are elongated parallel to one of the fabrics and other grains that are oblique to the same fabrics suggests that most of the low-grade monazite grains are not detrital, but grew during or after deformation of the sedimentary rocks.

Microprobe chemical dates obtained for six monazite grains from sample S371 are all younger than the minimum deposition age of the LBF (Sections 6.1; 6.4.1; 7.4) indicating that these six grains, at least, are not detrital (Chapter 6). However, the fact that the six grains dated are all of metamorphic age does not rule out the possibility that detrital grains are preserved in low grade LBF samples. Identification of two monazite grains of detrital age in Transects 3 and 4 (Chapter 6) indicates that other detrital monazite grains are probably preserved in lower grade samples. It is also possible that, in some instances, detrital monazite acted as a precursor to metamorphic monazite via *in situ* recrystallization combined with overgrowth of new material. This hypothesis has not been verified in the LBF samples. Wing et al. (2003) identified low-grade composite metamorphic monazite grains composed of a detrital core surrounded by a metamorphic overgrowth. In the LBF, at least one monazite grain showing an apparently composite texture was recognised. Grain S371-05 (Fig. 3.11) displays a composite texture and may be analogous to the composite grains of Wing et al. (2003). No trace analyses were obtained for this grain, hence the age of the core is unknown. A maximum age can be inferred for the overgrowth which grew parallel to S1.

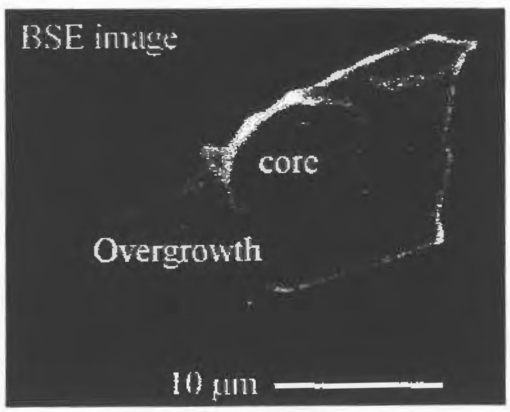

Figure 3.12 : BSE image of grain S371-05. The grain displays a composite texture. The core is granular and subrounded, whereas the rim is elongated parallel to S1, which constrains the age of overgrowth to the time of S1 development. No ages are available for this grain. Low-grade composite monazite grains were identified by Wing et al. (2003) and ages for these grains revealed a detrital core surrounded by a metamorphic overgrowth.

In the LBF, allanite, a common precursor to monazite (Smith and Barreiro, 1990; Kingsbury et al., 1993; Bingen et al., 1996; Wing et al., 2003), has not been identified. On the other hand, xenotime and apatite, two other phosphate phases, occur at low grade with monazite. Xenotime is scarce and exhibits an irregular shape with numerous embayments. Apatite is more abundant and varies from granular to euhedral. In the LBF, monazite is not observed in contact with xenotime and is only rarely observed with apatite. Contact with apatite is straight and does not suggest a reaction between the two minerals. Hence, no precursor to monazite was positively identified in the LBF metasedimentary rocks.

Here it is proposed that the LBF pelites have a suitable bulk rock composition to allow monazite crystallisation before upper greenschist facies conditions are reached, and all monazite precursors are consumed. This hypothesis would explain the lack of monazite precursors and the presence of monazite at low metamorphic grade. Eighteen LBF metapelite samples were analysed by Johns (2002). The Al_2O_3 and CaO values from Johns' (2002) analyses are normalized to Shaw's (1956) average pelite composition and plotted on a diagram adapted from Wing et al. (2003; Fig. 7). The dashed line represents the limit of stability for allanite and monazite in biotite and garnet zones as inferred from two sample suites in northern New England representing a Buchan and a Barrovian regional terranes (Wing et al., 2003). The compositions of the LBF samples cover a range of values on both sides of the stability limit of Wing et al. (2003) for monazite and allanite (Fig. 7.2). Eleven of the LBF samples collected by Johns (2002) plot in the allanite stability field, six of which are very close to the stability line. Because all monazite grains analysed in the present study are from LBF samples, it is reasonable to assume that their bulk rock compositions are similar to Johns' (2002) data. The widespread presence of monazite in the LBF upper greenschist rocks suggests that the range of Al_2O_3 and CaO composition suitable for formation of monazite at upper greenschist conditions is broader in the LBF than that observed by Wing et al. (2003) in their New England samples. This discrepancy between the LBF and observations from Wing et al. (2003) suggests that the compositional stability field of monazite depends on many factors, including the bulk composition, and that it may not be possible to establish a universal range of composition for monazite in metamorphic rocks.

The relative abundance of phosphate minerals (apatite, monazite, and xenotime) was estimated qualitatively from X-ray maps of Ca, Ce, P and Y on Bt-Ms, Bt-Ms-Crd±And and Bt-Ms-Crd samples (Chapter 3). These X-ray maps indicate that xenotime content decreases with metamorphic grade while apatite and monazite become more abundant. No monazite grain was found in contact with xenotime and most xenotime grains show very resorbed grain boundaries. These observations suggest that xenotime becomes unstable at higher metamorphic grade and possibly leaves the mineral assemblage. BSE images also reveal that monazite size consistently increases with metamorphic grade. Monazite grains tend to be more euhedral and prismatic at higher grade. Increase in size and abundance of monazite grains at higher metamorphic grade correlates with previous observations (Rubatto et al., 2001).

Most studies (Bingen and van Breemen, 1998; Broska and Siman, 1998; Pyle and Spear, 2003a; Wing et al., 2003) documented breakdown of monazite during prograde metamorphism. This study shows that monazite is relatively stable through the whole range of metamorphic conditions that the LBF experienced. Despite some embayed grains, monazite never disappears from the mineral assemblage. This suggests that monazite was likely consumed at some point during metamorphism but only to a limited extent. The coexistence of embayed monazite with euhedral monazite grains is attributed to the complex monazite growth history (Section 7.4). Monazites displaying embayments are more abundant around the sillimanite isograd (T3; S375 and S378).

Monazite grains occur in various settings in the LBF metasedimentary rocks. At lower grades, monazite is commonly associated with micas, either included in the mica grains or located along their grain boundaries. Grains located in the matrix were also locally identified. In lower grade samples displaying compositional layering consisting of alternating psammitic and more pelitic beds, monazite is most abundant in pelitic beds. The predominant association of monazite with pelites has been demonstrated by many other studies (Lanzirotti and Hanson, 1996; Rasmussen et al., 2001; Spear and Pyle, 2002).

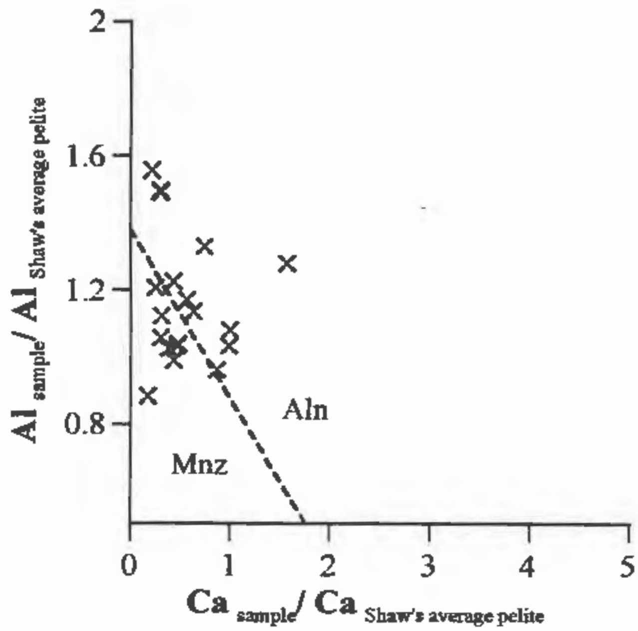

Figure 3.13 : Plot of Al_2O_3 and CaO content of LBF samples (Johns, 2002) referenced to Shaw's average pelite. The dashed line represents the limit of stability for Aln and Mnz in Bt and Grt zones as inferred by Wing et al. (2003) from two sample suites in northern New England representing a Buchan and a Barrovian regional terranes. Shaw's average pelite (1956) contains 2.18 % Cao and 16.62 % Al_2O_3. Samples from the LBF have bulk compositions plotting in both the Mnz stability zone and the Aln stability zone. Diagram after Wing et al., 2003.

In higher grade samples (above the sillimanite-in isograd), monazite is also commonly associated with biotite. Many monazite inclusions have been observed in cordierite and garnet porphyroblasts. Locally, grains were also identified in the Kfs-Pl-Qtz-Sil matrix.

Migmatite samples contain abundant monazite, although the grains are not uniformly distributed in the rock. Monazite grains are predominantly located in the mesosome part of the migmatites, whereas the leucosome contains little or no monazite. In the mesosome, monazite grains are found as inclusions in biotite or garnet porphyroblasts and are also very common within cordierite formed after breakdown of Bt-Sil (Chapter 3). Locally the Kfs-Qtz-Pl leucosome contains monazite associated with relict biotite grains.

The Mg X-ray map from sample S388 (Fig. 3.14), a stromatic migmatite with centimetre-thick leucosome layers, overlain with monazite locations identified from matching Ce and P spots, shows clearly the preferential distribution of monazite grains in the mesosome. On the Mg X-ray map, monazite grains (white spots) are restricted to the Bt-Crd-Sil melanosome. There are few monazite grains located in the leucosome and most are contiguous with relict biotite or skeletal garnet.

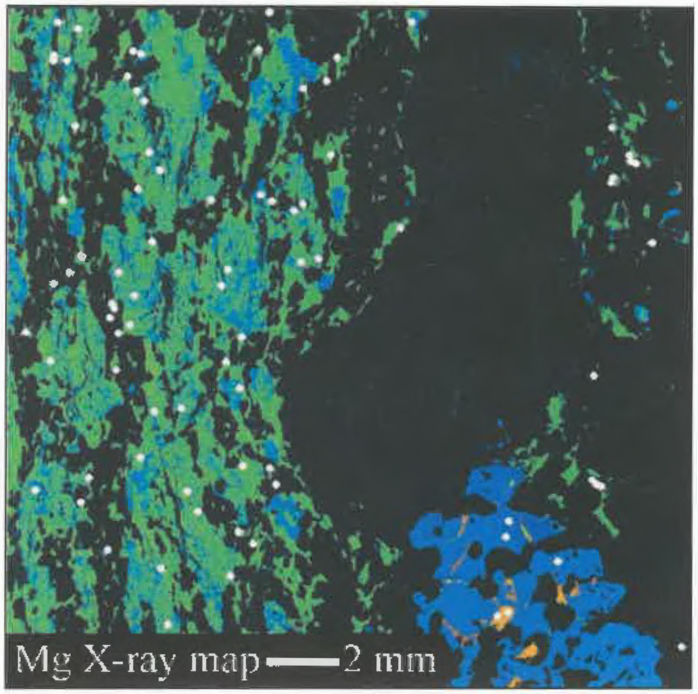

Figure 3.14: Magnesium X-ray map obtained from a thin section of sample S388. The large blue porphyroblast in the lower right is a residual garnet in the leucosome. Orange grains in garnet are biotite. The green and blue minerals on the left are biotite (solid green) and cordierite (blue mottled green) grains. The black material is the Qtz-Kfs-Pl leucosome. White circles are monazite grains identified from matching spots on superimposed Ce and P X-ray maps.

The absence of monazite in the leucosome has important geochemical implications. In most granitic rocks, accessory minerals contain as much as 60% of trace elements such as Zr, REEs, Y, Th, and U (Watt and Harley, 1993). Monazite is one of the main accessory minerals to trap LREEs, Th and to a lesser extent U and Y. Vapour-absent dehydration melting of pelitic metasedimentary rocks generally yields compositionally peraluminous melts (Patino Douce and Johnston, 1991). Because of the peraluminous composition, the most likely host phase for LREE's, Th and U is monazite. The stability of allanite, apatite and titanite is hindered by the generally low CaO content of peraluminous melts (Watt and Harley, 1993). Hence, an important proportion of the LREE's, Th, and U budget of the rock is locked inside the monazite grains and the abundance of these elements in the leucosome is mainly controlled by monazite behaviour during melting. This depends on a few factors: the solubility of monazite in the melt and its dissolution rate, the petrological setting of the grain (i.e., matrix grain, partially or totally included, inclusion in a phase participating in the melt-reaction or in a refractory mineral), and the efficiency of the melt segregation and the entrainment process.

If monazite dissolves in the melt, the leucosome will be enriched in LREEs, Th, U and Y relative to the mesosome. Depending on the melt saturation in PO_4 and LREEs, and its temperature, monazite dissolution rate will vary. Montel (1986) showed that monazite solubility is relatively low in felsic melts and dramatically reduced in peraluminous melts, with monazite being relatively insoluble in dry peraluminous granite (Watt and Harley, 1993). The solubility of monazite is relatively low and if melt extraction occurs faster than the dissolution rate, monazite may only dissolve partially. Hence, monazite is unlikely to dissolve completely in a peraluminous melt. In the case of rapid melt extraction, consumption of monazite may be very minor relative to its total volume. Consequently, dry peraluminous melts will be depleted in LREEs, Th and U relative to the mesosome. It is also documented that efficient melt extraction may entrain refractory accessory minerals (Watt and Harley, 1993). By this process minerals that did not participate to the melting reaction may still end up in the melt. The resulting leucosome will be enriched in LREEs, Th and U depending on the effectiveness of the entrainment process. Only monazite included in major phases that break down during the melting process is likely to be entrained.

The absence of monazite in the leucosome of S388 indicates that under the ambient conditions monazite did not crystallise from the melt. It also suggests that entrainment of residual minerals was relatively minor. The rare monazite grains, garnet porphyroblasts, and biotite grains in the leucosome likely came from the nearby mesosome and were entrained in the melt. This is verified by the presence, in the leucosome, of monazite grains older than the melting event (grain S397-02, Section 7.4). On the other hand, euhedral prismatic monazite of age correlative with the melting event (S401-01; Section 7.4) in some leucosome suggests that melt was sufficiently saturated in PO_4 and LREEs to crystallise monazite. Interestingly, magmatic monazite (crystallised from melt), rare in millimetre-scale leucosome, is abundant in peraluminous granite, collected in the same area and interpreted to be derived from partial melting of the LBF metasedimentary rocks. The granite also contains older metamorphic monazite inherited from the sedimentary rocks (grain S397-02; Section 7.) suggesting that older monazite grains were not dissolved by the melt when entrained.

Centimetre-thick leucosome veins (S388) contain very few monazite grains, while larger granitic bodies (S397) contain abundant magmatic and inherited monazite grains. This suggests that for the LBF metasedimentary rocks the amount of partial melting had a significant influence on monazite behaviour. Although S388 contains up to 50% leucosome, little or no monazite crystallised from the leucosome, suggesting that the melt had not reached saturation in PO_4 and LREEs, leading to crystallisation of monazite. Greater amount of melt or melting of a source with major mineral phases being initially richer in LREEs produce a melt saturated in PO_4 and LREEs causing crystallisation of monazite during cooling. Both hypotheses may explain the abundant magmatic monazite grains in S397. Also, a greater amount of melting means that more monazite grains would have been released into the melt when major phases broke down.

3.5 Summary.

Monazite is present in every metamorphic zone of the LBF. The low- to medium- CaO and Al_2O_3 content of the LBF likely permitted monazite to first appear at greenschist facies. Size and modal abundance of monazite increase with metamorphic grade. Near the sillimanite isograd, monazite displays embayments, especially grains located within fibrolite clusters. Finally, monazite is absent from leucosome veins, but abundant in the granitic bodies.

4. Analytical methods and procedures

4.1 Chemical dating of monazite

Electron microprobe (EMP) analysis has been used for many decades by geoscientists to determine the chemical composition of minerals. Applications cover a broad range of topics from geochemistry and mineralogy to thermobarometry. However, because dating rocks generally involves measurements of isotopic ratios, the EMP has not been widely used as an analytical tool in geochronology. Although there have been a few attempts to date U-rich minerals using EMP (Cameron-Shiman, 1978; Cuney et al., 1982), early applications did not lead to widespread use of EMP because suitable minerals are relatively rare and restricted to very specific geological settings, and analytical issues and resetting of dated minerals compromised the results.

The recognition of monazite as a valid geochronometer, notably by Parrish (1990), attracted more attention for the use of this mineral in geochronology. Suzuki and Adachi (1991) presented the basic rationale for chemical dating of monazite. They proposed that if monazite contains very little common Pb and generally shows concordant U/Pb and Th/Pb ages, "the Pb content of monazite is proportional to the Th and U contents and the time elapsed since the formation" (Suzuki and Adachi, 1991; Suzuki et al., 1991). They applied EMP analysis to monazite of known age and verified the direct relation between its radioactive element content and the age of the monazite crystal. This provided information to distinguish between various age populations of monazite. Montel et al. (1996) performed a well documented study of monazite using EMP chemical dating. They were the first to calculate an age directly from chemical data, and to demonstrate its correlation with results obtained from isotopic methods. They provided basic information for EMP dating and the essential statistical methods and age calculation equations. Williams et al. (1999) also contributed to the refinement of the technique, and introduced the concept of age domain mapping using X-ray mapping by EMP.

In the last few years, increasing interest in a range of *in situ* dating techniques has brought renewed attention to EMP chemical dating of monazite. The growing interest in this technique is evident from the large number of papers published on this topic in the last few years (e.g., Scherrer et al., 2000; Williams and Jercinovic, 2002; Pyle et al., 2003). This chapter summarises the main current technical and methodological aspects of EMP chemical dating of monazite.

4.1.1 Basics of chemical dating of monazite

The use of EMP for chemical dating has significantly expanded the use of monazite as a geochronometer. EMP enables *in situ* analysis, as well as X-ray elemental mapping of entire grains. The combination of these two procedures is the core of the technique. The technique is based on the following assumptions (Montel et al., 1996): (1) no common Pb is initially present or the amount is below detection limits (Parrish, 1990), and (2) the mineral is a closed chemical system, i.e. no partial gain or loss of U, Th or Pb has occurred. The absence of non-radiogenic (common) Pb enables chemical measurements of total Pb to be used without isotopic data (^{204,206,207,208}Pb), assuming that all Pb is formed by decay of ^{232}Th, ^{235}U and ^{238}U. It is also assumed that the isotopes of U and Th are present in their natural crustal ratios, that the half-lives of the parent isotopes are known, and that no isotopic fractionation occurred. Monazite has been shown to behave as a closed system under most geological conditions. The age (i.e. time since crystallisation) is calculated using the basic equation of radioactive decay (details in Section 4.3).

Using the high spatial resolution of the EMP (1-2 μm) and its ability to do chemical mapping, Montel et al. (1996) and Williams et al. (1999) were able to recognise multiple age domains within single monazite grains and to resolve complex tectonic histories of areas that had previously only revealed a few, typically discordant ages. Single point analyses made possible the quantification of the variation in age through the grain by traversing a single grain. This ability to do point analyses is an advantage over other methods that measure the whole monazite grain and may therefore combine different age domains. Compositional mapping, using secondary X-rays for selected elements (Pb, Th, U, and Y), reveals the geometry of different chemical domains. Point analysis allows correlation of chemical domains with age domains. *In situ* analysis of grains in their full petrographic context provides an important source of information to interpret chemical ages.

Ages are based on trace analyses of four elements: Pb, Th, U and Y. Y is analysed to correct for its interference on Pb Mα and its bearing on zoning and petrogenetic information. The three other elements are used for the age calculation. The precision and accuracy of the trace analyses are critical. Since the detection limit of the EMP is relatively low (e.g., 40-100 ppm), the trace element content is the main factor affecting the precision of analyses. In ideal conditions, trace element analysis using high beam currents and high-resolution crystals yield detection limits on the order of tens of ppm. Therefore, the concentrations of the trace elements in the grain, in particular Pb, and hence the age of the grain, will greatly affect the error. The younger age limit for reliable dating of a monazite grain is generally ca. 100-200 Ma depending on its radiogenic Pb content. Optimal analytical conditions on Proterozoic monazite commonly generate error on individual spots of 2-4%. Total error on a date obtained from multiple samples (spot analyses) within a single age domain can be as low as 1-2% or less.

4.1.2 Applications of electron microprobe dating of monazite

Chemical dating of monazite by EMP allows a broad range of applications. First, by using information related to the petrological setting of the dated grains, the technique can provide time constraints on microstructure development. A good example is described by Shaw et al. (2001) who established the timing of deformation by dating monazite from different textural settings (e.g. parallel to a S2 fabric, or within a mylonite). Combined with single grain dating and observations of the relation to microstructures, the study of monazite from different locations (e.g. within a porphyroblast or in the matrix) can provide important constraints on the timing of metamorphic events relative to microstructure development.

The chemical composition of monazite is another important source of information. Different generations of monazite growth may have different chemical compositions. For instance, Foster et al. (2000) used chemical variation to recognise timing of porphyroblast growth. They constrained the timing of garnet growth by recognising depletion in Y content between monazite included in the garnet (older and richer in Y) and monazite in the matrix (younger and depleted in Y), the Y being preferentially partitioned into garnet. Also, using the chemical composition of monazite, single grain X-ray mapping, and textural relations with other minerals, Pyle and Spear (2003a) recognised four different generations of monazite within migmatitic gneisses from New Hampshire. The use of EMP and its applications to the study of monazite was a key aspect in all the studies mentioned above.

4.2 EMP analysis

Electron microprobe analysis is widely used in Earth Sciences in a broad variety of fields. The high spatial resolution, short analytical time, and non-destructive nature make it a very useful tool for earth scientists. The electron microprobe allows precise chemical analysis of a small sample volume on a surface of less than ~2 μm in diameter. Electron microprobe analysis is the main component of this study. For this research, analyses were done on the electron microprobe (EMP), a JEOL JXA-8200 Superprobe, at the Dalhousie Regional Electron Microprobe Laboratory. The instrument is equipped with 5 spectrometers comprising the following crystals: spectrometer #1) TAP, LDE1, LIF, PET; spectrometer #2) PET, LIF; spectrometer #3) TAPH, LDE2H; spectrometer #4) TAP3, LDE2; and spectrometer #5) PETH, LIFH. Spectrometers #1,3, and 4 are equipped with a proportional flow counter using argon gas, whereas spectrometers #2 and 5 are equipped with a proportional sealed counter using xenon gas.

This section provides basic information on EMP analysis in order to better understand the reasoning behind each procedure, and the limits and errors resulting from EMP analysis in the context of chemical dating of monazite.

4.2.1 Sample preparation

For EMP analysis, rock samples have to be prepared as polished thin sections. Polished thin sections used in this research have all been prepared at the Dalhousie facility. They have an average thickness of ~ 40 μm. Normally in this process a disc made of lead (Pb) is used for polishing. The use of a lead lap for polishing raises serious concerns because microprobe dating is based on the analysis in trace mode of four elements (Pb, U, Th, and Y), of which Pb is the most critical one: it is therefore essential to avoid Pb contamination. Special attention was given to the cleaning of the thin sections in order to reduce the Pb contamination to a minimum (a more detailed discussion is given in Section 4.3.1.4). Also, we may note that routine major element analysis of monazite is not affected by Pb contamination, as this element is not analysed at all in this procedure. Thin sections are cleaned using an ultrasound bath, soap and alcohol to remove oil that may have accumulated during the polishing process. This is important for long analytical times at high current, where oil trapped between the rock and the coating can boil and evaporate, destroying the carbon layer.

4.2.2 Background and principles

X-ray microanalysis is the basic to the electron microprobe. Briefly, excited electrons from an incident electron beam hit the surface of the sample, ejecting electrons from the inner shells (Reed, 1993). The restoration of these electrons by electrons from the outer shells results in the production of characteristic X-rays. The wavelength and the intensity of the specific X-rays are used to determine the nature and quantity of an element in the material (Scott and Love, 1983).

In more detail, an electron beam is produced in a vacuum chamber using an electron gun. The latter is an electron emitter (e.g. a tungsten filament) that is heated by a current to produce electrons escaping the tungsten atoms. The filament is maintained at a negative potential to accelerate electrons through the anode aperture (Reed, 1993). Emitted electrons are focused into a narrow beam using a combination of magnetic lenses called condensers. The focus (or diameter) of the electron beam is controlled by varying the intensity of the electromagnetic field of the condenser lenses (Reed, 1996).

Incident electrons from the beam will eventually collide with atoms from the surface or at shallow depth within the sample. The extent and the shape of the interaction volume depends on both the average density of the material and the energy of the incident electrons (Scott and Love, 1983). The collisions between incident electrons and specimen atoms will produce different effects. These are classified in two categories: elastic scattering and inelastic scattering phenomena.

In elastic scattering, the electron trajectory is deflected, but little or no energy is lost. Back-scattered electrons (BSE) are the main results from elastic scattering. They are incident electrons strongly deflected from their trajectory by atomic nucleii. The probability of back-scattering increases with larger nucleus and consequently with higher atomic number. Hence, back-scattered electrons are very useful for imaging and zoning recognition in minerals as their intensity distribution reflects the variation in average atomic number of the material. Materials with greatest average atomic number display the brightest colours on a BSE image.

Inelastic scattering results from loss of energy from the incident electron and its transfer to the target atoms. Phenomena produced are secondary electrons, auger electrons, Bremsstrahlung (continuum X-rays), fluorescence and characteristic X-rays. Here, we will pay more attention to characteristic X-ray production. Other inelastic scattering effects are used in imaging techniques. For further details, refer to Reed (1996) and references therein.

Characteristic X-rays are the result of inner-shell ionisation caused by incident electron bombardment. Incident electrons with sufficient energy can remove electrons from atomic inner shells during collision. This creates vacancies which are generally filled by electrons from an outer shell. The difference in energy is dissipated in the form of X-rays. These X-rays are characteristic for each element and also have distinct energies depending on both the location of the initial vacancy and the source of the transition electron. The most energetic radiation is produced by K-shell vacancies filled by electrons from the next orbital, the L-shell (Reed, 1993).

The electron microprobe system is consequently designed to record the characteristic X-ray signals produced by the interaction between the specimen and the electron beam, deconvolve signals from various wavelengths, and measure their respective intensities. A detailed description of an EMP system is beyond the scope of this thesis. Readers are referred to Reed (1996) and Scott and Love (1983) for more information on EMP analysis.

4.2.3 Background correction

Because intensities measured at the peak are not net intensities, but combined background and element peak intensities, it is necessary to subtract the background value to obtain the net intensity at the peak position. The background correction assumes that background under the peak position is linear. Background is calculated by measuring a lower and upper background from both sides of the peak and is interpolated at peak position (Fig. 4.1). Lower and upper backgrounds must be as close as possible to the peak while avoiding neighbouring interference and peak tails. In general, background positions are set once for a specific element at specific analytical settings and background correction is efficiently applied. However, as discussed in Section 4.2.10, the background positions with the least interference are not always located at the same position. The following equation presents how background correction is determined by the software employed on the JEOL-8200.

Background correction:

$$I_{net} = I_{peak} - \frac{I_{PBH}\,\overline{PB_L} + I_{PBL}\,\overline{PB_H}}{\overline{PB_L} + \overline{PB_H}} \qquad \text{(eq. 4.1)}$$

where, I_{peak} : X - ray intensity at peak position

I_{PBH}, I_{PBL}: X - ray intensities of backgrounds on low - angle side and high - angle side

$\overline{PB_L}$, $\overline{PB_H}$: Distance between peak position and background measurement position

Figure 4.1: Interpolated background below a Pb Mα peak from a wavelength dispersive spectrometry (WDS) scan on monazite (PETH crystal, P10 gas, 15 kV, 200nA). Units on Y-axis are counts per seconds (cps).

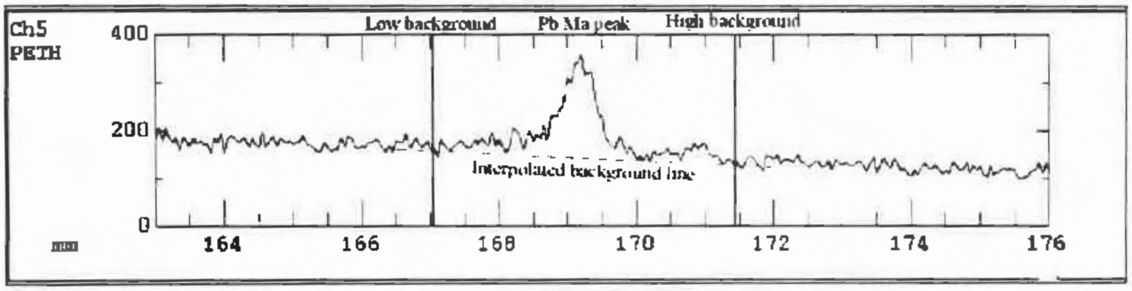

4.2.4 Coating

Samples analysed by EMP must be coated for two reasons. The coating allows non-thermally conductive specimens to dissipate the heat produced by the energy accumulated at the sample surface. Also, it avoids the build-up of a charge at the surface of the specimen. Electrical potential formed at the surface where the incident beam falls on the specimen could produce deflection of the beam as well as specimen current instability (Scott and Love, 1983).

Various materials can be used; the most common are carbon, aluminium, copper, silver, and gold. For this study, carbon coating was used for all the samples. A single thin coat was used for major element analysis at 20nA and a thicker coat was used for trace analysis at 200 nA.

Carbon thickness for major element analysis was on the order of ~200 Å (=20 nm), but trace analysis requires a thicker coating of about 400 Å (=40 nm) to reduce burning off the coating and minimise permanent damages on the sample. One of the main issues with carbon coating, for long counting times, is that current charging occurs at the sample surface deflecting the beam, which causes instability and reduces specimen current. Also, the poor thermal conductivity of carbon coating causes permanent damage to the sample surface. To prevent such problems, Jercinovic et al. (2002) proposed using gold coating.

4.2.5 Overlap problem

One of the challenges in EMP analysis of monazite is the presence of numerous interferences between X-ray lines (Scherrer et al., 2000; Pyle et al., 2002). Monazite is a LREE phosphate containing a substantial amount of Th and minor Y, Pb, and U. Hence, monazite includes a large number of elements having similar atomic numbers and a similar electronic configuration. Therefore, when subjected to an electron beam, X-rays emitted by these elements will have very similar energies and will occupy neighbouring

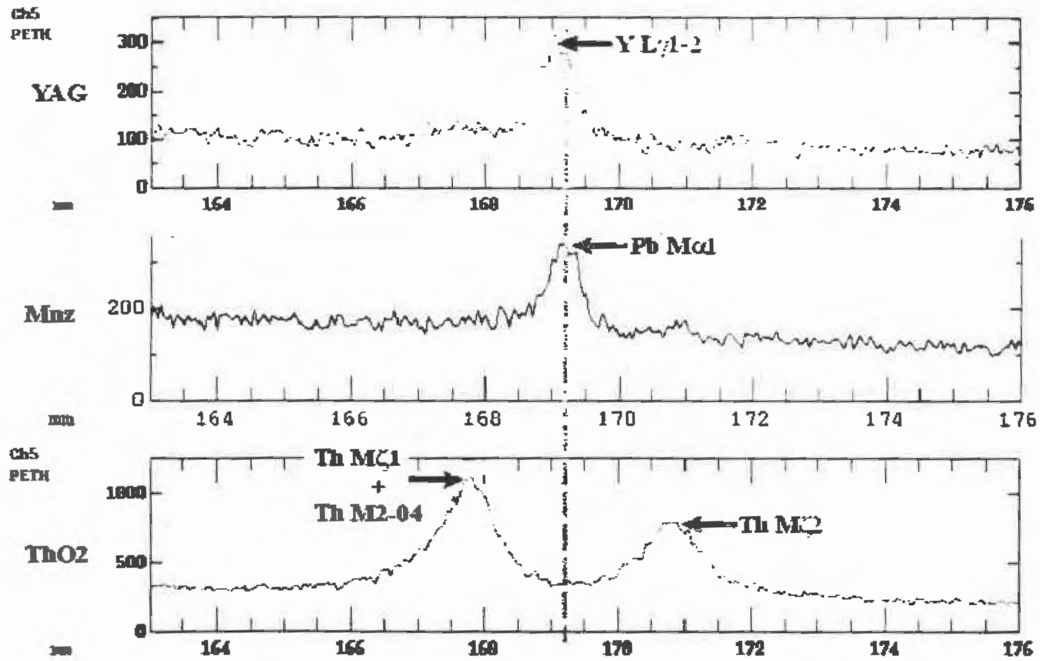

Figure 4.2: WDS scans (PETH crystal, P10 gas, 15 kV, 200 nA) of the Pb $M\alpha_1$ region obtained from an yttrium-rich garnet (YAG) standard, a monazite grain (Mnz) and a thorium oxide (ThO_2) standard. The Y $L\gamma_{1-2}$ peak is located at the same position than the Pb $M\alpha_1$ in monazite, hence correction for yttrium is required. Thorium peaks are not located at the Pb $M\alpha_1$ position but their combined peak tails increase the number of counts measured at the Pb position. Also, presence of the Th peaks on both sides of the Pb peak commend to select background positions away from the Th interference.

positions in the X-ray spectra. The situation is complicated by the fact that each element produces several peaks (mainly L-lines for actinides and M-lines for U, Th, Pb) issued from all the possible radiations caused by beam interaction. Due to the nature of X-rays, peaks always cover a certain range (a narrow bell shape), and two peaks with distinct mean values may overlap partially if they are close enough. A higher order peak of one element may occupy almost the same position as the first order peak of another element.

To measure the net intensity of a peak accurately, it is necessary to avoid peak overlap which artificially increases the count value at a peak position. Careful setting of the background positions away from neighbouring interfering peaks is very important. Inadequate background positions (i.e., located on the tail of a neighbour peak) make the background higher and consequently reduce the value of the net intensity. These considerations make the choice of the analytical line for an element critical, as the line with the highest intensity may not be free of interference. The choice depends on various factors. In trace analysis, higher intensity lines are generally favoured unless errors from overlap corrections are larger than counting statistics errors (Pyle et al., 2003).

In the case of monazite analysis, Lα lines are used for lanthanides (REE's) unless there is interference, in which case a Lβ line is used. Detailed tables with X-ray lines used for major element analysis and trace element analysis of monazite are given in Appendix 1 (Tables A1.6; A1.9; and A1.11). Overlap can be an important issue, especially in trace element mode, where the first order peak of a trace element present in only few hundreds or thousands of ppm may overlap with a higher order peak from a major element. For instance, in some cases, the intensity input from overlap of Pb Mα with Y Lγ_{1-2} and Th (M2-04 + Mζ_{1-2}) can be as much as ~5-8% (Pyle et al., 2003). Overlap from Th and Y peaks on Pb Mα can translate into a difference of tens of millions of years in age. Section 4.2.11 describes the procedure for overlap correction and Appendix 2 presents the correction factors measured for this study.

4.2.6 <u>Standards and calibration</u>

Calibration of the electron microprobe is a very important step in the analytical routine. The precision of the results depends on the quality of the calibration. Normally, calibration is done on a standard as similar as possible in composition to the unknown. The count rate from the standard is used to calculate the concentration of the same element in the unknown using the k-ratio (counts measured in the unknown/ counts measured in the standard) and applying ZAF corrections (corrections for the matrix effect considering atomic number (Z), absorption (A), and characteristic fluorescence (F)). In order to minimise the ZAF correction as many phosphates as possible should be used as standards (e.g, $CePO_4$, $LaPO_4$).

In major element analysis, we systematically ran a control monazite of known composition before starting an analytical session. The results from the control analysis are compared with the known composition and re-calibration is done for elements giving values beyond the usual error range. During the analysis, the control is checked regularly to monitor drift and ensure that the calibration remains accurate. For trace element analysis, because a much higher precision is required, all the measured elements are systematically calibrated before the beginning of every analytical session. A final but critical consideration is the analytical conditions for standardisation. Different analytical conditions are used for major element analysis and trace element analysis. Calibration must be done at the same conditions (similar count rate) as analysis of the unknown. However, in calibrating at high current with a standard rich in an element that is found only in trace quantities in the unknown (for example, calibrating Pb with crocoite (64.11 wt% PbO) for monazite with a few hundred ppm Pb) one has to be careful not to set the pulse-height analyser (PHA) window too narrow because of the possible shift of energy pulse to higher values (Pyle et al., 2003). Appendix 1 (Table A1.7) provides the list standards used in this study. Appendix 1 (Tables A1.3; A1.4; A1.6; A1.8; A1.9) presents the analytical conditions for major and trace elements analysis.

4.2.7 Thin section X-ray mapping procedure

Thin section X-ray mapping is used to locate monazite and other phosphate phases. It is done at high current, in scan mode, using the WDS spectrometers. Up to five elements can be mapped at the same time while also obtaining a BSE image from the mapped area. This procedure is very useful, especially in fine-grained rocks, where monazite grains are rare and hard to find in BSE imaging mode (Williams and Jercinovic, 2002). It also provides a complete inventory of all the monazite grains in a thin section and their various petrological settings. We experimented with various analytical conditions during the study, but the combination of elements that provided the most useful information on REE phosphates and their petrological setting was Ca, Ce, P, Y, Mg plus a BSE image. Analytical conditions are listed in Appendix 1.

4.2.8 Major element analysis and procedure

Major element analysis consists of the quantitative determination of the chemical composition at a specific spot in a monazite grain using WDS spectrometers. Quantitative analysis of monazite includes analysis of major and minor elements while trace elements (e.g., Pb, S, Eu, Yb) are neglected. In order to reduce analytical time, four spectrometers simultaneously analyse the monazite grain. The fifth spectrometer on the Dalhousie JEOL 8200 microprobe is equipped with crystals for light element analysis and could not be used for analysing elements normally contained in monazite. Appendix 1 provides a detailed description of the procedure to follow as well as all the analytical conditions used for major element analysis (Tables A1.3; A1.4; A1.6). Readers are referred to Pyle et al. (2003) and Scherrer et al. (2000) for further information on the choice of analytical settings, peak selection, and avoidable overlaps.

Quantitative determination of monazite major element composition requires careful settings to overcome analytical challenges. First, X-rays have to be judiciously chosen to avoid or at least minimise overlap. The PHA window has to be set to filter out most of the unwanted energy pulses (e.g. background and continuum X-rays) while including most of the signal from the analysed peak. Calibration must be done before analysis, or a control analysis has to be run, and backgrounds must be located adequately to avoid interference. Selection of grains for analysis is determined from the results of chemical mapping. For every grain or chemical domain, 3-10 points are analysed to establish the average chemical composition.

4.2.9 Single grain X-ray mapping

Elemental X-ray maps can be acquired using WDS spectrometers. Up to five elements can be done simultaneously. To increase the count rate, analysis is done at high current. The elements of interest are Y, for its petrological significance, the parent elements, Th and U, and daughter Pb. The grains to be mapped are selected according to features such as interesting texture or zoning observed with BSE imaging.

Mapping is done to reveal chemical zoning patterns which may be significant for the chemical age. Zoning in U, Th and Pb commonly, but not systematically, correlates with age domains. The geometry and location of the age domains provide insights on the timing of monazite growth. Well described examples of this type of study are given in Pyle and Spear (2003a) and Williams et al. (1999). Analytical settings and procedures for single grain X-ray mapping are provided in Appendix 1.

4.2.10 Trace element analysis and chemical dating

Trace element analysis is the basis for monazite chemical dating. It is, therefore, essential to obtain numbers that are as precise as possible. Only four elements are considered (Pb, Th, U and Y). At this stage the choice of X-ray lines is critical, especially in the case of Pb. For this study, Pb Mα was used. This X-ray line is subject to more interference than Pb Mβ, but the gain in intensity counterbalances it. The intensity ratio for Pb Mβ/Pb Mα is about ~ 0.8. Pyle et al. (2003) also demonstrated that unless monazite is Th-rich (~ 10 % ThO_2 or more), the interference correction error is minimal compared to loss in counts and the related increase in counting error. The last, but critical, issue in trace analysis is the selection of background for each chemical domain, as discussed in greater detail in the following section.

To apply an appropriate ZAF correction the average major element composition must be calculated for every grain and chemical domain. These values are transformed into element wt % and used as fixed values for mass absorption analysis. This, of course, requires that major element analysis and X-ray mapping were done prior to trace analysis. The analysis of Pb, Th, U and Y is done simultaneously, so the parameters will be the same for each element measured within a single analysis. About 3-10 analyses are done within each grain or chemical domain to establish an average age.

In this study, counts were optimised by using a higher intensity current (200 nA), a high-sensitivity crystal for Pb (PETH), and longer background and peak counting times (300 sec at background positions and 600 sec at peak position). These conditions allowed us to reach detection limits of 40–60 ppm for Pb, and 100-200 ppm for U, Th and Y, depending on the abundance of these elements.

4.2.11 Background selection

Selection of an appropriate background is very important especially for trace elements where the peak-to-background ratio is smaller. Background noise is subtracted from the peak measurement to give the net number of counts. Monazite contains many elements with X-ray lines that have mutual interference, rendering the background selection very difficult. The presence of an interfering peak at a pre-selected background position will artificially increase its value. This problem would be easy to solve if interfering peaks were always located at the same spot and if they always had the same width. However, the distribution of neighbouring interfering peaks depends on the chemical composition of monazite; these background positions must be determined for each chemical domain. Therefore, for every domain, it is important to scan the area of the peak to be analysed in order to choose the best location for the backgrounds. Backgrounds selected on an interfering peak will artificially increase the background and inversely reduce the value of the unknown element, resulting in a younger age in the case of Pb or older in the case of U and Th. Backgrounds should be chosen as close as possible to the main peak while avoiding interfering peaks. Background is interpolated under the peak as a linear function. Jercinovic et al. (2002) proposed that a six point background selection and extrapolation as a curve provides more accurate results. The equation for linear background correction is shown in section 4.2.2. The detailed procedure for WDS scan and background selection is presented in Appendix 1.

4.2.12 Peak overlap correction

Some interfering peaks lie at the same position or very close to the analysed peak of a specific element. In trace analysis, this is a problem particular for Pb $M\alpha_1$ which overlaps with Y $L\gamma_{1-2}$ and Th ($M2\text{-}04 + M\zeta_{1-2}$), and U $M\beta$ which overlaps with Th $M\gamma$.

Overlap at the peak position increases the net intensity, which in the case of Pb would give an older age. To obtain the true net intensity at the peak, a correction must be applied to the count value. The proportion of counts originating from overlap by an element *x* on an element *y* can be estimated by analysing an *x* standard, free of element *y*, at the same peak position and measuring the intensity of the signal. As relative proportions of various peaks of a same element are constant, the ratio of measured *y* in the *y*-free *x* standard to the *x* content of the standard can be used to estimate the contribution of the overlap of element *x* on the *y* peak (Pyle et al., 2003). The following equation shows the mathematical expression of the latter reasoning:

General equation for correcting interference of *x* on *y*:

$$CF_{x-y} = y_{k-ratio}^{std,x} \Big/ x_{k-ratio}^{std,x} \times y_{k-ratio}^{std,x} \qquad \text{(eq. 4.2)}$$

Figure 4.3: Example of two Th peaks in monazite. The Th Mβ peak is 58% of the intensity of the Th Mα peak used in trace analysis. Therefore, this ratio could be applied in a case where the main peak of an element is located at the same position as Th Mβ. The intensity of overlap will equal 58% of the count intensity measured for the Th Mα peak.

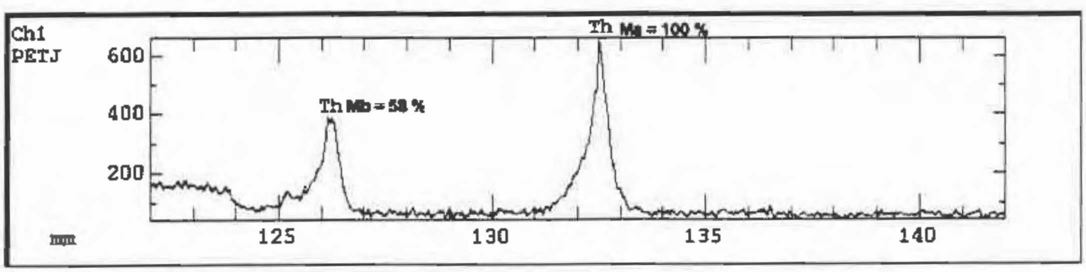

Correction factors (CF) are used to correct for the effect of overlap of Y $L\gamma_{1-2}$ and Th (M2-04 + $M\zeta_{1-2}$) on Pb $M\alpha_1$ and Th Mγ on U Mβ. The following equation shows how the factors are applied to correct the combined effect of Y $L\gamma_{1-2}$ and Th (M2-04 + $M\zeta_{1-2}$) (Pyle et al., 2003) on Pb $M\alpha_1$:

$$Pb_{corr(wt\%)}^{unk} = Pb_{uncorr(wt\%)}^{unk} - \left[\left(CF_{Th-Pb}\right)\left(Th_{k-ratio}^{unk}\right) + \left(CF_{Y-Pb}\right)\left(Y_{k-ratio}^{unk}\right)\right] \qquad \text{(eq. 4.3)}$$

4.3 Sources of error, estimation and propagation

4.3.1 Sources of error

Among the quantifiable sources of error, we can distinguish errors arising from the counting statistics during X-ray analysis, errors resulting from calibration, and errors due to correction for peak overlap. Non-quantifiable errors are selection of background position, selection of PHA window, chemical heterogeneity of the monazite grain, beam damage, and potential Pb contamination.

4.3.1.1 Counting statistics and error calculation

In EMP analysis, the first source of error comes from the counting statistics of X-rays. Because X-rays are random events, X-ray counting statistics represents a Poisson distribution. Consequently, each measurement will have an associated error which will decrease with increasing counts. The count rate must be maximised on single measurement in order to minimise the counting error. Note that the counting error is also sensitive to the peak/background ratio (P/B): with P/B increasing the standard deviation decreases. On the JEOL-8200 at Dalhousie, the relative standard deviation value is automatically calculated by the JEOL software using equation 4-4.

Standard deviation in X – ray counting :

$$S.D.\ (\%) = \frac{100}{I_{net}} \sqrt{\frac{I_{peak}}{t_{peak}} + \left(\frac{\overline{L_{PBH}}}{L}\right)^2 \frac{I_{PBL}}{t_{PBL}} + \left(\frac{\overline{L_{PBL}}}{L}\right)^2 \frac{I_{PBH}}{t_{PBH}}} \qquad \text{(eq. 4.4)}$$

$t_{peak}, t_{PBL}, t_{PBH}$: Counting time (in seconds) at the peak, and of the background signals at the low and high angles

$\overline{L_{PBH}} + \overline{L_{PBL}}$: Respectively, distance from the low and high background position to the peak position

$L = \overline{L_{PBH}} + \overline{L_{PBL}}$

Because of the way that net peak intensity is calculated, the counting errors on both peak and background measurements must be combined. The following equations present the standard deviation on net intensity (including error from peak and background) and the relative standard deviation.

Standard deviation (cps)

(eq. 4.5):

$$\sigma_{P-B}=\sqrt{\left(\frac{N_P}{t_P^2}\right)+\left(\frac{N_B}{t_B^2}\right)}$$

Relative standard deviation (%)

(eq. 4.6):

$$\varepsilon_{P-B}=\sqrt{\left(\frac{N_P}{t_P^2}\right)+\left(\frac{N_B}{t_B^2}\right)}\Bigg/\left(\frac{N_P}{t_P}\right)-\left(\frac{N_B}{t_B}\right)$$

Where, N_P = peak intensity in counts per second (cps)

N_B = background intensity (cps)

t_P = measuring time on peak position (sec)

t_B = measuring time on background position (sec)

4.3.1.2 Errors from calibration

The weight % value for an element is calculated through the k-ratio, which is the intensity of the element in the unknown over the intensity of the same element in the standard. Counting errors from measurements of peak and background in both the unknown and the standard must therefore be combined. This can be worked out by calculating the standard deviation and relative standard deviation on k-ratio using the two following equations (Pyle et al., 2002):

Standard deviation on k-ratio:

$$\sigma^2_{P-B,k-ratio}=\left(\frac{1}{2\left(\frac{N_{P,unk}}{t^2_{P,unk}}+\frac{N_{B,unk}}{t^2_{B,unk}}\right)^{1/2}\left(\frac{N_{P,std}}{t^2_{P,std}}+\frac{N_{B,std}}{t^2_{B,std}}\right)^{1/2}}\right)^2\sigma^2_{P-B,unk}$$

$$+\left(-\frac{1}{2}\bullet\frac{\left(\frac{N_{P,unk}}{t^2_{P,unk}}+\frac{N_{B,unk}}{t^2_{B,unk}}\right)^{1/2}}{\left(\frac{N_{P,std}}{t^2_{P,std}}+\frac{N_{B,std}}{t^2_{B,std}}\right)^{3/2}}\right)^2\sigma^2_{P-B,std}$$

(eq. 4.7)

relative standard deviation of the k-ratio:

$$\varepsilon_{P-B,k-ratio} = \sqrt{\varepsilon^2_{P-B,std} + \varepsilon^2_{P-B,unk}} \qquad \text{(eq. 4.8)}$$

4.3.1.3 Errors from overlap correction

Overlap correction introduces more counting errors because it is based on the ratio of intensity measurements. The effect is generally low on the total error, on the order of ~ 0.1-0.005 %. To be rigorous, however, it is important to propagate the error on k-ratio from each measurement used in the correction through the equation for corrected Pb and corrected U (Section 4.2.11; Appendix 2).

4.3.1.4 Risk of Pb contamination and other non-quantifiable errors

Among the many sources of non-quantifiable error, the risk of Pb contamination is certainly the most serious one. The use of a Pb lap during preparation of our samples introduces a risk of contamination that is difficult to assess and to control. Large deposits of Pb in cracks around the monazite grains can easily be revealed with WDS X-ray mapping. However smearing of Pb on the surface of the monazite grain is probably unrecognisable even with X-ray mapping due to the natural presence of radiogenic Pb in monazite and its spatial heterogeneity. Although careful cleaning should reduce the Pb contamination, ideally, polishing should be done on a Pb-free disc.

In order to assess the importance of potential Pb contamination, we analysed Pb on quartz, a Pb-free mineral, in trace mode. Results show values of ~ 40 ppm which is just about the detection limit making this value indistinguishable from background noise. However, quartz is a hard mineral and monazite may behave differently during polishing. We also re-polished some thin sections using a Pb-free lap and re-analysed the same monazite grains a second time. In most cases, the results were similar within error. A few grains that gave unusually old ages (1900-2300 Ma) during the first analytical session, yielded ages within the range of 1750-1920 Ma after being cleaned and re-polished on a Pb-free lap. These results indicate that Pb contamination can be significant and that polishing of thin sections on Pb lap should be avoided. However, the overall consistency and within-error variation of chemical ages suggests that contamination of Pb was not critical.

PHA window settings can cut off energy pulses if they are set too narrow. This cannot be quantified, but a large window and regular control checks should eliminate this potential source of error. Chemical heterogeneity is another source of error, but as it mainly relates to the ZAF correction, its effect on the overall precision of the age is minimal. As long as major chemical domains are dealt with separately, intra-domain chemical variations should not be a concern. Beam damage is another important issue. If the coating is too thin, beam burns during analysis can affect the results.

The final concern is the background selection for trace analysis. The error associated with this is hard to estimate. However, if background positions are systematically determined for each chemical domain, the contribution to the error should be minor.

4.3.2 Error propagation and calculation:

The various quantifiable errors involved in chemical dating of monazite should all be accounted for and propagated through the age equation. Errors are added in quadrature (equation 4-9). The relative error for U and Pb is the error on the corrected value.

$$\text{Total error on a spot age} = \sqrt{\varepsilon_U^2 + \varepsilon_{Th}^2 + \varepsilon_{Pb}^2} \quad \text{(eq. 4.9)}$$

A detailed description of the error calculation and propagation is provided in Appendix 2.

4.4 Age calculation and statistical treatment:

If the acquisition of precise chemical data for trace elements is critical, the processing and interpretation of the data is also important. It is essential to apply appropriate statistical treatment to the data and to propagate all source of errors rigorously. Appendix 2 provides an extensive description of the equations used to propagate error and calculate ages in this study. Chapter 6 also provides information on statistical modelling used to discriminate between populations.

4.4.1 Montel's equation:

The acquired data are used to calculate an age (t) by solving the following equation (Montel et al., 1996):

$$Pb = {}^{232}Th \times [e^{232\lambda t} - 1] + \varpi\, {}^{238}U \times [e^{238\lambda t} - 1] + \varpi\, {}^{235}U \times [e^{235\lambda t} - 1] \quad \text{(eq. 4.10)}$$

where

- Pb, Th, U are in ppm
- 232λ, 235λ, 238λ are the radioactive decay constants of ^{232}Th, ^{235}U, and ^{238}U, respectively Montel et al., 1996
- ϖ is the relative crustal abundance of U isotopes.
- Pb is the total amount of radiogenic Pb produced by all the parent atoms.

The age (t) is calculated by iteration, by comparing calculated Pb with measured Pb. This equation is derived from the general equation for radioactive decay (e.g. Faure, 1977):

$$D^* = N\,(e^{\lambda t} - 1) \qquad \text{(eq. 4.11)}$$

where,

- D* is the amount of radiogenic daughter,
- N is the present amount of the radioactive parent atoms,
- λ is the decay constant for each parent species,
- t is the time since the system is closed.

An age is calculated for each spot analysed within a single grain or chemical domain. The age of the grain or chemical domain is the weighted average of all the spot ages (eq. A2.22; Section 6.4). At least 5 analyses are required to give an age statistically meaningful.

Throughout this study, data were obtained using the various steps described in this chapter, error was rigorously propagated, and the ages were calculated and analysed according to the statistical test and techniques presented above and in Chapter 6. The results are discussed in Chapter 6 and the complete data set and analytical settings are provided in Appendices 1 and 6.

5. Monazite geochemistry

5.1 Introduction

It is widely recognised that information on the metamorphic evolution of a rock can be extracted from the chemical signature of its metamorphic minerals. Traditionally, major rock-forming minerals attracted most of the attention. However, the slow diffusion rate of many trace elements, for which accessory minerals are important sinks, and their potential for recording metamorphic history (Spear and Pyle, 2002), combined with the important role of accessory minerals in geochronology, have led to increasing research efforts in understanding the geochemistry and paragenesis of these minerals. Monazite is of special interest because it is an established geochronometer (Parrish, 1990), which has recently been the focus of *in situ* dating techniques using the electron microprobe (Montel et al., 1996; Williams et al., 1999) and other microbeam techniques.

A better understanding of monazite chemical behaviour through various metamorphic conditions is necessary to interpret monazite ages fully. Part of the present study aimed to investigate the chemical composition of metamorphic monazite and its variation with increasing metamorphic grade. Like other metamorphic minerals, the composition of monazite depends on three main factors: the bulk composition of the rock, the nature of coexisting mineral assemblages, and the pressure-temperature (P-T) conditions.

Previous studies documented the chemical variation of metamorphic monazite (Bea and Montero, 1999; Zhu and O, 1999; Pyle et al., 2001). The range in metamorphic grade as well as composition of the samples vary widely between studies. Samples for this study were all collected from a single lithological unit, the Paleoproterozoic Longstaff Bluff Formation (LBF), which experienced a wide range of metamorphic conditions from greenschist facies to granulite facies (Section 2.4). Given that the samples all belong to the same lithological unit and were taken from the semipelitic to pelitic horizons, variations in bulk rock composition should be minimised. Hence, variations in monazite composition should be mainly controlled by changes in the accompanying mineral assemblage and P-T conditions rather than by the protolith composition. Samples were collected along five transects described in detail in Chapter 3. The P-T conditions of each transect are given in Section 2.4

Results from the chemical investigation of LBF monazite are presented in this chapter. The focus is on data obtained from major element analysis, whereas Chapter 6 specifically deals with the geochronological data obtained from trace analysis of Pb, Th, U, and Y.

The first section of the chapter presents background information on monazite crystallographic structure and chemistry. The following sections contain results from the study of chemical zoning, characterisation of the variation in abundance of each element through various transects and petrological settings, and the assessment of the level of correlation between elements, and relevance of substitution mechanisms.

5.2 Monazite structure and composition

Monazite is an anhydrous orthophosphate of the type $A(PO_4)$, like xenotime and pretulite, and its crystal structure is monoclinic whereas the other two are tetragonal. The A-sites of monazite are preferentially filled by large trivalent cations, generally rare earth elements (REE) (Boatner, 2002). However, not all REEs fit well in the A-site and the dominant cations are light rare earth elements (LREE). In most monazite, La + Ce + Nd account for more than 75% of the cations occupying the A-site (Spear and Pyle, 2002). Other LREE, Pr and Sm, are also found in monazite, but together they only account for 3-5% of the A-site cations. Heavy rare earth elements (HREE), Dy and Gd, are also incorporated into monazite but they generally make up less than 1% of the cations. Ca and Th also commonly occupy A-sites. Their abundance varies from 2-10% of the cations (Section 5.3.2, Tables 5.1 and 5.2). Lastly, monazite incorporates small amounts of Si, U, and Y, and the abundance of these elements can vary from 0% to 2%, with Y values occasionally reaching as high as 4-5% (Pyle et al., 2001). Because of its affinity for Th and to a lesser extent for U, monazite can host high concentrations of these elements, making monazite the main source of radioactivity in many rocks. Bea and Montero

(1999) demonstrated that monazite controls the U budget in the leucosome of migmatitic metapelites. The radioactive element content of some metamorphic monazite reach values as high as 20% ThO_2 and 3% UO_2 (Watt, 1995). Despite its enrichment in U and Th, monazite does not display radioactively-induced structural damage nor show any evidence of metamictisation (Seydoux-Guillaume et al., 2002). Even though monazite does not generally incorporate common Pb at the time of crystallisation as shown by many studies (e.g., Parrish, 1990), its structure has the capacity to retain Pb produced by radioactive decay (Harrison et al., 2002). This is an important characteristic which enables radiogenic lead (Pb*), and therefore geochronological information, to be retained within the grain and renders monazite a valuable geochronometer. The issues of Pb diffusion and system closure are discussed in detail in Chapter 6.

In nature, monazite is generally a solid solution among three end-members. These are pure REE monazite (LREE-PO_4), brabantite ($Ca(Th,U)(PO_4)$), and huttonite ($(Th,U)SiO_4$). Substitutions between end-members account for most chemical variations in natural monazite (Townsend et al., 2000). The main substitutions are (Zhu and O'Nions, 1999):

Brabantite:	$2LREE^{3+} \rightarrow Th^{4+} + Ca^{2+}$	$2LREE^{3+} \rightarrow U^{4+} + Ca^{2+}$
Huttonite:	$LREE^{3+} + P^{5+} \rightarrow Th^{4+} + Si^{4+}$	$LREE^{3-} + P^{5+} \rightarrow U^{4+} + Si^{4+}$

Brabantite and huttonite are paired-substitution mechanisms. Thorium and U both have a suitable atomic radius to enter the monazite structure; however, neither of them is a trivalent (3+) cation: they rather are tetravalent (4+). Hence, to maintain the neutral charge balance, Th and U need to be associated with another element of complementary charge. Coupling of Th^{4+} or U^{4+} with Ca^{2+} preserves the electronic balance by substituting for 2 $LREE^{3+}$. Th^{4+} or U^{4+} may also be coupled with Si^{4+} and together substitute for 1 $LREE^{3+}$ + 1 P^{5+}. In brabantite substitution, Ca^{2+} fills an A-site left vacant by a LREE, while in huttonite the Si^{4+} cation occupies the 4-fold P^{5+} site (Spear and Pyle, 2002). Yttrium and HREE (Gd and Dy) are trivalent cations that substitute directly for LREEs. Section 5.5 presents results on monazite substitutions from this study.

Table 5.1: Selected analyses of monazites from literature. All reported analyses were acquired using an EMP; analytical conditions are described in the respective publications. Results are presented in oxide weight percent (wt %).

Sample/ grain	LM1A/	LM1D2/	Kinzi-gitic/	Strona -litic/	Strona -litic/	Primary zones/	Repla-cement zones/	DG136/	K986/
	H	H	-	Var. 1	Var. 2	IR 20	IR 20	mate6	incd3
**Analyses	38/1	87/3	1	1	1	-	-	-	-
P_2O_5	29.12	29.01	28.89	28.59	29.70	30.2	30.5	30.0	30.5
SiO_2	0.12	0.94	n.a.	n.a.	n.a.	0.27	0.36	0.4	0.39
CaO	0.97	1.99	0.68	0.90	0.68	0.98	0.49	0.87	1.07
ThO_2	4.02	12.91	5.97	5.35	5.70	2.7	2.7	4.17	4.55
UO_2	n.d.	1.27	1.01	0.72	0.28	n.a.	n.a.	0.38	0.93
Y_2O_3	0.72	1.63	2.51	1.41	0.17	0.90	0.52	1.28	2.96
La_2O_3	14.13	12.04	10.47	12.43	13.68	16.9	17.5	12.6	10.9
Ce_2O_3	29.75	24.84	23.70	33.83	33.08	32.3	33.3	28.2	27.3
Pr_2O_3	3.19	2.56	n.a.	n.a.	n.a.	2.8	3.0	2.98	2.75
Nd_2O_3	12.92	10.79	15.37	10.75	12.41	10.7	10.8	11.5	11.0
Sm_2O_3	1.06	0.45	5.57	2.27	0.67	1.2	1.1	1.89*	2.08*
Gd_2O_3	1.65	1.64	2.03	0.88	0.16	n.a.	n.a.	1.17	1.51
Dy_2O_3	0.58	0.93	0.57	0.43	0.04	0.28	0.21	n.a.	n.a.
Total	99.01	101.48	98.94	98.74	97.53	99.3	100.5	95.6	95.9
Source	1	1	2	2	2	3	3	4	4

Note:[1]Pyle & Spear (2003a), [2]Bea & Montero (1999), [3]Townsend et al. (2000), [4]Foster et al. (2002).

n.a.= element not analysed, n.d.= element value not determined because below detection limits

** In Foster et al. (2002) values were presented as SmO rather than Sm_2O_3.*

*** All values in oxide weight percent (wt %).*

Many studies using various analytical methods have reported metamorphic monazite with a large range of composition (Table 5.1).

5.3 <u>LBF monazite chemical zoning</u>

Metamorphic monazite is known to display compositional zoning as highlighted by numerous studies (Bea and Montero, 1999; Zhu and O'Nions, 1999; Pyle and Spear, 2003a). Chemical zoning is commonly reflected in back-scattered electron (BSE) images.

In this study, most BSE images were obtained using settings for major element analysis (20 nA, 15 kV). However, some images taken at 15 kV and 20 nA may fail to show zoning if the contrast between zones is too weak. In this study, consistent correlation between X-ray maps and BSE images indicates that, in most cases, the chemical zoning is revealed on a BSE image using major element analysis conditions. Use of a greater beam current and higher accelerating voltage enhances contrast between chemical zones.

BSE imaging is a qualitative analytical method that images the relative variation in average atomic number of the observed surface. It does not provide information on specific element distribution nor quantitative information on the chemical content. For these reasons, WDS X-ray maps were used along with BSE images. WDS X-ray mapping can generate maps of specific elements to characterise their zoning. These maps can also be calibrated using spot analyses to generate semi-quantitative data. Williams et al. (1999) used this technique to create age domain maps of monazite grains. For this study, element X-ray maps were not calibrated for semi-quantitative image analysis, but were used only to characterise the variation of specific elements within a single grain.

The zoning seen in BSE images typically reflects variation in content of more than one element. Previous studies (e.g., Zhu and O'Nions, 1999) showed that most elements can be zoned in monazite. Zoning in BSE images was reported by some authors to reflect mainly the concentration of Th (Watt and Harley, 1993; Watt, 1995), whereas Pyle et al. (2001) observed that it generally corresponds to Y zoning. Foster et al. (2002) described that in most cases zonation visible in BSE images correlates with zoning on Y and Th maps. In this study, only Pb, U, Th, and Y maps were acquired because of their significance in dating and help in targeting the location of spots for chemical dating. Results from this study indicate that chemical zoning is controlled by the concentration of both Y and Th. Previous studies demonstrated that, in specific geological contexts, zoning of Pb, Th, U, and Y often, but not always, correlates with age domains (Montel et al., 1996; Williams et al., 1999). Other studies, however, observed a lack of correspondence between chemical zoning and age zoning (Cocherie et al., 1998; Rubatto et al., 2001). This may be the result of a different geological history between samples investigated in these studies. For instance, Cocherie et al. (1998) interpreted the weak correlation between chemical zoning and age domains to reflect heterogeneous recrystallization of an older component that reset the U-Th-Pb system. Finally, the geometry of the zoning can also bear valuable information on the metamorphic evolution of the rock (Pyle and Spear, 2003a).

BSE images and X-ray maps from monazite grains of all grades were acquired. Monazite from low- to medium-grade rocks is generally relatively homogeneous (Fig. 5.1a,b; Fig. 5.2a,b). Locally, some grains show restricted zones of slightly different composition, but no distinct or consistent zoning pattern. For instance, S374-03 (Fig. 5.2b) is homogeneous with respect to U and Y, but the Th and Pb maps reveal small diffuse zones of slightly higher content. This type of poorly defined and low contrast zoning is relatively common in low- to medium-grade samples and generally consists of small irregular patches.

Conversely, monazite from high-grade samples commonly displays well-defined zoning (Fig. 5.1c-h; Fig. 5.2c-f). Most monazite grains from migmatitic samples are zoned. Hence, the discussion of chemical zoning is restricted to monazite from

Figure 5.1: (Next page). Examples of zoning patterns observed on BSE images of representative monazite grains from various grades. All mineral abbreviations after Kretz (1983). a) S371-19 (T1) is from a Bt-Ms-Qtz sample and the monazite grain shows a weak zoning on the BSE image. b) S366map2 (T2) from a Bt-Crd-Ms-Qtz±And sample shows a weak and poorly defined zoning common in medium-grade samples. c) S383-01 (T4) from a Bt-Grt-Sil-Kfs-Pl-Qtz incipient migmatite shows a simple concentric zoning with a light euhedral prismatic core and a darker rounded rim. d) S397-01 (T5) from a leucocratic Crd-Kfs-Pl-Qtz-Grt monzogranite shows a simple concentric rim with a darker euhedral prismatic core and a light euhedral prismatic rim. Note the inverted core-rim colour pattern in comparison with S383-01. e) S392-07 (T4) from a Bt-Grt-Sil-Kfs-Pl-Qtz migmatite displays a darker anhedral and resorbed core wrapped by two discontinuous rims. The outermost rim has the lightest colour tone. f) S392-01 (T4) from a Bt-Grt-Sil-Kfs-Pl-Qtz migmatite presents a complex concentric zoning pattern. A darker anhedral and resorbed core is enveloped by multiple rims of various shapes and tones. g) S392-17 (T4)from a Bt-Grt-Sil-Kfs-Pl-Qtz migmatite shows a patchy zoning pattern. The grain is rounded and shows a large embayment on the right side. h) S401-01 (T5) from a leucocratic Crd-Kfs-Pl-Qtz-Grt monzogranite displays a prismatic euhedral grain with a patchy zoning pattern on the BSE image.

Figure 5.1

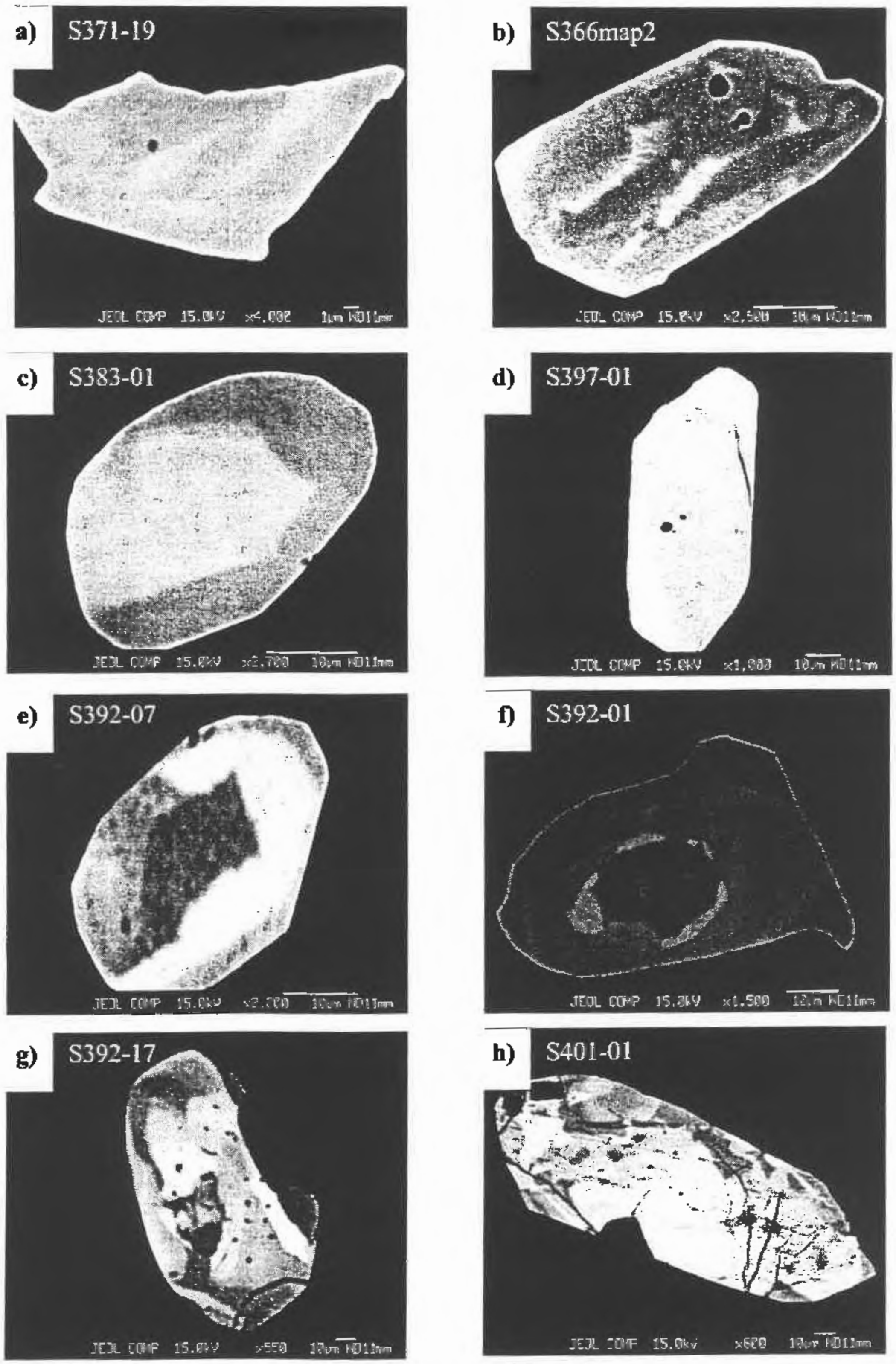
a) S371-19
b) S366map2
c) S383-01
d) S397-01
e) S392-07
f) S392-01
g) S392-17
h) S401-01

Figure 5.2: WDS X-ray maps of Pb, U, Th, and Y showing the zoning pattern for each element on selected representative monazite grains. Colours represent the relative abundance of an element, in increasing order: blue, green, yellow and red. Mineral abbreviations after Kretz (1983).

a) S371-09 (T1) is from a Bt-Ms-Qtz sample. Y and U show no zoning while Th and Pb are weakly zoned.

b) S374-03 (T3) from a Bt-Crd-Ms-Qtz±And sample shows no zoning in U and Pb, and a weak and poorly defined zoning in Th and Y. The minute zone of high Pb content is located on the site of an inclusion. Pb from lap likely accumulated there after the inclusion fell off the thin section during polishing.

c) S383-01 (T4) from a Bt-Grt-Sil-Kfs-Pl-Qtz incipient migmatite shows a distinct and simple concentric zoning in all four elements, although Th zonation is not as clearly defined.

d) S392map5 (T4) from a Bt-Grt-Sil-Kfs-Pl-Qtz migmatite has a strong zoning in Y and to lesser extent in U while Th and Pb are not clearly zoned.

e) S388-02 (T4) from a Bt-Grt-Sil-Kfs-Pl-Qtz migmatite presents a distinct complex concentric zoning pattern in all four elements.

f) S392-17 (T4) from a Bt-Grt-Sil-Kfs-Pl-Qtz migmatite presents a patchy zoning in Y, the three other elements are not clearly zoned.

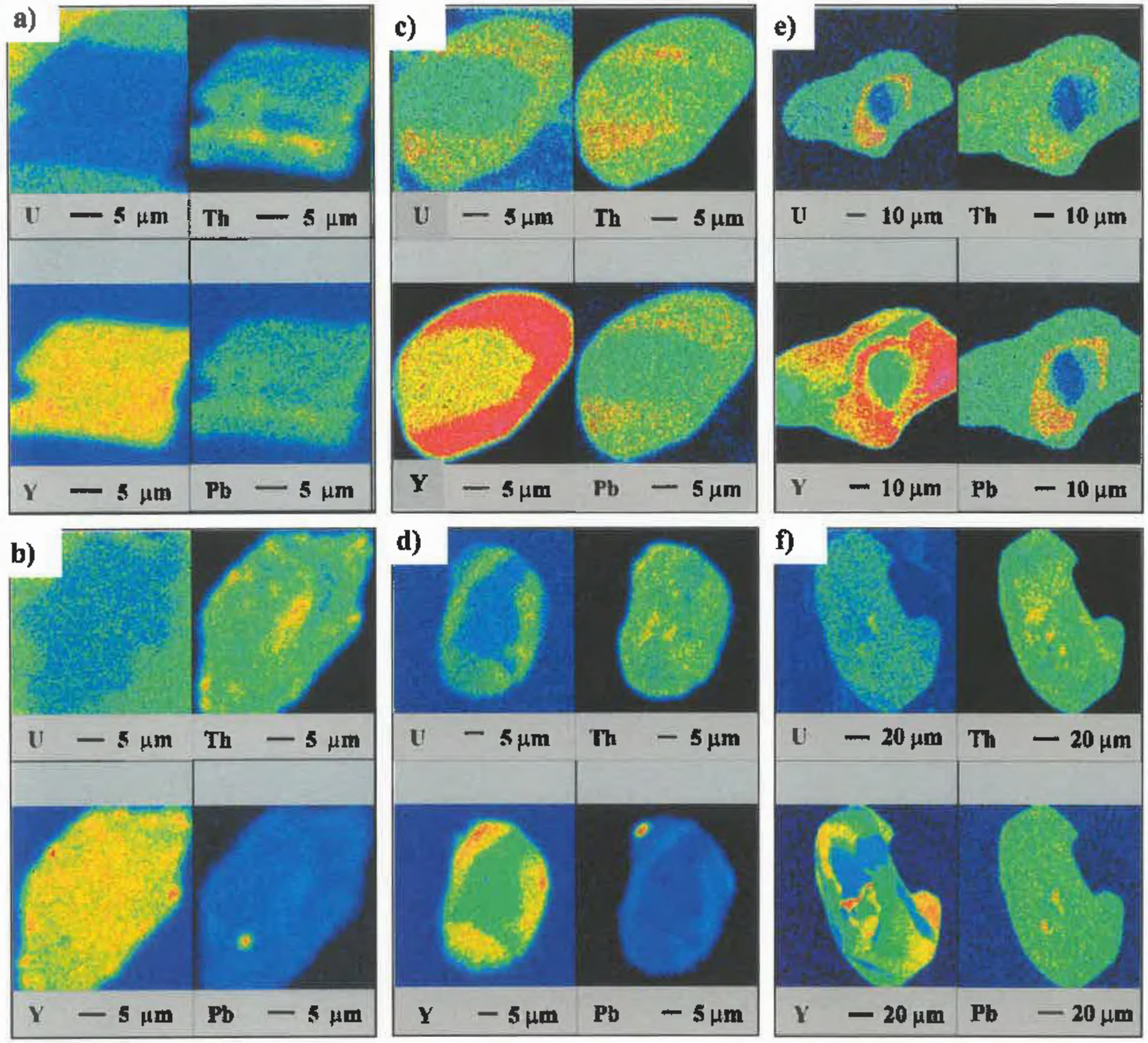

Transect 4 (T4) and Transect 5 (T5). Both transects are above the sillimanite isograd (Ch. 2). These rocks vary from incipient migmatites to peraluminous granites derived from melting of sedimentary rocks (Chapter 3). The migmatites progress from schistose metapelites with rare millimetre-scale veinlets, to interlayered centimetre-size leucosome veins with Bt-Crd-Sil mesosome forming stromatic migmatites, to large pockets of granite (Chapter 3, Appendix 4).

Zoning patterns in monazite were categorized and defined by Zhu and O'Nions (1999). Zoned monazite from the LBF displays two main types of zoning. The most common type is concentric zoning that may be simple (core surrounded by a simple rim; Fig. 5.1c,d; Fig. 5.2c,d) or more complex (core of variable shape enveloped by two or more circular rims that may be discontinuous; Fig. 5.2e). The number of rims is variable, but monazite commonly shows one or two rims, and locally three. Cores of zoned monazite exhibit different shapes. Some grains have a euhedral prismatic core (Fig. 5.1c,d) whereas other grains have a rounded core (Fig. 5.2e); in some cases embayments can be found along the core periphery (Fig. 5.1e,f). Rims can also exhibit a euhedral prismatic (Fig. 5.1d) or rounded shape (Fig. 5.1c), and locally show embayments along the grain boundary (Fig. 5.1g). The other type of zoning commonly observed is a "patchy" pattern defined by multiple patches of different composition that are irregular in size, non-concentric, and randomly distributed in the grain (Fig. 5.1g,h; Fig. 5.2f). This pattern is mainly found in monazite in the leucosomes.

The composition of various domains in zoned monazite was also examined. The investigation was restricted to monazite with concentric zoning because results can easily be grouped in two categories: core and rim analyses. Because of the role of U, Th, and Y in chemical dating, the focus was to compare these elements in cores and rims. For each zone, core or rim, all analyses with a good cation total ($1.975 < \text{total} < 2.025$; based on cations/4.000 oxygens) were averaged for comparison.

Histograms of Th content for cores and rims (Fig. 5.3a,b) show no difference in the distribution of compositions, with 0.057 ± 0.027 in cores and 0.057 ± 0.021

cations/4.000 oxygens in rims. A scattergram (Fig. 5.4a) plotting values of both core and rim for each grain reveals that in 74 % of the grains the rim is richer in Th than the core.

Analysis of the distribution of U values (Fig. 5.3c,d) in rims and cores of zoned monazite shows that U values do not have a strong preferential distribution, although 80% of the cores have U < 0.007 cations/ 4.000 oxygens, whereas only 54% of rims have U < 0.007 cations/ 4.000 oxygens. Similarly, the calculated average U content for the cores is 0.004 ± 0.005 and for the rims is 0.006 ± 0.006 cations/ 4.000 oxygens. The difference between core and rim average U content is very subtle and the two are not statistically different. Therefore, there may arguably be no difference between the overall core and rim composition.

Histograms of Y content (Fig. 5.3e,f) reveal that rims tend to be richer in Y than cores. The average composition of the cores is 0.034 ± 0.014 cations/ 4.000 oxygens whereas rims average is 0.040 ± 0.018 cations/4.000 oxygens. A scattergram (Fig. 5.4b) plotting Y values of both the core and rim for each grain was also produced, showing that in 70% of the grains the rim is richer in Y relative to the core. The symbol plot of Y content in zoned monazite (5.4b) also shows that the difference in Y content between core and rim is greater than the difference in Th content.

Gadolinium shows a subtle difference in concentration between rims and cores of zoned monazite. The histograms (Fig. 5.5a,b) show a shift of the average Gd content towards slightly greater values from 0.019 ± 0.005 cations/ 4.000 oxygens in cores to 0.021 ± 0.005 in rims.

Figure 5.3: (Next page) Histograms of Th, U, and Y values measured in cores and rims of zoned monazites. "*x*" is the arithmetical average calculated for each transect in cations/ 4.000 oxygens. a-b) Histograms of Th content in cores and rims of zoned monazite respectively. No noticeable difference between the two diagrams. c-d) Histograms of U content in cores and rims. Average composition of rims is slightly greater with a wider range of values. e-f) Histograms of Y content in cores and rims. Rims have a greater average Y content.

Figure 5.3

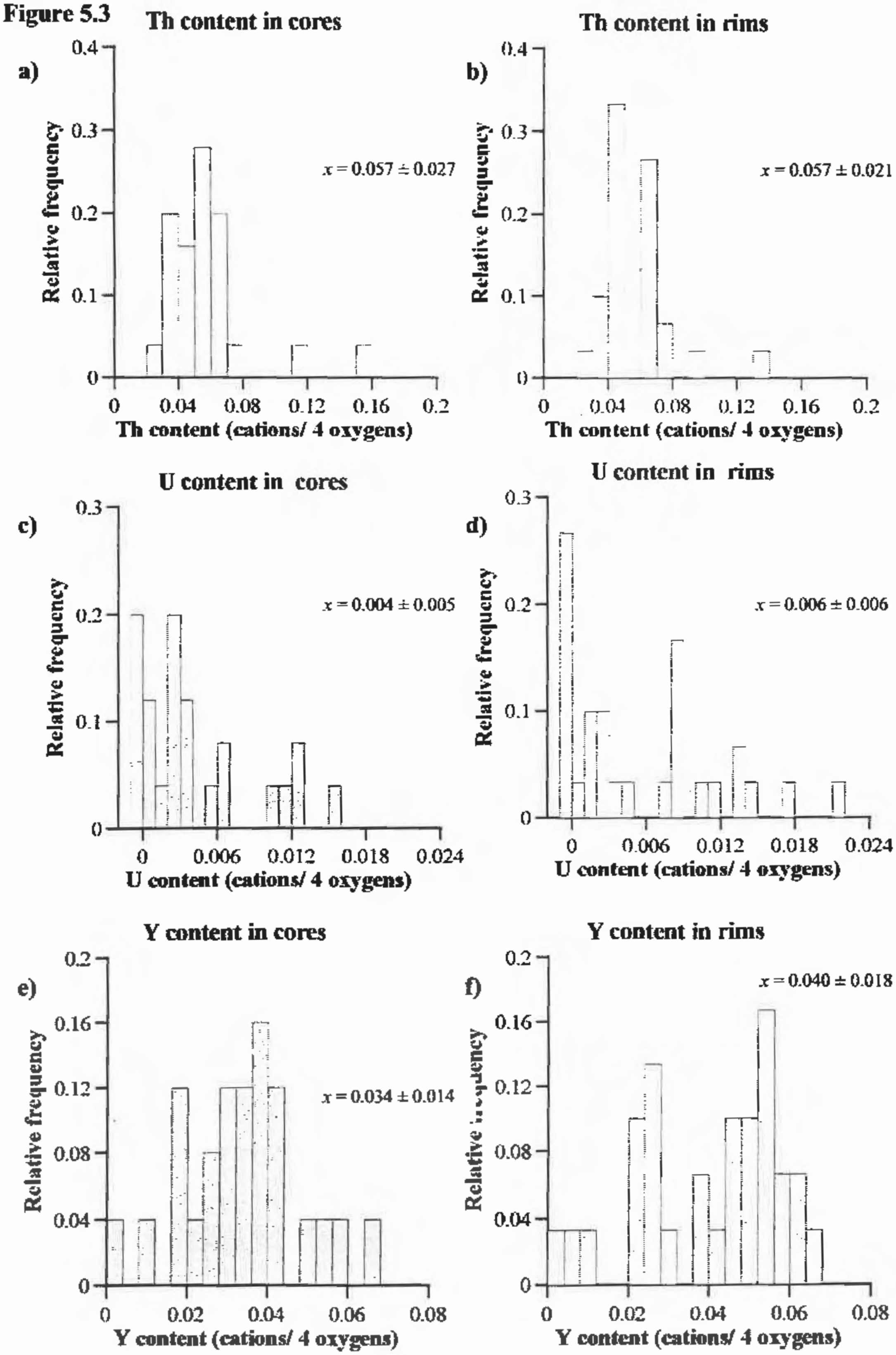
Th content in cores
a)
Relative frequency
$x = 0.057 \pm 0.027$
Th content (cations/ 4 oxygens)
Th content in rims
b)
Relative frequency
$x = 0.057 \pm 0.021$
Th content (cations/ 4 oxygens)
U content in cores
c)
Relative frequency
$x = 0.004 \pm 0.005$
U content (cations/ 4 oxygens)
U content in rims
d)
Relative frequency
$x = 0.006 \pm 0.006$
U content (cations/ 4 oxygens)
Y content in cores
e)
Relative frequency
$x = 0.034 \pm 0.014$
Y content (cations/ 4 oxygens)
Y content in rims
f)
$x = 0.040 \pm 0.018$
Y content (cations/ 4 oxygens)

Yttrium is enriched in the rims relative to the cores, while U and Gd only show subtle increase in content in rims and that Th content is stable. Locally, cores richer than the rims in one or more elements are also observed. Zhu and O'Nions (1999) also reported occurrences of such inverted zoning. Gd, U, and Y are preferentially present in greater amounts in the rim relative to the core, but there is no specific dominant composition for cores or rims. The range of values observed in the rims is similar to the range in values found in the cores, only the average value is higher in the rims.

The Th, U, and Y zoning patterns show that the LBF monazites do not display any systematic correspondence between the distribution of these elements. This was also noted by Pyle et al. (2001) who interpreted the non-correspondence between Th and Y as an indication that Th and Y distribution in monazite is controlled by independent reservoirs. Major Y sinks are garnet and xenotime in pelitic rocks (Pyle, 2001; Pyle and Spear, 2003b), whereas zircon may be an important controlling factor for the Th budget under certain conditions (Bea, 1996).

Previous studies have examined the boundary between distinct chemical zones and concluded that compositional change is generally sharp without a distinguishable transition zone (e.g., Zhu and O'Nions, 1999). This means that either no solid-state diffusion of elements occurred after closure of the chemical system, or the diffusion range was smaller than the maximum resolution of the imaging technique used. Hence, it is generally well accepted that zoning in unaltered monazite has sharp boundaries. Crowley and Ghent (1999) showed that even monazite with hydrothermally recrystallized rims generally displays a sharp boundary between rim and core.

This study did not focus on the nature of the boundary between different compositional zones in metamorphic monazite as this is already well documented (Zhu and O'Nions, 1999). Few line scans using WDS were obtained from zoned grains. Compositional profiles were obtained for Y and Th. Results generally agree with patterns observed on X-ray maps and BSE images. Locally, X-ray line scans show a decoupling between Th and Y, where Y is strongly zoned and Th has a constant distribution

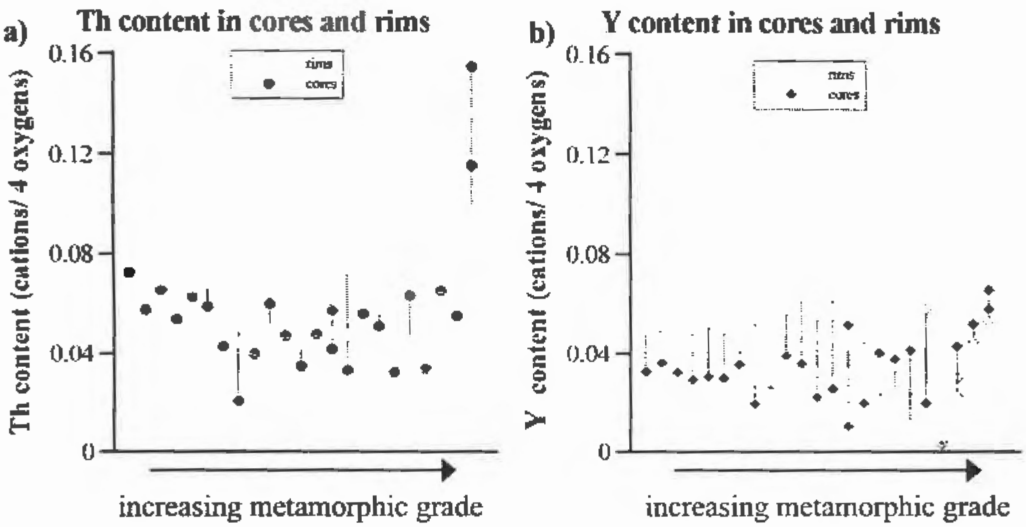

Figure 5.4: Figures 5.4a-b below present the compositional variation between core and rim of individual grains for Th and U content respectively. Rim (s) and core (s) from the same grain have the same *x* value and are linked by a solid line. On the abscissa, the grains are ordered according to their increasing sample number. This corresponds roughly to an increase, from the left to the right, of the metamorphic grade and abundance of leucosome in the rock. All grains are from samples collected in T4 or T5. Only grains exhibiting a concentric zoning pattern were considered in this diagram. Note compositional variation between core and rim is greater for Y than for Th. Th content is also commonly greater than Y content.

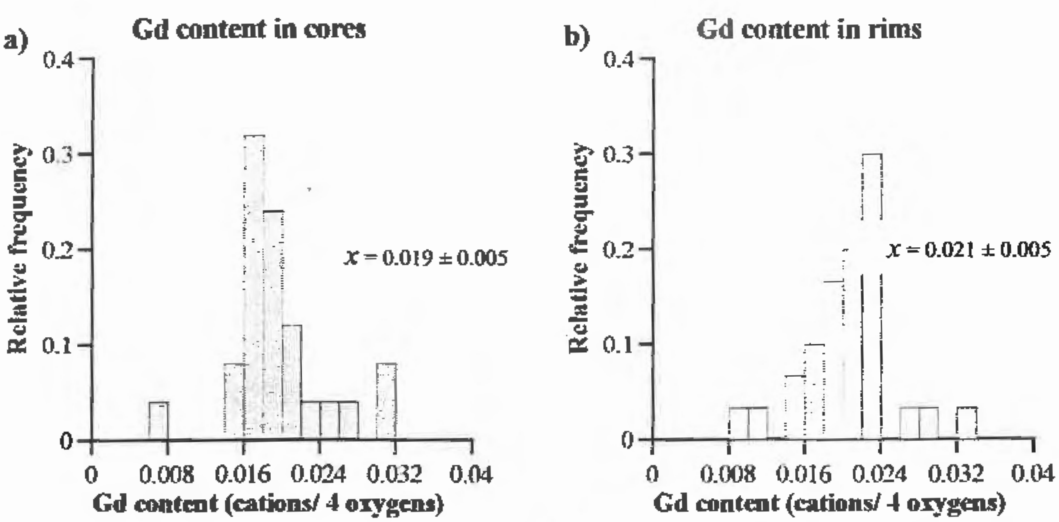

Figure 5.5: Histograms 5.5a-b below present the distribution of Gd values measured in cores and rims of zoned monazites. "*x*" is the arithmetical average calculated from all the data available for the zone with the standard deviation (± cations/ 4 oxygens).

throughout the chemical zones, or vice-versa. This supports observations made with some X-ray maps that these two elements vary independently. In other grains, Y and Th vary antithetically. For instance, Figure 5.6 shows a line scan through monazite grain S392-09 where high Th zones correspond to low Y zones, and vice-versa. The line scans correlate with results from Th and Y X-ray maps.

5.4 Major element chemistry

This study investigated the major element chemistry of monazite (technical details and settings given in Chapter 4 and Appendix 1). Both qualitative and quantitative analyses were obtained using WDS. Analytical conditions were optimised specifically for monazite analysis. Elements analysed were, in alphabetical order: Ca, Ce, Dy, Gd, La, Nd, P, Pr, Sm, Si, Th, U, and Y. Unless otherwise mentioned results in this chapter are reported in cations/ 4.000 oxygens. Section 5.4.1 addresses the issue of the reproducibility of the results using the Dalhousie JEOL 8200. The following sections present results from major element analysis.

5.4.1 Reproducibility of the results

The level of reproducibility of the results is a very important issue. To be able to draw conclusions from the results obtained from different monazite grains or chemical zones, one must be able to show that the variation in the results is not caused by analytical error or the resolution limit of the technique, but reflects real chemical changes. To achieve the best precision in the analysis of monazite, the choice of standards and controls used is the first important step. At the beginning of the implementation process, all REE`s were standardised using the Drake and Weill (1972) synthetic glass REE standards. Synthetic $CePO_4$ and $LaPO_4$ produced at RPI (Pyle, pers. comm.) were later used to reduce matrix effect. The switch to phosphate standards for the two main REE components of monazite improved the precision and reproducibility of the results (Fig. 5.7). A few other changes were made during the implementation process, e.g. Ce and La were moved from the PETJ to the LIF crystal and ThO_2 and UO_2 were used rather than metal standards. As recommended by Pyle et al.

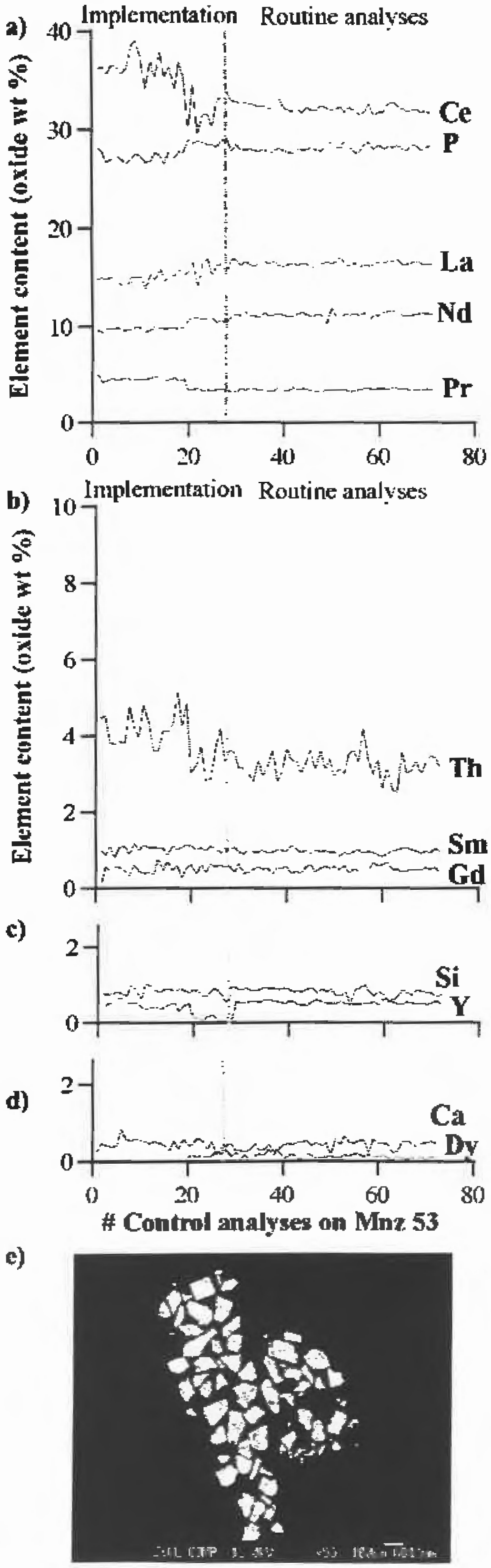

Figure 5.7 : Figures a-d) on the left present results of replicate analyses undertaken on Mnz 53, an in-house monazite control. Note that analyses acquired during the implementation period are also plotted. Most analyses used in this study were acquired during the routine analysis period. U is not plotted because its low content is commonly below the detection limit. In e) a BSE image shows the grain mount of Mnz 53. Appendices 1 provides details on Mnz 53 composition.

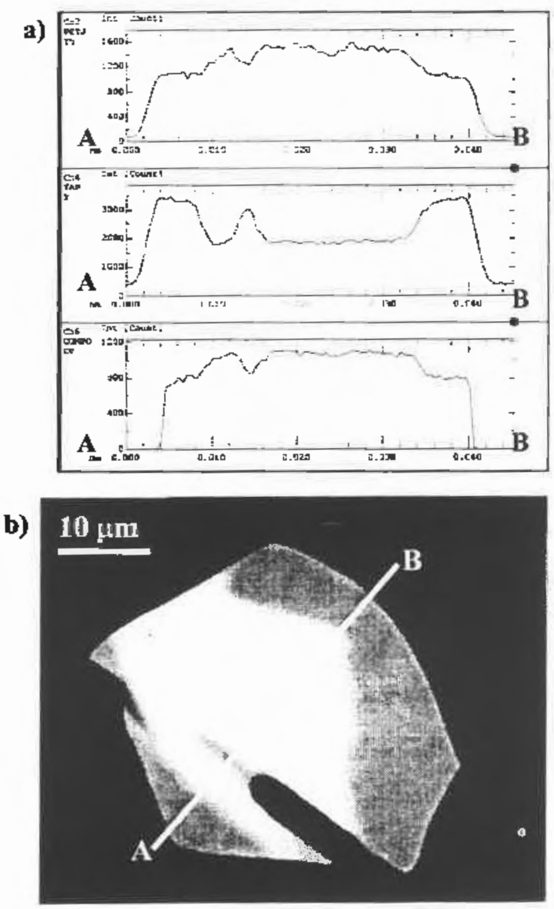

Figure 5.6 : A BSE image of grain S392-09 is shown in b) above. The A-B line marks the location of the WDS line scan. The Th, and Y WDS line scan profiles are presented in a) above. Note in this grain Th and Y vary in an antithetical manner. The Y zones are more contrasted.

(2003) and Scherrer et al. (2000), standards with high element concentrations were preferentially chosen.

Figure 5.7a-d shows replicate analyses of Mnz 53, an in-house control used since the beginning of the implementation process, with results for different elements. Mnz 53 is a set of monazite grains mounted with epoxy and is part of a set of standards provided by Ward™. During the implementation period results were unstable for some elements, but improvement in both the procedure and analytical settings provided better precision and an acceptable level of reproducibility. In BSE imaging mode Mnz 53 grains appeared quite homogeneous, and replicate analyses seem to show that compositional variations, if any, are minor.

Accuracy of the analytical settings used for this study was verified by multiple spot analyses on samples previously analysed by other EMP laboratories. For this purpose, the Dalhousie Regional Electron Microprobe Laboratory (DREML) collaborated with other universities to characterise the chemical composition of four monazite samples provided by M. Bersch from U. Alabama. Results from the Dalhousie EMP are similar to those obtained by other laboratories which used both EMP and LA-ICP-MS techniques. Repeated analyses of the monazite samples yielded a reasonable level of reproducibility. The same settings were used to analyse Mnz 53 during routine analyses and the consistency of the results confirmed their accuracy.

5.4.2 Results

Results from the chemical investigation of the LBF monazites are presented below. For each element in each transect, all analyses with a good cation total ($1.975 < \text{total} < 2.025$; based on cations/4.000 oxygens) were averaged together. Results are grouped by transect because despite the fact they cross isograds the short transect length (2-4 km) means that samples from a same transect experienced similar P-T conditions. Histograms showing the relative frequencies of each element within each transect are presented in Figures 5.8 to 5.19. These graphs provide a sense of the dominant value of the element at each grade and also show the range of values found. An average value (x)

is also calculated for each transect. Elements are grouped into four sets: the LREE`s, comprising Ce, La, Nd, Pr, and Sm; the HREE`s, comprising Gd and Dy; the key elements for geochronology: U, Th, and Y; and other cations: P, Si, and Ca. Below is a selection of representative analyses for different samples (Table 5.2). Full description of the samples can be found in Appendix 4.

Table 5.2: Representative monazite compositions from this study. Mineral abbreviations after Kretz (1983).

Grain	**S366-07**	**S371-19**	**S373-04**	**S378-03**	**S383-02**	**S392-05**	**S392-01**	**S397-01**
Mineral	Bt-Ms-Qtz-Crd	Bt-Ms-Qtz	Bt-Ms-Crd-Qtz	Bt-Ms-Crd-Qtz-Pl-Sil-And-	Bt-Kfs-Pl- Qtz-Sil- Grt-	Bt-Kfs-Pl- Crd-Qtz-Sil-Grt-	Bt-Kfs-Pl- Crd-Qtz-Sil-Grt-	Kfs-Pl-Qtz-Crd-Grt-Sil
Transect	2	1	3	3	4	4	4	5
Analysis #	159	169	56	252	554	282	212	120
P_2O_5	28.94	29.84	29.48	28.98	29.07	28.50	29.15	29.33
SiO_2	0.22	0.37	0.27	0.26	0.23	0.19	0.12	0.34
CaO	0.98	0.92	0.84	0.85	0.83	1.36	0.83	1.47
ThO_2	4.47	4.33	4.55	5.99	5.51	6.83	4.63	6.58
UO_2	0.27	0.26	0.22	0.02	0.29	0.30	0.034	0.79
Y_2O_3	1.12	1.02	1.25	1.02	1.67	1.51	2.45	2.18
La_2O_3	14.24	14.33	14.46	12.52	14.19	13.13	12.99	12.34
Ce_2O_3	27.88	28.02	28.09	31.60	31.09	30.18	30.92	26.06
Pr_2O_3	3.49	3.57	3.53	4.69	4.33	4.45	4.34	3.29
Nd_2O_3	12.73	12.85	12.45	10.73	9.93	10.00	10.31	11.35
Sm_2O_3	2.06	2.00	2.05	2.08	1.94	2.15	1.68	1.87
Gd_2O_3	1.54	1.32	1.36	1.58	1.23	1.31	1.60	1.76
Dy_2O_3	0.49	0.51	0.58	0.00	0.00	0.00	0.00	0.79
Total	98.43	99.34	99.14	100.31	100.31	99.91	99.06	98.15

Note: Values in oxide weight percent (wt %).

5.4.2.1 Light rare-earth elements (LREE):

5.4.2.1.1 Cerium, lanthanum, and neodymium:

Figures 5.8a-e, 5.9a-e, and 5.10a-e show relative frequency histograms of Ce, La, and Nd content per transect. All three elements present a decrease in abundance from T1 to T5. Variations in content of the three elements from T1 to T3 are minor relative to variations from T3 to T5. The three elements decrease in varying amounts from 10% to 18%. Average Ce content varies from 0.448 ± 0.030 cation/4.000 oxygens in T1 to 0.436 ± 0.036 in T3 and 0.373 ± 0.042 in T5. Lanthanum content varies from 0.204 ± 0.019 cations/ 4.000 oxygens in T1 to 0.204 ± 0.021 in T3 and 0.168 ± 0.026 in T5. Nd content varies from an average of 0.170 ± 0.015 in T1 to 0.164 ± 0.017 in T3 and 0.152 ± 0.012 cations/ 4.000 oxygens in T5 (Table 5.3).

5.4.2.1.2 Praseodymium and samarium:

Figures 5.11a-e and 5.13a-e respectively show the variation in Pr and Sm content per transect. Sm seems unaffected by the variation in metamorphic grade. Unlike all other LREE`s, Sm does not show a decrease in abundance with increasing metamorphic grade. Sm shows a very small increase from 0.027 cations/ 4.000 oxygens in T1 to 0.03 in T5. Note that the 0.030 average in T5 includes few anomalously high Sm values. If these values are excluded, the average composition in T5 is similar within error to all other previous transects. On the other hand, Pr presents variations similar to other LREE. Average Pr content is relatively stable from T1 to T4 and drops greatly from T4 to T5.

5.4.2.2 Heavy rare-earth elements (HREE):

5.4.2.2.1 Gadolinium and dysprosium:

Figure 5.14a-e shows increasing Gd abundance with increasing metamorphic grade. From T1 to T5 the average content in Gd and the range of values steadily increase. The Gd average composition varies from 0.017 ± 0.002 cations/ 4.000 oxygens in T1 to 0.018 ± 0.003 in T3 and 0.022 ± 0.005 in T5. No diagram of Dy is presented, but average values were calculated per transect. The results show that like Gd, Dy becomes more

Figures 5.8 & 5.9: (Next page) Histograms of the relative frequencies of Ce and La values measured in monazites from each transect. Average content "*x*" with standard deviation (± cations/4.000 oxygens) is given for each transect to the right of the histograms. 5.8a-e) Histograms of Ce content in Transects 1 to 5. Note that average content and range of values do not vary much between T1 and T3 and steadily decreases from T3 to T5. 5.9a-e) Histograms of La content in Transects 1 to 5. Similarly to Ce, average content and range of values do not vary much between T1 and T3, and steadily decreases from T3 to T5.

Figure 5.8

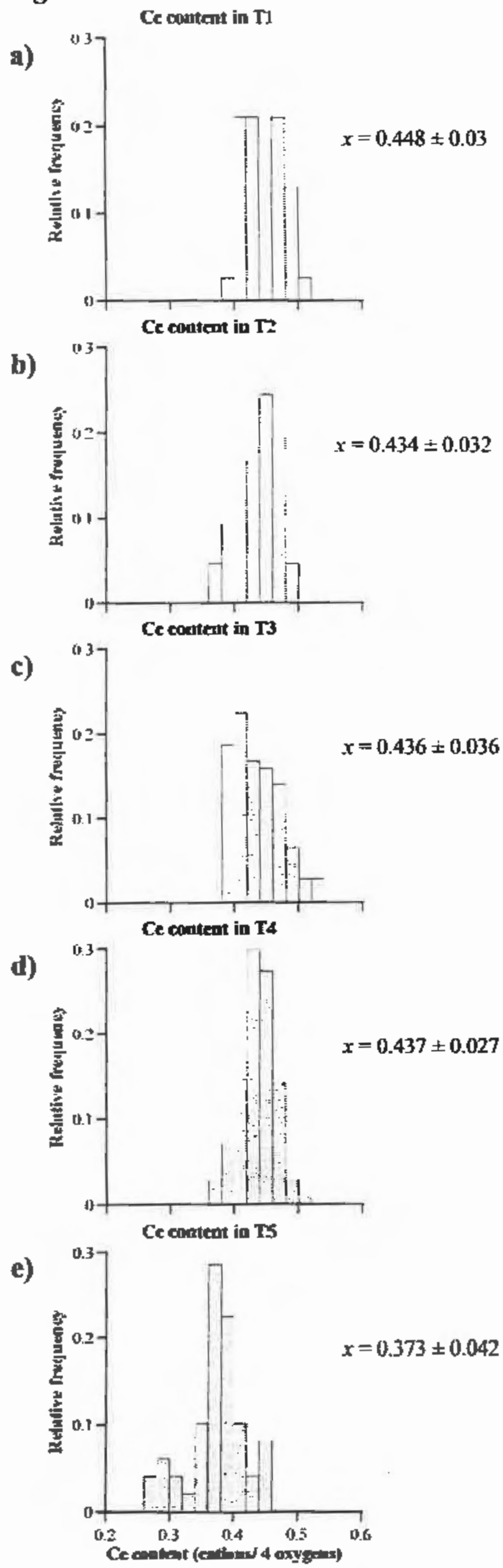

Figure 5.9

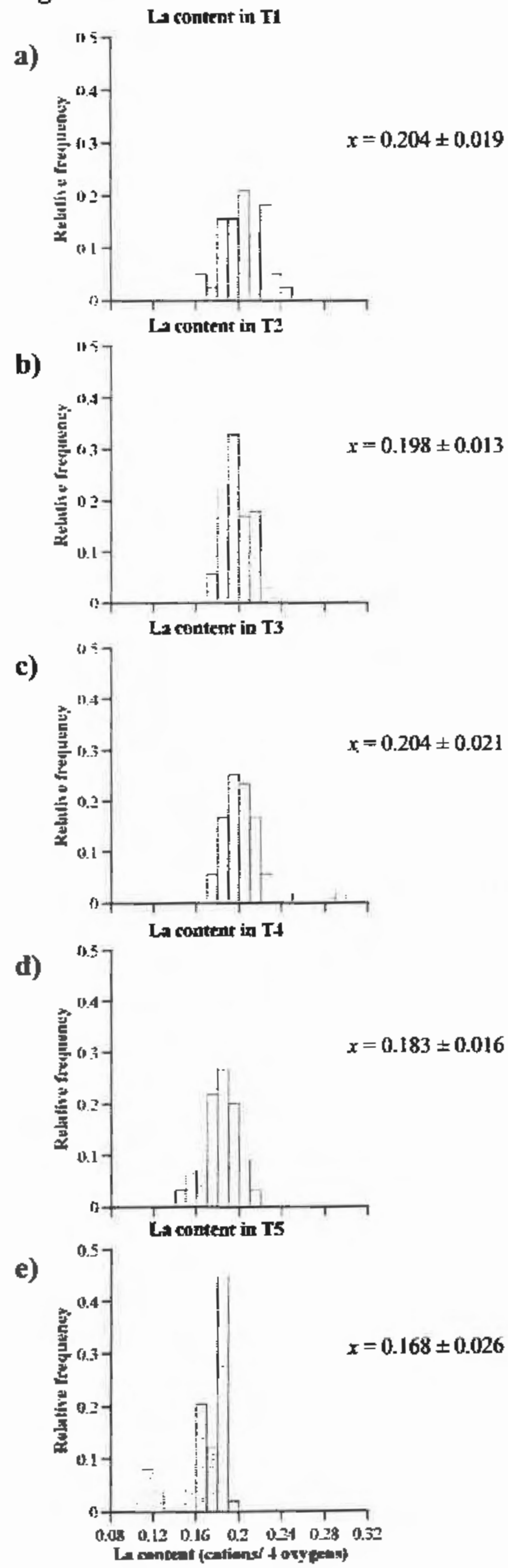

abundant in monazite with increasing metamorphic grade (Table 5.3).

5.4.2.3 Calcium and silicium:

Figures 5.16a-e and 5.17a-e display variations of Ca and Si content in monazite with increasing metamorphic grade. These histograms reveal an increasing abundance in Ca and Si from lower to higher grade transects. In the case of Ca, changes from T1 to T3 are very subtle, but from T3 to T5 changes are sharp with Ca averages shifting to greater values. Average Ca content in T1 is 0.030 ± 0.010 cations/ 4.000 oxygens, 0.036 ± 0.016 in T3 and 0.083 ± 0.023 in T5 (Table 5.3). In T5, no Ca value smaller than 0.014 were found while this corresponds to the highest value found in T1. Silicon does not show a systematic variation and average values remain similar in the first four transects. However, the range of Si values measured increases with grade, and in T5, Si displays a large increase relative to other transects (Table 5.4). Increase in Ca content from T1 to T5 is greater than for Si. This is important for examining the relative importance of brabantite and huttonite substitution mechanisms.

5.4.2.4 Phosphorus:

The P content in monazite from Transects 1-5 varies within a narrow range (Fig. 5.12a-e), and does not show any trend related to metamorphic grade. In fact, average P composition is similar in all transects, varying between 0.977 ± 0.017 cations/ 4.000 oxygens in T4 and 0.985 ± 0.019 in T2 (Table 5.3). The relatively stable P content, and the range of values very close to 1, indicate that substitutions in the 4-fold site occupied by P are not common and not dependent on the metamorphic grade. Correspondingly the Si content varies between 0.008 ± 0.005 in T3 and 0.014 ± 0.008 cations/ 4.000 oxygens in T5. The amount of Si measured almost exactly corresponds to

Figures 5.10 & 5.11: (Next page) Histograms of relative frequencies of Nd and Pr values measured in monazite from each transect. Average content "x" with standard deviation (± cations/4.000 oxygens) is given for each transect to the right of the histograms. 5.10a-e) Histograms of Nd content in Transects 1 to 5. Note that average content and range of values vary slightly from T1 to T3 and decreases between T3 and T4. 5.11a-e) Histograms of Pr content in Transects 1 to 5. Average content and range of values do not vary much from T1 to T4 and drastically decreases between T4 and T5.

Figure 5.10

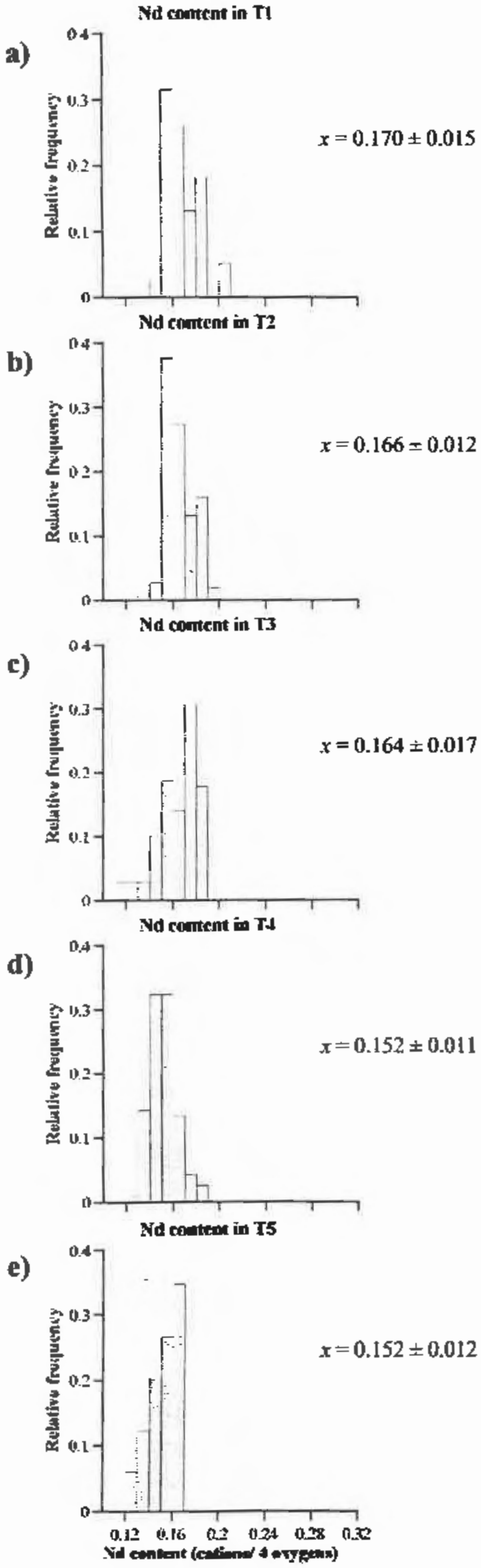

Figure 5.11

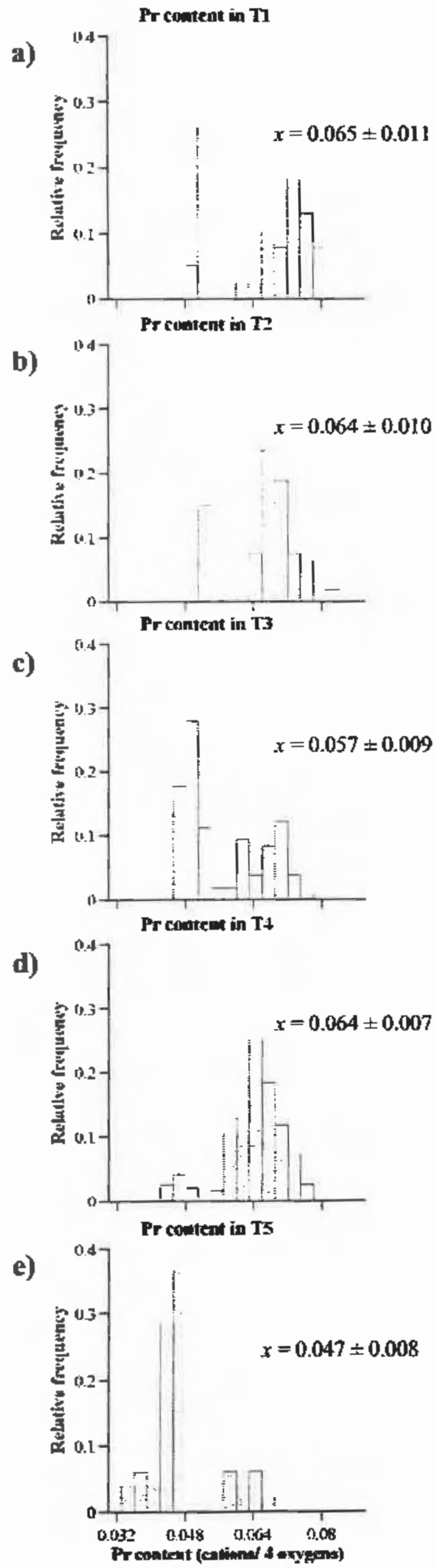

[P] –1. Silicon has an atomic radius similar to P, suggesting that most, if not all, Si incorporated in monazite substitutes for P in the 4-fold site.

5.4.3 Elements for geochronology

5.4.3.1 Thorium:

Histograms of Th content (Fig. 5.19a-e) show a distinct increase in content with increasing metamorphic grade. Similar to other elements, there is practically no variation in content between T1 and T3. However, the average composition of Th varies from 0.039 ± 0.019 in T1 to 0.041 ± 0.016 in T3 and 0.077 ± 0.025 cations/ 4.000 oxygens in T5.

5.4.3.2 Uranium:

Uranium content steadily increases from T1 to T5 (Fig. 5.15a-e). Similar to other elements, the increase is relatively small from T1 to T3, but much more important from T3 to T5 (Table 5.3). The range of values is much bigger in T4, but gets narrower in T5.

5.4.3.3 Yttrium:

Yttrium (Fig. 5.18a-e) also presents an important increase in content with higher metamorphic grade. The average Y content increases at every transect. The increase is minor from T1 to T3, but greater from T3 to T5 (Table 5.3). The range of Y values measured in T4 and T5 is much larger in comparison to the narrow range of values found in T1 and T2.

5.5 Pearson's correlation coefficient

Variation of all elements through every transect has been presented in the previous sections. The correspondence in the way that two sets of independent data vary

Figures 5.12 & 5.13: (Next page) Histograms of relative frequencies of P and Sm values measured in monazite from each transect. Average content "*x*" with standard deviation (± cations/4.000 oxygens) is given for each transect to the right of the histograms. 5.12a-e) Histograms of P content in Transects 1 to 5. Note that average content and range of values do not vary much from T1 to T3 and steadily decreases from T3 to T5. 5.13a-e) Histograms of Sm content in Transects 1 to 5. Similarly to P, average content and range of values do not vary much from T1 to T3 and steadily decreases from T3 to T5.

Figure 5.12

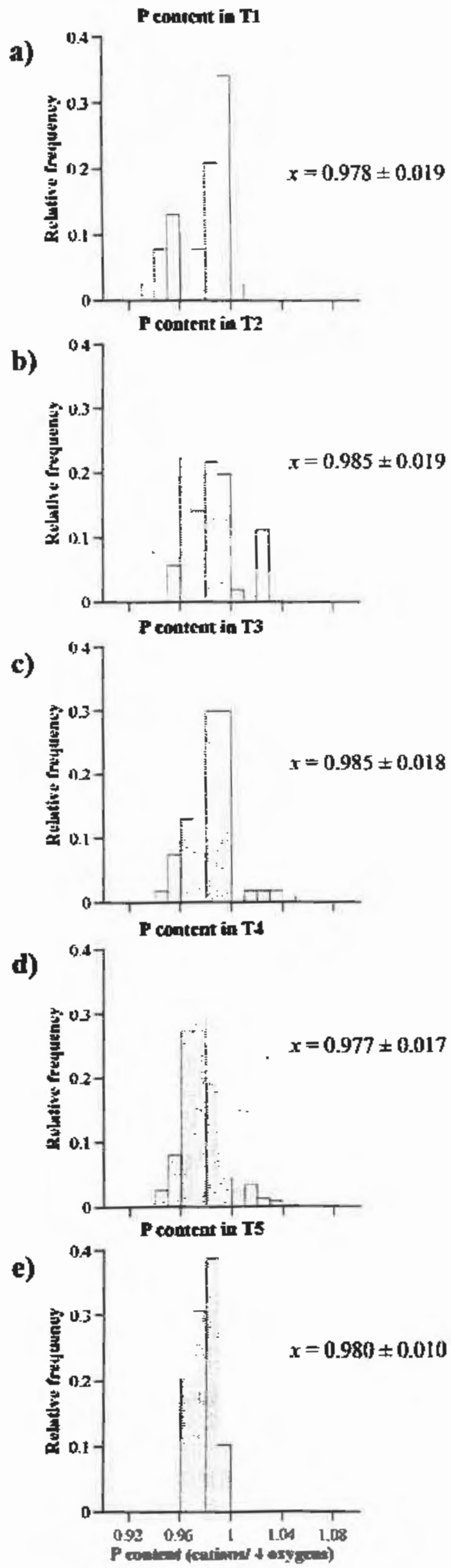

Figure 5.13

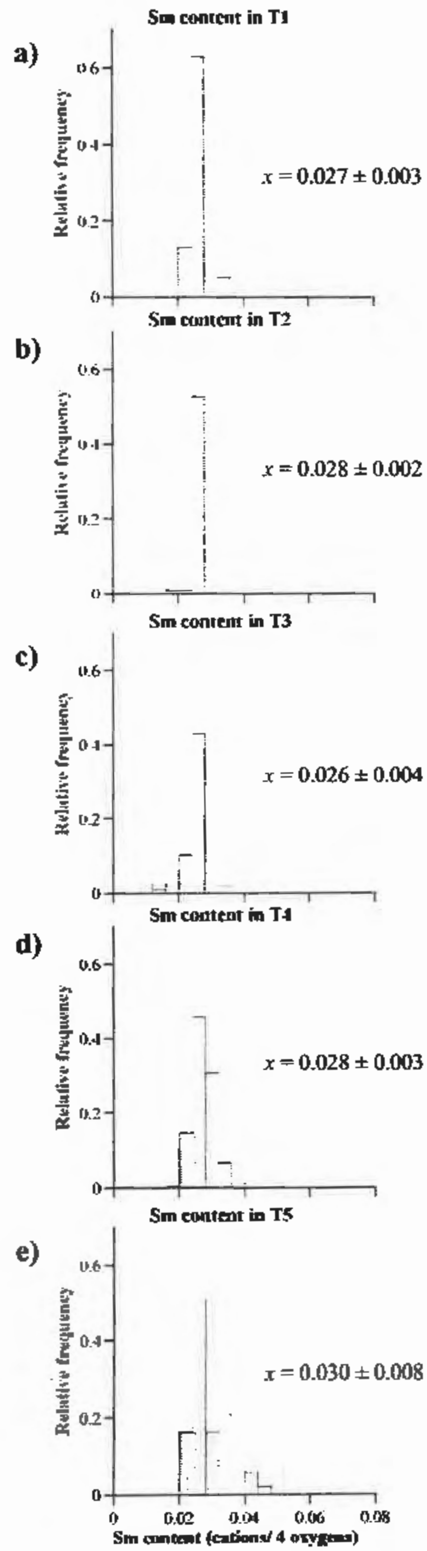

is termed correlation. This section analyses the level of correlation between all elements by using Pearson`s correlation coefficient. This is a statistical tool that measures the possibility that a relationship exists between two independent variables. Pearson's correlation coefficient can only verify the strength of a linear relationship between two sets of data, by measuring how closely variations of both variables are associated (Milton, 1992). The value of Pearson's correlation coefficient is calculated using an Excel™ function. Values can vary from -1 to +1. The sign before the Pearson's coefficient value reflects the slope of the linear relationship. Positive values indicate that large values from both sets of data tend to be paired. A negative value indicates an inverse correlation with small values from the first set being paired with large values from the second set, and vice-versa. In other words, a negative sign indicates that the values vary in an antithetical manner. The number indicates the quality of the correlation, a zero meaning that data are not correlated (random) while a value of ±1 means that the data show a perfect linear correlation.

Pearson's correlation coefficient was applied to major element analyses acquired through this study. All possible pairs of elements were tested and Table 5.4 below shows element pairs with the highest correlation coefficient. Measures of correlation between various elements can be insightful in determining which elements play a major role in the chemical variation of monazite. It is important to manipulate these data with care, especially in complex system where variations involve three or more elements.

The strongest correlation coefficient was calculated for Ca+Si vs Th+U. This supports the suggestion made earlier that these elements are incorporated into monazite via paired substitution mechanisms. Further discussion of substitution mechanisms is

Figures 5.14 & 5.15: (Next page) Histograms of relative frequencies of U and Gd values measured in monazite from each transect. Average content "x" with standard deviation (± cations/4.000 oxygens) is given for each transect to the right of the histograms. 5.14a-e) Histograms of Gd content in Transects 1-5. Similarly to U, average content and range of values steadily increase from T1 to T5. But, variations in average Gd content are not greater from T3 to T5. 5.15a-e) Histograms of U content in Transects 1 to 5. Note that average content and range of values steadily increases from T1 to T5 with greater variations from T3 to T5.

Figure 5.14

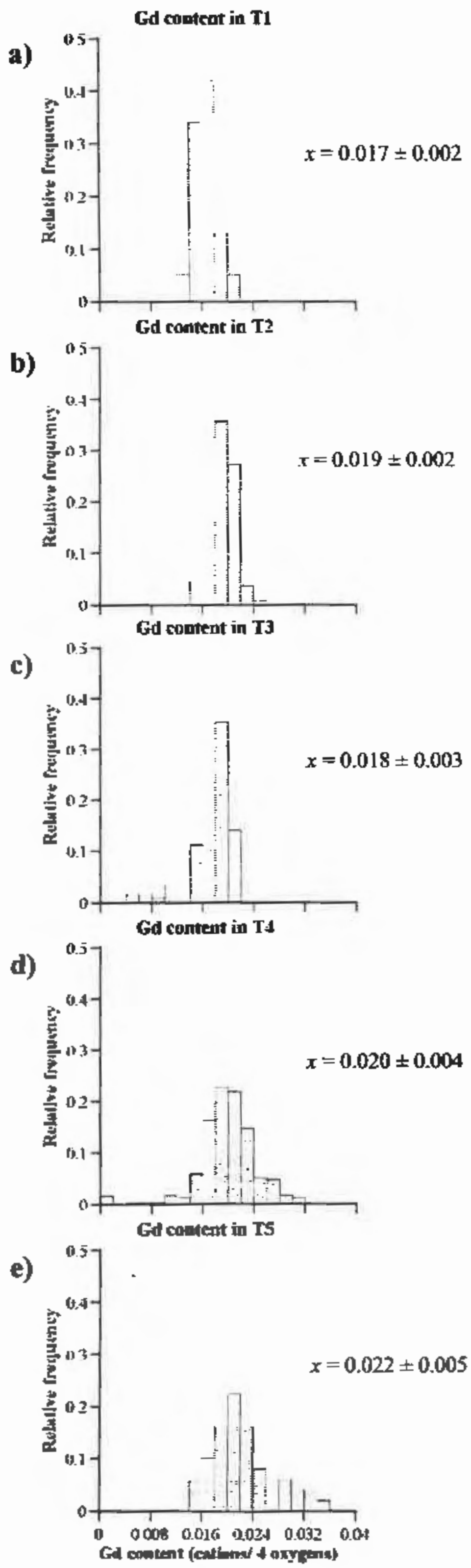

Figure 5.15

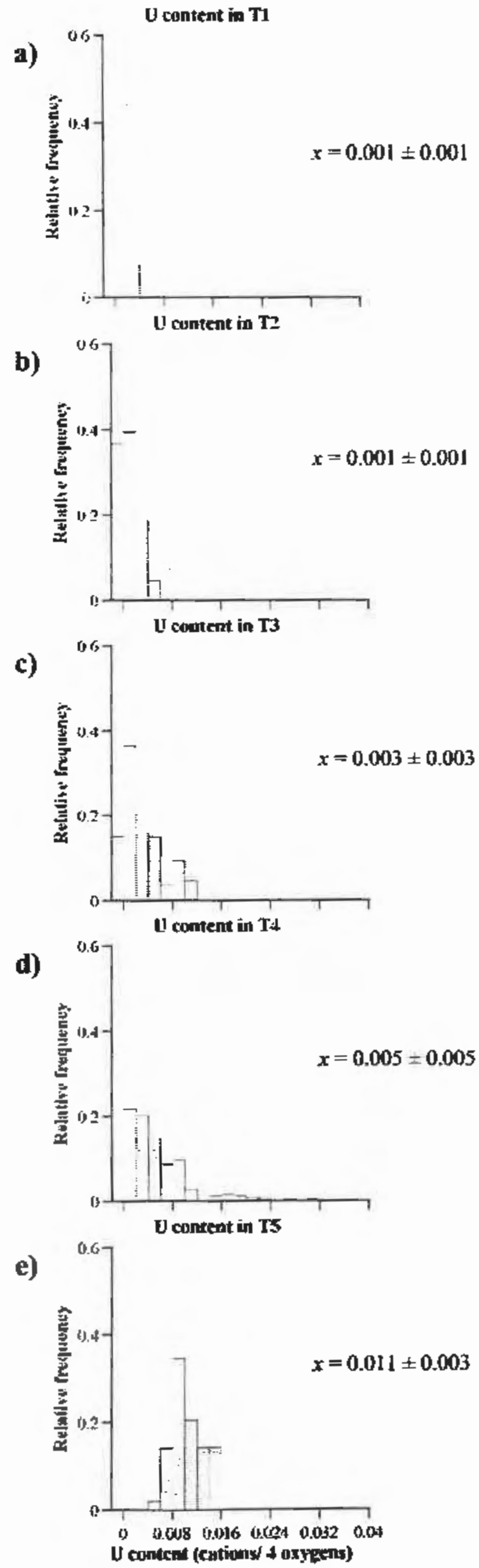

Table 5.3: Pairs showing best Pearson's correlation coefficient value. Data from all the transects were used for calculations.

Element pair	Pearson's factor	Level of correlation	Element pair	Pearson's factor	Level of correlation
Ca+Si vs Th+U	0.91	strong +	Pr vs Dy	-0.85	moderate -
Ca vs Th	0.81	moderate +	LREE vs Th+U+Ca+Si	-0.83	moderate -
Ce vs Pr	0.75	moderate +	La vs Ca	-0.74	moderate -
Ca vs U	0.67	moderate +	Ce vs Dy	-0.74	moderate -
Sm vs Gd	0.66	moderate +	La vs Th	-0.71	moderate -
Ca vs Y	0.62	moderate +	Y+HREE vs Th+U+Ca+Si	-0.69	moderate -
Y+HREE vs LREE	0.55	moderate +	Ce vs Ca	-0.66	moderate -
P vs Dy	0.53	moderate +	La vs Y	-0.62	moderate -
Y vs U	0.51	moderate +	P vs Pr	-0.55	moderate -
			Y vs Nd	-0.53	moderate -
			Ce vs P	-0.50	moderate -
			Ce vs Th	-0.50	moderate -

presented in Section 5.5. Ca shows a strong positive correlation with U and Y. Hence, Y and U also show a good positive correlation. Other positive correlations exist between LREE's, as these elements all tend to be less abundant with higher grade. Phosphorus yielded a moderate correlation value with Dy and Pr. In the previous section, it was

Figures 5.16 & 5.17: (Next page) Histograms of relative frequencies of Ca and Si values measured in monazite from each transect. Average content "x" with standard deviation (± cations/4.000 oxygens) is given for each transect to the right of the histograms. 5.16a-e) Histograms of Ca content in Transects 1 to 5. Note that average content and range of values do not vary much from T1 to T3 and greatly increases from T3 to T5. 5.17a-e) Histograms of Si content in Transects 1 to 5. Silicon slightly decreases from T1 to T4 and greatly increase between T4 and T5.

Figure 5.16

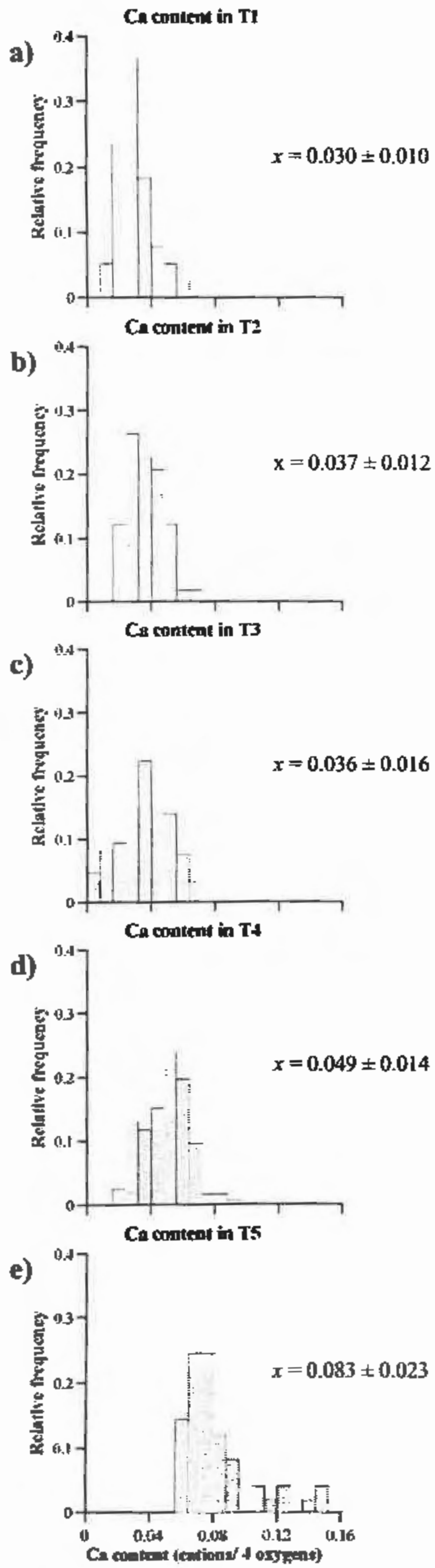

Figure 5.17

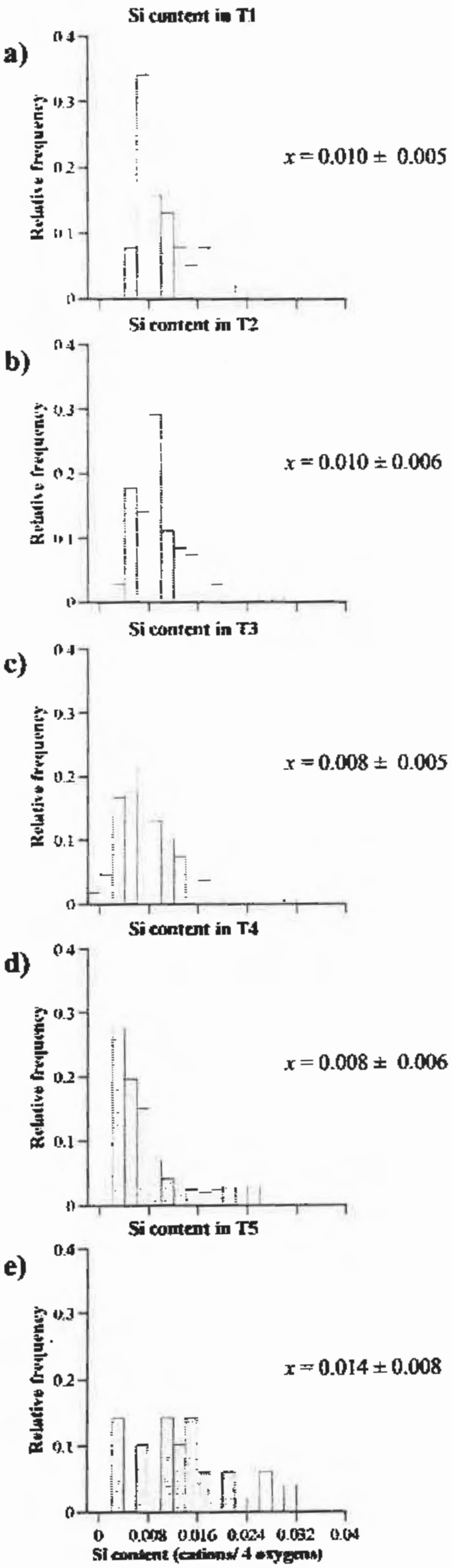

shown that the overall variation in P content is minor. Consequently, correlations with P may not bear much significance.

Interestingly Y+HREE vs LREE yields a moderate positive correlation. Y+HREE vs U+Th+Ca+Si has a negative correlation, while Y is generally positively correlated with U and Ca, and negatively correlated with LREE. This might suggest that HREE are positively correlated with LREE as shown between Gd and Sm. Previous sections showed that HREE increase with metamorphic grade whereas LREE decrease. This unexpected correlation may indicate that the increase in HREE is not only controlled by metamorphic grade, but also by the Ca+U+Th+Si abundance which controls the abundance of LREE.

Both Th and Y are negatively correlated with LREE, but there is no correlation between the variation in these two elements. This agrees with observations from chemical zoning that there was no apparent coupling between these elements. This supports the suggestion that the abundance of Th and Y is controlled by two independent reservoir systems (Pyle et al., 2001).

5.6 Substitution end-members

If Th and U are incorporated into monazite only via huttonite and brabantite substitutions, a plot of Ca+Si/Th+U content should show a linear correlation (Zhu and O'Nions, 1999; Spear and Pyle, 2002). Pearson`s correlation coefficient calculated with analyses from this study also indicates a strong linear relationship between these two pairs of elements (Section 5.5). All major element analyses are plotted in Figures 5.23a-c. Figure 5.23a shows a strong linear correlation between the Si+Ca and Th+U data. The

Figures 5.18 & 5.19: (Next page). Histograms of relative frequency of Y and Th values measured in monazite from each transect. Average content "x" with standard deviation (± cations/4.000 oxygens) is given for each transect to the right of the histograms. 5.18a-e) Histograms of Y content in Transects 1 to 5. The average content and range of values steadily increases from T1 to T3 and double between T3 and T4. From T4 to T5 the average data only slightly increases. 5.19a-e) Histograms of Th content in Transects 1-5. Similarly to Y, average content and range of values steadily increases from T1 to T3 and greatly increases from T3 to T5.

Figure 5. 18

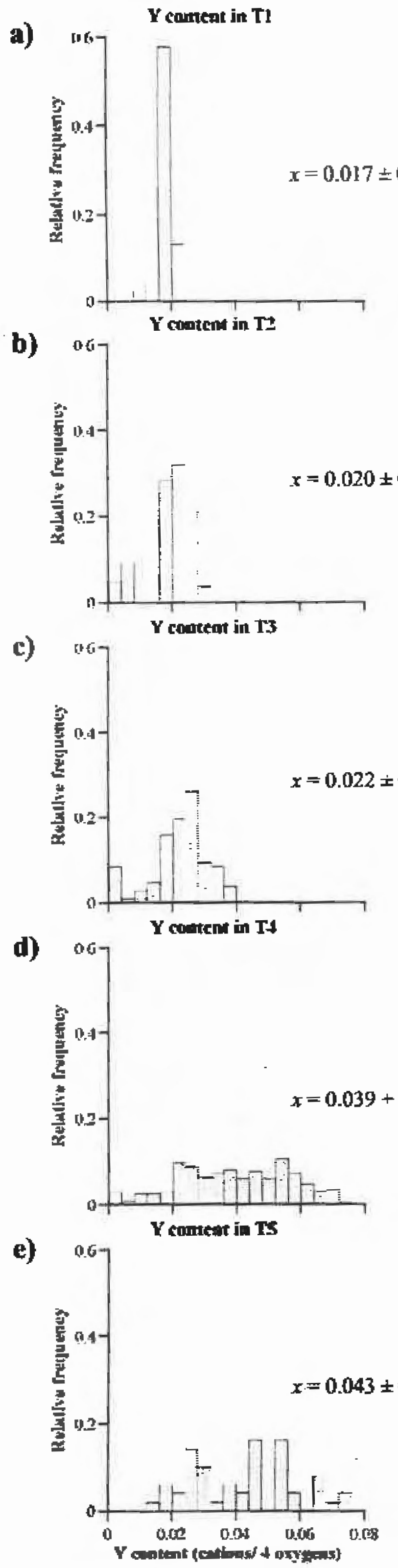

Figure 5.19

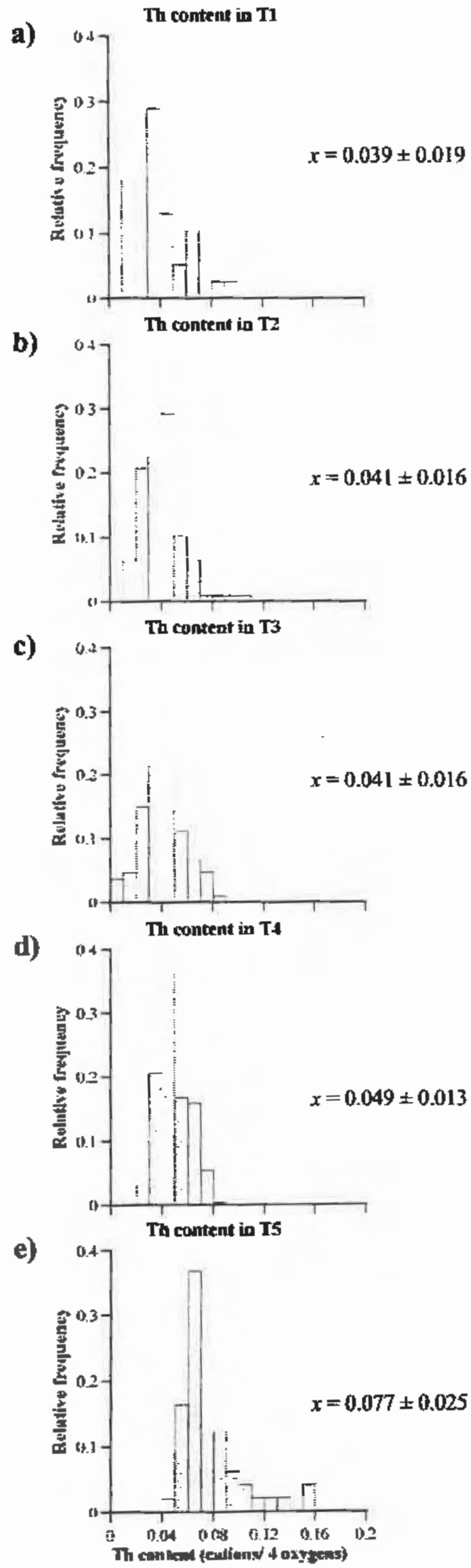

straight line has a slope of 1 and represents a theoretical perfect linear correlation between Si+Ca and Th+U. Results from this study show a very strong fit with this line. The data plotted show an excess of Ca+Si vs U+Th. The present amount of Th+U is smaller than the quantity incorporated at the time of crystallisation because of radioactive decay. Hence, the decay of Th and U into Pb* may explain, at least partially, the deficit in Th and U relative to Si and Ca. Also, part of the scattering of the data on either side of the theoretical line is probably the result of analytical error.

5.7 Synthesis

The previous sections presented the variation in content for each element through each transect. For this study, element variations were also compared for each petrological setting, each thin section, and each mineral assemblage. Petrological setting did not show any strong correlation with the element content (Fig. 5.22). Data grouped by thin section or mineral assemblage showed variations similar to data categorised per transect (Fig.5.20 and 5.21). The transect grouping was chosen to simplify the graphic representation.

Table 5.3 below presents a synthesis of the variations in average content for each element in each transect. This provides a broader perspective on changes happening in LBF monazite with increasing metamorphic grade. Results show that all LREE (except Sm) decrease in abundance with increasing metamorphic grade whereas Ca, Si, HREE, U, Th, and Y increase. The P content is roughly the same between all transects. From the observations made through the study of the chemical variations of monazite with increasing metamorphic grade, some interesting trends are revealed. First, almost all elements are involved in the substitution mechanisms and vary with grade. Only the P content remains stable through all transects likely because there are few cations suitable to fit in the 4-fold site occupied by P. Analysis of Si revealed that it accounts for most of the difference between the P content and 1 (i.e., in a stochiometric monazite there should

Figures 5.20 & 5.21: Next page. 5.20a-e) Ternary diagrams showing the variation in Y+HREE, Th+U+Ca+Si, and LREE content from Transect 1 to 5. 5.21a-e) Ternary diagrams showing the variation in Y, Th, and U content from Transect 1 to 5.

Figure 5.20

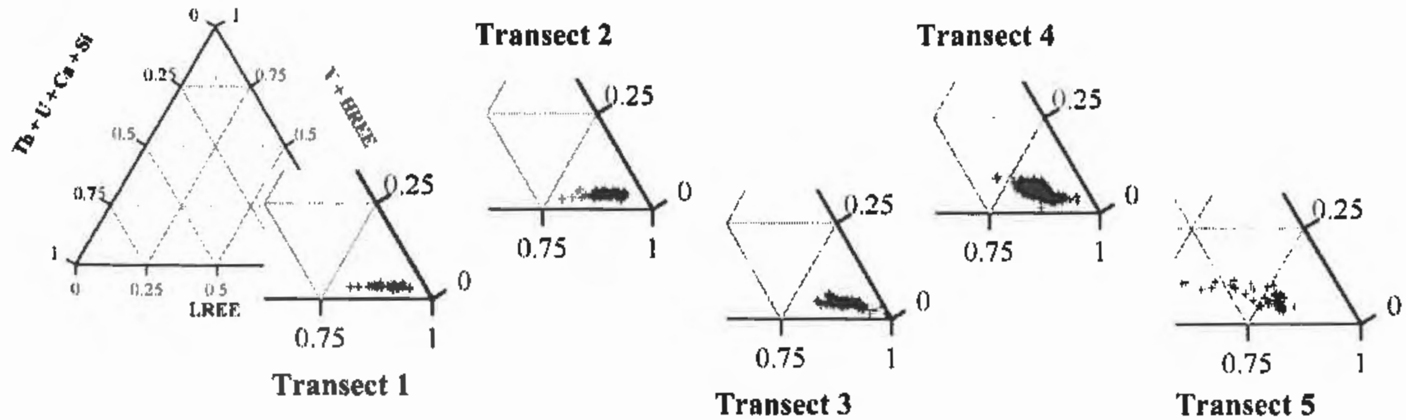

Figure 5.21

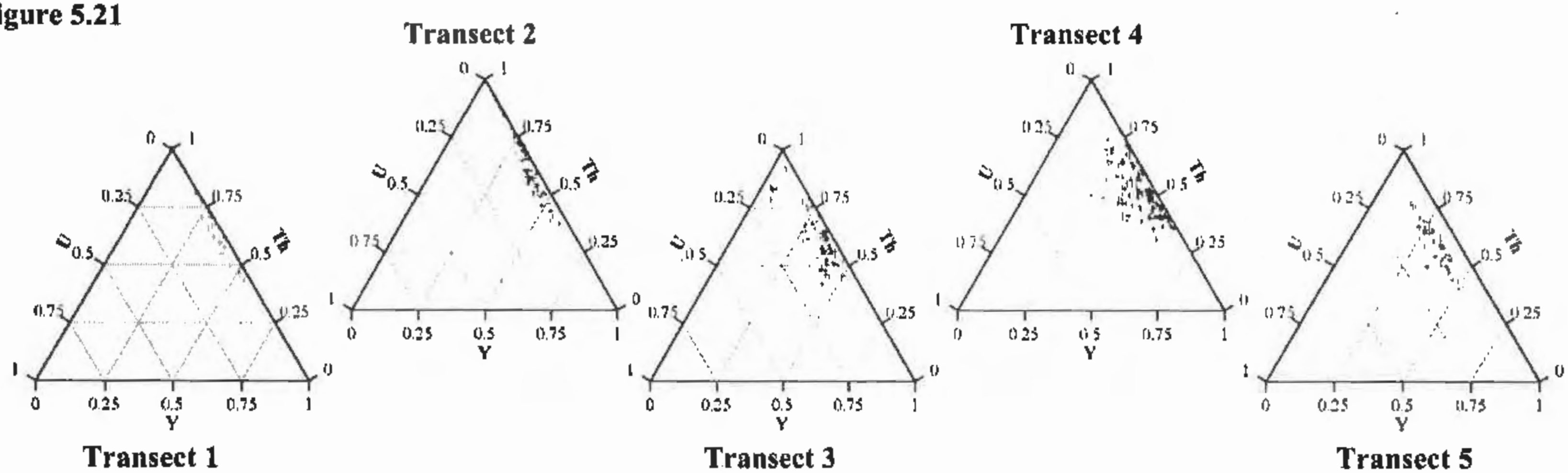

Table 5.4: Synthesis table presenting the average content for each element in each transect with the variation between transects. Average presented is in cations/ 4 oxygens. Variation is in percent (%). Avg = average.

	T1 Avg	T2 Avg	±% T1-T2	T3 Avg	±% T2-T3	±% T1-T3	T4 Avg	±% T3-T4	T5 Avg	±% T4-T5	±% T1-T5
Ce	0.448	0.434	-3	0.436	0.5	-3	0.436	0.1	0.373	-15	-17
P	0.978	0.985	0.7	0.985	0.0	0.7	0.976	-0.9	0.980	0.3	0.2
Si	0.010	0.010	0.0	0.008	-27	-27	0.008	5	0.014	80	39
Pr	0.065	0.064	-2	0.057	-11	-12	0.064	13	0.047	-26	-27
La	0.204	0.198	-3	0.204	3	0.0	0.183	-10	0.168	-8	-18
Ca	0.030	0.037	23	0.036	-1	21	0.049	35	0.083	68	176
Y	0.017	0.020	14	0.022	14	30	0.040	77	0.042	7	147
Nd	0.170	0.166	-2	0.164	-1	-3	0.152	-7	0.152	0.0	-10
Th	0.039	0.041	5	0.041	-1	4	0.049	20	0.078	59	98
Sm	0.027	0.028	6	0.026	-7	-2	0.028	5	0.030	7	10
Gd	0.017	0.019	14	0.018	-8	5	0.020	14	0.022	10	31
Dy	0.001	0.002	67	0.004	100	233	0.001	-80	0.008	850	533
U	0.001	0.001	50	0.003	167	300	0.005	50	0.011	125	1250
Total O	2.007	2.005	-0.1	2.005	0.0	-0.1	2.012	0.3	2.007	-0.2	0.0
Si + Ca	0.040	0.047	17	0.044	-7	9	0.057	30	0.097	70	141
Th + U	0.040	0.042	.7	0.044	5	12	0.054	21	0.088	64	122
Y + HREE	0.035	0.041	16	0.044	8	25	0.060	36	0.072	21	106
Th+U+ Ca+Si	0.080	0.090	11	0.088	-1	10	0.111	25	0.185	67	130
LREE	0.914	0.890	-3	0.888	-0.3	-3	0.864	-3	0.770	-11	-16

be 1 P per 4 oxygens). This suggests that Si occupies the 4-fold site in the monazite structure. The relatively small and stable Si content reveals that the huttonite substitution is not the dominant mechanism in the incorporation of Th and U in monazite (Fig. 5.23c). It also suggests that Si content of monazite is not sensitive to metamorphic grade.

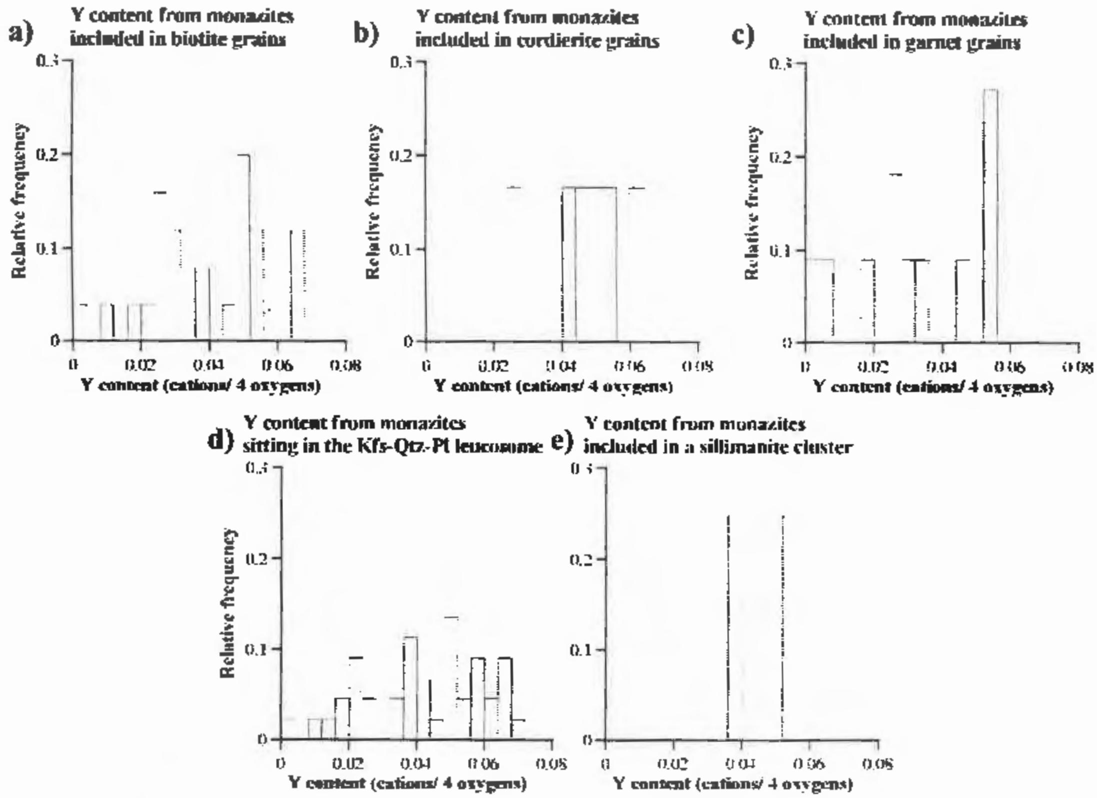

Figure 5. 22 : Above and on the right, histograms of Y values from monazites within migmatitic samples are presented for different petrological settings. From these diagrams, no setting versus composition relationship was observed.

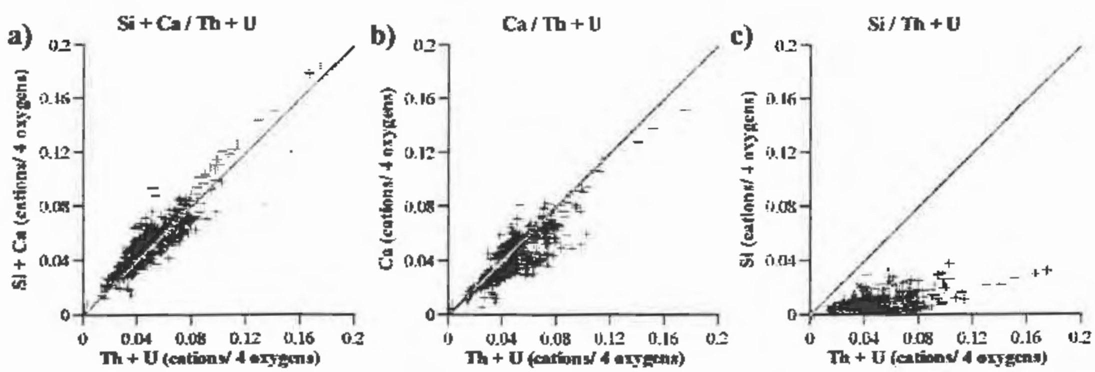

Figure 5.23 : Scattergrams presented below highlight the relationship between the Si + Ca and Th + U pairs. The solid grey line has a slope of 1 and represents the hypothetical case of a perfect paired substitution. In Figure a) the fit of data from the LBF with the theoretical line is very close supporting that Th+U are incorporated in monazite via brabantite and huttonite paired substitutions. Plot of Ca in b) shows that brabantite is the dominant substitution. Plot of Si in c) reveals that participation of Si to substitution is rather small relatively to Ca.

Finally, the systematic decrease in LREEs combined with the increase in Ca, HREEs, Si, Th, U, and Y, and the strong negative correlation between these two groups of elements indicate that substitutions in metamorphic monazite are dominated bybrabantite paired-substitutions and direct trivalent ion-substitution (i.e., Y or HREE directly replacing LREE). Systematic variations of many elements with increasing transect number strongly suggests that substitution mechanisms are influenced by metamorphism.

5.8 Discussion of LBF monazite chemical zoning

Study of LBF monazites from various metamorphic grades using Pb, Th, U, and Y X-ray maps as well as BSE images revealed that chemical zoning is weak in lower grade samples, whereas monazite from migmatite commonly displays a distinct zoning (Chapter 5). Low-grade monazite locally shows chemical heterogeneity, but it rarely translates into a distinct zoning pattern. Most high-grade monazite from migmatites presents a distinct chemical zoning. Concentric zonation is the most common zoning pattern in monazite, although many monazite grains also exhibit a patchy or irregular chemical zoning.

The chemistry of monazite with concentric zoning was given particular attention. Results showed that Gd, Th, U, and Y from rims of monazites with concentric zoning are generally enriched relative to the core, although the opposite was also observed. It was also recognised that variations in Y and Th in zoned monazite are not correlated. The decoupling in chemical zoning of Y and Th indicates that the two elements are controlled by independent factors, which suggests that sources or sinks for these two elements are likely two different mineral phases, as suggested by Pyle et al. (2001). Uranium also shows variations uncorrelated with Th and Y.

A good understanding of monazite chemical zoning is important for the interpretation of the nature of textures between different domains. Another issue is whether the chemical zoning reflects simply a local variation in the availability of an element at the time of crystallisation, or if it indicates discontinuous reactions in response to a change in the system conditions, thus releasing or trapping quantities of components common to monazite. Understanding the various processes responsible for monazite chemical zonation, and recognising which ones may apply to grains from this study, will help to interpret the nature of the chemical zoning.

A variety of mechanisms can control chemical zonation in monazite. These are overgrowth, regrowth, intergrowth, replacement and recrystallization (Zhu and O'Nions, 1999). The causes are numerous and may vary between different samples. Possible mechanisms include diffusion of elements within monazite because of diffusion rate lower than crystallisation rate, variation in composition of the fluid from which the mineral is crystallising, high-temperature recrystallization, fluid alteration causing overgrowth or recrystallization of a portion of the grain, and metamorphic reaction influencing the stability of REE-bearing phases. All of these mechanisms could have operated in the LBF samples. To determine the exact role of each mechanism in the zoning of LBF monazite was beyond the scope of this study. However, some of these concepts can be applied to specific examples in order to better constrain the significance and the nature of each chemical zone.

The geometry of the chemical zones can be a useful source of information on the processes that caused the chemical zonation as well as yielding information on the grain growth history. For instance, euhedral monazite cores likely crystallised in favourable environments such as saturated melt and were not consumed prior to overgrowth. In another case, a rounded monazite core could indicate a detrital grain while an embayed core indicates that partial resorption preceded overgrowth. Hence, to understand the growth history of a monazite grain it is necessary to consider not only the chemistry of the various zones and their age, but also their textures.

Grain S388-01 (Figures 5.24; 5.23; 6.18; 6.21), located in a garnet porphyroblast, shows a concentric zoning pattern consisting of three distinct chemical zones: a core, an inner rim and an outer rim. The core is rounded and has a regular contact with the inner rim. The inner rim and the outer rim exhibit an irregular contact with narrow cuspate embayments and variable outer rim thickness. The BSE image of S388-01 distinguishes clearly between the inner and the outer rim, whereas the core is faint. The contact between the inner and outer rim is drawn in Figure 5.22. The shape of the contact suggests that the inner rim of monazite was resorbed prior to the overgrowth.

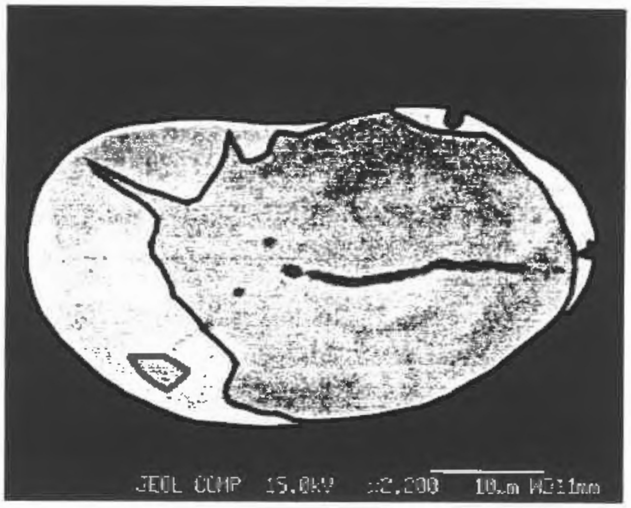

Figure 5.24: BSE image of grain S388-01. Two distinct zones are visible. The darker core and inner rim are contoured with the black line. The zone is irregular with distinct cuspate embayments present in the upper left. In the lower left, a small dark zone is detached from the core. This inner rim contour correlates with the Y X-ray map (Fig. 6.21). Within the darker core and inner rim variations in tone exist, but they are not distinct enough to be drawn.

Chemical dating (Section 6.4.4 and 7.9) revealed that the core and the outer rim have similar ages while the inner rim is older. Contrary to normal expectations, the oldest component is not the geometric core of the grain but the inner rim. By combining the age data with the information from the chemical zoning, it becomes possible to interpret this particular distribution of ages. The similarity between the ages of the core and the outer rim and their similar Y content indicates that they likely are the same chemical zone. This geometry is easily explained if an embayed core was overgrown by a younger rim. The presence of the younger core results from the section of the grain, which cuts through one of the embayments enveloped by the younger rim (Fig. 7.6). An explanation for this pattern of chemical zoning is proposed in Section 7.9. In many other cases, the texture of the chemical zones are used to interpret the ages obtained from each zone.

In summary, monazite chemical zoning is particularly strong in migmatitic samples. Both patchy and concentric zoning is observed. Rims of monazite that display concentric zoning are generally enriched in Gd, Th, U, and Y relative to the core. Thorium, U, and Y vary independently from each other suggesting that the budget of these elements is controlled by different mineral systems. Embayments were observed on both cores and rims of monazite grains. In at least one case (S388-01), monazite is inferred to have a core with large embayments enveloped by a younger overgrowth. The thin section cuts through one of the large embayments filled by the younger overgrowth, resulting in an unusual chemical and age zoning pattern.

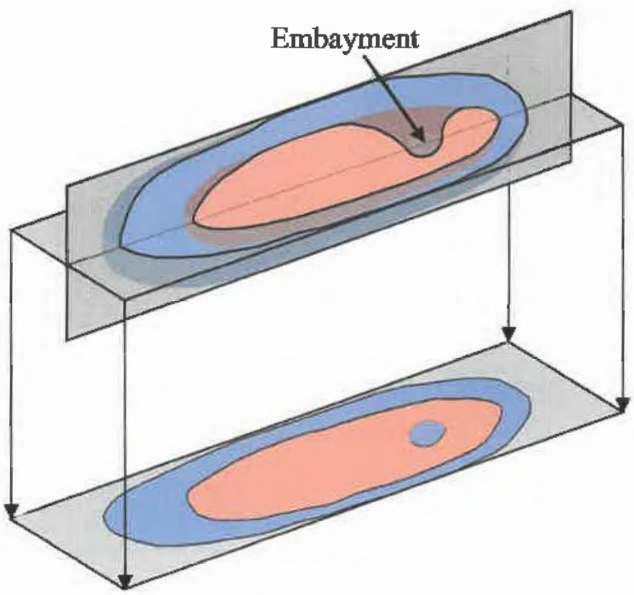

Figure 5.25 : The upper diagram is a 3D representation of the chemical zoning of grain S388-01. Geometry of the zoning is inferred from the Y X-ray map (Fig. 6.21) and the spot age distribution in the grain. The lower diagram is a plan view of the grain. The older component, shown in pink, presents a large embayment. The younger zone, shown in blue, envelops the core. The planar section of the grain cuts through the embayment and the resulting plan view show a concentric chemical zoning with similar ages in the core and the outer rim.

5.9 Discussion of LBF monazite chemical variation

Monazite compositions from the various metamorphic grades and petrological settings of the LBF were investigated using an EMP (Chapter 5). Comparison of the abundance of each element in each transect provides a clear picture of the chemical variations affecting monazite with increasing metamorphic grade.

Analysis of the abundance of Ca, Si, Th, and U shows that a strong linear relationship exists between Si+Ca and Th+U (Section 5.5; Fig. 5.22). This confirms that Th and U are incorporated in monazite through brabantite and huttonite substitutions as documented in previous studies (Zhu and O'Nions, 1999; Spear and Pyle, 2002). The results also demonstrate an excess of Ca relative to Si indicating that brabantite is the dominant substitution.

Analyses show that P content does not vary significantly with increasing metamorphic grade. This is not surprising since P constitutes the basic structure of monazite via the phosphate radical $-PO_4^{2-}$ and that the chemical bonds between P^{5+} and the four oxygens are much stronger than between the A-site and the phosphate molecule. Analyses reveal that P content is consistently slightly lower than the ideal 1P:4O, and that the difference correlates with Si, which agrees with the assumption that Si cations occupy the 4-fold site.

The LREEs generally show a systematic decrease in abundance with increasing metamorphic grade, whereas Y, Ca, Si, Th, and U become more abundant with increasing grade. Greater abundance of Ca, Si, Th, and U indicates that the substitution via these mechanisms increases with metamorphic grade. Globally Ca, Si, Th, U, and HREEs become more abundant with increasing metamorphic grade at the expense of the LREEs. This correlation suggests that metamorphic grade strongly influences the composition of metamorphic monazite. Two main processes can explain this. First, element partitioning at equilibrium between monazite and other minerals sharing common elements will vary with increasing metamorphic grade if the distribution coefficient is temperature- or pressure- dependent (Pyle et al., 2001). Secondly, the nature of the accompanying mineral assemblage at the time of crystallisation affects the chemical composition of monazite because the presence or absence of other mineral phases sharing common elements with monazite will exert an influence on the budget of these elements, and hence the composition of monazite.

Gadolinium arguably shows a small increase from T1 to T5. Pyle et al. (2001) reported Gd values averaging around 0.02 cations/ 4 oxygens, with no significant variation in Gd content with increasing metamorphic grade. Average values for Gd from this study give similar results. Analyses for Dy are rare since this element was added to the routine late in the implementation and the element was not systematically analysed. Available data show higher Dy at higher metamorphic grade.

Yttrium shows a significant increase in abundance with metamorphic grade. Pyle et al. (2001) reported a steady increase in Y content for monazite that grew in xenotime-bearing assemblages. This study did not emphasise the equilibrium between xenotime and monazite; therefore, information on xenotime equilibrium with monazite is incomplete. From X-ray maps (Chapter 3), we inferred that xenotime is present in the mineral assemblage until the sillimanite isograd. Low-grade monazite (T1) may have grown in equilibrium with xenotime but, at higher grade, xenotime clearly shows partial resorption, and equilibrium with the latest generation of monazite is unlikely. However, older monazite still present in the sample may have grown in equilibrium with xenotime.

In the LBF monazite, the average content of Y increases slightly from T1 to T3, but there is a steep increase between T3 and T4 along with a much broader range of values, ranging from 0.002 to 0.073 cations/ 4.000 oxygens. A wider range of values was also noted for other elements in high-grade monazite. The presence of different generations of monazite, which likely crystallized under different metamorphic conditions and were accompanied by different mineral assemblages, probably accounts for part of the range in content values. The rest of the variation can probably be attributed to the chemical zoning. For instance, monazite with patchy zoning, generally grains from leucosomes or granites, yield a wide range of compositions within a single episode of monazite growth.

Pyle et al. (2001) reported a steady increase in Y in monazite growing in xenotime-bearing assemblages and a narrower range of values for monazite in xenotime-absent assemblages. This study documented a minor but steady increase in Y content from T1 to T3 where xenotime progressively leaves the mineral assemblage and a sudden increase in Y between T3 and T4. Embayments and resorption textures found in skeletal garnets of samples S383 (T4) suggest that garnet is also being consumed. The breakdown of garnet could release the Y necessary to explain the sudden increase around the sillimanite isograd. However, the scarcity of garnet in the lower and middle-amphibolite facies rocks of the LBF is not consistent with this hypothesis.

In summary, monazite composition varies within each transect and the ranges of values tends to increase at higher metamorphic grade. There is a general and systematic variation in all elements but P with increasing metamorphic grade. Heavy rare earth elements, Ca, Si, Th, U and Y, increase with metamorphic grade while LREEs correspondingly diminish. Changes in composition appear to be more dramatic from T3 to T4 which marks the transition from Bt-Crd-Ms-Pl-Qtz-Sil rocks to Bt-Kfs-Pl-Qtz-Sil±Grt migmatites. As proposed for Y variation, reactions between major and possibly accessory phases is suspected to be responsible for sharp compositional variations coinciding with the sillimanite-in isograd and the onset of migmatisation.

6. Geochronology

6.1 Monazite geochronology

The U-Th-Pb chemical dating technique of monazite by EMP was employed in this study to investigate the monazite growth history in a sequence of Paleoproterozoic turbidites, the Longstaff Bluff Formation (LBF), at metamorphic grades ranging from upper greenschist to granulite facies (Chapter 2). This technique was chosen for its high spatial resolution making it possible to analyse monazite grains of size as small as ~5 μm in diameter (Montel et al., 1996). Its ability to provide information on element distribution within the grain and the preservation of the petrological setting are other key advantages of the technique (Williams et al., 1999).

The LBF is an excellent candidate to apply this technique for the following reasons: the Paleoproterozoic age of the rocks ensures that the Pb content of most grains is high enough to yield an acceptable 2σ error, available U-Pb dates for the study area provide a framework for comparison of the results, metapelites are abundant and show a large range in metamorphic grade. The main questions that the geochronological component of this study aimed to shed light on were, in no particular order, the documentation of all episodes of monazite growth, the recognition of detrital grains, testing the existence of an age gradient throughout the study area, the linkage of the different episodes of monazite growth with structural and metamorphic information, and verifying the relationship between the textural, chemical and age variation found in LBF monazite.

Monazite grains were selected from transects crossing the various isograds of the study area (Fig. 3.1). Within each transect, specific grains from different petrological settings were analysed to provide a regional picture of the variation in the timing of monazite growth throughout the area. This chapter presents results from the chemical dating of monazite as well as explaining data analysis and age calculation, and provides a summary of available isotopic ages for the LBF. Samples and control trace analyses, analytical settings, counting error calculation, and analytical procedure are in Appendices

1,2,3, and 7. Distribution and variation of the monazite chemical ages are presented in the following sections.

6.2 Geochronological background

The northern flank of the Trans-Hudson Orogen (THO) on Baffin Island was the subject of few previous geoscientific investigations (Morgan et al., 1975; Tippett, 1985; Jackson et al., 1990; Henderson and Parrish, 1992; Bethune and Scammell, 2003). The most recent was a three-year (2000-2002) multicomponent mapping project held through a joint partnership between the Geological Survey of Canada (GSC) and the Canada-Nunavut Geoscience Office (C-NGO). A U-Pb dating study is being conducted as part of this project to constrain the tectonic and magmatic history of the project area. Preliminary results were published in Wodicka et al. (2002) and Wodicka et al. (2003). Further work using thermal ionisation mass spectrometry (TIMS) is currently being carried out at the GSC facilities in Ottawa. In-situ chemical dating of monazite serves to complement and provide constraints at higher spatial resolution than the available data. Conversely, isotopic dates provide some verification of the results of the monazite chemical dating technique. Table 6.1 presents a compilation of the main isotopic ages for the LBF; a detailed geochronological inventory is presented in Chapter 7. A brief review of the geochronology of the study area is presented below with emphasis on the Paleoproterozoic period during which the LBF was deposited, deformed and metamorphosed, ca. 1.9-1.8 Ga (Hoffman, 1988).

Constraints on the deposition of the LBF turbidites were provided by the analysis of detrital zircon from siliciclastic units throughout the study area. The maximum deposition age for the LBF, which forms the uppermost unit of the Piling Group (PG), is constrained at 1915±8 Ma (Wodicka et al., 2003) based on the youngest detrital zircon found. The minimum deposition age is 1897+7/-4 Ma (Wodicka et al., 2002), the age of igneous zircon obtained from a megacrystic monzogranite interpreted to intrude the LBF (Corrigan et al., 2001; further details in Section 7.5). Other available geochronological data suggest that multiple metamorphic events were recorded in the study area. Metamorphic monazite from Paleoproterozoic granites and Archean basement yielded a range of dates from ca.1833 Ma to ca.1877 Ma (Wodicka et al., 2003). Titanite also revealed metamorphic ages from 1841+13/-9 Ma to ~1800 Ma (Wodicka et al., 2003). These data indicate the range of possible ages for the LBF monazites. The tectonic interpretation of the isotopic ages is discussed in Chapter 7 .

Table 6.1: Summary of the main geochronological constraints available for the deposition and metamorphism of the LBF. All ages are U-Pb dates acquired using TIMS technique. Full data set of available U-Pb dates for the study area and the central Baffin area in Chapter 7.

Age (Ma)	Mineral	Interpretation	Rock type	Source
1915±8	Zircon	Maximum deposition age	Siliciclastic rocks from the LBF	Wodicka et al. (2003)
1897+7/-4	Zircon	Crystallization age	K-feldspar megacrystic monzogranite	Wodicka et al. (2002)
~1877-1874	Monazite	Age of metamorphism	Archean monzogranite	Wodicka et al. (2003)
~1856	Monazite	Age of metamorphism	Archean granitoid	Wodicka et al. (2003)
1846+16/-12	Titanite	Age of metamorphism	Archean monzogranite	Wodicka, pers. comm.
1839-1833	Monazite	Age of metamorphism	K-feldspar megacrystic monzogranite	Wodicka pers. comm.
1835±1	Monazite	Crystallization age	white anatexic monzogranite	Wodicka, pers. comm.

6.3 Dating technique

In EMP chemical dating of monazite (Montel et al., 1996; Pyle et al., 2002; Williams and Jercinovic, 2002), ages are based on trace analyses of 4 elements: Pb, Th, U and Y (Chapter 4 and Appendix 1). Y is analysed to correct for its interference on Pb, and its bearing on zoning and petrogenetic information. The three other elements are used for the age calculation. The younger age limit for reliable dating of a monazite grain is generally between 100-200 Ma depending on its radiogenic Pb content. In this study, counts were optimised by using a higher intensity current (200 nA), a high-sensitivity crystal (PETH) for Pb, and longer background and peak counting time (300 sec at each of the two background positions, and 600 sec at peak position; all analytical settings described in Appendix 1). These conditions allowed us to reach detection limits of 40–60 ppm for Pb, and 100-200 ppm for U, Th and Y depending on the abundance of these elements.

6.4 Age and error calculations

Throughout this chapter, ages calculated from a single analysis are referred to as spot ages. Ages calculated from all spot ages of a grain or a domain are referred to as grain/domain average ages. Spot ages are calculated from EMP trace analyses of Pb, U, Th and Y on selected monazite grains. A detailed analytical procedure is described in Appendix 1. Prior to trace analysis, X-ray maps (Pb, Th, U, and Y) are produced from the grain. These maps are used to determine whether or not the grain is zoned and also serve to choose the location of the analyses. Analytical settings are adjusted to each individual grain or chemical domain, where applicable (i.e., where the chemical zones are large enough, or the number of zones is not too high, e.g. < 4, or the zoning pattern is not too complex). A number of spots (5-10) are analysed in each chemical domain or grain.

The spot age is calculated using the equation of Montel et al. (1996; see Section 4.4.1.1). Each age is calculated for the analytical conditions at the time of analysis and using corrected values of Pb and U. Corrections are made for Y $L\zeta_{1-2}$ and Th (M2-04 + $M\zeta_{1-2}$) peaks overlapping Pb $M\alpha$ as well as for Th $M\gamma$ overlapping U $M\beta$ (Section 4.2.11). Correction factors were measured on the JEOL-8200 Superprobe at Dalhousie University using Pb- and U-free YAG and ThO_2 standards (Appendix 1). Analytical error was determined for each spot age from the counting statistics using equations from Pyle et al. (2003; Appendix 2). The error calculation takes into account the standardisation, background corrections, corrections for overlap and counting error from each analysed spot. Spot ages bearing a 1σ error greater than 10% were automatically rejected and not included in calculation of the weighted average. The age for a grain or chemical domain is the calculated average weighted with the statistical error of every spot age. The weighted average is calculated using the specific function in Isoplot/Ex (rev. 2.49) from

Ludwig (2001). An example of results from trace analyses performed on grain S388-16 (grain description in Appendix 5) is given in Table 6.2.

Age variability within a single grain is not automatically interpreted as age zoning unless there is clear correspondence with element X-ray maps showing distinct chemical domains. In this case, ages are treated separately and a weighted average for each domain is calculated. A statistical test is then applied to verify if the two ages are statistically distinguishable. The critical value test, proposed by Fleck et al. (1977), is commonly used in $^{40}Ar/^{39}Ar$ geochronology to test for the existence of an age plateau. This test is based on the Student's t distribution and has the advantage of taking into account the standard deviation of the two ages under consideration. According to the critical value test, two distinct chemical zones can be considered as two distinct age domains with a 95% level of confidence only if the difference between the two average ages is greater than the calculated critical value (Eq. 6.1). If the difference is smaller, the two age domains must be considered statistically indistinguishable from each other. This test is also used to verify that replicate ages of a same grain yielded the same age within error. All replicate ages should differ from each other by a value smaller than the critical value. The critical value (C.V.) equation from Fleck et al. (1977) is presented below:

$$C.V. = 1.960\,(\sigma_1^2 + \sigma_2^2)^{1/2} \qquad \text{(eq. 6.1)}$$

where, σ_1 and σ_2 are the standard deviations of the two ages.

Once all grain/domain average ages have been calculated, it is first necessary to determine how many different age populations are present in the sample and, second, to determine as precisely as possible the average age and limits of each population. This can be a non-trivial task when two or more populations with relatively close values are mixed together. In this case, it is useful to apply statistical modelling to distinguish between the various age populations. For this study, age modelling used the least squares method as described in Montel et al. (1996). Results of modelling and further details on the technique are presented in Section 6.6.

Table 6.2: Representative trace element analyses: Example from grain S388-16, an elongated subhedral grain included in a biotite and parallel to the mineral cleavage. The monazite grain displays a concentric zoning with 2 rims and spot analyses were located in all zones . The sample is migmatitic and the biotite is part of the melanosome component (Fig. 6.20). Two values are reported for Pb and U: uncorrected values and interference corrected values.

Analysis #	Pb			Th		U corrected			Y		Age	
	ppm uncorr.	ppm corr.	± 1 σ[1]	ppm	± 1 σ[2]	ppm uncorr.	ppm corr.	± 1 σ[1]	ppm	± 1 σ[2]	Ma	± 2 σ[3]
91	5192	4947	0.49 %	41 153	0.26 %	5777	5399	1.02 %	22 780	0.16 %	1752	40.6 Ma
92	4629	4381	0.53 %	36 608	0.27 %	4963	4628	1.15 %	23 767	0.15 %	1764	45.8 Ma
93	4968	4707	0.50 %	40 801	0.26 %	4849	4475	1.18 %	24 717	0.15 %	1774	46.4 Ma
94	5038	4765	0.50 %	40 160	0.26 %	5083	4715	1.13 %	26 121	0.15 %	1787	45.2 Ma
95	5181	4887	0.50 %	39 495	0.26 %	5637	5275	1.04 %	28 605	0.14 %	1789	42.2 Ma
96	5297	5017	0.49 %	44 544	0.25 %	5038	4629	1.15 %	26 291	0.15 %	1760	44.8 Ma
97	5000	4747	0.50 %	39 942	0.26 %	5342	4976	1.09 %	23 858	0.15 %	1760	43.0 Ma
98	4938	4686	0.51 %	37 155	0.27 %	5756	5416	1.02 %	24 097	0.15 %	1772	41.4 Ma
99	4964	4711	0.50 %	36 852	0.27 %	6037	5699	0.98 %	24 213	0.15 %	1760	39.8 Ma
Average	-	-	-	-	-	-	-	-	-	-	**1768**	**14.4 Ma**

[1] *The error is the relative standard deviation on the k-ratio of both peak and background measurements for the corrected value.*
[2] *The error is the relative standard deviation on the k-ratio of both peak and background measurements for the measured value.*
[3] *Error on the age results from the cumulative error on each element propagated through the age equation (see Pyle et al. 2003).*

6.5 Results:

Geochronological data obtained through this study are presented in the following sections. Within this chapter, errors on spot ages and grain/domain average ages are all presented at a 2σ level of confidence. Throughout this study, grain/domain average ages are interpreted to represent the best estimate of the age of an individual monazite grain or domain. For each transect, two sets of diagrams are used to present the data.

The first set presents a compilation of all spot ages for one given transect. It combines two histograms of frequency distribution which serve to illustrate the range of ages measured and to reveal the most frequent values. The two histograms of spot ages are superposed and have a bin size of 20 and 10 Ma respectively. According to statistical rules the bin size should be larger than the sizes used in this study. The relatively small age variation between analysed grains requires a smaller bin size to depict changes in age distribution. For this purpose, arbitrary bin sizes of 20 Ma and 10 Ma were chosen.

The second set of diagrams presents results for the grain/domain average ages. A histogram of frequency distribution shows the grain/domain average ages using a 20 Ma bin size. A cumulative probability distribution curve is plotted in the same diagram and overlies the grain/domain average ages histogram. The cumulative probability curve is the sum of all probabilities calculated at every time value for each age. The probabilities are calculated from the grain/domain average ages using their respective standard deviations, assuming a normal probability distribution for each age. The cumulative probability curve is a simple visual representation of the age distribution that clearly marks the dominant, or most common, ages within a set. The cumulative probability curve generally represents more realistically the distribution of ages by weighting each age according to its own analytical error. It shows the effect of uncertainties in age, which the frequency distribution does not. Frequency histograms and cumulative distribution curves were produced using Isoplot/Ex (rev. 2.49) from Ludwig (2001).

6.5.1 Transect 1 (T1)

Transect 1 is the northernmost transect sampled in this study (Fig. 3.1). It is characterised by the lowest metamorphic grade. All samples collected in this transect contain Bt-Ms-Qtz. Six grains were analysed for chemical dating with a total of 35 trace analyses. Grains are generally homogeneous in age. One spot age calculated at 1384 Ma was rejected as an erroneous outlier. The reason for this age discrepancy is not known, but it may have been caused by the presence of an inclusion in subsurface, or by contamination of the surface, or by charging problems. A spot age of 1844 Ma was also rejected because it was located close to the grain edge. The following figures present the distribution of the remaining age results.

Monazite from T1 can be grouped into two sets based on their textural setting (Table 6.3). Thin section work and field observations showed the presence of two planar fabrics: S1 (schistosity) and S2 (spaced cleavage), both defined by mica orientation. Monazite was classified depending on whether it is oriented parallel to one of the fabrics or if it has no preferred orientation. Grains selected for dating were either parallel to S1 (Fig. 6.4) or S2 (Fig. 6.3). Elongated monazite grains that grew parallel to a fabric (S1 or S2) are interpreted to be syn- to post-fabric development. Therefore ages obtained from these grains provide a minimum age for the development of the fabrics.

The spot ages histograms (Fig. 6.1) show two clusters of ages around ca. 1750 Ma and ca. 1840 Ma. This suggests that monazite from T1 belongs to two distinct age populations. The cumulative probability curve and the histogram of grain/domain average ages (Fig. 6.2) present the same two predominant ages. Hence, ages obtained for T1 can be divided into two age groups.

Table 6.3 reveals a correlation between the textural setting and the chemical age of the grains. Grains parallel to S2 (Fig. 6.3)are systematically younger than S1-parallel grains, which agrees with the relative age inferred from the relationship between the two fabrics. S2 grains are all similar in age, however the S1 set is not as consistent. The S1-parallel

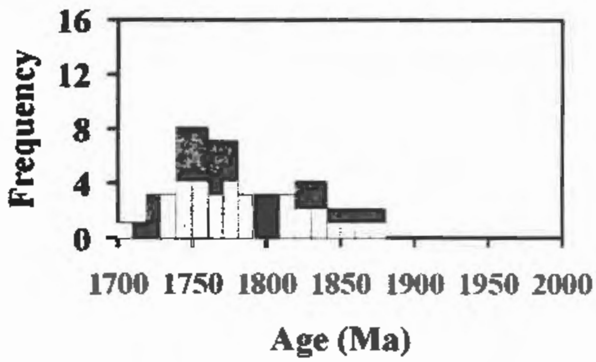

Figure 6.1 : Histogram of frequency distribution of spot ages from T1 (dark grey bins = 20 Ma, light grey bins = 10 Ma).

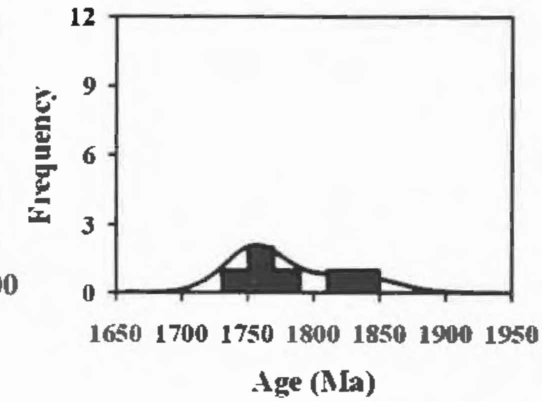

Figure 6.2 : Cumulative probability distribution curve and histogram of frequency distribution for grain/domain average ages in T1 (bins are 20 Ma).

Table 6.3: Grain/domain average ages from T1. "n" is the number of spot analyses performed on the grain used for age calculation. "r' is the number of analyses from this grain that were rejected. Grain descriptions are reported in Appendix 5, analytical settings in Appendix 1, and trace analyses in Appendix 7. From this transect, no included grains were analysed.

Setting	Grain category	Age ± error (2σ)	Grain/zone	Analyses
Parallel to S1	Fabric parallel grain	1840 ± 56 Ma	S371-18	n = 7, r = 1
Parallel to S1	Fabric parallel grain	1815 ± 63 Ma	S371-21	n = 5
Parallel to S1	Fabric parallel grain	1741 ± 48 Ma	S371-20	n = 6
Parallel to S2	Fabric parallel grain	1771 ± 51 Ma	S371-09	n = 5, r = 1
Parallel to S2	Fabric parallel grain	1756 ± 47 Ma	S371-19	n = 4
Parallel to S2	Fabric parallel grain	1756 ± 36 Ma	S371-06	n = 6
-	Included grain	-	-	-
-	Matrix grain	-	-	-

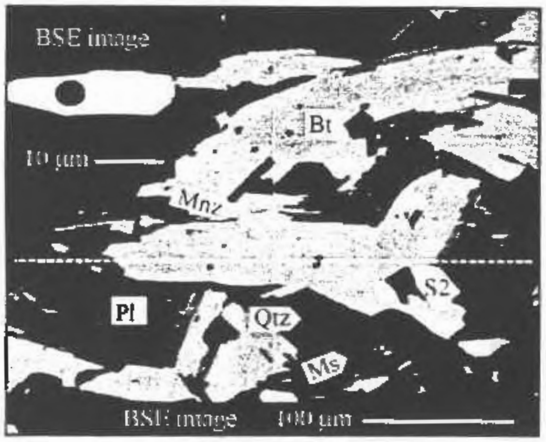

Figure 6.3 : BSE images of grain S371-06 (1756 ± 36 Ma), elongated and parallel to S2.

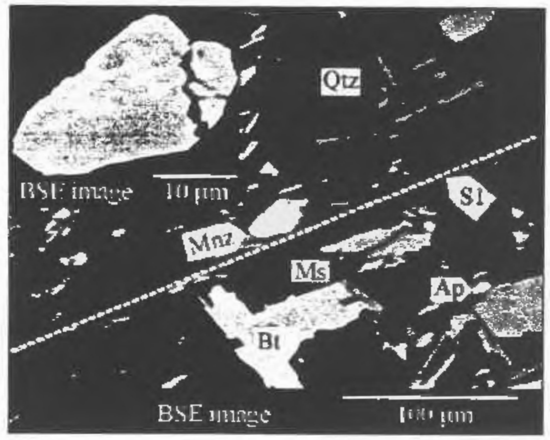

Figure 6.4 : BSE images of grain S371-20 (1741±48 Ma), granular, slightly elongated, parallel to S1, but with an age similar to S2-parallel grains.

set includes two older grains, 1840±56 Ma (S371-18) and 1815±63 Ma (S371-21), and a grain of distinctly younger age, 1741 ± 48 Ma (S371-20), similar to ages from the S2 set.

6.5.2 Transect 2 (T2)

Transect 2 is located about 25 km south-west of T1 (Fig. 3.1). This transect crosses the Crd-in and And-in isograds. Analysed samples, S366 and S367, contain the assemblage Bt-Crd-Ms-Qtz±And±Pl. Transect 2 samples show a well defined schistosity (S1) and include porphyroblasts of cordierite locally associated with andalusite. No monazite grains included in cordierite were dated from this transect.

Nine grains were analysed from this transect, with a total of 52 spot analyses. Grains are relatively homogenous and do not display any distinct age domains. Analyses (n=10) from 2 grains were not compiled because they were analysed early in the process of implementing the EMP chemical dating technique, and the procedure followed at this time lacked key steps (e.g., background selection using WDS scan and X-ray maps). Figures 6.5 and 6.6 present distributions of the 42 remaining ages obtained from the study of 7 grains.

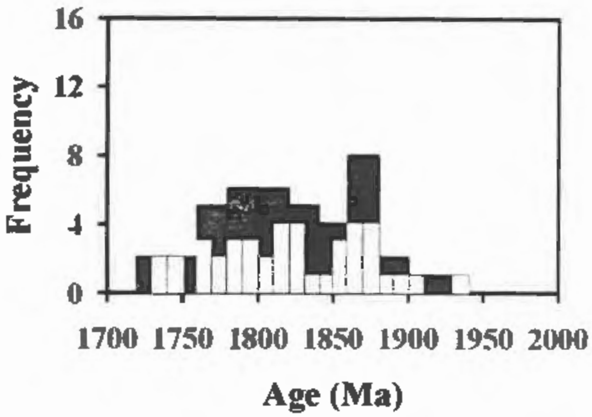

Figure 6.5 : Histogram of frequency distribution of spot ages from T2 (dark grey bins = 20 Ma, light grey bins = 10 Ma).

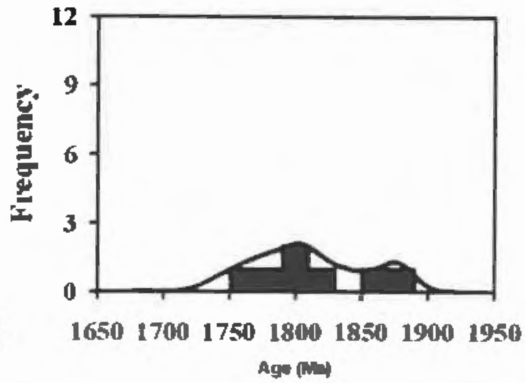

Figure 6.6 : Cumulative probability distribution curve and histogram of frequency distribution for grain/domain average ages in T2 (bins are 20 Ma).

Table 6.4: Grain/domain average ages for T2. "n" is the number of spot analyses performed on the grain used for age calculation. Grain descriptions are reported in Appendix 5, analytical settings in Appendix 1, and trace analyses in Appendix 7. From this transect, no included grain was analysed:

Setting	Grain category	Age ± error (2σ)	Grain/zone	Analyses
Parallel to S1	Fabric parallel grain	1878 ± 25 Ma	S366map1	n=8
Parallel to S1	Fabric parallel grain	1823 ± 37 Ma	S366map2	n=6
Oblique to S1	Fabric parallel grain	1751 ± 35 Ma	S366-07	n=5
Overgrown by S2	Fabric parallel grain	1853 ± 39 Ma	S366-16	n=7
-	Included grain	-	-	-
Matrix	Matrix grain	1805 ± 26 Ma	S367-10	n=6
Matrix	Matrix grain	1791 ± 33 Ma	S366-15	n=5
Matrix	Matrix grain	1775 ± 32 MA	S367map1	n=5

Dark grey bins (20 Ma) from the spot age histogram (Fig. 6.5) show two predominant ages, although the distribution of the 10 Ma bins (light grey) does not. The cumulative distribution curve and the histogram of grain/domain average ages (Fig. 6.6) also presents the same distribution. Grains from T2 display two main age clusters (Fig.

6.6) that show a certain range in the measured ages. Table 6.4 lists all grain/domain average ages obtained from T2.

The 1878±25 Ma (S366map1) and 1823±37 Ma (S366map2; Fig. 6.8) ages are from prismatic grains with long axes parallel to S1. The 1853±39 Ma (S366-16) age is from a granular, rounded grain overgrown or partly included by a biotite grain parallel to S2, suggesting that the grain is older than S2. The timing inferred from the textural settings of older grains generally corresponds with older measured ages.

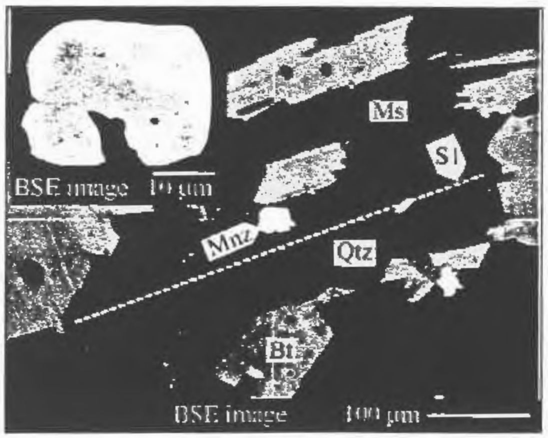

Figure 6.7 : BSE images of grain S366-07 which yielded an age of 1751 ± 35. Grain is oblique to the S1 fabric defined by micas and lack a preferred orientation.

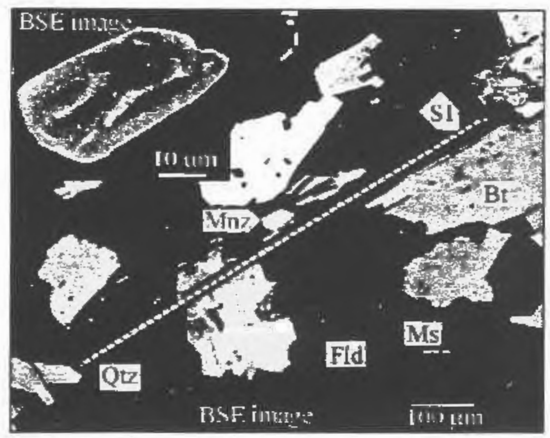

Figure 6.8 : BSE images of grain S366map2 which yielded an age of 1823±37 Ma. Grain is parallel to S1 fabric defined by micas.

The 1805±26 Ma (S367-10) age was obtained from a sub-prismatic grain showing embayments (resorption?) on more than 40% of its periphery. Due to its location in the middle of a quartz-feldspar matrix, bordered on one side by a biotite grain, no textural constraint on the timing of growth of this grain could be retrieved. The 1791±33 Ma (S366-15) age came from a sub-prismatic grain located in a quartz-feldspar matrix. The S1 fabric is well-developed in mica-rich zones around the grain, but the grain itself does not show evidence of a preferred orientation parallel to the fabric. Timing of growth is unclear, although likely to be younger than the fabric, as inferred from the lack of a preferred orientation. The 1775±32 Ma (S367map1) value was yielded by a granular monazite bearing few minor embayments and also located in the quartz-feldspar matrix.

The youngest grain dated at 1751±35 Ma (S366-07; Fig. 6.7) is a blocky grain oblique to S1 and lacking preferred orientation suggesting that this grain grew after the S1 fabric. This grain provides a minimum age for the S1 fabric.

In summary, older grains from this transect are texturally related to the older S1 fabric (Fig. 6.8) or, in one case, embayed and overgrown by S2. Younger ages come from grains that either had no clear relation with S1 or S2 as they were located in the quartz-feldspar matrix or, in one case, overgrow S1 (Fig. 6.7). The broad age range suggests that simultaneous growth of all grains from equivalent textural settings was unlikely. One explanation is that low-grade monazite generally contains little Pb and little U, therefore the error on individual ages is quite large. This large analytical error is probably partly responsible for the observed range of ages. On the other hand, it is also possible that the age range measured in grains from equivalent textural setting results from either diachronous growth of these grains or recrystallization of the older component of the grain. Recrystallization may be driven by different mechanisms such as new P-T conditions and fluid interaction.

6.5.3 Transect 3 (T3)

Transect 3 is located about 44 km south-south-east of T1 and 36 km south-east of T2 (Fig. 3.1). The transect crosses the Sil-in and And-out isograds. Samples from this transect commonly contain cordierite porphyroblasts. Some samples also contain fibrolite formed after breakdown of andalusite and muscovite (see Chapter 3 for details). Samples analysed generally contain Bt-Crd-Ms-Pl-Qtz±Sil. Fourteen grains from T3 were analysed, for a total of 81 spot analyses. Grains are relatively homogeneous and do not display any distinct age domains. Analyses (n=8) from two grains obtained early in the development of the technique were not compiled because the analytical procedure may have been unreliable. This section will discuss results from the analysis of twelve grains (n=73).

The frequency distribution histogram of spot ages (Fig. 6.9) presents a unimodal pattern, very similar to a normal distribution. The 20 Ma (dark grey) and the 10 Ma (light grey) bin sets show similar distribution pattern. The average ages histogram (Fig. 6.10) shows two predominant age clusters and a distinctly older component. The cumulative probability curve (Fig. 6.10) also shows two peaks at ca. 1800 and ca. 1840 Ma. Table 6.5 lists all grain/ domain average ages obtained for T3.

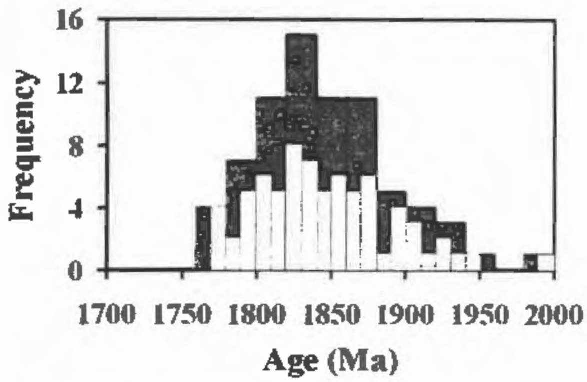

Figure 6.9 : Histogram of frequency distribution of spot ages from T3 (dark grey bins = 20 Ma, light grey bins = 10 Ma).

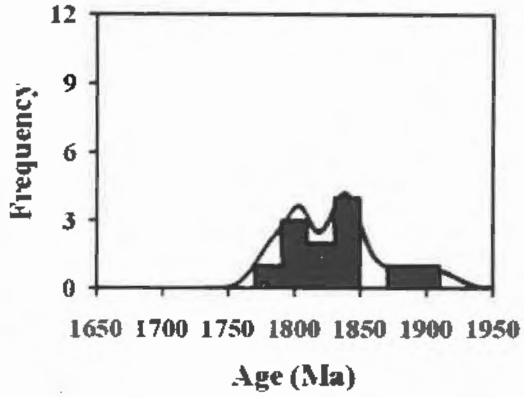

Figure 6.10 : Cumulative probability distribution curve and histogram of frequency distribution for grain/ domain average ages in T3 (bins are 20 Ma).

The unusually old age of 1908±29 Ma (S375-12; Fig. 6.11) was obtained from one grain located in the quartz-feldspar matrix in a mica-poor layer. The grain is sub-prismatic with rounded edges. This age is statistically indistinguishable to the maximum deposition age known for the LBF (Table 6.1; Section 7.2). Based on the grain habit (prismatic with rounded edges), its setting (a sandy bed in a semipelite), and its age, the grain is interpreted as detrital.

Grains S374-03 (1875±33 Ma; Fig. 6.13) and S373-01 (1818±26 Ma) are included in cordierite porphyroblasts, while grain S374-01 (1844±20 Ma) shows numerous embayments interpreted as resorption and is located in a sillimanite cluster (Fig. 6.14). Despite the range of ages from 1818±26 Ma (S373-01) to 1875±33 Ma (S374-03) measured in included monazite grains, no value from the ca. 1800 Ma cluster or younger was obtained.

Table 6.5: Grain/domain average ages for T3. "n" is the number of spot analyses performed on the grain used for age calculation. Grain descriptions are reported in Appendix 5, analytical settings in Appendix 1, and trace analyses in Appendix 7. From this transect, no fabric parallel grain was analysed.

Setting	Grain category	Age ± error (2σ)	Grain/zone	Analyses
-	Fabric parallel grain	-	-	-
Incl. in Crd	Included grain	1875 ± 33 Ma	S374-03	n=9
Incl. in Crd	Included grain	1818 ± 26 Ma	S373-01	n=5
Incl. in fibrolite cluster	Included grain	1844 ± 20 Ma	S374-01	n=6
Matrix	Matrix grain	1908 ± 29 Ma	S375-12	n=8
Matrix	Matrix grain	1847 ± 28 Ma	S374-02	n=6
Matrix	Matrix grain	1836 ± 18 Ma	S374-05	n=8
Matrix	Matrix grain	1836 ± 24 Ma	S375-11	n=6
Matrix	Matrix grain	1818 ± 39 Ma	S374-04	n=5
Matrix	Matrix grain	1805 ± 15 Ma	S373-02	n=5
Matrix	Matrix grain	1795 ± 23 Ma	S373-03	n=5
Matrix	Matrix grain	1792 ± 24 Ma	S373-05	n=5
Matrix	Matrix grain	1777 ± 23 Ma	S373-04	n=5

Monazite grains from the matrix show a large range of ages from 1777±23 Ma (S373-04) to 1908±29 Ma (S375-12). S375-12 is interpreted to be a detrital grain as discussed previously. The rest of the matrix grains can be divided into two groups roughly corresponding to the ca.1800 Ma and ca.1840 Ma age clusters. One grain, S374-04 (1818±39 Ma), does not clearly belong to either of the two age groups. Grain S373-04 (1777±23 Ma; Fig. 6.12) is distinctly younger than other grains from the ca. 1800 Ma cluster.

Three monazite grains from the matrix yielded ages in the older cluster (ca. 1840 Ma). Grain S374-05 yielded an age of 1836±18 Ma; the grain is included in a mica cluster. Ages of 1847±28 Ma and 1836±24 Ma were obtained from S374-02 and

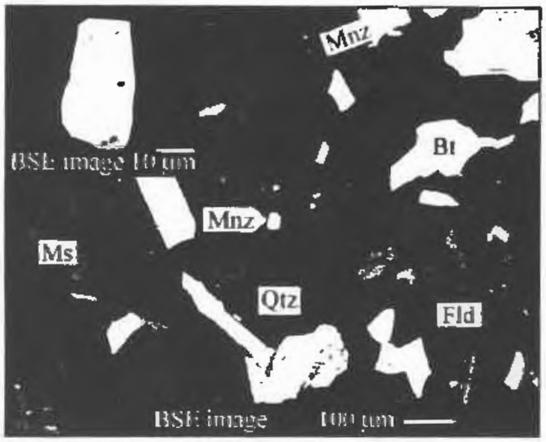

Figure 6.11 : BSE images of grain S375-12 which yielded an age of 1908±29 Ma. The grain is elongated and rounded, and located in the quartz-feldspar matrix.

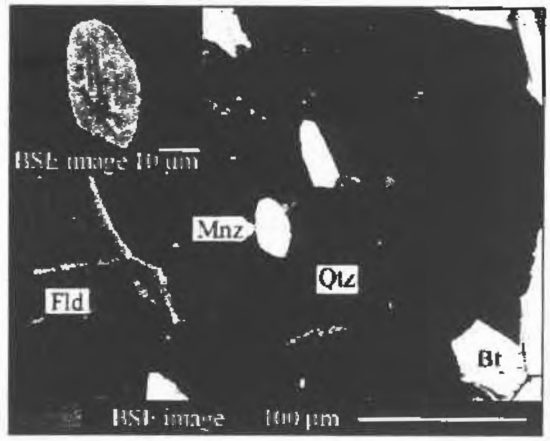

Figure 6.12 : BSE images of grain S373-04 which yielded an age of 1777±23 Ma. The grain is elliptic and rounded, and sits in the quartz-feldspar matrix.

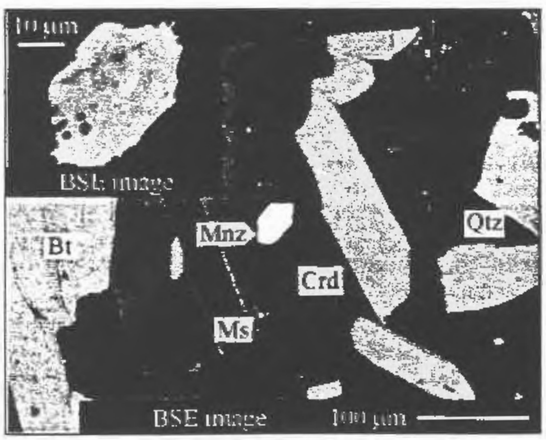

Figure 6.13 : BSE images of grain S374-03 which yielded an age of 1875±33 Ma. Grain is included in a cordierite porphyroblast.

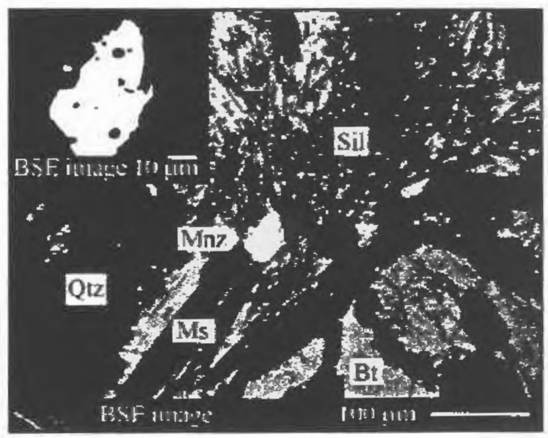

Figure 6.14 : BSE images of grain S374-01 which yielded an age of 1844±20 Ma. Grain is located in a fibrolite cluster and bordered by muscovite.

S375-11 respectively. Both grains are located in the quartz-feldspar matrix with no clear constraint on timing of growth relative to other metamorphic minerals or micro-fabrics.

Monazite grain S374-04, 1818±39 Ma, is from a grain partly bordered by mica and quartz-feldspar matrix. The grain has a sharp grain boundary against mica indicating growth late- to post-mica formation. The grain also has a large embayment. No textural evidence relates this grain to either specific age cluster

The younger age cluster comprises three monazite grains that yielded ages from 1792±24 Ma (S373-05) to 1805±15 Ma (S373-02). Two of these grains, S373-02 and S373-03, are in the quartz-feldspar matrix and they show a regular grain boundary with subprismatic shape. Grain S373-05 with an age of 1792±24 Ma formed along the grain boundary between a biotite crystal and the quartz-feldspar matrix, and displays a subprismatic shape.

In summary, ages from T3 monazite grains show two predominant age clusters at ca.1800 Ma and ca. 1840 Ma. Monazite grains from the older cluster represent an inclusion in cordierite porphyroblast (S374-03), matrix grains (S374-05, S374-02, and S375-11) and one grain in a fibrolite cluster (S374-01). The younger age cluster includes monazite located in the matrix. An older grain from the matrix dated at 1908±29 Ma (S375-12) is interpreted to be detrital, whereas a monazite inclusion in a cordierite porphyroblast, S374-03 (1875±33 Ma), may record an older episode of monazite growth. Two grains, S374-04 (1818±39 Ma) with an age intermediate between the two age clusters and S373-04 (1777±23 Ma) which is distinctly younger than the youngest age cluster, could not be confidently grouped with either of the two age clusters identified in T3. These results suggest that at least two monazite-forming events, corresponding to the ca. 1800 Ma and ca. 1840 Ma age clusters, affected the LBF in the T3 area. Monazite grains included in cordierite provide a maximum age for the porphyroblast growth. Further investigation using geochemical data may help to determine whether ages recorded by S374-03 (1875±33 Ma) and S373-01 (1818 ± 26 Ma) are distinct episodes of monazite growth or if they belong to one of the identified age clusters.

6.5.4 Transect 4 (T4)

Transect 4 is located 58 km south of T1 and 31 km south-west of T3. Transect 4 does not cross any isograd, but is characterised by the Bt-Crd-Kfs-Pl-Qtz-Sil±Grt mineral assemblage. Samples from T4 are migmatitic metasedimentary rocks that experienced partial melting with a southward increase in leucosome abundance. Whereas the northernmost part of the transect shows little evidence of melting, with sparsely distributed millimetre-scale leucosomes parallel to compositional layering (transposed bedding), the southernmost outcrops display centimetre-scale leucosomes, alternating with leucosome-poor semipelitic beds to form a well-defined migmatitic layering. Pockets of leucosome are also common and locally disrupt the rock structure.

In Transect 4, monazite grains were selected from a variety of petrological settings to investigate possible age variations. Monazite grains from T4 are abundant, large and typically zoned. Grains from T4 were therefore used to implement and test the chemical dating technique and many grains have been dated more than once.

In the early dating attempts, ages varying from ca. 1600 Ma to 2300 Ma were obtained from some grains, although many grains showed geologically significant ages (ca. 1750-1900 Ma). The discrepancy between results is explained by variation of analytical conditions (e.g., PHA window, beam current, use of different standards), analytical procedure (e.g., absence of background selection using WDS scan, various counting time) and sample preparation (various coating thickness, Pb lap polishing). Based on our initial experience, a routine procedure with specific analytical settings was adopted, allowing us to reach reasonable level of accuracy and precision in the results. Replicate trace analyses generally reproduce the initial results within a 95% level confidence, i.e. they differ from the initial results by a value less than the critical value (Section 6.3 and Eq. 6.1). All T4 ages reported here were acquired using the current analytical protocol (Appendix 1). When possible, grains analysed in the early days of the technique development were re-analysed using the standard routine; these cases are noted below.

In order to verify reproducibility of the results and to check the possibility of Pb contamination (Section 4.3.1.4) many grains from T4 were also analysed a second time using the same standard routine. All analytical conditions were similar, except that thin sections were re-polished on a Pb-free lap before the second run of analyses. Where grains or domains were analysed twice, results from both analytical sessions are presented.

Fourteen grains from T4 were analysed, for a total of 168 analyses. Grains from this transect commonly display chemical zoning which in some cases corresponds to age zoning. Where there is no clear evidence of age zoning, an average age was calculated for the whole grain. If distinct age domains were identified, they were averaged individually. Analyses (n=30) from 4 grains obtained early in the development of the technique were not included in averages for reasons discussed previously. This section presents the results from 10 grains (n=148).

The 20 Ma bins (dark grey) in the spot age histogram (Fig. 6.15) show a pattern similar to a normal distribution with two peaks. The 10 Ma bins (light grey) reveal the presence of two predominant age clusters. The average age histogram (Fig. 6.16) indicates the presence of at least two main clusters at ca.1790 Ma and ca.1840 Ma. The average age histogram also shows two grains or domains with an age between 1880-1900 Ma and 1900-1920 Ma respectively. Similar older ages were identified in T3. Finally, the cumulative probability curve (Fig. 6.16) correlates with the average age histogram, but also highlights that the two main age clusters on the histograms are in fact two pairs of dominant ages. The first pair comprises a minor peak at ca. 1765 Ma and a major peak at ca. 1790 Ma. The second pair reveals a minor peak at ca.1820 Ma and a major peak at ca. 1850 Ma. Further analysis of zoning and petrological setting is presented below, in order to establish the significance of individual ages and the relationship between age clusters. Table 6.6 lists all the grain/ domain average ages obtained for T4.

The oldest age in T4 was obtained from monazite S392-05 (1913±26 Ma; Fig. 6.19; Table 6.6). This grain is partly included in biotite. Grain S392-05 displays distinct concentric zoning, but ages from core and rim are statistically indistinguishable from each other. Textural setting and grain habit do not clearly suggest a detrital origin for this grain. Grain S392-05 is similar within error to both the youngest detrital zircon known from the LBF (1915±8Ma; Wodicka et al., 2003) and the emplacement of the 1897+7/-4 Ma megacrystic monzogranite (Wodicka et al., 2002), which is the oldest event known to have affected the LBF after its deposition.

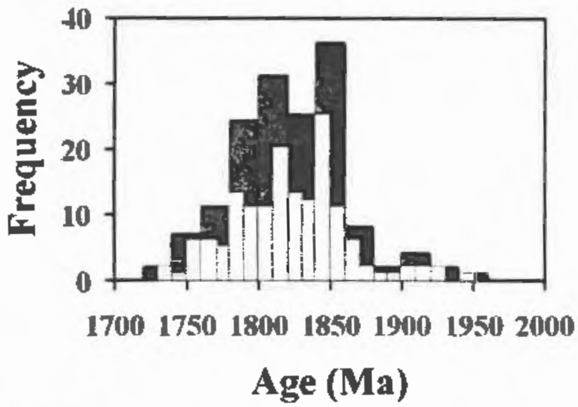

Figure 6.15 : Histogram of frequency distribution of spot ages from T4 (dark grey bins = 20 Ma and light grey bins = 10 Ma).

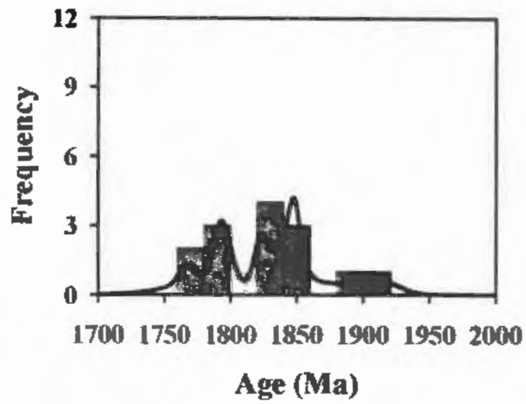

Figure 6.16 : Cumulative probability distribution curve and histogram of frequency distribution for grain/domain average ages in T4 (bins are 20 Ma).

Table 6.6: Grain/domain average ages for T4. "n" is the number of spot analyses performed on the grain used for age calculation. Grain descriptions are reported in Appendix 5, analytical settings in Appendix 1, and trace analyses in Appendix 7. From this transect, no fabric parallel grain was analysed.

Setting	Grain category	Age ± error (2σ)	Grain/zone	Analyses
-	Fabric parallel grain	-	-	-
Incl. in Grt	Included grain	1855 ± 29 Ma	S392map5	n=8
Incl. in Grt	Included grain	1848 ± 08 Ma	S388-01 inner rim	n=8
Incl. in Grt	Included grain	1835 ± 17 Ma	S383-02	n=13
Incl. in Grt	Included grain	1792 ± 12 Ma	S388-01 core	n=10
Incl. in Grt	Included grain	1791 ± 13 Ma	S388-02	n=21
Incl. in Bt	Included grain	1913 ± 26 Ma	S392-05	n=9
Incl. in Bt	Included grain	1836 ± 26 Ma	S392-01 core	n=10
Incl. in Bt	Included grain	1822 ± 09 Ma	S383-07	n=12
Incl. in Bt	Included grain	1761 ± 46 Ma	S392-01 rim	n=1
Incl. in Bt	Included grain	1768 ± 14 Ma	S388-16	n=9
Matrix	Matrix grain	1798 ± 13 Ma	S383-01	n=9
Leucosome	Matrix grain	1885 ± 34 Ma	S392-06 core	n=5
Leucosome	Matrix grain	1848 ± 12 Ma	S392-17	n=16
Leucosome	Matrix grain	1822 ± 33 Ma	S392-06 rim	n=8

Additionally, grain S392-05 is correlative in age with grain S375-12 from T3 (1908±29 Ma). Hence, this grain is interpreted to be detrital in origin.

Other studies have successfully dated older monazite preserved in garnet porphyroblasts (Montel et al., 2000; Terry et al., 2000). Because garnet porphyroblasts are present in migmatites from the high-grade LBF, special attention was paid to monazite from this setting. Monazite grains included in garnet may have been shielded from interaction with the rest of the rock and therefore may preserve old ages. The timing of the garnet growth is important. If garnet grew early in the thermal history of the rock, included monazite should be older than matrix monazite and should not preserve ages from the younger events. If garnet grew during the last metamorphic event, it could have included grains from the latest as well as the earliest events that affected the rock. If the garnet is fractured, late hydrothermal fluids may have possibly reacted with monazite to form a younger rim.

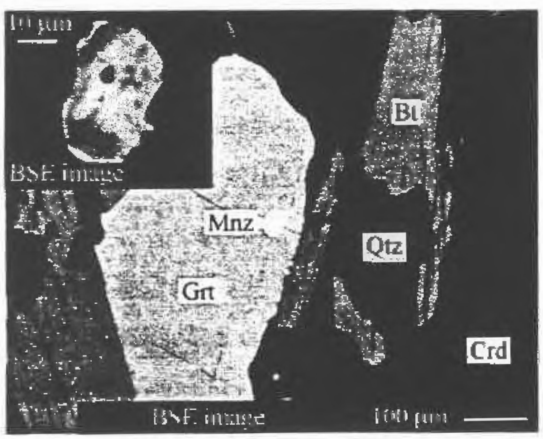

Figure 6.17 : BSE images of grain S392map5 which yielded an age of 1855±29 Ma. Grain is included in a garnet porphyroblast and shows no clear age zoning.

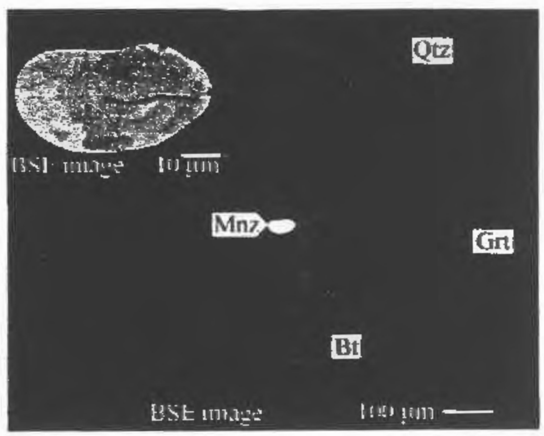

Figure 6.18 : BSE images of grain S388-01, included in garnet, which has two distinct age domains that yielded ages of 1848±8 Ma and 1792±12 Ma.

In T4, four grains included in garnet porphyroblasts were dated. Garnet in S383, S388 and S392map5 is resorbed and textural relationships suggest that they grew prior to formation of migmatites (Chapter 3). Monazite grain S392map5 (Fig. 6.17) is included in an elongated garnet porphyroblast parallel to the migmatitic layering. The reliability of the results acquired from grain S392map5 during the first run of analyses was hindered by a stage problem. Ages were older than any obtained with the standard routine and highly variable, from 1850 Ma to 2350 Ma, for a grain showing relatively simple chemical zoning. X-ray maps revealed the presence of a discontinuous rim, with minor Th- and U-enriched zones in the core. Variable ages are thought to be caused by problems with the stage. The generally older ages could be explained by the fact that despite meticulous cleaning efforts some Pb smeared over the surface of the sample during polishing and may not have been removed. An excess of Pb relative to measured Th and U will produce an older age. Due to analytical problems, the results from the first analytical session were considered dubious and discarded. To resolve the age of this grain, a second run of analyses was acquired. The new results yielded an average age of 1855±29 Ma. The chemical zoning did not translate into an age zoning.

Grain S388-01 (Fig. 6.18, 6.21), also included in garnet, displays distinct concentric chemical zoning on X-ray maps. In order to test the reproducibility of the results and verify the presence of an age zoning, this grain was analysed a second time. The challenge was to discriminate between distinct age domains. During the first set of analyses the core, the inner rim, and the outer rim were analysed. The second run of analyses only re-examined the outer rim and the core.

Results from trace analyses performed on S388-01 show an unusual variation in age. Comparison of results from both analytical sessions confirmed that the grain does not have a simple concentric age zoning with an older core and younger rims. The spot analyses gave similar ages for the core and the outer rim. Inner rim ages are consistently older than both the core and the outer rim. The distribution of spot ages is shown on the Y X-ray map in Figure 6.21. Plotting of the spot ages clearly shows that intermediate ages come from spot analyses located at the margin of two chemical domains (Fig. 6.21). The similarity in age between the core and the outer rim, which are statistically indistinguishable from each other, suggests that they are contemporaneous and may be considered a single age domain. Hence, ages from the core and the outer rim are averaged together. For age calculation, only ages clearly located in one of the two domains are used in the average. Other ages located on the margin of the two chemical domains (shown in grey circles in Fig.6.21) were not used because they may be dubious. Calculated age for the older component (inner rim) of S388-01 is 1848±08 Ma and the younger component (outer rim + core) has an average age of 1792±12 Ma. The significance and interpretation of the age similarity between core and outer rim, and implications in terms of the chemical zoning geometry are discussed in detail in Chapter 7.

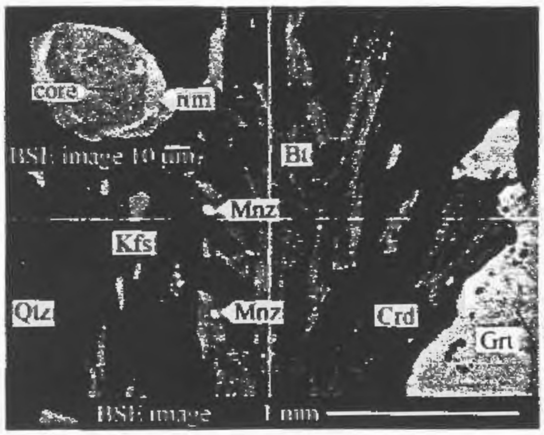

Figure 6.19 : BSE images of grain S392-05 which yielded an age of 1913±26 Ma. Ages from the core and the rim are not statistically distinguishable.

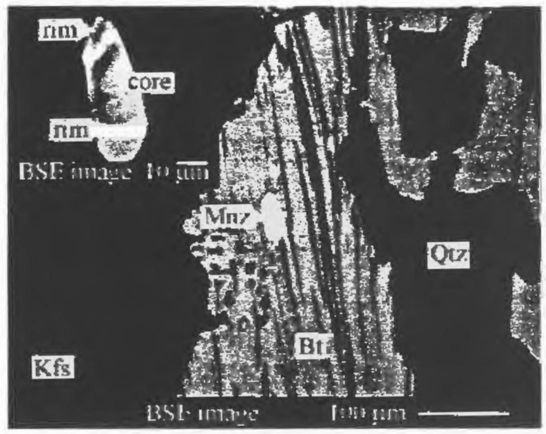

Figure 6.20 : BSE images of grain S388-16 that yielded an age of 1768 ±14 Ma. Grain is located in restitic biotite. Core and rims ages are not statistically distinguishable.

Monazite S383-02 (Fig. 6.22), an inclusion in garnet, was analysed twice. Results from both analytical sessions were statistically indistinguishable from each other and have been combined. The average age for the grain is 1835±17 Ma. The petrological setting of monazite grain S383-02 and the host garnet porphyroblast are presented in Figure 6.22. X-ray maps of Ce and P show the location of grain S383-02 and other monazite grains, and the Mg X-ray map highlights the locations of biotite and garnet porphyroblasts. The matrix is composed mainly of biotite-plagioclase-quartz-sillimanite and local K-feldspar. The garnet porphyroblast in Figure 6.22 displays an irregular shape with numerous embayments (Chapter 3, Appendix 4).

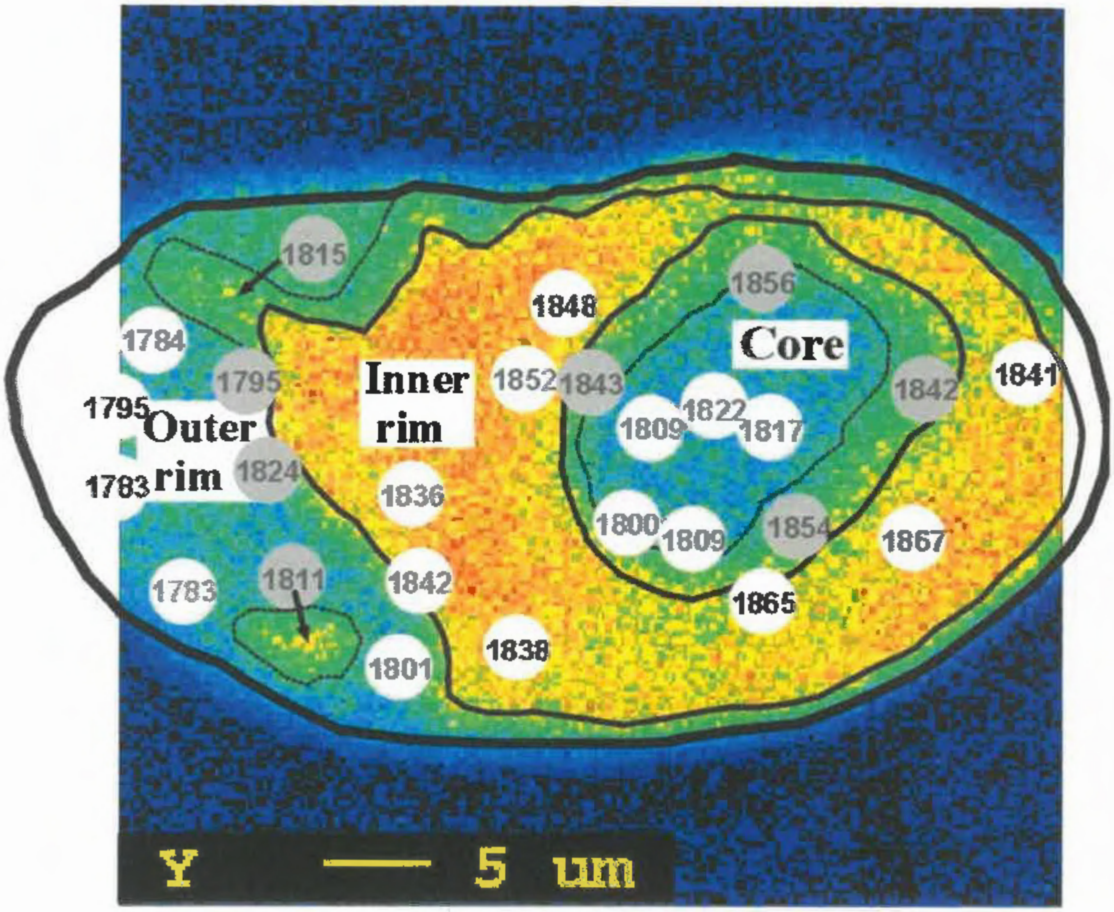

Figure 6.21 : Yttrium X-ray map of grain S388-01. Contour of the grain is drawn by a thick solid black line. Because the Y X-ray map area is smaller than the grain, the missing parts of the grain were drawn using a BSE image. The thin solid black line represents the limits of the inner rim interpreted from the X-ray map. Dotted black line outlines area of intermediate composition. White circles indicate spot ages used for the average age calculation. Spot ages in grey circles are located in the intermediate zones and were not considered in the average age calculation. Spot ages from the outer rim and the core were combined together because they are statistically indistinguishable from each other.

Grain S388-02, also included in a garnet porphyroblast, was analysed twice. Results from both analytical sessions were statistically indistinguishable and have been combined. Total average age for the grain is 1791±13 Ma. Monazite S388-02 is located in the same garnet porphyroblast as grain S388-01. Monazite grain S388-02 does not display any age zoning, despite its relatively complex zoning pattern (Fig. 5.2e).

Monazite included in garnet yielded ages as young as 1791±13 Ma (S388-02) and 1792±12 Ma (S388-01 core + outer rim). The two young ages were recorded in monazite grains included in the same garnet porphyroblast. Other monazite grains included in garnet, S383-02 (1835±17 Ma), inner rim of S388-01 (1848±08 Ma), and S392map5 (1855±29 Ma) gave older ages.

Four monazite grains included in Bt were dated. Grain S392-05 (1913±26 Ma; Fig. 6.19) is partly included in a biotite grain that is partially resorbed. This grain has an unusually old age and is interpreted to be detrital (see discussion earlier). The core of grain S392-01 gave an age of 1836±26 Ma whereas the rim was dated at 1761±46 Ma (Table 6.6). Grain S392-01 displays a well-defined concentric zoning with multiple zones. Only the outermost rim shows a statistically distinct age from the core. Monazites S383-07 (1822±09 Ma) and S388-16 (1768±14 Ma; Fig. 6.20) are included in biotite grains and are elongated parallel to the mineral cleavage.

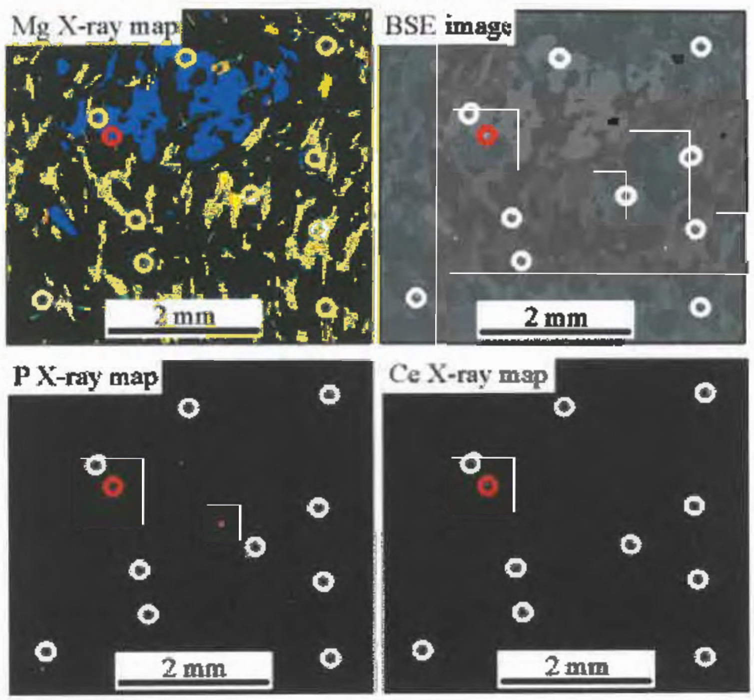

Figure 6.22 : BSE image and X-ray maps of a part of thin section S383 showing a garnet porphyroblast in a Bt-Qtz-Kfs-Pl -Sil matrix. White circles highlight occurrences of monazite as inferred from matching Ce and P X-ray maps. Red circle is grain S383-02 shown in further detail in Figure 5.2e. On the Mg map, the blue grain is garnet and the yellow grains are biotites.

Monazite grain S383-01 (1798±13 Ma) is located in the Qtz-Pl-Kfs matrix of S383. This grain is classified separately from the other grains because S383 is an incipient migmatite that contains less than 5% leucosome. The Qtz-Pl-Kfs matrix of this grain is a mix of the recrystallized psammitic component of the sample with metamorphic Pl and Kfs, whereas the two other matrix monazite grains are located in the leucosome.

Two matrix grains sitting in a Qtz-Pl-Kfs leucosome were dated. These grains are located in pockets of leucosome contiguous to Crd and partially altered Bt. Grain S392-06 is located at the grain boundary between Kfs and Qtz crystals. The grain displays concentric zoning. The core of S392-06 gave an age of 1885±34 Ma whereas the rim gave an age of 1822±33 Ma. Monazite S392-17, also located in a Qtz-Pl-Kfs leucosome, displays a complex patchy zoning pattern. Spot ages did not reveal age zoning, and averaged 1848±12 Ma.

In summary, monazite in T4 preserves a multi-stage growth history. Ages recorded by T4 monazite grains span from 1761±46 Ma (S392-01 rim) to 1913±26 Ma (S392-05). Two main age clusters are found around ca.1790 Ma and ca.1850 Ma (Fig. 6.16). Two minor age clusters are also present at ca.1765 Ma and ca.1820 Ma (Fig. 6.16). Two distinctly older monazite grains with ages of 1885±34 Ma (S392-06 core) and 1913±26 Ma (S392-05) respectively were found.

6.5.5 Transect 5 (T5)

Transect 5 is located 70 km south-east of T1 and 25 km south-east of T3. Samples from T5 are granites derived from partial melting of PG metasedimentary rocks (Section 3.4, 2.3). Field evidence shows a clear relationship between a granitic body (> 100 m^2) with edges branching into granitic veins, and then into migmatitic metasedimentary rocks. Large veins of leucosome become subparallel to migmatitic layering and split into smaller veinlets. Leucogranite pockets are common in the migmatitic metasedimentary rocks (details in Chapter 3).

Three monazite grains were analysed, for a total of 33 analyses. The grains are chemically zoned, but do not display a systematic age zoning. Different chemical domains were analysed separately. No ages were rejected.

The 20 Ma bins (dark grey) of spot ages (Fig. 6.23) show two predominant age clusters at ca.1800 Ma and ca.1840 Ma. The 10 Ma bins (light grey) present the same age distribution. The cumulative probability curve (Fig. 6.24) shows three peaks that correspond to the age of the three grains dated from this transect. The results taken on their own might not be meaningful because of the small size of T5 sample. However, T5 monazite ages correspond to age clusters obtained in previous transects.

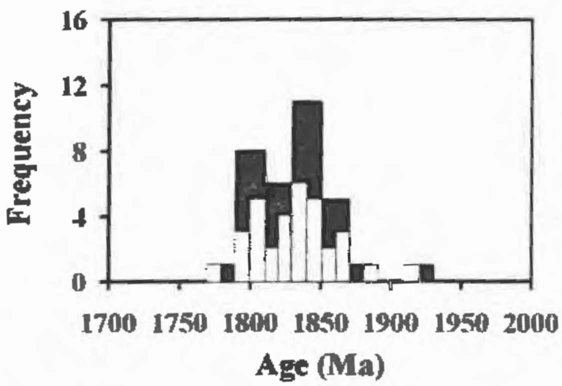

Figure 6.23 : Histogram of frequency distribution of spot ages from T5 (dark grey bins = 20 Ma and light grey bins = 10 Ma).

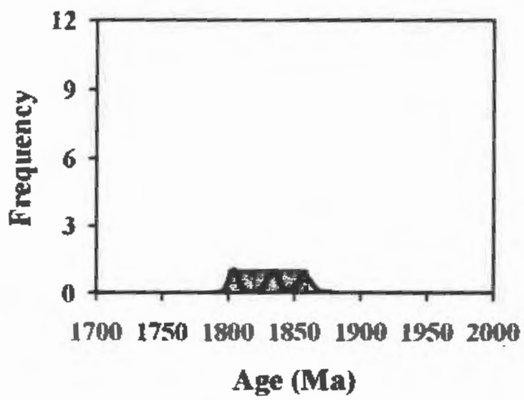

Figure 6.24 : Cumulative probability distribution curve and histogram for grain/domain average ages in T5 (bins are 20 Ma). Only three grains were analysed.

Grain S397-02, located in the leucogranite matrix, gave an age of 1858±11 Ma (Table 6.7). S397-02 is a sub-rounded grain, with a narrow lighter rim (Appendix 5). Grain S397-01 included in garnet yielded an age of 1834±09 Ma (Fig. 6.25). Grain S397-01 displays simple concentric zoning with both core and rim exhibiting a euhedral shape, and statistically indistinguishable ages. Another grain (S401-1), also located in the quartz-feldspar matrix, presents a prismatic euhedral habit and displays complex patchy zoning pattern (Fig. 6.26). The spot ages gave an average age of 1804±8 Ma. The grain does not present any age zoning despite the complex chemical zoning pattern

Table 6.7: Grain/domain average ages for T5. "n" is the number of spot analyses performed on the grain used for age calculation. Grain descriptions are reported in Appendix 5, analytical settings in Appendix 1, and trace analyses in Appendix 7.

Setting	Grain category	Age ± error (2σ)	Grain/zone	Analyses
Incl. in Grt	Included grain	1834 ± 09 Ma	S397-01	n=6
Granite	Matrix grain	1858 ± 11 Ma	S397-02	n=10
Granite	Matrix grain	1804 ± 08 Ma	S401-01	n=12

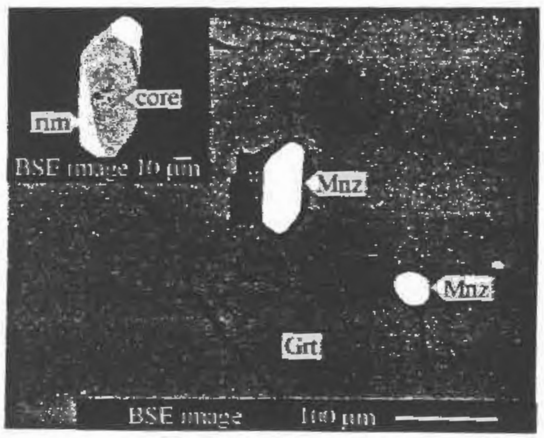

Figure 6.25 : BSE images of grain S397-01 that yielded an age of 1834±09 Ma. Ages from core and rim are statistically similar and were averaged. Grain is included in a garnet porphyroblast.

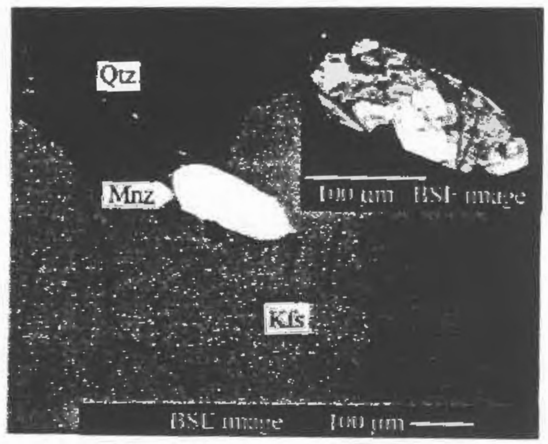

Figure 6.26 : BSE images of grain S401-01 that yielded an age of 1804 ±8 Ma. Grain is located on the edge of a K-feldspar grain. Grain is highly zoned but has no age zoning.

Monazite from T5 record three episodes of growth. These ages correlate well with episodes found in other previous transects. There are insufficient data to decipher in detail the history of this transect. Data from T5 need to be combined with data from other transects before making any interpretation.

6.5.6 Transect comparisons

Throughout the study area, 46 grains were analysed for chemical dating providing a total of 375 spot analyses. From these, 50 analyses were not regarded as reliable. The data compiled in the figures below include 325 analyses from 38 monazite grains. The distribution of monazite grain/domain average ages obtained from all transects is shown in Figure 6.27. Spot ages range from 1700 to 1980 Ma. The 20 Ma bin distribution shows a broad normal distribution skewed towards older ages. The 10 Ma (light grey) bins correlate this observation. The average age histogram (Fig. 6.28) displays a broad normal distribution with a large dominant cluster around ca.1840 Ma. The cumulative probability curve (Fig. 6.28) is more informative and reveals that two main peaks are present at ca.1800 Ma and ca.1840 Ma. Both the average age histogram and the probability curve show few but distinct older ages.

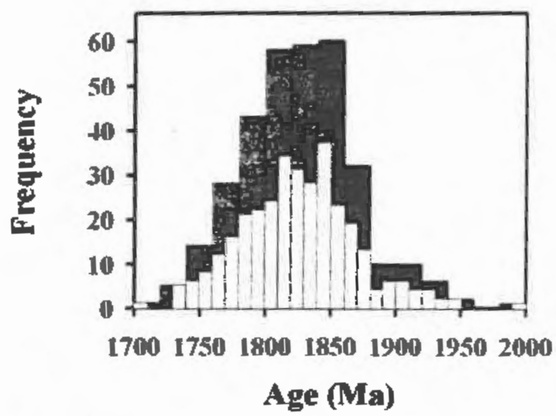

Figure 6.27 : Frequency distribution histogram of spot ages from all transects (dark grey bins = 20 Ma and light grey bins = 10 Ma).

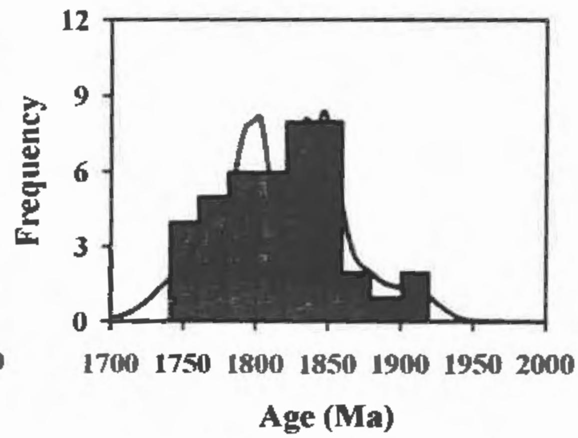

Figure 6.28 : Cumulative probability distribution curve and frequency distribution histogram of grain/domain average ages in all transects (bins are 20 Ma).

Figure 6.29, shows the cumulative probability curve from all transects (black). Probability curves presented earlier for each of the five transects are also shown (grey). Figure 6.29 highlights the contribution of each transect to the total probability curve. The specific age distribution within each transect, displayed by the grey probability curves, facilitates comparison between the transects. The composite figure of probability curves reveals that the ca.1790-1800 Ma and ca.1840-1850 Ma episodes of monazite growth are recorded in most transects. Transects 4 and 5 present an intermediate age cluster at ca. 1820-1830 Ma. Lower grade transects show a predominance of younger ages. All transects but T1 record monazite growth at ca. 1800 Ma. Only Transects 3 and 4 show older grains at ca. 1910 Ma. Finally, age clusters correlate between transects, although minor variations exist. Discussion of the significance of the variation in age between transects for specific episodes of monazite growth is addressed in Chapter 7.

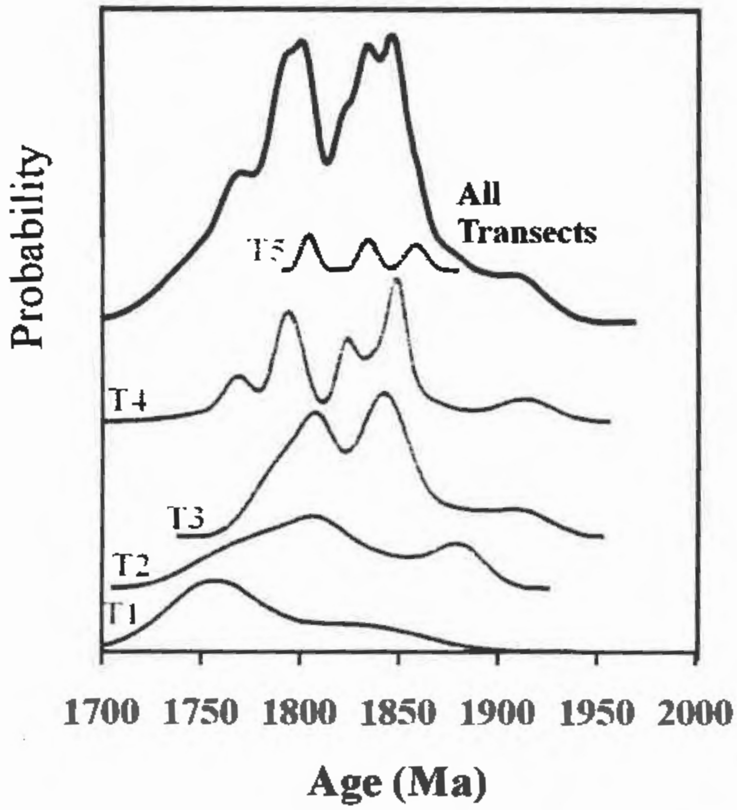

Figure 6.29 : Composite figure showing the cumulative probability curve of average ages of all transects, in black, with cumulative probability curves of average ages for each transect shown in grey. Probability curve profiles have not been altered and all transects have been fitted accordingly to the X-axis scale. The Y axis gives the relative variation in probability within each transect. Peaks represent ages with high probability values.

On the cumulative probability curve (Fig 6.29), the ca.1830 and ca.1850 Ma age clusters are not clearly distinguished; instead a broader peak with a double hinge is shown. On the other hand, the ca.1800 Ma peak is distinct in all plots but T1. A minor deflection on the younger shoulder of the curve from all transects is caused by younger ages mainly recorded in T1. The right shoulder of the cumulative curve from all transects presents a minor deflection due to older monazite ages from Transects 3 and 4. Note that younger ages are mostly recorded in the northern part of the study area (T1 and T2) and older ages are more common in the southern part of the area (T3-T5).

6.6 Age modelling

Finally, statistical discrimination of the various age populations recorded through the study area is required. This was done using least-squares modelling (Montel et al., 1996). Calculations were processed using software provided by J.-M. Montel. The least-squares model provides the best age estimate for a given number of population within the data set. The model assumes that grains from a single population plot along a normal probability distribution curve. Using each individual age and its respective standard error, the model calculates the probability that the sample age distribution is the result of a specific number of different populations mixed together. The model must first be applied assuming that the data set consists of a single population. If the calculated probability is too low (< 5% probability of the chi-square value), the data are remodelled assuming that two different populations are present. This continues until the model yields an acceptable probability. The software uses a chi-square test to verify the probability that all ages grouped within the same population, defined by the least-square model, belong to this population. The model must be accepted when the probability of the chi-square value exceeds 5% (Montel et al., 1996). If the probability is below this value, the model is invalid and the age distribution must be remodelled. This step is repeated until all populations yield an acceptable probability. Note that the presence of outliers, such as inherited detrital cores, may interfere with the results. All data from identified outliers must be removed.

All grain/domain average ages from all transects were modelled together. Monazite grains S392-05 (1913±26 Ma) and S375-12 (1908±29 Ma), interpreted as detrital, were not included in the modelling to avoid interference. Three grains dated at 1875±33 Ma (S374-03), 1878±25 Ma (S366map1) and 1885±34 Ma (S392-06 core) were also excluded from the modelling because they were interpreted as outliers. The data set of average ages was modelled for one single population and successively for larger number of populations until a satisfactory chi-square probability value was reached.

The results from modelling are presented in Table 6.8 and Figure 6.30. Figure 6.30 presents the data modelled with a 4 age population model. Age models using distribution of 1, 2 and 3 age populations were previously applied to the data set. However, only the 4 population distribution yielded an acceptable probability values for all populations. Ages calculated for these four populations are presented in Table 6.8. Modelled populations match the age clusters observed on the probability curves (Fig. 6.29).

Table 6.8 : Results from least squares modelling. Data are presented for each identified age group.

Age group	Weighted average (Ma)	2σ-err. of mean (±Ma)	CHI2	Probability	# of ages
Group #1	1766	9	3.7	88.2 %	9
Group #2	1799	5	6	65.1 %	9
Group #3	1829	5	6.9	73.2 %	11
Group #4	1850	5	3.3	85.1 %	8

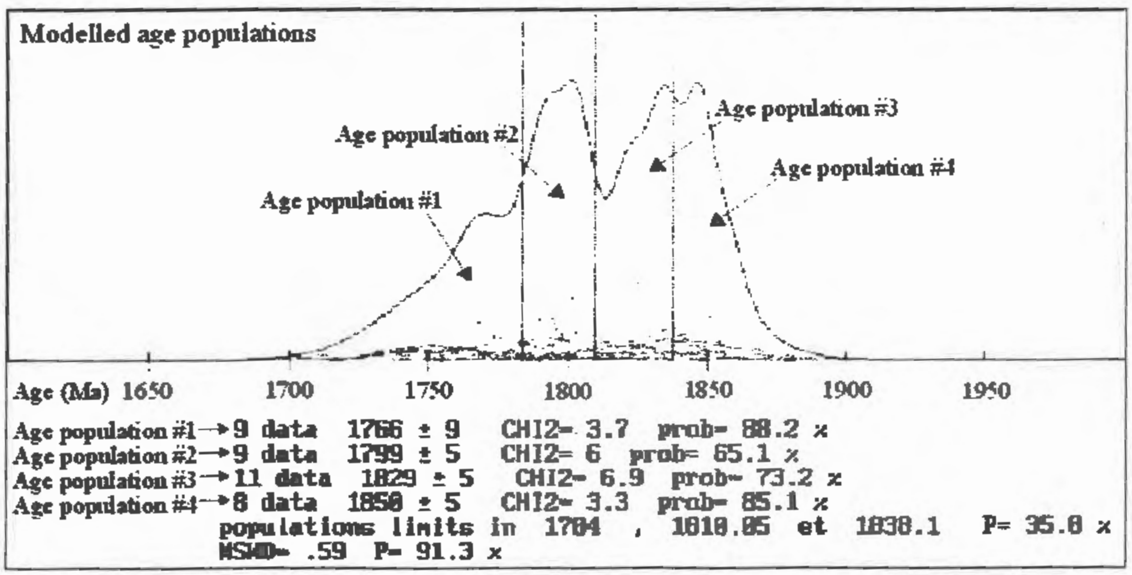

Figure 6.30: Age model produced using least-square modelling software provided by J.-M. Montel. Small curves are individual normal probability curves drawn for of each age data. The broader curve is the cumulative probability curve of all ages from every transects (excluding outliers and grains interpreted as detrital). Arrow indicates modelled age populations. Vertical bars are population limits.

6.7 Summary

In summary, the EMP chemical dating of LBF monazite reveals that growth of monazite in the LBF spanned over range of ca.100 My. The age data are mainly distributed around two broad age clusters. Further data analysis including statistical modelling and normal probability curve plots led to the suggestion that the two main broad peaks represent four age clusters. The oldest monazite grains analysed (S375-12 and S392-05) yielded ages of ca.1910 Ma and can arguably be interpreted as detrital as well as metamorphic (Section).A last group of three grains similar in age, ca. 1880 Ma, is also reported.

7. Discussion and conclusions

7.1 Introduction

This chapter mainly discusses the significance of the results obtained from the EMP chemical dating of LBF monazite. The first section provides a detailed review of available geochronological data for the study area and their interpretation. The second section discusses the significance of a chemical age and the notion of closure temperature for monazite. The following sections present a synthesis of the geochronological data obtained in this study and discuss the constraints that each age provides using information from the petrological setting of individual grains. Finally, geochronological information from chemical dating of LBF monazite grains is combined with available isotopic and geological data for this part of the Trans-Hudson Orogen (THO), and implications for the tectono-metamorphic evolution of the rocks from the study area are discussed.

7.2 Regional geochronological context and interpreted tectonic history

Zircon from the stratigraphically lowest basal quartzite (Dewar Lakes Formation) sampled just above an Archean dome revealed a source of exclusively Archean age. Another quartzite from the Flint Lake area (Fig. 2.2) revealed Archean zircons, but also showed a wider range of ages including some Paleoproterozoic zircons as young as 2159±16 Ma (Wodicka et al., 2003). A quartzitic sample from within the Bravo Lake Fm gave similar results, suggesting that the Dewar Lakes Formation and the Bravo Lakes Formation recorded a transition from a basin-margin siliciclastic depositional environment, fed by erosion of the Archean Rae craton, to a shallow-marine depositional environment fed by new and younger sources, possibly volcanic arcs. Analysis of detrital zircons from the LBF, which forms the highest stratigraphic unit of the Piling Group, yielded predominantly Paleoproterozoic ages ranging from 1990-1915 Ma. The youngest zircon yielded an age of 1915±8 Ma, hence providing a maximum depositional age for the LBF. The contrast with the lower units of the Piling Group indicates a drastic change in the sediments source (Wodicka et al., 2003).

A large K-feldspar megacrystic monzogranite pluton found in the southernmost part of the study area has been dated at 1897+7/-4 Ma (Wodicka et al., 2002). Although this pluton was originally thought to be a northern extension of the Cumberland Batholith, the 1897+7/-4 Ma age is significantly older than the Cumberland Batholith dated at ca.1870-1850 Ma further south (Wodicka and Scott, 1997; Scott, 1999). The 1897+7/-4 Ma K-feldspar megacrystic monzogranite was suspected to have caused the partial melting of the sedimentary rocks in the south of the study area where abundant migmatite and peraluminous leucogranite were found (Corrigan et al., 2001).

In support of this hypothesis, rafts and enclaves of migmatitic sedimentary rocks are common in the pluton. If these are Piling Group sedimentary rocks, it would provide a minimum age of sedimentation at 1897+7/-4 Ma. A mafic sill intruding the Bravo Lake Formation and dated at 1883.3±4.7 Ma was first thought to be pene-contemporaneous with sedimentation (Henderson and Parrish, 1992) and to provide a maximum age for deposition of the LBF. However, recent work now suggests that the mafic sills were intruded after deposition of the Bravo Lake Formation (Scott et al., 2002; Wodicka, pers. comm.). Another sill, also intruding the Bravo Lake Formation, yielded an age of 1897+10/-5 Ma (Wodicka, pers. comm.). The favoured hypothesis is now that the metasedimentary enclaves contained in the megacrystic monzogranite are Piling Group-related implying that the LBF is younger than 1915 Ma (age of the youngest zircon found near the bottom of the Longstaff Bluff Fm) but older than 1897 Ma (time of megacrystic monzogranite emplacement). Enclaves contained in the monzogranite show evidence of metamorphism prior to or during pluton emplacement. However, no regional metamorphic ages on either monazite or titanite correspond to the megacrystic monzogranite emplacement. The absence of metamorphic ages contemporaneous with the monzogranite emplacement suggests that the metamorphic event recorded by the enclaves was local, probably a high-temperature contact metamorphism (Wodicka, pers. comm.). The regional metamorphic ages recorded by monazite and titanite, which are consistently younger than the megacrystic monzogranite, implies that the regional melting event, evident from the southward increase in metamorphic grade and the abundance of migmatites, was not directly related to the 1897 Ma megacrystic monzogranite.

U-Pb TIMS work by Wodicka (pers. comm.) on a white monzogranite interpreted to be derived from sediments yielded an age of 1835±1 Ma that is inferred to be the age of partial melting. It is also suggested that this metamorphic event recognised in the south of the study area was synchronous with the main metamorphic event described north of the study area (D_{1P} in Corrigan et al., 2001). This metamorphism was the result of thrusting and folding as thin-skin deformation was ongoing over the area.

Another tectonic event affected the southern part of the study area at ca. 1800-1810 Ma (Wodicka et al., 2003, Wodicka pers. comm.); this is inferred to be responsible for the thrusting of the Bravo Lake Formation to its present structural position on top of some LBF turbidites. This would have also caused exhumation of higher-grade rocks south of the Great Southern Thrust (a major thrust surface that juxtaposed rocks from the Lower Piling with rocks of the Upper Piling Group during D_{1P}; de Kemp et al., 2002). This event is likely correlative with the thick-skinned deformation event (D_{2P} in Corrigan et al., 2001). Metamorphic monazite from Archean basement also yielded ages of 1877-1874 Ma and 1856 Ma (Wodicka et al., 2003). These ages mark the onset of regional metamorphism.

7.3 <u>Significance of chemical age, closure temperature and Pb diffusion in monazite</u>

Chemical ages calculated for monazite are based on its Pb, Th, and U content. The chemical age represents the time when diffusion of both radioactive parent and daughter elements stopped. In fact, the chemical age is the record of the time at which the U-Th-Pb monazite system closed: the time at which the parent as well as the daughter radioactive elements became immobile. This definition applies to mineral that grew above its closure temperature. If the mineral grew at conditions below its closure temperature, the age represents the time of mineral growth.

Because solid diffusion of elements in mineral phases is strongly dependent of temperature (Dodson, 1973), the time at which diffusion of radioactive parent and daughter elements stopped corresponds to a specific temperature. Dodson (1973) demonstrated that the range of temperature over which radioactive elements become immobile is short relative to the long half-life of elements such as Th and U. The temperature below which elements from a chemical system become immobile is called closure temperature.

Knowledge of the closure temperature of a chemical or isotopic system bears great significance in the interpretation of the age. In monazite, diffusion studies of Pb were carried out to more accurately restrain the range of monazite closure temperatures. The earlier Pb diffusion studies of Smith and Giletti (19971997) found closure temperature in the order of 500°C and 650°C for monazite crystals of 10 and 100 μm respectively. However, many studies report monazite grains that retained older ages through later magmatic or metamorphic temperatures as high as 710±30°C (Parrish, 1990) or 850°C (Spear and Parrish, 1996) suggesting that monazite has a higher closure temperature. Most recent work from Cherniak et al. (2004) on Pb diffusion in monazite reveals that diffusion rates of Pb in monazite are low. Closure temperature calculated from the results of Cherniak et al. (2004) give values of 950°C and 1050°C for monazite grains of 10 and 100 μm respectively at a cooling rate of 10°C/Ma. These latest results suggest that monazite has an ability to retain Pb more efficiently than zircon. Finally, other factors such as fluid interaction may lower the closure temperature of monazite and cause the resetting of the chemical system likely by dissolution (Hawkins and Bowring, 1997; Townsend et al., 2000).

For the LBF, the earlier considerations on monazite closure temperature imply that, since metamorphic conditions did not exceed 900°C in the area (Table 2.1), older generations of monazite were not likely to be reset by subsequent metamorphic events. However, hydrothermal events (Hawkins and Bowring, 1997; Townsend et al., 2000) or even dissolution and reprecipitation of monazite in response to changes affecting the matrix phases (Ayers et al., 1999) could have caused resetting of monazite U-Th-Pb system.

7.4 Age distribution.

Data obtained from EMP chemical dating of monazite from the LBF reveal a range of ages from ca.1740 Ma to ca.1910 Ma. Graphical representation of age data using histograms and cumulative probability curves (Chapter 6) show that the data are not randomly distributed, but cluster around few values. These age clusters can be interpreted as distinct age populations. The spread of ages either around each cluster would then represent a normal distribution resulting from analytical error.

Results from statistical modelling are compared to the age distribution within each transect using cumulative probability curves. The following section presents the variation in age distribution in each transect. Age variation between transect is examined and correlation between transects is proposed. Figure 7.1 presents normal probability curves drawn from grain/domain average ages for each transect (grey) the cumulative probability curve for all transects (black). Results from statistical modelling are also shown.

In Figure 7.1, one can observe that data within each transect cluster around specific values. These age clusters possibly represent different episodes of monazite growth. The age of the populations modelled is indicated on top of Figure 7.1 and is projected through the probability curves (dashed grey lines). Correlation between age clusters and the four modelled age populations is relatively good, although not perfect. Figure 7.1 shows that not all age clusters are present in every transect. The number of clusters is variable from one transect to another and, importantly, the position of each cluster also varies slightly. These two observations are important in interpreting results from age modelling. The age population modelling assumes a single value for each age population, however it is possible that the same event occurs at a different time in different transects. Variation in the number of age clusters shown on Figure 7.1 and in the

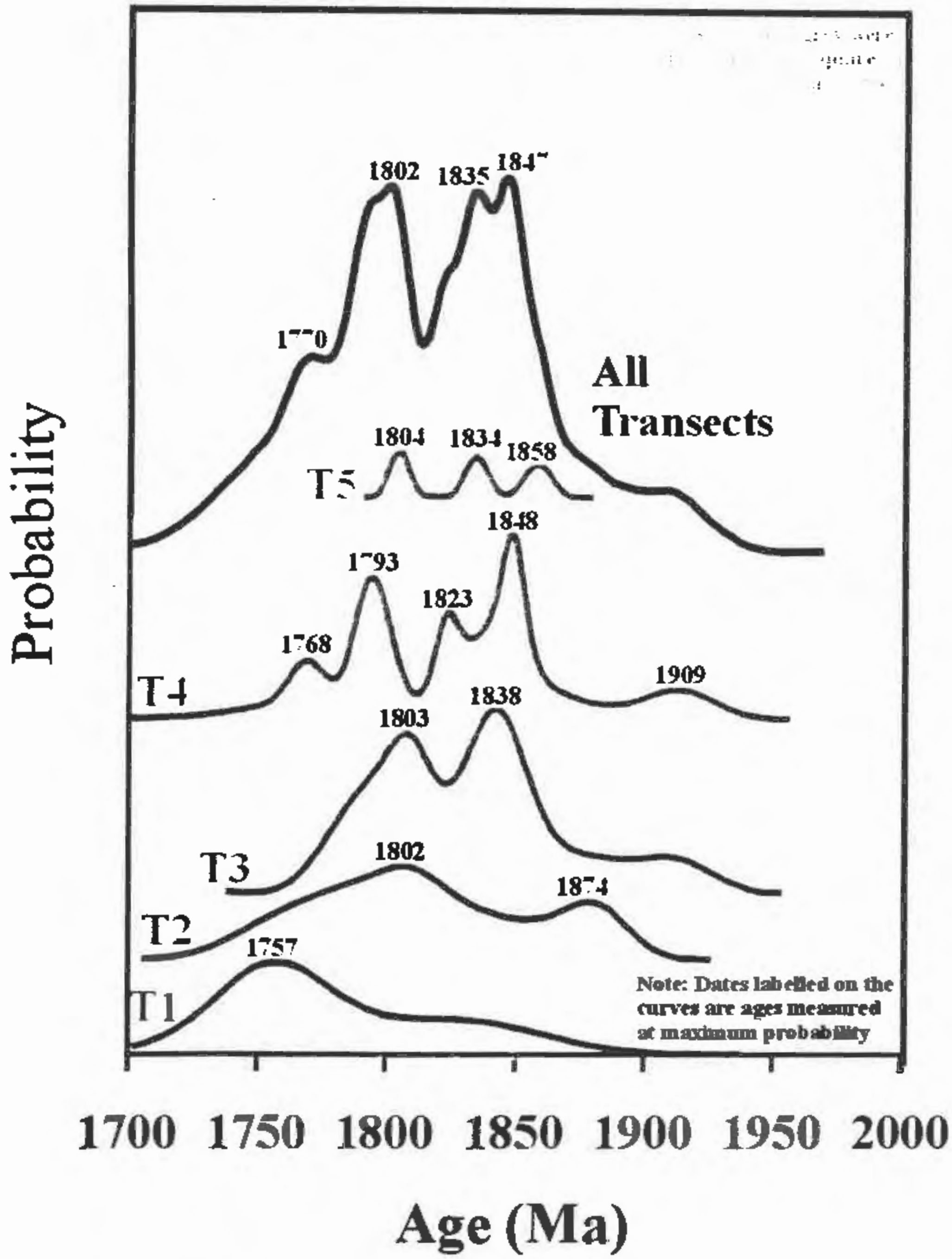

Figure 7.1 : Composite figure showing the cumulative probability curve of average ages of all transects, in black, with cumulative probability curves of average ages for each transect, in grey. Probability curve profiles have not been altered and all transects have been fitted according to the X-axis scale. The Y axis gives the relative variation in probability within each transect. Peaks represent ages with high probability values. Age populations determined from statistical modelling are shown in grey.

position of these age clusters is interpreted to reflect spatial variation in the monazite growth history.

The two sets of ages not included in the modelling (outliers) are also distinguishable in Figure 7.1. The first set (E_0) comprises two grains that gave ages of 1908±29 Ma (S375-12) and 1913±26 Ma (S392-05) and are probably detrital (Table 7.1). The second set consists of three grains dated at 1875±33 Ma (S374-03), 1878±25 Ma (S366map1), and 1885±34 Ma (S392-06 core; Table 7.2), which are slightly younger than the first set and distinctly older than the rest of the LBF monazite dated. These three grains are very similar in age. Despite no clear textural resemblance could be drawn between these grains, they possibly represent an earlier phase (E_1) of monazite growth. This event would be the first record of monazite growth in the LBF. Ages from E_0 and E_1 are grouped separately in this section, but the large error on the age of these grains relative to the age difference do not allow to firmly state that these age clusters are distinct (details in Section 7.5).

The second oldest episode of monazite growth (E_2) documented in the LBF corresponds to the 1850±5 Ma modelled age population. Two age clusters in T3 and T4 as well as one grain from T5 correlates with this event. Ages consistently get younger from T5 to T3, varying from 1858 Ma to 1848 Ma and 1838 Ma. If these grains all correspond to the same monazite-forming event, the northward younging of ages indicates the existence of an age gradient. A record of this event in T1 and T2 is not clear from the probability curves, although results presented in Table 6.3 and 6.4 revealed that in each transect one grain yielded ages at ca. 1840-1850 Ma and may be correlated with this event. The few E_2 ages yielded by grains from T1 and T2 in the north may indicate that E_2 mainly affected the northern part of the study area. However, north of the study area, some monazite and titanite grains also yielded ages similar to E_2 (Wodicka, pers. comm.). List of all grains grouped in E_2 is given in Table 7.3.

The second age population defined from modelling was 1829±5 Ma (E_3). Probability curves reveal that only one age cluster from T4 and one grain in T5 show ages correlative with this event. Age variation between T4 and T5 suggests that this monazite-forming event was recorded earlier in T5. The age gradient would be younging towards the north similarly to the E_2 event. However, data are too scarce to firmly support the presence of an age gradient. The lack of correlative age clusters in other transects is tentatively explained by the possibility that E_3 may be a local episode of monazite growth restricted to the southern part of the study area. List of monazite grains grouped in E_3 is provided in Table 7.4. Since the distribution of age clusters suggests that E_3 was not recorded in T3 and that the 1838 Ma age cluster in T3 is interpreted to be correlative with E_2 grain, ages from 1810 to 1830Ma were assigned to the nearest event, E_2 or E_4 (Tables 7.3 and 7.5).

Distinct age clusters correlative with the third model age population (E_4), 1799±5 Ma, are found in T2 to T4. One grain in each of T1 and T5 also yielded correlative ages. Ages of the three correlative age clusters are very similar and no age gradient is observed (Fig. 7.1). The two grains in T1 and T5 also present very similar ages. The record of this event is more widespread and correlative ages are also found further north. This contrasts with E_2 and E_3 that show a northward younging age gradient and were arguably more restricted to the south. The list of grains grouped in this event is given in Table 7.5.

The youngest age population (E_5), 1766±9 Ma, defined from modelling is mainly found in T1 and T2 although rare occurrences were recorded in T3 and T4. This suggests that this event was more local and mainly affected the northern part of the study area.

In summary, E_0 and E_1 are possibly distinct events, but the large error on the ages does not allow to confirm this hypothesis. The modelled age populations correspond roughly to age clusters on the transect probability curves. The age cluster distribution reveals that E_2 and E_3 monazite-forming events were not recorded simultaneously throughout the transects. The age distribution for E_2 and E_3 suggests that monazite grew asynchronously through the study area during these two events. Age data indicate that monazite first grew in the south and then progressed to the north. Hence, the modelled age populations E_2 and E_3 correspond to the average age of each of this event that was recorded progressively through the field area. Data for E_4 indicate that this episode of monazite growth was recorded synchronously within all transects. Finally, the latest event, E_5, was mainly recorded in the northern part of the area, although, single data were measured in T3 and T4. Correlation between age clusters is presented in Figure 7.2.

7.5 Interpretation of monazite chemical ages and constraints on the LBF history

The multiple episodes of monazite growth recorded in the LBF agree with field evidence for a complex tectono-metamorphic history (Corrigan et al., 2001; Scott et al., 2002a; Allan and Pattison, 2003; Berniolles, 2003). Results from U-Pb TIMS dating (Wodicka et al., 2002; Wodicka et al., 2003; Section 7.2) also suggest that the study area experienced a complex history, recorded at least partially by monazite grains.

As presented above in Section 7.4, six distinct monazite age groups are recognised throughout the study area. Four of these groups are interpreted as distinct episodes of monazite growth within the LBF. One group comprises two grains interpreted as detrital (Section 6.4). The last group includes three grains close in age that are considered as outliers in statistical modelling. Each of the monazite age group is examined in the following section. Constraints on the tectono-metamorphic and microstructural development of the LBF provided by the different episodes of monazite growth recorded throughout the field area are presented and discussed. Comparison with isotopic ages is also provided.

The oldest data (E_0) come from two monazite grains that yielded ages of 1908±29 Ma (S375-12) and 1913±26 Ma (S392-05) respectively. These grains are interpreted as detrital (Section 6.4) and indicate that sources for the LBF were, partially at least, young Paleoproterozoic rocks. The two detrital grains correlate with results from the conventional TIMS U-Pb dating of LBF detrital zircons that gave ages as young as 1915±8 Ma (Wodicka et al., 2003; Section 7.4).

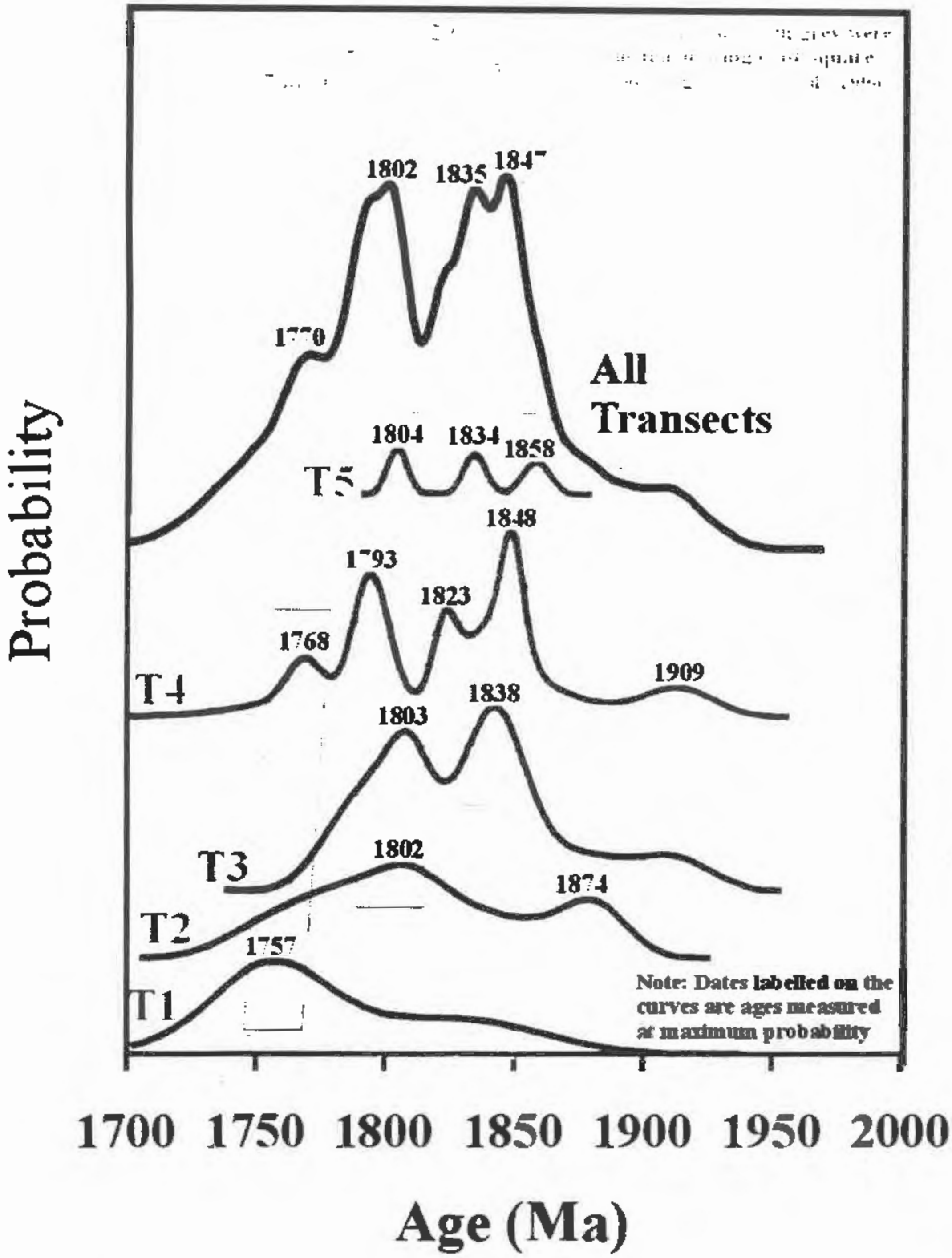

Figure 7.2 : Composite figure showing the cumulative probability curve of average ages of all transects, in black, with cumulative probability curves of average ages for each transect shown in grey. Probability curve profiles have not been altered and all transects have been fitted accordingly to the X-axis scale. The Y axis gives the relative variation in probability within each transect. Peaks represent ages with higher probability values. Grey boxes represent proposed correlation between age clusters from different transects.

Table 7.1: Monazite grain/domain average ages grouped in detrital age group (E_0). Grain descriptions are reported in Appendix 5 and spot age data in Appendix 6. Relevant figures for each grain are indicated in parenthesis in the Texture column.

Transect	Setting	Grain category	Age ± 2σ (Ma)	Grain	Texture
T1	-	-	-	-	-
T2	-	-	-	-	-
T3	Interstitial in Qtz-Kfs	Matrix grain	1908±29	S375-12	Subprismatic, rounded edges (Fig. 6.11)
T4	Included in Bt	Included grain	1913±26	S392-05	Subhedral, concentric zoning (Fig. 6.19)
T5	-	-	-	-	-

The second age group represents the record of the oldest monazite chemical ages since deposition of the LBF and comprises three grains of age ranging from 1875 to 1885 Ma. These grains, similar in age, may represent the earliest record, in the LBF, of a monazite-forming event (E_1). The relatively large error on the age of these grains (ca. ±30 Ma) and the small number of data (3), makes it difficult to discriminate with confidence if the data represent a distinct episode of monazite growth or if they belong to another age group. Statistically the grains from E_1 are not distinct from E_0 or E_2 as calculated from statistical modelling, although grains from E_0 are statistically distinct from E_2. Petrological setting and chemistry of each grain are used to verify the possibility that age cluster E_1 is a distinct episode of monazite growth.

Data from Wodicka et al. (2002) revealed that the emplacement of the megacrystic monzogranite to the south of T5 occurred at 1897+4/-7 Ma. Both detrital monazite grains as well as the three grains from E_1 may legitimately be attributed to the emplacement of the megacrystic monzogranite because they are not statistically distinguishable. Textural information strongly suggests that S375-12 (1908±29 Ma) is detrital. However, textural information from S392-05 (1913±26 Ma) does not as clearly point towards a detrital origin. The relationship of the grains from E_1 relative to the emplacement of the megacrystic monzogranite also cannot be clearly established. The three grains come from different transects and are located in different settings (Table 7.2).

Table 7.2: List of monazites grain/domain average ages grouped in Event 1 (E_1). Grain descriptions are reported in Appendix 5 and spot age data in Appendix 7. Relevant figure(s) for each grain are indicated in parenthesis in the Texture column.

Transect	Setting	Grain category	Age ± 2σ (Ma)	Grain	Texture
T1	-	-	-	-	-
T2	Parallel to S1	Fabric parallel grain	1878±25	S366map1	Prismatic, subhedral
T3	Included in Crd	Included grain	1875±33	S374-03	Granular, anhedral, embayed
T4	Leucosome	Matrix grain	1885±34	S392-06	Anhedral, embayed
T5	-	-	-	-	-

Results from trace analyses of Th, U, and Y were used to try distinguishing between E_0 and E_1 age populations (Fig. 7.3). Grain S375-12 and the core of S392-05 have composition relatively distinct from the four other grains or domains. The three grains from E_1 have a relatively similar composition. The rim of S392-05 also has a composition similar to the three grains from E_1. Trace analyses for the rim of S392-05 gave an age of 1881±59 Ma and 1921±29 Ma in the core, but, because they were statistically indistinguishable from each other, ages from both domains were combined. Based on chemical composition, it is proposed that the rim and the core be considered as the record of two distinct episodes of monazite growth. Ages from the core and the rim, although not statistically different, are similar toS375-12 and E_1 respectively. To discriminate if the E_1 ages are the record of the granite emplacement, or if they represent an episode associated with a different tectonic event, the data are not sufficient. Note that metamorphic monazite dated by TIMS (Wodicka, pers. comm.) yielded ages at ca. 1877-1874 Ma in the Dewar Lakes area (Table 6.1). The average age of E_1 grains is closer to these monazite ages measured by TIMS than the age of the monzogranite emplacement.

Using the petrological setting constraints on the metamorphic history can be inferred from these monazite grains. Grain S374-03 is included in a cordierite grain and shows minor embayments indicating that cordierite growth occurred after the grain crystallised at 1875±33 Ma. Embayments on the monazite grain indicate that monazite was partially consumed prior to cordierite growth. The core of grain S392-06 is 1885±34 Ma. The core is rounded and has an irregular boundary. One cuspate embayment is present. These observations indicate that prior to growth of the rim the core was partially consumed. The last grain is S366map1 which gave an average age of 1878±25 Ma. This grain is subprismatic and parallel to the mica fabric. This fabric is tentatively interpreted to be S1. Hence, S366 map1 provides a minimum age of 1878±25 Ma for development of S1, since the parallelism of the monazite grain suggest that it likely grew during or after S1. This is older than the S1 maximum age (1840±56 Ma) inferred from grain S371-18. Because of the large error on S371-18, caused by the low U and Pb in the grain, S366map1 and S371-18 ages are not statistically different. The weighted average of the four grains grouped in E_1, including S392-05 rim, is 1879±17 Ma.

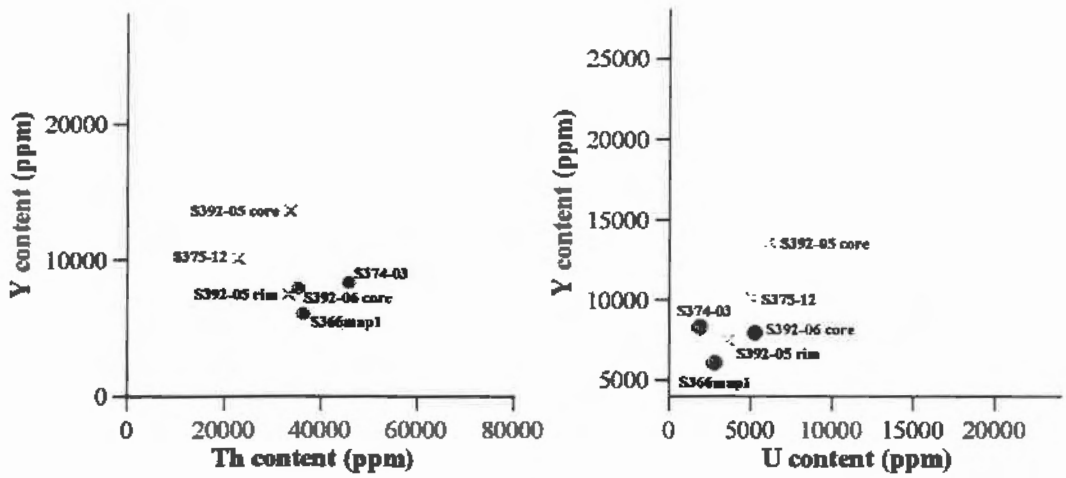

Figure 7.3 : Plot of Y vs Th content and Y vs U content of grains from both E_0 and E_1. X represents detrital grains and circles grains from E_1. Content of Th, U and Y is from trace analyses proceeded on the grains.

The second event (E_2) modelled at 1850±5 Ma is correlated by an age cluster in T3 and T4. Single grains correlative to this event are found in T1, T2 and T5. Based on the probability distribution curve, ages are interpreted to get younger northward (Fig. 7.8). Ten grain/domain average ages are attributed to this event. The petrological setting of these grains indicates that this episode of monazite growth predated the development of garnet and low-temperature cordierite. Table 7.3 lists the grains with their petrological setting and textural features.

Two grains, S388-01 and S392map5, included in a garnet porphyroblast provide a maximum age for the garnet growth. Grain S388-01 is zoned and the rim (Table 7.5) is interpreted as a late hydrothermal recrystallization of the grain. The garnet porphyroblast is cracked and fluids may have circulated through the cracks of the garnet porphyroblast. The unusual shape of the monazite core with long and narrow cuspate embayments can be realistically explained by an inward progressive recrystallization likely caused by hydrothermal fluids. Grain S388-02 is included in the same garnet porphyroblast than S388-01 and presents an age similar to the recrystallized rim of S388-01. Monazite S388-02 has patchy zoning pattern which has been interpreted by other studies (Stern and Sanborn, 1998; Ayers et al., 1999) as the result of differential recrystallization or replacement. Other studies (Hawkins and Bowring, 1997; Townsend et al., 2000) also reported that grains with patchy zoning commonly yield younger ages that are likely related to partial resetting by recrystallization of the grain. Accordingly, S388-02 displays the same younger age than S388-01 rim. Additionally, both monazite grains are included in the same garnet porphyroblast and cracks in the garnet are visible around both monazite grains. Hence, S388-02 would be the result of a complete recrystallization via fluid interaction. Finally, the LBF shows a predominant location of patchy monazite in leucosome and granitic material derived from metapelites melting suggesting that melt interaction played an important role in the origin of the patchy zoning pattern, which would agree with observations from other studies mentioned earlier (Stern and Sanborn, 1998; Ayers et al., 1999).

Grain S397-02 located in a granite matrix is granular and rounded unlike typical magmatic monazite grains. This suggests that the grain was consumed partially during or before granite emplacement. Hence, granite must be younger than the monazite grain at 1858±11 Ma. Another grain, S392-17, located in the leucosome component of a migmatite shows a large embayment and provides an upper limit for the age of migmatisation, which is interpreted to be contemporaneous with the production of

Table 7.3: List of monazite grain/domain average ages grouped in Event 2 (E_2). Grain descriptions are reported in Appendix 5 and spot age data in Appendix 7. Relevant figure(s) for each grain are indicated in parenthesis in the Texture column.

Transect	Setting	Grain category	Age ± 2σ (Ma)	Grain	Texture
T1	Parallel to S1	Fabric parallel grain	1840±56	S371-18	Anhedral, elongated, parallel to S1
T2	Overgrown by S2	Fabric parallel grain	1853±39	S366-16	Rounded, irregular boundary, minor embayments
T3	Contiguous with Qtz-Ms	Matrix grain	1847±28	S374-02	Subhedral, one side has an irregular boundary with embayments
T3	In fibrolite cluster	Included grain	1844±20	S374-01	Numerous embayments, anhedral (Fig. 6.14)
T3	Within Ms cluster	Matrix grain	1836±18	S374-05	Prismatic, many small embayments, straight inclusions
T3	Along Qtz-Bt grain boundary	Matrix grain	1836±24	S375-11	Euhedral, prismatic
T4	Included in Grt	Included grain	1855±29	S392-map5	Embayed, irregular boundary (Fig. 5.2d; 6.17)
T4	Leucosome	Matrix grain	1848±12	S392-17	Complex zoning, large embayments one side (Fig. 5.1g; 5.2f)
	Included in Grt	Included grain	1848±08	S388-01 core	Irregular core with cuspate embayments, cracked (Fig. 6.18; 6.21; 7.2)
T4	In Bt cluster	Included grain	1836±26	S392-01 core	Resorbed core, multiple zoning (Fig. 5.1f)
T5	Leucogranite	Matrix	1858±11	S397-02	Granular, subrounded

peraluminous leucogranite, at 1848±12 Ma. Note that S392-17 also displays a patchy zoning. Grain S366-16 (1853±39 Ma) is overgrown by S2 and provides a maximum age for the development of S2. In T1, a grain parallel to S1 gave an age of 1840±56 Ma. Finally, matrix grains in T3 gave ages ranging from 1836 Ma to 1847 Ma. Record of this event is reported by Wodicka (2003) who dated metamorphic monazite that yielded an age of ca. 1856 Ma. This age is interpreted as the onset of metamorphism. Data from chemical dating of monazite suggest that the E_2 event was regional because correlative ages are in every transect. The petrological setting of the grains also indicates that the E_2 event occurred prior to growth of low-temperature cordierite and garnet porphyroblasts but after or synchronously with the development of the S1 fabric. The record of this event was masked by later metamorphic events.

The third event (E_3) corresponds to the age population modelled at 1829±5 Ma. From the age distribution on the probability curves, this event is interpreted to be recorded only in Transects 4 and 5. Two monazite grains included in garnet, S383-02 and S397-01, yielded similar ages of 1835±17 Ma and 1834±09 Ma respectively providing a maximum age for growth of garnet. These garnet porphyroblast are interpreted to be from the same generation than the garnet porphyroblasts including monazite grains from E_2.

Table 7.4: List of monazite grain/domain average ages grouped in Event 3 (E_3). Grain descriptions are reported in Appendix 5 and spot age data in Appendix 7. Relevant figure(s) for each grain are indicated in parenthesis in the Texture column.

Transect	Setting	Grain category	Age ± 2σ (Ma)	Grain	Texture
T1	-	-	-	-	-
T2	-	-	-	-	-
T3	-	-	-	-	-
T4	Included in Grt	Included grain	1835±17	S383-02	Elongated (Fig. 6.22)
T4	Leucosome	Matrix grain	1822±33	S392-06 rim	Rim partially embayed
T4	Included in Bt	Included grain	1822±09	S383-07	Subhedral, elongated, concentric zoning, parallel to cleavage (Fig. 6.22)
T5	included in Grt	Included grain	1834±09	S397-01	Zoned, euhedral core and rim (Fig. 5.1d; 6.25)

The maximum age for garnet growth is provided by the youngest included monazite grain or domain which does not show indication of possible recrystallization. Hence, the garnet-forming event may be younger or synchronous to crystallisation of E_3 monazite grains. Consequently, it is reasonable to propose that garnet growth is associated with the E_3 event.

Available isotopic data from TIMS suggest that an event related to thin-skinned deformation (D_{1P} in Corrigan et al., 2001) culminated at ca. 1838-1835 Ma (Wodicka, pers. comm.) and caused the partial melting of the LBF metasedimentary rocks in the south. This event correlates well with the E_3 event of monazite growth. However, information from the petrological setting of monazite grains does not suggest that this event was related to a major melting event. Ages of monazite from the study area rather suggest that partial melting of the LBF metasedimentary rocks and migmatisation occurred around ca. 1800 Ma during the E_4 monazite forming event as discussed below.

The fourth monazite-forming event (E_4) occurred at ca.1800 Ma and the corresponding modelled age population was 1799±5 Ma. This event is abundantly recorded throughout the study area. Age clusters correlative with this event are found in T2, T3 and T4. Single grains of similar ages are also found in T1 and T5. Information from chemical ages and petrological setting suggests that some grains formed during E_4 event grew during partial melting partial of the metasedimentary rocks.

Monazite S401-01, a well-shaped euhedral grain dated at 1804±08 Ma, is located in a leucogranite formed from the partial melting of the LBF metasedimentary rocks. Another grain, S383-01, located in the Qtz-Kfs-Pl leucosome of a migmatitic sample was dated at 1798±13 Ma. Additionally, numerous matrix grains from T2 and T3 (Table 7.5) also gave ages of ca.1800 Ma. These data strongly suggest that melting occurred at ca. 1800 Ma. Oppositely, TIMS ages indicate that the migmatisation event occurred between 1830-1835 Ma (Wodicka, pers. comm.). The discrepancy between these two interpretations is not clear. Since the samples dated by both methods were collected from locations ~40 km apart, it is possible that two different generations of leucosome were sampled. This would imply that the LBF metasedimentary rocks melted twice, which has not been documented.

Garnet porphyroblasts, interpreted to be younger or contemporaneous with E_3, are generally resorbed. Garnet porphyroblasts located in the Qtz-Kfs-Pl leucosome of the migmatitic samples display a skeletal habit with multiple major embayments interpreted as resulting from resorption and the grain also contains numerous fractures. Hence, the young ages obtained from S388-01 rim and S388-02 can be attributed to interaction with fluids associated to the melting event that circulated the garnet network of cracks (Fig.6.18)

Table 7.5: List of monazite grain/domain average ages grouped in Event 4 (E_4). Grain descriptions are reported in Appendix 5 and spot age data in Appendix 7. Relevant figure(s) for each grain are indicated in parenthesis in the Texture column.

Transect	Setting	Grain category	Age ± 2σ (Ma)	Grain	Texture
T1	Parallel to S1	Fabric parallel grain	1815±63	S371-21	Subhedral, elongated, straight edges
T2	Parallel to S1	Fabric parallel grain	1823±37	S366map2	subhedral, subprismatic, elongated, parallel to S1 (Fig. 5.1b; 6.8)
T2	Bt-Qtz grain boundary	Matrix grain	1805±26	S367-10	grain resorbed (embayed) on half of its grain boundary
T2	Bordered by Bt and Qtz-Pl	Matrix grain	1791±33	S366-15	subhedral, few inclusions, zoned
T3	Contiguous with Ms and Qtz-Pl	Matrix grain	1818±39	S374-04	one large embayments, straight boundary with micas
T3	Included in Crd	Included grain	1818±26	S373-01	anhedral, granular, irregular boundary
T3	Interstitial between Qtz-Kfs	Matrix grain	1805±15	S373-02	granular, one small embayment
T3	Qtz-Kfs-Pl matrix	Matrix grain	1795±23	S373-03	subhedral, subprismatic
T3	Contiguous with a Bt grain	Matrix grain	1792±24	S373-05	subhedral, straight edges, prismatic
T4	Leucosome	Matrix grain	1798±13	S383-01	euhedral core, rounded rim (Fig. 5.1c; 5.2c; 6.22)
T4	Included in Grt	Included grain	1792±12	S388-01rim	anhedral, granular, irregular rim, core with cuspate embayments (Fig. 6.18; 6.21; 7.2)
T4	Included in Grt	Included grain	1791±13	S388-02	anhedral, granular, complex zoning, numerous cracks (Fig. 5.2e)
T5	Leucogranite	Matrix grain	1804±08	S401-01	euhedral, complex zoning, prismatic (Fig. 5.1h; 6.26)

Two grains from T1 and T2, S371-21 (1815±63) and S366map2 (1823±37), parallel to S1 yielded ages correlative with E_4, although these ages are slightly older. This would attribute the development of S1 to the E_4 event that produced the fourth generation of monazite. However, S1 was earlier interpreted to be linked to the older D_{1P} event described in Corrigan et al. (2001). One explanation may arise from the large analytical errors of these two grains which makes them statistically indistinguishable from E_3 or even E_2 events. Hence, these two grains could in fact be formed during E_2. This example shows that the narrow time span between the multiple monazite-forming events that occurred in the LBF is challenging the limit of resolution of the chemical dating of monazite. Use of other information such as grain chemistry, zoning pattern and petrological setting generally successfully correlates with grain chemical ages that occasionally have larger errors.

The fifth and last event (E_5) occurred around ca.1770 Ma (age population modelled at 1766±9 Ma). The youngest event recorded in the LBF is mainly found in the northern part of the area. As highlighted by monazite grown parallel to S2, it is likely linked to the development of the S2 fabric in the north. It is possible that this event was more local. No TIMS ages are correlative for this age. Because of the generally small size of the grains bearing this age, it is likely that these grains could not be recovered from the crushing process preceding TIMS analysis or that bulk rock composition was not appropriate as LBF samples collected were psammites and wackes.

The existence of a younger grain in an older setting (S1) can be explained as the result of later monazite growth or recrystallization parallel to S1. In support of this hypothesis, the grain is not elongated to the same extent as the other two S1-parallel grains. Also, its age is similar to S2-parallel grain ages, corresponding to a known period of monazite growth.

Ages correlative with E_5 were also found in monazite grains partially included in resorbed biotite. This is unexpected as the textural relationship suggests that these should be older. A 1761±90 Ma age was yielded by the outermost rim of grain S392-01 and is interpreted to be from hydrothermal origin. The fluids could have migrated through biotite cleavage and fractures, providing that the grain was not perfectly sealed, and caused growth or resetting of the outermost rim. In the case of S388-16 (Fig.6.21), the 1768±14 Ma age is in the whole grain. The grain is parallel to the mica cleavage and would normally be interpreted to be syn-biotite growth. Hence, this age is difficult to explain in regards to its petrological setting. One explanation could be that the grain was epitaxial and replaced an earlier mineral or recrystallization of the grain was caused from hydrothermal fluid infiltration.

Table 7.6: List of monazite grain/domain average ages grouped in Event 5 (E_5). Grain descriptions are reported in Appendix 5 and spot age data in Appendix 7. Relevant figure(s) for each grain are indicated in parenthesis in the Texture column.

Transect	Setting	Grain category	Age ± 2σ (Ma)	Grain	Texture
T1	Parallel to S2	Fabric parallel grain	1771±51	S371-09	Subhedral, subprismatic (Fig. 5.2a)
T1	Parallel to S2	Fabric parallel grain	1756±36	S371-06	Elongated, straight edges (Fig. 6.3)
T1	Parallel to S2	Fabric parallel grain	1756±47	S371-19	Subprismatic (Fig. 5.1a)
T1	Parallel to S1	Fabric parallel grain	1741±48	S371-20	Anhedral, granular, fractured (Fig. 6.4)
T2	contiguous with Ms and Qtz-Pl	Matrix grain	1775±32	S367map1	Anhedral, granular, minor embayment on one side
T2	Oblique to S1	Fabric parallel grain	1751±35	S366-07	Square, subprismatic, oblique to S1 fabric, embayment (Fig. 6.7)
T3	Contiguous with Ms and Qtz	Matrix grain	1777±23	S373-04	Anhedral, granular (Fig. 6.12)
T4	Included in Bt	Included grain	1768±14	S388-16	Elongated, concentric zoning, discontinuous rim, parallel to Bt cleavage (Fig. 6.20)
T4	In Bt cluster	Included grain	1761±46	S392-01 rim	Discontinuous rim, embayed or minor overgrowth (Fig. 5.1f)
T5	-	-	-	-	-

LBF monazite grains yielded ages spanning over more than 100 My. These ages cluster around two main broad peaks (ca.1800 Ma and ca. 1840 Ma; Fig. 7.2), which, based on observation of age probability distribution in individual transects and statistical modelling, are likely combined peaks (younger broad peak, ca.1765Ma and ca.1800 Ma; older broad peak, ca.1830 Ma and ca.1850 Ma). In this study, the these four age cluster were discussed separately and evidence from petrological setting of monazite grains, statistical modelling and good correlation with known TIMS ages tend to support the hypothesis that these age clusters represent distinct episode of monazite growth. However, the large error on grain ages relative to the difference bet te different age cluster do not allow to dismiss completely the possibility that of more than

In summary, five distinct monazite-forming events are recognised in the LBF. Also two detrital grains were identified. Monazite-forming event (E_1) may be correlative with emplacement of the megacrystic monzogranite in the south or represent a younger metamorphic event yet unrelated to any specific metamorphic feature of the LBF. The second event (E_2) was more regional and pre-dated development of garnet and low-grade cordierite. Development of the S1 fabric is likely related to this event. Event E_2 was probably masked by later metamorphic event. The third event (E_3) seems to be restricted to the southern part of the study area and may be related to formation of garnet and cordierite porphyroblasts. The fourth monazite-forming event (E_4) was synchronously recorded throughout the study area and corresponds to the partial melting of the metasedimentary rocks. Finally, the last monazite-forming event (E_5) is related to the development of the a late mica fabric identified as S2.

7.6 Implications for the THO tectono-metamorphic history

The record of 5 episodes of monazite growth suggests a complex tectono-thermal history for the LBF. The recognition of potential age gradients is interesting in terms of tectonic evolution of the LBF. The northward younging of the E_2 and E_3 episodes of monazite growth correlates very well with the idea of a northward progression of the thin-skinned deformation. Faulting and thickening of the supracrustal material occurring early in the south correlates with monazite ages being older in the south and the progression of the deformation to the north is recorded by the northward younging monazite age gradient.

The synchronous development of the E_4 monazite generation throughout the study area indicates drastic changes in the nature or dynamics of the operating tectonic processes. The chemical age data for monazite suggest that this event, related to the partial melting of the sedimentary rocks, occurred synchronously throughout the transects. But it is more likely that the progression of the deformation occurred much faster than for previous events, so progression in age from the south to the north could not be recognised within the resolution of monazite chemical dating.

The last event mainly recorded in the northern part of the study area could represent the locking of active deformation in the south and progression of the deformation front further north. The geochronological data obtained from monazite chemical dating suggest that THO was active for a period spanning from ca.1880 Ma to 1770 Ma.

The good agreement of monazite ages yielded by chemical EMP dating confirms the potential of this technique for deciphering the thermal history of areas affected by multiple events. Preservation of the petrological setting of the analysed grains and information on their chemical content reveal to be very insightful in interpreting the grain ages. However, the lower resolution of the technique may require to use it in combination with another isotopic technique when attempting to distinguish between ages differing only by a small amount of time. The development of thermobarometry tools using monazite will give further significance to these ages.

7.7 :Suggestions for further work

Investigation of the LBF monazites provided useful information on the tectono-metamorphic history of the THO in this area as well as on monazite behaviour with increasing metamorphic grade. However, the limited extent of the study left many questions pending. Numerous problems certainly deserve greater attention from researchers. Areas of work for which further investigation would be complementary with this study and help understanding monazite behaviour under prograde metamorphic sequence are presented below.

1) Detailed examination of the bulk rock geochemistry of the samples is required to permit comparison with other prograde metamorphic sequences since bulk rock composition has been proven to be an important controlling factor for monazite stability under a range of metamorphic conditions.

2) A more extensive study of the distribution and nature of accessory phases in the LBF combined with element mapping tools, bulk rock geochemistry and the chemical characterisation of accessory minerals will provide a better understanding of the interplay between monazite and other accessory phases.

3) Further investigation of migmatites to better understand the behaviour of monazite during partial melting of metasedimentary rocks will be helpful.

4) Thermometry and barometry of monazite with accompanying mineral assemblage would give precise knowledge of the P-T conditions at the time of monazite equilibrium and provide significant information on the P-T-t history of the rock.

5) Investigation of monazite inclusions would reveal information on pre-monazite mineral assemblages and possibly P-T conditions.

6) SHRIMP analyses carried out on selected monazite grains previously dated by EMP chemical dating would allow to test the accuracy of the CHIME technique and confirm the validity of the results.

7.8 <u>Conclusions:</u>

1. In the LBF, monazite appears early in the prograde metamorphic sequence. Upper greenschist rocks contain small but widespread metamorphic monazite grains. The

low to moderate CaO content of the LBF possibly suppressed the stability field of allanite, a common precursor to monazite in metapelites, allowing monazite to appear first at upper greenschist facies.

2. The transition from the Kfs-Sil zone to the migmatite zone coincides with a significant increase in size and abundance of monazite and significant changes in monazite composition, notably a significant increase in Y content. Highly resorbed garnets are reported from this transition.

3. Increasing metamorphic grade strongly influences the composition of LBF monazite. The LREE content decreases, whereas the HREE, Ca, Th, U, Y content increases; the P and Si content is relatively stable. The broader spread in element content values observed at higher grade indicates that other factors than metamorphic grade also control monazite composition. Brabantite substitution is the main mechanism to incorporate Th and U in monazite.

4. Monazite is scarce in leucosomes, but abundant in granitic bodies. Inherited monazites were identified in the granite. Both monazite and xenotime with euhedral magmatic textures were identified in the granite suggesting a magmatic crystallisation. The absence of monazite from the leucosomes suggests that the melt was not yet saturated enough in PO_4 and LREE to crystallise monazite.

5. Based on EMP U-Th-Pb chemical dating of monazite 6 different age populations within LBF monazite were recognized. Detrital grains (E_0) older than 1908 Ma were identified. Episodes of monazite growth were dated at ca. 1878 Ma (E_1), 1850 Ma (E_2), 1830 Ma (E_3), 1800 Ma (E_4) and 1770 Ma (E_5).

6. Significance of E_1 was not resolved. E_1 ages are within error from E_0 grains that are probably detrital; E_1 monazite ages are also statistically similar to the age of the monzogranite emplacement in the south (1897+7/-4 Ma), and similar to metamorphic monazite ages reported by Wodicka et al. (ca.1877-1874 Ma; 2003).

7. E_2 monazite ages are correlative with thin-skinned deformation and petrological textures suggests it may be associated with cordierite growth and S1 development.

8. E_3 monazites ages are within error from E2 and E4, but normal probability plots, statistical modelling and petrological setting suggest that it represents a distinct episode of monazite growth. However, further work is required to confirm this hypothesis. Petrological data suggest that E_3 is associated to garnet growth.

9. E_4 monazite is interpreted to be associated to partial melting of the LBF in the south. This event is widespread in the study area.

10. E_5 monazite ages were mainly reported from monazite in T1. The parallelism of the grains with an S2 fabric suggests that these grains are syn- to post- S2 development

11. The age data indicate a northward younging of the E2 and E3 events. These two events are mainly recorded in the southernmost transects. E4 is synchronously recorded throughout the field area and E5 is mainly recorded in the northern part of the study area. This new information suggests a variation in the tectonic style through time and/ or a migration of the main deformation zone.

References

Allan, M. M. and Pattison, D. R. M. 2003. Deformation history and metamorphism of a synformal depression, Longstaff Bluff Formation metaturbidite, central Baffin Island, Nunavut. Geological Survey of Canada. Current Research. 2003-C15. 11 p.

Ayers, J. C., Miller, C., Gorisch, B. and Milleman, J. 1999. Textural development of monazite during high-grade metamorphism; hydrothermal growth kinetics, with implications for U, Th-Pb geochronology. American Mineralogist, **84**; 1766-1780.

Bea, F. and Montero, P. 1999. Behavior of accessory phases and redistribution of Zr, REE, Y, Th, and U during metamorphism and partial melting of metapelites in the lower crust; an example from the Kinzigite Formation of Ivrea-Verbano, NW Italy. Geochimica et Cosmochimica Acta, **63**; 1133-1153.

Berniolles, F. 2003. Cross-section through the Central Baffin Project area, Nunavut: Report of progress. Central Baffin Workshop, Program with abstracts, Geological Survey of Canada, p.4.

Bethune, K. M. and Scammell, R. J. 1997. Legend and descriptive notes, Koch Island area, District of Franklin, Northwest Territories (part of NTS 37 C). Geological Survey of Canada. Open File. 3391.

Bethune, K. M. and Scammell, R. J. 2003. Geology, geochronology, and geochemistry of Archean rocks in the Eqe Bay area, north-central Baffin Island, Canada; constraints on the depositional and tectonic history of the Mary River Group of northeastern Rae Province. Canadian Journal of Earth Sciences, **40**; 1137-1167.

Bingen, B., Demaiffe, D. and Hertogen, J. 1996. Redistribution of rare earth elements, thorium, and uranium over accessory minerals in the course of amphibolite to granulite facies metamorphism; the role of apatite and monazite in orthogneisses from southwestern Norway. Geochimica et Cosmochimica Acta, **60**; 1341-1354.

Bingen, B. and van Breemen, O. 1998. U-Pb monazite ages in amphibolite- to granulite-facies orthogneiss reflect hydrous mineral breakdown reactions; Sveconorwegian Province of SW Norway. Contributions to Mineralogy and Petrology, **132**; 336-353.

Boatner, L. A. 2002. Synthesis, structure and properties of monazite, pretulite and xenotime. Reviews in Mineralogy and Geochemistry, **48**; 87-121.

Broska, I. and Siman, P. 1998. The breakdown of monazite in the West-Carpathian Veporic orthogneisses and Tatric granites. Geologica Carpathica, **49**; 161-167.

Cameron-Shiman, M. 1978. Electron-microprobe study of uranium minerals and its application to some Canadian deposits. Ph.D. Thesis, Edmonton University, Edmonton, Alberta, Canada. 343 pages

Cherniak, D. J., Watson, E. B., Grove, M. and Harrison, T. M. 2004. Pb diffusion in monazite: A combined RBS/SIMS study. Geochimica et Cosmochimica Acta, **68**; 829-840.

Cocherie, A., Legendre, O., Peucat, J. J. and Kouamelan, A. N. 1998. Geochronology of polygenetic monazites constrained by in situ electron microprobe Th-U-total lead determination; implications for lead behaviour in monazite. Geochimica et Cosmochimica Acta, **62**; 2475-2497.

Corrigan, D., Scott, D. J. and St, O. M. R. 2001. Geology of the northern margin of the Trans-Hudson Orogen (Foxe fold belt), central Baffin Island, Nunavut. Geological Survey of Canada. Current Research. 27 pages.

Corrigan, D., St-Onge, M. R., Scott, D. J. and Wodicka, N. 2002. Tectonic context for the Central Baffin Island project, Nunavut: Age, Lithotectonic Framework and Extent of the Trans-Hudson Orogen. Central Baffin Workshop, Program with Abstracts, Geological Survey of Canada, p. 6.

Crowley, J. L. and Ghent, E. D. 1999. An electron microprobe study of the U-Th-Pb systematics of metamorphosed monazite; the role of Pb diffusion versus overgrowth and recrystallization. Chemical Geology, **157**; 285-302.

Cuney, M., Le Fort, P. and Wang, Z. X. 1982. Uranium and thorium geochemistry and mineralogy in the Manaslu leucogranite (Nepal, Himalaya). Symposium on Geology of Granites and their Metallogenic Relations, Science Press, 853-873.

de Kemp, E. A., Sherwin, T., Ryder, I., Davies, A. and Snyder, D. 2002. Detailed stratigraphic, structural, and three-dimensional mapping of the basal surface of the Paleoproterozoic Bravo Lake Formation, Nadluarjuk Lake area, Central Baffin Island, Nunavut. Geological Survey of Canada. Current Research. 2002-C18. 10 p.

Dodson, M. H. 1973. Closure temperature in cooling geochronological and petrological systems. Contributions to Mineralogy and Petrology, **40**; 259-274.

Drake, M. J. and Weill, D. F. 1972. New rare earth element standards for electron microprobe analysis. Chemical Geology, **10**; 179-181.

Dubach, K. and Carmichael, D. 2003. Coming full circle: more results on metamorphic isograds in central Baffin Island. Joint Central Baffin / Committee Bay workshop, Geological Survey of Canada, p.18-19.

Evans, J. A., Zalasiewicz, J. A., Fletcher, I., Rasmussen, B. and Pearce, N. J. G. 2002. Dating diagenetic monazite in mudrocks; constraining the oil window? Journal of the Geological Society of London, **159**; 619-622.

Faure, G. 1977. Principles of Isotope Geology. John Wiley & Sons, Inc. Intermediate geology series, 464 pages.

Finger, F., Broska, I., Roberts, M. P. and Schermaier, A. 1998. Replacement of primary monazite by apatite-allanite-epidote coronas in an amphibolite facies granite gneiss from the Eastern Alps. American Mineralogist, **83**; 248-258.

Fleck, R. J., Sutter, J. F. and Elliot, D. H. 1977. Interpretation of discordant $^{40}Ar/^{39}Ar$ age-spectra of Mesozoic tholeiites from Antarctica. Geochimica et Cosmochimica Acta, **41**; 15-32.

Foster, G., Gibson, H. D., Parrish, R., Horstwood, M., Fraser, J. and Tindle, A. 2002. Textural, chemical and isotopic insights into the nature and behaviour of metamorphic monazite. Chemical Geology, **191**; 183-207.

Foster, G., Kinny, P., Vance, D., Prince, C. and Harris, N. 2000. The significance of monazite U-Th-Pb age data in metamorphic assemblages; a combined study of monazite and garnet chronometry. Earth and Planetary Science Letters, **181**; 327-340.

Franz, G., Andrehs, G. and Rhede, D. 1996. Crystal chemistry of monazite and xenotime from Saxothuringian-Moldanubian metapelites, NE Bavaria, Germany. Fluid Inclusions., **8**; 1097-1118.

Harrison, T. M., Catlos, E. J. and Montel, J.-M. 2002. U-Th-Pb dating of phosphate minerals. Reviews in Mineralogy and Geochemistry, **48**; 523-558.

Hawkins, D. P. and Bowring, S. A. 1997. U-Pb systematics of monazite and xenotime; case studies from the Paleoproterozoic of the Grand Canyon, Arizona. Contributions to Mineralogy and Petrology, **127**; 87-103.

Hawkins, D. P. and Bowring, S. A. 1999. U-Pb monazite, xenotime and titanite geochronological constraints on the prograde to post-peak metamorphic thermal history of Paleoproterozoic migmatites from the Grand Canyon, Arizona. Contributions to Mineralogy and Petrology, **134**; 150-169.

Heaman, L. M., LeCheminant, A. N. and Rainbird, R. H. 1992. Nature and timing of the Franklin igneous events, Canada: implications for Late Proterozoic mantle plume and the breakup of Laurentia. Earth and Planetary Science Letters, **109**; p. 117-131.

Henderson, J. R. 1983. Structure and metamorphism of the Aphebian Penrhyn Group and its Archean basement complex in the Lyon Inlet area, Melville Peninsula, District of Franklin. Geological Survey of Canada. Bulletin. 324. 50 p.

Henderson, J. R. and Parrish, R. R. 1992. Geochronology and structural geology of the Early Proterozoic Foxe-Rinkian orogen, Baffin Island, N.W.T. Geological Survey of Canada. Current Activities Forum. p.12.

Hoffman, P. F. 1988. United Plates of America, the birth of a craton:Early Proterozoic assembly and growth of Laurentia. Annual Reviews of Earth and Planetary Sciences, **16**; p. 543-603.

Jackson, G. D. 1969. Reconnaissance of north-central Baffin Island. Geological Survey of Canada. Report of Activies. Paper 69-1, part A. p.171-176.

Jackson, G. D. and Berman, R. G. 2000. Precambrian metamorphic and tectonic evolution of northern Baffin Island, Nunavut, Canada. Canadian Mineralogist, **38**; 399-421.

Jackson, G. D., Hunt, P. A., Loveridge, W. D. and Parrish, R. R. 1990. Reconnaissance geochronology of Baffin Island, N.W.T. Geological Survey of Canada. Radiogenic Age and Isotopic Studies. Report 3, Paper 89-2. p. 123-148.

Jackson, G. D. and Taylor, F. C. 1972. Correlation of major Aphebian rock units in the northeastern Canadian Shield. Canadian Journal of Earth Sciences, **v. 9**; p. 1650-1669.

Jercinovic, M. J. and Williams, M. L. 2002. Background determination and instrumental parameters in electron microprobe age dating techniques. GSA Annual Meeting, Abstracts with Programs, Geological Society of America, **34**;67.

Johns, S. M. 2002. Nd Isotope constraints on the provenance and tectonic evolution of the Piling Group metasedimentary rocks, Baffin Island, Nunavut. Unpublished B.Sc. thesis, University of Saskatchewan, Saskatoon. 61 p.

Kingsbury, J. A., Miller, C. F., Wooden, J. L. and Harrison, T. M. 1993. Monazite paragenesis and U-Pb systematics in rocks of the eastern Mojave Desert, California, U.S.A.; implications for thermochronometry. Chemical Geology, **110**; 147-167.

Kretz, R. 1983. Symbols for rock-forming minerals. American Mineralogist, **68**; 277-279.

Lanzirotti, A. and Hanson, G. N. 1996. Geochronology and geochemistry of multiple generations of monazite from the Wepawaug Schist, Connecticut, USA; implications for monazite stability in metamorphic rocks. Contributions to Mineralogy and Petrology, **125**; 332-340.

Ludwig, K. R. 2001. Users manual for ISOPLOT/EX, version rev. 2.49 A geochronological toolkit for Microsoft Excel. Berkeley Geochronology Center. Special Publication No. 1a. 55 pages.

McLennan, S. M. 1989. Rare earth elements in sedimentary rocks; influence of provenance and sedimentary processes. Reviews in Mineralogy, **21**; 169-200.

Milodowski, A. E. and Zalasiewicz, J. A. 1991. Redistribution of rare earth elements during diagenesis of turbidite/hemipelagite mudrock sequences of Llandovery age from central Wales. Geological Society Special Publication, **57**; 101-124.

Milton, J. S. 1992. Statistical Methods in the Biological and Health Sciences. McGraw-Hill. Series in Probability and Statistics, 526 pages.

Modeland, S, and Francis, D. 2003. Bravo Lake Formation: a Paleoproterozoic line of fire. Joint Central Baffin / Committee Bay workshop, Program with abstracts, Geological Survey of Canada, Ottawa. p.56.

Montel, J. M. 1986. Experimental determination of the solubility of Ce monazite in SiO_2-Al_2O_3-K_2O-Na_2O melts at 800°C, 2 kbar under H_2O saturated conditions. Geology, **10**; 659-662.

Montel, J. M., Foret, S., Veschambre, M., Nicollet, C. and Provost, A. 1996. Electron microprobe dating of monazite. Chemical Geology, **131**; 37-53.

Montel, J. M., Kornprobst, J. and Vielzeuf, D. 2000. Preservation of old U-Th-Pb ages in shielded monazite; example from the Benmi Bousera Hercynian kinzigites (Morocco). Journal of Metamorphic Geology, **18**; 335-342.

Morgan, W. C. 1983. Lake Gillian, District of Franklin, Northwest Territories. Map 1560A, 1:250 000. Geological Survey of Canada.

Morgan, W. C., Bourne, J., Herd, R. K., Pickett, J. W. and Tippett, C. R. 1975. Geology of the Foxe Fold Belt, Baffin Island, District of Franklin; *in* Report of Activities, Part A; Geological Survey of Canada. Paper 75-1A,343-347.

Nesse, W. D. 1999. Introduction to Mineralogy; Oxford University Press, 464 p.

Overstreet, W. C. 1967. The geologic occurrence of monazite. U. S. Geological Survey. Professional Paper. 327 pages.

Parrish, R. R. 1990. U-Pb dating of monazite and its application to geological problems. Canadian Journal of Earth Sciences, **27**; 1431-1450.

Patino Douce, A. E. and Johnston, A. D. 1991. Phase equilibria and melt productivity in the pelitic system; implications for the origin of peraluminous granitoids and aluminous granulites. Contributions to Mineralogy and Petrology, **107**; 202-218.

Pyle, J. M. 2001. Distribution of select trace elements in pelitic metamorphic rocks: pressure, temperature, mineral assemblage, and reaction-history controls. PhD. Thesis, Renssaeler Polytechnic Institute, Troy, N.Y. 352 pages

Pyle, J. M. and Spear, F. S. 2003a. Four generations of accessory-phase growth in low-pressure migmatites from SW New Hampshire. American Mineralogist, **88**; 338-351.

Pyle, J. M. and Spear, F. S. 2003b. Yttrium zoning in garnet; coupling of major and accessory phases during metamorphic reactions. American Mineralogist, **88**; 708.

Pyle, J. M., Spear, F. S., Rudnick, R. L. and McDonough, W. F. 2001. Monazite-xenotime-garnet equilibrium in metapelites and a new monazite-garnet thermometer. Journal of Petrology, **42**; 2083-2107.

Pyle, J. M., Spear, F. S. and Wark, D. A. 2002. Electron microprobe analysis of REE in apatite, monazite and xenotime; protocols and pitfalls. Reviews in Mineralogy and Geochemistry, **48**; 337-362.

Pyle, J. M., Spear, F. S., Wark, D. A., Daniel, C. G. and Storm, L. C. 2003. Contributions to precision and accuracy of chemical ages of monazite. American Mineralogist, in press.

Rasmussen, B. 1996. Early-diagenetic REE-phosphate minerals (florencite, gorceixite, crandallite, and xenotime) in marine sandstones; a major sink for oceanic phosphorus. American Journal of Science, **296**; 601-632.

Rasmussen, B., Buick, R. and Taylor, W. R. 1998. Removal of oceanic REE by authigenic precipitation of phosphatic minerals. Earth and Planetary Science Letters, **164**; 135-149.

Rasmussen, B., Fletcher, I. R. and McNaughton, N. J. 2001. Dating low-grade metamorphic events by SHRIMP U-Pb analysis of monazite in shales. Geology, **29**; 963-966.

Reed, S. J. B. 1993. Electron Microprobe Analysis. Cambridge University Press. 326 pages.

Reed, S. J. B. 1996. Electron microprobe analysis and scanning electron microscopy in geology. Cambridge University Press. 201 pages.

Rubatto, D., Williams, I. S. and Buick, I. S. 2001. Zircon and monazite response to prograde metamorphism in the Reynolds Range, central Australia. Contributions to Mineralogy and Petrology, **140**; 458-468.

Scherrer, N. C., Engi, M., Gnos, E., Jakob, V. and Liechti, A. 2000. Monazite analysis; from sample preparation to microprobe age dating and REE quantification. Schweizerische Mineralogische und Petrographische Mitteilungen, **80**; 93-105.

Scott, D. J. 1997. Geology, U-Pb and Pb-Pb geochronology of the Lake Harbour area, Southern Baffin Island: implications for the Paleoproterozoic evolution of northeast Laurentia. Canadian Journal of Earth Sciences, **34**;140-155.

Scott, D. J. 1999. U-Pb geochronology of the eastern Hall Peninsula, southern Baffin Island, Canada; a northern link between the Archean of West Greenland and the Paleoproterozoic Torngat Orogen of northern Labrador. Precambrian Research **93**;5-26.

Scott, D. J., St Onge, M. R. and Corrigan, D. 2002. Geology of the Paleoproterozoic Piling Group and underlying Archean gneiss, central Baffin Island, Nunavut. Geological Survey of Canada. Current Research 2002-C17. 10 pages.

Scott, D. J., St-Onge, M. R. and Corrigan, D. 2003. Geology of the Archean Rae Craton and Mary River Group and the Paleoproterozoic Piling Group, central Baffin Island, Nunavut. Geological Survey of Canada. Current Research. 2003-C26. 12 p.

Scott, V. D. and Love, G. 1983. Quantitative Electron-Probe Microanalysis. Ellis Horwood Series Physics, 345.

Seydoux-Guillaume, A. M., Wirth, R., Nasdala, L., Gottschalk, M., Montel, J. M. and Heinrich, W. 2002. An XRD, TEM and Raman study of experimentally annealed natural monazite. Physics and Chemistry of Minerals, **29**; 240-253.

Shaw, C. A., Karlstrom, K. E., Williams, M. L., Jercinovic, M. J. and McCoy, A. M. 2001. Electron-microprobe monazite dating of ca. 1.71-1.63 Ga and ca. 1.45-1.38 Ga deformation in the Homestake shear zone, Colorado; origin and early evolution of a persistent intracontinental tectonic zone. Geology, **29**; 739-742.

Shaw, D. M. 1956. Geochemistry of pelitic rocks. Part III. Major elements and general geochemistry. Geological Society of America Bulletin, **67**; 919-934.

Smith, H. A. and Barreiro, B. 1990. Monazite U-Pb dating of staurolite grade metamorphism in pelitic schists. Contributions to Mineralogy and Petrology, **105**; 602-615.

Spear, F. S. and Parrish, R. R. 1996. Petrology and cooling rates of the Valhalla Complex, British Columbia, Canada. Journal of Petrology, **37**; 733-765.

Spear, F. S. and Pyle, J. M. 2002. Apatite, monazite, and xenotime in metamorphic rocks. Reviews in Mineralogy and Geochemistry, **48**; 293-335.

Stacey, J. R. and Pattison, D. R. M. 2003. Stratigraphy, structure, and petrology of a representative klippe of the Bravo Lake formation, Piling Group, central Baffin Island, Nunavut. Geological Survey of Canada. Current Research. 2003-C13. 11 p.

Stern, R. A. and Sanborn, N. 1998. Monazite U-Pb and Th-Ph geochronology by high-resolution secondary ion mass spectrometry; *in* Radiogenic age and isotopic studies: Report 11; Geological Survey of Canada, Current Research, no. 1998-F,1-18.

St-Onge, M. R., Lucas, S. B., Scott, D. J. and Wodicka, N. 1997. Crustal-scale architecture and tectonostratigraphy of the Quebec-Baffin segment of Trans-

Hudson Orogen. University of British Columbia, Canadian Lithoprobe Program. Report **61**;186-192.

St-Onge, M. R., Lucas, S. B., Scott, D. J. and Wodicka, N. 1999. Upper and lower plate juxtaposition, deformation and metamorphism during crustal convergence, Trans-Hudson Orogen (Quebec-Baffin segment), Canada. Precambrian Research **93**; 27-49.

St-Onge, M. R., Scott, D. J. and Corrigan, D. 2001a. Geology, Flint Lake, Nunavut; Geological Survey of Canada, Open File 3959, scale 1:100 000.

St-Onge, M. R., Scott, D. J. and Corrigan, D. 2001b. Geology, MacDonald River; Nunavut; Geological Survey of Canada, Open File 3958, scale 1:100 000.

St-Onge, M. R., Scott, D. J. and Corrigan, D. 2001c. Geology, Nadluardjuk Lake, Nunavut, Geological Survey of Canada, Open File 3960, scale 1:100 000.

St-Onge, M. R., Scott, D. J. and Corrigan, D. 2001d. Geology, Wordie Bay, Nunavut; Geological Survey of Canada, Open File 3961, scale 1:100 000.

St-Onge, M. R., Scott, D. J. and Wodicka, N. 2001. Terrane boundaries within Trans-Hudson Orogen (Quebec-Baffin segment), Canada; changing structural and metamorphic character from foreland to hinterland. Precambrian Research, **107**; 75-91.

St-Onge, M. R., Scott, D. J. and Wodicka, N. 2002. Review of crustal architecture and evolution in the Ungava Peninsula, Baffin Island area; connection to the Lithoprobe ECSOOT transect. Canadian Journal of Earth Sciences, **39**; 589-610.

Suzuki, K. and Adachi, M. 1991. Precambrian provenance and Silurian metamorphism of the Tsubonosawa Paragneiss in the South Kitakami Terrane, Northeast Japan, revealed by the chemical Th-U-total Pb isochron ages of monazite, zircon and xenotime. Geochemical Journal, **25**; 357-376.

Suzuki, K., Adachi, M. and Tanaka, T. 1991. Middle Precambrian provenance of Jurassic sandstone in the Mino Terrane, central Japan; Th-U-total Pb evidence from an electron microprobe monazite study. Sedimentary Geology, **75**; 141-147.

Taylor, F. C. 1982. Precambrian geology of the Canadian north borderlands; *in* Geology of the North Atlantic Borderlands, (ed.) J. W. Kerr, A. J. Fergusson, and L. C. Machan; Canadian Society of Petroleum Geologists. Memoir **7**; p.11-30.

Terry, M. P., Robinson, P., Hamilton, M. A. and Jercinovic, M. J. 2000. Monazite geochronology of UHP and HP metamorphism, deformation, and exhumation, Nordoyane, Western Gneiss region, Norway. American Mineralogist, **85**; 1651-1664.

Tippett, C. R. 1984. Supplementary data concerning "Geology of a transect through the southern margin of the Foxe fold belt, central Baffin Island, District of Franklin". Geological Survey of Canada. Open-File Report - Geological Survey of Canada. 1111. 84 p.

Tippett, C. R. 1985. Geology of a transect through the sourthern margin Foxe Fold Belt, Central Baffin Island, District of Franklin. Geological Survey of Canada. Open File. 1110. 77 p.

Townsend, K. J., Miller, C. F., D'Andrea, J. L., Ayers, J. C., Harrison, T. M. and Coath, C. D. 2000. Low temperature replacement of monazite in the Ireteba Granite, southern Nevada; geochronological implications. Chemical Geology, **172**; 95-112.

Vielreicher, N. M., Groves, D. I., Fletcher, I. R., McNaughton, N. J. and Rasmussen, B. 2003. Hydrothermal monazite and xenotime geochronology: A new direction for precise dating of orogenic gold mineralization. SEG Newsletter, **53**; 8 p.

Watt, G. R. 1995. High-thorium monazite-(Ce) formed during disequilibrium melting of metapelites under granulite-facies conditions. Mineralogical Magazine, **59**; 735-743.

Watt, G. R. and Harley, S. L. 1993. Accessory phase controls on the geochemistry of crustal melts and restites produced during water-undersaturated partial melting. Contributions to Mineralogy and Petrology, **114**; 550-566.

Williams, M. L. and Jercinovic, M. J. 2002. Microprobe monazite geochronology; putting absolute time into microstructural analysis. Journal of Structural Geology, **24**;1013-1028.

Williams, M. L., Jercinovic, M. J. and Terry, M. P. 1999. Age mapping and dating of monazite on the electron microprobe; deconvoluting multistage tectonic histories. Geology, **27**; 1023-1026.

Wing, B. A., Ferry, J. M. and Harrison, T. M. 2003. Prograde destruction and formation of monazite and allanite during contact and regional metamorphism of pelites: petrology and geochronology. Contributions to Mineralogy and Petrology, **145**; 228-250.

Wodicka, N. and Scott, D. J. 1997. A preliminary report on the U-Pb geochronology of the Meta Incognita Peninsula, southern Baffin Island, Northwest Territories. Geological Survey of Canada. Current Research. 1997-C. 167-178.

Wodicka, N., Scott, D. J., St-Onge, M. R. and Corrigan, D. 2002. A preliminary report on the U-Pb geochronology of the Northern margin of the Trans-Hudson Orogen, central Baffin Island, Nunavut. Geological Survey of Canada. Current Research. 2002-F7. 12 pages.

Wodicka, N., St Onge, M. R., Scott, D. J. and Corrigan, D. 2003. Paleoproterozoic evolution of the northern margin of Trans-Hudson Orogen, central Baffin Island, Nunavut: new U-Pb geochronological constraints. Joint Central Baffin / Committee Bay Workshop, Geological Survey of Canada- Continental Geoscience Division, p.56.

Zhu, X. K. and O, N. R. K. 1999. Monazite chemical composition; some implications for monazite geochronology. Contributions to Mineralogy and Petrology, **137**; 351-363.

Zhu, X. K. and O'Nions, R. K. 1999. Zonation of monazite in metamorphic rocks and its implications for high temperature thermochronology; a case study from the Lewisian terrain. Earth and Planetary Science Letters, **171**; 209-220.

Appendix 1

Procedure for monazite analysis and chemical dating using the JEOL 8200 Superprobe at Dalhousie University

A1.1 Pre-analysis specifications

Polished thin sections should be **free of any Pb contamination**. Ideally, thin sections should be entirely polished using a Pb-free disc. Samples polished using a lead lap need to be re-polished using a lead-free lap.

Sections should have a **double carbon coat** for any analysis (single grain mapping, thin section mapping, line analysis or trace element analysis) done using **200 nA** current. Otherwise, permanent beam damage is likely. Burning off the carbon coating may also affect the accuracy of results. For analysis done at 20nA (major element analysis), a single carbon coating is sufficient. A good cleaning is essential. It is recommended to first use soap and rinse. Then, use alcohol and ultrasonic bath to **get rid of all the oil** (often deposited on the thin section during the polishing process). At high current (~200 nA) oil trapped between the rock material and the carbon coating will heat up, boil, and blow off the coating.

Two reference points, using a sharp permanent marker, should be put on opposite corners of the upper surface for (re)location of analysed grains. For easy recognition in SEM, COMPO, or BSE imaging, the points should be drawn directly on the rock rather than the epoxy.

A1.2 Location of monazite grains

Locate the two marker points drawn on the thin section and take note of their coordinates. Also, make sure to note the orientation of the thin section and its position in the thin section holder. This is your best way to find again the analysed grains quickly (coordinates are in mm)! Two methods can be used to find the monazite grains in the thin section.

A1.2.1 Scanning in BSE mode

In BSE imaging mode, grains with higher average atomic number appear brighter. Because of its chemical composition monazite is generally one the brightest minerals in regular granitic, metapelitic, or sedimentary rocks. Its density (i.e. its mean atomic number) is much greater than most common silicates. By enhancing the contrast to merge into the dark background all the minerals with low mean atomic number (e.g. silicates and oxides), only the brighter spots due to minerals with high mean atomic number will remain visible. If the composition and/or the metamorphic grade of the rock is right, it is likely that some of the bright spots are monazite grains. Analyse the suspect bright spots with EDS (A1.3) until you find monazite. Then adjust the contrast to merge into the background all other minerals but the monazite. This will distinguish monazite and minerals with a similar or greater average atomic number (e.g., zircon, iron oxides and sulphides). Mineral textures and habit help to distinguish monazite from other bright minerals.

A1.2.2 Thin section X-ray mapping

X-ray chemical mapping of the full thin section or selected parts of it for characteristic elements (e.g., Mg, Ca, Ce, Y, P) provides information to locate monazite by finding matching spots of high concentration of elements specific to this mineral. It has the advantage of showing the distribution of monazite grains within the thin section. Up to 5 elements and a BSE image map can be simultaneously obtained. This method provides a lot of information on the rock texture and monazite in various settings. X-ray mapping requires more time than BSE scanning, but allows location of fine-grained monazites. By combining information from various element maps, it is possible to locate monazite and other phosphate phases accurately (e.g., Ce and P for monazite, Y and P for xenotime, Ca and P for apatite). Elements to be mapped can be changed, but possible combinations depend on spectrometer configuration (i.e. specific elements can only be analysed on certain crystals, so not all combinations are possible).

The selection of the interval, which is the perimeter (length x width) in mm of the area to be mapped, is your choice. Resolution depends on the pixel size you choose (from

1 μm to 100 μm). The time spent to produce a single map depends on the number of pixels (max: 800 x 800) and the dwell time (in msec) spent on each pixel. For an area of 16 x 16 mm with 800 x 800 pixels and a dwell time of 15 msec, it takes about 3hrs 30min to generate a map with a pixel size of 20 μm. In fine-grained schists, this level of resolution is good enough to reveal monazite and xenotime down to 10 μm in diameter. The level of resolution you need depends on the grain size of the rock analysed and the size of the smallest monazite grain you expect to find. Table A1.1 provides recommended analytical settings; the analytical procedure is given next.

Table A1.1: Typical thin section X-ray mapping analytical conditions

Acc. Voltage:	15 kV	Scan Type:	Stage (uni)
Probe current:	200 nA	Stage Drive:	Normal
Probe diam.:	0.5 μm	Pixels (X,Y):	800 x 800
Magnification:	40 x	Pixel Size (X, Y):	20.0 μm x 20.0 μm
		Dwell time:	15 msec

<u>Thin section X-ray mapping procedure</u>

1. In the upper Bar Menu go to the "*Analysis*" icon. From the menu choose "*Map Analysis*". In "*Sample*" choose "*MonaziteTrace*"
2. Go to "*Measurements*" > "*Element conditions*". Choose the elements to be mapped and verify that "*Measur. order*" is right (e.g., Ca on CH1 , Ce on CH5 , Mg on CH3, P on CH2 and Y on CH4)
3. Go back to "*Measurements*" and click on "*EOS conditions*". Adjust the settings according to the left column of Table A1.1.
4. Back to "*Measurements*", go to "*Stage cond.*" > "*Pos. Input*". A screen similar to Figure A1.1 should appear. Give a name to your map file in the "*Comment*" box. Verify that settings are similar to the right column of Table A1.1 above.
5. To select the area to be mapped, position your beam at the upper right corner of the desired area. Go to "*Store*" > "*Read*" > "*To start*". Go to "*Confirm*", the stage will move to every corner defining the area to be mapped. You must record each of these positions by hitting the "*Store*" button on the joystick pad every time the stage

moves to a new position. If you realise the position is wrong, hit "*Cancel*" and either relocate your start position or change the number of pixels in the X- or Y-axis. Complete recording by hitting the "*Apply*" button.

6. "*Close*" > "*Preset Measur.*" To see mapping in progress: Upper Bar Menu go to the "*Process*" icon > "*To map*" > "*Realtime*" > "*Start*"

Figure A1.1: Snapshot of the screen in mapping mode.

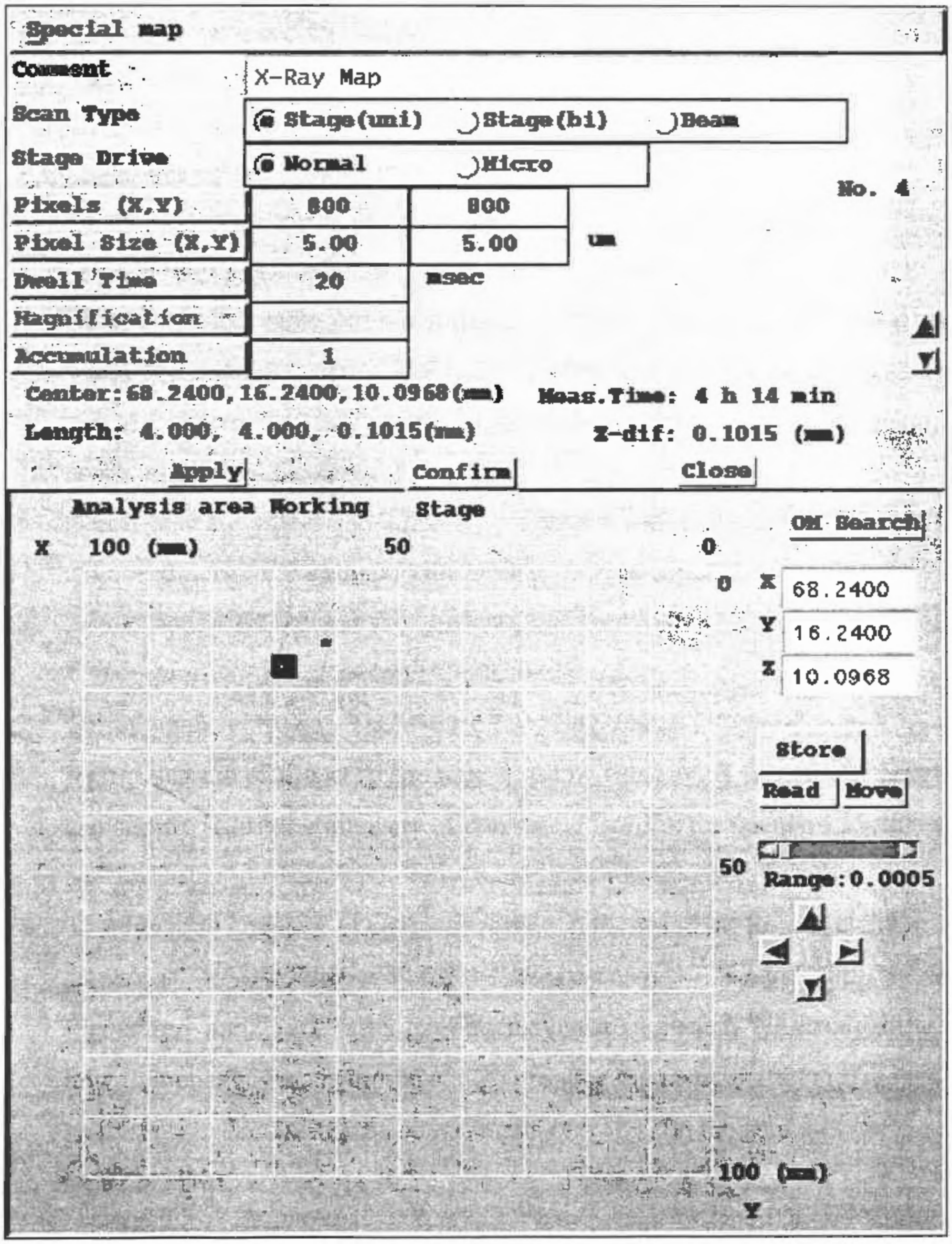

A1.3 Identification of monazite (EDS analysis)

Before spending time analysing and mapping a grain, confirmation of the nature of the grain should be obtained using quick qualitative EDS analysis.

Qualitative EDS analysis procedure

1. First turn off the "*PRB scan*" button (green button on your left goes off!)
2. Then, click on "*EDS*" icon on the very bottom tool bar; a screen will come up on your right.
3. Hit the "*Acquire*" button; the analysis will start. You can stop it after a few seconds, once you can clearly distinguish the different peaks. To do so, just hit the button again.

Since X-rays have characteristic energies, the solid-state detector records and separates the electrons received based on their energy. In qualitative electron dispersive spectrometry (EDS) analysis mode, a histogram of the abundance of electrons with the different energies is displayed using a bin size of 0.01 KeV (Figures A1.2-A1.5). The energy of the peak (in KeV) is characteristic for each element and its intensity (in counts per second) indicates its relative abundance. The EDS pattern provides information on the composition of the mineral. Monazite can easily be recognised to its typical pattern. Figure A1.2 provides an example of typical monazite qualitative EDS pattern and figures A1.3-A1.5 show typical EDS pattern measured from zircon, xenotime and apatite grains.

Figure A1.2: Typical qualitative EDS pattern of a monazite grain

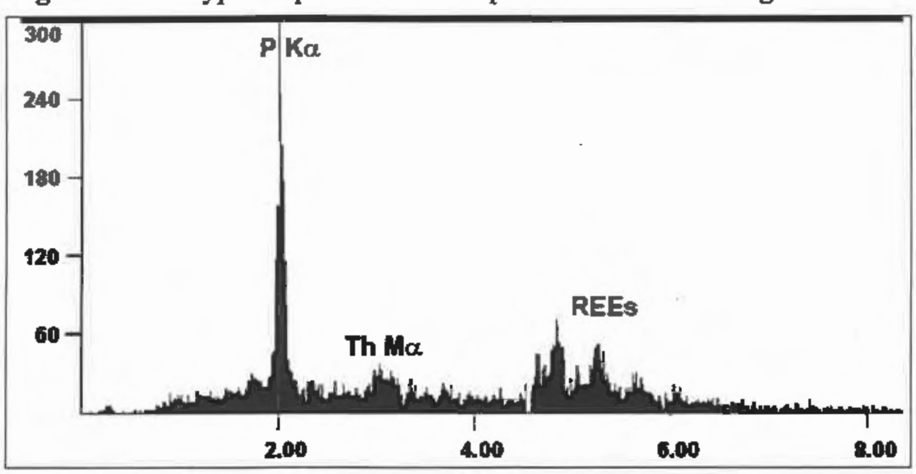

Figure A1.3: Typical qualitative EDS pattern of a zircon grain

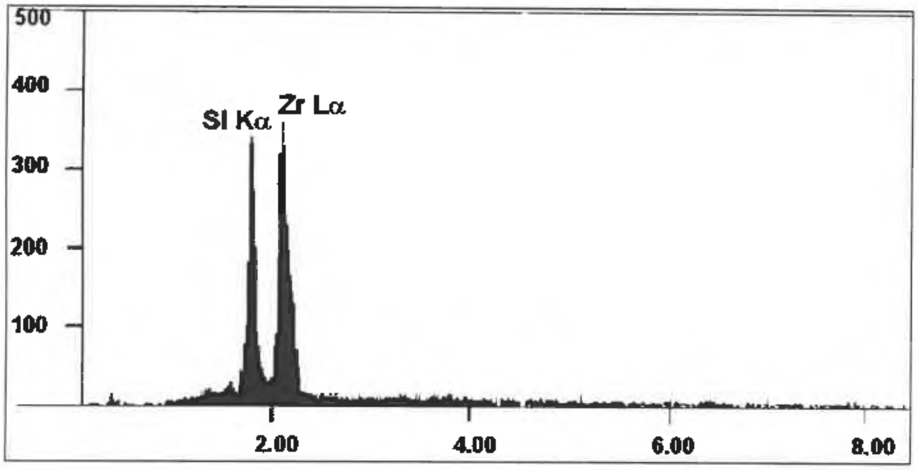

Figure A1.4: Typical qualitative EDS pattern of a xenotime grain

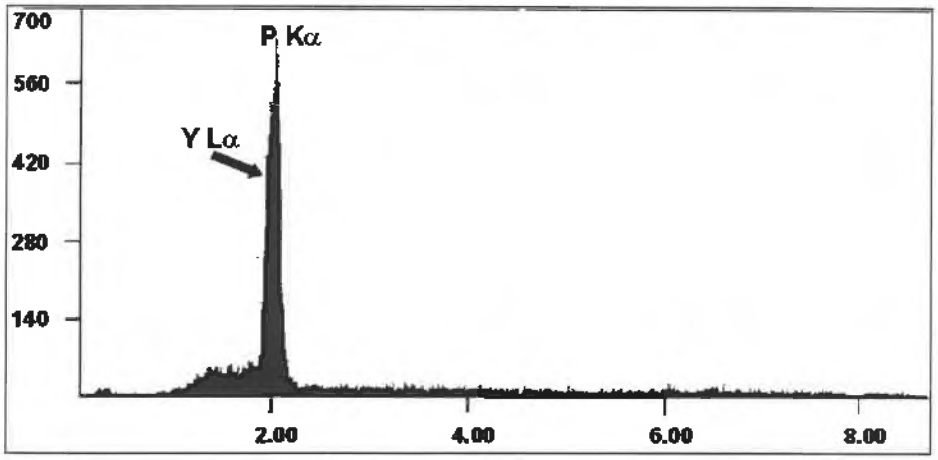

Figure A1.5: Typical qualitative EDS pattern of an apatite grain

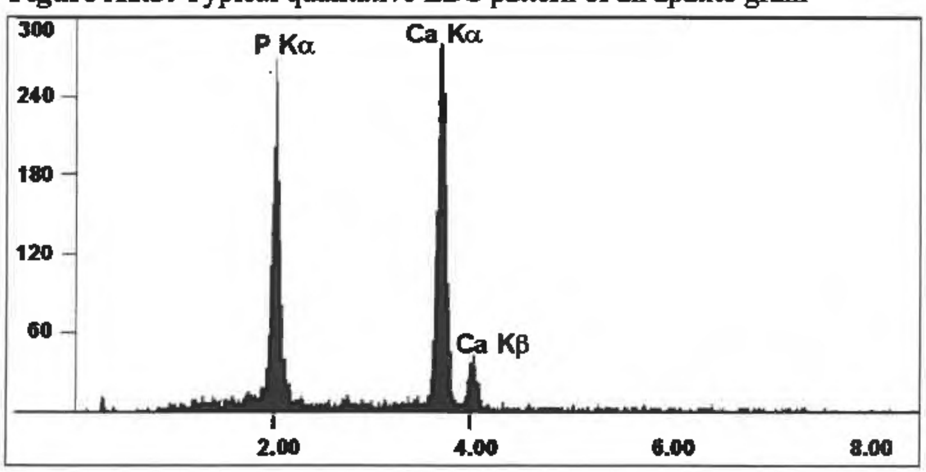

A1.4 Characterization of element distribution (BSE imaging and single grain X-ray mapping)

Before analysing monazite for major and trace element chemistry, it is important to assess the chemical homogeneity. You must verify if the grain is chemically homogeneous or zoned. In the case of a zoned grain, you need to know the geometry of the chemical zones. Each zone will have to be characterized for its major element content and will be analysed separately for trace element content.

Identification of chemical zonation is important because each zone will require a specific ZAF correction that will be defined by its average major element composition. Also, zoning in Pb, U, and Th **may, but not always**, indicate an age zonation.

A1.4.1 BSE imaging

The chemical homogeneity of the monazite can be evaluated by looking at the grain in BSE imaging mode and enhancing the contrast. Because the elements Pb, Th, U and Y have a high atomic number, and together they account for a significant proportion of the composition of monazite, BSE imaging will generally reflect zonation in these elements. BSE images should give you enough information to select the location of major element spot analyses. Later on, you can choose grains for dating based on BSE and major element data. However, it will be necessary to obtain an X-ray map of the grain before proceeding to trace element analysis.

Procedure for acquisition of a BSE image

1. Adjust the magnification and the contrast to the desired level. It is strongly recommended to save and print an image of your grain to locate your analyses and to keep in your records.
2. To take a picture simply hit the "*Photo*" button.
3. To print go to "*Utility*" > "*Graphics*" > "ImageMagick"
4. Find the picture in the folder, open, view at half-size, and print.

A1.4.2 Single grain X-ray mapping

Once a grain is chosen for dating, it is recommended to obtain an X-ray map for U, Th, Pb and Y in order to verify and constrain the zoning in these elements. It is important to identify the different chemical zones. Analytical conditions in trace analysis mode are set for each domain.

Table A1.2: Single grain X-ray mapping analytical conditions

Acc. Voltage:	15 kV	Scan Type:	Stage (uni) for grain > 60 µm Beam for grain < 60 µm
Probe current:	200 nA	Stage Drive:	Normal
Probe diam.:	0 µm	Pixel Size:	0 µm
Magnification:	vary with the size of the grain	Dwell time:	40 msec

Single grain X-ray mapping procedure

1. In the upper Bar Menu go to the "*Analysis*" icon. From the menu, choose "*Map Analysis*". In "*Sample*" choose "*MonaziteTrace*".
2. Go to "*Measurements*" > "*Element conditions*". Choose the elements to be mapped and verify that "*Measur. order*" is right (e.g., Pb on CH5, Th on CH1, U on CH2 and Y on CH4).
3. Go back to "*Measurements*" and click on "*EOS conditions*". Adjust the settings according to the left column of Table A1.2.
4. Back to "*Measurements*", go to "*Stage cond.*" > "*Pos. Input*". A window similar to Figure A1.1 appears. Give a name to your map file in the "*Comment*" box. Verify that settings are similar to the right column of Table A1.2.
5. Position your beam in the centre of the grain. Go to "*Store*" > "*Read*" > "*To center*". Go to "*Confirm*"; the stage will move to every corner defining the area to be mapped. You must record each of these positions by hitting the "*Store*" button on the joystick pad every time the stage moves to a new position. If you realise the position is wrong, hit "*Cancel*" and either relocate your start position or change the number of

pixels in the X- or Y-axis. Complete recording by hitting the "*Apply*" button, then "*Close*".

6. "*Measurement*"> "*Preset Measur.*" To see the mapping in progress: Upper Bar Menu go to the "*Process*" icon > "*To map*" > "*Realtime*" > "*Start*".

A1.5 Major element analysis

The next step is acquiring complete major element analyses to characterize monazite chemistry and to establish the ZAF correction to be used during trace element analysis.

Major element analysis procedure

1. On the upper bar menu, go to "*Analysis*" > "*Quantitative Analysis*" > "*Sample*" > "*Group*" > "*AgeDate*" > "*MonazMajor*"
2. Before starting, make sure the settings are correct. Go to "*Quantitative Analysis*" and verify that settings under "*EOS cond.*" correspond to Table A1.3, the settings under "*Measur. Order*" correspond to Table A1.4 and settings under "*Element Cond.*" correspond to Table A1.6.
3. Before starting analysis you must run a control sample to verify the accuracy of the calibration. Move the stage to the Monazite 53 sample.
4. To record the spot to analyse: under "*Quantitative Analysis*", go to "*Stage cond.*" > "*Pos. Input*" > "*Read & Apply*" > "*Close*"
5. To run analysis: go to "*Stage cond.*" > "*Pos. Input*" > "*One-by-one*" > "*Acquire*"
6. Verify that the results correspond to those in Table A1.5. For small variations, you can simply adjust the intensity of counts recorded in the standard for this element and for larger variations you must recalibrate for this specific element.
7. To adjust the intensity of counts recorded in the standard for this element go to "*Analysis*" > "*Standard analysis*" > "*Measurement*" > "*Check data*" > "*Net intensities*" and "*Save*" after data intensities are adjusted. While adjusting the values, note that changes made on the counts produce the inverse effect on the result of the analysis (i.e. decreasing the count intensity by 3% on the standard increases the wt % value by 3%).

8. To recalibrate an element: go to "*Analysis*" > "*Standard analysis*" > "*Sample*" Then, you choose the standard of the element to recalibrate. Table A1.7 lists all the standards used for major element analysis of monazite, and their compositions.
9. Once you have selected the standard, verify the analytical conditions. Press "*Acquire*". Afterwards, run another control analysis on Monazite 53 to verify that values are now within error. Once results on monazite control are satisfactory, you can start to analyse unknown monazites.
10. To record and run analysis on unknown monazite grain(s): go to "*Quantitative Analysis*", "*Stage cond.*" > "*Pos. Input*" > "*Read & Apply*". To enter many points, position the stage at the new spot location and record with "*Read & Apply*". Repeat for each spot. Go to "*Stage cond.*" and "*Preset measur.*" to start analysis.

Table A1.3: Major element analysis typical EOS conditions.

Acc. Voltage:	15 kV	Probe diam.:	0 μm
Probe current:	20 nA	Magnification:	4000 x

Table A1.4: Measurement order of the elements for major element analysis.

CH 1 (PETJ)	CH 2 (LIF)	CH 3	CH 4 (TAP)	CH 5 (LIFH)
Ca	Ce	-	Si	Gd
P	Dy	-	Y	Nd
Th	La	-	-	Pr
U	-	-	-	Sm

Table A1.5: Average composition of Monazite 53 control in oxide wt %.

Element	weight %	**Element**	weight %
CaO:	0.42	**Pr_2O_3:**	3.49
Ce_2O_3:	32.31	**SiO_2:**	0.81
Dy_2O_3:	0.14	**Sm_2O_3:**	1.00
Gd_2O_3:	0.54	**Th_2O_3:**	3.24
La_2O_3:	16.53	**UO_2:**	0.06
Nd_2O_3:	11.24	**Y_2O_3:**	0.52
P_2O_5:	28.26	**Total:**	98.55

Table A1.6: Element conditions for major analysis.

Element	Ca	Ce	Dy	Gd	La	Nd
Line	Kα	Lα	Lα	Lβ	Lα	Lβ
Standard	KK	$CePO_4$	REE4	REE1	$LaPO_4$	REE2
Spectrometer	1	2	2	5	2	5
Crystal	PETJ	LIF	LIF	LIFH	LIF	LIFH
Peak	107.542	178.195	132.790	128.470	185.443	150.671
Bkg H/L	5.0/5.0	3.0/3.0	5.5/2.3	1.0/1.0	5.0/5.0	5.15/5.89
High V. (V)	1610	1700	1700	1610	1700	1730
Gain	32	8	8	32	8	32
Baseline	1.0	0.2	0.2	1.0	0.2	1.0
Window Width (V)	8.0	9.3	-	9.0	8.0	8.0
Mode	Diff.	Diff.	Int.	Diff.	Diff.	Diff.
Peak (s)	40	40	40	40	40	40
Background (s)	20	20	20	20	20	20

Table A1.6 (continued): Element conditions for major analysis.

Element	P	Pr	Si	Sm	Th	U	Y
Line	Kα	Lβ	Kα	Lβ	Mα	Mβ	Lα
Standard	$CePO_4$	REE3	Sanidine	REE2	ThO_2	UO_2	YAG
Spectrometer	1	5	4	5	1	1	4
Crystal	PETJ	LIFH	TAP	LIFH	PETJ	PETJ	TAP
Peak	197.187	157.122	77.275	139.058	132.468	118.94	69.87
Bkg L/H	5.0/5.0	1.25/24.2	5.0/5.0	11.80/5.83	2.0/2.0	2.9/1.6	1.0/1.0
High V. (V)	1708	1730	1650	1730	1718	1700	1700
Gain	16	32	32	32	16	16	32
Baseline	2.0	1.0	1.0	1.0	4.0	2.0	3.5
Window Width (V)	4.0	8.0	8.0	8.0	4.5	4.0	5.0
Mode	Diff.	Diff.	Diff.	Diff.	Diff.	Diff.	Diff.
Peak (s)	40	40	40	40	40	40	40
Background (s)	20	20	20	20	20	20	20

Table A1.7: Standard for each element with its composition.

Element	Standard	Weight %	Element	Standard	Weight %
Ca	KK	CaO, 10.30 %	**Pr**	REE3	Pr2O3, 4.44 %
Ce	CePO4	Ce2O3, 69.81 %	**Si**	Sanidine	SiO2, 64.67 %
Dy	REE4	Dy2O3, 4.36 %	**Sm**	REE2	Sm2O3, 4.26 %
Gd	REE1	Gd2O3, 4.46 %	**Th**	ThO2	ThO2, 99.99 %
La	LaPO4	La2O3, 69.65 %	**U**	UO2	UO2, 98.87 %
Nd	REE2	Nd2O3, 4.26 %	**Y**	YAG	Y2O3, 57.06 %
P	CePO4	P2O5, 30.20 %	-	-	-

A1.6 Trace element analysis

Trace element analysis is a critical step in the dating procedure of monazite (see Appendix 2 for age calculation procedure). It is essential to follow rigorously each step to make sure that calibration and corrections are done adequately. It is also very important to recognize chemical domains and deal individually with each of them.

Trace element analysis procedure:

1. On the upper bar menu, go to "*Analysis*" > "*Quantitative Analysis*" > "*Sample*" > "*Group*" > "*AgeDate*" > "*MonaziteTrace*"
2. You must start by calibrating Pb, Th, U and Y: Go to "*Analysis*" > "*Standard Analysis*" > "*Sample*". Choose the standard depending on the element (Crocoite for Pb, ThO2 for Th, YAG for Y, and UO2 for U). Go to "*Measurement*", check "*EOS cond.*" with Table A1.8.
3. Check "*Element Conditions*", which should be similar to Table A1.9. Make sure that peak and background measuring times are 40 and 20 seconds respectively.
4. Run calibration, "*Stage cond.*" > "*Pos. Input*" > "*Read & Apply*" > "*Acquire*". If low compared to last calibration, check PHA, and adjust if necessary. Then, recalibrate following the same procedure.
5. Go to "*Analysis*" > "*Quantitative Analysis*". Before starting, make sure the settings are correct. Verify that "*EOS cond.*" settings correspond to Table A1.8.

6. Using X-ray maps of the grain to be dated you can identify the various chemical domains present. For every chemical domain, calculate the average major element composition. Transform the oxide wt % values into element wt % values using the Excel spreadsheet (*OxiConv.xls*) available on the service computer.
7. You must determine the position of low and high backgrounds for each element measured in trace mode within every chemical domain. Run a WDS scan. Go to "*Analysis*" > "*Qualitative*" > "*WDS Scan*". In "*Sample*" choose "*MonaziteWDSscan*". Verify that the settings correspond to Table A1.10. Record spot location ("*Stage cond.*" > "*Pos. Input*" > "*Read & Apply*") and proceed to analysis ("*Stage cond.*" > "*Preset measur.*").
8. You can view the analysis in real time: in the upper Bar Menu go to "*Process*" > "*WDS Scan*" > "*Realtime*" > "*Start*". Print the scan window (see Figure A1.6) and determine the background positions on both sides of each peak (see Figure A1.7). Positions have to be close to the peak of interest while also being as far as possible from any interfering peak.
9. Go to "*Element Cond.*" and insert the new values for background positions. Also verify that settings under "*Element Cond.*" correspond to Table A1.11 and do not forget to reset times to 600/300sec, (peak/background).
10. Enter the fixed weight calculated for all elements including O, except the four analysed in trace mode (Pb, Th, U and Y). Note that background positions and average element wt% values must be determined for each chemical domain.
11. Set up points on unknown monazite grain(s) and run analyses.
12. To calculate ages, plug in element (as ppm) and other required values in the Excel spread sheet available on the service computer.
13. Collect BSE images of analysed grains - burned marks show exact locations of analysed spots

Table A1.8: EOS conditions for calibration in trace analysis mode.

Acc. Voltage:	15 kV	Probe diam. (μm):	0
Probe current:	200 nA	Magnification:	4000 x

Figure A1.6: WDS scan of a monazite grain (Pb CH-5, Th CH-1, U CH-2 and Y CH-4)

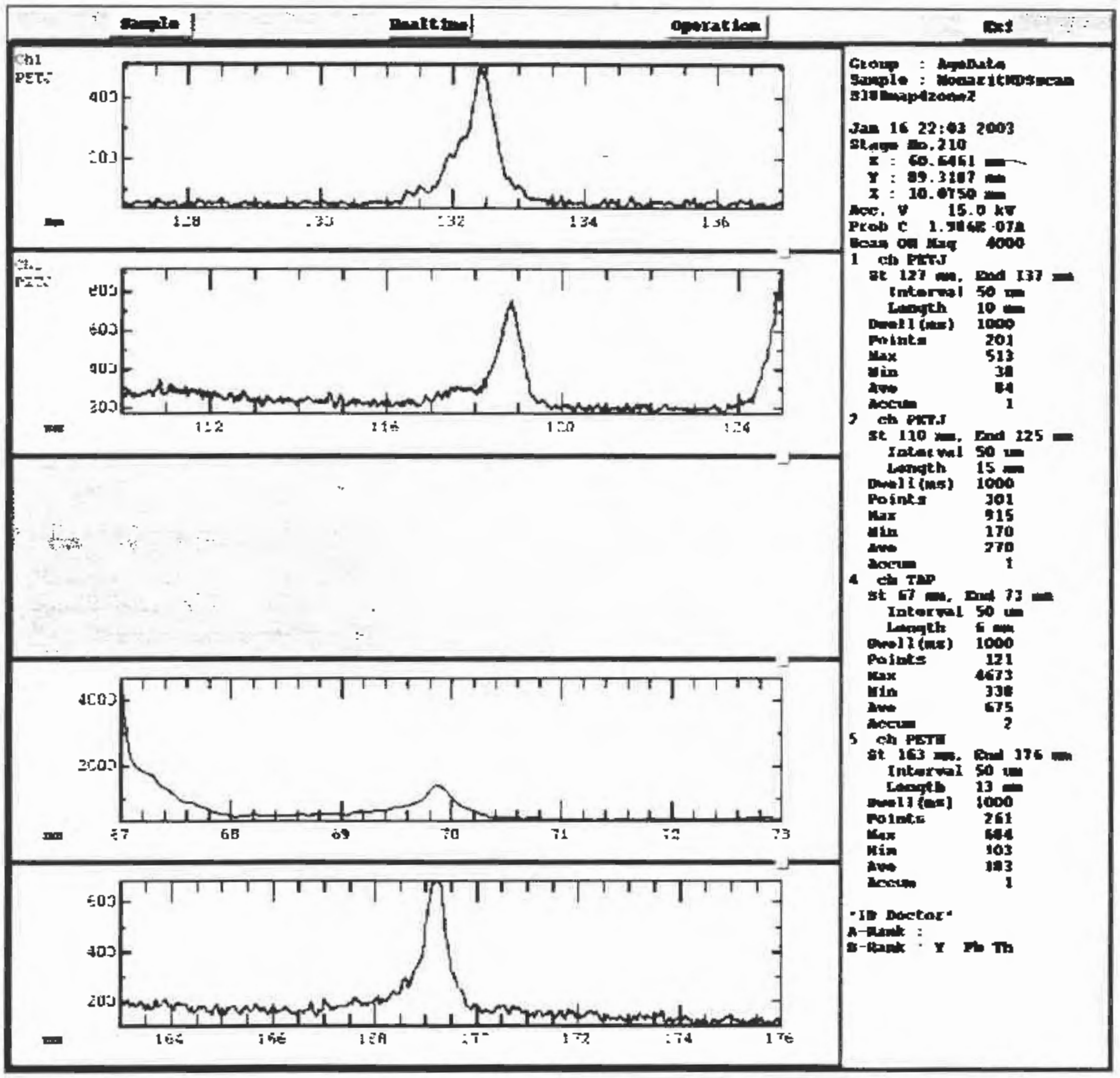

Figure A1.7: Interpolated background below a Pb Mα peak from a WDS scan on monazite (PETH crystal, P10, 15 kV, 200nA).

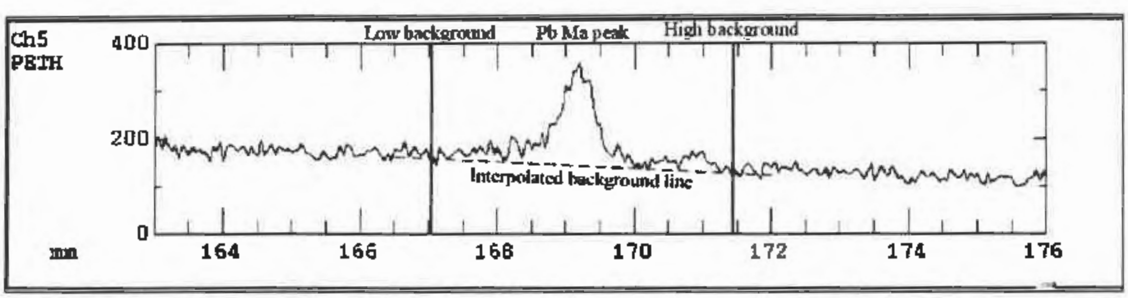

Table A1.9: Analytical settings for trace element analysis calibration

El.	Pb	Th	U	Y
Line	Mα	Mα	Mβ	Lα
Standard	Crocoite	ThO_2	UO_2	YAG
Spec	5	1	2	4
Xtal	PETH	PETJ	PETJ	TAP
Peak	169.198	132.468	118.898	69.870
Bkg L/H	3.3/4.0	2.0/2.0	5.0/5.0	1.0/1.0
High V. (V)	1700	1718	1700	1700
Gain	64	16	64	32
Baseline	0.7	4.0	2.5	3.5
Window Width (V)	3.5	4.5	2.8	5.0
Mode	Diff.	Diff.	Diff.	Diff.
Peak (s)	40	40	40	40
Back (s)	20	20	20	20

Table A1.10: WDS Scan analytical conditions

Acc. Voltage:	15 kV	Scan:	ON
Probe current:	200 nA	Magnification:	4000 x
Channel #1: Th			
Xtal:	PETJ	Interval:	50 μm
Start:	127 mm	Length:	10 mm
End:	137 mm	Dwell time:	1000 ms
Channel #2: U			
Xtal:	PETJ	Interval:	50 μm
Start:	110mm	Length:	15 mm
End:	125mm	Dwell time:	1000ms
Channel #4:Y			
Xtal:	TAP	Interval:	50 μm
Start:	67 mm	Length:	6 mm
End:	73 mm	Dwell time:	1000 ms
Channel #5: Pb			
Xtal:	PETH	Interval:	50 μm
Start:	163 mm	Length:	13 mm
End:	176 mm	Dwell time:	1000 ms

Table A1.11: Analytical conditions for trace element analysis.

Element	Pb	Th	U	Y
Line	Mα	Mα	Mβ	Lα
Standard	Crocoite	ThO_2	UO_2	YAG
Spectrometer	5	1	1	4
Crystal	PETH	PETJ	PETJ	TAP
Peak	169.198	132.468	118.940	69.870
Bkg L/H	3.0/4.0	2.0/2.0	2.9/1.6	1.0/1.0
High V. (V)	1700	1718	1700	1700
Gain	64	16	16	32
Baseline	1.2	4.0	2.0	3.5
Window Width (V)	2.5	4.5	4.0	5.0
Mode	Diff.	Diff.	Diff.	Diff.
Peak (s)	600	600	600	600
Background (s)	300	300	300	300

Appendix 2
Error and age calculation procedure

A2.1 Theory of counting statistics and age calculation

Quantification of errors in monazite chemical analysis is based on counting statistics. This arises from both the nature of X-rays and the functioning of an electron-microprobe (EMP). The following section describes each step in assessing error through the monazite dating procedure. Note that calculations are shown here in detail for illustrating the principles, but in practice all data are entered into an Excel spreadsheet and calculation of errors is automated.

Radiation produced through beam excitation is recorded by counters in the EMP. X-ray emission is a random phenomenon occurring through time, which obeys Poisson statistics (Scott and Love, 1983). The standard deviation (σ) of a typical Poisson distribution is equal to $\sqrt{N}$, where N is the number of counts.

This basic relation applies to EMP counting statistics. During a typical quantitative analysis, a spectrometer records a number of counts at the peak (N_p) through a length of time t_p. The standard deviation for peak measurement can be reported as $\sqrt{N_P}/t_P$. The spectrometer also measures counts from the background (N_B) during the length of time t_B, from which a standard deviation can also be calculated of the form $\sqrt{N_B}/t_B$.

A2.2 Intensity calculation

Measurement values are reported as intensity (I) expressed in counts per second (cps). The intensities from peak and background correspond to the following equations:

$$I_P = N_P / t_P \quad \text{(eq. A2.1)} \qquad \text{and} \qquad I_B = N_B / t_B \quad \text{(eq. A2.2)}$$

where

I_P, I_B = intensity (cps) at both peak and background positions.

N_P, N_B = total measured counts (cnts) at both peak and background positions.

t_P, t_B = measuring time (s) at both peak and background positions.

Because continuum X-rays (Bremsshtralung X-rays) and other phenomena produce a continuous background radiation through the whole X-ray spectrum, the intensity measured at the peak must be corrected for background noise. The net intensity is simply obtained by subtracting background intensity from the peak value.

$I_{net} = I_P - I_B$ (eq. A2.3)

Hence, error on the net intensity is calculated by summing the error from both peak and background. Note here that N/t can be replaced by I, especially if data are given on the print-out as intensity values.

General equations for standard deviation for peak and background,

$$\sigma_{P-B} = \sqrt{\left(\frac{N_P}{t_P^2}\right) + \left(\frac{N_B}{t_B^2}\right)} \quad \text{eq. (A2.4)} \quad \text{or} \qquad \sigma_{P-B} = \sqrt{\left(\frac{I_P}{t_P}\right) + \left(\frac{I_B}{t_B}\right)} \quad \text{(eq. A2.5)}$$

and relative standard deviation:

$$\varepsilon_{P-B} = \sqrt{\left(\frac{N_P}{t_P^2}\right) + \left(\frac{N_B}{t_B^2}\right)} \Bigg/ \left(\frac{N_P}{t_P}\right) - \left(\frac{N_B}{t_B}\right) \qquad \text{(eq. A2.6), or}$$

$$\varepsilon_{P-B} = \sqrt{\left(\frac{I_P}{t_P}\right) + \left(\frac{I_B}{t_B}\right)} \Bigg/ (I_P - I_B) \qquad \text{(eq. A2.7), or}$$

$$\varepsilon_{P-B} = \sigma_{P-B} / I_{net} * 100 \qquad \text{(eq. A2.8)}$$

However, background intensity cannot be directly measured underneath the peak, because peak and background signals are merged together and are indistinguishable from each other. This difficulty is overcome by measuring background intensities on both sides of the peak at interference-free positions and a linear interpolation allows estimation of the value under the peak position. Interpolated background is calculated through equation A2.9.

$$I_B = \frac{I_{BL} \times L_{BL} + I_{BH} \times L_{BH}}{L_{BL} + L_{BH}} \qquad \text{(eq. A2.9)}$$

I_{BL} = Count intensity (cps) measured at the low background position

I_{BH} = Count intensity (cps) measured at the high background position

L_{BL} = Distance (mm) of the low background position to the peak

L_{BH} = Distance (mm) of the high background position to the peak

Background positions should be selected based on a WDS scan obtained for every chemical domain and/or grain. The figure below shows an example of background positions selected on both sides of a Pb Mα peak with the interpolated linear background drawn in as a dotted line.

Figure A2.1: Interpolated background below a Pb Mα peak from a WDS scan on monazite (PETH crystal, P10, 15 kV, 200nA).

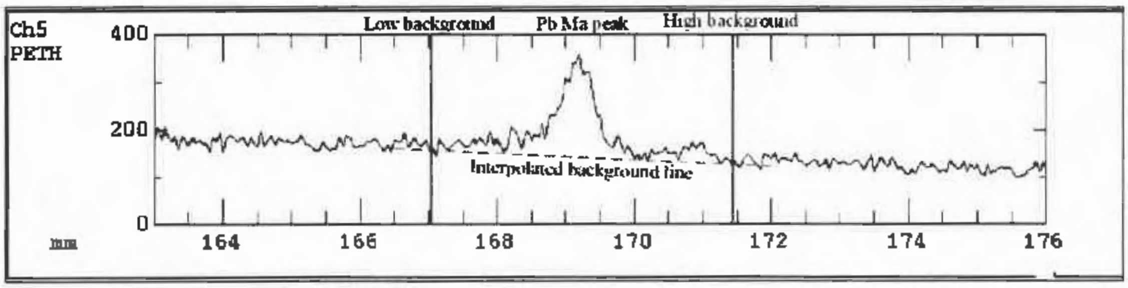

Because the interpolated background value (I_B) is a function of two independent measurements (I_{BL} and I_{BH}), the error inherent in each measurement must be incorporated into the I_B value before error is calculated on the net intensity (I_{net}). This can be done through the following equation by summing the standard deviation on both backgrounds:

$$\sigma I_B = \sqrt{\sigma^2 I_{BL} + \sigma^2 I_{BH}}. \quad \text{(eq. A2.10)}$$

The equation for calculating error on I_{net} (σ_{P-B}) then becomes,

$$\sigma_{P-B} = \sqrt{\sigma^2 I_P + \sigma^2 I_{BL} + \sigma^2 I_{BH}} \quad \text{(eq. A2.11)}$$

Both factors (denominators) that are used to normalize the counts (N), which are background distances from peak and counting time, must also be squared to preserve the unit relationship. Replacing the terms in the previous equation gives equation A2.12.

$$\sigma_{P-B}=\sqrt{\left(\frac{N_P}{t_P^2}\right)+\left(\frac{L_{BL}}{L_{BI}+L_{BH}}\right)^2\times\left(\frac{N_{BL}}{t_{BL}^2}\right)+\left(\frac{L_{BH}}{L_{BI}+L_{BH}}\right)^2\times\left(\frac{N_{BH}}{t_{BH}^2}\right)} \qquad \text{(eq. A2.12)}$$

Because of the relation I = N/t, the equation can be simplified to:

$$\sigma_{P-B}=\sqrt{\left(\frac{I_P}{t_P}\right)+\left(\frac{L_{BL}}{L_{BL}+L_{BH}}\right)^2\times\left(\frac{I_{BL}}{t_{BL}}\right)+\left(\frac{L_{BH}}{L_{BI}+L_{BH}}\right)^2\times\left(\frac{I_{BH}}{t_{BH}}\right)} \qquad \text{(eq. A2.13)}$$

Once error has been calculated on the net intensity (I_{net}) in the unknown, the error arising from standardisation must also be added. This is important because the EMP software uses the k-ratio (intensity unknown/intensity standard) to measure the proportion that a specific element contributes to the unknown sample. Therefore, the error on the k-ratio is the combination of the error on both peak and background from the standard and the unknown. Errors on I_{net} from the standard are calculated the same way as for the unknown. Relative standard errors are added in quadrature through equation A2.14:

$$\varepsilon_{P-B,k-ratio}=\sqrt{\varepsilon^2_{P-B,std}+\varepsilon^2_{P-B,unk}} \qquad \text{(eq. A2.14)}$$

Another important consideration in EMP analysis of monazite is the X-ray line interference problem. There are many overlaps between lines, although only three require correction. These are Y and Th lines interfering with Pb, and a Th line interfering with U. The effect of overlap is an increase in the measured signal. In trace element analysis for chemical dating, this results in a variation in age. To correct for this problem, we need to determine the amount of interference affecting Pb and U. Assessing the amount of interference from an element *y* on an element *x* is done by measuring the signal of *x* in a *x*-free standard of the element *y*. In the case of monazite dating, analyses were done at the Pb Mα position on ThO_2 and YAG (Yttrium-Aluminium-Garnet), both Pb-free standards, as well as at the U Mβ position on the ThO_2 (U-free) standard. Because these standards are Pb- and U-free, no signal should exist at the U and Pb peak positions. Consequently, all counts measured at the peak position are interpreted as interference. The relative intensity of overlap is obtained by calculating the ratio of $x_{\text{k-ratio}}/\, y_{\text{k-ratio}}$ in the x-free standard. K-ratios are used rather than count intensity to facilitate the matrix correction. Because peak ratios of an element are nearly constant, the ratio of y interfering peak (i.e., located at the x peak position) to the y main peak remains regular independent of the nature of the matrix. Therefore, peak ratios measured in the x-free standards can be used to determine the amount of overlap from a y interfering peak in monazite.

Figure A2.2: Example of two Th peaks in monazite. The Th Mβ peak is 58% of the intensity of the Th Mα peak used in trace analysis. Therefore, this ratio could be applied in a case where the main peak of an element is located at the same position as Th Mβ. The intensity of overlap will equal 58% of the intensity of the Th Ma peak.

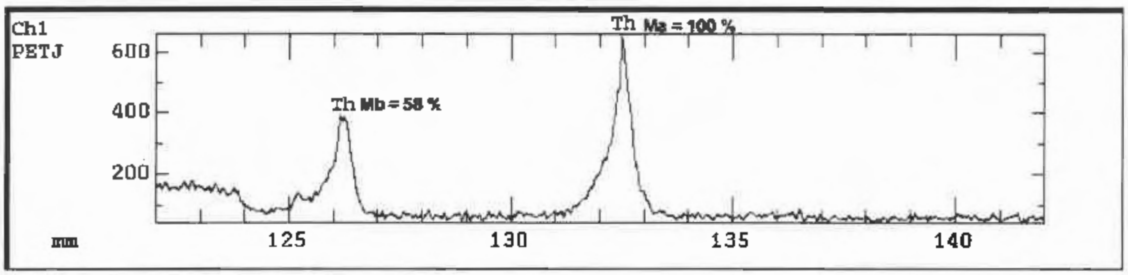

Measurements for Pb and U in ThO_2 and YAG, were done repeatedly and averaged. The average value can be used as a constant factor for all analyses done with the same instrument under the same analytical conditions. Corrections are done on the k-ratio prior to matrix correction. The correction is specific to every instrument.

Calculation of the correction factor:

$$CF_{x\text{-}y} = y^{std,x}_{k-ratio} \big/ x^{std,x}_{k-ratio} \quad \text{(eq. A2.15)}$$

Calculation of apparent Pb from the Th interference:

$$Pb^{app,unk}_{Th\ \text{interference},(wt\%)} = \left(CF_{Th-Pb}\right)\times\left(Th^{unk}_{k-ratio}\right)\times\left(Pb_{ZAF\ \text{factor}}\right)\times\left(Pb_{\text{std},\,wt\%}\right) \quad \text{(eq. A2.16)}$$

Correction of Pb for Y and Th interference:

$$\begin{aligned} Pb^{unk}_{corr(wt\%)} = Pb^{unk}_{uncorr(wt\%)} &- \left[\left(CF_{Th-Pb}\right)\times\left(Th^{unk}_{k-ratio}\right)\times\left(Pb_{ZAF\ \text{factor}}\right)\times\left(Pb_{\text{std},\,wt\%}\right)\right] \\ &- \left[\left(CF_{Y-Pb}\right)\times\left(Y^{unk}_{k-ratio}\right)\times\left(Pb_{ZAF\ \text{Factor}}\right)\times\left(Pb_{\text{std},\,wt\%}\right)\right] \end{aligned} \quad \text{(eq. A2.17)}$$

Calculated correction factor for interference of Y $L\zeta_{1-2}$ on Pb $M\alpha$: 0.0053
Calculated correction factor for interference of Th (M2-04 + $M\zeta_{1-2}$) on Pb $M\alpha$: 0.0015
Calculated correction factor for interference of Th $M\gamma$ on U $M\beta$: 0.0094

Correction for interference also introduces error due to uncertainty in the correction factor itself and on the measurement made for the interfering element in the unknown. The error on corrected values is calculated the following way Pyle et al. (2003):

Error on corrected U: (eq. A2.18)

$$\sigma^2_{U,\,corr,\,unk} = \sigma^2_{U,\,uncorr,\,unk} + \sigma^2_{U,\,Th-std}\left[\frac{(-Th,_{Th^\circ-std})(Th,_{unk})}{(U,_{U-std})(Th,Th_{-std})}\right]^2$$
$$+\sigma^2_{U,\,U-std}\left[\frac{(U,_{Th-std})(Th,_{Th^\circ-std})(Th,_{unk})}{(U,_{U-std})^2(Th,_{Th-std})}\right]^2 + \sigma^2_{Th,\,Th-std}\left[\frac{(U,_{Th-std})(Th,_{Th^\circ-std})(Th,_{unk})}{(U,_{U-std})(Th,_{Th-std})^2}\right]^2$$
$$+\sigma^2_{Th,\,Th^\circ-std}\left[\frac{(-U,_{Th-std})(Th,_{unk})}{(U,_{U-std})(Th,_{Th-std})}\right]^2 + \sigma^2_{Th,unk}\left[\frac{(-U,_{Th-std})(Th,_{Th^\circ-std})}{(U,_{U-std})(Th,_{Th-std})}\right]^2$$

Error on corrected Pb: (eq. A2.19)

$$\sigma^2_{Pb,\,corr,\,unk} = \sigma^2_{Pb,\,uncorr,\,unk} + \sigma^2_{Pb,\,Th-std}\left[\frac{(-Th,_{Th^\circ-std})(Th,_{unk})}{(Pb,_{Pb-std})(Th,_{Th-std})}\right]^2$$
$$+\sigma^2_{Pb,\,Pb-std}\left[\frac{(Pb,_{Th-std})(Th,_{Th^\circ-std})(Th,_{unk})}{(Pb,_{Pb-std})(Th,_{Th-std})} + \frac{(Pb,_{Y-std})(Y,_{Y^\circ-std})(Y,_{unk})}{(Pb,_{Pb-std})^2(Y,_{Y-std})}\right]^2 + \sigma^2_{Th,\,unk}\left[\frac{(-Pb,_{Th-std})(Th,_{Th^\circ-std})}{(Pb,_{Pb-std})(Th,_{Th-std})}\right]^2$$
$$+\sigma^2_{Th,\,Th-std}\left[\frac{(Pb,_{Th-std})(Th,_{Th^\circ-std})(Th,_{unk})}{(Pb,_{Pb-std})(Th,_{Th-std})^2}\right]^2 + \sigma^2_{Th,\,Th^\circ-std}\left[\frac{(-Pb,_{Th-std})(Th,_{unk})}{(Pb,_{Pb-std})(Th,_{Th-std})}\right]^2$$
$$+\sigma^2_{Pb,\,Y-std}\left[\frac{(-Y,_{Y^\circ-std})(Y,_{unk})}{(Pb,_{Pb-std})(Y,_{Y-std})}\right]^2 + \sigma^2_{Y,\,Y-std}\left[\frac{(-Pb,_{Y-std})(Y,_{Y^\circ-std})(Y,_{unk})}{(Pb,_{Pb-std})(Y,_{Y-std})^2}\right]^2 + \sigma^2_{Y,\,Y^\circ-std}\left[\frac{(-Pb,_{Y-std})(Y,_{unk})}{(Pb,_{Pb-std})(Y,_{Y-std})}\right]^2$$
$$+\sigma^2_{Y,unk}\left[\frac{(-Pb,_{Y-std})(Y,_{Y^\circ-std})}{(Pb,_{Pb-std})(Y,_{Y-std})}\right]^2$$

where each term is the value in counts per seconds (cps) measured in the specific standard. The superscript ° indicates calibration measurements done at 200 nA. All standard deviation values are also in counts per second (cps).

The age is calculated by iteration using the following equation from Montel et al. (1996):

$$Pb = {}^{232}Th / 232 \times [e^{232\lambda t} - 1] \times 208 + \varpi\, {}^{238}U/238.04 \times [e^{238\lambda t} - 1] \times 206$$
$$+ \varpi\, {}^{235}U/ 238.04 \times [e^{235\lambda t} - 1] \times 206 \qquad \text{(eq. A2.20)}$$

where

- Pb, Th, U are in ppm
- 232λ, 235λ, 238λ are the radioactive decay constants of ^{232}Th (4,95E-11), ^{235}U (9,85E-10), and ^{238}U (1,55E-10), respectively (Montel et al., 1996)
- ϖ is the relative crustal abundance of U isotopes ($^{238}U = 0.9928$ and $^{235}U = 0.0072$).
- Pb is the total amount of radiogenic Pb produced by all the parent atoms.
- t, time, is in years in the equation, but age is entered as My in the Excel™ age calculation spreadsheet used for age calculation.

Error is propagated through the age equation using the following equation:

$$\varepsilon_{age} = \sqrt{\varepsilon_{U,corr}^2 + \varepsilon_{Th}^2 + \varepsilon_{P,corrb}^2} \qquad \text{(eq. A2.21)}$$

The age for a grain or chemical domain is simply the average of all the spot ages obtained within the grain or chemical domain weighted with the individual error of each spot age. The weighted average is calculated using Isoplot/Ex (rev. 2.49) from Ludwig (2001).

$$\bar{x} = \frac{\sum\left\{ \left(x_i - \bar{x}\right) / \sigma_{x_i}^2 \right\}}{\sum\left(1 / \sigma_{x_i}^2 \right)} \qquad \text{(eq. A2.22)}$$

Error on the grain is calculated by summing and averaging the error from all analyses done within this grain or chemical zone using the following equation:

$$\sum \varepsilon = \sqrt{(\varepsilon_1 + \varepsilon_2 + \varepsilon_3 + \ldots)} / n \qquad \text{(eq. A2.23)}$$

A2.3 Worked example

Here is a worked example with data acquired from grain **S392-01**, analysis **#657**. The grain is a subhedral, zoned monazite included in biotite from a migmatitic metapelite at upper amphibolite facies. Analysis #657 is located on the rim of the grain.

Figure A2.3: Analytical conditions for trace analysis of the sample as showed on the print-out. Take note of background positions and counting times highlighted by boxes. Different background positions were used for standardisation. The background positions (in mm) used for calibration were: Pb = -3.5/+5.0, Th = -2.0/+2.0, U = -3.0/+3.0 and Y = -2.0/+2.0.

```
Measurement Condition
WDS elements
Element  X-ray Crystal   CH  Acc.v    Peak Pos.     (nm)      BG_L     BG_U (mm)
 1 Th    Ma     PETJ    ( 1)  15.0    132.527    0.41381    2.000    2.000
 2 U     Mb     PETJ    ( 2)  15.0    118.898    0.37160    2.500    4.000
 3 Y     La     TAP     ( 4)  15.0     69.884    0.64488    1.000    1.000
 4 Pb    Ma     PETH    ( 5)  15.0    169.199    0.52860    2.000    2.000

Element   Peak  Back            Pksk  Gain  High.V Base.L Window.W  Mode
 1 Th    360.0 180.0 (s)          1     16    1700   1.0     5.0 (V)  Dif
 2 U     360.0 180.0 (s)          1     64    1700   1.0     5.0 (V)  Dif
 3 Y     360.0 180.0 (s)          1     32    1700   2.0     6.0 (V)  Dif
 4 Pb    360.0 180.0 (s)          1     64    1700   1.2     2.5 (V)  Dif

Measurement Order of WDS
Order      Channel 1           2           3           4          5
  1                Th          U           -           Y          Pb

Calc. Elements :   La (Fixed)          Ce (Fixed)          Pr (Fixed)
                   Nd (Fixed)          Sm (Fixed)          Gd (Fixed)
                   Dy (Fixed)          Ca (Fixed)          Si (Fixed)
                   P  (Fixed)          O  (Fixed)
```

Figure A2.4: Data from standardisation (calibration) of Pb, Th, U, and Y. Intensities measured on peak and both background positions for each element are shown in a box.

```
Standard Data
Element    Standard name     Mass(%)    ZAF Fac.    Z         A         F
 1 Th      ThO2              87.8800    1.6363    1.9598    0.8349    1.0000
 2 U       UO2               87.1500    1.3150    1.5286    0.8603    1.0000
 3 Y       YAG               44.9300    2.6890    3.8386    0.7005    1.0000
 4 Pb      Crocoite          64.1100    2.4678    3.1295    0.7886    1.0000

Standard Intensity of WDS
Element   Curr.(A)     Net(cps) Bg-(cps) Bg+(cps)   S.D.(%)   Date
 1 Th    2.001E-07     12989.1    182.9    155.6      0.14    Nov 15 21:45 2003
 2 U     2.001E-07     21614.4    433.4    437.5      0.11    Nov 15 21:40 2003
 3 Y     2.001E-07     47672.5   4048.0    582.8      0.08    Nov 15 21:31 2003
 4 Pb    2.001E-07     38125.5    528.4    202.7      0.08    Nov 15 21:35 2003
```

Figure A2.5: Data acquired from trace analysis of the unknown at spot #657, intensities values measured at peak and both background positions, mass (%), K-raw (%) and ZAF factors are given for Pb, Th, U , and Th in the boxes. K-raw (%) is the k-ratio calculated by the EMP.

```
Unknown Specimen No. 657
 Group          : AgeDate          Sample  : MonaziteTrace
 UNK No.        :  657             Comment : S392-01-1
 Stage          :    X=   40.7773  Y=   90.3746  Z=    9.9930
 Acc. Voltage   :    15.0 (kV)     Probe Dia. : 0    Scan : On        Mag : 4000
 Dated on Nov 15 23:09 2003
 WDS only         No. of accumulation : 1

Curr.(A)  : 2.002E-07
Element Peak(mm) Net(cps)    Bg-     Bg+  S.D.(%)    D.L.(ppm)
 1 Th    132.531    339.5    73.1    71.8     0.34        43
 2 U     118.898    103.0   230.8   191.6     1.20        44
 3 Y      69.874   1328.3   958.4   673.7     0.22        20
 4 Pb    169.199    190.1   167.6   148.3     0.62        16

ZAF Metal
Element   Mass(%)    Atom(%)   X(%)   K-raw(%)    ZAF       Z        A        F
 Th        2.8773    0.4699   2.2960   2.6127   1.2532   1.1937   1.0498   1.0000
 U         0.5100    0.0812   0.4153   0.4765   1.2280   1.1882   1.0335   1.0000
 Y         1.4231    0.6065   1.2512   2.7848   1.1373   0.9424   1.2068   1.0000
 Pb        0.4125    0.0754   0.3195   0.4984   1.2912   1.0817   1.1937   1.0000
 La       11.1000    3.0278    Fixed
 Ce       26.4700    7.1581    Fixed
 Pr        3.8300    1.0299    Fixed
 Nd        9.3700    2.4615    Fixed
 Sm        1.5300    0.3856    Fixed
 Gd        1.3200    0.3181    Fixed
 Dy        0.0000    0.0000    Fixed
 Ca        0.5800    0.5483    Fixed
 Si        0.1100    0.1484    Fixed
 P        12.5400   15.3426    Fixed
 O        28.8600   68.3468    Fixed
 ------------------------------------------------------------     -------------
 Total   100.9329  100.0000   4.2820   6.3724     Iteration - 3
```

The rest of this section will show how probe data were used to calculate the chemical age of the grain at this spot and the counting error associated with it. All data used in the following sections can be found in the figures above. Calculations are done in logical order. When the same calculation applies to each element, only Pb is shown and results for other elements are given at the end of the section.

Step 1: Interpolated background

$$I_B = \frac{I_{BL} \times L_{BL} + I_{BH} \times L_{BH}}{L_{BL} + L_{BH}} \qquad \text{(eq. A2.9)}$$

Standard background:

Pb, $I_B = (528.4 * 3.5 + 202.7 * 5.0) / (3.5 + 5.0) = 336.81$ cps

Th = 169.25 cps, U = 435.45 cps and Y= 2315.40 cps

Unknown background:

Pb, $I_B = (167.6 * 2.0 + 148.3 * 2.0) / (2.0 + 2.0) = 157.95$ cps

Th = 72.45 cps, U = 206.68 cps and Y= 816.05 cps

Step 2: Intensity on peak

$I_P = I_{net} + I_B$ (eq. A2.3)

Standard peak intensity:

Pb, $I_P =$ 38 125.5 + 336.81 = 38 462.31 cps

Th = 13 158.35cps , U = 22 049.85 cps and Y= 49 987.90 cps

Unknown peak intensity:

Pb, $I_P = 190.1 + 157.95 = 348.05$ cps

Th = 411.95 cps, U = 309.68 cps and Y= 2144.35 cps

Step 3: Standard deviation on both peak and background

Standard deviations on both peak and background are simply added in quadrature through the following equation:

$$\sigma_{P-B}=\sqrt{\left(\frac{I_P}{t_P}\right)+\left(\frac{L_{BL}}{L_{BL}+L_{BH}}\right)^2\times\left(\frac{I_{BL}}{t_{BL}}\right)+\left(\frac{L_{BH}}{L_{BI}+L_{BH}}\right)^2\times\left(\frac{I_{BH}}{t_{BH}}\right)} \quad \text{eq. (A2.13)}$$

Standard peak and background standard deviation:

Pb,

$$\sigma_{P-B,std}=\sqrt{\left(\frac{38462.31}{40}\right)+\left(\frac{3.5}{3.5+5.0}\right)^2\times\left(\frac{528.4}{10}\right)+\left(\frac{5.0}{3.5+5.0}\right)^2\times\left(\frac{202.7}{10}\right)}=31.27\,\text{cps}$$

Th = 18.37 cps, U = 23.94 cps and Y= 36.95 cps

Unknown peak and background standard deviation:

Pb,

$$\sigma_{P-B,unk}=\sqrt{\left(\frac{348.05}{360}\right)+\left(\frac{2.0}{2.0+2.0}\right)^2\times\left(\frac{167.6}{90}\right)+\left(\frac{2.0}{2.0+2.0}\right)^2\times\left(\frac{148.3}{90}\right)}=1.36\,\text{cps}$$

Th = 1.24 cps, U = 1.43 cps and Y= 3.24 cps

Step 4: Relative standard deviations on peak and background

$\varepsilon_{P\text{-}B,\,std} = (\sigma_{P\text{-}B,\,std} * 100) / I_{net}$ and, $\varepsilon_{P\text{-}B,\,unk} = (\sigma_{P\text{-}B,\,unk} * 100) / I_{net}$

Standard relative standard deviations:

Pb, $\varepsilon_{P\text{-}B,\,std}$ = (31.27 * 100) / 38 125.5 = 0.08 %

Th = 0.14 %, U = 0.11 % and Y= 0.08 %

Unknown relative standard deviations:

Pb, $\varepsilon_{P\text{-}B,\,unk}$ = (1.36 * 100) / 190.1 = 0.71 %

Th = 0.37 %, U = 1.39 % and Y= 0.24 %

Step 5: Relative standard deviation on k-ratio

$$\varepsilon_{P-B,k-ratio}=\sqrt{\varepsilon^2_{P-B,std}+\varepsilon^2_{P-B,unk}}$$

Pb, $$\varepsilon_{P-B,k-ratio}=\sqrt{0.08^2+0.71^2}=0.72\ \%$$

Th = 0.39 %, U = 1.39 % and Y= 0.26 %

Step 6: Correction factor for interference of Y and Th lines on Pb Mα, and Th lines on U Mβ:

$$Pb^{unk}_{corr(wt\%)} = Pb^{unk}_{uncorr(wt\%)} - \left[\left(CF_{Th-Pb}\right)\times\left(Th^{unk}_{k-ratio}\right)\times\left(Pb_{ZAF\ factor}\right)\times\left(Pb_{std,\,wt\%}\right)\right] - \left[\left(CF_{Y-Pb}\right)\times\left(Y^{unk}_{k-ratio}\right)\times\left(Pb_{ZAF\ Factor}\right)\times\left(Pb_{std,\,wt\%}\right)\right]$$

Pb_{corr} = 4125 ppm - (0.0015 x 2.6127 x (1.2912 / 100) x 641 100 ppm) - (0.0053 x 2.7848 x (1.2912 / 100) x 641 100 ppm) = 3970 ppm

U_{corr} = 4837 ppm

Step 7: Relative standard deviation on corrected Pb

Equation A2.17, Pb_{corr} = 0.979 % and U_{corr} = 2.014 %

Table A2.1: Data required in equation A2.17

	Intensity (cps)	Std dev. (cps)
Pb, Th, std	56.8	4.78
Th, Th, std	13164.9	18.48
Th, Th°, std (calibration)	13193.2	18.525
Pb, Y, std	203.3	3.46
Y, Y, std	48137.8	37.24
Y, Y°, std (calibration)	48618.25	37.06
U, Th, std	199.6	5.89

Step 8: Age calculated by iteration using equation of Montel et al. 1996

$$Pb = {}^{232}Th/232 \times [e^{232\lambda t} - 1] \times 208 + \varpi\, {}^{238}U/238.04 \times [e^{238\lambda t} - 1] \times 206 + \varpi\, {}^{235}U/238.04 \times [e^{235\lambda t} - 1] \times 206 \qquad \text{(eq. A-1.20)}$$

Considering, Pb_{corr} = 3970 ppm, U_{corr} = 4837 ppm, Th = 28 773 ppm

$$3970 = 28\,773/232 \times [e^{4.95E\text{-}11 \times 1.831E+09} - 1] \times 208 + 0.9928 \times 4837/238.04 \times [e^{1.55E\text{-}10 \times 1.831E+09} - 1] \times 206 + 0.0072 \times 4837/238.04 \times [e^{9.85E\text{-}10 \times 1.831E+09} - 1] \times 207$$

Age = 1832 Ma

Step 9: Propagation of error through the age calculation

Pb_{corr} = 0.979 %, Th = 0.39 %, U_{corr} = 2.014 %

$$\varepsilon_{age} = \sqrt{\varepsilon^2_{U_{corr}} + \varepsilon^2_{Th} + \varepsilon^2_{Pb_{corr}}}$$

$$\varepsilon_{age} = \sqrt{2.014^2 + 0.39^2 + 0.979^2} = 2.27\%$$

#10- Standard deviation on the age:

2.27% x 1832 Ma / 100 = 41.7 Ma

1832 Ma ± 2.27 % or **1832 Ma ± 41.7 Ma** **References**

Appendix 3

Data for correction factor calculation

Table A3.1: Data from trace analysis of ThO_2 at Pb Mα and Th Mα positions (15 kV, 200 nA, Pb on PETH, Th on PET crystals, 40 sec. on peak and 20 sec. on backgrounds).

Trace Analysis	Intensity (cps)				Intensity (%)		Raw K-ratios (%)		Ratio Pb/Th
			Std dev. (P-B)		Rel. Std dev. (P-B)				
	Pb, ThO2	Th, ThO2	Pb, ThO2	Th, ThO2	Pb, ThO2	Th, ThO2	Pb, ThO2	Th, ThO2	
#596	49.8	13926.6	4.86	19.07	9.77	0.14	0.1293	99.8483	0.0013
#597	52.9	13900.1	4.87	19.06	9.21	0.14	0.1374	99.6091	0.0014
#598	52.4	13925.6	4.87	19.07	9.30	0.14	0.1359	99.7421	0.0014
#599	50.5	14007.9	4.87	19.13	9.64	0.14	0.1312	100.3815	0.0013
#600	43.5	13902.1	4.85	19.06	11.15	0.14	0.1130	99.5735	0.0011
#601	46.8	14043.2	4.86	19.15	10.38	0.14	0.1213	100.5841	0.0012
#602	53.9	14001.4	4.88	19.12	9.05	0.14	0.1399	100.2853	0.0014
#630	64.5	12422.3	4.71	17.92	7.31	0.14	0.1686	100.6425	0.0017
#631	69.8	12483.7	4.73	17.96	6.77	0.14	0.1827	101.1397	0.0018
#632	60.4	12513.7	4.70	17.98	7.79	0.14	0.1581	101.3323	0.0016
#633	56.9	12432.2	4.69	17.92	8.25	0.14	0.149	100.7229	0.0015
#634	66.0	12397.4	4.72	17.90	7.15	0.14	0.1726	100.4404	0.0017
#635	65.2	12464.8	4.72	17.94	7.23	0.14	0.1706	100.9867	0.0017
#636	62.2	12486.6	4.71	17.96	7.57	0.14	0.1628	101.1632	0.0016
#637	57.1	12343.0	4.69	17.86	8.22	0.14	0.1495	100.0501	0.0015
Average	**56.8**	**13150.0**	**4.78**	**18.47**	**8.59**	**0.14**	**0.1481**	**100.4334**	**0.0015**

Table A3.2: Data from trace analysis of ThO_2 at U MB and Th Mα positions (15 kV, 200 nA, U and Th on PET crystals, 40 sec. on peak and 20 sec. on backgrounds).

Trace Analysis	Intensity (cps) U, ThO2	Intensity (cps) Th, ThO2	Std dev. (P-B) U, ThO2	Std dev. (P-B) Th, ThO2	Intensity (%) Rel. Std Dev. (P-B) U, ThO2	Intensity (%) Rel. Std Dev. (P-B) Th, ThO2	Raw K-ratios (%) U, ThO2	Raw K-ratios (%) Th, ThO2	Raw K-ratios (%) Ratio U/Th
#603	155.7	14032.0	6.08	19.14	3.91	0.14	0.7694	100.3544	0.0077
#604	155.1	14004.4	6.08	19.12	3.94	0.14	0.7659	100.0792	0.0077
#605	154.1	14010.8	6.08	19.12	3.94	0.14	0.7611	100.2033	0.0076
#606	164.6	13978.7	6.10	19.10	3.71	0.14	0.8133	99.9732	0.0081
#607	157.2	13888.8	6.08	19.04	3.87	0.14	0.7767	99.3303	0.0078
#608	158.6	14054.6	6.09	19.15	3.84	0.14	0.7837	100.5159	0.0078
#609	164.1	14058.1	6.10	19.15	3.72	0.14	0.8106	100.5410	0.0081
#638	224.9	12420.4	5.69	17.92	2.53	0.14	1.0347	100.5763	0.0103
#639	239.3	12401.2	5.72	17.91	2.39	0.14	1.1016	100.4716	0.0110
#640	236.3	12415.1	5.72	17.92	2.42	0.14	1.0869	100.5339	0.0108
#641	229.9	12351.9	5.70	17.87	2.48	0.14	1.0578	100.0216	0.0106
#642	239.3	12462.1	5.72	17.95	2.39	0.14	1.1011	100.9147	0.0109
#643	241.0	12527.9	5.73	17.99	2.38	0.14	1.1088	101.4472	0.0109
#644	238.2	12584.2	5.72	18.03	2.40	0.14	1.0957	101.9030	0.0108
#645	235.7	12507.1	5.71	17.98	2.42	0.14	1.0845	101.2791	0.0107
Average	**199.6**	**13179.8**	**5.89**	**18.49**	**3.09**	**0.14**	**0.9435**	**100.5430**	**0.0094**

Table A3.3: Data from trace analysis of YAG at Pb Mα and Y Lα positions (15 kV, 200 nA, Y on TAP, Pb on PETH crystals, 40 sec. on peak and 20 sec. on backgrounds).

	Intensity (cps)				Intensity (%)		Raw K-ratios (%)		
			Std dev. (P-B)		Rel. Std dev. (P-B)				
Trace Analysis	**Pb, YAG**	**Y, YAG**	**Pb, YAG**	**Y, YAG**	**Pb, YAG**	**Y, YAG**	**Pb, YAG**	**Y, YAG**	**Ratio Pb/Y**
#610	203.4	48698.9	3.47	37.64	1.71	0.08	0.5268	98.4908	0.0054
#611	199.7	48719.4	3.46	37.65	1.73	0.08	0.5171	98.5323	0.0053
#612	199.9	48594.9	3.46	37.60	1.73	0.08	0.5181	98.3293	0.0053
#613	200.1	48332.0	3.46	37.52	1.73	0.08	0.5184	97.7487	0.0053
#614	198.5	48432.5	3.46	37.55	1.74	0.08	0.5144	98.0007	0.0053
#615	196.5	48723.0	3.45	37.65	1.75	0.08	0.5089	98.5396	0.0052
#616	193.7	48307.0	3.44	37.51	1.77	0.08	0.5016	97.6983	0.0052
#646	209.0	47677.3	3.46	36.90	1.66	0.08	0.5460	99.8623	0.0055
#647	204.3	47551.0	3.45	36.86	1.69	0.08	0.5337	99.5977	0.0054
#648	203.5	48121.5	3.44	37.05	1.69	0.08	0.5314	100.7423	0.0053
#649	211.0	48136.6	3.47	37.05	1.64	0.08	0.5509	100.7740	0.0055
#650	207.8	48020.8	3.46	37.01	1.66	0.08	0.5427	100.5315	0.0054
#651	212.4	47414.7	3.48	36.81	1.64	0.08	0.5546	99.2627	0.0056
#652	208.4	47722.5	3.46	36.91	1.66	0.08	0.5441	99.9070	0.0055
#653	202.0	47615.2	3.44	36.88	1.70	0.08	0.5275	99.6824	0.0053
Average	**203.3**	**48137.8**	**3.46**	**37.24**	**1.70**	**0.08**	**0.5291**	**99.1800**	**0.0053**

Table A3.4: Data from standardisation of elements for trace analysis (15 kV, 200 nA, 40 sec. on peak and 20 sec. on backgrounds).

		Intensity (cps)			Intensity (%)	Position (mm)		
Trace Analysis	**Net intensity**	**Std Dev. (P-B)**	**Bkg Low**	**Bkg High**	**Rel. Std Dev. (P-B)**	**Bkg Low**	**Bkg High**	**Peak**
Pb in crocoite (#597-602, #610-616)	38399.6	31.39	477.0	233.2	0.08	3.2	4.0	169.243
Pb in crocoite (#630-637, #646-653)	38237.7	31.32	539.3	205.5	0.08	3.5	5.0	169.195
Average	**38318.65**	**31.355**	-	-	**0.08**	-	-	-
Th in ThO2 (#597-602, #603-609)	14031.0	19.14	228.4	184.9	0.14	2.0	2.0	132.583
Th on ThO2 (#630-637, # 638-645)	12355.4	17.91	162.6	139.8	0.14	3.0	2.0	132.542
Average	**13193.2**	**18.525**	-	-	**0.14**	-	-	-
U in UO2 (#603-609)	20222.3	23.21	443.9	443.8	0.11	3.0	3.0	118.898
U in UO2 (#638-645)	21736.5	24.01	444.0	436.1	0.11	3.8	4.4	118.898
Average	**20979.4**	**23.61**	-	-	**0.11**	-	-	-
Y in YAG (#610-616)	49469.6	37.18	3336.5	540.8	0.08	2.0	2.0	69.889
Y in YAG (#646-653)	47766,9	36.94	3969.7	572.2	0.08	2.0	2.0	69.879
Average	**48618.25**	**37.06**	-	-	**0.08**	-	-	-

Appendix 4

Sample descriptions

S366
Transect 2
Bt- Ms-Pl-Qtz

UTM zone 18
7 623 300 m. N.
553 493 m. E.

Min.	**%**	**Size (mm)**	**Texture**
Qtz	50	0.04-0.3	Anhedral, heterogranular
Bt	30	0.3-0.8	Euhedral, elongated abundant radioactive halos
Ms	10	0.1-0.3	Euhedral, elongated
Pl	10	0.04-0.3	Anhedral, granular
Op	1	0.05-0.2	Anhedral, granular
Ap	<1	<0.08	Subhedral, subprismatic
Mnz / Zrn	1	<0.3	Granular, rounded

Field of view: 2.5 mm across
Type of light: Polarised light

Thin section description: The cleavage (S2) is defined by biotite oriented horizontally (E-W) in extinction. The main schistosity (S1) is defined by biotite and muscovite crystals oriented NE-SW. Bedding is also present in the sample, but not evident at the scale of the picture.

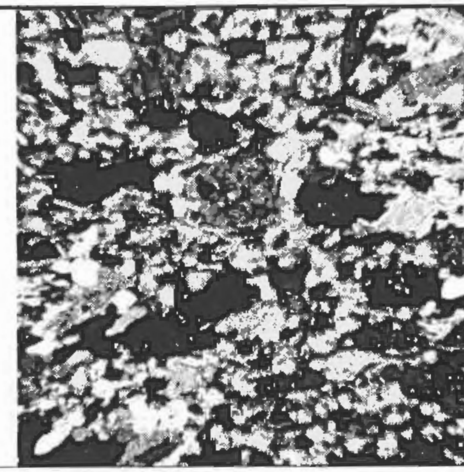

Field of view: 2.0 mm across
Type of light: Crossed polars

Thin section description: Same area as depicted in image on left under crossed-polars. Granoblastic and heterogranular texture of the matrix are more obvious. Note the spotty texture of biotite from radioactive damage induced by inclusions of zircon and monazite.

Sample description: Metasedimentary rock of psammitic composition with rare thin horizons of pelitic material. The rock has a granoblastic texture with a relatively heterogranular quartz-plagioclase matrix. Grain size varies from fine- to medium-grained. The micas are preferentially oriented along S1 or S2. The schistosity S1 is the best-developed foliation in the sample, especially in the thin pelitic horizons. Compositional layering is recognizable but not well defined. Graded bedding is locally observed. Two types of biotite grains are present in the sample. One population of biotite is anhedral with a darker colour and a weak pleochroism and the second population is euhedral, generally parallel to the planar fabric S1. Muscovite grains are smaller and narrower than biotite. Coalescent quartz with undulose extinction exists in local elliptic segregation of coarser quartz material.

S367 **Transect 2** **Bt-Crd-Ms-Pl -Qtz**			UTM zone 18 7 623 050 m. N. 553 754 m. E.
Min.	**%**	**Size (mm)**	**Texture**
Qtz	50	0.04-0.3	Anhedral, granular
Bt	25	0.2-0.6	Anhedral/ euhedral
Pl	10	0.04-0.3	Anhedral, granular
Ms	10	0.1-0.3	Euhedral
Crd	5	2-5	Anhedral, Poikiloblastic
Op	1	0.05-1	Anhedral/ prismatic
Ap	<1	0.02-0.1	Prismatic/ granular
Mnz/ Zrn	tr.	<0.04	Anhedral, granular

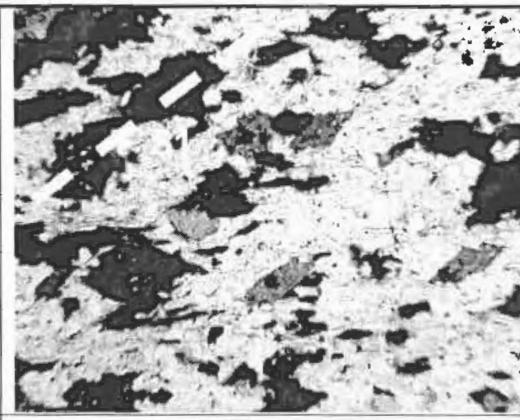

Field of view: 2 mm across
Type of light: Polarised light

Thin section description: Biotite crystals oriented NE-SW define the main schistosity S1. The sample has a granoblastic texture. Note the large dark anhedral biotite crystals.

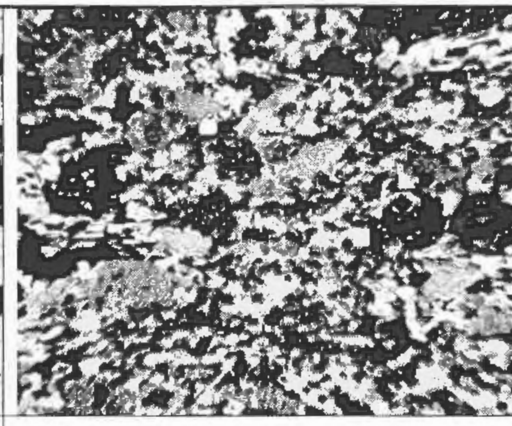

Field of view: 2 mm across
Type of light: Crossed polars

Thin section description: Same area depicted as image to left, but under crossed polars. The matrix has a granoblastic and equigranular texture. Biotite commonly display radioactive damage halo from zircon and monazite inclusions.

Sample description: Metasedimentary rock of psammitic composition with thin horizons of semipelitic material displaying a well-defined compositional layering corresponding to S0. The micas have a preferred orientation (S1) defining a fabric at low angle to S0. The two planar fabrics are subparallel. The rock is fine-to medium-grained with a dominant granoblastic texture. The quartz-plagioclase matrix is equigranular. Cordierite is relatively small with porphyroblast from 2-5 mm. Biotite is found as anhedral crystals of irregular shape that are darker and present a weaker pleochroism. Biotite is also commonly found with the more typical mica shape. These crystals are lighter and display a good pleochroism.

S371 Transect 1 Bt-Ms-Qtz			UTM zone 18 7 648 219 m. N. 573 776 m. E.
Min.	**%**	**Size (mm)**	**Texture**
Bt	40	0.1-0.3	Euhedral Parallel to S1 or S2
Qtz	35	0.02-0.15	Anh., Gran Equigranular, rounded
Ms	25	0.05-0.2	Euhdr. Par. S1 or S2
Ap	<1	0.01-0.08	Euh., Prism. Mainly found in the matrix
Op	<1	0.05-0.2	Anh./prism
Mnz/ Zrn	tr.	<0.03	Granular

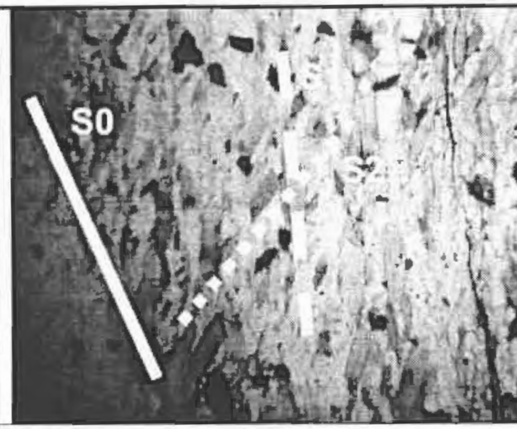

Field of view: 1.5 mm across
Type of light: Polarised light

Thin section description: The bedding (S0) is oriented NNW-SSE. Contact between a psammitic and a semipelitic bed located in the lower left defines S0. Biotite grains vertically oriented define the S1 foliation at low angle with S0. A weaker foliation (S2) oriented NE-SW is also defined by biotite grains.

Field of view: 1.5 mm across
Type of light: Crossed polars

Thin section description: Picture has the same orientation as image on the left. Biotite parallel to S1 is in extinction. S2 biotite grains are oblique to S1 and oriented NE-SW. The quartz matrix is fine-grained.

Sample description: Metasedimentary rock composed of alternating horizons of psammitic and pelitic material of thickness varying from 0.2-1 cm. The rock is fine-grained and presents a dominant lepidoblastic texture. Matrix quartz is relatively equigranular, although local elliptic segregation of coarser quartz is present. Three foliations were identified in this sample. The bedding (S0) is defined by compositional layering. The main schistosity is defined by the preferential orientation of micas (S1) and is at low angle relative to S0. A more subtle planar fabric also defined by mica orientation was identified and is interpreted as S2. The S2 fabric is at higher angle than S1 relatively to S0. The radioactive minerals (monazite and zircon) are very difficult to find because of their small size. Dark radioactively-induced halos are rarely recognised in micas.

S373 **Transect 3** **Bt-Crd-Ms-Pl-Qtz**			UTM zone 18 7 607 678 m. N. 587 960 m. E.
Min.	**%**	**Size (mm)**	**Texture**
Qtz	52	0.05-0.25	Anhedral, granular
Bt	25	0.1-1	Euhedral
Pl	10		Anhedral, granular
Ms	5	0.2-0.6	Euhedral
Crd	5	4 -10	Anhedral, poikiloblastic
Ap	1	0.02-0.1	Euhedral, prismatic
Op	2	0.05-0.5	Anhedral, granular
Mnz/Zrn	<1	<0.05	Anhedral, granular

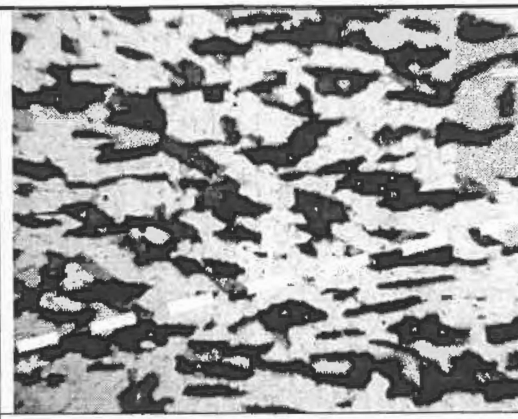

Field of view: 2.7 mm across
Type of light: Polarised light

Thin section description: A moderately developed S1 fabric is defined by the biotite oriented NE-SW. Biotite commonly contains dark haloes due to radioactively-induced damage by zircon or monazite inclusions.

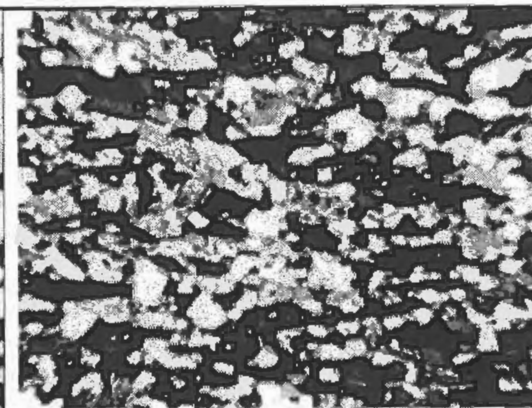

Field of view: 2.5 mm across
Type of light: Crossed polars

Thin section description: Same as left under crossed polars. The quartz-plagioclase is heterogranular. Some biotite grains are randomly oriented.

Sample description: Metasedimentary rock composed of an alternation of semipelitic and psammitic layers of thickness varying from 0.4 -1 cm. Psammite layers are larger and more abundant than semipelitic layers. The rock is medium-grained with a dominant granoblastic texture. The quartz-plagioclase matrix is heterogranular. Anhedral, dark biotite is very abundant. Numerous pleochroic radioactively-induced haloes are present in biotite. Biotite is also locally chloritized. A planar fabric, S1, defined by the micas is at low angle with the bedding (S0). The mica parallel to fabric S1 wraps around the cordierite porphyroblasts. Inclusions in cordierite define an older fabric oblique with S1.

S374
Transect 3
Bt-Crd-Ms-Pl-Qtz

UTM zone 18
7 607 678 m. N.
587 960 m. E.

Min.	**%**	**Size (mm)**	**Texture**
Qtz	40	0.05-0.4	Anhedral, granular
Bt	25	0.1-1	Euhedral,
Crd	15	5-10	Anhedral, poikiloblastic
Ms	10	0.2-0.6	Euhedral
Pl	10	0.05-0.4	Anhedral, granular
Op	<1	0.02-0.4	Anhedral, granular
Ap	<1	0.05-0.0.2	Euhedral, prismatic
Mnz/ Zrn	tr.	<0.05	Anhedral, granular

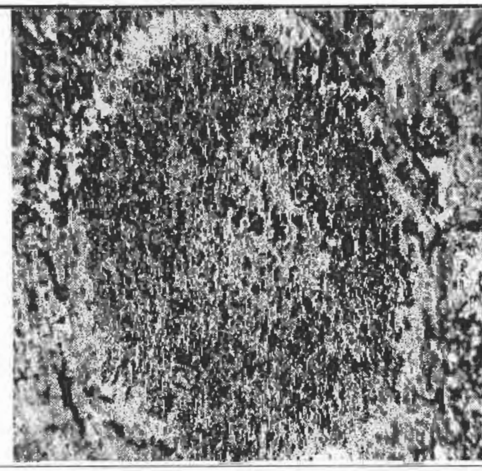

Field of view: 8 mm across
Type of light: Crossed polars

Thin section description: Cordierite porphyroblast with fresh core and rim altered to white micas and pinite. Inclusions in the cordierite define a fabric oblique to the external fabric (S1).

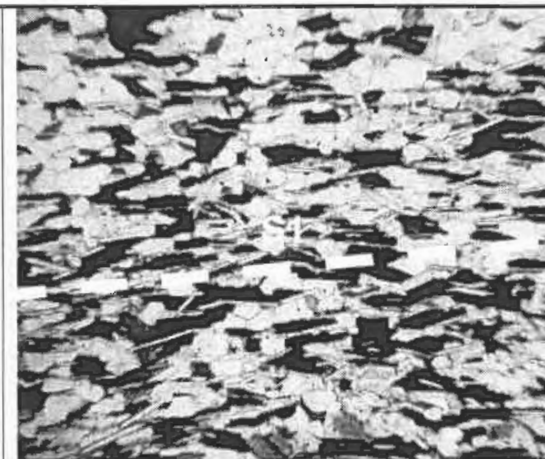

Field of view: 2.6 mm across
Type of light: Polarised light

Thin section description: The micas are mainly oriented NE-SW along S1. A steeper fabric also oriented NE-SW seems to have caused displacement between micas. This feature has not been related to S1 or S2 .65

Sample description: Metasedimentary rock mainly composed of an alternation of psammitic and semipelitic horizons of thickness varying from 0.4-1 cm. Psammite component is dominant in the rock. The rock has a grano-lepidoblastic texture. Anhedral dark biotite represents a minor proportion of all biotites. Biotite is locally chloritized. Large elliptical poikiloblastic crystals of cordierite are found in the more pelitic layers. Cordieritegives the rock a "spotted" aspect. Core of cordierite crystals is fresh, while the outer rim is retrograded to muscovite. The inner rim is probably a mix of very fine-grained white micas. The inclusions in cordierite define an internal fabric oblique to the external fabric (S1). The mica fabric is well developed in the pelitic layers but much weaker in the psammite layers. A weak second fabric is observed in the sample, but has not been related to S1 or S2.

S375
Transect 3
Bt-Ms-Pl-Qtz-Sil

UTM zone 18
7 607 205 m. N.
587 643 m. E.

Min.	%	Size (mm)	Texture
Qtz	50	0.1-0.5	Anhedral, granular
Bt	20	0.2-0.6	Euhedral
Pl	12	0.1-0.3	Anhedral, granular
Kfs	5	0.1-0.4	Anhedral, poikiloblastic
Ms	2	0.1-0.4	Euhedral, highly resorbed
Sil	4	0.05-0.1	Euhedral, prismatic
Grt	2	<0.2	Subhedral, granular
Crd	4	0.2-0.8	Anhedral, poikiloblastic
Mnz/ Zrn	tr.	<0.05	Anhedral, granular
Ap	<1	0.05-0.1	Euhedral, prismatic

Field of view: 2.3 mm across
Type of light: Polarised light

Thin section description: Fibrous minerals in the centre are fine-grained sillimanite needles forming clusters of fibrolite. Fibrolite formed in the samples after muscovite. No muscovite (Ms) is present near the cluster. All micas in the picture are biotite.

Field of view: 1.2 mm across
Type of light: Crossed polars

Thin section description: The mica in the centre-right is a partially resorbed muscovite crystal. Note the presence of fibrolite clusters in contact with it. Matrix comprises a mix of quartz, plagioclase, and local K-feldspar.

Sample description: Psammitic metasedimentary rock with abundant fibrolite clusters. The fibrolite clusters are 0.5-5 mm in diameter. The rock mainly has a granoblastic texture and grain size is heterogranular. Muscovite is rare and resorbed in the sample. K-feldspar and cordierite are present in minor amount. Cordierite is not as poikiloblastic and does not have an elliptic shape as in other samples that are Ms-bearing with no fibrolite. K-feldspar is the product of muscovite breakdown. Rare minute grains of garnet were identified. Garnet grains are granular to prismatic.

S378 **Transect 3** **Bt-Crd-Ms-Pl-Qtz**			UTM zone 18 7 606 451 m. N. 587 949 m. E.
Min.	**%**	**Size (mm)**	**Texture**
Qtz	35	0.05-0.25	Anhedral, granular
Bt	27	0.2-0.6	Euhedral, oriented
Ms	20	0.1-0.4	Euhedral, oriented
Crd	10	5-15	Anhedral, poikiloblastic
Pl	8	0.05-0.2	Anhedral, granular
Op	<1	<0.2	Anhedral
Ap	<1	0.02-0.1	Euhedral, prismatic
Mnz/ Zrn	tr.	<0.05	Anhedral, granular

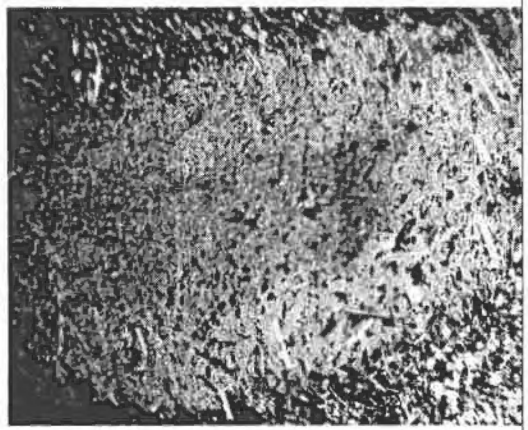

Field of view: 6 mm across
Type of light: Crossed polars

Thin section description: Large cordierite porphyroblast with inclusion trail in the outer rim slightly oblique to the external fabric (S1). The inclusions in the core are randomly oriented. The whole porphyroblast is retrograded to fine-grained white-micas

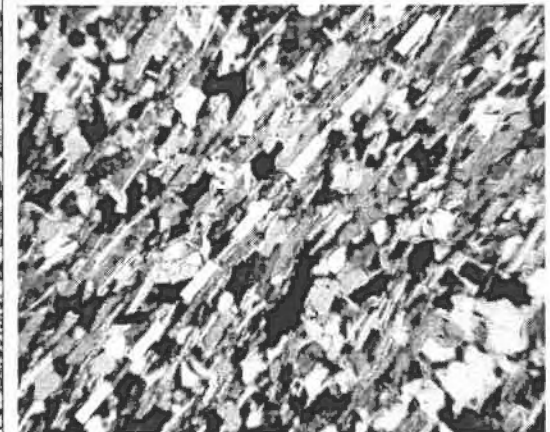

Field of view: 2 mm across
Type of light: Crossed polars

Thin section description: Pelitic horizons with a strongly developed S1 fabric. No evidence was found for an S2 fabric.

Sample description: Metasedimentary rock comprising psammitic and pelitic layers of thickness varying from 0.4-1.5 cm. Numerous cordierite porphyroblasts are present in the more pelitic layers. The S1 fabric wraps around the cordierite crystals. Biotite is locally chloritized, especially around the cordierite porphyroblasts. Muscovite is abundant and stable in this sample. No sillimanite was identified.

S383, Transect 4
Incipient migmatite
Bt-Crd-Grt-Kfs-Qtz-Sil

UTM zone 18
7 592 200 m. N.
580 651 m. E.

Min.	**%**	**Size (mm)**	**Texture**
Bt	25	0.5-2	Euhedral, locally resorbed
Kfs	25	0.5-4	Anhedral
Pl	20	0.5-4	Anhedral
Qtz	15	0.5-2	Anhedral
Crd	10	0.5-4	Anhedral
Grt	5	0.5-2	Anhedral, porphyroblastic
Ap	<1	<0.1	Euhedral, prismatic
Mnz/ Zrn	<1	<0.1	Anhedral, granular

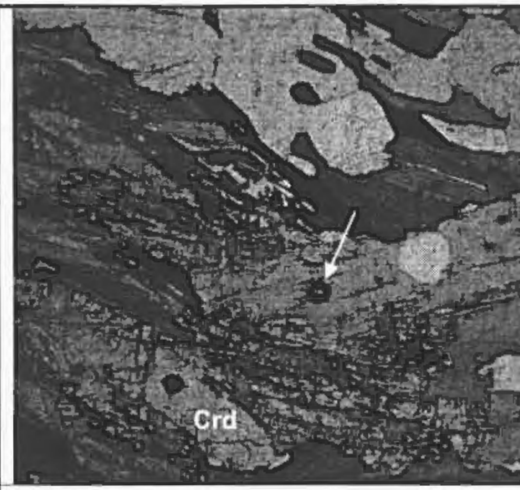

Field of view: 0.8 mm across
Type of light: Polarised light

Thin section description: Biotite and sillimanite partially consumed to form contiguous cordierite porphyroblast. In the centre (arrow), a monazite grain surrounded by a pleochroic halo is included in a biotite grain.

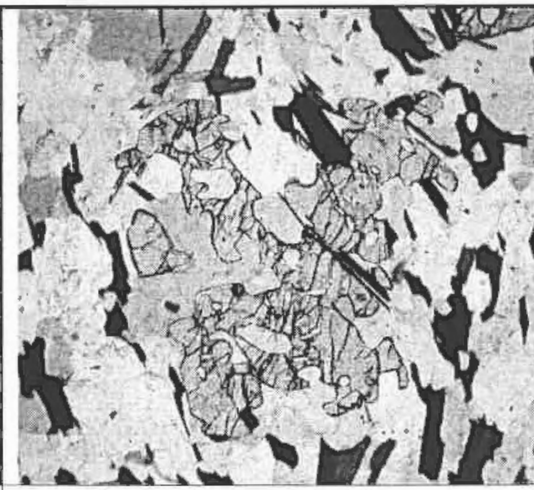

Field of view: 2.6 mm across
Type of light: Polarised light

Thin section description: Skeletal garnet porphyroblast in a quartz-plagioclase matrix. Some of the surrounding biotite is also partially consumed. Monazite inclusions were identified in the garnet.

Sample description: This sample is an incipient migmatite with probably less than 5% of melt extracted. Leucosome veinlets are rare and thin. Areas surrounding the leucosome show resorbed biotite with cordierite and K-feldspar. Coarsening of the matrix is observed close to leucosome veinlets. Most of the sample is a Bt-Grt-Kfs-Pl-Qtz-Sil-bearing rock with no evidence of partial melting. Monazite and zircon are larger in this sample, up to 0.1 mm in diameter. No muscovite is present. Garnet is partially resorbed. The rock has a predominant granoblastic texture.

S384, Transect 4
Migmatite
Bt-Crd-Grt-Kfs-Qtz-Sil

UTM zone 18
7 592 200 m. N.
580 651 m. E.

	Min.	**%**	**Size (mm)**	**Texture**
Leucosome (40%)	Kfs	40	0.5-4	Anhedral
	Pl	25	0.5-4	Anhedral
	Qtz	20	0.5-2	Anhedral
	Crd	15	0.5-3	Anhedral
Melanosome (60 %)	Bt	35	0.5-3	Euhedral, resorbed
	Kfs	20	0.5-2	Anhedral
	Crd	20	0.5-3	Anhedral, elliptic
	Sil	15	0.5-1.5	Euhedral, inclusions in Crd
	Pl	10	0.5-2	Anhedral
	Mnz/ Zrn	<1	0.5-0.15	Anhedral, granular

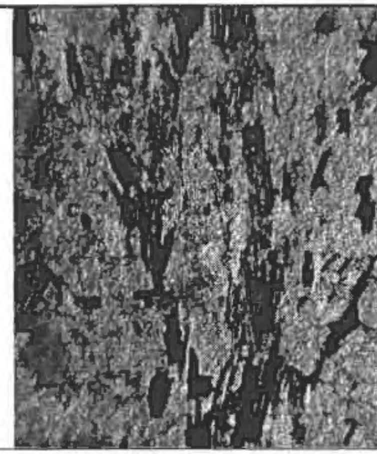

Field of view: 6 mm across
Type of light: Polarised light

Thin section description: The picture shows partially resorbed biotite crystals, in dark, the grey areas comprise essentially altered cordierite with minor amounts of K-feldspar and sillimanite.

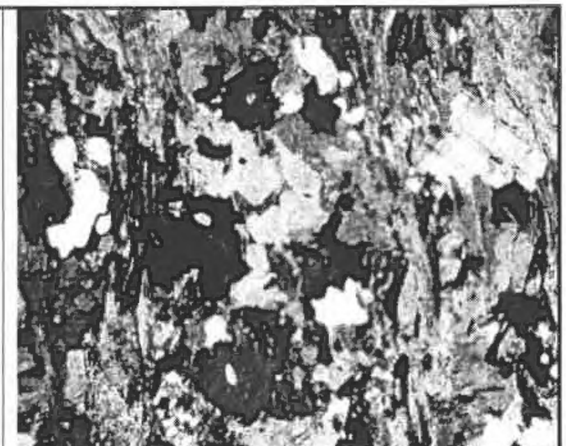

Field of view: 8 mm across
Type of light: Crossed polars

Thin section description: Partially resorbed biotite crystals with altered cordierite, sillimanite and K-feldspar.

Sample description: Stromatic migmatite with abundant leucosome, up to 40%. The sample shows a well-defined migmatitic layering. Schistosity (S1) and cleavage (S2) are not preserved. The sample is relatively altered. Cordierite is all retrograded to white micas and locally altered to pinnite. Cordierite commonly contains clusters of sillimanite. Accessory minerals, monazite and zircon, are larger and easier to identify. Monazite included in cordierite typically has a moat of altered cordierite surrounding it.

S388, Transect 4 **Migmatite** **Bt-Crd-Grt-Kfs-Qtz-Sil**				UTM zone 18 7 590 377 m. N. 580 658 m. E.
Min.		**%**	**Size (mm)**	**Texture**
Leucosome (40%)	Kfs	35	10-30	Anhedral
	Pl	35	10-30	Anhedral
	Qtz	25	5-20	Anhedral
	Grt	5	5-30	Anhedral, skeletal
Melanosome (60%)	Bt	30	2-8	Euhedral, resorbed
	Crd	25	5-15	Anhedral, elliptic
	Pl	25	5-15	Anhedral
	Sil	10	2-6	Euhedral
	Kfs	10	5-10	Anhedral

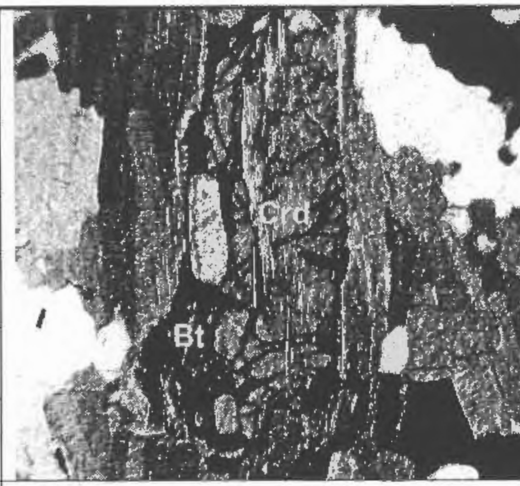

Field of view: 4.5 mm across
Type of light: Crossed polars

Thin section description: Fractured grey coarse crystal in the centre is a cordierite (Crd) grain and white fibres in the core are sillimanite inclusions. Surrounding minerals are biotite (Bt), plagioclase and K-feldspar. Matrix is coarse with irregular grain boundaries.

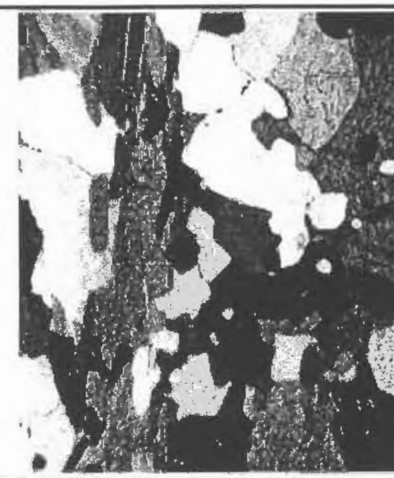

Field of view: 3.1 mm across
Type of light: Crossed polars

Thin section description: In the centre-left a thin vertical band of partially resorbed biotite forms the restitic material. On both sides are veinlets of granitic leucosome mainly composed of K-feldspar, plagioclase and quartz with local garnet and biotite schlieren.

Sample description: Stromatic migmatite with a well-defined migmatitic layering. Veins of leucosome vary from 0.2-2 cm in width. Cordierite is mainly restricted to the melanosome. Few skeletal garnet grains are located in the leucosome along with partially resorbed biotite crystals. Leucosome has a granitic composition and comprises mainly K-feldspar, plagioclase and quartz with local garnet and biotite schlieren. The leucosome is coarse-grained with a granoblastic texture.

S390, Transect 4
Migmatite

UTM zone 18
7 589 659 m. N.
580 646 m. E.

	Min.	%	Size (mm)	Texture
Leucosome (60%)	Kfs	50	10-30	Anhedral
	Pl	30	10-30	Anhedral
	Qtz	20	5-20	Anhedral
Melanosome (40%)	Bt	30	2-8	Euhedral, resorbed
	Crd	30	5-10	Anhedral, elliptic
	Pl	15	5-10	Anhedral
	Sil	10	2-6	Euhedral
	Kfs	10	5-10	Anhedral

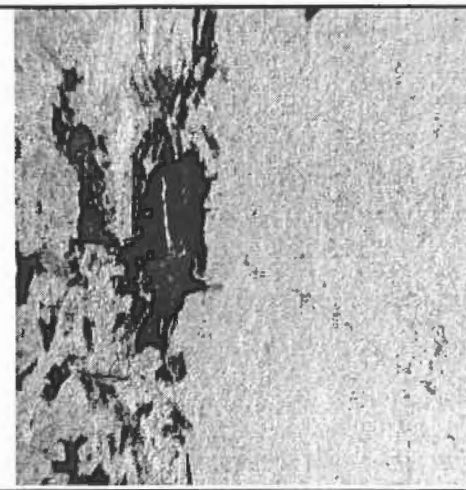

Field of view: 8 mm across
Type of light: Polarised light

Thin section description: In the left side is the melanosome bearing Bt+Crd +Kfs+Pl+Sil. The light area in the right side is the leucosome bearing Kfs+Pl+Qtz. Dark minerals are biotite crystals.

Field of view: 8 mm across
Type of light: Crossed polars

Thin section description: Picture is same as previous seen under crossed polars. Leucosome displays large grains with irregular grain boundary and a granoblastic texture.

Sample description: Stromatic migmatite with a well-defined migmatitic layering. Veins of leucosome vary from 0.2-3 cm in width. Cordierite is mainly restricted to the melanosome. Leucosome has a granitic composition and comprises mainly K-feldspar, plagioclase and quartz with few partially resorbed biotite crystals and thin biotite schlierens. The leucosome is coarse-grained with a granoblastic texture.

S392, Transect 4
Migmatite
Bt-Crd-Grt-Kfs-Qtz-Sil

UTM zone 18
7 588 997 m. N.
580 927 m. E.

	Min.	**%**	**Size (mm)**	**Texture**
Leucosome (60%)	Kfs	35	3-10	Anhedral
	Pl	35	3-10	Anhedral
	Qtz	25	3-8	Anhedral
	Grt	5	1-5	Anhedral, resorbed
Melanosome (40%)	Bt	25	1-4	Euhedral, resorbed
	Crd	25	2-4	Anhedral
	Sil	20	1-4	Euhedral
	Grt	15	1-5	Anhedral, resorbed
	Pl	15	2-4	Euhedral

Field of view: 3 mm across
Type of light: Polarised light

Thin section description: Irregular and elongated garnet (arrow) is located in a thin leucosome pocket. Darker minerals are resorbed biotite crystals with contiguous cordierite.

Field of view: 3 mm across
Type of light: Crossed polars

Thin section description: The picture is the same than on the left. Extinct minerals are garnets. Light-gray minerals are quartz and feldspars. Garnet has an irregular shape.

Sample description: Stromatic migmatite with a well-defined migmatitic layering. Veins of leucosome vary from 0.2-1 cm in width. Cordierite is mainly restricted to the melanosome and textures indicate it formed after biotite and sillimanite breakdown. Abundant skeletal garnets is located in both the leucosome and melanosome. Garnet crystals are elongated and have very irregular grain boundaries suggesting partial resorption. Leucosome has a granitic composition and comprises mainly K-feldspar, plagioclase and quartz with local garnets and biotite schlierens. The leucosome is coarse-grained with a granoblastic texture.

S394, Transect 4
Migmatite
Bt-Crd-Grt-Kfs-Sil-Qtz

UTM zone 18
7 581 032 m. N.
594 185 m. E.

	Min.	**%**	**Size (mm)**	**Texture**
Leucosome (60%)	Kfs	35	4-20	Anhedral
	Pl	30	4-20	Anhedral
	Qtz	20	4-12	Anhedral
	Grt	15	2-15	Anhedral, resorbed
Melanosome (40%)	Bt	45	5-10	Euhedral, resorbed
	Crd	20	4-12	Anhedral
	Pl	10	4-12	Anhedral
	Sil	25	2-6	Euhedral

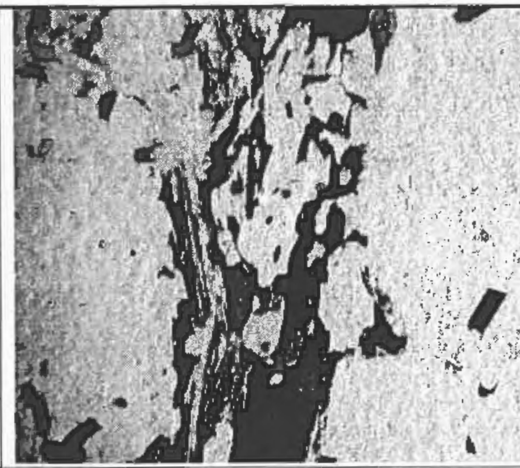

Field of view: 6 mm across
Type of light: Polarised light

Thin section description: In the centre, thin band of restitic material, mainly biotite, sillimanite and cordierite, with leucosome of granitic composition on both sides. Few biotite grains are isolated in the leucosome.

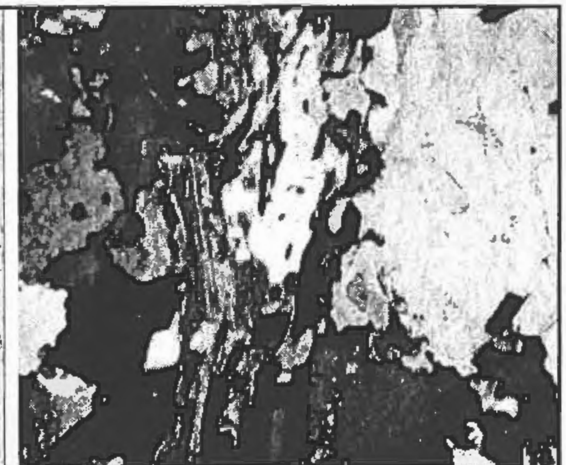

Field of view: 6 mm across
Type of light: Crossed polars

Thin section description: Same area as depicted in image to left, but under crossed polars. Leucosome is coarse-grained with very irregular grain boundaries between minerals.

Sample description: The sample is metatexite that presents a slightly undulating migmatitic layering. The structure of the rock is not disrupted. Leucosome is abundant and forms veins up to 2 cm in width. Melanosome is mostly composed of restitic material, biotite and sillimanite, as well as cordierite and local plagioclase. Leucosome is coarse-grained with irregular-shaped K-feldspar, plagioclase and quartz grains. Local embayed garnet and partially resorbed biotite porphyroblasts were identified in the leucosome.

S397, Transect 5
Syenogranite
Kfs-Pl-Qtz-Grt

UTM zone 18
7 580 302 m. N.
594 301 m. E.

	Min.	**%**	**Size (mm)**	**Texture**
Granite (80 %)	Kfs	40	2-10	Anhedral
	Pl	25	2-10	Anhedral
	Qtz	20	1-4	Anhedral
	Grt	5	2-10	Euh., prism./ anh., resorbed
Enclaves (20 %)	Bt	35	1-4	Euhedral, resorbed
	Crd	35	2-6	Anhedral, granular
	Sil	25	0.5-2	Euhedral
	Grt	5	1-6	Anhedral, resorbed, skeletal

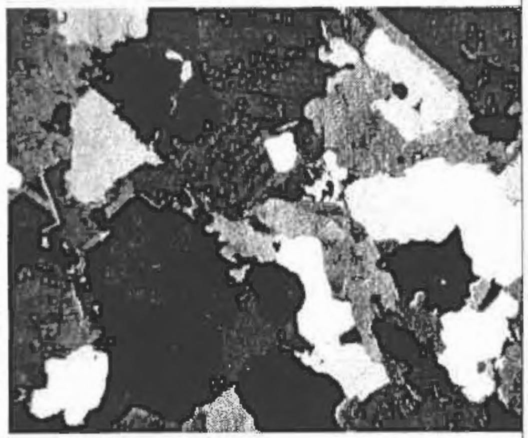

Field of view: 6 mm across
Type of light: Crossed polars

Thin section description: Massive coarse-grained syenogranite mainly composed of K-feldspar, plagioclase and quartz. Contact between crystals is very irregular.

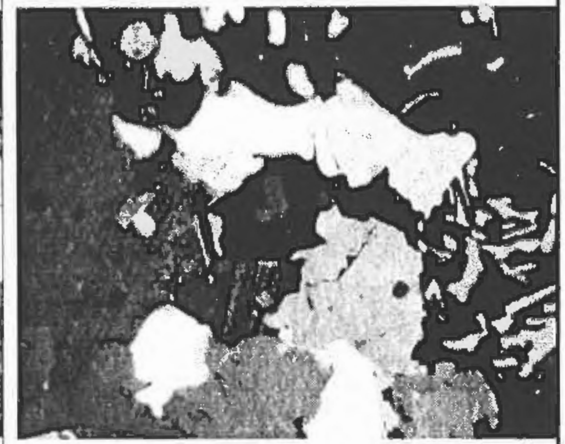

Field of view: 6 mm across
Type of light: Crossed polars

Thin section description: A large skeletal and resorbed garnet crystal is located on the right and top part of the picture. The garnet is extinct. Matrix comprises large irregular crystals of K-feldspar, plagioclase and quartz.

Sample description: Coarse-grained syenogranite with irregular compositional foliation defined by abundant biotite schlieren and metasedimentary enclaves. The metasedimentary enclaves comprise Bt-Crd-Grt-Sil and probably correspond to restitic material formed during partial melting. Both nice euhedral and skeletal garnet porphyroblasts are found in the sample. These suggest that the rock inherited garnet from the sample as well as crystallizing new garnet. The syenogranite minerals show no indication of deformation.

S399, Transect 5
Migmatite
Bt-Crd-Kfs-Pl-Qtz-Sil

UTM zone 18
7 580 302 m. N.
594 301 m. E.

	Min.	**%**	**Size (mm)**	**Texture**
Leucosome (60%)	Kfs	35	1-4	Anhedral
	Pl	35	1-4	Anhedral
	Qtz	25	0.5-2	Anhedral
Melanosome (40%)	Crd	25	0.5-2	Anhedral, elliptic crystals
	Bt	25	0.2-2	Euhedral, resorbed
	Sil	15	0.2-1	Euhedral, abundant inclusions in Crd
	Kfs	10	0.5-2	Anhedral
	Grt	5	0.4-2	Anhedral, resorbed

Field of view: 6 mm across
Type of light: Polarised light
Thin section description: Coarse leucosome of granitic composition on the right. Melanosome comprising sillimanite (shiny bright needles), biotite (brown crystals), cordierite, and K-feldspar are on the left.

Field of view: 2 mm across
Type of light: Polarised light
Thin section description: On the right; coarse leucosome of granitic composition. On the left, melanosome with a large cordierite located between the two dark masses of biotite. Cordierite is altered to pinnite. A monazite crystal surrounded by an alteration moat is located on the right edge of the cordierite.

Sample description: Stromatic migmatite with abundant leucosome horizons. Leucosome bands of thickness up to 2-3 cm. Leucosome typically composed of Kfs-Pl-Qtz. The melanosome comprises partially consumed biotite and sillimanite as well as K-feldspar and cordierite crystals formed at the expense of biotite and sillimanite. Migmatitic layering undulating but not disrupted. The leucosome locally contains biotite schlieren.

S401, Transect 5
Syenogranite
Kfs-Pl-Qtz-Grt

UTM zone 18
7 578 948 m. N.
593 261 m. E.

Min.	**%**	**Size (mm)**	**Texture**
Kfs	45	2-10	Anhedral
Pl	25	2-10	Anhedral
Qtz	20	1-4	Anhedral
Grt	10	2-10	Subhedral to euhedral, granular
Bt	5	1-4	Euhedral
Sil	1	0.5-2	Euhedral, aggregates
Mnz/ Zrn	<1	0.05-0.2	granular to euhedral
Op	<1	0.5-3	anhedral, granular
Ap	<1	0.5-2	Euhedral, prismatic

Field of view: 3 mm across
Type of light: Polarised light

Thin section description: Subhedral garnet grain located in the middle of a large K-feldspar crystal. Garnet is fresh and shows no resorption.

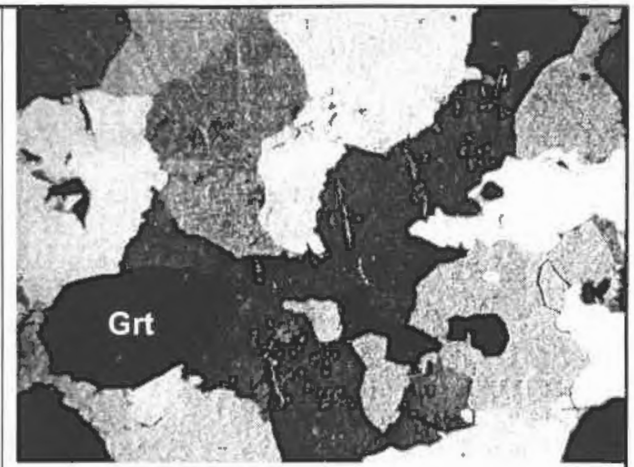

Field of view: 6 mm across
Type of light: Crossed polars

Thin section description: The extinct crystal on the left is a garnet. The picture highlights the granoblastic texture of the rock. The matrix minerals (quartz, plagioclase and K-feldspar) are coarse, 5-15 mm. Contact between grains is very irregular.

Sample description: The sample is a coarse and massive syenogranite bearing Bt-Crd-Grt. Elongated aggregates of Bt-Grt-Sil are locally observed and are interpreted to represent the remnants of highly assimilated metasedimentary enclaves. Aggregates are 10-30 cm long and 1-10 cm in width. Thin biotite schlieren were also observed on the outcrop. The granite has no foliation. Garnet is abundant in the granite and commonly displays a euhedral to anhedral habit suggesting that most of the garnet grains probably crystallised in the granite.

Appendix 5

Monazite grain descriptions

Grain	Picture	Trans.	Miner. parag.	Habit	Setting	Chemistry	Chem. zoning	Size (μm)	Area (sq. μm)	Comments	Age (Ma)	St. Dev. (Ma ± 2σ)	Map
S371-01		#1	bt-mu-qz±pl	skeletal, elong., irregular	in mu along bt boundary	Th~5.89% Y~0.67% U~0.01%	homo.	8 x 45	360	skeletal	-	-	-
S371-02	none	#1	bt-mu-qz±pl	subhedr., square-like, irregular border	elongated along S1	Th~6.67% Y~0.91% U~0.01%	homo.	15 x 30	450	-	-	-	-
S371-03	none	#1	bt-mu-qz±pl	....	....	Th~3.17% Y~0.83% U~0%	homo.	...	...	-	-	-	-
S371-05		#1	bt-mu-qz±pl	subhedr., prismatic	in bt cluster	Th~3.84% Y~0.78% U~0.03%	homo.	10 x 25	250	elongated along S1? (cleavage)	-	-	-
S371-06		#1	bt-mu-qz±pl	subhedr., prismatic, elong.	in bt, parallel to grain boundary	Th~6.88% Y~0.86% U~0%	homo.	8 x 15	120	parallel to S2 (cleavage)	1756	36	Yes
S371-07		#1	bt-mu-qz±pl	anhedral, granular, elliptical	in bt and mu cluster, elongated along S1	Th~4.81% Y~0.82% U~0.06%	homo.	12 x 23	276	paralle to S1 (schistosity)	-	-	-
S371-08	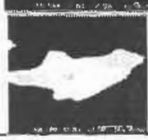	#1	bt-mu-qz±pl	anhedral, irregular shape,	....	Th~5.05% Y~0.87% U~0.08%	homo.	12 x 40	277	-	-	-	-

Grain	Picture	Trans.	Miner. parag.	Habit	Setting	Chemistry	Chem. zoning	Size (µm)	Area (sq. µm)	Comments	Age (Ma)	St. Dev. (Ma ± 2σ)	Map
S371-09	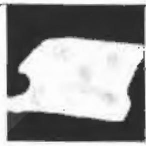	#1	bt-mu-qz±pl	subhedr., prismatic	in bt and mu cluster, elongated along S2	Th~4.91% Y~0.94% U~0.03%	homo.	12 x 40	278	-	1771	51	Yes
S371-10		#1	bt-mu-qz±pl	anhedral, irregular shape	along bt-mu-qz grain boundary	Th~4.62% Y~0.91% U~0.04%	homo.	22 x 38	836	-	-	-	-
S371-11		#1	bt-mu-qz±pl	anhedral, fractured, irregular shape	located within bt-mu cluster	Th~5.64% Y~0.94% U~0.04%	slightly zoned	18 x 35	630	fractured or possibly coalescent grains	-	-	-
S371-12		#1	bt-mu-qz±pl	subhedr., elong., prismatic	along bt-mu grain boundary, parallel to S1	Th~7.63% Y~0.89% U~0.09%	slightly zoned	10 x 22	220	-	-	-	-
S371-13	none	#1	bt-mu-qz±pl	....	....	Th~4.22% Y~0.57% U~0%	....	....	....	....	-	-	-
S371-14	none	#1	bt-mu-qz±pl	subhedr., prismatic	along bt-mu grain boundary, parallel to S1	Th~4.20% Y~0.80% U~0%	homo.	12 x 20	200	-	-	-	-

Grain	Picture	Trans.	Miner. parag.	Habit	Setting	Chemistry	Chem. zoning	Size (µm)	Area (sq. µm)	Comments	Age (Ma)	St. Dev. (Ma ± 2σ)	Map
S371-15	none	#1	bt-mu-qz±pl	subhedr., prismatic	along bt-mu grain boundary, parallel to S1	Th~5.49% Y~0.89% U~0%	homo.	10 x 25	250	-	-	-	-
S371-16	none	#1	bt-mu-qz±pl	subhedr., prismatic	along bt-mu grain boundary, parallel to S1	Th~2.57% Y~0.80% U~0%	homo.	15 x 25	375	-	-	-	-
S371-17	none	#1	bt-mu-qz±pl	subhedr., prismatic	along bt-mu grain boundary, parallel to S1	Th~1.91% Y~0.69% U~0%	homo.	20 x 25	500	-	-	-	-
S371-18		#1	bt-mu-qz±pl	anhedral, elong.	within matrix, bordered by mu-qz	n.a.	slightly zoned	7 x 35	245	elongated along S1	1840	56	Yes
S371-19		#1	bt-mu-qz±pl	subhedr., prismatic	along bt-mu grain boundary	Th~3.99% Y~0.87% U~0.23%	slightly zoned	13 x 19	247	2 sides straighter, 2 sides irregular	1756	47	Yes
S371-20		#1	bt-mu-qz±pl	anhedral, granular, oval	along bt-mu grain boundary, parallel to S1	Th~2.33% Y~0.73% U~0.12%	slightly zoned	10 x 20	200	fractured	1741	48	Yes

Grain	Picture	Trans.	Miner. parag.	Habit	Setting	Chemistry	Chem. zoning	Size (µm)	Area (sq. µm)	Comments	Age (Ma)	St. Dev. (Ma ± 2σ)	Map
S371-21	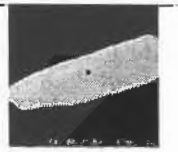	#1	bt-mu-qz±pl	euhedral, prismatic, elong.	along bt-mu grain boundary, parallel to S1	Th~2.99% Y~0.90% U~0.11%	slightly zoned	9 x 22	198	-	1815	63	Yes
S366-01		#2	bt-crd-mu-qz ±pl	granular, rounded	bordered by mu and bt	Th~4.0% Y~0.78% U~0.1%	homo.	16 x 18	227	-	-	-	No
S366-02		#2	bt-crd-mu-qz ±pl	subhedr., prism., elong.	bordered by bt and qz	Th~4.23% Y~0.93% U~0.28%	homo.	8 x 22	176	irregular grain boundary (resorbed?)	-	-	No
S366-03		#2	bt-crd-mu-qz ±pl	anhedral	bordered by bt and qz	Th~6.56% Y~0.92% U~0.03%	homo.	20 x 35	700	irregular grain boundary (resorbed?)	-	-	-
S366-04		#2	bt-crd-mu-qz ±pl	anhedral, elong., granular	within matrix with qz + pl	Th~7.65% Y~0.86% U~0.05%	homo.	12 x 30	360	-	-	-	-
S366-06		#2	bt-crd-mu-qz ±pl	anhedral, irregular	within micas cluster	Th~4.37% Y~0.96% U~0.01%	homo.	15 x 40	600	flat edges parallel to S2	-	-	-
S366-07		#2	bt-crd-mu-qz ±pl	subhedr., prism., granular	in mu cluster, bordered by qz	Th~3.67% Y~0.87% U~0.29%	slightly zoned	23 x 30	690	square-like, indented	1751	35	Yes
S366-08		#2	bt-crd-mu-qz ±pl	subhedr., granular, subprism.	along grain boundary, bordered by qz-bt	Th~5.36% Y~1.08% U~0.04%	homo.	10 x 20	200	fractured	-	-	-

Grain	Picture	Trans.	Miner. parag.	Habit	Setting	Chemistry	Chem. zoning	Size (µm)	Area (sq. µm)	Comments	Age (Ma)	St. Dev. (Ma ± 2σ)	Map
S366-09	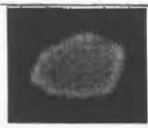	#2	bt-crd-mu-qz ±pl	granular, rounded	included in bt	Th~6.79% Y~0.87% U~0%	homo.	5 x 4	20	-	-	-	-
S366-10		#2	bt-crd-mu-qz ±pl	subhedr., granular, prism.	along grain boundary, bordered by qz-bt	Th~6.09% Y~0.97% U~0.02%	homo.	15 x 20	300	fractured	-	-	-
S366-11		#2	bt-crd-mu-qz ±pl	subhedr., elong., prism.	along bt grain boundary, bordered by qz-bt	Th~5.25% Y~0.94% U~0.03%	homo.	20 x 50	1000	-	-	-	-
S366-12	none	#2	bt-crd-mu-qz ±pl	subhedr., granular, subprism.	bordered by bt and qz	Th~5.16% Y~0.97% U~0.02%	homo.	15 x 20	300	irregular grain boundary	-	-	-
S366-13	none	#2	bt-crd-mu-qz ±pl	subhedr., granular, subprism.	bordered by bt and qz	Th~4.95% Y~0.97% U~0%	homo.	10 x 20	200	-	-	-	-
S366-14	none	#2	bt-crd-mu-qz ±pl	....	....	totals too low	....	....	....	-	-	-	-
S366-15		#2	bt-crd-mu-qz ±pl	subhedr., prismatic	bordered by bt and matrix of qz + pl	Th~3.91% Y~0.93% U~0.08%	slightly zoned	24 x 30	720	-	1791	33	Yes
S366-16		#2	bt-crd-mu-qz ±pl	granular, rounded	within bt, in contact with qz matrix	Th~3.25% Y~0.92% U~0.18%	slightly zoned	25 x 30	750	irregular boundary related to cracks in bt	1853	39	Yes

Grain	Picture	Trans.	Miner. parag.	Habit	Setting	Chemistry	Chem. zoning	Size (μm)	Area (sq. μm)	Comments	Age (Ma)	St. Dev. (Ma ± 2σ)	Map
S366 map1		#2	bt-crd-mu-qz ±pl	subhedr., prismatic	bordered by bt-qz	totals too low	slightly zoned	15 x 25	375	parallel to S1	1878	25	Yes
S366 map2		#2	bt-crd-mu-qz ±pl	subhedr., prismatic	bordered by bt-qz	totals too low	slightly zoned	20 x 45	900	parallel to S1	1823	37	Yes
S367-01		#2	bt-crd-mu-qz ±pl	anhedral, granular, elliptical	interstitial within qz + kfs matrix	Th~3.02% Y~1.11% U~0.23%	homo.	5 x 15	75	-	-	-	-
S367-02		#2	bt-crd-mu-qz ±pl	subhedr., prismatic	interstitial, in matrix, between 2 bt grains and qz	Th~4.14% Y~1.23% U~0.29%	homo.	10 x 20	200	-	-	-	-
S367-03		#2	bt-crd-mu-qz ±pl	anhedral, granular, rounded	along bt and qz grain boundary	Th~4.61% Y~1.27% U~0.25%	homo.	12 x 15	180	-	-	-	-
S367-04	none	#2	bt-crd-mu-qz ±pl	anhedral, granular, irregular	interstitial, in matrix qz grains	Th~2.99% Y~1.15% U~0.27%	homo.	10 x 20	200	-	-	-	-
S367-05		#2	bt-crd-mu-qz ±pl	subhedr., prismatic	in matrix, bordered by qz-kfs-ap	Th~4.28% Y~1.25% U~0.36%	homo.	12 x 18	216	in contact with euhedral, stable, prismatic ap	-	-	-
S367-06		#2	bt-crd-mu-qz ±pl	euhedral, prismatic	within matrix bordered by qz	Th~4.17% Y~1.21% U~0.29%	homo.	9 x 14	126	-	-	-	-

Grain	Picture	Trans.	Miner. parag.	Habit	Setting	Chemistry	Chem. zoning	Size (μm)	Area (sq. μm)	Comments	Age (Ma)	St. Dev. (Ma ± 2σ)	Map
S367-07	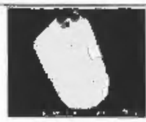	#2	bt-crd-mu-qz ±pl	subhedr., prismatic	....	totals too low	homo.	10 x 15	150	-	-	-	-
S367-08		#2	bt-crd-mu-qz ±pl	euhedral, prismatic	within matrix bordered by qz	Th~4.05% Y~1.21% U~0.44%	homo.	12 x 15	180	stable subeuhedral crystals (3) of ap in proximity (within less than 70 um radius)	-	-	-
S367-09	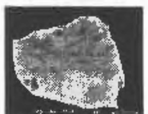	#2	bt-crd-mu-qz ±pl	anhedral, granular, subprism.	within matrix bordered by qz	Th~2.37% Y~1.04% U~0.18%	homo.	14 x 18	252	grain boundary relatively irregular	-	-	-
S367-10		#2	bt-crd-mu-qz ±pl	subhedr., subprism.	along bt grain boundary, bordered by qz-bt	Th~2.78% Y~1.19% U~0.31%	homo.	12 x 18	216	irregular grain boundary (resorbed?)	1805	26	No
S367-11	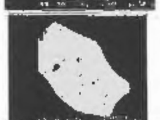	#2	bt-crd-mu-qz ±pl	subhedr., prismatic	....	n.a.	homo.	22 x 37	814	-	-		
S367 map1		#2	bt-crd-mu-qz ±pl	anhedral, granular, rounded	within matrix, bordered by mu-qz	totals too low	slightly zoned	12 x 22	264	1 side of the grain in contact with bt is irregular (resorbed)	1775	32	Yes
S373-01		#3	bt-crd-mu-qz ±pl	anhedral, granular, elliptical	within a qz inclusion in crd	Th~3.52% Y~1.18% U~0.36%	homo.	13 x 39	507	-	1818	26	No
S373-02		#3	bt-crd-mu-qz ±pl	anhedral, granular, elliptical	in matrix, along qz-kfs grain boundary	Th~4.62% Y~1.58% U~0.70%	homo.	10 x 25	250	-	1805	15	Yes

Grain	Picture	Trans.	Miner. parag.	Habit	Setting	Chemistry	Chem. zoning	Size (µm)	Area (sq. µm)	Comments	Age (Ma)	St. Dev. (Ma ± 2σ)	Map
S373-03		#3	bt-crd-mu-qz ±pl	subhedr.	in matrix, along qz-kfs-mu grain boundary	Th~3.12% Y~0.95% U~0.24%	homo.	19 x 37	703	kfs in contact with mnz are slightly altered	1795	23	Yes
S373-04		#3	bt-crd-mu-qz ±pl	anhedral, granular, elliptical	in matrix, along qz–kfs-mu grain boundary	Th~4.67% Y~1.18% U~0.22%	slightly zoned	17 x 30	510	kfs and mu in contact with mnz are slightly altered	1777	23	Yes
S373-05		#3	bt-crd-mu-qz ±pl	subhedr., prismatic, straight edges	in matrix, along bt-qz grain boundary	Th~4.70% Y~1.43% U~0.45%	slightly zoned	20 x 28	560		1792	24	Yes
S374-01		#3	bt-crd-mu-qz-sil±plag	anhedral, irregular	within fibrolite cluster	Th~3.38% Y~1.25% U~0.41%	slightly zoned	30 x 45	1350	very irregular boundary (resorption or interstitial growth?)	1844	20	Yes
S374-02	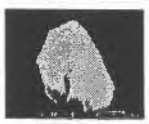	#3	bt-crd-mu-qz-sil±plag	subhedr., prismatic	interstitial, within matrix, bordered by qz-mu	Th~4.16% Y~1.24% U~0.33%	slightly zoned	21 x 26	546	1 side has irregular boundary (resorption or interstitial growth?)	1847	28	Yes
S374-03		#3	bt-crd-mu-qz-sil±plag	anhedral, granular, oval	included in crd	Th~4.62% Y~1.14% U~0.20%	slightly zoned	23 x 32	736	grain boundary locally irregular with embayments	1875	31	Yes
S374-04	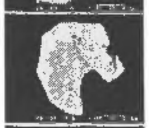	#3	bt-crd-mu-qz-sil±plag	subhedr., granular, "kidney-shaped"	interstitial, within matrix	Th~4.23% Y~1.17% U~0.28%	slightly zoned	22 x 41	902	2 large embayments, slightly cracked	1818	39	Yes
S374-05	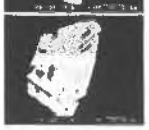	#3	bt-crd-mu-qz-sil±plag	anhedral, prismatic, irregular boundary	within mu cluster	Th~4.54% Y~1.53% U~0.63%	moder. zoning	31 x 38	1178	irregular boundary, elongated, linear inclusions, embayments	1836	18	Yes

Grain	Picture	Trans.	Miner. parag.	Habit	Setting	Chemistry	Chem. zoning	Size (µm)	Area (sq. µm)	Comments	Age (Ma)	St. Dev. (Ma ± 2σ)	Map
S374-06		#3	bt-crd-mu-qz-sil±plag	granular, square-like	bordered by crd-qz	Th~4.09% Y~1.15% U~0.21%	....	28 x 35	980	-	-	-	-
S375-01		#3	bt-crd-mu-qz-sil±plag	subhedr., prismatic	included in bt	Th~6.30% Y~1.15% U~0.83%	....	19 x 26	494	-	-	-	-
S375-02		#3	bt-crd-mu-qz-sil±plag	subhedr., prismatic	within qz + kfs matrix	Th~2.08% Y~0.88% U~0.38%	distinct zoning	17 x 29	493	embayments	-	-	-
S375-03		#3	bt-crd-mu-qz-sil±plag	anhedral	interstitial, bordered by bt-qz	Th~3.64% Y~0.86% U~0.31%	strongly zoned	26 x 56	1456	irregurlar border	-	-	-
S375-04		#3	bt-crd-mu-qz-sil±plag	anhedral, granular, irregular shape	in matrix, bordered by qz-kfs	Th~0.36% Y~0.67% U~0.25%	slightly zoned	46 x 50	2300	**anomalous Th values!!!**	-	-	-
S375-06		#3	bt-crd-mu-qz-sil±plag	anhedral, granular, rounded	along bt-qz grain boundary	Th~6.38% Y~1.14% U~0.89%	....	20 x 27	540	may be a composite grain.....	-	-	-
S375-07		#3	bt-crd-mu-qz-sil±plag	anhedral, granular, rounded	in matrix, interstitial, bordered by qz-kfs	Th~5.44% Y~0.85% U~0.27%	....	9 x 11	99	irregular boundary, embayments	-	-	-
S375-08		#3	bt-crd-mu-qz-sil±plag	subhedr., granular, square-like	in matrix, interstitial, bordered by qz-kfs	Th~6.91% Y~1.09% U~0.74%	....	15 x 17	255	embayment	-	-	-

Grain	Picture	Trans.	Miner. parag.	Habit	Setting	Chemistry	Chem. zoning	Size (μm)	Area (sq. μm)	Comments	Age (Ma)	St. Dev. (Ma ± 2σ)	Map
S375-09		#3	bt-crd-mu-qz-sil±plag	subhedr., prismatic, granular	in matrix, interstitial, bordered by kfs	Th~5.14% Y~0.99% U~0.65%	homo.	13 x 24	312	-	-	-	-
S375-10		#3	bt-crd-mu-qz-sil±plag	anhedral, elliptical, granular	in matrix, bordered by bt-kfs-qz	Th~5.07% Y~0.90% U~0.23%	homo.	15 x 22	330	irregular boundary, minor embayments	-	-	-
S375-11		#3	bt-crd-mu-qz-sil±plag	subhedr., prismatic, granular	....	Th~3.43% Y~0.07% U~0.46%	slightly zoned	18 x 37	666	-	1836	24	Yes
S375-12	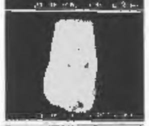	#3	bt-crd-mu-qz-sil±plag	subhedr., prismatic,	within matrix, included in kfs	Th~2.58% Y~0.07% U~0.24%	slightly zoned	18 x 40	720	-	1908	29	Yes
S375-13	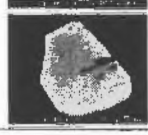	#3	bt-crd-mu-qz-sil±plag	anhedral, square-like	included in bt	Th~4.48% Y~0.10% U~0.59%	slightly zoned	15 x 18	270	-	-	-	-
S378-01		#3	bt-mu-qz-sil±plag	subhedr., prismatic	in the matrix	Th~7.68% Y~1.21% U~0.14%	...	12 x 21	252	-	-	-	-
S378-02		#3	bt-mu-qz-sil±plag	anhedral, granular, "drop-shaped"	along grain boundary of crd-qz-kfs	Th~8.36% Y~0.96% U~0.04%	...	15 x 18	270	-	-	-	-
S378-03		#3	bt-mu-qz-sil±plag	anhedral, elong., narrow	included in crd	Th~5.96% Y~1.17% U~0.09%	...	9 x 63	504	-	-	-	-

Grain	Picture	Trans.	Miner. parag.	Habit	Setting	Chemistry	Chem. zoning	Size (μm)	Area (sq. μm)	Comments	Age (Ma)	St. Dev. (Ma ± 2σ)	Map
S378-04	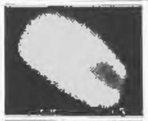	#3	bt-mu-qz-sil±plag	anhedral, granular, rounded	....	Th~6.29% Y~0.80% U~0.01%	...	15 x 24	360	a major embayment on one side	-	-	-
S378-05		#3	bt-mu-qz-sil±plag	anhedral, skeletal	included in crd, in the core area	Th~5.30% Y~0.91% U~0.01%	..	12 x 40	480	irregular boundary, major embayments	-	-	-
S378-06	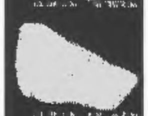	#3	bt-mu-qz-sil±plag	subhedr., prismatic	in matrix, bordered by qz-kfs	Th~4.76% Y~0.91% U~0.0%	homo.	18 x 32	576	...	1764	27	No
S378-07		#3	bt-mu-qz-sil±plag	anhedral, "drop-shaped"	....	Th~3.83% Y~0.89% U~0.01%	...	22 x 38	836	irregular contour	1887	69	No
S378-08	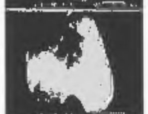	#3	bt-mu-qz-sil±plag	anhedral, irregular, embay-ments	along bt-mu cluster, bordered by qz-kfs	Th~6.66% Y~1.15% U~0.15%	distinct zoning	15 x 27	405	irregular contour, major embayments, resorption....	-	-	-
S383-01		#4	bt-grt-sil-kfs	anhedral, granular, rounded	core; loca-ted in KFS xtal	Th~8.03% Y~1.55% U~0.30%	distinct zoning	25 x 38	950	high Th core, euhedral shape	1808	21	Yes
S383-02		#4	bt-grt-sil-kfs	subhedr., prismatic	rim	Th~7.82% Y~2.40% U~0.92%	distinct zoning	25 x 38	950	granular, rounded rim	1793	16	Yes
S383-03		#4	bt-grt-sil-kfs	subhedr., elong., prismatic	included in grt	Th~4.14% Y~1.47% U~0.28%	homo.	12 x 58	696	-	1835	17	Yes
		#4	bt-grt-sil-kfs	subhedr., elong., prismatic	included in grt	Th~4.87% Y~1.63% U~0.44%	homo.	12 x 22	264	-	-	-	-

Grain	Picture	Trans.	Miner. parag.	Habit	Setting	Chemistry	Chem. zoning	Size (µm)	Area (sq. µm)	Comments	Age (Ma)	St. Dev. (Ma ± 2σ)	Map
S383-04	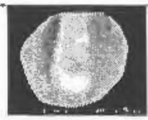	#4	bt-grt-sil-kfs	anhedral, granular, rounded	included in kfs, alteration halo	Th~6.99% Y~2.09% U~0.87%	moder. zoning	11 x 21	231	-	-	-	-
S383-05		#4	bt-grt-sil-kfs	anhedral, granular, rounded	included in kfs, alteration halo	Th~7.24% Y~2.04% U~0.77%	moder. zoning	28 x 44	1232	-	-	-	-
S383-06		#4	bt-grt-sil-kfs	anhedral, granular, rounded	included in bt	Th~6.33% Y~1.89% U~0.64%	slightly zoned	23 x 31	713	-	-	-	-
S383-07		#4	bt-grt-sil-kfs	subhedr., elong., prismatic	included in bt, parallel to cleavage	Th~7.14% Y~1.88% U~0.61%	distinct zoning	22 x 40	880	-	1822	9	Yes
S383-08		#4	bt-grt-sil-kfs	subhedr., prismatic	included in kfs, bt on one side	Th~6.95% Y~1.80% U~0.52%	slightly zoned	13 x 28	364	-	-	-	-
S383-09	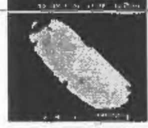	#4	bt-grt-sil-kfs	anhedral, elong., granular, elliptical	....	Th~6.18% Y~1.96% U~0.81%	homo.	15 x 38	570	minor embayments	-	-	-
S384-01		#4	bt-grt-sil-kfs	anhedral, embayed	interstitial, within kfs + qz matrix	Th~4.64% Y~2.43% U~0.23%	....	25 x 40	1000	very irregular boundary (interstitial growth?)	-	-	-
S384-02		#4	bt-grt-sil-kfs	anhedral, granular, rounded	partly included in bt	totals too low	....	25 x 30	750	-	-	-	-
S384-03		#4	bt-grt-sil-kfs	anhedral, embayed	within a sil cluster	totals too low	....	22 x 45	990	very irregular boundary (interstitial growth?)	-	-	-

Grain	Picture	Trans.	Miner. parag.	Habit	Setting	Chemistry	Chem. zoning	Size (μm)	Area (sq. μm)	Comments	Age (Ma)	St. Dev. (Ma ± 2σ)	Map
S384-04		#4	bt-grt-sil-kfs	anhedral, embayed	partly included in bt	totals too low	....	14 x 28	392	very irregular boundary, numerous embayments (resorption or interstitial growth?)	-	-	-
S384-05		#4	bt-grt-sil-kfs	anhedral, granular, subprism.	included in bt, and bordered by sil	Th~4.35% Y~2.57% U~0.24%	....	18 x 22	396	fractured, embayed by growth of a sil grain	-	-	-
S384-06	none	#4	bt-grt-sil-kfs	....	....	Th~4.65% Y~0.90% U~0.06%	....	....	....	....	-	-	-
S388-01		#4	bt-grt-sil-kfs	anhedral, granular, oval	included in grt	Th~4.9% Y~1.18% U~0.99%	outer rim	26 x 45	1170	rounded grain included in grt and with three distinct chemical zones	1800	9	Yes
S388-01		#4	bt-grt-sil-kfs	anhedral, granular, oval	included in grt	Th~5.66% Y~2.55% U~2.45%	inner rim	26 x 45	1170	rounded grain inlcuded in grt and with three distinct chemical zones	1847	7	Yes
						Th~2.30% Y~0.93% U~0.27%	core				1853	11	
S388-02		#4	bt-grt-sil-kfs	anhedral, granular, oval	included in grt	Th~4.65 Y~0.90% U~0.06%	distinct zoning	50 x 115	5750	complex zoning	1791	11	Yes
S388-03	none	#4	bt-grt-sil-kfs	....	included in grt	Th~3.77% Y~1.37% U~0.66%	....	....	....	....	-	-	-
S388-04	none	#4	bt-grt-sil-kfs	....	included in crd	Th~4.92% Y~1.65% U~0.51%	....	....	....	....	-	-	-

Grain	Picture	Trans.	Miner. parag.	Habit	Setting	Chemistry	Chem. zoning	Size (μm)	Area (sq. μm)	Comments	Age (Ma)	St. Dev. (Ma ± 2σ)	Map
S388-05	none	#4	bt-grt-sil-kfs	....	in sil-crd	Th~4.92% Y~2.23% U~0.63%	....	....	....	....	-	-	-
S388-06	none	#4	bt-grt-sil-kfs	....	in kfs-qz matrix	Th~5.18% Y~2.72% U~0.79%	....	....	....	....	-	-	-
S388-07	none	#4	bt-grt-sil-kfs	....	in kfs-qz matrix	Th~4.69% Y~2.34% U~0.64%	....	....	....	....	-	-	-
S388-08	none	#4	bt-grt-sil-kfs	....	included in bt	Th~4.77% Y~2.29% U~0.81%	....	....	....	....	-	-	-
S388-09	none	#4	bt-grt-sil-kfs	....	included in crd	Th~5.40% Y~1.90% U~0.88%	....	....	....	....	-	-	-
S388-10	none	#4	bt-grt-sil-kfs	....	included in bt	Th~5.46% Y~2.37% U~0.69%	....	....	....	....	-	-	-
S388-11	none	#4	bt-grt-sil-kfs	....	included in bt	Th~4.42% Y~1.15% U~0.48%	....	....	....	....	-	-	-
S388-13	none	#4	bt-grt-sil-kfs	....	in kfs-qz matrix	Th~4.07% Y~2.29% U~1.05%	....	....	....	....	-	-	-
S388-14	none	#4	bt-grt-sil-kfs	....	included in bt	totals too low	....	....	....	....	-	-	-
S388-16	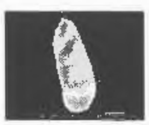	#4	bt-grt-sil-kfs	subhedral, prism., elong.	included in bt	totals too low	distinct zoning	17 x 45	765	elongated along bt cleavage, circular zoning (core + rim)	1768	14	Yes

Grain	Picture	Trans.	Miner. parag.	Habit	Setting	Chemistry	Chem. zoning	Size (µm)	Area (sq. µm)	Comments	Age (Ma)	St. Dev. (Ma ± 2σ)	Map
S390-01	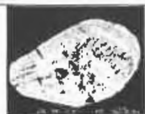	#4	crd-grt-kfs	anhedral, granular, oval	in matrix, along qz-kfs grain boundary	Th~7.37% Y~2.30% U~0.40%	distinct zoning	70 x 105	7350	grain located between qz and kfs, complex zoning, numerous, inclusions and fractures	-	-	-
S390-02		#4	crd-grt-kfs	anhedral, subprism., granular	in matrix, within kfs, bordered partly by qz	Th~6.61% Y~2.76% U~0.45%	slightly zoned	133 x 144	19 152	located on the margin of a kfs grain, fracture, few inclusions, zoned of break-down…?	-	-	-
S390-03		#4	crd-grt-kfs	anhedral, granular	included in bt	Th~7.51% Y~2.98% U~0.47%	slightly zoned	25 x 33	825	included in bt, slightly fractured, locally irregular grain boundary	-	-	-
S390-04		#4	crd-grt-kfs	anhedral, granular	in matrix, included in qz	Th~6.10% Y~2.28% U~0.26%	slightly zoned	26 x 32	832	included in qz, zoning pattern might reflect partial fracturing	-	-	-
S390-05		#4	crd-grt-kfs	anhedral, granular, subprism.	included in kfs	Th~5.98% Y~2.36% U~0.33%	distinct zoning	36 x 48	1728	zoning not circular, but still show core and rim	1724	9	No
S390-06		#4	crd-grt-kfs	anhedral, rounded, fractured	along bt and matrix boundary	Th~5.38% Y~2.07% U~0.21%	distinct zoning	44 x 48	1064	shape suggests interstitial base…	-	-	-
S390-07		#4	crd-grt-kfs	subhedral, prismatic	included in bt	Th~4.16% Y~1.45% U~0.08%	distinct zoning	16 x 30	480	large fracture, core-to-rim zoning, parallel to bt cleavage	-	-	-
S390-08		#4	crd-grt-kfs	subhedral, elong.	included in crd	totals too low	homo.	10 x 50	500	moat of altered crd around the mnz grain	-	-	-
S390-09	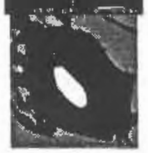	#4	crd-grt-kfs	subhedr., prism., elong.	included in crd	Th~5.29% Y~2.17% U~0.19%	….	20 x 45	900	moat of altered crd around the mnz grain	-	-	-

Grain	Picture	Trans.	Miner. parag.	Habit	Setting	Chemistry	Chem. zoning	Size (μm)	Area (sq. μm)	Comments	Age (Ma)	St. Dev. (Ma ± 2σ)	Map
S390-10	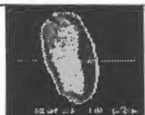	#4	crd-grt-kfs	anhedral, subprism., granular	included in crd	Th~5.11% Y~1.03% U~0.04%	distinct zoning	10 x 18	180	moat of altered crd around the mnz grain	-	-	-
S390-11		#4	crd-grt-kfs	anhedral, rounded, granular	matrix	Th~4.43% Y~3.28% U~0.23%	homo.	35 x 35	1225	-	-	-	-
S390-12	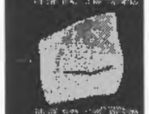	#4	crd-grt-kfs	subhedral, prism.	included in bt	none	homo.	25 x 31	775	-	-	-	-
S390-13	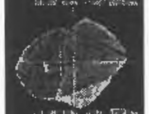	#4	crd-grt-kfs	subhedr., prism., fractured	partly included in bt and kfs	none	homo.	55 x 60	3300	-	-	-	-
S390-15		#4	crd-grt-kfs	subhedr., prism.,	included in crd	Th~3.61% Y~2.12% U~0.55%	homo.	29 x 63	1827	moat of altered crd around the mnz grain (chem. calc. with trace analysis results)	1895	18	No
S390-16		#4	crd-grt-kfs	subhedr., prism.	included in bt	Th~3.06% Y~2.17% U~0.34%	homo	20 x 40	800	mnz grain parallel to bt cleavage	1971	23	No
S390-17		#4	crd-grt-kfs	anhedral, granular, subprism.	matrix	none	distinct zoning	100 x 140	14 000	grain with abundant cracks and inclusions, complex zoning pattern	-	-	-
S390-18		#4	crd-grt-kfs	anhedral, granular, rounded	in qz matrix bordered by bt	Th~3.79% Y~1.72% U~0.49%	distinct zoning	39 x 44	1716	irregular boundary, in contact with unstable bt (resorbed), minor embayments, circular inclusion	1914	27	No
S390-20		#4	crd-grt-kfs	anhedral, granular, rounded	matrix	totals too low	slightly zoned	43 x 62	2666	-	-	-	-

Grain	Picture	Trans.	Miner. parag.	Habit	Setting	Chemistry	Chem. zoning	Size (μm)	Area (sq. μm)	Comments	Age (Ma)	St. Dev. (Ma ± 2σ)	Map
S392-01		#4	crd-grt-kfs	subhedr., prism.	in biotite	Th~5.65% Y~1.62% U~0.06%	distinct zoning	36 x 57	2052	core-to-rim zoning, with multiple subdomains	1831	24	No
S392-02	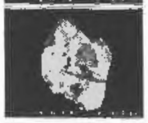	#4	crd-grt-kfs	subhedr., subprism.	included in bt	Th~5.71% Y~1.11% U~0%	distinct zoning	100 x 100	10 000	core-to-rim zoning, with multiple subdomains	-	-	Yes
S392-03		#4	crd-grt-kfs	anhedral, granular, elong.	matrix	Th~6.47% Y~1.28% U~0.05%	slightly zoned	28 x 61	1708	transversal fracture, single round inclusion	-	-	-
S392-04		#4	crd-grt-kfs	anhedral, irregular	along bt and matrix grain boundary	Th~6.19% Y~1.32% U~0.01%	distinct zoning	41 x 50	2050	one straight side, irregular boundary for remaining sides, moderately fractured	-	-	-
S392-05		#4	crd-grt-kfs	subhedral, prism., granular	partly included in bt and qz matrix	Th~5.98% Y~1.54% U~0.18%	distinct zoning	48 x 50	2400	rim-to-core zoning, euhedral zoning pattern	1913	26	No
S392-06		#4	crd-grt-kfs	anhedral, granular, rounded	matrix	Th~3.53% Y~1.38% U~0.67%	core rim	33 x 42	1386	rim-to-core zoning (chem. calc. with trace analysis results)	1885 1822	34 33	Yes
S392-07		#4	crd-grt-kfs	subhedr., granular, oval	....	Th~3.36% Y~1.17% U~0.48%	distinct zoning	26 x 36	936	-	-	-	-
S392-08		#4	crd-grt-kfs	subhedr., subprism.	matrix and grt boundary	Th~6.05% Y~1.73% U~0.52%	distinct zoning	31 x 34	1054	sharp narrow embayment (sil needle), core-to-rim zoning, line profile obtained	-	-	-
S392-09	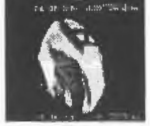	#4	crd-grt-kfs	anhedral, granular, rounded	....	Th~5.65% Y~1.06% U~0.57%	distinct zoning	32 x 39	1248	core-to-rim zoning, moderate fracturation, grain boundary locally irregular	-	-	-

Grain	Picture	Trans.	Miner. parag.	Habit	Setting	Chemistry	Chem. zoning	Size (µm)	Area (sq. µm)	Comments	Age (Ma)	St. Dev. (Ma ± 2σ)	Map
S392-17	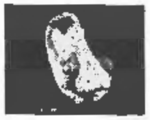	#4	crd-grt-kfs	anhedral, granular	....	Th~3.92% Y~0.34% U~0.47% Th~3.20% Y~1.25% U~0.56%	zone 1 zone 2	83 x 150	12 450	complex zoning pattern	1848	12	No
S392 map5		#4	crd-grt-kfs	anhedral, granular	included in grt	totals too low	light zoning	22 x 34	748	light zoning, irregular boundary (analysis redone in Nov. 2003)	1855	29	Yes
S394-18		#5	crd-grt-kfs	euhedral, prism.	matrix	Th~7.27% Y~1.77% U~1.28%	distinct zoning	46 x 67	3082	core-to-rim zoning pattern, moderately cracks and few inclusions	-	-	-
S396-26		#5	crd-grt-kfs	anhedral, granular	included in grt	Th~7.45% Y~2.08% U~1.44%	homo. to light zoning	46 x 117	5382	weak zoning, peanut-shaped, moat	-	-	-
S397-01		#5	crd-grt-kfs	euhedral, prism.	inluded in grt	Th~5.37% Y~1.85% U~1.50% Th~5.87% Y~1.46% U~0.99%	core rim	37 x 68	2516	nice euhedral grain with straight boundaries, core-to-rim zoning pattern (chem. calc. with trace analysis results)	1838 1827	6 15	Yes
S397-02		#5	crd-grt-kfs	anhedral, granular, subround.	in matrix, bordered by qz-bt	Th~7.29% Y~1.40% U~0.92%	light zoning	36 x 39	1404	light zoning, undefined pattern	1858	11	Yes
S397-03		#5	crd-grt-kfs	anhedral, triangular, elong.	included in bt	Th~ 6.70% Y~2.26% U~1.14%	distinct zoning	45 x 140	6300	complex zoning	-	-	-

Grain	Picture	Trans.	Miner. parag.	Habit	Setting	Chemistry	Chem. zoning	Size (μm)	Area (sq. μm)	Comments	Age (Ma)	St. Dev. (Ma ± 2σ)	Map
S399-4.1		#5	crd-grt-kfs	subhedr., prism., granular	included in crd	Th~8.54% Y~1.53% U~0%	distinct zoning	63 x 92	5796	moat of altered crd around the mnz grain, square-like inclusions (sil?!)	-	-	-
S399-8.1	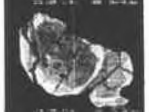	#5	crd-grt-kfs	anhedral, granular, irregular	along grt margin; matrix?	Th~7.58% Y~1.86% U~0.52%	distinct zoning	40 x 68	2720	major fractures, complex zoning pattern	-	-	-
S399-8.2		#5	crd-grt-kfs	anhedral, granular, irregular	within grt, along sil grain	Th~7.63% Y~2.02% U~0.83%	moder. zoning	38 x 62	2356	numerous inclusions rounded to cylindrical	-	-	-
S399-04		#5	crd-grt-kfs	anhedral, granular,	included in crd	none	....	30 x 45	1350	moat of altered crd around the mnz grain	-	-	-
S399-04		#5	crd-grt-kfs	anhedral, granular,	included in crd	none	....	35 x 55	1925	moat of altered crd around the mnz grain	-	-	-
S401-01		#5	crd-grt-kfs	subhedr., prism.	included in kfs	Th~9.33% Y~1.82% U~1.08%	distinct zoning	71 x 158	11 218	very complex zoning pattern, major fracturing	1804	8	Yes
S401-02	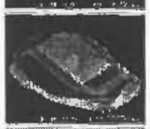	#5	crd-grt-kfs	subhedr., prism.	partly in kfs bordered by qz	Th~13.64% Y~2.87% U~1.52%	distinct zoning	38 x 48	1824	euhedral, core-to-rim zoning pattern	-	-	-
S403-01		#5	crd-grt-kfs	anhedral, irregular	....	none	distinct	70 x 210	14 700	-	-	-	-

Appendix 6

Major element analyses

Mnz Grain	Analysis #	Ce	P	Si	Pr	La	Ca	Y	Nd	Th	Sm	Gd	Dy	U	Total / 4O
S366-01	265	0.4664	0.9804	0.0084	0.0708	0.1964	0.0224	0.0172	0.1620	0.0344	0.0296	0.0172	0.0000	0.0008	2.006
	266	0.4696	0.9912	0.0060	0.0688	0.1944	0.0196	0.0180	0.1616	0.0264	0.0280	0.0180	0.0000	0.0004	2.002
	267	0.4512	0.9772	0.0112	0.0704	0.1808	0.0344	0.0180	0.1580	0.0548	0.0308	0.0176	0.0000	0.0004	2.005
	Average	**0.4624**	**0.9829**	**0.0085**	**0.0700**	**0.1905**	**0.0255**	**0.0177**	**0.1605**	**0.0385**	**0.0295**	**0.0176**	**0.0000**	**0.0005**	**2.004**
S366-02	268	0.4304	0.9756	0.0096	0.0656	0.1796	0.0524	0.0232	0.1492	0.0724	0.0284	0.0180	0.0000	0.0016	2.006
	269	0.4596	0.9808	0.0084	0.0664	0.1820	0.0320	0.0212	0.1552	0.0496	0.0300	0.0180	0.0000	0.0004	2.004
	270	0.4600	0.9600	0.0124	0.0672	0.1880	0.0380	0.0216	0.1608	0.0556	0.0312	0.0204	0.0000	0.0008	2.016
	Average	**0.4500**	**0.9721**	**0.0101**	**0.0664**	**0.1832**	**0.0408**	**0.0220**	**0.1551**	**0.0592**	**0.0299**	**0.0188**	**0.0000**	**0.0009**	**2.009**
S366-03	271	0.4668	0.9660	0.0100	0.0724	0.1920	0.0312	0.0220	0.1592	0.0488	0.0268	0.0172	0.0000	0.0004	2.013
	272	0.4468	0.9736	0.0100	0.0692	0.1824	0.0408	0.0196	0.1560	0.0624	0.0280	0.0176	0.0000	0.0004	2.007
	273	0.4500	0.9592	0.0172	0.0708	0.1852	0.0368	0.0176	0.1584	0.0680	0.0280	0.0200	0.0000	0.0004	2.012
	Average	**0.4545**	**0.9663**	**0.0124**	**0.0708**	**0.1865**	**0.0363**	**0.0197**	**0.1579**	**0.0597**	**0.0276**	**0.0183**	**0.0000**	**0.0004**	**2.011**
S366-04	274	0.4300	0.9496	0.0236	0.0676	0.1764	0.0524	0.0172	0.1484	0.0976	0.0284	0.0192	0.0000	0.0008	2.011
	275	0.4628	0.9708	0.0124	0.0688	0.1840	0.0340	0.0172	0.1536	0.0568	0.0280	0.0192	0.0000	0.0004	2.008
	276	0.4632	0.9696	0.0140	0.0668	0.1836	0.0340	0.0208	0.1544	0.0540	0.0308	0.0176	0.0000	0.0004	2.009
	Average	**0.4520**	**0.9633**	**0.0167**	**0.0677**	**0.1813**	**0.0401**	**0.0184**	**0.1521**	**0.0695**	**0.0291**	**0.0187**	**0.0000**	**0.0005**	**2.009**
S366-06	115	0.4552	0.9808	0.0108	0.0732	0.1964	0.0272	0.0196	0.1608	0.0332	0.0284	0.0200	0.0000	0.0000	2.006
	116	0.4612	0.9820	0.0100	0.0664	0.1960	0.0264	0.0204	0.1580	0.0356	0.0280	0.0216	0.0000	0.0000	2.006
	117	0.4308	0.9900	0.0160	0.0684	0.1788	0.0368	0.0208	0.1588	0.0500	0.0284	0.0176	0.0000	0.0000	1.997
	Average	**0.4491**	**0.9843**	**0.0123**	**0.0693**	**0.1904**	**0.0301**	**0.0203**	**0.1592**	**0.0396**	**0.0283**	**0.0197**	**0.0000**	**0.0000**	**2.003**
S366-07	118	0.4648	0.9904	0.0064	0.0752	0.1932	0.0152	0.0208	0.1704	0.0172	0.0316	0.0188	0.0000	0.0000	2.004
	119	0.4556	0.9900	0.0064	0.0692	0.2044	0.0220	0.0208	0.1608	0.0276	0.0264	0.0192	0.0000	0.0000	2.002
	120	0.4364	0.9880	0.0084	0.0704	0.1796	0.0460	0.0264	0.1552	0.0508	0.0244	0.0168	0.0000	0.0008	2.003
	121	0.4448	0.9784	0.0160	0.0708	0.1928	0.0340	0.0200	0.1568	0.0448	0.0280	0.0168	0.0000	0.0000	2.004
	157	0.4064	0.9928	0.0104	0.0512	0.2168	0.0308	0.0220	0.1828	0.0304	0.0292	0.0200	0.0060	0.0020	2.001
	158	0.3912	0.9936	0.0076	0.0504	0.2100	0.0492	0.0256	0.1768	0.0428	0.0276	0.0188	0.0064	0.0032	2.003
	159	0.4092	0.9820	0.0088	0.0512	0.2104	0.0424	0.0240	0.1824	0.0408	0.0284	0.0204	0.0064	0.0024	2.009
	160	0.4184	0.9912	0.0056	0.0524	0.2180	0.0276	0.0228	0.1876	0.0248	0.0268	0.0200	0.0064	0.0024	2.004
	161	0.4200	0.9896	0.0072	0.0536	0.2184	0.0268	0.0204	0.1884	0.0264	0.0288	0.0184	0.0048	0.0016	2.005
	Average	**0.4274**	**0.9884**	**0.0085**	**0.0605**	**0.2048**	**0.0327**	**0.0225**	**0.1735**	**0.0340**	**0.0279**	**0.0188**	**0.0033**	**0.0014**	**2.004**
S366-08	122	0.4456	0.9848	0.0088	0.0712	0.1896	0.0396	0.0220	0.1512	0.0476	0.0252	0.0176	0.0000	0.0000	2.004
	123	0.4216	0.9928	0.0116	0.0676	0.1892	0.0432	0.0240	0.1576	0.0492	0.0248	0.0160	0.0000	0.0004	1.998
	124	0.4256	0.9896	0.0160	0.0712	0.1852	0.0388	0.0228	0.1552	0.0488	0.0276	0.0176	0.0000	0.0008	1.999

Mnz Grain	Analysis #	Ce	P	Si	Pr	La	Ca	Y	Nd	Th	Sm	Gd	Dy	U	Total / 4O
S366-08 (cnt'd)	Average	0.4309	0.9891	0.0121	0.0700	0.1880	0.0405	0.0229	0.1547	0.0485	0.0259	0.0171	0.0000	0.0004	2.000
S366-09	125	0.4228	0.9716	0.0276	0.0672	0.1928	0.0436	0.0184	0.1488	0.0612	0.0268	0.0160	0.0000	0.0000	1.997
S366-10	126	0.4412	0.9932	0.0128	0.0736	0.1932	0.0284	0.0180	0.1572	0.0392	0.0232	0.0164	0.0000	0.0000	1.997
	127	0.4100	0.9572	0.0380	0.0604	0.1888	0.0600	0.0180	0.1376	0.1020	0.0180	0.0124	0.0000	0.0000	2.002
	128	0.4508	0.9832	0.0132	0.0752	0.1924	0.0316	0.0184	0.1520	0.0440	0.0260	0.0140	0.0000	0.0000	2.001
	Average	0.4312	0.9763	0.0229	0.0691	0.1918	0.0409	0.0182	0.1489	0.0616	0.0235	0.0147	0.0000	0.0000	1.999
S366-11	277	0.4580	0.9752	0.0084	0.0700	0.1904	0.0324	0.0204	0.1600	0.0480	0.0272	0.0188	0.0000	0.0004	2.010
	278	0.4356	0.9720	0.0100	0.0704	0.1812	0.0464	0.0228	0.1612	0.0628	0.0280	0.0180	0.0000	0.0012	2.010
	279	0.4632	0.9764	0.0088	0.0680	0.1920	0.0280	0.0188	0.1604	0.0420	0.0296	0.0200	0.0000	0.0004	2.008
	129	0.4420	0.9784	0.0148	0.0748	0.1976	0.0348	0.0172	0.1584	0.0448	0.0272	0.0156	0.0000	0.0000	2.006
	130	0.4388	0.9820	0.0116	0.0700	0.1936	0.0376	0.0200	0.1572	0.0480	0.0268	0.0188	0.0000	0.0000	2.005
	131	0.4496	0.9856	0.0096	0.0752	0.1916	0.0312	0.0192	0.1624	0.0376	0.0252	0.0168	0.0000	0.0000	2.004
	132	0.4296	0.9800	0.0116	0.0772	0.1936	0.0408	0.0204	0.1596	0.0508	0.0260	0.0168	0.0000	0.0000	2.007
	Average	0.4453	0.9785	0.0107	0.0722	0.1914	0.0359	0.0198	0.1599	0.0477	0.0271	0.0178	0.0000	0.0003	2.007
S366-12	133	0.4232	0.9944	0.0088	0.0772	0.1700	0.0468	0.0236	0.1548	0.0520	0.0276	0.0172	0.0000	0.0004	1.996
	134	0.4452	0.9864	0.0120	0.0772	0.1880	0.0296	0.0172	0.1608	0.0416	0.0268	0.0168	0.0000	0.0000	2.002
	Average	0.4342	0.9904	0.0104	0.0772	0.1790	0.0382	0.0204	0.1578	0.0468	0.0272	0.0170	0.0000	0.0002	1.999
S366-13	135	0.4204	0.9928	0.0084	0.0696	0.1812	0.0460	0.0236	0.1512	0.0576	0.0268	0.0172	0.0000	0.0000	1.995
	136	0.4612	0.9856	0.0084	0.0744	0.1940	0.0236	0.0172	0.1612	0.0316	0.0264	0.0184	0.0000	0.0000	2.002
	Average	0.4408	0.9892	0.0084	0.0720	0.1876	0.0348	0.0204	0.1562	0.0446	0.0266	0.0178	0.0000	0.0000	1.999
S366-15	140	0.4388	0.9832	0.0192	0.0732	0.1856	0.0344	0.0188	0.1564	0.0476	0.0264	0.0168	0.0000	0.0000	2.001
	141	0.4524	0.9916	0.0088	0.0812	0.1876	0.0220	0.0184	0.1648	0.0280	0.0272	0.0188	0.0000	0.0000	2.001
	142	0.4532	0.9760	0.0136	0.0736	0.1828	0.0384	0.0180	0.1568	0.0528	0.0256	0.0156	0.0000	0.0000	2.007
	143	0.4668	0.9840	0.0060	0.0812	0.2036	0.0208	0.0168	0.1620	0.0244	0.0264	0.0164	0.0000	0.0000	2.008
	144	0.4344	0.9816	0.0132	0.0752	0.1796	0.0412	0.0200	0.1568	0.0544	0.0272	0.0192	0.0000	0.0000	2.003
	145	0.4560	0.9868	0.0092	0.0724	0.1848	0.0364	0.0200	0.1560	0.0408	0.0252	0.0168	0.0000	0.0000	2.005
	145	0.4208	0.9956	0.0060	0.0532	0.2180	0.0192	0.0228	0.1896	0.0160	0.0312	0.0192	0.0068	0.0024	2.001
	146	0.4308	0.9928	0.0036	0.0520	0.2340	0.0176	0.0180	0.1848	0.0176	0.0288	0.0172	0.0056	0.0008	2.004
	147	0.4104	0.9980	0.0060	0.0512	0.2184	0.0300	0.0212	0.1864	0.0248	0.0268	0.0188	0.0064	0.0020	2.001
	148	0.3988	0.9852	0.0188	0.0500	0.2080	0.0412	0.0196	0.1768	0.0464	0.0296	0.0188	0.0072	0.0012	2.002
	149	0.4080	0.9912	0.0104	0.0544	0.2120	0.0372	0.0212	0.1780	0.0340	0.0268	0.0212	0.0064	0.0012	2.002
	Average	0.4337	0.9878	0.0104	0.0652	0.2013	0.0308	0.0195	0.1699	0.0352	0.0274	0.0181	0.0029	0.0007	2.003
S366-16	151	0.4156	1.0052	0.0048	0.0528	0.2212	0.0176	0.0188	0.1904	0.0152	0.0276	0.0196	0.0060	0.0012	1.996

Mnz Grain	Analysis #	Ce	P	Si	Pr	La	Ca	Y	Nd	Th	Sm	Gd	Dy	U	Total / 4O
S366-16 (cnt'd)	152	0.4036	0.9888	0.0140	0.0484	0.2116	0.0380	0.0200	0.1836	0.0404	0.0276	0.0176	0.0060	0.0012	2.001
	153	0.4104	0.9948	0.0084	0.0508	0.2168	0.0256	0.0208	0.1896	0.0260	0.0284	0.0192	0.0064	0.0020	1.999
	154	0.3944	0.9984	0.0076	0.0480	0.2064	0.0464	0.0240	0.1784	0.0416	0.0268	0.0184	0.0060	0.0028	2.000
	155	0.4048	0.9912	0.0160	0.0492	0.2124	0.0320	0.0184	0.1840	0.0376	0.0276	0.0188	0.0036	0.0020	1.998
	Average	**0.4058**	**0.9957**	**0.0102**	**0.0498**	**0.2137**	**0.0319**	**0.0204**	**0.1852**	**0.0322**	**0.0276**	**0.0187**	**0.0056**	**0.0018**	**1.999**
S366map1	60	0.3688	1.0208	0.0132	0.0488	0.1900	0.0512	0.0040	0.1712	0.0532	0.0296	0.0228	0.0068	0.0000	1.981
	61	0.3920	1.0304	0.0096	0.0536	0.2032	0.0268	0.0024	0.1772	0.0256	0.0304	0.0200	0.0060	0.0000	1.977
	62	0.3836	1.0264	0.0096	0.0492	0.1940	0.0484	0.0036	0.1664	0.0452	0.0280	0.0204	0.0052	0.0000	1.980
	63	0.3896	1.0284	0.0108	0.0512	0.1980	0.0312	0.0032	0.1776	0.0300	0.0296	0.0216	0.0072	0.0000	1.978
	64	0.3764	1.0216	0.0116	0.0484	0.1932	0.0528	0.0036	0.1688	0.0496	0.0292	0.0204	0.0064	0.0000	1.982
	Average	**0.3821**	**1.0255**	**0.0110**	**0.0502**	**0.1957**	**0.0421**	**0.0034**	**0.1722**	**0.0407**	**0.0294**	**0.0210**	**0.0063**	**0.0000**	**1.980**
S366map2	7	0.3948	1.0208	0.0100	0.0528	0.2096	0.0264	0.0044	0.1788	0.0280	0.0316	0.0212	0.0048	0.0000	1.983
	8	0.3684	1.0252	0.0092	0.0492	0.1972	0.0540	0.0048	0.1724	0.0476	0.0296	0.0204	0.0048	0.0000	1.983
	9	0.3744	1.0248	0.0104	0.0504	0.2016	0.0468	0.0056	0.1740	0.0416	0.0276	0.0196	0.0044	0.0000	1.982
	10	0.4040	1.0248	0.0072	0.0504	0.2148	0.0240	0.0048	0.1812	0.0240	0.0268	0.0168	0.0024	0.0000	1.982
	11	0.3980	1.0276	0.0052	0.0512	0.2136	0.0204	0.0044	0.1820	0.0192	0.0328	0.0220	0.0044	0.0000	1.981
	12	0.4008	1.0244	0.0060	0.0524	0.2200	0.0260	0.0044	0.1756	0.0272	0.0268	0.0152	0.0028	0.0000	1.982
	Average	**0.3901**	**1.0246**	**0.0080**	**0.0511**	**0.2095**	**0.0329**	**0.0047**	**0.1773**	**0.0313**	**0.0292**	**0.0192**	**0.0039**	**0.0000**	**1.982**
S366	**Average**	**0.4288**	**0.9899**	**0.0111**	**0.0637**	**0.1966**	**0.0348**	**0.0177**	**0.1658**	**0.0428**	**0.0277**	**0.0183**	**0.0021**	**0.0006**	**2.000**
S367-01	*491	0.4940	0.9576	0.0080	0.0704	0.2172	0.0236	0.0220	0.1660	0.0196	0.0292	0.0176	0.0000	0.0012	2.026
	492	0.4768	0.9680	0.0084	0.0680	0.2116	0.0280	0.0248	0.1592	0.0264	0.0268	0.0192	0.0000	0.0012	2.019
	493	0.4636	0.9660	0.0092	0.0664	0.2052	0.0444	0.0244	0.1568	0.0368	0.0260	0.0188	0.0000	0.0036	2.021
	Average	**0.4702**	**0.9670**	**0.0088**	**0.0672**	**0.2084**	**0.0362**	**0.0246**	**0.1580**	**0.0316**	**0.0264**	**0.0190**	**0.0000**	**0.0024**	**2.020**
S367-02	494	0.4460	0.9700	0.0080	0.0656	0.1900	0.0504	0.0284	0.1560	0.0472	0.0324	0.0192	0.0000	0.0032	2.017
	495	0.4632	0.9680	0.0068	0.0672	0.1976	0.0388	0.0260	0.1584	0.0380	0.0304	0.0212	0.0000	0.0028	2.018
	496	0.4692	0.9644	0.0048	0.0640	0.1996	0.0396	0.0256	0.1636	0.0384	0.0312	0.0188	0.0000	0.0028	2.022
	497	0.4824	0.9608	0.0060	0.0704	0.2100	0.0288	0.0256	0.1592	0.0280	0.0292	0.0212	0.0000	0.0016	2.024
	Average	**0.4652**	**0.9658**	**0.0064**	**0.0668**	**0.1993**	**0.0394**	**0.0264**	**0.1593**	**0.0379**	**0.0308**	**0.0201**	**0.0000**	**0.0026**	**2.020**
S367-03	*499	0.4648	0.9532	0.0080	0.0688	0.2016	0.0480	0.0260	0.1604	0.0472	0.0296	0.0184	0.0000	0.0020	2.028
	500	0.4644	0.9656	0.0076	0.0668	0.2008	0.0360	0.0260	0.1608	0.0380	0.0324	0.0200	0.0000	0.0012	2.020
	501	0.4700	0.9648	0.0068	0.0684	0.2012	0.0340	0.0260	0.1652	0.0332	0.0292	0.0200	0.0000	0.0020	2.021
	502	0.4492	0.9608	0.0080	0.0636	0.1924	0.0504	0.0300	0.1596	0.0500	0.0312	0.0224	0.0000	0.0040	2.022
	Average	**0.4612**	**0.9637**	**0.0075**	**0.0663**	**0.1981**	**0.0401**	**0.0273**	**0.1619**	**0.0404**	**0.0309**	**0.0208**	**0.0000**	**0.0024**	**2.021**

Mnz Grain	Analysis #	Ce	P	Si	Pr	La	Ca	Y	Nd	Th	Sm	Gd	Dy	U	Total / 4O
S367-04	504	**0.4952**	**0.9592**	**0.0060**	**0.0664**	**0.2044**	**0.0300**	**0.0220**	**0.1616**	**0.0312**	**0.0288**	**0.0184**	**0.0000**	**0.0012**	**2.024**
	*505	0.5124	0.9552	0.0016	0.0648	0.2108	0.0212	0.0224	0.1692	0.0312	0.0312	0.0184	0.0000	0.0012	2.029
	*506	0.5040	0.9604	0.0032	0.0728	0.2096	0.0204	0.0228	0.1644	0.0196	0.0264	0.0212	0.0000	0.0012	2.025
	*507	0.4808	0.9572	0.0040	0.0680	0.2004	0.0372	0.0280	0.1652	0.0320	0.0316	0.0212	0.0000	0.0044	2.028
	508	0.4808	0.9632	0.0032	0.0716	0.1984	0.0372	0.0272	0.1556	0.0328	0.0320	0.0184	0.0000	0.0040	2.024
	Average	**0.4808**	**0.9632**	**0.0032**	**0.0716**	**0.1984**	**0.0372**	**0.0272**	**0.1556**	**0.0328**	**0.0320**	**0.0184**	**0.0000**	**0.0040**	**2.024**
S367-05	509	0.4720	0.9672	0.0052	0.0684	0.2040	0.0416	0.0236	0.1612	0.0296	0.0280	0.0204	0.0000	0.0016	2.023
	*510	0.4812	0.9628	0.0052	0.0684	0.1944	0.0400	0.0272	0.1672	0.0312	0.0272	0.0244	0.0000	0.0020	2.026
	*511	0.4684	0.9508	0.0060	0.0688	0.1964	0.0480	0.0288	0.1564	0.0456	0.0296	0.0200	0.0000	0.0040	2.027
	*512	0.4712	0.9576	0.0056	0.0664	0.1912	0.0556	0.0268	0.1572	0.0436	0.0300	0.0204	0.0000	0.0044	2.028
	513	0.4612	0.9600	0.0076	0.0652	0.1928	0.0504	0.0264	0.1588	0.0456	0.0324	0.0204	0.0000	0.0036	2.024
	Average	**0.4666**	**0.9636**	**0.0064**	**0.0668**	**0.1984**	**0.0460**	**0.0250**	**0.1600**	**0.0376**	**0.0302**	**0.0204**	**0.0000**	**0.0026**	**2.024**
S367-06	*514	0.4640	0.9520	0.0152	0.0636	0.2024	0.0444	0.2640	0.1592	0.0448	0.0296	0.0204	0.0000	0.0032	2.026
	515	0.4732	0.9580	0.0144	0.0664	0.1964	0.0360	0.0256	0.1604	0.0372	0.0304	0.0208	0.0000	0.0024	2.022
	*516	0.4824	0.9492	0.0112	0.0668	0.1976	0.0412	0.0288	0.1616	0.0384	0.0300	0.0196	0.0000	0.0036	2.030
	*517	0.4640	0.9556	0.0116	0.0712	0.2004	0.0320	0.0224	0.1576	0.0344	0.0288	0.0200	0.0000	0.0012	2.026
	Average	**0.4732**	**0.9580**	**0.0144**	**0.0664**	**0.1964**	**0.0360**	**0.0256**	**0.1604**	**0.0372**	**0.0304**	**0.0208**	**0.0000**	**0.0024**	**2.022**
S367-07	519	0.4104	0.9728	0.0116	0.0640	0.1820	0.0644	0.0300	0.1560	0.0644	0.0272	0.0248	0.0000	0.0044	2.013
	520	0.4104	0.9660	0.0144	0.0672	0.1856	0.0664	0.0280	0.1544	0.0688	0.0280	0.0224	0.0000	0.0044	2.016
	521	0.4452	0.9700	0.0068	0.0660	0.1936	0.0440	0.0264	0.1664	0.0412	0.0336	0.0212	0.0000	0.0032	2.018
	522	0.4304	0.9652	0.0088	0.0700	0.1952	0.0504	0.0304	0.1620	0.0472	0.0320	0.0236	0.0000	0.0044	2.020
	523	0.4452	0.9672	0.0084	0.0664	0.1896	0.0500	0.0276	0.1600	0.0488	0.0300	0.0216	0.0000	0.0040	2.018
	Average	**0.4283**	**0.9682**	**0.0100**	**0.0667**	**0.1892**	**0.0550**	**0.0285**	**0.1598**	**0.0541**	**0.0302**	**0.0227**	**0.0000**	**0.0041**	**2.017**
S367-08	524	0.4492	0.9720	0.0092	0.0680	0.1956	0.0440	0.0264	0.1596	0.0376	0.0296	0.0208	0.0000	0.0040	2.016
	525	0.4444	0.9636	0.0300	0.0656	0.1912	0.0412	0.0264	0.1596	0.0376	0.0284	0.0216	0.0000	0.0044	2.014
	526	0.4544	0.9664	0.0100	0.0684	0.1956	0.0420	0.0256	0.1668	0.0364	0.0280	0.0220	0.0000	0.0044	2.020
	527	0.4588	0.9660	0.0152	0.0664	0.1972	0.0428	0.0260	0.1580	0.0376	0.0272	0.0200	0.0000	0.0032	2.018
	Average	**0.4517**	**0.9670**	**0.0161**	**0.0671**	**0.1949**	**0.0425**	**0.0261**	**0.1610**	**0.0373**	**0.0283**	**0.0211**	**0.0000**	**0.0040**	**2.017**
S367-09	528	0.4856	0.9660	0.0044	0.0704	0.2156	0.0244	0.0204	0.1636	0.0220	0.0264	0.0204	0.0000	0.0020	2.021
	529	0.4800	0.9688	0.0056	0.0712	0.2120	0.0212	0.0232	0.1680	0.0172	0.0296	0.0216	0.0000	0.0016	2.020
	530	0.4772	0.9688	0.0064	0.0672	0.2128	0.0252	0.0220	0.1660	0.0232	0.0268	0.0204	0.0000	0.0020	2.018
	531	0.4732	0.9708	0.0044	0.0700	0.2060	0.0280	0.0228	0.1692	0.0248	0.0276	0.0212	0.0000	0.0012	2.019
	532	0.4808	0.9644	0.0048	0.0708	0.2064	0.0280	0.0252	0.1684	0.0228	0.0280	0.0220	0.0000	0.0012	2.023

Mnz Grain	Analysis #	Ce	P	Si	Pr	La	Ca	Y	Nd	Th	Sm	Gd	Dy	U	Total / 4O
S367-09 (cnt'd)	Average	**0.4794**	**0.9678**	**0.0051**	**0.0699**	**0.2106**	**0.0254**	**0.0227**	**0.1670**	**0.0220**	**0.0277**	**0.0211**	**0.0000**	**0.0016**	**2.020**
S367-10	163	0.3996	0.9948	0.0072	0.0492	0.2088	0.0412	0.0264	0.1872	0.0304	0.0268	0.0208	0.0068	0.0040	2.004
	164	0.4028	0.9932	0.0060	0.0496	0.2124	0.0420	0.0236	0.1864	0.0340	0.0276	0.0176	0.0060	0.0032	2.005
	165	0.4248	0.9936	0.0032	0.0524	0.2248	0.0236	0.0228	0.1896	0.0144	0.0308	0.0188	0.0068	0.0012	2.007
	166	0.4140	0.9880	0.0052	0.0536	0.2228	0.0252	0.0256	0.1936	0.0208	0.0284	0.0204	0.0072	0.0020	2.007
	167	0.4092	0.9944	0.0052	0.0496	0.2172	0.0316	0.0272	0.1864	0.0256	0.0292	0.0196	0.0056	0.0032	2.004
	Average	**0.4101**	**0.9928**	**0.0054**	**0.0509**	**0.2172**	**0.0327**	**0.0251**	**0.1886**	**0.0250**	**0.0286**	**0.0194**	**0.0065**	**0.0027**	**2.005**
S367map1	3	0.3820	1.0220	0.0092	0.0520	0.2036	0.0344	0.0048	0.1868	0.0304	0.0320	0.0216	0.0048	0.0000	1.984
	4	0.3716	1.0232	0.0092	0.0496	0.1992	0.0532	0.0052	0.1720	0.0480	0.0288	0.0188	0.0044	0.0000	1.983
	5	0.3444	1.0064	0.0252	0.0464	0.1836	0.0768	0.0044	0.1636	0.0856	0.0260	0.0188	0.0040	0.0000	1.984
	6	0.3560	1.0156	0.0188	0.0468	0.1920	0.0584	0.0048	0.1724	0.0636	0.0284	0.0204	0.0044	0.0000	1.982
	Average	**0.3635**	**1.0168**	**0.0156**	**0.0487**	**0.1946**	**0.0557**	**0.0048**	**0.1737**	**0.0569**	**0.0288**	**0.0199**	**0.0044**	**0.0000**	**1.983**
S367	**Average**	**0.4437**	**0.9750**	**0.0090**	**0.0632**	**0.2013**	**0.0406**	**0.0234**	**0.1663**	**0.0377**	**0.0292**	**0.0205**	**0.0014**	**0.0025**	**2.014**
S371-01	146	0.4564	0.9888	0.0104	0.0772	0.1816	0.0268	0.0132	0.1628	0.0392	0.0248	0.0152	0.0000	0.0000	1.997
	147	0.4280	0.9912	0.0176	0.0704	0.1640	0.0400	0.0152	0.1532	0.0680	0.0232	0.0172	0.0000	0.0000	1.988
	Average	**0.4422**	**0.9900**	**0.0140**	**0.0738**	**0.1728**	**0.0334**	**0.0142**	**0.1580**	**0.0536**	**0.0240**	**0.0162**	**0.0000**	**0.0000**	**1.993**
S371-02	148	0.4072	0.9788	0.0236	0.0668	0.1672	0.0588	0.0180	0.1488	0.0868	0.0220	0.0164	0.0000	0.0004	1.995
	149	0.4516	0.9904	0.0080	0.0780	0.1880	0.0248	0.0200	0.1612	0.0324	0.0264	0.0196	0.0000	0.0000	2.000
	Average	**0.4294**	**0.9846**	**0.0158**	**0.0724**	**0.1776**	**0.0418**	**0.0190**	**0.1550**	**0.0596**	**0.0242**	**0.0180**	**0.0000**	**0.0002**	**1.998**
S371-03	150	0.4608	0.9904	0.0064	0.0788	0.1924	0.0240	0.0172	0.1616	0.0280	0.0252	0.0176	0.0000	0.0000	2.003
	Average	**0.4608**	**0.9904**	**0.0064**	**0.0788**	**0.1924**	**0.0240**	**0.0172**	**0.1616**	**0.0280**	**0.0252**	**0.0176**	**0.0000**	**0.0000**	**2.003**
S371-05	153	0.4672	0.9916	0.0088	0.0664	0.1916	0.0216	0.0128	0.1608	0.0320	0.0244	0.0156	0.0000	0.0004	1.993
	154	0.4540	0.9864	0.0088	0.0788	0.2028	0.0244	0.0144	0.1548	0.0348	0.0248	0.0160	0.0000	0.0000	2.000
	155	0.4556	0.9872	0.0072	0.0744	0.1888	0.0292	0.0212	0.1556	0.0360	0.0268	0.0180	0.0000	0.0004	2.000
	Average	**0.4589**	**0.9884**	**0.0083**	**0.0732**	**0.1944**	**0.0251**	**0.0161**	**0.1571**	**0.0343**	**0.0253**	**0.0165**	**0.0000**	**0.0003**	**1.998**
S371-06	156	0.4684	0.9448	0.0172	0.0740	0.1972	0.0404	0.0172	0.1632	0.0604	0.0248	0.0140	0.0000	0.0000	2.022
	157	0.4672	0.9440	0.0132	0.0700	0.1940	0.0484	0.0200	0.1552	0.0656	0.0268	0.0168	0.0000	0.0000	2.021
	Average	**0.4678**	**0.9444**	**0.0152**	**0.0720**	**0.1956**	**0.0444**	**0.0186**	**0.1592**	**0.0630**	**0.0258**	**0.0154**	**0.0000**	**0.0000**	**2.022**
S371-07	334	0.5016	0.9528	0.0072	0.0668	0.2036	0.0244	0.0160	0.1664	0.0352	0.0304	0.0204	0.0000	0.0004	2.026
	353	0.4908	0.9552	0.0072	0.0732	0.2012	0.0236	0.0176	0.1644	0.0372	0.0316	0.0200	0.0000	0.0004	2.023
	354	0.4876	0.9564	0.0084	0.0728	0.1964	0.0268	0.0180	0.1652	0.0392	0.0308	0.0196	0.0000	0.0012	2.022
	355	0.4716	0.9448	0.0116	0.0680	0.1876	0.0396	0.0196	0.1624	0.0668	0.0324	0.0188	0.0000	0.0008	2.024
	Average	**0.4833**	**0.9521**	**0.0091**	**0.0713**	**0.1951**	**0.0300**	**0.0184**	**0.1640**	**0.0477**	**0.0316**	**0.0195**	**0.0000**	**0.0008**	**2.023**

Mnz Grain	Analysis #	Ce	P	Si	Pr	La	Ca	Y	Nd	Th	Sm	Gd	Dy	U	Total / 4O
S371-08	*335	0.4968	0.9312	0.0064	0.0696	0.2028	0.0276	0.0192	0.1652	0.0412	0.0296	0.0164	0.0000	0.0004	2.027
	*350	0.4708	0.9416	0.0100	0.0668	0.1936	0.0392	0.0208	0.1632	0.0464	0.0308	0.0192	0.0000	0.0012	2.026
	*351	0.4920	0.9488	0.0068	0.0684	0.2088	0.0268	0.0204	0.1672	0.0400	0.0312	0.0152	0.0000	0.0012	2.027
	*352	0.5032	0.9472	0.0064	0.0676	0.2120	0.0272	0.0160	0.1600	0.0420	0.0292	0.0156	0.0000	0.0004	2.028
	Average	-	-	-	-	-	-	-	-	-	-	-	-	-	-
S371-09	*336	0.5044	0.9476	0.0080	0.0752	0.2044	0.0244	0.0184	0.1608	0.0380	0.0296	0.0168	0.0000	0.0000	2.028
	*346	0.4936	0.9512	0.0068	0.0660	0.2108	0.0268	0.0216	0.1620	0.0412	0.0252	0.0150	0.0000	0.0000	2.026
	*347	0.5004	0.9500	0.0064	0.0664	0.2080	0.0264	0.0192	0.1604	0.0412	0.0292	0.0184	0.0000	0.0000	2.026
	*348	0.5020	0.9476	0.0060	0.0684	0.2070	0.0244	0.0200	0.1648	0.0372	0.0308	0.0192	0.0000	0.0004	2.029
	*349	0.4700	0.9424	0.0128	0.0644	0.1912	0.0412	0.0228	0.1620	0.0588	0.0280	0.0204	0.0000	0.0008	2.025
	Average	-	-	-	-	-	-	-	-	-	-	-	-	-	-
S371-10	*337	0.4916	0.9468	0.0080	0.0684	0.1968	0.0372	0.0208	0.1696	0.0428	0.0328	0.0228	0.0000	0.0004	2.026
	*342	0.4844	0.9428	0.0108	0.0668	0.1960	0.0332	0.0208	0.1668	0.0552	0.0304	0.0200	0.0000	0.0004	2.028
	*343	0.5044	0.9548	0.0052	0.0728	0.2032	0.0196	0.0196	0.1672	0.0284	0.0304	0.0192	0.0000	0.0008	2.026
	*344	0.5020	0.9504	0.0060	0.0684	0.2032	0.0228	0.0200	0.1700	0.0332	0.0296	0.0216	0.0000	0.0008	2.028
	*345	0.4932	0.9372	0.0108	0.0704	0.1944	0.0332	0.0180	0.1660	0.0552	0.0320	0.0208	0.0000	0.0000	2.031
	Average	-	-	-	-	-	-	-	-	-	-	-	-	-	-
S371-11	*338	0.4780	0.9444	0.0104	0.0628	0.2064	0.0416	0.0200	0.1488	0.0640	0.0364	0.0192	0.0000	0.0008	2.027
	339	0.4892	0.9512	0.0100	0.0664	0.2052	0.0300	0.0196	0.1568	0.0464	0.0300	0.0188	0.0000	0.0000	2.024
	*340	0.4900	0.9444	0.0100	0.0672	0.2024	0.0312	0.0184	0.1620	0.0520	0.0288	0.0200	0.0000	0.0004	2.027
	*341	0.5012	0.9416	0.0080	0.0692	0.2104	0.0288	0.0196	0.1608	0.0468	0.0264	0.0172	0.0000	0.0004	2.031
	Average	0.4892	0.9512	0.0100	0.0664	0.2052	0.0300	0.0196	0.1568	0.0464	0.0300	0.0188	0.0000	0.0000	2.024
S371-12	[illegible]	[illegible]	[illegible]	[illegible]	[illegible]	[illegible]	[illegible]	[illegible]	0.1696	[illegible]	[illegible]	[illegible]	[illegible]	[illegible]	[illegible]
	[illegible]	[illegible]	[illegible]	[illegible]	[illegible]	0.1760	0.0688	0.0340	[illegible]	[illegible]	0.0320	[illegible]	[illegible]	[illegible]	[illegible]
	*355	[illegible]	[illegible]	[illegible]	[illegible]	[illegible]	0.0428	[illegible]	[illegible]	[illegible]	[illegible]	[illegible]	[illegible]	[illegible]	[illegible]
	359	0.4524	0.9360	0.0216	0.0636	0.1824	0.0492	0.0200	0.1584	0.0904	0.0288	0.0172	0.0000	0.0008	2.021
	151	0.4312	0.9792	0.0136	0.0708	0.1828	0.0420	0.0196	0.1580	0.0584	0.0260	0.0180	0.0000	0.0000	2.000
	152	0.4496	0.9888	0.0116	0.0772	0.1780	0.0300	0.0168	0.1592	0.0420	0.0260	0.0164	0.0000	0.0004	1.996
	Average	0.4444	0.9680	0.0156	0.0705	0.1811	0.0404	0.0188	0.1585	0.0636	0.0269	0.0172	0.0000	0.0004	2.006
S371-13	158	0.4940	0.9544	0.0096	0.0744	0.2112	0.0300	0.0112	0.1584	0.0400	0.0232	0.0152	0.0000	0.0000	2.022
	159	0.4796	0.9728	0.0072	0.0724	0.2068	0.0308	0.0132	0.1536	0.0372	0.0228	0.0156	0.0000	0.0000	2.012
	Average	0.4868	0.9636	0.0084	0.0734	0.2090	0.0304	0.0122	0.1560	0.0386	0.0230	0.0154	0.0000	0.0000	2.017
S371-14	160	0.4748	0.9620	0.0120	0.0784	0.2016	0.0332	0.0172	0.1592	0.0384	0.0260	0.0168	0.0000	0.0000	2.020

Mnz Grain	Analysis #	Ce	P	Si	Pr	La	Ca	Y	Nd	Th	Sm	Gd	Dy	U	Total / 4O
S371-14 (cnt'd)	Average	**0.4748**	**0.9620**	**0.0120**	**0.0784**	**0.2016**	**0.0332**	**0.0172**	**0.1592**	**0.0384**	**0.0260**	**0.0168**	**0.0000**	**0.0000**	**2.020**
S371-15	161	0.4732	0.9548	0.0112	0.0748	0.2008	0.0388	0.0184	0.1548	0.0492	0.0280	0.0180	0.0000	0.0000	2.022
	Average	**0.4732**	**0.9548**	**0.0112**	**0.0748**	**0.2008**	**0.0388**	**0.0184**	**0.1548**	**0.0492**	**0.0280**	**0.0180**	**0.0000**	**0.0000**	**2.022**
S371-16	162	0.4932	0.9636	0.0080	0.0780	0.1988	0.0196	0.0172	0.1676	0.0236	0.0292	0.0180	0.0000	0.0000	2.017
	Average	**0.4932**	**0.9636**	**0.0080**	**0.0780**	**0.1988**	**0.0196**	**0.0172**	**0.1676**	**0.0236**	**0.0292**	**0.0180**	**0.0000**	**0.0000**	**2.017**
S371-17	163	0.5060	0.9608	0.0060	0.0752	0.2164	0.0164	0.0148	0.1676	0.0176	0.0264	0.0152	0.0000	0.0000	2.022
	Average	**0.5060**	**0.9608**	**0.0060**	**0.0752**	**0.2164**	**0.0164**	**0.0148**	**0.1676**	**0.0176**	**0.0264**	**0.0152**	**0.0000**	**0.0000**	**2.022**
S371-19	169	0.4028	0.9920	0.0144	0.0512	0.2076	0.0388	0.0212	0.1800	0.0388	0.0272	0.0172	0.0064	0.0024	2.000
	170	0.4068	0.9868	0.0132	0.0512	0.2104	0.0392	0.0196	0.1804	0.0428	0.0264	0.0168	0.0056	0.0024	2.002
	171	0.4316	0.9896	0.0088	0.0544	0.2308	0.0196	0.0144	0.1856	0.0196	0.0276	0.0144	0.0052	0.0016	2.004
	172	0.3972	0.9884	0.0176	0.0496	0.2064	0.0444	0.0188	0.1748	0.0520	0.0264	0.0160	0.0048	0.0028	2.000
	173	0.4232	0.9952	0.0076	0.0536	0.2208	0.0248	0.0176	0.1856	0.0268	0.0268	0.0156	0.0012	0.0012	2.000
	Average	**0.4123**	**0.9904**	**0.0123**	**0.0520**	**0.2152**	**0.0334**	**0.0183**	**0.1813**	**0.0360**	**0.0269**	**0.0160**	**0.0046**	**0.0021**	**2.001**
S371-20	200	0.4200	0.9888	0.0080	0.0528	0.2156	0.0260	0.0184	0.1940	0.0296	0.0276	0.0180	0.0024	0.0016	2.003
	201	0.4220	1.0000	0.0064	0.0520	0.2252	0.0244	0.0160	0.1832	0.0232	0.0260	0.0168	0.0024	0.0008	1.999
	202	0.4372	1.0028	0.0036	0.0532	0.2380	0.0152	0.0132	0.1748	0.0144	0.0260	0.0152	0.0020	0.0012	1.997
	203	0.4360	0.9988	0.0060	0.0512	0.2436	0.0144	0.0128	0.1796	0.0124	0.0268	0.0160	0.0016	0.0004	2.000
	204	0.4164	0.9968	0.0064	0.0516	0.2280	0.0276	0.0172	0.1856	0.0272	0.0264	0.0140	0.0020	0.0012	2.001
	Average	**0.4263**	**0.9974**	**0.0061**	**0.0522**	**0.2301**	**0.0215**	**0.0155**	**0.1834**	**0.0214**	**0.0266**	**0.0160**	**0.0021**	**0.0010**	**2.000**
S371-21	206	0.4028	0.9968	0.0160	0.0464	0.2204	0.0372	0.0164	0.1740	0.0452	0.0236	0.0144	0.0000	0.0004	1.994
	207	0.4320	0.9936	0.0056	0.0504	0.2280	0.0196	0.0204	0.1880	0.0176	0.0280	0.0176	0.0008	0.0012	2.003
	208	0.4436	0.9640	0.0068	0.0580	0.2208	0.0196	0.0220	0.2084	0.0200	0.0336	0.0208	0.0028	0.0012	2.022
	209	0.4164	0.9964	0.0076	0.0520	0.2232	0.0260	0.0176	0.1856	0.0280	0.0292	0.0156	0.0004	0.0012	1.999
	210	0.4192	0.9920	0.0080	0.0536	0.2136	0.0188	0.0212	0.2048	0.0172	0.0308	0.0212	0.0016	0.0008	2.003
	Average	**0.4228**	**0.9886**	**0.0088**	**0.0521**	**0.2212**	**0.0242**	**0.0195**	**0.1922**	**0.0256**	**0.0290**	**0.0179**	**0.0011**	**0.0010**	**2.004**
S371	**Average**	**0.4485**	**0.9784**	**0.0102**	**0.0655**	**0.2039**	**0.0298**	**0.0173**	**0.1693**	**0.0385**	**0.0268**	**0.0170**	**0.0010**	**0.0006**	**2.007**
S373-01	37	0.4260	0.9932	0.0068	0.0508	0.2260	0.0204	0.0232	0.1804	0.0212	0.0284	0.0172	0.0068	0.0020	2.002
	38	0.3948	0.9936	0.0068	0.0496	0.2096	0.0456	0.0296	0.1768	0.0380	0.0284	0.0176	0.0064	0.0056	2.003
	39	0.4140	0.9884	0.0124	0.0504	0.2216	0.0304	0.0232	0.1788	0.0320	0.0264	0.0156	0.0068	0.0024	2.002
	40	0.3904	0.9892	0.0088	0.0496	0.2144	0.0524	0.0260	0.1708	0.0480	0.0276	0.0172	0.0068	0.0036	2.005
	41	0.4196	0.9964	0.0096	0.0528	0.2164	0.0220	0.0232	0.1860	0.0208	0.0284	0.0160	0.0060	0.0024	2.000
	Average	**0.4090**	**0.9922**	**0.0089**	**0.0506**	**0.2176**	**0.0342**	**0.0250**	**0.1786**	**0.0320**	**0.0278**	**0.0167**	**0.0066**	**0.0032**	**2.002**
S373-02	43	0.3892	0.9960	0.0096	0.0468	0.2036	0.0484	0.0316	0.1736	0.0400	0.0296	0.0172	0.0088	0.0056	2.000

Mnz Grain	Analysis #	Ce	P	Si	Pr	La	Ca	Y	Nd	Th	Sm	Gd	Dy	U	Total / 4O
S373-02 (cnt'd)	44	0.3848	0.9936	0.0080	0.0460	0.2016	0.0540	0.0344	0.1740	0.0428	0.0284	0.0200	0.0092	0.0064	2.003
	45	0.3956	0.9940	0.0072	0.0468	0.1988	0.0536	0.0360	0.1696	0.0404	0.0276	0.0172	0.0088	0.0080	2.004
	46	0.3932	0.9920	0.0060	0.0488	0.2024	0.0528	0.0324	0.1708	0.0452	0.0284	0.0196	0.0080	0.0044	2.004
	47	0.3904	0.9940	0.0108	0.0448	0.1960	0.0532	0.0336	0.1740	0.0412	0.0316	0.0208	0.0056	0.0064	2.003
	Average	**0.3906**	**0.9939**	**0.0083**	**0.0466**	**0.2005**	**0.0524**	**0.0336**	**0.1724**	**0.0419**	**0.0291**	**0.0190**	**0.0081**	**0.0062**	**2.003**
S373-03	48	0.4120	0.9840	0.0116	0.0496	0.2148	0.0416	0.0216	0.1752	0.0432	0.0252	0.0180	0.0068	0.0024	2.006
	49	0.4408	0.9932	0.0056	0.0520	0.2256	0.0208	0.0168	0.1844	0.0200	0.0228	0.0144	0.0036	0.0020	2.002
	50	0.4376	0.9900	0.0044	0.0516	0.2256	0.0232	0.0220	0.1836	0.0216	0.0232	0.0152	0.0044	0.0024	2.005
	51	0.3908	0.9996	0.0036	0.0488	0.1960	0.0588	0.0352	0.1676	0.0420	0.0244	0.0176	0.0084	0.0096	2.002
	52	0.3924	0.9960	0.0044	0.0464	0.2012	0.0592	0.0348	0.1696	0.0416	0.0240	0.0168	0.0072	0.0100	2.004
	Average	**0.4147**	**0.9926**	**0.0059**	**0.0497**	**0.2126**	**0.0407**	**0.0261**	**0.1761**	**0.0337**	**0.0239**	**0.0164**	**0.0061**	**0.0053**	**2.004**
S373-04	54	0.4092	0.9848	0.0104	0.0476	0.2096	0.0404	0.0236	0.1824	0.0428	0.0268	0.0180	0.0072	0.0016	2.005
	55	0.3992	0.9856	0.0100	0.0500	0.2092	0.0476	0.0248	0.1768	0.0492	0.0268	0.0180	0.0060	0.0016	2.005
	56	0.4072	0.9880	0.0108	0.0508	0.2112	0.0360	0.0264	0.1760	0.0408	0.0280	0.0180	0.0076	0.0020	2.003
	57	0.4032	0.9944	0.0092	0.0508	0.2064	0.0372	0.0252	0.1808	0.0372	0.0284	0.0188	0.0064	0.0024	2.000
	Average	**0.4047**	**0.9882**	**0.0101**	**0.0498**	**0.2091**	**0.0403**	**0.0250**	**0.1790**	**0.0425**	**0.0275**	**0.0182**	**0.0068**	**0.0019**	**2.003**
S373-05	59	0.3944	0.9936	0.0072	0.0460	0.1972	0.0564	0.0368	0.1684	0.0412	0.0276	0.0184	0.0084	0.0088	2.005
	60	0.3976	0.9872	0.0068	0.0484	0.1992	0.0552	0.0316	0.1760	0.0460	0.0284	0.0184	0.0080	0.0056	2.008
	61	0.4148	0.9856	0.0100	0.0500	0.2100	0.0372	0.0232	0.1808	0.0404	0.0276	0.0180	0.0052	0.0016	2.005
	62	0.3856	0.9924	0.0084	0.0476	0.2032	0.0532	0.0332	0.1740	0.0432	0.0284	0.0204	0.0084	0.0056	2.004
	63	0.4012	0.9884	0.0072	0.0480	0.2156	0.0464	0.0268	0.1740	0.0424	0.0288	0.0172	0.0044	0.0048	2.006
	Average	**0.3987**	**0.9894**	**0.0079**	**0.0480**	**0.2050**	**0.0497**	**0.0303**	**0.1746**	**0.0426**	**0.0282**	**0.0185**	**0.0069**	**0.0053**	**2.006**
S373	**Average**	**0.4035**	0.9914	0.0082	0.0489	0.2090	0.0436	0.0281	0.1760	0.0384	**0.0273**	**0.0177**	**0.0069**	**0.0045**	**2.004**
S374-01	68	0.4248	0.9932	0.0060	0.0504	0.2116	0.0280	0.0268	0.1776	0.0308	0.0280	0.0152	0.0052	0.0028	2.001
	69	0.4216	0.9968	0.0044	0.0520	0.2128	0.0200	0.0244	0.1888	0.0224	0.0272	0.0200	0.0072	0.0020	2.000
	Average	**0.4122**	**0.9927**	**0.0066**	**0.0498**	**0.2096**	**0.0353**	**0.0274**	**0.1793**	**0.0336**	**0.0277**	**0.0179**	**0.0065**	**0.0036**	**2.001**
S374-02	71	0.4032	0.9940	0.0060	0.0508	0.2000	0.0488	0.0272	0.1720	0.0408	0.0276	0.0184	0.0088	0.0048	2.003
	72	0.4052	0.9940	0.0080	0.0508	0.2000	0.0428	0.0272	0.1744	0.0412	0.0272	0.0196	0.0064	0.0048	2.002
	73	0.4120	0.9868	0.0132	0.0476	0.1940	0.0424	0.0280	0.1744	0.0476	0.0268	0.0196	0.0064	0.0020	2.001
	74	0.4312	0.9888	0.0064	0.0520	0.2072	0.0268	0.0280	0.1808	0.0292	0.0276	0.0168	0.0080	0.0012	2.004
	75	0.4212	0.9904	0.0076	0.0492	0.2128	0.0284	0.0208	0.1824	0.0296	0.0312	0.0212	0.0064	0.0016	2.003
	Average	**0.4146**	**0.9908**	**0.0082**	**0.0501**	**0.2028**	**0.0378**	**0.0262**	**0.1768**	**0.0377**	**0.0281**	**0.0191**	**0.0072**	**0.0029**	**2.003**
S374-03	77	0.4108	0.9856	0.0104	0.0500	0.2116	0.0344	0.0260	0.1824	0.0360	0.0276	0.0220	0.0064	0.0020	2.006

Mnz Grain	Analysis #	Ce	P	Si	Pr	La	Ca	Y	Nd	Th	Sm	Gd	Dy	U	Total / 4O
S374-03 (cnt'd)	78	0.4176	0.9864	0.0080	0.0512	0.2128	0.0316	0.0244	0.1792	0.0352	0.0288	0.0196	0.0076	0.0020	2.005
	79	0.4080	0.9856	0.0124	0.0508	0.2064	0.0392	0.0252	0.1748	0.0480	0.0260	0.0184	0.0060	0.0012	2.002
	80	0.4052	0.9924	0.0108	0.0500	0.2116	0.0384	0.0216	0.1776	0.0404	0.0260	0.0200	0.0056	0.0008	2.000
	81	0.4096	0.9848	0.0108	0.0492	0.2040	0.0424	0.0212	0.1776	0.0496	0.0272	0.0200	0.0052	0.0020	2.004
	Average	**0.4102**	**0.9870**	**0.0105**	**0.0502**	**0.2093**	**0.0372**	**0.0237**	**0.1783**	**0.0418**	**0.0271**	**0.0200**	**0.0062**	**0.0016**	**2.003**
S374-04	82	0.4152	0.9860	0.0112	0.0496	0.2060	0.0368	0.0252	0.1804	0.0424	0.0268	0.0172	0.0040	0.0020	2.003
	83	0.4448	0.9920	0.0048	0.0500	0.2384	0.0204	0.0208	0.1756	0.0196	0.0208	0.0116	0.0036	0.0016	2.004
	84	0.3976	0.9964	0.0044	0.0480	0.2092	0.0476	0.0264	0.1756	0.0424	0.0256	0.0184	0.0044	0.0044	2.001
	85	0.4020	0.9872	0.0128	0.0480	0.1996	0.0468	0.0268	0.1784	0.0516	0.0248	0.0164	0.0052	0.0024	2.002
	86	0.4220	0.9840	0.0084	0.0508	0.2028	0.0332	0.0256	0.1860	0.0372	0.0300	0.0188	0.0052	0.0016	2.006
	Average	**0.4163**	**0.9891**	**0.0083**	**0.0493**	**0.2112**	**0.0370**	**0.0250**	**0.1792**	**0.0386**	**0.0256**	**0.0165**	**0.0045**	**0.0024**	**2.003**
S374-05	88	0.4120	0.9924	0.0072	0.0512	0.2188	0.0280	0.0252	0.1816	0.0280	0.0260	0.0200	0.0092	0.0020	2.002
	89	0.3936	0.9868	0.0056	0.0496	0.1952	0.0564	0.0396	0.1760	0.0412	0.0260	0.0200	0.0084	0.0100	2.008
	90	0.3908	0.9920	0.0072	0.0464	0.2032	0.0484	0.0300	0.1784	0.0448	0.0284	0.0192	0.0088	0.0048	2.002
	91	0.3880	0.9940	0.0044	0.0480	0.1936	0.0544	0.0396	0.1748	0.0420	0.0260	0.0192	0.0100	0.0096	2.004
	92	0.3916	0.9900	0.0128	0.0468	0.1992	0.0476	0.0288	0.1756	0.0508	0.0300	0.0180	0.0076	0.0020	2.001
	Average	**0.3952**	**0.9910**	**0.0074**	**0.0484**	**0.2020**	**0.0470**	**0.0326**	**0.1773**	**0.0414**	**0.0273**	**0.0193**	**0.0088**	**0.0057**	**2.004**
S374-06	93	0.4156	0.9848	0.0092	0.0464	0.2136	0.0368	0.0208	0.1804	0.0388	0.0288	0.0208	0.0072	0.0020	2.005
	94	0.4152	0.9916	0.0080	0.0480	0.2008	0.0360	0.0288	0.1812	0.0364	0.0284	0.0180	0.0072	0.0020	2.002
	95	0.4180	0.9908	0.0072	0.0460	0.2028	0.0368	0.0216	0.1824	0.0372	0.0300	0.0204	0.0076	0.0020	2.003
	96	0.4224	0.9896	0.0080	0.0492	0.2012	0.0344	0.0260	0.1832	0.0352	0.0276	0.0196	0.0064	0.0012	2.004
	Average	**0.4178**	**0.9892**	**0.0081**	**0.0474**	**0.2046**	**0.0360**	**0.0243**	**0.1818**	**0.0369**	**0.0287**	**0.0197**	**0.0071**	**0.0018**	**2.004**
S374	**Average**	**0.4108**	**0.9896**	**0.0084**	**0.0493**	**0.2069**	**0.0383**	**0.0265**	**0.1789**	**0.0384**	**0.0274**	**0.0190**	**0.0067**	**0.0030**	**2.003**
S375-01	308	0.4464	0.9736	0.0020	0.0620	0.1872	0.0576	0.0252	0.1440	0.0624	0.0264	0.0180	0.0000	0.0084	2.013
	309	0.4404	0.9820	0.0028	0.0604	0.1768	0.0608	0.0288	0.1408	0.0612	0.0256	0.0180	0.0000	0.0108	2.008
	310	0.4724	0.9700	0.0040	0.0712	0.1896	0.0348	0.0188	0.1564	0.0468	0.0300	0.0168	0.0000	0.0032	2.014
	Average	**0.4531**	**0.9752**	**0.0029**	**0.0645**	**0.1845**	**0.0511**	**0.0243**	**0.1471**	**0.0568**	**0.0273**	**0.0176**	**0.0000**	**0.0075**	**2.012**
S375-02	311	0.4772	0.9824	0.0012	0.0624	0.1924	0.0368	0.0304	0.1480	0.0292	0.0244	0.0172	0.0000	0.0096	2.012
	312	0.5300	0.9820	0.0028	0.0696	0.2120	0.0116	0.0128	0.1452	0.0140	0.0204	0.0096	0.0000	0.0000	2.010
	313	0.5280	0.9784	0.0032	0.0708	0.2116	0.0104	0.0116	0.1528	0.0128	0.0200	0.0120	0.0000	0.0004	2.012
	Average	**0.5117**	**0.9809**	**0.0024**	**0.0676**	**0.2053**	**0.0196**	**0.0183**	**0.1487**	**0.0187**	**0.0216**	**0.0129**	**0.0000**	**0.0033**	**2.011**
S375-03	314	0.5360	0.9680	0.0144	0.0608	0.2560	0.0056	0.0076	0.1192	0.0244	0.0116	0.0060	0.0000	0.0004	2.010
	315	0.5188	0.9660	0.0220	0.0552	0.2504	0.0092	0.0196	0.1128	0.0344	0.0112	0.0076	0.0000	0.0000	2.008

Mnz Grain	Analysis #	Ce	P	Si	Pr	La	Ca	Y	Nd	Th	Sm	Gd	Dy	U	Total / 4O
S375-03 (cnt'd)	316	0.4836	0.9752	0.0016	0.0596	0.2216	0.0384	0.0272	0.1252	0.0400	0.0188	0.0144	0.0000	0.0076	2.014
	Average	**0.5128**	**0.9697**	**0.0127**	**0.0585**	**0.2427**	**0.0177**	**0.0181**	**0.1191**	**0.0329**	**0.0139**	**0.0093**	**0.0000**	**0.0027**	**2.011**
S375-04	317	0.5128	0.9868	0.0020	0.0604	0.2980	0.0044	0.0084	0.1188	0.0008	0.0100	0.0064	0.0000	0.0004	2.010
	318	0.4956	0.9876	0.0000	0.0556	0.2892	0.0080	0.0180	0.1248	0.0032	0.0164	0.0116	0.0000	0.0000	2.010
	319	0.4832	0.9932	0.0012	0.0624	0.2352	0.0196	0.0216	0.1336	0.0084	0.0224	0.0156	0.0000	0.0084	2.005
	320	0.5104	0.9868	0.0000	0.0588	0.2976	0.0048	0.0088	0.1252	0.0008	0.0124	0.0044	0.0000	0.0000	2.010
	Average	**0.5005**	**0.9886**	**0.0008**	**0.0593**	**0.2800**	**0.0092**	**0.0142**	**0.1256**	**0.0033**	**0.0153**	**0.0095**	**0.0000**	**0.0022**	**2.009**
S375-06	*360	0.4672	0.9464	0.0000	0.0656	0.1984	0.0564	0.0260	0.1520	0.0608	0.0244	0.0172	0.0000	0.0032	2.030
	*361	0.4680	0.9412	0.0104	0.0664	0.1900	0.0456	0.0236	0.1600	0.0680	0.0280	0.0196	0.0000	0.0072	2.026
	*362	0.4544	0.9544	0.0040	0.0636	0.1920	0.0640	0.0292	0.1508	0.0612	0.0256	0.0164	0.0000	0.0124	2.026
	363	0.4496	0.9616	0.0036	0.0680	0.1880	0.0624	0.0272	0.1452	0.0600	0.0252	0.0184	0.0000	0.0120	2.021
	*364	0.4788	0.9732	0.0084	0.0640	0.1984	0.0448	0.0208	0.1540	0.0504	0.0264	0.0188	0.0000	0.0064	2.025
	Average	**0.4496**	**0.9616**	**0.0036**	**0.0680**	**0.1880**	**0.0624**	**0.0272**	**0.1452**	**0.0600**	**0.0252**	**0.0184**	**0.0000**	**0.0120**	**2.021**
S375-07	365	0.4812	0.9604	0.0076	0.0656	0.2256	0.0304	0.0216	0.1536	0.0376	0.0224	0.0120	0.0000	0.0024	2.021
	366	0.4740	0.9536	0.0092	0.0676	0.2116	0.0388	0.0152	0.1564	0.0544	0.0240	0.0152	0.0000	0.0020	2.022
	367	0.4644	0.9484	0.0104	0.0724	0.1944	0.0448	0.0160	0.1604	0.0656	0.0268	0.0176	0.0000	0.0028	2.024
	Average	**0.4732**	**0.9541**	**0.0091**	**0.0685**	**0.2105**	**0.0380**	**0.0176**	**0.1568**	**0.0525**	**0.0244**	**0.0149**	**0.0000**	**0.0024**	**2.022**
S375-08	368	0.4336	0.9584	0.0048	0.0676	0.1872	0.0652	0.0272	0.1488	0.0712	0.0284	0.0180	0.0000	0.0104	2.021
	369	0.4324	0.9656	0.0044	0.0624	0.1844	0.0652	0.0324	0.1444	0.0688	0.0256	0.0196	0.0000	0.0104	2.016
	*370	0.4668	0.9472	0.0080	0.0680	0.1904	0.0472	0.0172	0.1640	0.0644	0.0292	0.0200	0.0000	0.0036	2.026
	*371	0.4696	0.9492	0.0080	0.0708	0.1936	0.0420	0.0188	0.1660	0.0556	0.0280	0.0212	0.0000	0.0028	2.026
	Average	**0.4330**	**0.9620**	**0.0046**	**0.0650**	**0.1858**	**0.0652**	**0.0298**	**0.1466**	**0.0700**	**0.0270**	**0.0188**	**0.0000**	**0.0104**	**2.018**
S375-09	372	0.4420	0.9564	0.0032	0.0620	0.1848	0.0676	0.0260	0.1548	0.0664	0.0300	0.0188	0.0000	0.0120	2.024
	373	0.4856	0.9588	0.0040	0.0692	0.1960	0.0336	0.0184	0.1628	0.0416	0.0308	0.0192	0.0000	0.0028	2.023
	374	0.4776	0.9600	0.0040	0.0664	0.1936	0.0420	0.0172	0.1616	0.0472	0.0288	0.0188	0.0000	0.0052	2.022
	375	0.4876	0.9564	0.0036	0.0752	0.1980	0.0256	0.0200	0.1716	0.0344	0.0324	0.0172	0.0000	0.0024	2.024
	*376	0.4744	0.9512	0.0032	0.0696	0.1936	0.0492	0.0276	0.1548	0.0504	0.0288	0.0176	0.0000	0.0076	2.028
	Average	**0.4732**	**0.9579**	**0.0037**	**0.0682**	**0.1931**	**0.0422**	**0.0204**	**0.1627**	**0.0474**	**0.0305**	**0.0185**	**0.0000**	**0.0056**	**2.024**
S375-10	377	0.4816	0.9616	0.0064	0.0708	0.1940	0.0284	0.0196	0.1628	0.0380	0.0336	0.0208	0.0000	0.0020	2.020
	*378	0.4868	0.9512	0.0072	0.0700	0.1984	0.0332	0.0228	0.1652	0.0444	0.0292	0.0148	0.0000	0.0020	2.035
	*379	0.4808	0.9380	0.0088	0.0708	0.2028	0.0264	0.0212	0.1612	0.0532	0.0268	0.0144	0.0000	0.0020	2.037
	*380	0.4964	0.9480	0.0072	0.0716	0.2160	0.0264	0.0172	0.1616	0.0420	0.0252	0.0132	0.0000	0.0016	2.027
	381	0.4720	0.9492	0.0120	0.0660	0.2144	0.0396	0.0180	0.1524	0.0596	0.0220	0.0148	0.0000	0.0028	2.023

Mnz Grain	Analysis #	Ce	P	Si	Pr	La	Ca	Y	Nd	Th	Sm	Gd	Dy	U	Total / 4O
S375-10 (cnt'd)	Average	0.4768	0.9554	0.0092	0.0684	0.2042	0.0340	0.0188	0.1576	0.0488	0.0278	0.0178	0.0000	0.0024	2.021
S375-11	175	0.4280	1.0400	0.0036	0.0468	0.2028	0.0148	0.0012	0.1524	0.0296	0.0236	0.0148	0.0036	0.0044	1.966
	176	0.4400	1.0188	0.0036	0.0504	0.2056	0.0108	0.0016	0.1616	0.0320	0.0272	0.0164	0.0072	0.0032	1.979
	177	0.4424	1.0176	0.0040	0.0512	0.2052	0.0152	0.0016	0.1604	0.0284	0.0284	0.0164	0.0060	0.0044	1.982
	178	0.4580	0.9976	0.0032	0.0508	0.2092	0.0164	0.0020	0.1712	0.0280	0.0284	0.0204	0.0064	0.0036	1.996
	179	0.4328	1.0232	0.0040	0.0504	0.1976	0.0120	0.0016	0.1648	0.0304	0.0292	0.0184	0.0064	0.0044	1.976
	Average	0.4402	1.0194	0.0037	0.0499	0.2041	0.0138	0.0016	0.1621	0.0297	0.0274	0.0173	0.0059	0.0040	1.979
S375-12	181	0.4532	1.0084	0.0036	0.0524	0.1984	0.0228	0.0020	0.1644	0.0252	0.0280	0.0184	0.0088	0.0048	1.990
	182	0.4160	1.0312	0.0064	0.0516	0.1992	0.0096	0.0016	0.1732	0.0256	0.0296	0.0192	0.0080	0.0008	1.972
	183	0.4356	1.0272	0.0068	0.0528	0.1896	0.0124	0.0012	0.1728	0.0260	0.0276	0.0160	0.0056	0.0008	1.975
	184	0.4256	1.0452	0.0040	0.0488	0.2068	0.0080	0.0008	0.1632	0.0136	0.0252	0.0164	0.0064	0.0020	1.966
	Average	0.4326	1.0280	0.0052	0.0514	0.1985	0.0132	0.0014	0.1684	0.0226	0.0276	0.0175	0.0072	0.0021	1.976
S375-13	*186	0.4008	1.0368	0.0056	0.0464	0.1920	0.0296	0.0024	0.1548	0.0436	0.0264	0.0192	0.0032	0.0060	1.967
	*187	0.3988	1.0504	0.0032	0.0460	0.1892	0.0260	0.0020	0.1536	0.0384	0.0260	0.0184	0.0012	0.0044	1.960
	*188	0.3988	1.0492	0.0044	0.0480	0.1860	0.0272	0.0016	0.1552	0.0388	0.0248	0.0150	0.0020	0.0060	1.960
	*189	0.4032	1.0528	0.0068	0.0452	0.1564	0.0204	0.0016	0.1548	0.0352	0.0260	0.0192	0.0008	0.0036	1.956
	Average	-	-	-	-	-	-	-	-	-	-	-	-	-	-
S375	Average	0.4691	0.9833	0.0060	0.0611	0.2119	0.0285	0.0150	0.1502	0.0359	0.0243	0.0154	0.0017	0.0043	2.006
S378-01	248	0.4456	0.9668	0.0164	0.0680	0.1820	0.0384	0.0212	0.1548	0.0656	0.0276	0.0204	0.0000	0.0000	2.007
	249	0.4284	0.9784	0.0136	0.0624	0.1724	0.0584	0.0292	0.1392	0.0716	0.0284	0.0200	0.0000	0.0024	2.005
	Average	0.4370	0.9726	0.0150	0.0652	0.1772	0.0484	0.0252	0.1470	0.0686	0.0280	0.0202	0.0000	0.0012	2.006
S378-02	250	0.4516	0.9632	0.0168	0.0644	0.1792	0.0436	0.0204	0.1480	0.0736	0.0284	0.0196	0.0000	0.0000	2.009
	251	0.4424	0.9600	0.0168	0.0676	0.1800	0.0440	0.0196	0.1536	0.0768	0.0284	0.0204	0.0000	0.0008	2.011
	Average	0.4470	0.9616	0.0168	0.0660	0.1796	0.0438	0.0200	0.1508	0.0752	0.0284	0.0200	0.0000	0.0004	2.010
S378-03	252	0.4592	0.9740	0.0104	0.0676	0.1832	0.0360	0.0216	0.1520	0.0540	0.0284	0.0208	0.0000	0.0004	2.008
	253	0.4296	0.9776	0.0092	0.0684	0.1724	0.0644	0.0304	0.1356	0.0756	0.0232	0.0192	0.0000	0.0020	2.008
	254	0.4780	0.9752	0.0100	0.0708	0.1952	0.0220	0.0220	0.1572	0.0308	0.0288	0.0208	0.0000	0.0000	2.011
	Average	0.4556	0.9756	0.0099	0.0689	0.1836	0.0408	0.0247	0.1483	0.0535	0.0268	0.0203	0.0000	0.0008	2.009
S378-04	255	0.4688	0.9660	0.0124	0.0672	0.1884	0.0380	0.0152	0.1504	0.0588	0.0256	0.0204	0.0000	0.0000	2.011
	256	0.4700	0.9628	0.0176	0.0708	0.1908	0.0344	0.0156	0.1496	0.0532	0.0280	0.0188	0.0000	0.0004	2.012
	257	0.4536	0.9564	0.0312	0.0704	0.1824	0.0412	0.0196	0.1552	0.0572	0.0264	0.0200	0.0000	0.0000	2.014
	Average	0.4641	0.9617	0.0204	0.0695	0.1872	0.0379	0.0168	0.1517	0.0564	0.0267	0.0197	0.0000	0.0001	2.012
S378-05	258	0.4648	0.9752	0.0060	0.0696	0.1840	0.0352	0.0200	0.1520	0.0520	0.0292	0.0204	0.0000	0.0004	2.009

Mnz Grain	Analysis #	Ce	P	Si	Pr	La	Ca	Y	Nd	Th	Sm	Gd	Dy	U	Total / 4O
S378-05 (cnt'd)	259	0.4652	0.9740	0.0084	0.0728	0.1924	0.0296	0.0184	0.1544	0.0464	0.0292	0.0176	0.0000	0.0000	2.008
	260	0.4596	0.9852	0.0060	0.0736	0.1884	0.0280	0.0188	0.1504	0.0448	0.0292	0.0180	0.0000	0.0000	2.002
	Average	**0.4632**	**0.9781**	**0.0068**	**0.0720**	**0.1883**	**0.0309**	**0.0191**	**0.1523**	**0.0477**	**0.0292**	**0.0187**	0.0000	**0.0001**	**2.007**
S378-06	261	0.4632	0.9864	0.0076	0.0712	0.1784	0.0296	0.0200	0.1572	0.0412	0.0264	0.0180	0.0000	0.0000	2.001
	262	0.4688	0.9872	0.0060	0.0696	0.1836	0.0244	0.0188	0.1584	0.0360	0.0308	0.0192	0.0000	0.0000	2.003
	263	0.4556	0.9740	0.0092	0.0724	0.1824	0.0392	0.0200	0.1548	0.0540	0.0276	0.0204	0.0000	0.0000	2.010
	Average	**0.4625**	**0.9832**	**0.0076**	**0.0711**	**0.1815**	**0.0311**	**0.0196**	**0.1568**	**0.0437**	**0.0283**	**0.0192**	**0.0000**	**0.0000**	**2.005**
S378-08	324	0.4400	0.9612	0.0132	0.0648	0.1836	0.0496	0.0256	0.1460	0.0824	0.0264	0.0160	0.0000	0.0008	2.010
	325	0.4668	0.9664	0.0072	0.0720	0.1908	0.0304	0.0204	0.1556	0.0544	0.0292	0.0192	0.0000	0.0000	2.012
	326	0.4520	0.9612	0.0064	0.0628	0.1868	0.0528	0.0268	0.1496	0.0680	0.0292	0.0164	0.0000	0.0044	2.017
	327	0.4632	0.9792	0.0056	0.0716	0.1884	0.0248	0.0256	0.1612	0.0388	0.0292	0.0200	0.0000	0.0000	2.008
	Average	**0.4555**	**0.9670**	**0.0081**	**0.0678**	**0.1874**	**0.0394**	**0.0246**	**0.1531**	**0.0609**	**0.0285**	**0.0179**	**0.0000**	**0.0013**	**2.012**
S378	**Average**	**0.4563**	**0.9716**	**0.0115**	**0.0689**	**0.1842**	**0.0382**	**0.0215**	**0.1518**	**0.0568**	**0.0280**	**0.0193**	**0.0000**	**0.0006**	**2.009**
S383-01 rim	547	0.4092	0.9748	0.0032	0.0588	0.1796	0.0660	0.0532	0.1392	0.0700	0.0260	0.0220	0.0000	0.0084	2.011
	551	0.4052	0.9784	0.0024	0.0592	0.1832	0.0668	0.0476	0.1420	0.0708	0.0252	0.0200	0.0000	0.0084	2.010
	552	0.4076	0.9768	0.0028	0.0648	0.1788	0.0672	0.0504	0.1400	0.0696	0.0268	0.0188	0.0000	0.0076	2.011
	Average	**0.4073**	**0.9767**	**0.0028**	**0.0609**	**0.1805**	**0.0667**	**0.0504**	**0.1404**	**0.0701**	**0.0260**	**0.0203**	**0.0000**	**0.0081**	**2.011**
S383-01 core	548	0.4296	0.9676	0.0108	0.0640	0.1924	0.0528	0.0332	0.1464	0.0708	0.0228	0.0180	0.0000	0.0020	2.011
	549	0.4324	0.9700	0.0108	0.0644	0.1832	0.0516	0.0320	0.1456	0.0720	0.0276	0.0160	0.0000	0.0024	2.009
	550	0.4352	0.9640	0.0108	0.0612	0.1848	0.0572	0.0328	0.1452	0.0756	0.0264	0.0164	0.0000	0.0032	2.013
	Average	**0.4324**	**0.9672**	**0.0108**	**0.0632**	**0.1868**	**0.0539**	**0.0327**	**0.1457**	**0.0728**	**0.0256**	**0.0168**	**0.0000**	**0.0025**	**2.011**
S383-01	Average	**0.4199**	**0.9719**	0.0068	**0.0621**	**0.1837**	**0.0603**	**0.0415**	**0.1431**	**0.0715**	**0.0258**	**0.0185**	0.0000	**0.0053**	**2.011**
S383-02	553	0.4796	0.9796	0.0040	0.0648	0.2188	0.0244	0.0292	0.1392	0.0320	0.0216	0.0160	0.0000	0.0008	2.010
	554	0.4504	0.9740	0.0092	0.0624	0.2072	0.0352	0.0352	0.1404	0.0496	0.0264	0.0160	0.0000	0.0024	2.009
	555	0.4520	0.9836	0.0040	0.0640	0.2108	0.0412	0.0288	0.1356	0.0452	0.0204	0.0156	0.0000	0.0052	2.006
	556	0.4760	0.9824	0.0056	0.0616	0.2212	0.0220	0.0304	0.1412	0.0280	0.0224	0.0152	0.0000	0.0012	2.008
	557	0.4700	0.9812	0.0032	0.0672	0.2128	0.0244	0.0324	0.1400	0.0324	0.0248	0.0168	0.0000	0.0028	2.008
	Average	**0.4656**	0.9802	**0.0052**	**0.0640**	**0.2142**	**0.0294**	**0.0312**	**0.1393**	**0.0374**	**0.0231**	**0.0159**	**0.0000**	**0.0025**	**2.008**
S383-03	559	0.4624	0.9760	0.0080	0.0652	0.2096	0.0256	0.0348	0.1464	0.0368	0.0248	0.0180	0.0000	0.0012	2.009
	560	0.4676	0.9800	0.0068	0.0648	0.2076	0.0260	0.0320	0.1428	0.0372	0.0224	0.0184	0.0000	0.0012	2.007
	561	0.4652	0.9784	0.0080	0.0632	0.2056	0.0272	0.0344	0.1408	0.0408	0.0236	0.0164	0.0000	0.0024	2.006
	562	0.4692	0.9680	0.0080	0.0624	0.2088	0.0344	0.0320	0.1420	0.0476	0.0244	0.0140	0.0000	0.0032	2.013
	563	0.4256	0.9756	0.0048	0.0588	0.1904	0.0624	0.0412	0.1392	0.0612	0.0232	0.0188	0.0000	0.0112	2.012

Mnz Grain	Analysis #	Ce	P	Si	Pr	La	Ca	Y	Nd	Th	Sm	Gd	Dy	U	Total / 4O
S383-03 (cnt'd)	Average	0.4580	0.9756	0.0071	0.0629	0.2044	0.0351	0.0349	0.1422	0.0447	0.0237	0.0171	0.0000	0.0038	2.009
S383-04 rim	565	0.4320	0.9760	0.0032	0.0540	0.1844	0.0636	0.0448	0.1408	0.0632	0.0224	0.0172	0.0000	0.0100	2.012
	566	0.4212	0.9796	0.0036	0.0576	0.1816	0.0604	0.0464	0.1400	0.0656	0.0240	0.0180	0.0000	0.0092	2.008
	569	0.4244	0.9736	0.0056	0.0548	0.1772	0.0676	0.0448	0.1408	0.0708	0.0228	0.0184	0.0000	0.0100	2.011
	570	0.4128	0.9856	0.0036	0.0592	0.1768	0.0644	0.0556	0.1348	0.0644	0.0192	0.0180	0.0000	0.0108	2.005
	Average	0.4226	0.9787	0.0040	0.0564	0.1800	0.0640	0.0479	0.1391	0.0660	0.0221	0.0179	0.0000	0.0100	2.009
S383-04 core	567	0.4548	0.9624	0.0172	0.0604	0.2012	0.0372	0.0332	0.1436	0.0608	0.0220	0.0152	0.0000	0.0028	2.010
	568	0.4464	0.9652	0.0124	0.0592	0.1928	0.0376	0.0392	0.1552	0.0548	0.0284	0.0172	0.0000	0.0032	2.012
	Average	0.4506	0.9638	0.0148	0.0598	0.1970	0.0374	0.0362	0.1494	0.0578	0.0252	0.0162	0.0000	0.0030	2.011
S383-04	Average	0.4319	0.9737	0.0076	0.0575	0.1857	0.0551	0.0440	0.1425	0.0633	0.0231	0.0173	0.0000	0.0077	2.010
S383-05 rim	571	0.4248	0.9788	0.0028	0.0556	0.1840	0.0612	0.0524	0.1412	0.0644	0.0208	0.0160	0.0000	0.0076	2.010
	572	0.4216	0.9816	0.0032	0.0556	0.1808	0.0644	0.0524	0.1368	0.0656	0.0228	0.0148	0.0000	0.0084	2.008
	576	0.4176	0.9768	0.0028	0.0572	0.1772	0.0656	0.0572	0.1380	0.0688	0.0232	0.0164	0.0000	0.0092	2.010
	Average	0.4213	0.9791	0.0029	0.0561	0.1807	0.0637	0.0540	0.1387	0.0663	0.0223	0.0157	0.0000	0.0084	2.009
S383-05 core	573	0.4600	0.9756	0.0088	0.0624	0.2004	0.0288	0.0280	0.1564	0.0424	0.0252	0.0176	0.0000	0.0024	2.008
	574	0.4320	0.9488	0.0184	0.0580	0.1808	0.0520	0.0372	0.1524	0.0840	0.0276	0.0200	0.0000	0.0044	2.016
	575	0.4372	0.9692	0.0040	0.0584	0.1860	0.0656	0.0320	0.1424	0.0700	0.0228	0.0176	0.0000	0.0092	2.015
	Average	0.4431	0.9645	0.0104	0.0596	0.1891	0.0488	0.0324	0.1504	0.0655	0.0252	0.0184	0.0000	0.0053	2.013
S383-05	Average	0.4322	0.9718	0.0067	0.0579	0.1849	0.0563	0.0432	0.1445	0.0659	0.0237	0.0171	0.0000	0.0069	2.011
S383-06 rim	577	0.4300	0.9720	0.0032	0.0576	0.1832	0.0620	0.0532	0.1396	0.0620	0.0244	0.0180	0.0000	0.0092	2.014
	578	0.4364	0.9764	0.0024	0.0572	0.1824	0.0564	0.0528	0.1392	0.0576	0.0236	0.0188	0.0000	0.0084	2.012
	579	0.4288	0.9776	0.0036	0.0580	0.1848	0.0624	0.0456	0.1368	0.0620	0.0224	0.0192	0.0000	0.0092	2.011
	Average	0.4317	0.9753	0.0031	0.0576	0.1835	0.0603	0.0505	0.1385	0.0605	0.0235	0.0187	0.0000	0.0089	2.012
S383-06 core	580	0.4516	0.9664	0.0140	0.0644	0.1956	0.0384	0.0292	0.1488	0.0600	0.0212	0.0180	0.0000	0.0024	2.010
	581	0.4732	0.9676	0.0092	0.0628	0.2020	0.0308	0.0284	0.1552	0.0452	0.0232	0.0136	0.0000	0.0020	2.013
	582	0.4540	0.9652	0.0120	0.0644	0.1968	0.0352	0.0308	0.1492	0.0560	0.0264	0.0184	0.0000	0.0024	2.012
	Average	0.4596	0.9664	0.0117	0.0639	0.1981	0.0348	0.0295	0.1511	0.0537	0.0236	0.0167	0.0000	0.0023	2.012
S383-06	Average	0.4457	0.9709	0.0074	0.0607	0.1908	0.0475	0.0400	0.1448	0.0571	0.0235	0.0177	0.0000	0.0056	2.012
S383-07 rim	587	0.4192	0.9728	0.0040	0.0620	0.1740	0.0636	0.0528	0.1416	0.0684	0.0256	0.0192	0.0000	0.0088	2.012
	588	0.4196	0.9728	0.0040	0.0620	0.1780	0.0632	0.0540	0.1400	0.0660	0.0264	0.0196	0.0000	0.0080	2.013
	Average	0.4194	0.9728	0.0040	0.0620	0.1760	0.0634	0.0534	0.1408	0.0672	0.0260	0.0194	0.0000	0.0084	2.013
S383-07 core	584	0.4432	0.9564	0.0196	0.0660	0.1872	0.0392	0.0296	0.1536	0.0716	0.0272	0.0168	0.0000	0.0012	2.011
	585	0.4676	0.9704	0.0084	0.0672	0.1936	0.0276	0.0276	0.1616	0.0416	0.0276	0.0180	0.0000	0.0008	2.012

Mnz Grain	Analysis #	Ce	P	Si	Pr	La	Ca	Y	Nd	Th	Sm	Gd	Dy	U	Total / 4O
S383-07 core (cnt'd)	586	0.4292	0.9696	0.0052	0.0592	0.1856	0.0672	0.0352	0.1388	0.0760	0.0260	0.0124	0.0000	0.0080	2.013
	Average	**0.4467**	**0.9655**	**0.0111**	**0.0641**	**0.1888**	**0.0447**	**0.0308**	**0.1513**	**0.0631**	**0.0269**	**0.0157**	**0.0000**	**0.0033**	**2.012**
S383-07	**Average**	**0.4358**	**0.9684**	**0.0082**	**0.0633**	**0.1837**	**0.0522**	**0.0398**	**0.1471**	**0.0647**	**0.0266**	**0.0172**	**0.0000**	**0.0054**	**2.012**
S383-08 rim	592	0.4176	0.9736	0.0084	0.0608	0.1800	0.0628	0.0508	0.1412	0.0656	0.0252	0.0076	0.0000	0.0168	2.011
	593	0.4180	0.9696	0.0048	0.0592	0.1744	0.0732	0.0504	0.1380	0.0716	0.0260	0.0112	0.0000	0.0180	2.015
	Average	**0.4178**	**0.9716**	**0.0066**	**0.0600**	**0.1772**	**0.0680**	**0.0506**	**0.1396**	**0.0686**	**0.0256**	**0.0094**	**0.0000**	**0.0174**	**2.013**
S383-08 core	589	0.4316	0.9564	0.0184	0.0612	0.1776	0.0536	0.0356	0.1536	0.0772	0.0272	0.0200	0.0000	0.0024	2.014
	590	0.4676	0.9616	0.0116	0.0744	0.1964	0.0304	0.0272	0.1576	0.0440	0.0256	0.0008	0.0000	0.0192	2.017
	591	0.4564	0.9644	0.0128	0.0660	0.1988	0.0424	0.0268	0.1484	0.0560	0.0248	0.0008	0.0000	0.0160	2.014
	Average	**0.4519**	**0.9608**	**0.0143**	**0.0672**	**0.1909**	**0.0421**	**0.0299**	**0.1532**	**0.0591**	**0.0259**	**0.0072**	**0.0000**	**0.0125**	**2.015**
S383-08	**Average**	**0.4382**	**0.9651**	**0.0112**	**0.0643**	**0.1854**	**0.0525**	**0.0382**	**0.1478**	**0.0629**	**0.0258**	**0.0081**	**0.0000**	**0.0145**	**2.014**
S383-09 rim	594	0.4264	0.9748	0.0036	0.0584	0.1812	0.0660	0.0452	0.1444	0.0588	0.0260	0.0112	0.0000	0.0172	2.014
	597	0.4284	0.9740	0.0040	0.0592	0.1792	0.0668	0.0472	0.1424	0.0572	0.0272	0.0116	0.0000	0.0180	2.015
	599	0.4268	0.9724	0.0044	0.0580	0.1784	0.0664	0.0472	0.1432	0.0604	0.0272	0.0100	0.0000	0.0212	2.016
	Average	**0.4272**	**0.9737**	**0.0040**	**0.0585**	**0.1796**	**0.0664**	**0.0465**	**0.1433**	**0.0588**	**0.0268**	**0.0109**	**0.0000**	**0.0188**	**2.015**
S383-09 core	595	0.4436	0.9708	0.0064	0.0636	0.1916	0.0564	0.0332	0.1440	0.0596	0.0236	0.0060	0.0000	0.0156	2.015
	596	0.4564	0.9624	0.0136	0.0644	0.1952	0.0400	0.0380	0.1520	0.0484	0.0260	0.0020	0.0000	0.0192	2.018
	598	0.4516	0.9684	0.0120	0.0656	0.1936	0.0452	0.0380	0.1464	0.0516	0.0236	0.0020	0.0000	0.0160	2.014
	Average	**0.4505**	**0.9672**	**0.0107**	**0.0645**	**0.1935**	**0.0472**	**0.0364**	**0.1475**	**0.0532**	**0.0244**	**0.0033**	**0.0000**	**0.0169**	**2.016**
S383-09	**Average**	**0.4389**	**0.9705**	**0.0073**	**0.0615**	**0.1865**	**0.0568**	**0.0415**	**0.1454**	**0.0560**	**0.0256**	**0.0071**	**0.0000**	**0.0179**	**2.015**
S383	**Average**	**0.4400**	**0.9720**	**0.0075**	**0.0614**	**0.1906**	**0.0500**	**0.0396**	**0.1441**	**0.0586**	**0.0245**	**0.0152**	**0.0000**	**0.0078**	**2.011**
S384-01	166	0.4152	0.9692	0.0036	0.0760	0.1944	0.0532	0.0528	0.1584	0.0500	0.0268	0.0180	0.0000	0.0020	2.020
	*167	0.4376	0.9520	0.0036	0.0740	0.1592	0.0556	0.0556	0.1608	0.0508	0.0300	0.0200	0.0000	0.0016	2.032
	168	0.4496	0.9684	0.0024	0.0724	0.1988	0.0464	0.0496	0.1524	0.0352	0.0288	0.0168	0.0000	0.0024	2.023
	Average	**0.4324**	**0.9688**	**0.0030**	**0.0742**	**0.1966**	**0.0498**	**0.0512**	**0.1554**	**0.0426**	**0.0278**	**0.0174**	**0.0000**	**0.0022**	**2.021**
S384-02	172	0.4340	0.9764	0.0048	0.0676	0.1792	0.0516	0.0524	0.1588	0.0396	0.0292	0.0192	0.0000	0.0032	2.019
	173	0.4260	0.9748	0.0036	0.0692	0.1980	0.0520	0.0496	0.1516	0.0400	0.0288	0.0204	0.0000	0.0028	2.020
	*174	0.4380	0.9684	0.0036	0.0568	0.1848	0.0524	0.0640	0.1540	0.0372	0.0264	0.0208	0.0000	0.0032	2.026
	175	0.4292	0.9788	0.0036	0.0672	0.1760	0.0524	0.0516	0.1572	0.0456	0.0284	0.0212	0.0000	0.0020	2.014
	Average	**0.4297**	**0.9767**	**0.0040**	**0.0680**	**0.1844**	**0.0520**	**0.0512**	**0.1559**	**0.0417**	**0.0288**	**0.0203**	**0.0000**	**0.0027**	**2.018**
S384-03 core	178	0.4288	0.9808	0.0008	0.0732	0.1944	0.0580	0.0372	0.1468	0.0428	0.0284	0.0192	0.0000	0.0036	2.017
	179	0.4368	0.9740	0.0028	0.0652	0.1996	0.0592	0.0344	0.1560	0.0432	0.0264	0.0180	0.0000	0.0040	2.021
	Average	**0.4328**	**0.9774**	**0.0018**	**0.0692**	**0.1970**	**0.0586**	**0.0358**	**0.1514**	**0.0430**	**0.0274**	**0.0186**	**0.0000**	**0.0038**	**2.019**

Mnz Grain	Analysis #	Ce	P	Si	Pr	La	Ca	Y	Nd	Th	Sm	Gd	Dy	U	Total / 4O
S384-03 rim	176	0.4244	0.9836	0.0032	0.0660	0.1928	0.0604	0.0444	0.1476	0.0448	0.0248	0.0176	0.0000	0.0032	2.014
	177	0.4300	0.9760	0.0032	0.0692	0.1988	0.0640	0.0404	0.1428	0.0476	0.0256	0.0152	0.0000	0.0032	2.020
	180	0.4196	0.9720	0.0028	0.0732	0.1872	0.0608	0.0432	0.1600	0.0460	0.0304	0.0204	0.0000	0.0032	2.022
	Average	**0.4247**	**0.9772**	**0.0031**	**0.0695**	**0.1929**	**0.0617**	**0.0427**	**0.1501**	**0.0461**	**0.0269**	**0.0177**	**0.0000**	**0.0032**	**2.019**
S384-03	Average	**0.4279**	**0.9773**	**0.0026**	**0.0694**	**0.1946**	**0.0605**	**0.0399**	**0.1506**	**0.0449**	**0.0271**	**0.0181**	**0.0000**	**0.0034**	**2.019**
S384-04	*181	0.4368	0.9604	0.0032	0.0712	0.2132	0.0488	0.0488	0.1556	0.0464	0.0284	0.0168	0.0000	0.0024	2.030
	*182	0.4352	0.9656	0.0028	0.0724	0.1972	0.0524	0.0524	0.1540	0.0420	0.0248	0.0154	0.0000	0.0024	2.025
	183	0.4312	0.9696	0.0028	0.0688	0.1972	0.0520	0.0508	0.1564	0.0412	0.0296	0.0196	0.0000	0.0016	2.022
	Average	**0.4312**	**0.9696**	**0.0028**	**0.0688**	**0.1972**	**0.0520**	**0.0508**	**0.1564**	**0.0412**	**0.0296**	**0.0196**	**0.0000**	**0.0016**	**2.022**
S384-05	184	0.4244	0.9676	0.0040	0.0720	0.1888	0.0536	0.0600	0.1540	0.0432	0.0288	0.0212	0.0000	0.0028	2.024
	185	0.4416	0.9696	0.0036	0.0708	0.1816	0.0476	0.0556	0.1568	0.0404	0.0268	0.0204	0.0000	0.0020	2.022
	*186	0.4312	0.9628	0.0060	0.0724	0.1924	0.0496	0.0512	0.1604	0.0440	0.0252	0.0236	0.0000	0.0008	2.026
	187	0.4428	0.9852	0.0100	0.0672	0.1996	0.0356	0.0216	0.1588	0.0460	0.0204	0.0156	0.0000	0.0000	2.004
	188	0.4360	0.9932	0.0040	0.0624	0.1880	0.0484	0.0532	0.1432	0.0388	0.0208	0.0172	0.0000	0.0012	2.007
	Average	**0.4362**	**0.9789**	**0.0054**	**0.0681**	**0.1895**	**0.0463**	**0.0476**	**0.1532**	**0.0421**	**0.0242**	**0.0186**	**0.0000**	**0.0015**	**2.014**
S384-06	169	0.4712	0.9684	0.0068	0.0728	0.2016	0.0276	0.0200	0.1664	0.0364	0.0252	0.0180	0.0000	0.0000	2.016
	*170	0.4652	0.9508	0.0116	0.0736	0.2128	0.0308	0.0188	0.1584	0.0496	0.0280	0.0160	0.0000	0.0012	2.025
	171	0.4208	0.9768	0.0048	0.0708	0.1988	0.0624	0.0336	0.1524	0.0476	0.0280	0.0164	0.0000	0.0032	2.019
	Average	**0.4460**	**0.9726**	**0.0058**	**0.0718**	**0.2002**	**0.0450**	**0.0268**	**0.1594**	**0.0420**	**0.0266**	**0.0172**	**0.0000**	**0.0016**	**2.017**
S384	**Average**	**0.4330**	**0.9756**	**0.0039**	**0.0696**	**0.1926**	**0.0521**	**0.0441**	**0.1541**	**0.0428**	**0.0269**	**0.0185**	**0.0000**	**0.0024**	**2.018**
S388-01outer rim	409	0.4664	0.9540	0.0064	0.0676	0.1832	0.0552	0.0280	0.1588	0.0436	0.0340	0.0232	0.0000	0.0092	2.030
	410	0.4660	0.9564	0.0040	0.0684	0.1852	0.0588	0.0244	0.1572	0.0460	0.0320	0.0228	0.0000	0.0088	2.030
	411	0.4592	0.9656	0.0044	0.0672	0.1848	0.0528	0.0224	0.1580	0.0436	0.0328	0.0224	0.0000	0.0084	2.022
	Average	**0.4639**	**0.9587**	**0.0049**	**0.0677**	**0.1844**	**0.0556**	**0.0249**	**0.1580**	**0.0444**	**0.0329**	**0.0228**	**0.0000**	**0.0088**	**2.027**
S388-01inner rim	412	0.4052	0.9772	0.0056	0.0560	0.1620	0.0820	0.0588	0.1420	0.0524	0.0284	0.0240	0.0000	0.0224	2.016
	415	0.4208	0.9708	0.0032	0.0596	0.1752	0.0828	0.0492	0.1380	0.0504	0.0288	0.0220	0.0000	0.0208	2.022
	Average	**0.4130**	**0.9740**	**0.0044**	**0.0578**	**0.1686**	**0.0824**	**0.0540**	**0.1400**	**0.0514**	**0.0286**	**0.0230**	**0.0000**	**0.0216**	**2.019**
S388-01 core	413	0.4896	0.9712	0.0016	0.0660	0.2120	0.0324	0.0220	0.1520	0.0248	0.0276	0.0160	0.0000	0.0040	2.020
	414	0.5068	0.9664	0.0012	0.0688	0.2236	0.0180	0.0172	0.1588	0.0168	0.0288	0.0160	0.0000	0.0008	2.024
	Average	**0.4982**	**0.9688**	**0.0014**	**0.0674**	**0.2178**	**0.0252**	**0.0196**	**0.1554**	**0.0208**	**0.0282**	**0.0160**	**0.0000**	**0.0024**	**2.022**
S388-01	Average	**0.4591**	**0.9659**	**0.0038**	**0.0648**	**0.1894**	**0.0546**	**0.0317**	**0.1521**	**0.0397**	**0.0303**	**0.0209**	**0.0000**	**0.0106**	**2.023**
S388-02 High Y	416	0.4432	0.9664	0.0048	0.0600	0.1740	0.0564	0.0480	0.1556	0.0432	0.0340	0.0268	0.0000	0.0100	2.022
	419	0.4424	0.9684	0.0020	0.0648	0.1788	0.0472	0.0604	0.1532	0.0316	0.0348	0.0284	0.0000	0.0100	2.022

Mnz Grain	Analysis #	Ce	P	Si	Pr	La	Ca	Y	Nd	Th	Sm	Gd	Dy	U	Total / 4O
S388-02 High Y (cnt'd)	**Average**	**0.4428**	**0.9674**	**0.0034**	**0.0624**	**0.1764**	**0.0518**	**0.0542**	**0.1544**	**0.0374**	**0.0344**	**0.0276**	**0.0000**	**0.0100**	**2.022**
S388-02 Low Y	417	0.4644	0.9640	0.0044	0.0628	0.1820	0.0536	0.0280	0.1560	0.0452	0.0312	0.0228	0.0000	0.0076	2.022
	418	0.4864	0.9692	0.0008	0.0720	0.2028	0.0168	0.0236	0.1732	0.0152	0.0380	0.0216	0.0000	0.0008	2.021
	Average	**0.4754**	**0.9666**	**0.0026**	**0.0674**	**0.1924**	**0.0352**	**0.0258**	**0.1646**	**0.0302**	**0.0346**	**0.0222**	**0.0000**	**0.0042**	**2.022**
S388-02	*420	0.4288	0.9660	0.0044	0.0584	0.1772	0.0812	0.0512	0.1384	0.0504	0.0272	0.0192	0.0000	0.0220	2.025
	*421	0.4560	0.9600	0.0048	0.0632	0.1792	0.0548	0.0408	0.1540	0.0440	0.0320	0.0272	0.0000	0.0096	2.026
	Average	**0.4591**	**0.9670**	**0.0030**	**0.0649**	**0.1844**	**0.0435**	**0.0400**	**0.1595**	**0.0338**	**0.0345**	**0.0249**	**0.0000**	**0.0071**	**2.022**
S388-03	*423	0.4700	0.9456	0.0060	0.0660	0.1896	0.0588	0.0284	0.1564	0.0444	0.0344	0.0280	0.0000	0.0084	2.036
	*424	0.4728	0.9528	0.0040	0.0640	0.1836	0.0572	0.0268	0.1584	0.0452	0.0316	0.0256	0.0000	0.0080	2.032
	*425	0.4816	0.9568	0.0008	0.0644	0.1964	0.0448	0.0416	0.1536	0.0264	0.0312	0.0212	0.0000	0.0104	2.031
	*426	0.4984	0.9552	0.0024	0.0680	0.2000	0.0244	0.0244	0.1716	0.0224	0.0372	0.0236	0.0000	0.0016	2.029
	*427	0.4988	0.9368	0.0040	0.0664	0.2040	0.0316	0.0240	0.1688	0.0352	0.0392	0.0252	0.0000	0.0012	2.035
	Average	-	-	-	-	-	-	-	-	-	-	-	-	-	-
S388-04	*428	0.5128	0.9496	0.0044	0.0652	0.2044	0.0360	0.0224	0.1528	0.0360	0.0284	0.0192	0.0000	0.0008	2.032
	*429	0.4668	0.9560	0.0016	0.0600	0.1908	0.0600	0.0380	0.1504	0.0444	0.0320	0.0228	0.0000	0.0092	2.031
	*430	0.5068	0.9444	0.0056	0.0672	0.1944	0.0424	0.0224	0.1536	0.0400	0.0320	0.0192	0.0000	0.0000	2.034
	*431	0.4576	0.9528	0.0072	0.0656	0.1760	0.0532	0.0640	0.1488	0.0504	0.0372	0.0232	0.0000	0.0032	2.029
	*432	0.4720	0.9556	0.0016	0.0604	0.1908	0.0644	0.0300	0.1496	0.0484	0.0272	0.0216	0.0000	0.0096	2.031
	Average	-	-	-	-	-	-	-	-	-	-	-	-	-	-
S388-05	*433	0.4660	0.9584	0.0024	0.0612	0.1520	0.0544	0.0572	0.1464	0.0424	0.0268	0.0276	0.0000	0.0068	2.029
	*434	0.4600	0.9580	0.0036	0.0596	0.1520	0.0544	0.0588	0.1452	0.0468	0.0292	0.0228	0.0000	0.0060	2.027
	*435	0.4624	0.9588	0.0020	0.0588	0.1568	0.0532	0.0556	0.1500	0.0428	0.0200	0.0224	0.0000	0.0072	2.028
	*436	0.4716	0.9580	0.0012	0.0572	0.1392	0.0540	0.0416	0.1472	0.0456	0.0308	0.0248	0.0000	0.0068	2.029
	*437	0.4920	0.9452	0.0080	0.0656	0.1956	0.0428	0.0248	0.1524	0.0476	0.0320	0.0240	0.0000	0.0016	2.032
	Average	-	-	-	-	-	-	-	-	-	-	-	-	-	-
S388-06	*438	0.4608	0.9496	0.0068	0.0660	0.1752	0.0476	0.0676	0.1500	0.0476	0.0280	0.0260	0.0000	0.0048	2.030
	*439	0.4640	0.9532	0.0064	0.0644	0.1748	0.0452	0.0660	0.1548	0.0436	0.0284	0.0324	0.0000	0.0048	2.028
	*440	0.4572	0.9544	0.0056	0.0648	0.1736	0.0560	0.0632	0.1476	0.0488	0.0272	0.0220	0.0000	0.0084	2.028
	*441	0.4464	0.9564	0.0088	0.0636	0.1696	0.0540	0.0632	0.1480	0.0528	0.0296	0.0280	0.0000	0.0048	2.025
	*442	0.4500	0.9544	0.0024	0.0660	0.1892	0.0612	0.0272	0.1428	0.0452	0.0284	0.0192	0.0000	0.0136	2.030
	443	**0.4608**	**0.9612**	**0.0064**	**0.0620**	**0.1796**	**0.0452**	**0.0588**	**0.1464**	**0.0432**	**0.0300**	**0.0232**	**0.0000**	**0.0056**	**2.022**
	Average	**0.4608**	**0.9612**	**0.0064**	**0.0620**	**0.1796**	**0.0452**	**0.0588**	**0.1464**	**0.0432**	**0.0300**	**0.0232**	**0.0000**	**0.0056**	**2.022**
S388-07	444	0.4572	0.9620	0.0048	0.0620	0.1752	0.0544	0.0528	0.1480	0.0528	0.0252	0.0224	0.0000	0.0048	2.022

Mnz Grain	Analysis #	Ce	P	Si	Pr	La	Ca	Y	Nd	Th	Sm	Gd	Dy	U	Total / 4O
S388-07 (cnt'd)	445	0.5084	0.9516	0.0056	0.0756	0.1968	0.0292	0.0212	0.1584	0.0312	0.0280	0.0208	0.0000	0.0020	2.029
	446	0.4492	0.9664	0.0072	0.0660	0.1708	0.0496	0.0628	0.1448	0.0476	0.0272	0.0220	0.0000	0.0048	2.019
	447	0.4736	0.9640	0.0008	0.0704	0.1852	0.0496	0.0432	0.1464	0.0336	0.0272	0.0212	0.0000	0.0100	2.026
	448	0.4408	0.9676	0.0056	0.0660	0.1720	0.0528	0.0628	0.1500	0.0484	0.0272	0.0208	0.0000	0.0060	2.019
	449	0.4572	0.9680	0.0048	0.0640	0.1700	0.0520	0.0576	0.1504	0.0440	0.0260	0.0200	0.0000	0.0064	2.020
	Average	**0.4644**	**0.9633**	**0.0048**	**0.0673**	**0.1783**	**0.0479**	**0.0501**	**0.1497**	**0.0429**	**0.0268**	**0.0212**	**0.0000**	**0.0057**	**2.023**
S388-08	450	0.4488	0.9608	0.0028	0.0648	0.1816	0.0576	0.0496	0.1496	0.0516	0.0280	0.0232	0.0000	0.0064	2.025
	451	0.4648	0.9660	0.0024	0.0640	0.1776	0.0560	0.0392	0.1508	0.0424	0.0276	0.0216	0.0000	0.0108	2.023
	452	0.4704	0.9636	0.0024	0.0680	0.1812	0.0560	0.0364	0.1512	0.0424	0.0244	0.0184	0.0000	0.0096	2.025
	453	0.4584	0.9640	0.0056	0.0672	0.1812	0.0416	0.0616	0.1464	0.0388	0.0292	0.0224	0.0000	0.0048	2.021
	454	0.4600	0.9628	0.0080	0.0648	0.1780	0.0424	0.0600	0.1484	0.0436	0.0280	0.0200	0.0000	0.0048	2.020
	Average	**0.4611**	**0.9643**	**0.0053**	**0.0653**	**0.1789**	**0.0467**	**0.0536**	**0.1485**	**0.0416**	**0.0283**	**0.0213**	**0.0000**	**0.0068**	**2.021**
S388-09	455	0.4488	0.9628	0.0036	0.0668	0.1804	0.0600	0.0436	0.1528	0.0528	0.0284	0.0184	0.0000	0.0060	2.024
	456	0.4508	0.9660	0.0028	0.0644	0.1808	0.0688	0.0388	0.1464	0.0500	0.0256	0.0192	0.0000	0.0104	2.024
	457	0.4616	0.9672	0.0024	0.0640	0.1860	0.0500	0.0376	0.1548	0.0428	0.0284	0.0192	0.0000	0.0072	2.021
	458	0.4656	0.9644	0.0032	0.0672	0.1840	0.0564	0.0308	0.1496	0.0476	0.0272	0.0188	0.0000	0.0076	2.023
	459	0.4468	0.9652	0.0032	0.0656	0.1792	0.0568	0.0536	0.1496	0.0524	0.0268	0.0180	0.0000	0.0052	2.022
	460	0.4516	0.9696	0.0020	0.0632	0.1780	0.0652	0.0392	0.1476	0.0492	0.0272	0.0180	0.0000	0.0104	2.022
	Average	**0.4542**	**0.9659**	**0.0029**	**0.0652**	**0.1814**	**0.0595**	**0.0406**	**0.1501**	**0.0491**	**0.0273**	**0.0186**	**0.0000**	**0.0078**	**2.023**
S388-10	462	0.4428	0.9656	0.0040	0.0664	0.1804	0.0576	0.0484	0.1480	0.0536	0.0288	0.0208	0.0000	0.0048	2.021
	463	0.4540	0.9672	0.0020	0.0664	0.1832	0.0572	0.0400	0.1500	0.0476	0.0268	0.0204	0.0000	0.0076	2.022
	464	0.4420	0.9680	0.0048	0.0636	0.1740	0.0540	0.0584	0.1504	0.0480	0.0296	0.0204	0.0000	0.0064	2.020
	465	0.4452	0.9684	0.0052	0.0640	0.1740	0.0544	0.0552	0.1512	0.0496	0.0260	0.0200	0.0000	0.0060	2.019
	466	0.4480	0.9684	0.0036	0.0648	0.1768	0.0588	0.0452	0.1480	0.0516	0.0288	0.0208	0.0000	0.0056	2.020
	467	0.4416	0.9736	0.0028	0.0628	0.1748	0.0540	0.0544	0.1528	0.0464	0.0268	0.0208	0.0000	0.0060	2.017
	Average	**0.4456**	**0.9685**	**0.0037**	**0.0647**	**0.1772**	**0.0560**	**0.0503**	**0.1501**	**0.0495**	**0.0278**	**0.0205**	**0.0000**	**0.0061**	**2.020**
S388-11	473	0.4368	0.9832	0.0016	0.0644	0.1764	0.0660	0.0332	0.1468	0.0488	0.0272	0.0184	0.0000	0.0104	2.013
	469	0.4588	0.9768	0.0012	0.0664	0.1844	0.0556	0.0292	0.1476	0.0440	0.0272	0.0176	0.0000	0.0080	2.016
	470	0.4940	0.9624	0.0060	0.0716	0.1976	0.0316	0.0212	0.1560	0.0340	0.0296	0.0180	0.0000	0.0008	2.022
	471	0.4764	0.9616	0.0096	0.0696	0.1988	0.0364	0.0204	0.1572	0.0388	0.0316	0.0188	0.0000	0.0016	2.021
	472	0.4732	0.9676	0.0064	0.0720	0.1936	0.0344	0.0192	0.1640	0.0368	0.0312	0.0192	0.0000	0.0008	2.018
	Average	**0.4678**	**0.9703**	**0.0050**	**0.0688**	**0.1902**	**0.0448**	**0.0246**	**0.1543**	**0.0405**	**0.0294**	**0.0184**	**0.0000**	**0.0043**	**2.018**
S388-13	482	0.4344	0.9772	0.0024	0.0640	0.1852	0.0484	0.0528	0.1548	0.0332	0.0288	0.0260	0.0000	0.0092	2.016

Mnz Grain	Analysis #	Ce	P	Si	Pr	La	Ca	Y	Nd	Th	Sm	Gd	Dy	U	Total / 4O
S388-13 (cnt'd)	484	0.4200	0.9852	0.0020	0.0676	0.1816	0.0528	0.0536	0.1548	0.0344	0.0284	0.0240	0.0000	0.0084	2.012
	480	0.4276	0.9740	0.0040	0.0668	0.1800	0.0584	0.0520	0.1532	0.0392	0.0280	0.0228	0.0000	0.0116	2.018
	481	0.4356	0.9732	0.0048	0.0660	0.1796	0.0520	0.0408	0.1636	0.0384	0.0300	0.0268	0.0000	0.0080	2.018
	483	0.4320	0.9780	0.0036	0.0660	0.1780	0.0476	0.0552	0.1560	0.0348	0.0316	0.0240	0.0000	0.0084	2.015
	Average	**0.4299**	**0.9775**	**0.0034**	**0.0661**	**0.1809**	**0.0518**	**0.0509**	**0.1565**	**0.0360**	**0.0294**	**0.0247**	**0.0000**	**0.0091**	**2.016**
S388-14	486	0.4152	0.9784	0.0056	0.0612	0.1728	0.0576	0.0588	0.1560	0.0504	0.0280	0.0252	0.0000	0.0048	2.014
	487	0.3944	0.9884	0.0052	0.0608	0.1684	0.0584	0.0608	0.1572	0.0540	0.0272	0.0252	0.0000	0.0052	2.006
	488	0.4184	0.9844	0.0028	0.0636	0.1772	0.0584	0.0456	0.1524	0.0452	0.0280	0.0244	0.0000	0.0092	2.011
	489	0.4180	0.9960	0.0020	0.0652	0.1812	0.0556	0.0296	0.1520	0.0432	0.0288	0.0232	0.0000	0.0088	2.003
	490	0.4144	0.9868	0.0036	0.0600	0.1716	0.0564	0.0560	0.1532	0.0472	0.0288	0.0244	0.0000	0.0060	2.008
	Average	**0.4121**	**0.9868**	**0.0038**	**0.0622**	**0.1742**	**0.0573**	**0.0502**	**0.1542**	**0.0480**	**0.0282**	**0.0245**	**0.0000**	**0.0068**	**2.008**
S388-16outer rim	66	0.4028	1.0172	0.0068	0.0420	0.1984	0.0428	0.0248	0.1608	0.0356	0.0268	0.0212	0.0092	0.0000	1.988
	72	0.3912	1.0180	0.0072	0.0440	0.1920	0.0444	0.0268	0.1644	0.0376	0.0280	0.0244	0.0092	0.0000	1.988
	Average	**0.3970**	**1.0176**	**0.0070**	**0.0430**	**0.1952**	**0.0436**	**0.0258**	**0.1626**	**0.0366**	**0.0274**	**0.0228**	**0.0092**	**0.0000**	**1.988**
S388-16inner rim	67	0.3856	1.0192	0.0092	0.0448	0.1876	0.0440	0.0260	0.1652	0.0416	0.0284	0.0228	0.0104	0.0000	1.985
	71	0.3904	1.0108	0.0108	0.0468	0.1812	0.0444	0.0276	0.1716	0.0428	0.0300	0.0224	0.0104	0.0000	1.990
	Average	**0.3880**	**1.0150**	**0.0100**	**0.0458**	**0.1844**	**0.0442**	**0.0268**	**0.1684**	**0.0422**	**0.0292**	**0.0226**	**0.0104**	**0.0000**	**1.987**
S388-16 core	68	0.4000	1.0184	0.0056	0.0444	0.1948	0.0448	0.0240	0.1620	0.0368	0.0268	0.0216	0.0096	0.0000	1.989
	69	0.3956	1.0156	0.0076	0.0428	0.1824	0.0452	0.0264	0.1664	0.0432	0.0284	0.0228	0.0112	0.0000	1.988
	70	0.3912	1.0108	0.0080	0.0464	0.1944	0.0456	0.0280	0.1644	0.0400	0.0296	0.0236	0.0104	0.0000	1.992
	Average	**0.3956**	**1.0149**	**0.0071**	**0.0445**	**0.1905**	**0.0452**	**0.0261**	**0.1643**	**0.0400**	**0.0283**	**0.0227**	**0.0104**	**0.0000**	**1.990**
S388-16	Average	**0.3938**	**1.0157**	**0.0079**	**0.0445**	**0.1901**	**0.0445**	**0.0262**	**0.1650**	**0.0397**	**0.0283**	**0.0227**	**0.0101**	**0.0000**	**1.989**
S388	Average	**0.4434**	**0.9755**	**0.0045**	**0.0627**	**0.1829**	**0.0510**	**0.0411**	**0.1541**	**0.0424**	**0.0289**	**0.0217**	**0.0013**	**0.0063**	**2.016**
S390-01 High Y	227	0.4108	0.9700	0.0084	0.0640	0.1592	0.0568	0.0716	0.1444	0.0688	0.0316	0.0236	0.0000	0.0024	2.012
	228	0.4124	0.9844	0.0052	0.0660	0.1700	0.0636	0.0644	0.1300	0.0596	0.0276	0.0216	0.0000	0.0040	2.009
	Average	**0.4116**	**0.9772**	**0.0068**	**0.0650**	**0.1646**	**0.0602**	**0.0680**	**0.1372**	**0.0642**	**0.0296**	**0.0226**	**0.0000**	**0.0032**	**2.011**
S390-01 Low Y	225	0.4312	0.9752	0.0064	0.0628	0.1716	0.0604	0.0384	0.1392	0.0680	0.0308	0.0228	0.0000	0.0040	2.011
	226	0.4256	0.9732	0.0064	0.0640	0.1724	0.0680	0.0328	0.1416	0.0712	0.0316	0.0224	0.0000	0.0044	2.014
	229	0.4276	0.9816	0.0056	0.0632	0.1696	0.0672	0.0364	0.1404	0.0668	0.0276	0.0200	0.0000	0.0028	2.009
	Average	**0.4281**	**0.9767**	**0.0061**	**0.0633**	**0.1712**	**0.0652**	**0.0359**	**0.1404**	**0.0687**	**0.0300**	**0.0217**	**0.0000**	**0.0037**	**2.011**
S390-01	Average	**0.4215**	**0.9769**	**0.0064**	**0.0640**	**0.1686**	**0.0632**	**0.0487**	**0.1391**	**0.0669**	**0.0298**	**0.0221**	**0.0000**	**0.0035**	**2.011**
S390-02	230	0.4144	0.9848	0.0040	0.0616	0.1644	0.0612	0.0624	0.1388	0.0596	0.0320	0.0216	0.0000	0.0032	2.008
	231	0.4176	0.9832	0.0056	0.0656	0.1624	0.0620	0.0544	0.1388	0.0604	0.0304	0.0232	0.0000	0.0048	2.008

Mnz Grain	Analysis #	Ce	P	Si	Pr	La	Ca	Y	Nd	Th	Sm	Gd	Dy	U	Total / 4O
S390-02 (cnt'd)	232	0.3848	0.9976	0.0048	0.0580	0.1560	0.0792	0.0704	0.1300	0.0648	0.0280	0.0236	0.0000	0.0056	2.003
	Average	**0.4056**	**0.9885**	**0.0048**	**0.0617**	**0.1609**	**0.0675**	**0.0624**	**0.1359**	**0.0616**	**0.0301**	**0.0228**	**0.0000**	**0.0045**	**2.007**
S390-03	233	0.4100	0.9928	0.0052	0.0652	0.1592	0.0612	0.0692	0.1396	0.0484	0.0280	0.0216	0.0000	0.0048	2.005
	234	0.3988	0.9872	0.0056	0.0604	0.1580	0.0748	0.0604	0.1320	0.0716	0.0288	0.0236	0.0000	0.0048	2.006
	235	0.4056	0.9860	0.0052	0.0604	0.1580	0.0644	0.0664	0.1392	0.0652	0.0284	0.0232	0.0000	0.0036	2.006
	Average	**0.4048**	**0.9887**	**0.0053**	**0.0620**	**0.1584**	**0.0668**	**0.0653**	**0.1369**	**0.0617**	**0.0284**	**0.0228**	**0.0000**	**0.0044**	**2.006**
S390-04	236	0.4336	0.9816	0.0040	0.0640	0.1784	0.0496	0.0484	0.1448	0.0540	0.0280	0.0204	0.0000	0.0020	2.009
	237	0.4260	0.9776	0.0080	0.0648	0.1744	0.0536	0.0508	0.1464	0.0588	0.0284	0.0180	0.0000	0.0032	2.010
	238	0.4328	0.9856	0.0032	0.0644	0.1800	0.0484	0.0456	0.1432	0.0532	0.0292	0.0184	0.0000	0.0020	2.006
	Average	**0.4308**	**0.9816**	**0.0051**	**0.0644**	**0.1776**	**0.0505**	**0.0483**	**0.1448**	**0.0553**	**0.0285**	**0.0189**	**0.0000**	**0.0024**	**2.009**
S390-05 rim	239	0.4284	0.9852	0.0032	0.0656	0.1772	0.0492	0.0624	0.1368	0.0456	0.0288	0.0236	0.0000	0.0028	2.009
	240	0.4404	0.9860	0.0044	0.0628	0.1812	0.0524	0.0476	0.1392	0.0476	0.0260	0.0168	0.0000	0.0032	2.008
	241	0.4352	0.9876	0.0032	0.0624	0.1772	0.0508	0.0536	0.1416	0.0480	0.0268	0.0188	0.0000	0.0024	2.008
	244	0.4236	0.9792	0.0064	0.0644	0.1712	0.0460	0.0676	0.1396	0.0572	0.0300	0.0204	0.0000	0.0020	2.008
	Average	**0.4319**	**0.9845**	**0.0043**	**0.0638**	**0.1767**	**0.0496**	**0.0578**	**0.1393**	**0.0496**	**0.0279**	**0.0199**	**0.0000**	**0.0026**	**2.008**
S390-05 core	242	0.4336	0.9760	0.0044	0.0664	0.1664	0.0532	0.0440	0.1504	0.0616	0.0312	0.0220	0.0000	0.0020	2.012
	243	0.4304	0.9844	0.0028	0.0652	0.1812	0.0656	0.0384	0.1392	0.0564	0.0264	0.0168	0.0000	0.0048	2.012
	245	0.4448	0.9744	0.0040	0.0648	0.1824	0.0588	0.0360	0.1400	0.0628	0.0252	0.0176	0.0000	0.0028	2.014
	Average	**0.4363**	**0.9783**	**0.0037**	**0.0655**	**0.1767**	**0.0592**	**0.0395**	**0.1432**	**0.0603**	**0.0276**	**0.0188**	**0.0000**	**0.0032**	**2.013**
S390-05	Average	**0.4338**	**0.9818**	**0.0041**	**0.0645**	**0.1767**	**0.0537**	**0.0499**	**0.1410**	**0.0542**	**0.0278**	**0.0194**	**0.0000**	**0.0029**	**2.010**
S390-06 rim	75	0.4244	0.9904	0.0076	0.0696	0.1472	0.0532	0.0652	0.1496	0.0456	0.0272	0.0236	0.0000	0.0024	2.006
	76	0.4324	0.9828	0.0064	0.0664	0.1664	0.0484	0.0640	0.1500	0.0432	0.0280	0.0208	0.0000	0.0016	2.011
	77	0.4368	0.9780	0.0092	0.0688	0.1608	0.0544	0.0672	0.1476	0.0436	0.0248	0.0212	0.0000	0.0016	2.014
	Average	**0.4312**	**0.9837**	**0.0077**	**0.0683**	**0.1581**	**0.0520**	**0.0655**	**0.1491**	**0.0441**	**0.0267**	**0.0219**	**0.0000**	**0.0019**	**2.010**
S390-06 core	78	0.4324	0.9912	0.0044	0.0712	0.1656	0.0616	0.0420	0.1492	0.0428	0.0276	0.0180	0.0000	0.0032	2.009
	79	0.4320	0.9992	0.0048	0.0708	0.1556	0.0668	0.0372	0.1504	0.0416	0.0248	0.0172	0.0000	0.0048	2.005
	80	0.4360	0.9948	0.0040	0.0696	0.1608	0.0600	0.0396	0.1516	0.0444	0.0232	0.0200	0.0000	0.0028	2.007
	81	0.4544	0.9612	0.0228	0.0736	0.1720	0.0428	0.0256	0.1516	0.0608	0.0276	0.0192	0.0000	0.0008	2.013
	Average	**0.4387**	**0.9866**	**0.0090**	**0.0713**	**0.1635**	**0.0578**	**0.0361**	**0.1507**	**0.0474**	**0.0258**	**0.0186**	**0.0000**	**0.0029**	**2.009**
S390-06	Average	**0.4355**	**0.9854**	**0.0085**	**0.0700**	**0.1612**	**0.0553**	**0.0487**	**0.1500**	**0.0460**	**0.0262**	**0.0200**	**0.0000**	**0.0025**	**2.009**
S390-07 rim	82	0.4428	0.9800	0.0076	0.0680	0.1556	0.0520	0.0572	0.1524	0.0476	0.0272	0.0184	0.0000	0.0012	2.013
	83	0.4296	0.9908	0.0068	0.0660	0.1556	0.0496	0.0592	0.1504	0.0416	0.0288	0.0204	0.0000	0.0024	2.008
	84	0.4196	0.9872	0.0072	0.0696	0.1644	0.0536	0.0584	0.1516	0.0428	0.0264	0.0228	0.0000	0.0016	2.011

Mnz Grain	Analysis #	Ce	P	Si	Pr	La	Ca	Y	Nd	Th	Sm	Gd	Dy	U	Total / 4O
S390-07 rim (cnt'd)	85	0.4364	0.9864	0.0036	0.0692	0.1556	0.0568	0.0476	0.1548	0.0452	0.0284	0.0200	0.0000	0.0032	2.012
	Average	**0.4321**	**0.9861**	**0.0063**	**0.0682**	**0.1578**	**0.0530**	**0.0556**	**0.1523**	**0.0443**	**0.0277**	**0.0204**	**0.0000**	**0.0021**	**2.011**
S390-07 core	86	0.4620	0.9780	0.0056	0.0724	0.1724	0.0500	0.0276	0.1532	0.0424	0.0252	0.0196	0.0000	0.0016	2.018
	87	0.4980	0.9716	0.0084	0.0748	0.1844	0.0192	0.0188	0.1660	0.0240	0.0288	0.0192	0.0000	0.0000	2.015
	88	0.4720	0.9652	0.0152	0.0780	0.1880	0.0292	0.0208	0.1604	0.0380	0.0280	0.0188	0.0000	0.0004	2.015
	Average	**0.4773**	**0.9716**	**0.0097**	**0.0751**	**0.1816**	**0.0328**	**0.0224**	**0.1599**	**0.0348**	**0.0273**	**0.0192**	**0.0000**	**0.0007**	**2.016**
S390-07	Average	**0.4515**	**0.9799**	**0.0078**	**0.0711**	**0.1680**	**0.0443**	**0.0414**	**0.1555**	**0.0402**	**0.0275**	**0.0199**	**0.0000**	**0.0015**	**2.013**
S390-08	89	0.4168	1.0040	0.0048	0.0644	0.1600	0.0712	0.0460	0.1396	0.0472	0.0224	0.0204	0.0000	0.0036	2.004
	90	0.4016	1.0092	0.0072	0.0628	0.1524	0.0808	0.0592	0.1328	0.0448	0.0228	0.0184	0.0000	0.0080	2.001
	91	0.4212	0.9940	0.0080	0.0680	0.1520	0.0588	0.0588	0.1484	0.0484	0.0240	0.0192	0.0000	0.0016	2.005
	92	0.4140	0.9852	0.0224	0.0692	0.1640	0.0708	0.0448	0.1400	0.0472	0.0260	0.0184	0.0000	0.0040	2.010
	93	0.4316	0.9900	0.0092	0.0700	0.1488	0.0556	0.0572	0.1468	0.0460	0.0232	0.0224	0.0000	0.0024	2.008
	Average	**0.4170**	**0.9965**	**0.0103**	**0.0669**	**0.1554**	**0.0674**	**0.0532**	**0.1415**	**0.0467**	**0.0237**	**0.0198**	**0.0000**	**0.0039**	**2.006**
S390-09	95	0.4372	0.9796	0.0060	0.0672	0.1656	0.0596	0.0488	0.1500	0.0508	0.0256	0.0180	0.0000	0.0020	2.015
	96	0.4468	0.9824	0.0064	0.0664	0.1684	0.0560	0.0440	0.1500	0.0460	0.0256	0.0192	0.0000	0.0016	2.012
	97	0.4416	0.9836	0.0068	0.0704	0.1616	0.0648	0.0548	0.1408	0.0440	0.0244	0.0200	0.0000	0.0020	2.015
	Average	**0.4419**	**0.9819**	**0.0064**	**0.0680**	**0.1652**	**0.0601**	**0.0492**	**0.1469**	**0.0469**	**0.0252**	**0.0191**	**0.0000**	**0.0019**	**2.014**
S390-10 rim	98	0.4456	0.9732	0.0108	0.0720	0.1548	0.0516	0.0628	0.1512	0.0444	0.0272	0.0204	0.0000	0.0020	2.016
	99	0.4348	0.9816	0.0128	0.0704	0.1488	0.0540	0.0648	0.1456	0.0448	0.0276	0.0208	0.0000	0.0016	2.012
	Average	**0.4402**	**0.9774**	**0.0118**	**0.0712**	**0.1518**	**0.0528**	**0.0638**	**0.1484**	**0.0446**	**0.0274**	**0.0206**	**0.0000**	**0.0018**	**2.014**
S390-10 core	100	0.4576	0.9624	0.0244	0.0736	0.1772	0.0400	0.0212	0.1544	0.0568	0.0264	0.0160	0.0000	0.0008	2.012
	101	0.4752	0.9656	0.0176	0.0836	0.1736	0.0276	0.0232	0.1624	0.0380	0.0264	0.0188	0.0000	0.0000	2.014
	102	0.4580	0.9820	0.0068	0.0740	0.1624	0.0556	0.0328	0.1452	0.0488	0.0260	0.0160	0.0000	0.0008	2.014
	Average	**0.4636**	**0.9700**	**0.0163**	**0.0771**	**0.1711**	**0.0411**	**0.0257**	**0.1540**	**0.0479**	**0.0263**	**0.0169**	**0.0000**	**0.0005**	**2.013**
S390-10	Average	**0.4542**	**0.9730**	**0.0145**	**0.0747**	**0.1634**	**0.0458**	**0.0410**	**0.1518**	**0.0466**	**0.0267**	**0.0184**	**0.0000**	**0.0010**	**2.013**
S390-11	106	0.4224	0.9720	0.0168	0.0776	0.1532	0.0500	0.0700	0.1532	0.0400	0.0284	0.0232	0.0000	0.0020	2.019
	107	0.4232	0.9808	0.0168	0.0780	0.1476	0.0484	0.0700	0.1468	0.0388	0.0276	0.0232	0.0000	0.0016	2.014
	108	0.4360	0.9736	0.0172	0.0776	0.1428	0.0504	0.0700	0.1492	0.0408	0.0264	0.0220	0.0000	0.0020	2.017
	109	0.4416	0.9748	0.0160	0.0736	0.1456	0.0496	0.0672	0.1492	0.0404	0.0276	0.0208	0.0000	0.0020	2.017
	Average	**0.4308**	**0.9753**	**0.0167**	**0.0767**	**0.1473**	**0.0496**	**0.0693**	**0.1496**	**0.0400**	**0.0275**	**0.0223**	**0.0000**	**0.0019**	**2.017**
S390-20	328	0.3664	0.9772	0.0076	0.0596	0.1520	0.0916	0.0700	0.1384	0.0660	0.0280	0.0248	0.0000	0.0304	2.012
	329	0.3928	0.9804	0.0092	0.0696	0.1512	0.0564	0.0592	0.1508	0.0720	0.0272	0.0256	0.0000	0.0080	2.003
	330	0.3668	0.9760	0.0088	0.0644	0.1412	0.0864	0.0732	0.1428	0.0700	0.0304	0.0224	0.0000	0.0268	2.009

Mnz Grain	Analysis #	Ce	P	Si	Pr	La	Ca	Y	Nd	Th	Sm	Gd	Dy	U	Total / 4O
S390-20 (cnt'd)	331	0.3976	0.9836	0.0032	0.0684	0.1508	0.0724	0.0560	0.1412	0.0664	0.0268	0.0192	0.0000	0.0192	2.005
	332	0.3684	0.9840	0.0060	0.0584	0.1452	0.0912	0.0684	0.1352	0.0648	0.0296	0.0320	0.0000	0.0236	2.007
	Average	**0.3784**	**0.9802**	**0.0070**	**0.0641**	**0.1481**	**0.0796**	**0.0654**	**0.1417**	**0.0678**	**0.0284**	**0.0248**	**0.0000**	**0.0216**	**2.007**
S390	**Average**	**0.4276**	**0.9822**	**0.0081**	**0.0678**	**0.1631**	**0.0577**	**0.0522**	**0.1454**	**0.0519**	**0.0274**	**0.0207**	**0.0000**	**0.0043**	**2.010**
S392-01outer rim	211	0.4460	0.9744	0.0076	0.0640	0.1940	0.0348	0.0388	0.1528	0.0488	0.0256	0.0232	0.0000	0.0000	2.010
S392-01inner rim	210	0.4440	0.9780	0.0020	0.0620	0.1916	0.0440	0.0368	0.1532	0.0568	0.0228	0.0184	0.0000	0.0000	2.010
S392-01outer core	213	0.4720	0.9508	0.0244	0.0724	0.1864	0.0236	0.0104	0.1712	0.0576	0.0264	0.0176	0.0000	0.0000	2.013
S392-01 core	212	0.4500	0.9808	0.0048	0.0628	0.1904	0.0356	0.0520	0.1464	0.0420	0.0232	0.0212	0.0000	0.0004	2.010
S392-01	Average	**0.4530**	**0.9710**	**0.0097**	**0.0653**	**0.1906**	**0.0345**	**0.0345**	**0.1559**	**0.0513**	**0.0245**	**0.0201**	**0.0000**	**0.0001**	**2.011**
S392-02outer rim	216	0.4432	0.9804	0.0064	0.0588	0.2152	0.0320	0.0468	0.1328	0.0476	0.0212	0.0212	0.0000	0.0000	2.006
S392-02inner rim	214	0.4804	0.9404	0.0256	0.0716	0.1872	0.0356	0.0032	0.1640	0.0744	0.0232	0.0120	0.0000	0.0000	2.018
S392-02 core	215	0.4728	0.9800	0.0036	0.0668	0.2100	0.0216	0.0200	0.1580	0.0332	0.0240	0.0184	0.0000	0.0000	2.009
S392-02	Average	**0.4655**	**0.9669**	**0.0119**	**0.0657**	**0.2041**	**0.0297**	**0.0233**	**0.1516**	**0.0517**	**0.0228**	**0.0172**	**0.0000**	**0.0000**	**2.011**
S392-03	217	0.4464	0.9620	0.0188	0.0684	0.1836	0.0328	0.0228	0.1632	0.0600	0.0280	0.0228	0.0000	0.0008	2.010
	218	0.4504	0.9636	0.0204	0.0648	0.1792	0.0344	0.0252	0.1580	0.0636	0.0260	0.0204	0.0000	0.0004	2.006
	219	0.4456	0.9804	0.0152	0.0620	0.1804	0.0300	0.0336	0.1528	0.0528	0.0264	0.0204	0.0000	0.0000	2.000
	Average	**0.4475**	**0.9687**	**0.0181**	**0.0651**	**0.1811**	**0.0324**	**0.0272**	**0.1580**	**0.0588**	**0.0268**	**0.0212**	**0.0000**	**0.0004**	**2.005**
S392-04 rim	221	0.4692	0.9608	0.0192	0.0672	0.1888	0.0292	0.0160	0.1580	0.0560	0.0280	0.0180	0.0000	0.0000	2.010
	222	0.4568	0.9804	0.0004	0.0648	0.1960	0.0476	0.0280	0.1404	0.0564	0.0220	0.0172	0.0000	0.0000	2.010
	Average	**0.4630**	**0.9706**	**0.0098**	**0.0660**	**0.1924**	**0.0384**	**0.0220**	**0.1492**	**0.0562**	**0.0250**	**0.0176**	**0.0000**	**0.0000**	**2.010**
S392-04 core	220	0.4444	0.9840	0.0012	0.0588	0.1836	0.0516	0.0404	0.1484	0.0564	0.0232	0.0176	0.0000	0.0000	2.010
	Average	**0.4444**	**0.9840**	**0.0012**	**0.0588**	**0.1836**	**0.0516**	**0.0404**	**0.1484**	**0.0564**	**0.0232**	**0.0176**	**0.0000**	**0.0000**	**2.010**
S392-04	Average	**0.4568**	**0.9751**	**0.0069**	**0.0636**	**0.1895**	**0.0428**	**0.0281**	**0.1489**	**0.0563**	**0.0244**	**0.0176**	**0.0000**	**0.0000**	**2.010**
S392-05 rim	280	0.4472	0.9536	0.0212	0.0672	0.1856	0.0356	0.0268	0.1552	0.0616	0.0332	0.0260	0.0000	0.0012	2.015
	281	0.4524	0.9576	0.0224	0.0720	0.1868	0.0292	0.0224	0.1608	0.0560	0.0304	0.0212	0.0000	0.0008	2.012
	Average	**0.4498**	**0.9556**	**0.0218**	**0.0696**	**0.1862**	**0.0324**	**0.0246**	**0.1580**	**0.0588**	**0.0318**	**0.0236**	**0.0000**	**0.0010**	**2.014**
S392-05 core	282	0.4420	0.9652	0.0076	0.0648	0.1936	0.0584	0.0320	0.1428	0.0624	0.0296	0.0176	0.0000	0.0028	2.019
	283	0.4316	0.9716	0.0028	0.0680	0.1772	0.0408	0.0400	0.1672	0.0456	0.0396	0.0296	0.0000	0.0016	2.016
	284	0.4132	0.9892	0.0048	0.0664	0.1648	0.0428	0.0420	0.1680	0.0464	0.0384	0.0272	0.0000	0.0016	2.005
	Average	**0.4289**	**0.9753**	**0.0051**	**0.0664**	**0.1785**	**0.0473**	**0.0380**	**0.1593**	**0.0515**	**0.0359**	**0.0248**	**0.0000**	**0.0020**	**2.013**
S392-05	Average	**0.4373**	**0.9674**	**0.0118**	**0.0677**	**0.1816**	**0.0414**	**0.0326**	**0.1588**	**0.0544**	**0.0342**	**0.0243**	**0.0000**	**0.0016**	**2.013**
S392-07outer rim	396	0.4776	0.9592	0.0116	0.0668	0.2120	0.0312	0.0232	0.1496	0.0276	0.0340	0.0284	0.0000	0.0028	2.024
	401	0.4804	0.9612	0.0100	0.0696	0.2068	0.0252	0.0212	0.1692	0.0236	0.0320	0.0220	0.0000	0.0012	2.022

Mnz Grain	Analysis #	Ce	P	Si	Pr	La	Ca	Y	Nd	Th	Sm	Gd	Dy	U	Total / 4O
S392-07outer rim (cnt'd)	402	0.4724	0.9628	0.0140	0.0704	0.1996	0.0320	0.0208	0.1628	0.0316	0.0320	0.0208	0.0000	0.0008	2.020
	403	0.4744	0.9644	0.0096	0.0724	0.2024	0.0292	0.0228	0.1652	0.0264	0.0340	0.0196	0.0000	0.0012	2.022
	Average	**0.4762**	**0.9619**	**0.0113**	**0.0698**	**0.2052**	**0.0294**	**0.0220**	**0.1617**	**0.0273**	**0.0330**	**0.0227**	**0.0000**	**0.0015**	**2.022**
S392-07inner rim	397	0.4696	0.9540	0.0200	0.0748	0.1948	0.0368	0.0132	0.1668	0.0336	0.0344	0.0200	0.0000	0.0052	2.024
	398	0.4788	0.9540	0.0196	0.0728	0.1960	0.0340	0.0116	0.1624	0.0320	0.0352	0.0200	0.0000	0.0056	2.022
	399	0.4872	0.9492	0.0228	0.0736	0.1896	0.0288	0.0100	0.1712	0.0312	0.0352	0.0200	0.0000	0.0048	2.024
	400	0.4800	0.9524	0.0200	0.0744	0.1948	0.0344	0.0100	0.1676	0.0332	0.0324	0.0204	0.0000	0.0044	2.024
	Average	**0.4789**	**0.9524**	**0.0206**	**0.0739**	**0.1938**	**0.0335**	**0.0112**	**0.1670**	**0.0325**	**0.0343**	**0.0201**	**0.0000**	**0.0050**	**2.024**
S392-07 core	404	0.4580	0.9692	0.0036	0.0712	0.1968	0.0460	0.0384	0.1516	0.0312	0.0304	0.0204	0.0000	0.0056	2.023
	405	0.4512	0.9728	0.0048	0.0684	0.1868	0.0504	0.0424	0.1556	0.0320	0.0300	0.0200	0.0000	0.0064	2.021
	406	0.4524	0.9724	0.0052	0.0688	0.1908	0.0484	0.0428	0.1524	0.0328	0.0288	0.0188	0.0000	0.0064	2.020
	407	0.4508	0.9716	0.0036	0.0656	0.1872	0.0508	0.0428	0.1556	0.0336	0.0304	0.0220	0.0000	0.0068	2.021
	Average	**0.4531**	**0.9715**	**0.0043**	**0.0685**	**0.1904**	**0.0489**	**0.0416**	**0.1538**	**0.0324**	**0.0299**	**0.0203**	**0.0000**	**0.0063**	**2.021**
S392-07	Average	**0.4694**	**0.9619**	**0.0121**	**0.0707**	**0.1965**	**0.0373**	**0.0249**	**0.1608**	**0.0307**	**0.0324**	**0.0210**	**0.0000**	**0.0043**	**2.022**
S392-08 rim	1	0.4276	0.9704	0.0040	0.0680	0.2016	0.0424	0.0576	0.1452	0.0456	0.0256	0.0264	0.0000	0.0024	2.017
	6	0.4196	0.9760	0.0052	0.0668	0.1928	0.0408	0.0568	0.1484	0.0444	0.0276	0.0304	0.0000	0.0028	2.012
	7	0.4240	0.9684	0.0060	0.0664	0.1960	0.0412	0.0556	0.1516	0.0480	0.0296	0.0264	0.0000	0.0028	2.016
	8	0.4164	0.9804	0.0036	0.0640	0.1928	0.0412	0.0640	0.1456	0.0448	0.0264	0.0284	0.0000	0.0024	2.010
	Average	**0.4219**	**0.9738**	**0.0047**	**0.0663**	**0.1958**	**0.0414**	**0.0585**	**0.1477**	**0.0457**	**0.0273**	**0.0279**	**0.0000**	**0.0026**	**2.014**
S392-08 core	2	0.4324	0.9536	0.0220	0.0684	0.1872	0.0468	0.0204	0.1588	0.0620	0.0324	0.0272	0.0000	0.0056	2.017
	3	0.4260	0.9480	0.0260	0.0712	0.1832	0.0452	0.0216	0.1592	0.0672	0.0348	0.0268	0.0000	0.0068	2.016
	4	0.4348	0.9576	0.0240	0.0680	0.1880	0.0420	0.0160	0.1536	0.0628	0.0320	0.0268	0.0000	0.0056	2.012
	5	0.4236	0.9516	0.0248	0.0640	0.1864	0.0444	0.0220	0.1588	0.0644	0.0368	0.0304	0.0000	0.0076	2.015
	9	0.4244	0.9588	0.0232	0.0688	0.1828	0.0416	0.0196	0.1628	0.0616	0.0336	0.0248	0.0000	0.0064	2.011
	Average	**0.4282**	**0.9539**	**0.0240**	**0.0681**	**0.1855**	**0.0440**	**0.0199**	**0.1586**	**0.0636**	**0.0339**	**0.0272**	**0.0000**	**0.0064**	**2.014**
S392-08	Average	**0.4254**	**0.9628**	**0.0154**	**0.0673**	**0.1901**	**0.0428**	**0.0371**	**0.1538**	**0.0556**	**0.0310**	**0.0275**	**0.0000**	**0.0047**	**2.014**
S392-09	12	0.4556	0.9540	0.0240	0.0664	0.1856	0.0300	0.0232	0.1652	0.0512	0.0320	0.0224	0.0000	0.0048	2.014
	13	0.4392	0.9760	0.0056	0.0624	0.1892	0.0528	0.0268	0.1580	0.0476	0.0280	0.0200	0.0000	0.0076	2.013
	14	0.4636	0.9432	0.0292	0.0688	0.1840	0.0288	0.0152	0.1728	0.0560	0.0324	0.0184	0.0000	0.0048	2.017
	15	0.4500	0.9580	0.0276	0.0624	0.1836	0.0304	0.0244	0.1664	0.0536	0.0300	0.0188	0.0000	0.0044	2.010
	16	0.4576	0.9504	0.0256	0.0628	0.1904	0.0300	0.0232	0.1692	0.0528	0.0308	0.0184	0.0000	0.0044	2.015
	17	0.4572	0.9472	0.0252	0.0688	0.1844	0.0328	0.0252	0.1656	0.0540	0.0312	0.0216	0.0000	0.0052	2.018
	Average	**0.4539**	**0.9548**	**0.0229**	**0.0653**	**0.1862**	**0.0341**	**0.0230**	**0.1662**	**0.0525**	**0.0307**	**0.0199**	**0.0000**	**0.0052**	**2.015**

Mnz Grain	Analysis #	Ce	P	Si	Pr	La	Ca	Y	Nd	Th	Sm	Gd	Dy	U	Total / 4O
S392-17 High Y	81	0.3880	1.0156	0.0060	0.0460	0.2012	0.0452	0.0216	0.1708	0.0364	0.0272	0.0240	0.0088	0.0000	1.991
	Average	**0.3880**	**1.0156**	**0.0060**	**0.0460**	**0.2012**	**0.0452**	**0.0216**	**0.1708**	**0.0364**	**0.0272**	**0.0240**	**0.0088**	**0.0000**	**1.991**
S392-17 Low Y	76	0.4140	0.9944	0.0212	0.0504	0.2032	0.0288	0.0040	0.1864	0.0384	0.0300	0.0204	0.0020	0.0000	1.994
	77	0.4172	0.9900	0.0200	0.0476	0.2068	0.0336	0.0040	0.1836	0.0408	0.0312	0.0208	0.0024	0.0000	1.998
	Average	**0.4156**	**0.9922**	**0.0206**	**0.0490**	**0.2050**	**0.0312**	**0.0040**	**0.1850**	**0.0396**	**0.0306**	**0.0206**	**0.0022**	**0.0000**	**1.996**
S392-17 Medium Y	74	0.3960	1.0092	0.0144	0.0488	0.1984	0.0340	0.0164	0.1772	0.0316	0.0296	0.0268	0.0076	0.0000	1.990
	75	0.4040	1.0084	0.0128	0.0448	0.2012	0.0328	0.0140	0.1768	0.0320	0.0320	0.0256	0.0060	0.0000	1.990
	78	0.3884	1.0100	0.0084	0.0472	0.2188	0.0440	0.0116	0.1700	0.0384	0.0280	0.0220	0.0060	0.0000	1.993
	79	0.3960	1.0040	0.0160	0.0504	0.2004	0.0312	0.0128	0.1820	0.0328	0.0328	0.0260	0.0068	0.0000	1.992
	80	0.3964	1.0020	0.0160	0.0492	0.2060	0.0328	0.0104	0.1808	0.0356	0.0312	0.0268	0.0056	0.0000	1.993
	Average	**0.3962**	**1.0067**	**0.0135**	**0.0481**	**0.2050**	**0.0350**	**0.0130**	**0.1774**	**0.0341**	**0.0307**	**0.0254**	**0.0064**	**0.0000**	**1.992**
S392-17	Average	**0.4000**	**1.0042**	**0.0144**	**0.0481**	**0.2045**	**0.0353**	**0.0119**	**0.1785**	**0.0358**	**0.0303**	**0.0241**	**0.0057**	**0.0000**	**1.993**
S392map5 rim	86	0.3624	1.0404	0.0040	0.0460	0.1980	0.0596	0.0048	0.1664	0.0380	0.0272	0.0232	0.0088	0.0000	1.979
	87	0.3764	1.0372	0.0064	0.0476	0.1960	0.0580	0.0036	0.1636	0.0376	0.0264	0.0208	0.0068	0.0000	1.980
	88	0.3752	1.0320	0.0028	0.0476	0.1968	0.0456	0.0048	0.1820	0.0292	0.0320	0.0264	0.0084	0.0000	1.983
	Average	**0.3713**	**1.0365**	**0.0044**	**0.0471**	**0.1969**	**0.0544**	**0.0044**	**0.1707**	**0.0349**	**0.0285**	**0.0235**	**0.0080**	**0.0000**	**1.981**
S392map5 core	83	0.3972	1.0204	0.0076	0.0508	0.2072	0.0280	0.0028	0.1832	0.0284	0.0300	0.0220	0.0072	0.0000	1.985
	84	0.4008	1.0212	0.0076	0.0460	0.2164	0.0308	0.0028	0.1744	0.0312	0.0264	0.0204	0.0052	0.0000	1.983
	85	0.3800	1.0240	0.0104	0.0476	0.2060	0.0384	0.0024	0.1748	0.0416	0.0276	0.0212	0.0048	0.0000	1.979
	Average	**0.3927**	**1.0219**	**0.0085**	**0.0481**	**0.2099**	**0.0324**	**0.0027**	**0.1775**	**0.0337**	**0.0280**	**0.0212**	**0.0057**	**0.0000**	**1.982**
S392map5	Average	**0.3820**	**1.0292**	**0.0065**	**0.0476**	**0.2034**	**0.0434**	**0.0035**	**0.1741**	**0.0343**	**0.0283**	**0.0223**	**0.0069**	**0.0000**	**1.982**
S392	**Average**	**0.4370**	**0.9763**	**0.0133**	**0.0627**	**0.1938**	**0.0380**	**0.0241**	**0.1623**	**0.0450**	**0.0297**	**0.0223**	**0.0015**	**0.0023**	**2.008**
S394-18outer rim	28	0.4328	0.9744	0.0068	0.0596	0.1756	0.0776	0.0304	0.1380	0.0624	0.0252	0.0188	0.0000	0.0136	2.015
	Average	**0.4328**	**0.9744**	**0.0068**	**0.0596**	**0.1756**	**0.0776**	**0.0304**	**0.1380**	**0.0624**	**0.0252**	**0.0188**	**0.0000**	**0.0136**	**2.015**
S394-18inner rim	24	0.4412	0.9656	0.0064	0.0668	0.1876	0.0776	0.0228	0.1364	0.0676	0.0232	0.0140	0.0000	0.0108	2.020
	27	0.4412	0.9628	0.0068	0.0632	0.1800	0.0808	0.0232	0.1404	0.0720	0.0240	0.0160	0.0000	0.0116	2.022
	Average	**0.4412**	**0.9642**	**0.0066**	**0.0650**	**0.1838**	**0.0792**	**0.0230**	**0.1384**	**0.0698**	**0.0236**	**0.0150**	**0.0000**	**0.0112**	**2.021**
S394-18 core	25	0.4296	0.9672	0.0068	0.0640	0.1728	0.0776	0.0464	0.1360	0.0632	0.0252	0.0184	0.0000	0.0128	2.020
	26	0.4448	0.9644	0.0104	0.0612	0.1800	0.0696	0.0404	0.1348	0.0680	0.0224	0.0140	0.0000	0.0084	2.018
	Average	**0.4372**	**0.9658**	**0.0086**	**0.0626**	**0.1764**	**0.0736**	**0.0434**	**0.1354**	**0.0656**	**0.0238**	**0.0162**	**0.0000**	**0.0106**	**2.019**
S394	**Average**	**0.4379**	**0.9669**	**0.0074**	**0.0630**	**0.1792**	**0.0766**	**0.0326**	**0.1371**	**0.0666**	**0.0240**	**0.0162**	**0.0000**	**0.0114**	**2.019**
S396-26	19	0.4060	0.9772	0.0036	0.0572	0.1672	0.0856	0.0452	0.1412	0.0712	0.0248	0.0204	0.0000	0.0144	2.014
	20	0.4112	0.9732	0.0024	0.0620	0.1736	0.0776	0.0480	0.1412	0.0676	0.0272	0.0216	0.0000	0.0116	2.017

Mnz Grain	Analysis #	Ce	P	Si	Pr	La	Ca	Y	Nd	Th	Sm	Gd	Dy	U	Total / 4O
S396-26 (cnt'd)	21	0.4476	0.9680	0.0076	0.0636	0.1844	0.0584	0.0316	0.1504	0.0464	0.0260	0.0184	0.0000	0.0152	2.018
	22	0.4084	0.9732	0.0032	0.0584	0.1652	0.0832	0.0460	0.1420	0.0724	0.0280	0.0216	0.0000	0.0148	2.016
	23	0.4012	0.9604	0.0120	0.0568	0.1684	0.0808	0.0524	0.1448	0.0852	0.0256	0.0204	0.0000	0.0092	2.018
S396	**Average**	**0.4149**	**0.9704**	**0.0058**	**0.0596**	**0.1718**	**0.0771**	**0.0446**	**0.1439**	**0.0686**	**0.0263**	**0.0205**	**0.0000**	**0.0130**	**2.016**
S397-01 rim	118	0.3728	0.9880	0.0128	0.0436	0.1840	0.0684	0.0436	0.1596	0.0636	0.0260	0.0232	0.0096	0.0080	2.004
	119	0.3796	0.9824	0.0120	0.0476	0.1872	0.0620	0.0448	0.1648	0.0588	0.0264	0.0236	0.0104	0.0076	2.008
	120	0.3792	0.9868	0.0136	0.0476	0.1808	0.0628	0.0460	0.1612	0.0596	0.0256	0.0232	0.0100	0.0068	2.004
	Average	**0.3892**	**0.9899**	**0.0041**	**0.0492**	**0.1811**	**0.0715**	**0.0502**	**0.1523**	**0.0567**	**0.0235**	**0.0184**	**0.0068**	**0.0130**	**2.005**
S397-01 core	121	0.3768	0.9992	0.0020	0.0456	0.1860	0.0684	0.0544	0.1556	0.0524	0.0220	0.0168	0.0096	0.0120	2.001
	122	0.3744	0.9980	0.0040	0.0424	0.1824	0.0728	0.0552	0.1556	0.0520	0.0220	0.0180	0.0104	0.0152	2.002
	123	0.3736	0.9996	0.0036	0.0424	0.1844	0.0776	0.0528	0.1484	0.0580	0.0232	0.0160	0.0100	0.0120	2.002
	124	0.3876	0.9908	0.0032	0.0460	0.1860	0.0716	0.0476	0.1564	0.0584	0.0220	0.0176	0.0072	0.0108	2.005
	Average	**0.3853**	**0.9923**	**0.0040**	**0.0475**	**0.1820**	**0.0731**	**0.0509**	**0.1514**	**0.0570**	**0.0234**	**0.0178**	**0.0076**	**0.0128**	**2.003**
S397-01	Average	**0.4164**	**0.9725**	**0.0063**	**0.0595**	**0.1750**	**0.0734**	**0.0411**	**0.1458**	**0.0656**	**0.0266**	**0.0204**	**0.0004**	**0.0119**	**2.004**
S397-02	127	0.3896	0.9832	0.0152	0.0468	0.1864	0.0684	0.0256	0.1636	0.0660	0.0252	0.0188	0.0064	0.0088	2.004
	128	0.3840	0.9868	0.0148	0.0456	0.1856	0.0676	0.0252	0.1640	0.0652	0.0272	0.0196	0.0064	0.0092	2.002
	129	0.3820	0.9884	0.0120	0.0460	0.1892	0.0728	0.0396	0.1580	0.0640	0.0232	0.0160	0.0064	0.0068	2.005
	130	0.3844	0.9868	0.0156	0.0476	0.1844	0.0660	0.0256	0.1608	0.0656	0.0268	0.0204	0.0068	0.0100	2.001
	131	0.3864	0.9792	0.0148	0.0448	0.1896	0.0668	0.0380	0.1636	0.0656	0.0260	0.0176	0.0064	0.0076	2.006
	132	0.3892	0.9796	0.0176	0.0456	0.1860	0.0688	0.0284	0.1636	0.0668	0.0248	0.0204	0.0064	0.0088	2.006
	133	0.3828	0.9756	0.0248	0.0456	0.1860	0.0640	0.0268	0.1668	0.0740	0.0256	0.0180	0.0068	0.0060	2.003
	Average	**0.3855**	**0.9828**	**0.0164**	**0.0460**	**0.1867**	**0.0678**	**0.0299**	**0.1629**	**0.0667**	**0.0255**	**0.0187**	**0.0065**	**0.0082**	**2.004**
S397-03 High Y	136	0.3660	0.9900	0.0084	0.0432	0.1808	0.0648	0.0724	0.1524	0.0576	0.0248	0.0208	0.0108	0.0108	2.003
	139	0.3712	0.9908	0.0040	0.0456	0.1852	0.0736	0.0528	0.1576	0.0612	0.0252	0.0184	0.0072	0.0116	2.005
	141	0.3616	0.9876	0.0108	0.0440	0.1692	0.0736	0.0696	0.1536	0.0628	0.0268	0.0208	0.0116	0.0120	2.004
	Average	**0.3842**	**0.9817**	**0.0189**	**0.0464**	**0.1857**	**0.0659**	**0.0274**	**0.1635**	**0.0688**	**0.0260**	**0.0190**	**0.0067**	**0.0081**	**2.004**
S397-03 Low Y	135	0.3848	0.9876	0.0140	0.0460	0.1932	0.0632	0.0248	0.1624	0.0620	0.0300	0.0184	0.0056	0.0092	2.001
	137	0.3848	0.9832	0.0136	0.0440	0.1864	0.0680	0.0316	0.1672	0.0624	0.0276	0.0204	0.0076	0.0088	2.006
	138	0.3804	0.9884	0.0116	0.0464	0.1880	0.0600	0.0384	0.1636	0.0544	0.0296	0.0228	0.0092	0.0096	2.002
	140	0.3800	0.9816	0.0148	0.0472	0.1880	0.0700	0.0280	0.1632	0.0668	0.0272	0.0220	0.0072	0.0092	2.005
	142	0.4024	0.9780	0.0160	0.0460	0.1900	0.0628	0.0184	0.1688	0.0636	0.0284	0.0200	0.0048	0.0076	2.007
	Average	**0.3753**	**0.9848**	**0.0133**	**0.0450**	**0.1820**	**0.0685**	**0.0458**	**0.1600**	**0.0637**	**0.0265**	**0.0206**	**0.0088**	**0.0098**	**2.004**
S397-03	Average	**0.3855**	**0.9828**	**0.0164**	**0.0460**	**0.1867**	**0.0678**	**0.0299**	**0.1629**	**0.0667**	**0.0255**	**0.0187**	**0.0065**	**0.0082**	**2.004**

Mnz Grain	Analysis #	Ce	P	Si	Pr	La	Ca	Y	Nd	Th	Sm	Gd	Dy	U	Total / 4O
S397	**Average**	**0.4151**	**0.9899**	**0.0069**	**0.0569**	**0.1869**	**0.0634**	**0.0238**	**0.1527**	**0.0536**	**0.0264**	**0.0197**	**0.0026**	**0.0075**	**2.004**
S399-4a	1	0.4208	0.9776	0.0148	0.0756	0.1804	0.0532	0.0268	0.1436	0.0740	0.0260	0.0000	0.0000	0.0000	2.008
	2	0.4220	0.9776	0.0144	0.0732	0.1612	0.0568	0.0396	0.1480	0.0792	0.0316	0.0000	0.0000	0.0000	2.003
	3	0.4140	0.9884	0.0040	0.0712	0.1720	0.0676	0.0500	0.1396	0.0660	0.0264	0.0000	0.0000	0.0000	2.011
	4	0.4408	0.9584	0.0244	0.0712	0.1748	0.0516	0.0168	0.1516	0.0872	0.0300	0.0000	0.0000	0.0000	2.008
	5	0.4392	0.9488	0.0180	0.0744	0.1872	0.0532	0.0288	0.1536	0.0804	0.0276	0.0000	0.0000	0.0000	2.017
	Average	**0.4274**	**0.9702**	**0.0151**	**0.0731**	**0.1751**	**0.0565**	**0.0324**	**0.1473**	**0.0774**	**0.0283**	**0.0000**	**0.0000**	**0.0000**	**2.009**
S399-8.1	6	0.4100	0.9688	0.0036	0.0660	0.2108	0.0700	0.0460	0.1336	0.0792	0.0232	0.0000	0.0000	0.0040	2.015
	7	0.4352	0.9604	0.0156	0.0716	0.2080	0.0516	0.0276	0.1404	0.0712	0.0248	0.0000	0.0000	0.0064	2.012
	8	0.4056	0.9808	0.0040	0.0652	0.2036	0.0600	0.0476	0.1364	0.0716	0.0244	0.0000	0.0000	0.0060	2.006
	9	0.4348	0.9548	0.0196	0.0712	0.1912	0.0524	0.0176	0.1456	0.0864	0.0248	0.0000	0.0000	0.0020	2.017
	10	0.4192	0.9948	0.0020	0.0660	0.1864	0.0548	0.0572	0.1348	0.0508	0.0264	0.0000	0.0000	0.0084	2.001
	11	0.4316	0.9792	0.0024	0.0736	0.2120	0.0448	0.0488	0.1404	0.0436	0.0292	0.0000	0.0000	0.0056	2.012
	12	0.4240	0.9840	0.0020	0.0660	0.2040	0.0520	0.0512	0.1344	0.0548	0.0276	0.0000	0.0000	0.0068	2.007
	13	0.4096	0.9776	0.0076	0.0676	0.1912	0.0548	0.0596	0.1380	0.0728	0.0248	0.0000	0.0000	0.0020	2.006
	14	0.4500	0.9500	0.0196	0.0712	0.1992	0.0456	0.0092	0.1500	0.0804	0.0284	0.0000	0.0000	0.0008	2.020
	15	0.4128	0.9816	0.0036	0.0680	0.2048	0.0528	0.0524	0.1408	0.0604	0.0268	0.0000	0.0000	0.0036	2.007
	16	0.4488	0.9444	0.0200	0.0752	0.2004	0.0492	0.0156	0.1492	0.0820	0.0252	0.0000	0.0000	0.0044	2.020
	*17	0.4576	0.9348	0.0224	0.0804	0.2060	0.0448	0.0100	0.1520	0.0760	0.0292	0.0000	0.0000	0.0048	2.023
	Average	**0.4256**	**0.9706**	**0.0091**	**0.0692**	**0.2011**	**0.0535**	**0.0393**	**0.1403**	**0.0685**	**0.0260**	**0.0000**	**0.0000**	**0.0045**	**2.011**
S399-8.2	18	0.4040	0.9696	0.0048	0.0676	0.1880	0.0696	0.0544	0.1344	0.0812	0.0224	0.0000	0.0000	0.0036	2.021
	*19	0.4296	0.9420	0.0200	0.0676	0.1928	0.0528	0.0192	0.1448	0.0908	0.0244	0.0000	0.0000	0.0000	2.036
	20	0.4080	0.9788	0.0036	0.0648	0.1932	0.0724	0.0448	0.1324	0.0740	0.0220	0.0000	0.0000	0.0132	2.008
	21	0.4220	0.9716	0.0036	0.0684	0.1972	0.0684	0.0452	0.1332	0.0672	0.0228	0.0000	0.0000	0.0108	2.017
	22	0.4092	0.9832	0.0024	0.0636	0.2036	0.0584	0.0592	0.1320	0.0508	0.0292	0.0000	0.0000	0.0104	2.013
	23	0.4396	0.9604	0.0144	0.0692	0.1988	0.0544	0.0272	0.1392	0.0772	0.0256	0.0000	0.0000	0.0064	2.012
	24	0.4392	0.9780	0.0008	0.0732	0.2152	0.0432	0.0472	0.1416	0.0408	0.0276	0.0000	0.0000	0.0064	2.013
	*25	0.4496	0.9284	0.0224	0.0764	0.2036	0.0476	0.0084	0.1476	0.0784	0.0244	0.0000	0.0000	0.0016	2.050
	Average	**0.4203**	**0.9736**	**0.0049**	**0.0678**	**0.1993**	**0.0611**	**0.0463**	**0.1355**	**0.0652**	**0.0249**	**0.0000**	**0.0000**	**0.0085**	**2.014**
S399	**Average**	**0.4246**	**0.9713**	**0.0093**	**0.0697**	**0.1947**	**0.0562**	**0.0397**	**0.1406**	**0.0696**	**0.0262**	**0.0000**	**0.0000**	**0.0046**	**2.012**
S401-01 High Y	99	0.3500	0.9812	0.0148	0.0372	0.1576	0.0892	0.0732	0.1516	0.0776	0.0260	0.0232	0.0132	0.0124	2.008
	106	0.3516	0.9788	0.0204	0.0416	0.1672	0.0824	0.0592	0.1492	0.0824	0.0268	0.0220	0.0136	0.0088	2.004
	Average	**0.3508**	**0.9800**	**0.0176**	**0.0394**	**0.1624**	**0.0858**	**0.0662**	**0.1504**	**0.0800**	**0.0264**	**0.0226**	**0.0134**	**0.0106**	**2.006**

Mnz Grain	Analysis #	Ce	P	Si	Pr	La	Ca	Y	Nd	Th	Sm	Gd	Dy	U	Total / 4O
S401-01 Medium Y	104	0.3508	0.9672	0.0264	0.0424	0.1564	0.0948	0.0476	0.1556	0.0956	0.0312	0.0244	0.0112	0.0072	2.011
	105	0.3572	0.9752	0.0196	0.0436	0.1632	0.0952	0.0320	0.1600	0.0876	0.0304	0.0240	0.0100	0.0112	2.010
	107	0.3552	0.9780	0.0204	0.0444	0.1612	0.0908	0.0324	0.1600	0.0912	0.0292	0.0244	0.0088	0.0088	2.005
	Average	**0.3544**	**0.9735**	**0.0221**	**0.0435**	**0.1603**	**0.0936**	**0.0373**	**0.1585**	**0.0915**	**0.0303**	**0.0243**	**0.0100**	**0.0091**	**2.009**
S401-01 Low Y	100	0.3800	0.9640	0.0308	0.0452	0.1664	0.0768	0.0180	0.1672	0.0880	0.0276	0.0236	0.0092	0.0096	2.006
	101	0.3716	0.9680	0.0268	0.0436	0.1688	0.0844	0.0160	0.1668	0.0884	0.0296	0.0260	0.0088	0.0096	2.008
	102	0.3756	0.9708	0.0300	0.0452	0.1648	0.0792	0.0184	0.1636	0.0856	0.0316	0.0248	0.0072	0.0084	2.005
	103	0.3732	0.9816	0.0176	0.0436	0.1796	0.0768	0.0248	0.1624	0.0756	0.0276	0.0240	0.0088	0.0084	2.004
	Average	**0.3751**	**0.9711**	**0.0263**	**0.0444**	**0.1699**	**0.0793**	**0.0193**	**0.1650**	**0.0844**	**0.0291**	**0.0246**	**0.0085**	**0.0090**	**2.006**
S401-01	Average	**0.3628**	**0.9739**	**0.0230**	**0.0430**	**0.1650**	**0.0855**	**0.0357**	**0.1596**	**0.0858**	**0.0289**	**0.0240**	**0.0101**	**0.0094**	**2.007**
S401-02outer rim	113	0.2944	0.9748	0.0272	0.0384	0.1168	0.1380	0.0532	0.1264	0.1368	0.0412	0.0296	0.0124	0.0144	2.004
	Average	**0.2944**	**0.9748**	**0.0272**	**0.0384**	**0.1168**	**0.1380**	**0.0532**	**0.1264**	**0.1368**	**0.0412**	**0.0296**	**0.0124**	**0.0144**	**2.004**
S401-02inner rim	112	0.3140	0.9884	0.0124	0.0420	0.1168	0.1068	0.0668	0.1460	0.0940	0.0516	0.0332	0.0172	0.0136	2.003
	116	0.3172	0.9868	0.0116	0.0428	0.1224	0.1148	0.0588	0.1408	0.1004	0.0488	0.0332	0.0140	0.0136	2.006
	Average	**0.3156**	**0.9876**	**0.0120**	**0.0424**	**0.1196**	**0.1108**	**0.0628**	**0.1434**	**0.0972**	**0.0502**	**0.0332**	**0.0156**	**0.0136**	**2.004**
S401-02outer core	111	0.2960	0.9816	0.0216	0.0364	0.1136	0.1220	0.0660	0.1380	0.1160	0.0488	0.0344	0.0144	0.0132	2.002
	114	0.2980	0.9800	0.0224	0.0396	0.1148	0.1280	0.0548	0.1364	0.1280	0.0444	0.0300	0.0136	0.0124	2.002
	115	0.3220	0.9848	0.0164	0.0456	0.1228	0.1060	0.0548	0.1444	0.1028	0.0504	0.0300	0.0128	0.0092	2.002
	Average	**0.3053**	**0.9821**	**0.0201**	**0.0405**	**0.1171**	**0.1187**	**0.0585**	**0.1396**	**0.1156**	**0.0479**	**0.0315**	**0.0136**	**0.0116**	**2.002**
S401-02core	109	0.2668	0.9640	0.0324	0.0356	0.1016	0.1516	0.0664	0.1252	0.1592	0.0420	0.0308	0.0140	0.0160	2.006
	110	0.2636	0.9740	0.0304	0.0356	0.1024	0.1484	0.0656	0.1248	0.1508	0.0440	0.0316	0.0148	0.0156	2.002
	Average	**0.2652**	**0.9690**	**0.0314**	**0.0356**	**0.1020**	**0.1500**	**0.0660**	**0.1250**	**0.1550**	**0.0430**	**0.0312**	**0.0144**	**0.0158**	**2.004**
S401-02	Average	**0.2965**	**0.9793**	**0.0218**	**0.0395**	**0.1139**	**0.1270**	**0.0608**	**0.1353**	**0.1235**	**0.0464**	**0.0316**	**0.0142**	**0.0135**	**2.003**
S401	**Average**	**0.3316**	**0.9764**	**0.0224**	**0.0413**	**0.1410**	**0.1050**	**0.0475**	**0.1481**	**0.1095**	**0.0371**	**0.0276**	**0.0120**	**0.0113**	**2.005**

**Analysis not used in the average because the cation total does not fall between 1.975 and 2.025 cations/ 4.000 oxygens.*

Appendix 7

Trace element analyses

Grain #:	S366-07	Acc. Voltage:	15 kV	Bkg: 300 sec.	
Chemical zone:	homogeneous	Anal. Current:	200 nA	Pb Ma / PETH	Th Ma / PETJ
Analyses#:	365-369	Peak:	600 sec.	U Mb / PETJ	Y La / TAP

Spot #	Pb uncorr. (ppm)	Pb corr. (ppm)	Pb error (%)	Th (ppm)	Th error (%)	U uncorr. (ppm)	U corr. (ppm)	U error (%)	Y (ppm)	Y error (%)	Age (Ma)	S.D. 2s (Ma)	S.D. 2s (%)
1	3196	3091.90	0.6755	29807	0.2880	2553	2280.52	2.4134	8228	0.2864	1748.5	88	5.05
2	3991	3875.85	0.5754	39969	0.2340	2327	1960.60	2.6611	8186	0.2882	1772.5	97	5.47
3	4163	4041.99	0.5598	40280	0.2331	3090	2720.75	2.0482	8828	0.2703	1737.0	74	4.28
4	4826	4688.71	0.5073	43880	0.2198	4217	3814.46	1.5520	10251	0.2379	1748.0	58	3.31
5	3196	3091.90	0.6755	29807	0.2880	2553	2280.52	2.4134	8228	0.2864	1748.5	88	5.05

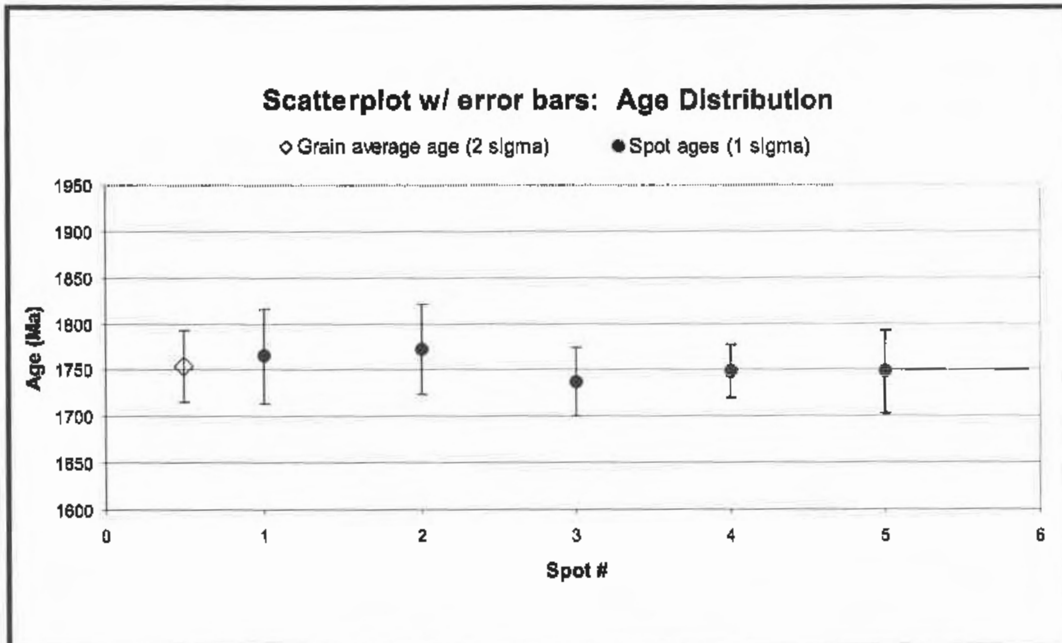

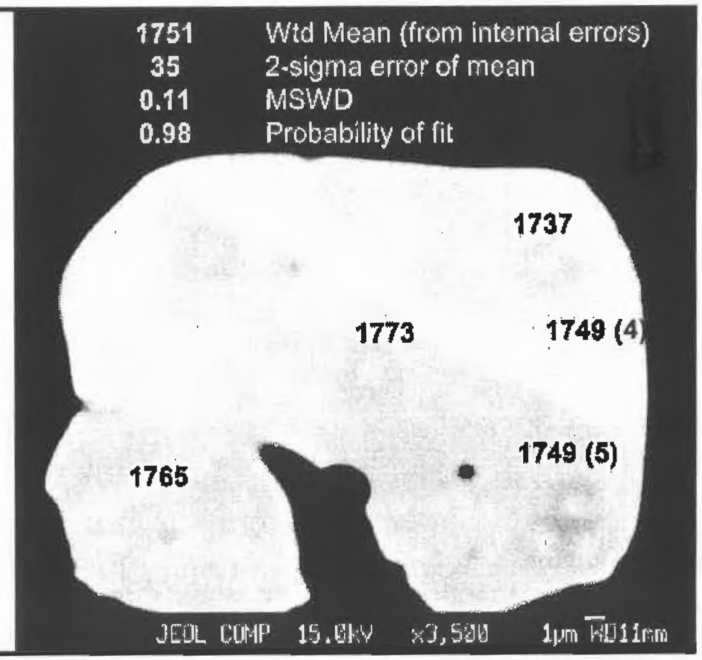

Grain #:	S366-15	Acc. Voltage:	15 kV	Bkg: 300 sec.	
Chemical zone:	homogeneous	Anal. Current:	200 nA	Pb Ma / PETH	Th Ma / PETJ
Analyses#:	657-666	Peak: 600 sec.		U Mb / PETJ	Y La / TAP

Spot #	Pb uncorr. (ppm)	Pb corr. (ppm)	Pb error (%)	Th (ppm)	Th error (%)	U uncorr. (ppm)	U corr. (ppm)	U error (%)	Y (ppm)	Y error (%)	Age (Ma)	S.D. 2s (Ma)	S.D. 2s (%)
1	4722	4595.77	0.5055	41450	0.2266	4206	3823.97	1.5908	9264	0.2541	1785.0	60	3.38
2	4522	4398.79	0.5202	41570	0.2263	3494	3110.83	1.8795	8901	0.2630	1789.0	70	3.94
3	2747	2665.84	0.7426	25357	0.3253	1861	1628.33	3.3198	7275	0.3123	1824.0	125	6.84
4	3819	3707.34	0.5838	35470	0.2550	2593	2266.59	2.4577	8347	0.2777	1821.5	93	5.09
5	4530	4406.72	0.5197	40736	0.2316	3853	3477.61	1.7195	9016	0.2602	1776.0	65	3.63

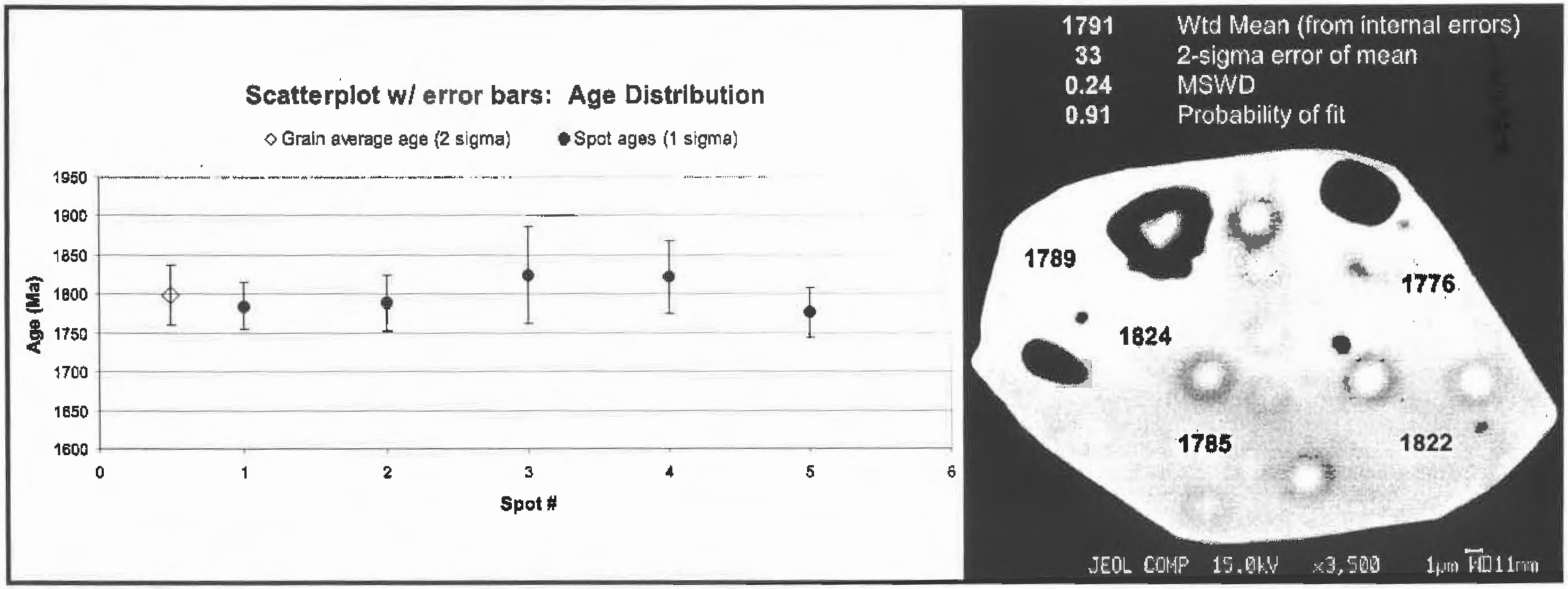

Grain #:	S366-16	Acc. Voltage: 15 kV	Bkg: 300 sec.	
Chemical zone:	homogeneous	Anal. Current: 200 nA	Pb Ma / PETH	Th Ma / PETJ
Analyses#:	354-356	Peak: 600 sec.	U Mb / PETJ	Y La / TAP

Spot #	Pb uncorr. (ppm)	Pb corr. (ppm)	Pb error (%)	Th (ppm)	Th error (%)	U uncorr. (ppm)	U corr. (ppm)	U error (%)	Y (ppm)	Y error (%)	Age (Ma)	S.D. 2s (Ma)	S.D. 2s (%)
1	3646	3543.97	0.6008	34152	0.2624	2066	1753.10	3.2430	7413	0.3091	1875.0	124	6.62
2	3219	3118.63	0.6583	28979	0.2956	2101	1835.90	3.1762	7891	0.2924	1874.5	122	6.52
3	5077	4950.23	0.4812	48604	0.2059	2901	2453.96	2.4041	8405	0.2782	1847.0	91	4.93
4	4180	4065.51	0.5470	38909	0.2398	2576	2219.10	2.6522	8241	0.2823	1856.5	101	5.44
5	4280	4161.52	0.5386	42120	0.2268	2502	2115.29	2.7352	8286	0.2811	1797.5	101	5.60
6	3686	3578.23	0.5969	31734	0.2768	2825	2534.52	2.4156	8393	0.2774	1871.0	94	5.02
7	3751	3642.86	0.5898	33942	0.2637	2503	2192.09	2.7112	8149	0.2847	1863.2	104	5.58

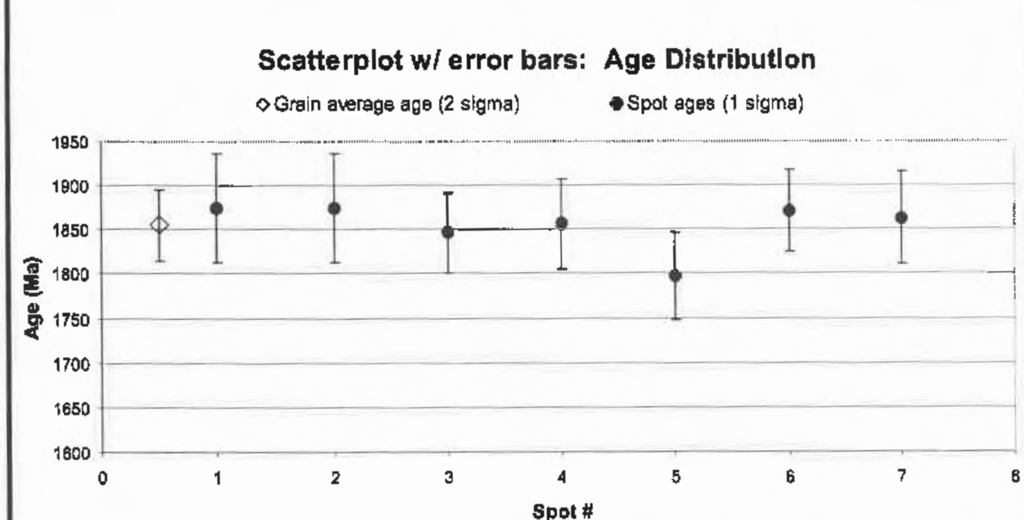

1853	Wtd Mean (from internal errors)
39	2-sigma error of mean
0.28	MSWD
0.95	Probability of fit

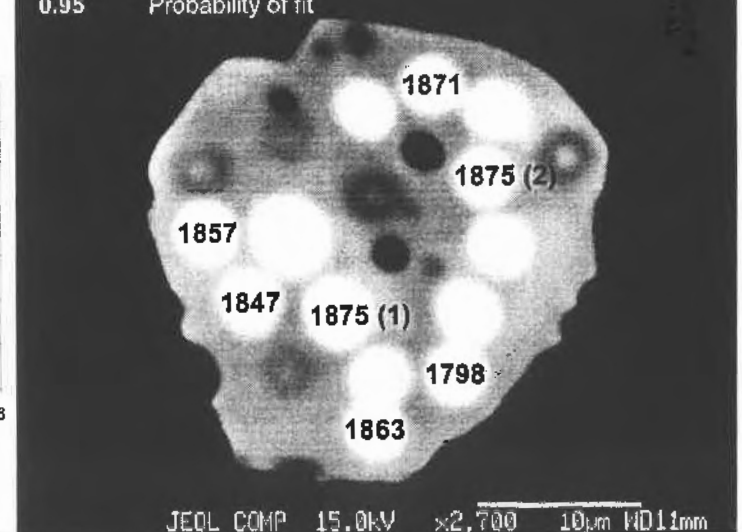

Grain #: S366map1
Chemical zone: homogeneous
Analyses#: 657-668

Acc. Voltage: 15 kV
Anal. Current: 200 nA
Peak: 600 sec.

Bkg: 300 sec.
Pb Ma / PETH   Th Ma / PETJ
U Mb / PETJ   Y La / TAP

Spot #	Pb uncorr. (ppm)	Pb corr. (ppm)	Pb error (%)	Th (ppm)	Th error (%)	U uncorr. (ppm)	U corr. (ppm)	U error (%)	Y (ppm)	Y error (%)	Age (Ma)	S.D. 2s (Ma)	S.D. 2s (%)
1	4861	4775.50	0.5070	42657	0.2091	3679	3487.80	1.4699	6708	0.3165	1850.0	58	3.15
2	4154	4060.02	0.5656	37984	0.2252	2622	2274.04	2.0865	5977	0.3496	1880.5	82	4.36
3	3088	3009.18	0.7007	27116	0.2815	2301	2053.35	2.3299	5636	0.3670	1864.0	91	4.91
4	5149	5041.03	0.4896	43568	0.2063	4108	3706.40	1.3988	6877	0.3099	1890.0	57	3.01
5	5037	4930.65	0.4968	41132	0.2141	4623	4245.98	1.2597	7008	0.3050	1865.0	51	2.76
6	3547	3464.64	0.6324	31276	0.2559	2394	2108.01	2.2553	5504	0.3754	1903.5	90	4.72
7	2776	2705.29	0.7598	23233	0.3134	2314	2102.03	2.3131	5200	0.3938	1874.5	92	4.92
8	4740	4643.86	0.5167	43347	0.2070	2629	2231.31	2.0907	5527	0.3751	1930.2	84	4.34

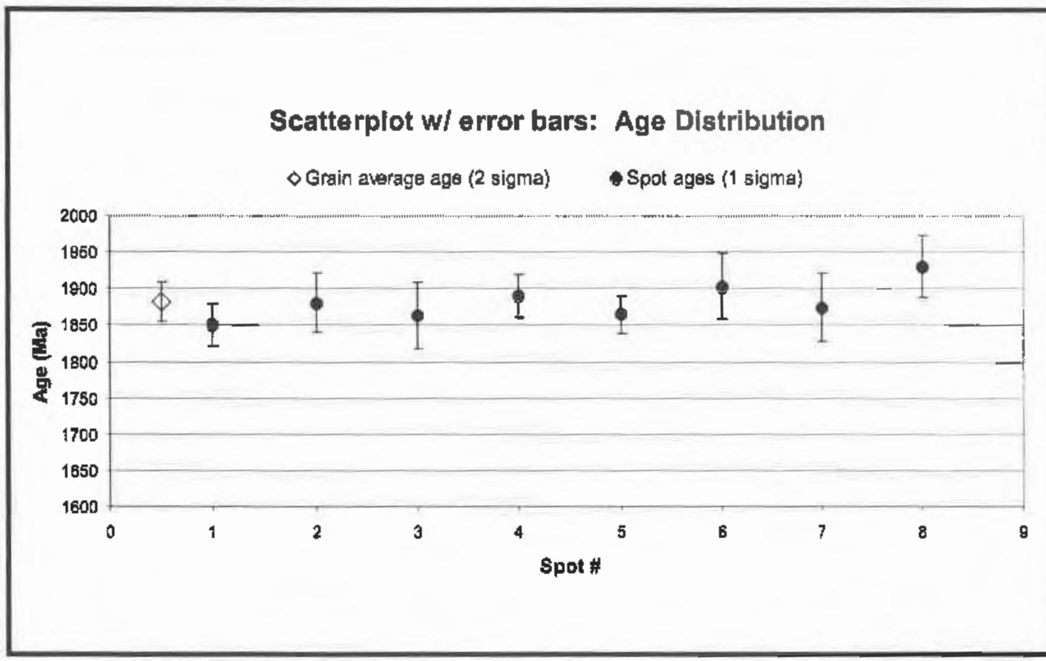

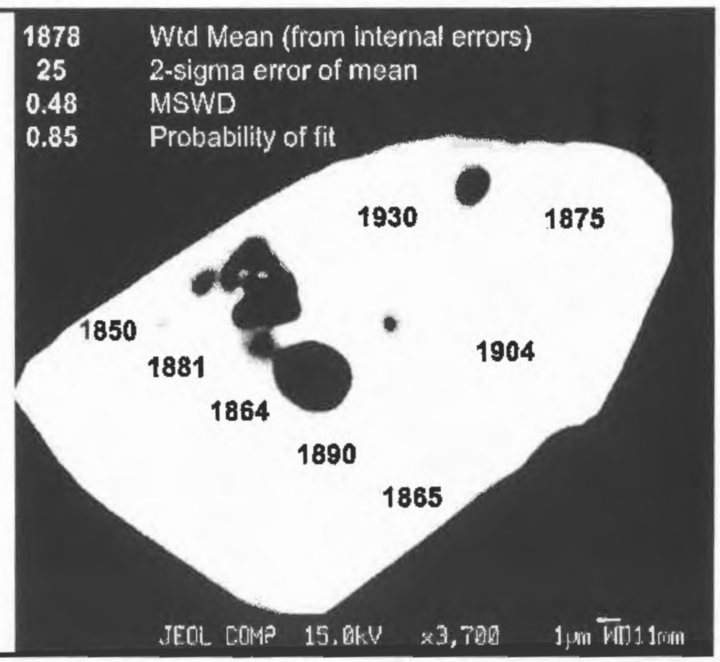

Grain #:	8366map2	Acc. Voltage:	15 kV	Bkg: 300 sec.	
Chemical zone:	homogeneous	Anal. Current:	200 nA	Pb Ma / PETH	Th Ma / PETJ
Analyses#:	41-46	Peak: 600 sec.		U Mb / PETJ	Y La / TAP

Spot #	Pb uncorr. (ppm)	Pb corr. (ppm)	Pb error (%)	Th (ppm)	Th error (%)	U uncorr. (ppm)	U corr. (ppm)	U error (%)	Y (ppm)	Y error (%)	Age (Ma)	S.D. 2s (Ma)	S.D. 2s (%)
1	2541	2459.20	0.7908	22038	0.3257	1923	1721.75	2.8212	6619	0.3289	1861.5	110	5.90
2	2317	2232.96	0.8524	19549	0.3555	2013	1834.62	2.7040	7199	0.3060	1827.0	105	5.72
3	3734	3628.89	0.5947	35225	0.2368	2441	2118.14	2.2848	7609	0.2928	1816.5	86	4.75
4	3492	3390.72	0.6239	32531	0.2496	2287	1989.07	2.4216	7515	0.2957	1831.0	92	5.03
5	3423	3320.66	0.6335	31676	0.2542	2472	2181.96	2.2527	7749	0.2881	1802.0	85	4.72
6	4507	4398.62	0.5220	43769	0.2059	2650	2247.83	2.1376	6881	0.3202	1820.0	81	4.43

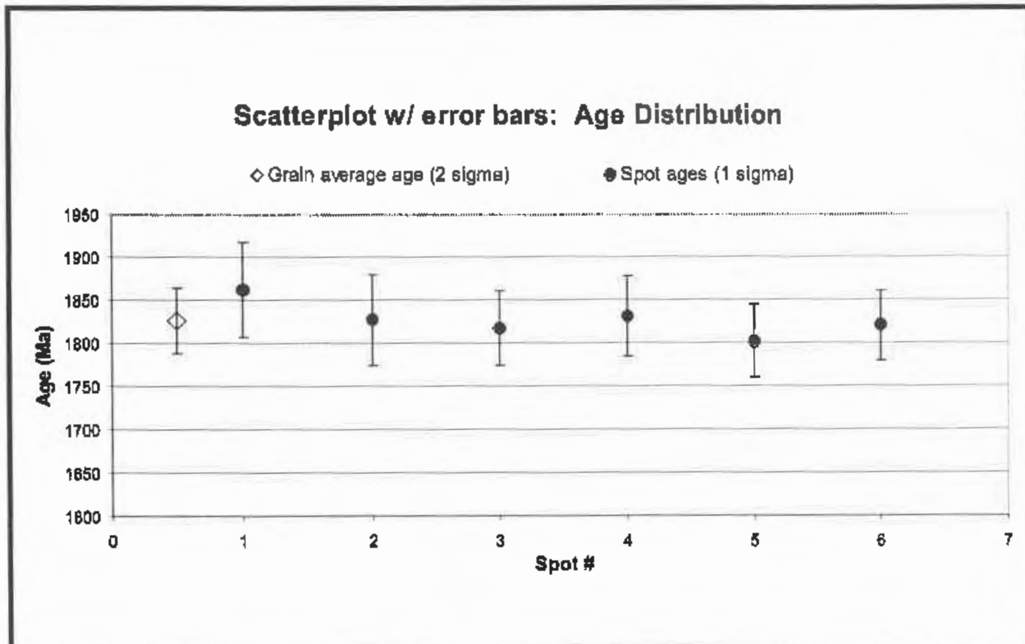

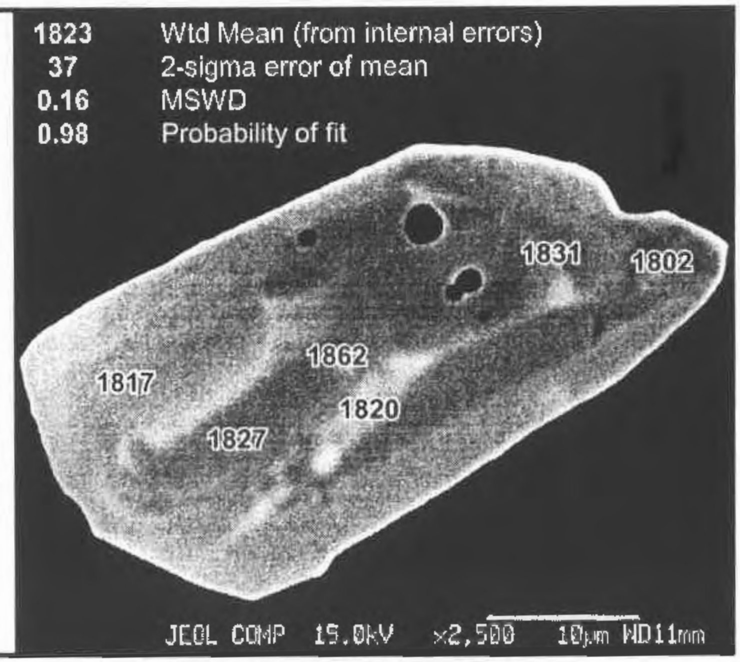

Grain #: S367-10
Chemical zone: homogeneous
Analyses#: 496-501

Acc. Voltage: 15 kV
Anal. Current: 200 nA
Peak: 600 sec.

Bkg: 300 sec.
Pb Ma / PETH Th Ma / PETJ
U Mb / PETJ Y La / TAP

Spot #	Pb uncorr. (ppm)	Pb corr. (ppm)	Pb error (%)	Th (ppm)	Th error (%)	U uncorr. (ppm)	U corr. (ppm)	U error (%)	Y (ppm)	Y error (%)	Age (Ma)	S.D. 2s (Ma)	S.D. 2s (%)
1	3186	3071.71	0.6535	21286	0.3842	4496	4302.10	1.4061	10529	0.2361	1785.0	57	3.21
2	2967	2851.93	0.6902	19375	0.4137	4103	3926.60	1.5245	10866	0.2300	1814.5	63	3.46
3	4129	3994.34	0.5449	29464	0.3012	5307	5038.03	1.2258	11630	0.2146	1793.3	50	2.76
4	1909	1823.08	0.9731	14000	0.5365	2063	1935.68	2.8540	8178	0.2931	1853.0	114	6.13
5	2315	2221.52	0.8330	16346	0.4730	2859	2710.26	2.1076	8752	0.2765	1817.0	84	4.64
6	4071	3956.72	0.5478	33549	0.2741	3948	3641.26	1.5960	8929	0.2729	1814.5	62	3.43

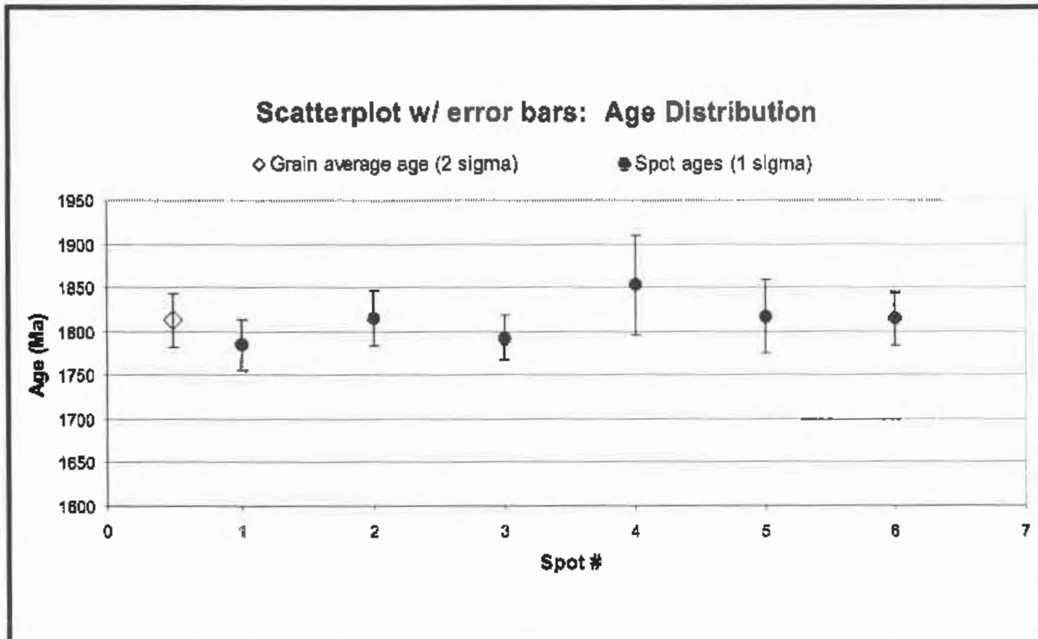

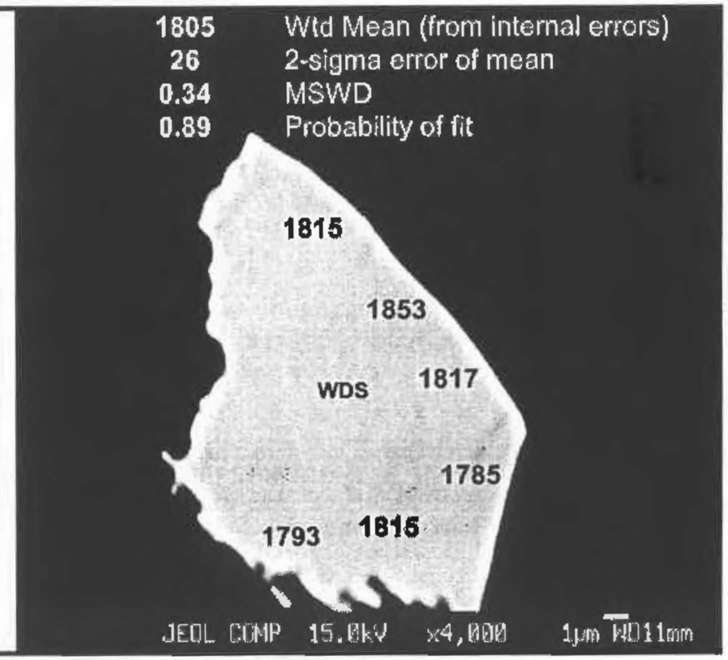

Grain #:	S367map1	Acc. Voltage:	15 kV	Bkg: 300 sec.	
Chemical zone:	homogeneous	Anal. Current:	200 nA	Pb Ma / PETH	Th Ma / PETJ
Analyses#:	47-51	Peak: 600 sec.		U Mb / PETJ	Y La / TAP

Spot #	Pb uncorr. (ppm)	Pb corr. (ppm)	Pb error (%)	Th (ppm)	Th error (%)	U uncorr. (ppm)	U corr. (ppm)	U error (%)	Y (ppm)	Y error (%)	Age (Ma)	S.D. 2s (Ma)	S.D. 2s (%)
1	3364	3257.86	0.6248	30447	0.2608	2816	2536.55	2.0904	8298	0.2739	1767.5	78	4.40
2	3975	3863.50	0.5556	37247	0.2284	2802	2459.42	2.1138	8049	0.2620	1798.5	79	4.40
3	4267	4147.76	0.5299	41839	0.2120	3089	2703.69	1.9413	8352	0.2736	1731.5	70	4.06
4	5482	5342.10	0.4514	54248	0.1802	3469	2967.68	1.7694	9140	0.2540	1769.0	65	3.68
5	6026	5885.65	0.4260	58797	0.1716	3640	3095.95	1.7042	8612	0.2676	1806.6	64	3.54

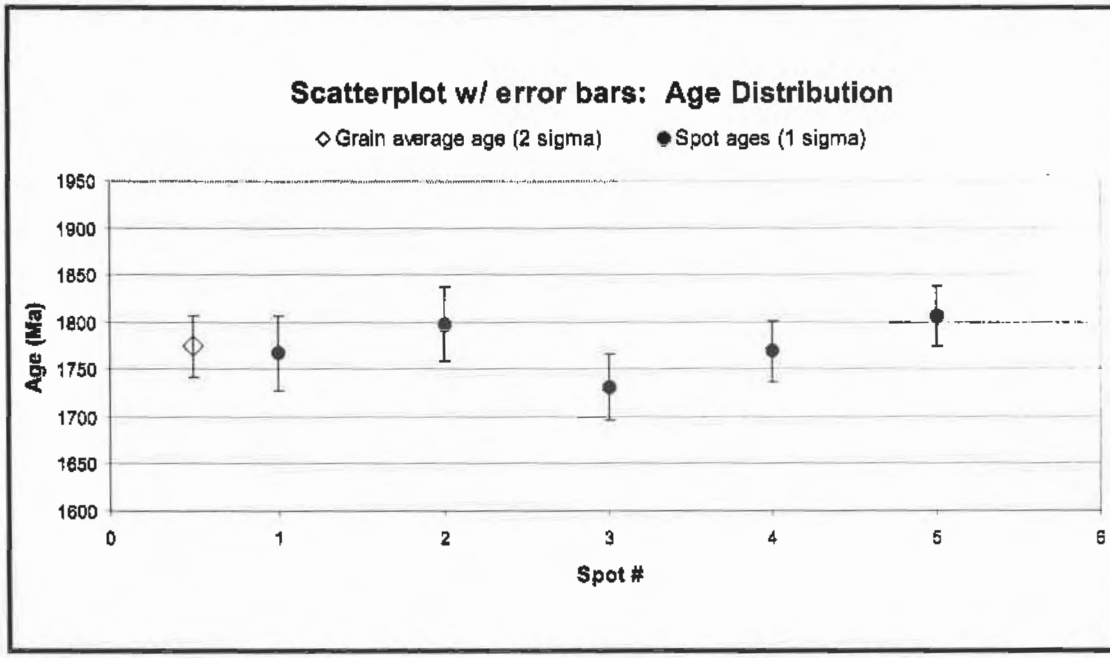

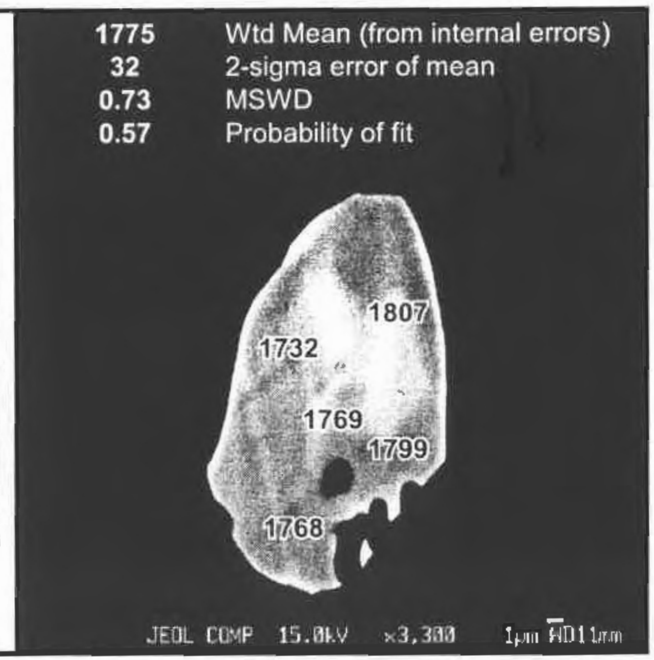

Grain #: 5371-06
Chemical zone: homogeneous
Analyses#: 122-127

Acc. Voltage: 15 kV
Anal. Current: 200 nA
Peak: 600 sec.

Bkg: 300 sec.
Pb Ma / PETH Th Ma / PETJ
U Mb / PETJ Y La / TAP

Spot #	Pb uncorr. (ppm)	Pb corr. (ppm)	Pb error (%)	Th (ppm)	Th error (%)	U uncorr. (ppm)	U corr. (ppm)	U error (%)	Y (ppm)	Y error (%)	Age (Ma)	St.Dev. (Ma ± 2s)	St.Dev. (% ± 2s)
1	3423	3336.09	0.6346	35762	0.2324	1859	1531.08	2.7598	5479	0.3823	1741.0	99	5.69
2	3354	3265.81	0.6446	35101	0.2354	1608	1486.22	2.8377	5715	0.3686	1739.0	102	5.85
3	3625	3530.74	0.6097	37648	0.2242	1955	1607.79	2.6415	6064	0.3501	1743.0	95	5.45
4	4844	4730.49	0.5002	51283	0.1851	2292	1819.81	2.3122	6551	0.3282	1760.8	84	4.75
5	5218	5101.03	0.4766	53770	0.1798	2708	2212.58	1.9875	6630	0.3249	1777.3	73	4.11
6	3874	3779.78	0.5813	40280	0.2154	2051	1681.21	2.5294	5740	0.3677	1756.3	92	5.22

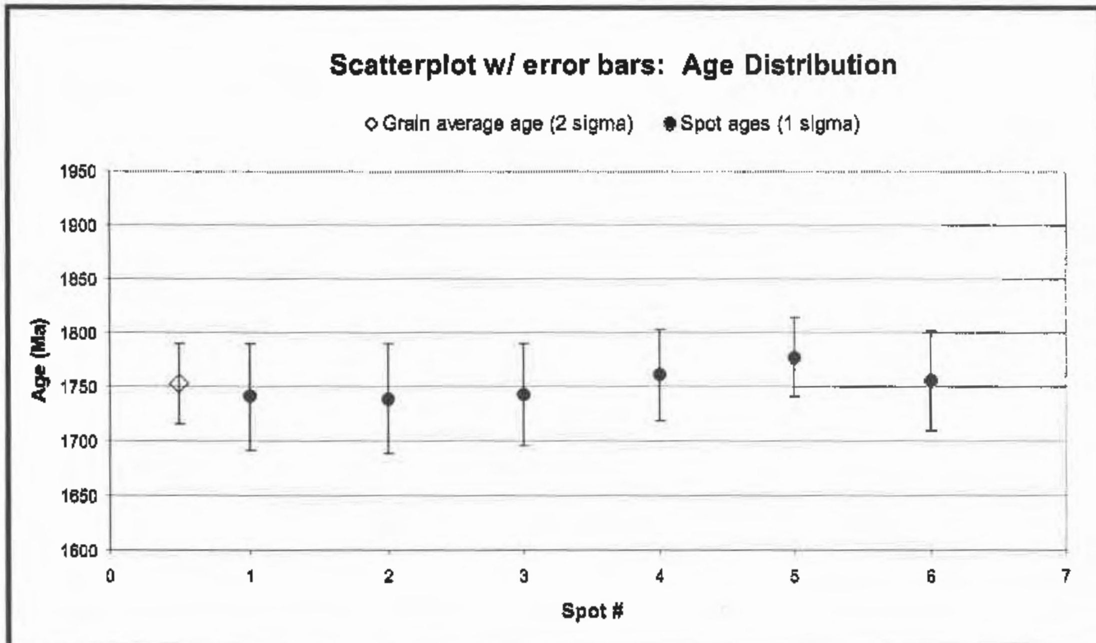

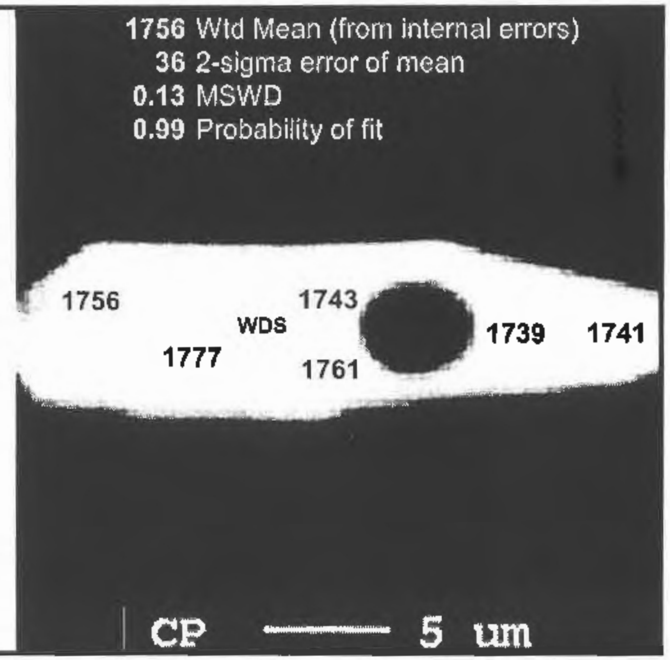

Chemical zone: S371-09
Chemical zone: homogeneous
Analyses#: 116-121

Acc. Voltage: 15 kV
Anal. Current: 200 nA
Peak: 600 sec.

Bkg: 300 sec.
Pb Ma / PETH Th Ma / PETJ
U Mb / PETJ Y La / TAP

Spot #	Pb uncorr. (ppm)	Pb corr. (ppm)	Pb error (%)	Th (ppm)	Th error (%)	U uncorr. (ppm)	U corr. (ppm)	U error (%)	Y (ppm)	Y error (%)	Age (Ma)	S.D. 2s (Ma)	S.D. 2s (%)
1	2882	2790.59	0.7343	27560	0.2780	2113	1861.23	2.4829	7096	0.3171	1752.0	91	5.22
2	5079	4964.90	0.4913	54126	0.1797	2172	1673.89	2.4856	6254	0.3563	1776.6	90	5.09
3	2498	2417.25	0.8196	25657	0.2919	1182	947.72	4.3073	6098	0.3619	1788.0	157	8.79
4	3087	3001.54	0.6960	31923	0.2517	1495	1202.95	3.4526	5825	0.3777	1781.0	126	7.07
5	2093	2025.14	0.9440	20908	0.3371	1169	978.32	4.3309	5212	0.4161	1782.0	159	8.90
6	2404	2333.45	0.8435	23195	0.3130	[illegible]	1094.32	[illegible]	[illegible]	[illegible]	[illegible]	146	8.00

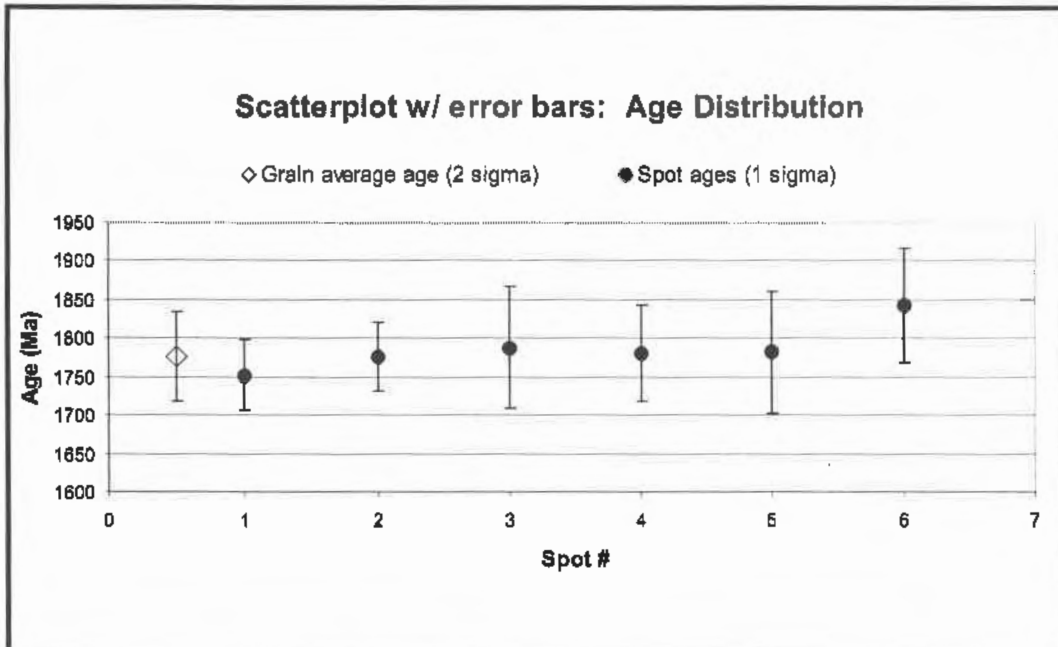

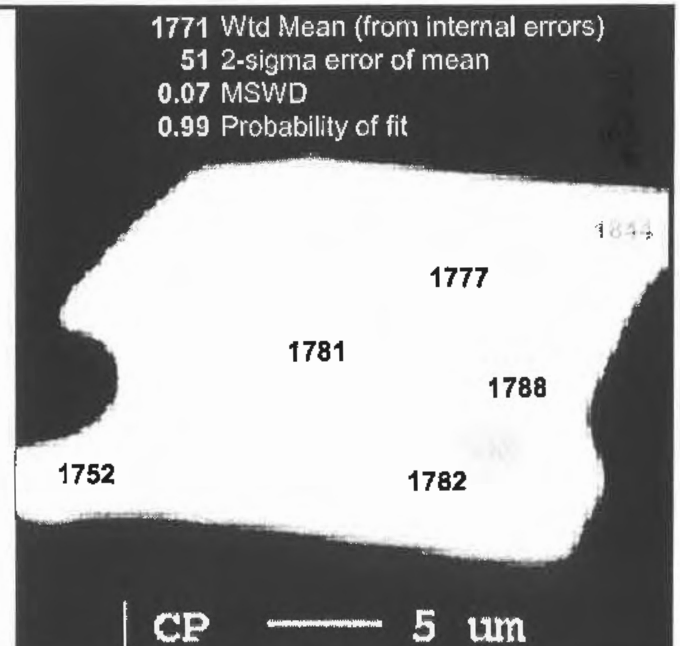

Grain #: S371-18
Chemical zone: homogeneous
Analyses#: 128-135

Acc. Voltage: 15 kV
Anal. Current: 200 nA
Peak: 600 sec.

Bkg: 300 sec.
Pb Ma / PETH Th Ma / PETJ
U Mb / PETJ Y La / TAP

Spot #	Pb uncorr. (ppm)	Pb corr. (ppm)	Pb error (%)	Th (ppm)	Th error (%)	U uncorr. (ppm)	U corr. (ppm)	U error (%)	Y (ppm)	Y error (%)	Age (Ma)	S.D. 2s (Ma)	S.D. 2s (%)
1	5161	5051.68	0.4777	54854	0.1771	1867	1381.37	2.9459	5592	0.3763	1815.7	109	5.99
2	3773	3680.35	0.5895	39457	0.2175	1236	873.83	4.3360	5665	0.3707	1855.4	163	8.77
3	2773	2697.01	0.7393	27304	0.2773	1217	967.23	4.3516	5310	0.3915	1878.0	166	8.85
4	2521	2449.05	0.7963	25057	0.2942	1257	1027.93	4.2103	5132	0.4035	1828.0	157	8.59
5	2250	2181.99	0.8707	21862	0.3235	1083	883.34	4.8519	5089	0.4060	1867.5	185	9.88
6	2821	2743.37	0.7292	26934	0.2798	1606	1359.68	3.3380	5550	0.3763	1847.0	127	6.86
7	1696	1638.91	1.0979	16137	0.4025	1051	903.86	4.9638	4562	0.4466	1814.0	185	10.20

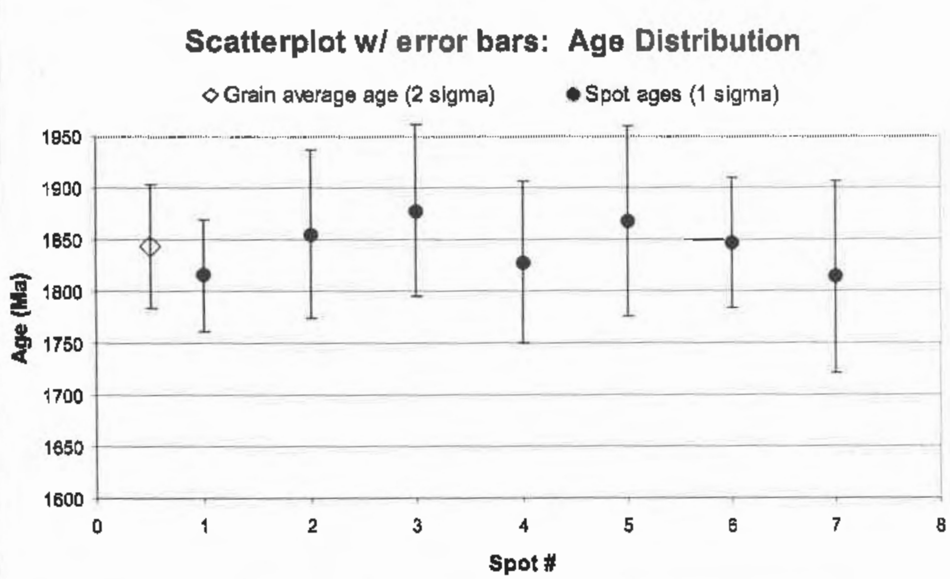

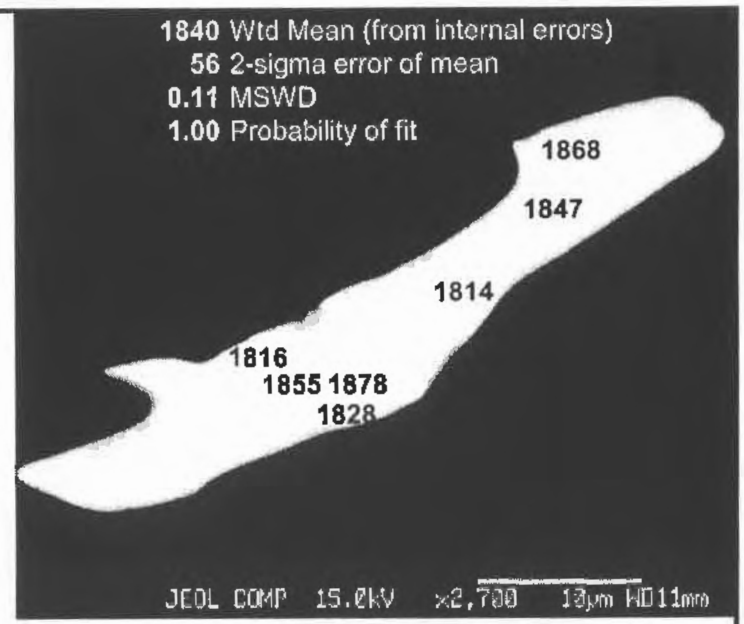

Grain #:	S371-19	Acc. Voltage: 15 kV	Bkg: 300 sec.	
Chemical zone:	homogeneous	Anal. Current: 200 nA	Pb Ma / PETH	Th Ma / PETJ
Analyses#:	370-373	Peak: 600 sec.	U Mb / PETJ	Y La / TAP

Spot #	Pb uncorr. (ppm)	Pb corr. (ppm)	Pb error (%)	Th (ppm)	Th error (%)	U uncorr. (ppm)	U corr. (ppm)	U error (%)	Y (ppm)	Y error (%)	Age (Ma)	S.D. 2s (Ma)
1	4165	4054.77	0.5536	42024	0.2271	2343	1957.32	2.6438	7344	0.3137	1777.0	96
2	4621	4499.08	0.5168	46770	0.2113	2900	2470.29	2.1816	8082	0.2869	1740.0	79
3	3222	3126.27	0.6650	32270	0.2735	1935	1639.64	3.1277	6929	0.3298	1761.5	113
4	4219	4110.47	0.5489	43249	0.2229	2393	1995.94	2.5964	6986	0.3284	1754.0	94

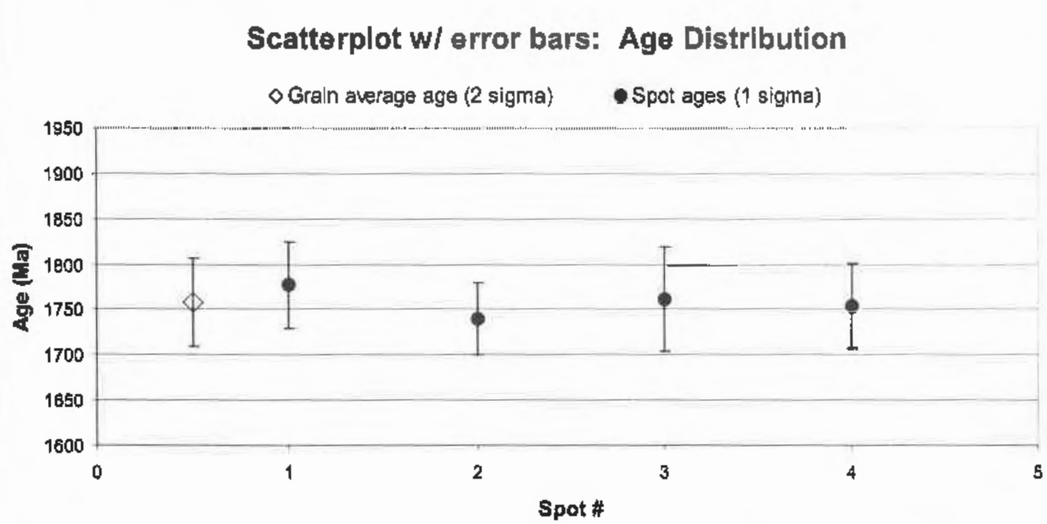

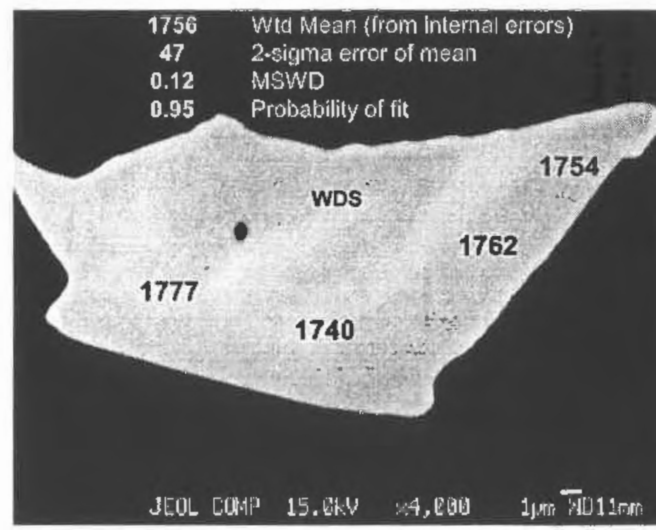

Grain #: S371-20
Chemical zone: homogeneous
Analyses#: 374-379

Acc. Voltage: 15 kV
Anal. Current: 200 nA
Peak: 600 sec.

Bkg: 300 sec.
Pb Ma / PETH Th Ma / PETJ
U Mb / PETJ Y La / TAP

Spot #	Pb uncorr. (ppm)	Pb corr. (ppm)	Pb error (%)	Th (ppm)	Th error (%)	U uncorr. (ppm)	U corr. (ppm)	U error (%)	Y (ppm)	Y error (%)	Age (Ma)	S.D. 2s (Ma)	S.D. 2s (%)
1	4536	4423.20	0.5303	48041	0.2076	2195	1753.58	2.8393	6862	0.3344	1752.5	102	5.80
2	1609	1545.95	1.1772	15381	0.4813	1195	1054.93	4.8800	5339	0.4151	1735.0	175	10.09
3	2892	2803.52	0.7323	29810	0.2910	1551	1280.28	3.8599	6443	0.3520	1763.5	139	7.88
4	4171	4057.25	0.5619	44471	0.2187	2038	1629.80	3.0262	7441	0.3109	1736.5	107	6.18
5	2196	2115.32	0.9106	21095	0.3756	1746	1553.63	3.4200	6646	0.3421	1707.5	122	7.12
6	3203	3109.79	0.6786	31657	0.2775	2141	1851.42	2.8480	6726	0.3393	1746.5	103	5.89

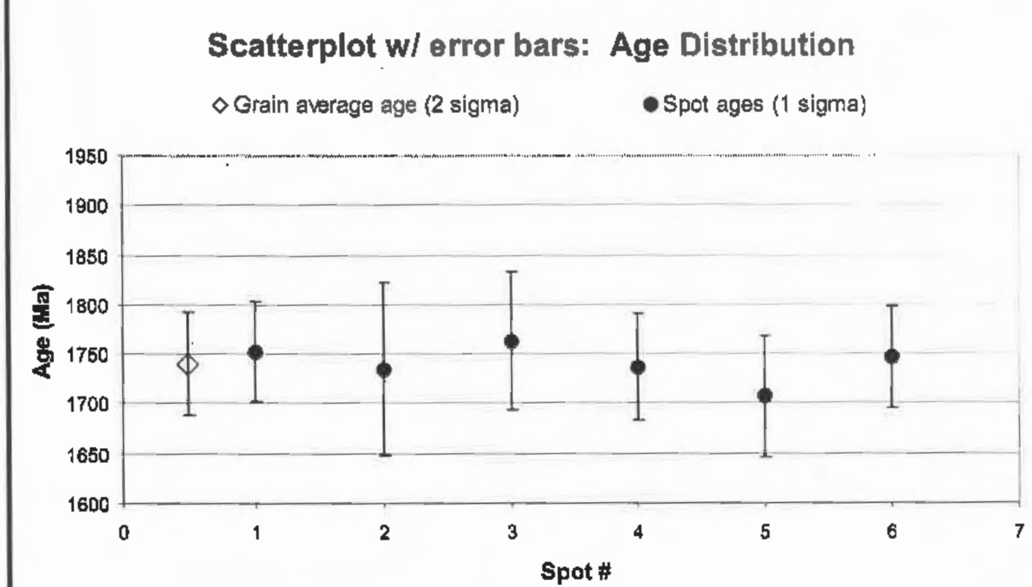

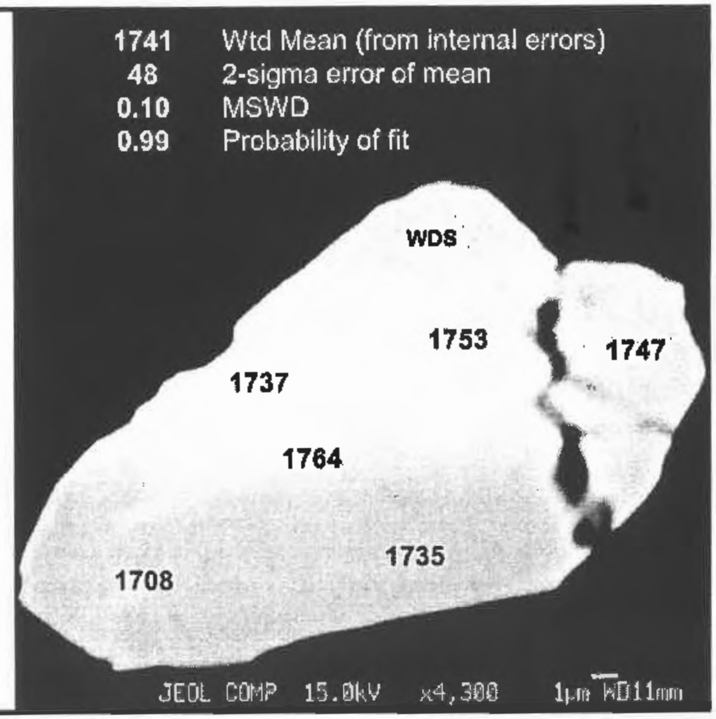

Grain #: S371-21
Chemical zone: homogeneous
Analyses#: 381-385

Acc. Voltage: 15 kV
Anal. Current: 200 nA
Peak: 600 sec.

Bkg: 300 sec.
Pb Ma / PETH Th Ma / PETJ
U Mb / PETJ Y La / TAP

Spot #	Pb uncorr. (ppm)	Pb corr. (ppm)	Pb error (%)	Th (ppm)	Th error (%)	U uncorr. (ppm)	U corr. (ppm)	U error (%)	Y (ppm)	Y error (%)	Age (Ma)	S.D. 2s (Ma)	S.D. 2s (%)
1	2157	2067.92	0.8978	18499	0.4158	1713	1544.45	3.8272	7967	0.2935	1839.0	145	7.91
2	3262	3169.96	0.6510	32727	0.2707	1889	1589.52	3.6351	6456	0.3547	1773.0	128	7.21
3	2198	2100.61	0.8858	19076	0.4061	1701	1527.16	3.8623	8834	0.2685	1830.0	146	7.97
4	2414	2314.83	0.8225	21668	0.3653	1672	1472.57	3.9375	8702	0.2721	1826.0	148	8.08
5	2594	2503.80	0.7753	23699	0.3413	1782	1563.90	3.7056	7395	0.3139	1818.0	138	7.61

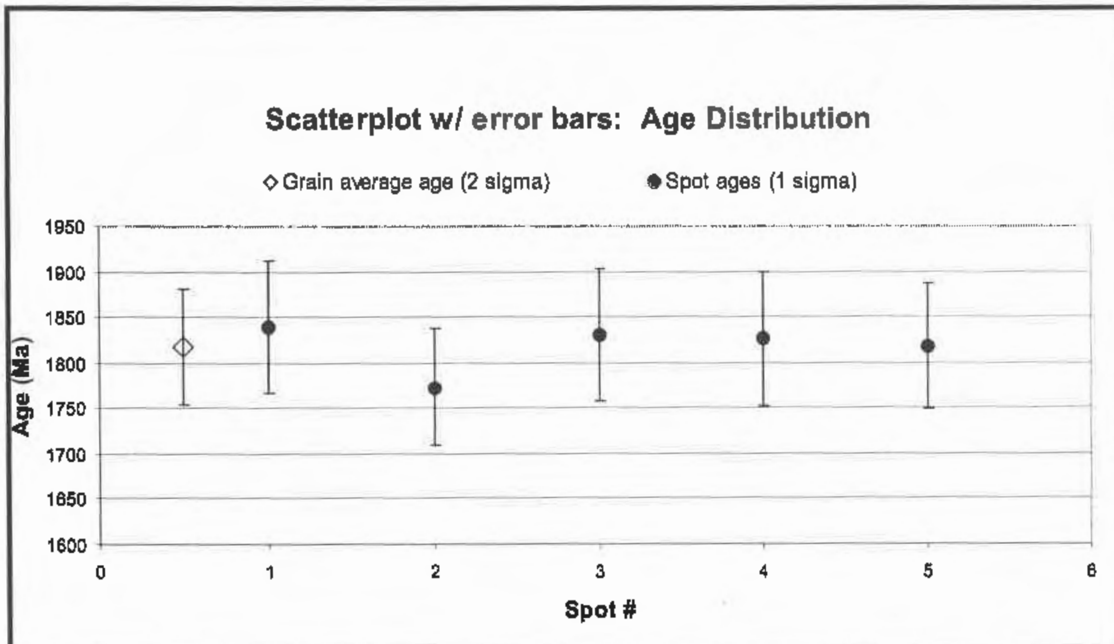

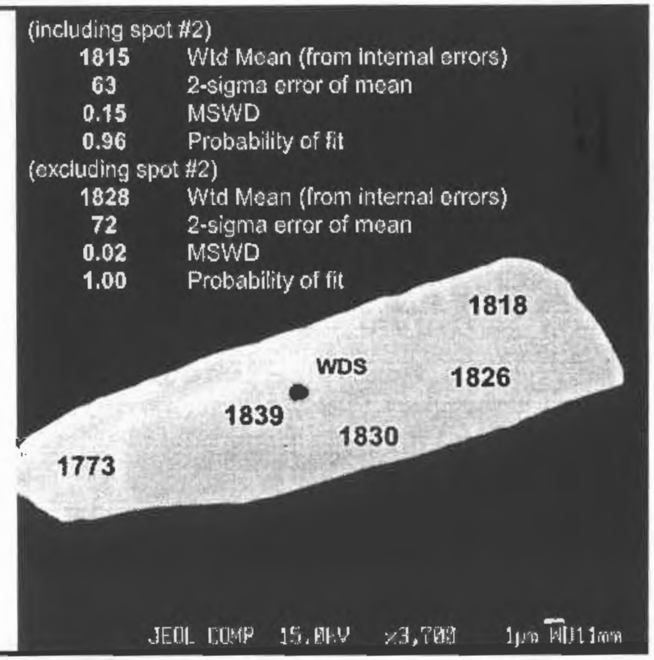

Grain #:	S373-01	Acc. Voltage:	15 kV	Bkg: 300 sec.	
Chemical zone:	homogeneous	Anal. Current:	200 nA	Pb Ma / PETH	Th Ma / PETJ
Analyses#:	251-255	Peak:	600 sec.	U Mb / PETJ	Y La / TAP

Spot #	Pb uncorr. (ppm)	Pb corr. (ppm)	Pb error (%)	Th (ppm)	Th error (%)	U uncorr. (ppm)	U corr. (ppm)	U error (%)	Y (ppm)	Y error (%)	Age (Ma)	S.D. 2s (Ma)	S.D. 2s (%)
1	5901	5751.68	0.4339	36211	0.2520	9230	8898.51	0.7382	12633	0.2194	1797.3	32	1.81
2	3335	3221.31	0.6338	28866	0.2962	2363	2099.07	2.3767	9450	0.2806	1888.5	94	4.96
3	3749	3635.75	0.5824	32349	0.2727	2930	2633.91	1.9553	8949	0.2948	1858.0	77	4.13
4	3609	3501.00	0.5979	34169	0.2622	2251	1938.05	2.4869	8103	0.3218	1824.7	94	5.17
5	3084	2980.85	0.6703	26979	0.3111	2280	2033.42	2.4529	8473	0.3087	1858.5	95	5.13

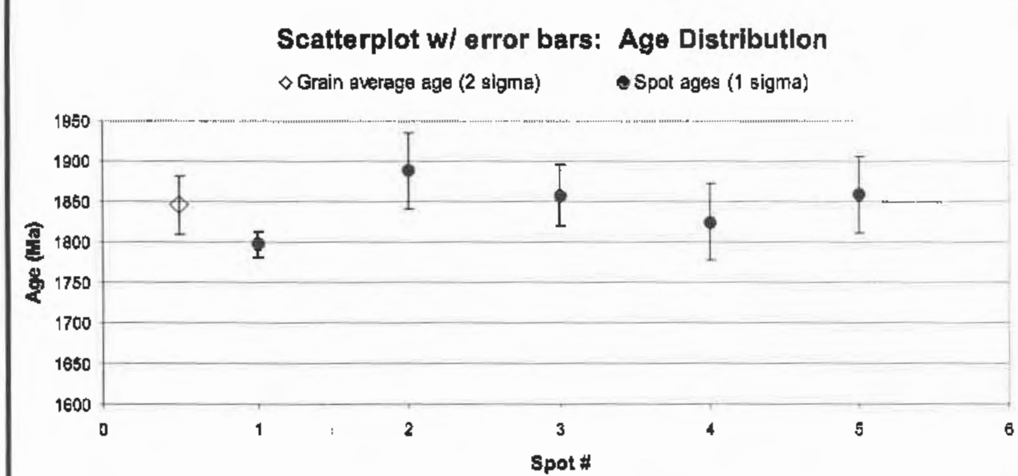

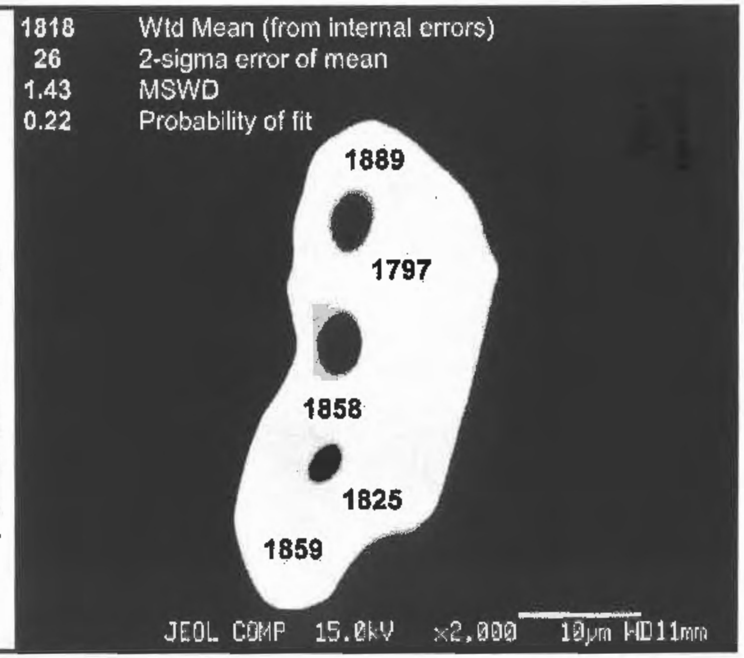

Grain #:	S373-02	Acc. Voltage: 15 kV	Bkg: 300 sec.
Chemical zone:	homogeneous	Anal. Current: 200 nA	Pb Ma / PETH Th Ma / PETJ
Analyses#:	256-260	Peak: 600 sec.	U Mb / PETJ Y La / TAP

Spot #	Pb uncorr. (ppm)	Pb corr. (ppm)	Pb error (%)	Th (ppm)	Th error (%)	U uncorr. (ppm)	U corr. (ppm)	U error (%)	Y (ppm)	Y error (%)	Age (Ma)	S.D. 2s (Ma)	S.D. 2s (%)
1	6183	6040.51	0.4251	43316	0.2237	8206	7808.02	0.8121	10887	0.2294	1805.5	34	1.91
2	6849	6698.43	0.4011	38749	0.2419	11464	11108.58	0.6276	12407	0.2057	1810.3	29	1.59
3	5842	5703.09	0.4399	38360	0.2432	8449	8097.06	0.7901	11110	0.2253	1802.3	34	1.89
4	6044	5899.95	0.4323	40457	0.2352	8709	8337.64	0.7767	11433	0.2208	1788.3	33	1.86
5	5401	5273.23	0.4620	36140	0.2540	7435	7103.57	0.8751	10110	0.2446	1821.0	38	2.06

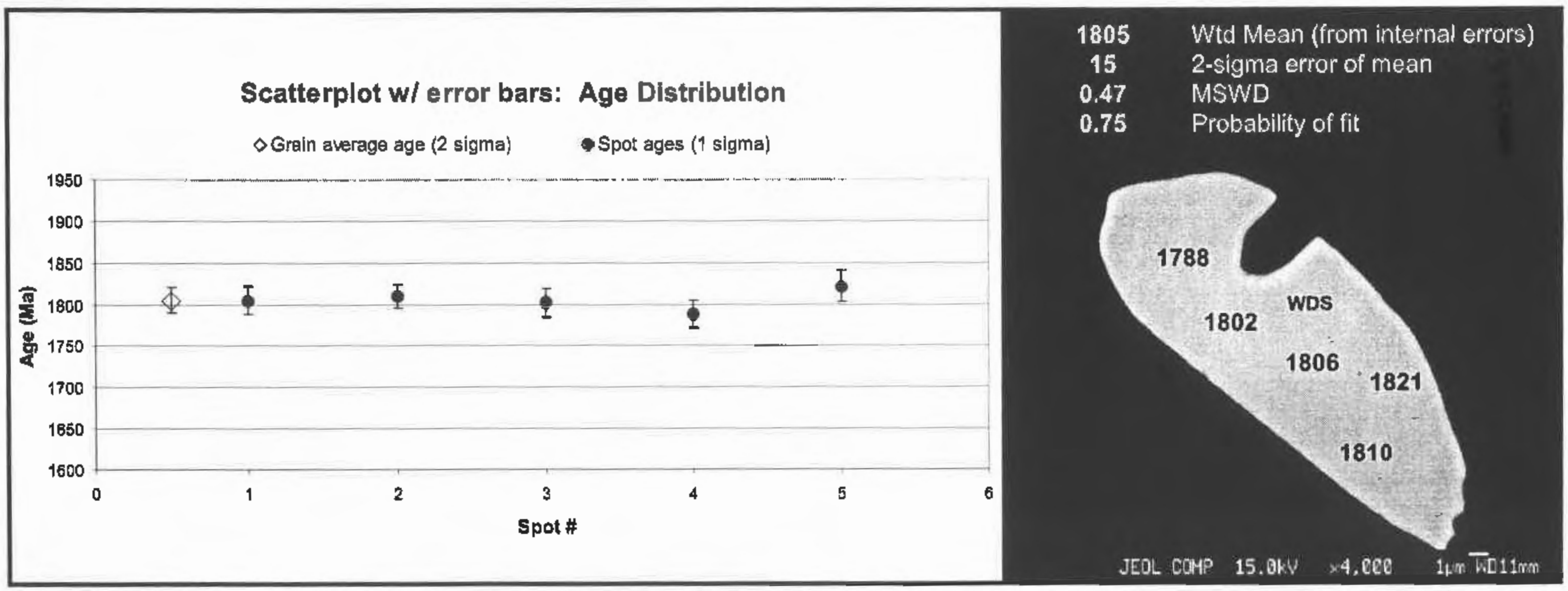

Grain #: S373-03
Chemical zone: homogeneous
Analyses#: 267-271

Acc. Voltage: 15 kV
Anal. Current: 200 nA
Peak: 600 sec.

Bkg: 300 sec.
Pb Ma / PETH Th Ma / PETJ
U Mb / PETJ Y La / TAP

Spot #	Pb uncorr. (ppm)	Pb corr. (ppm)	Pb error (%)	Th (ppm)	Th error (%)	U uncorr. (ppm)	U corr. (ppm)	U error (%)	Y (ppm)	Y error (%)	Age (Ma)	S.D. 2s (Ma)	S.D. 2s (%)
1	3812	3698.61	0.5839	35113	0.2579	2785	2466.14	1.9676	8600	0.2771	1804	75	4.18
2	2525	2434.46	0.7937	22464	0.3582	1854	1646.81	2.8725	7589	0.3086	1835	110	6.01
3	3701	3586.26	0.5961	32213	0.2741	3253	2958.00	1.7231	9130	0.2627	1794	66	3.70
4	4925	4796.20	0.4911	40669	0.2329	5138	4764.74	1.1617	9667	0.2509	1778	46	2.58
5	6416	6263.95	0.4172	46075	0.2138	8273	7849.68	0.7683	11661	0.2140	1800	33	1.86

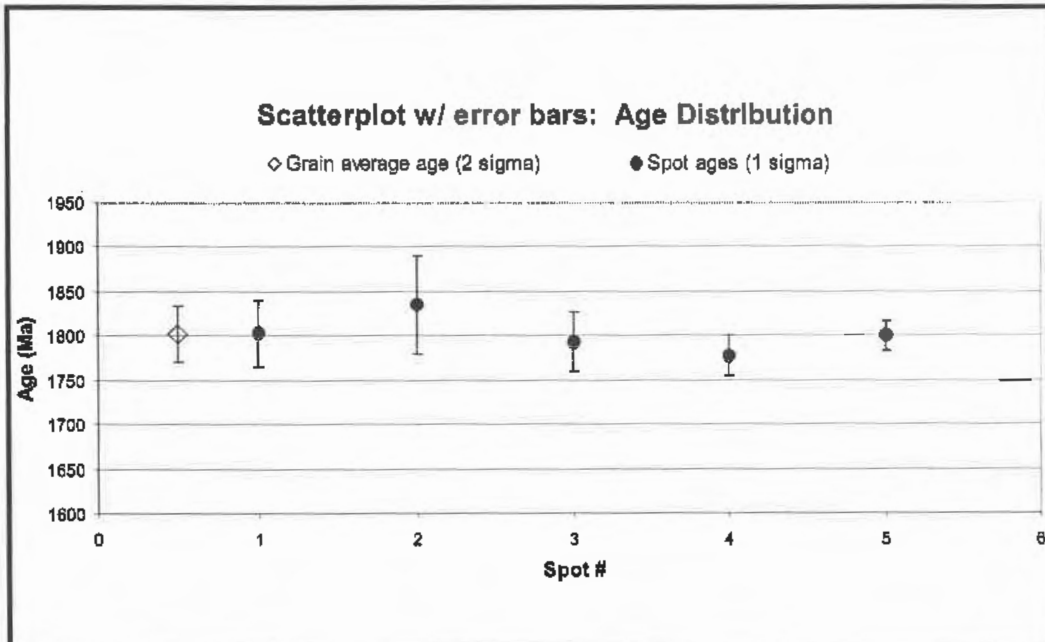

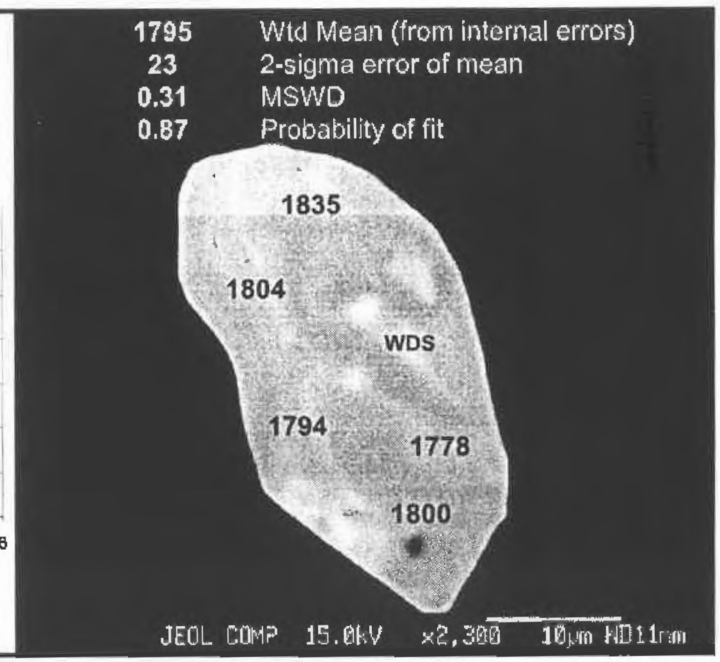

Grain #:	S373-04	Acc. Voltage:	15 kV	Bkg: 300 sec.	
Chemical zone:	homogeneous	Anal. Current:	200 nA	Pb Ma / PETH	Th Ma / PETJ
Analyses#:	458-462	Peak: 600 sec.		U Mb / PETJ	Y La / TAP

Spot #	Pb uncorr. (ppm)	Pb corr. (ppm)	Pb error (%)	Th (ppm)	Th error (%)	U uncorr. (ppm)	U corr. (ppm)	U error (%)	Y (ppm)	Y error (%)	Age (Ma)	S.D. 2s (Ma)	S.D. 2s (%)
1	3787	3674.94	0.5936	36844	0.2505	2271	1933.17	2.6164	8223	0.2834	1801.5	97	5.40
2	3752	3644.01	0.5975	36365	0.2528	2314	1980.57	2.5709	7814	0.2964	1799.0	96	5.31
3	3161	3062.50	0.6767	28676	0.2995	2263	2000.65	2.6014	7711	0.2994	1828.5	99	5.42
4	6904	6764.33	0.4041	41844	0.2298	11387	11003.22	0.8600	11944	0.2072	1771.0	29	1.64
5	5129	5004.95	0.4834	44500	0.2202	4900	4491.21	1.3135	8622	0.2728	1770.0	50	2.85

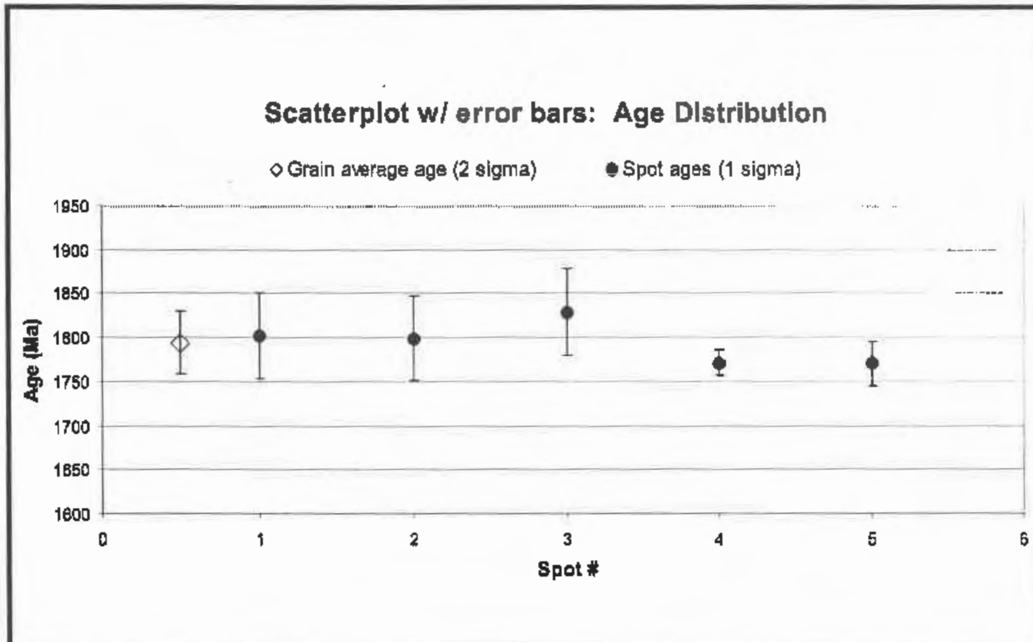

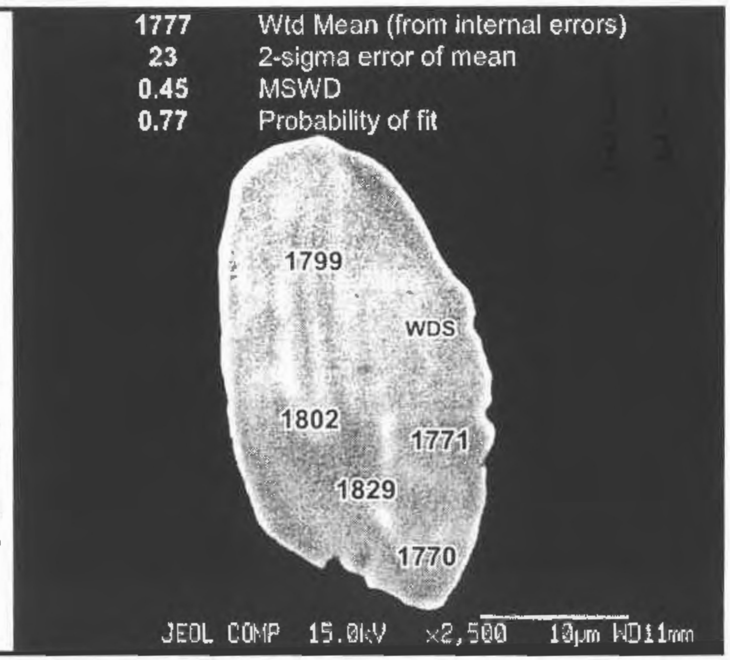

Grain #:	S373-05	Acc. Voltage:	15 kV	Bkg: 300 sec.	
Chemical zone:	homogeneous	Anal. Current:	200 nA	Pb Ma / PETH	Th Ma / PETJ
Analyses#:	453-457	Peak: 600 sec.		U Mb / PETJ	Y La / TAP

Spot #	Pb uncorr. (ppm)	Pb corr. (ppm)	Pb error (%)	Th (ppm)	Th error (%)	U uncorr. (ppm)	U corr. (ppm)	U error (%)	Y (ppm)	Y error (%)	Age (Ma)	S.D. 2s (Ma)	S.D. 2s (%)
1	4626	4504.67	0.5138	39080	0.2414	4237	3878.31	1.4821	8998	0.2614	1817.5	58	3.19
2	4098	3982.42	0.5577	35856	0.2563	3451	3122.15	1.7736	8749	0.2674	1811.2	68	3.76
3	3924	3813.89	0.5747	37809	0.2469	2505	2158.00	2.3831	7863	0.2935	1797.0	89	4.94
4	4546	4427.66	0.5197	44183	0.2219	2900	2493.79	2.1006	7992	0.2898	1789.0	78	4.36
5	6332	6189.78	0.4222	43334	0.2251	9024	8626.01	0.7885	10869	0.2230	1778.8	33	1.87

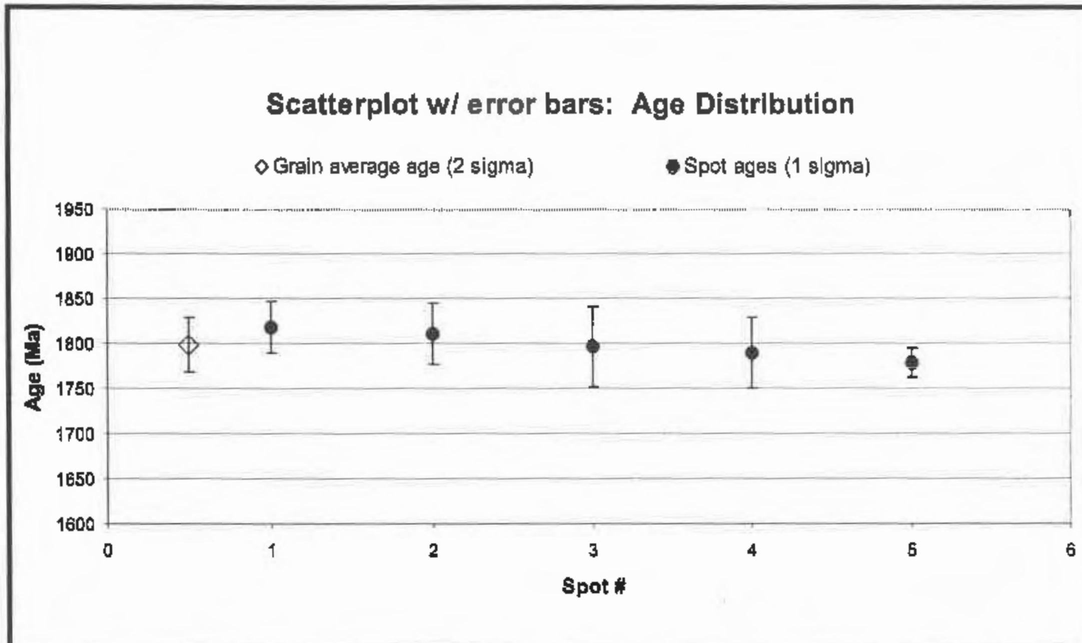

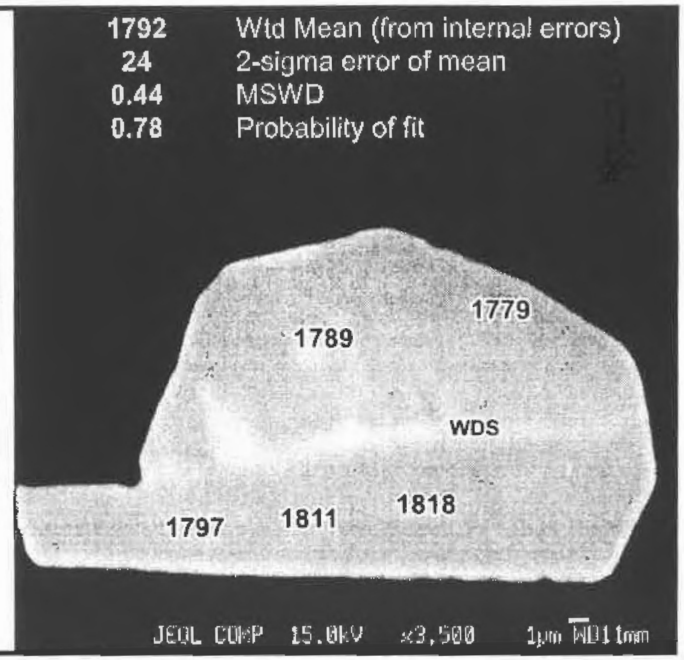

Grain #: S374-01	Acc. Voltage: 15 kV	Bkg: 300 sec.	
Chemical zone: homogeneous	Anal. Current: 200 nA	Pb Ma / PETH	Th Ma / PETJ
Analyses#: 272-277	Peak: 600 sec.	U Mb / PETJ	Y La / TAP

Spot #	Pb uncorr. (ppm)	Pb corr. (ppm)	Pb error (%)	Th (ppm)	Th error (%)	U uncorr. (ppm)	U corr. (ppm)	U error (%)	Y (ppm)	Y error (%)	Age (Ma)	S.D. 2s (Ma)	S.D. 2s (%)
1	6320	6176.52	0.4162	37861	0.2455	9914	9567.05	0.6812	11730	0.2166	1818.3	31	1.69
2	3551	3434.82	0.6076	29808	0.2912	2707	2434.27	2.0326	9602	0.2565	1899.5	82	4.29
3	3927	3606.49	0.5661	36004	0.2545	2460	2129.94	2.2351	9304	0.2642	1865.3	87	4.65
4	6465	6322.47	0.4114	39881	0.2373	9421	9055.28	0.7113	11360	0.2233	1852.9	32	1.73
5	2984	2883.59	0.6892	26166	0.3203	2151	1911.59	2.5075	8247	0.2927	1865.0	98	5.25
6	3387	3277.17	0.6268	28639	0.2991	2656	2396.01	2.0618	9020	0.2700	1877.5	82	4.36

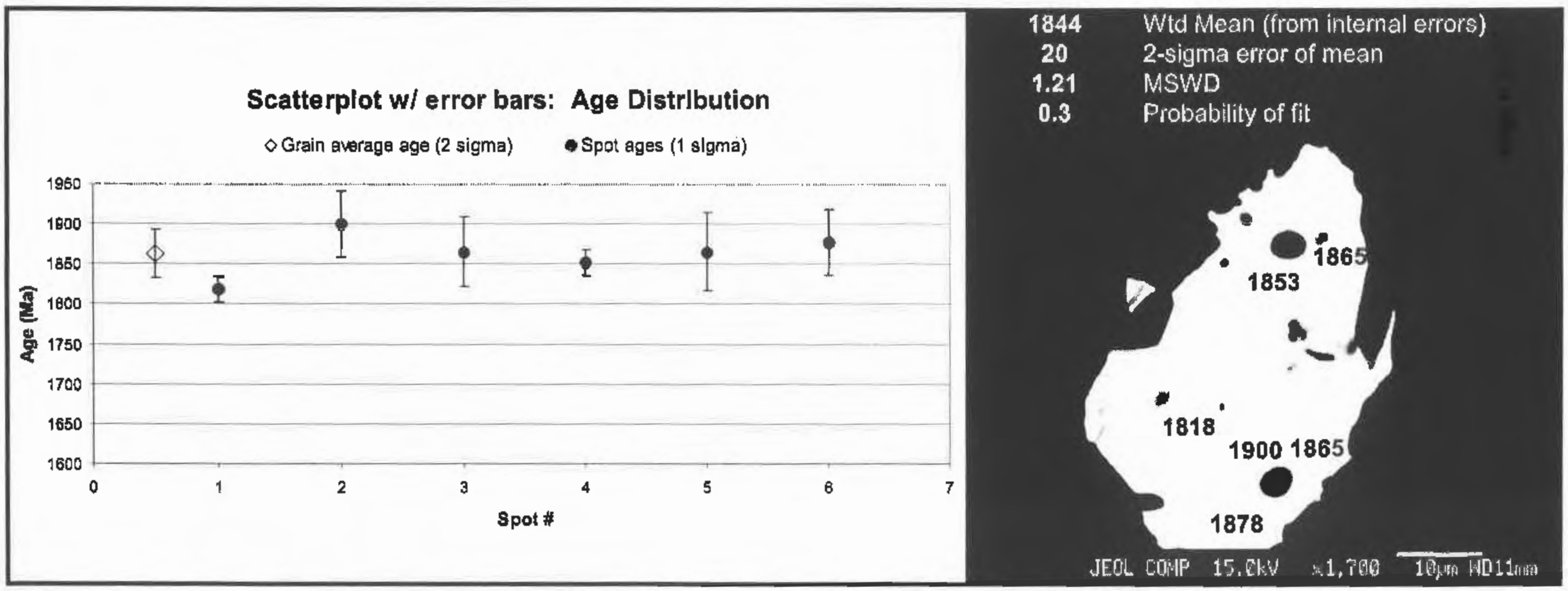

Grain #:	8374-02	Acc. Voltage:	15 kV	Bkg: 300 sec.	
Chemical zone:	homogeneous	Anal. Current:	200 nA	Pb Ma / PETH	Th Ma / PETJ
Analyses#:	278-283	Peak: 600 sec.		U Mb / PETJ	Y La / TAP

Spot #	Pb uncorr. (ppm)	Pb corr. (ppm)	Pb error (%)	Th (ppm)	Th error (%)	U uncorr. (ppm)	U corr. (ppm)	U error (%)	Y (ppm)	Y error (%)	Age (Ma)	S.D. 2s (Ma)	S.D. 2s (%)
1	4199	4068.01	0.5581	39102	0.2397	2650	2281.38	2.0847	10122	0.2435	1841.0	80	4.35
2	3528	3414.53	0.6303	32611	0.2725	2246	1947.40	2.4140	8934	0.2710	1846.0	93	5.03
3	2468	2366.88	0.8285	21157	0.3763	1833	1639.91	2.8952	8983	0.2692	1869.0	114	6.08
4	5733	5597.18	0.4542	40293	0.2351	7170	6800.47	0.8785	10533	0.2359	1841.0	38	2.05
5	3376	3273.66	0.6510	31087	0.2825	2101	1816.44	2.5708	7840	0.3044	1862.5	99	5.34
6	3215	3113.11	0.6754	29059	0.2968	2064	1798.16	2.6126	8052	0.2973	1874.0	102	5.44

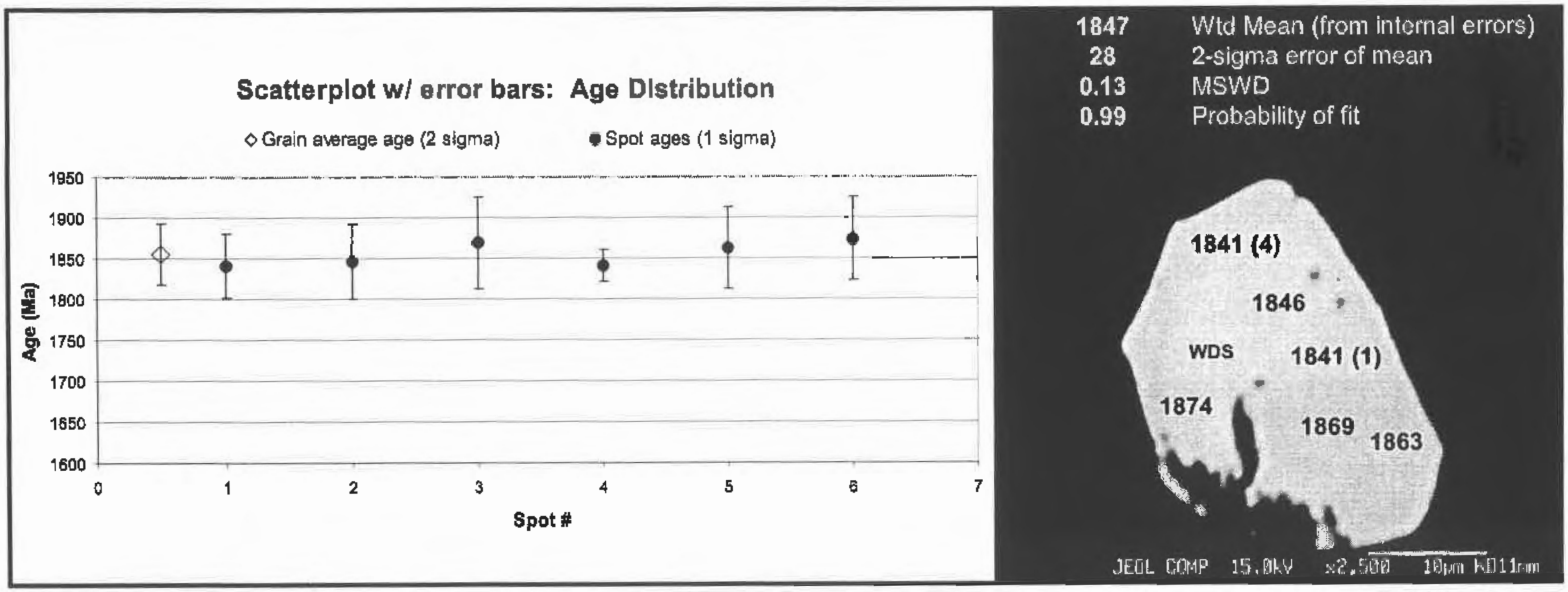

Grain #: S374-03	Acc. Voltage: 15 kV	Bkg: 300 sec.	
Chemical zone: homogeneous	Anal. Current: 200 nA	Pb Ma / PETH	Th Ma / PETJ
Analyses#: 284-292	Peak: 600 sec.	U Mb / PETJ	Y La / TAP

Spot #	Pb uncorr. (ppm)	Pb corr. (ppm)	Pb error (%)	Th (ppm)	Th error (%)	U uncorr. (ppm)	U corr. (ppm)	U error (%)	Y (ppm)	Y error (%)	Age (Ma)	S.D. 2s (Ma)	S.D. 2s (%)
1	5784	5643.37	0.4566	57045	0.1864	2652	2125.86	2.1643	8918	0.2717	1869.7	83	4.45
2	4543	4420.87	0.5335	44256	0.2205	2171	1764.21	2.5684	8433	0.2844	1872.0	99	5.27
3	4805	4684.66	0.5131	46207	0.2143	2426	2001.03	2.3151	7973	0.2987	1878.8	90	4.77
4	4243	4123.44	0.5585	39795	0.2373	2217	1851.70	2.5026	8713	0.2757	1898.5	98	5.16
5	4875	4752.14	0.5082	47695	0.2097	2316	1877.16	2.4209	8071	0.2854	1870.5	93	4.97
6	4360	4237.94	0.5485	41748	0.2297	2250	1876.57	2.4615	8749	0.2751	1871.8	95	5.07
7	4346	4228.15	0.5495	40632	0.2341	2198	1824.92	2.5245	8406	0.2849	1915.5	100	5.20
8	4049	3938.53	0.5756	38170	0.2440	2069	1718.72	2.6563	7870	0.3009	1900.0	104	5.46
9	5409	5278.97	0.4747	55874	0.1889	2371	1857.63	2.3687	7864	0.3022	1818.8	89	4.89

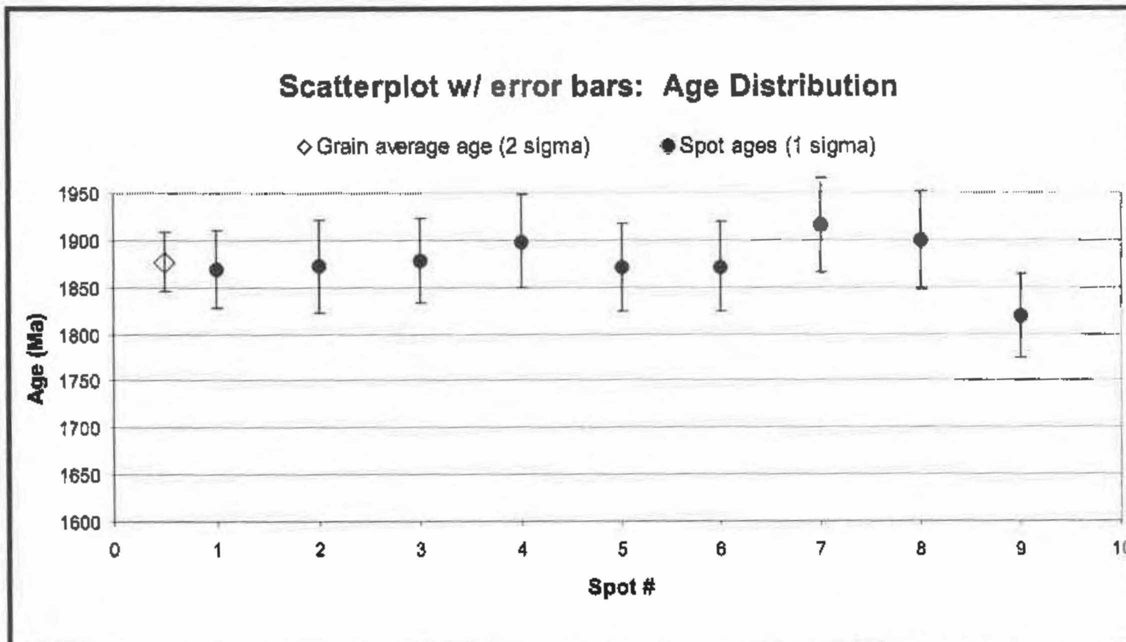

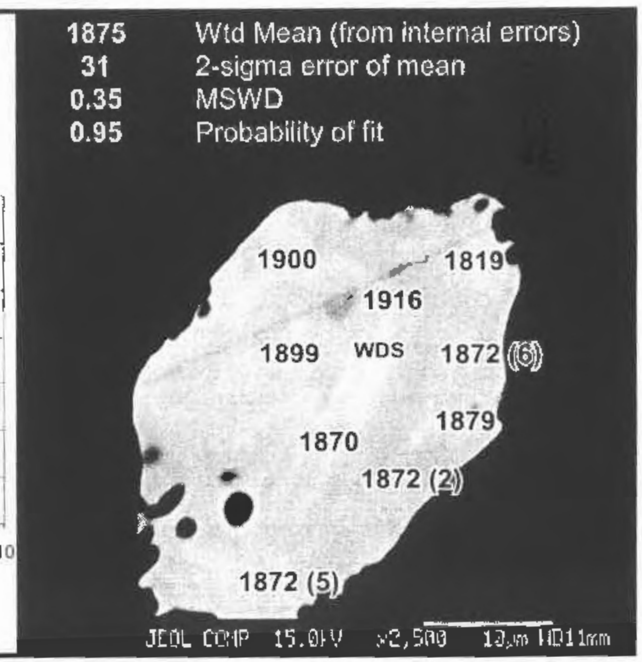

Grain #: 8374-04
Chemical zone: homogeneous
Analyses#: 448-452

Acc. Voltage: 15 kV
Anal. Current: 200 nA
Peak: 600 sec.

Bkg: 300 sec.
Pb Ma / PETH Th Ma / PETJ
U Mb / PETJ Y La / TAP

Spot #	Pb uncorr. (ppm)	Pb corr. (ppm)	Pb error (%)	Th (ppm)	Th error (%)	U uncorr. (ppm)	U corr. (ppm)	U error (%)	Y (ppm)	Y error (%)	Age (Ma)	S.D. 2s (Ma)	S.D. 2s (%)
1	3426	3320.92	0.6597	30767	0.2857	2516	2234.32	2.3667	8204	0.2824	1832.5	91	4.95
2	3538	3436.42	0.6436	32974	0.2718	2303	2000.90	2.5759	7513	0.3051	1833.0	98	5.35
3	3372	3271.13	0.6660	30916	0.2842	2385	2101.94	2.4827	7698	0.2980	1822.0	94	5.18
4	4386	4261.99	0.5531	41540	0.2311	3040	2658.59	2.0103	9004	0.2609	1780.5	75	4.21
5	3828	3713.43	0.6086	35030	0.2602	2705	2383.94	2.2239	8521	0.2734	1824.5	85	4.65

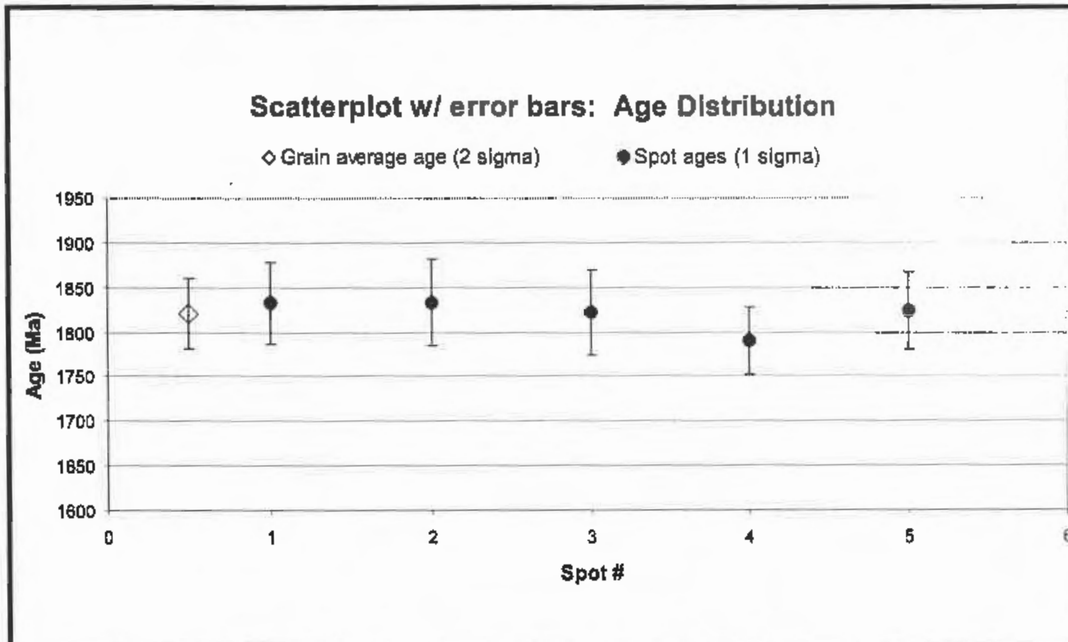

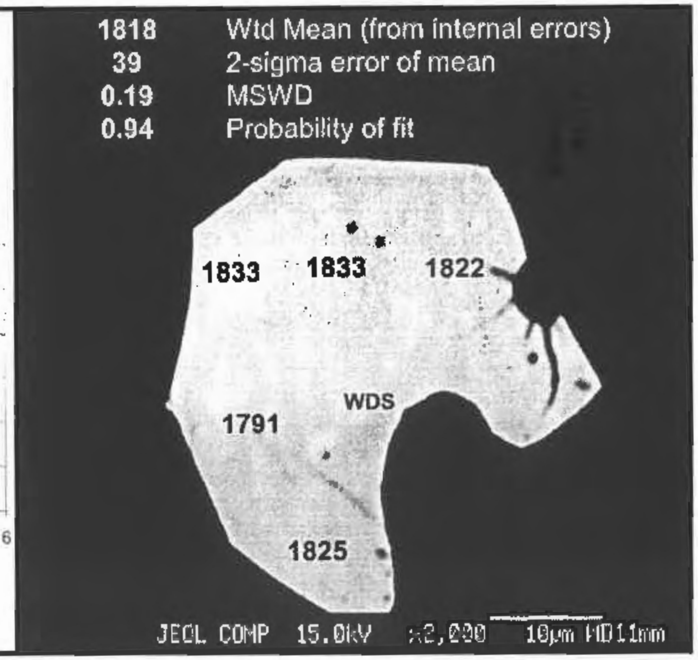

Grain #: S374-05
Chemical zone: homogeneous
Analyses#: 440-447

Acc. Voltage: 15 kV
Anal. Current: 200 nA
Peak: 600 sec.

Bkg: 300 sec.
Pb Ma / PETH Th Ma / PETJ
U Mb / PETJ Y La / TAP

Spot #	Pb uncorr. (ppm)	Pb corr. (ppm)	Pb error (%)	Th (ppm)	Th error (%)	U uncorr. (ppm)	U corr. (ppm)	U error (%)	Y (ppm)	Y error (%)	Age (Ma)	S.D. 2s (Ma)	S.D. 2s (%)
1	2770	2669.64	0.7404	23313	0.3532	2391	2177.92	2.4503	8602	0.2695	1833.0	95	5.18
2	6961	6807.61	0.3990	43777	0.2246	10273	9870.96	0.7118	12100	0.2033	1827.0	31	1.72
3	4321	4194.27	0.5371	40135	0.2381	2801	2432.45	2.1492	9481	0.2489	1838.)	82	4.47
4	7280	7125.46	0.3896	39779	0.2404	12205	11840.18	0.6245	12752	0.1950	1835.8	29	1.57
5	4701	4570.38	0.5078	45222	0.2195	2783	2367.11	2.1778	9274	0.2540	1824.0	82	4.50
6	2790	2683.17	0.7381	22714	0.3606	2468	2260.48	2.3817	9424	0.2494	1857.0	94	5.05
7	2481	2385.47	0.8068	20173	0.3950	1912	1727.79	3.0131	8446	0.2738	1924.5	121	6.29
8	4606	4489.26	0.5137	38991	0.2431	3977	3619.05	1.5634	8477	0.2743	1844.8	62	3.34

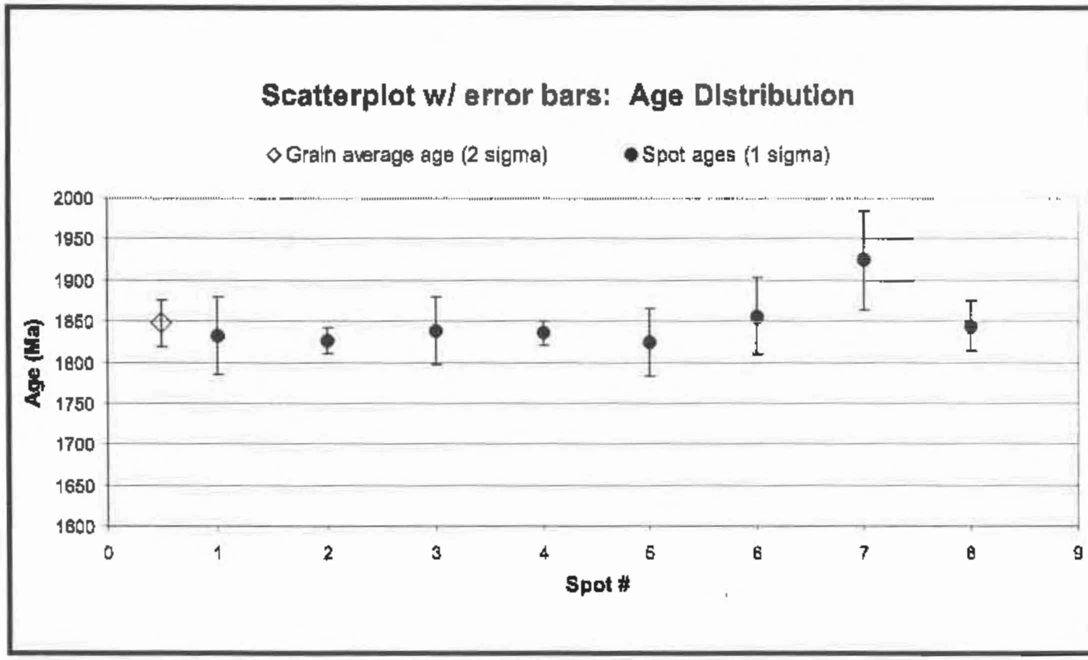

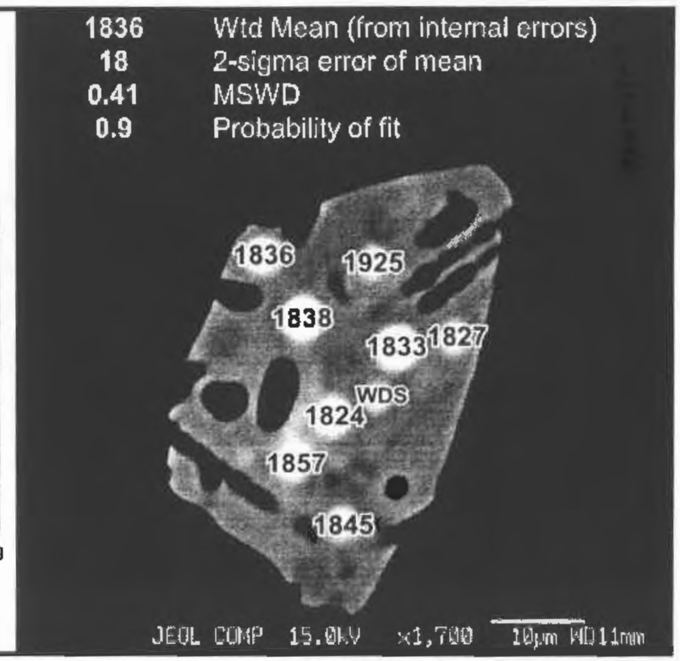

Grain #:	8375-11	Acc. Voltage: 15 kV	Bkg: 300 sec.	
Chemical zone:	homogeneous	Anal. Current: 200 nA	Pb Ma / PETH	Th Ma / PETJ
Analyses#:	657-668	Peak: 600 sec.	U Mb / PETJ	Y La / TAP

Spot #	Pb uncorr. (ppm)	Pb corr. (ppm)	Pb error (%)	Th (ppm)	Th error (%)	U uncorr. (ppm)	U corr. (ppm)	U error (%)	Y (ppm)	Y error (%)	Age (Ma)	S.D. 2s (Ma)	S.D. 2s (%)
1	5363	5237.39	0.7691	28643	0.3585	9094	8832.33	1.2080	10840	0.3044	1838.7	55	2.97
2	5376	5231.32	0.7702	25974	0.3845	9603	9365.97	1.1581	13382	0.2547	1855.0	54	2.90
3	5295	5152.75	0.7775	23476	0.4137	9952	9747.92	1.1251	13422	0.2540	1859.5	53	2.87
4	3150	3041.37	1.1105	28275	0.3614	2221	1982.51	4.0697	8917	0.3597	1842.5	156	8.47
5	4782	4671.54	0.8268	26127	0.3825	8329	8090.43	1.2910	9415	0.3435	1800.3	57	3.17
6	5316	5188.88	0.7737	28544	0.3595	9138	8877.25	1.2041	11028	0.3001	1822.3	54	2.96

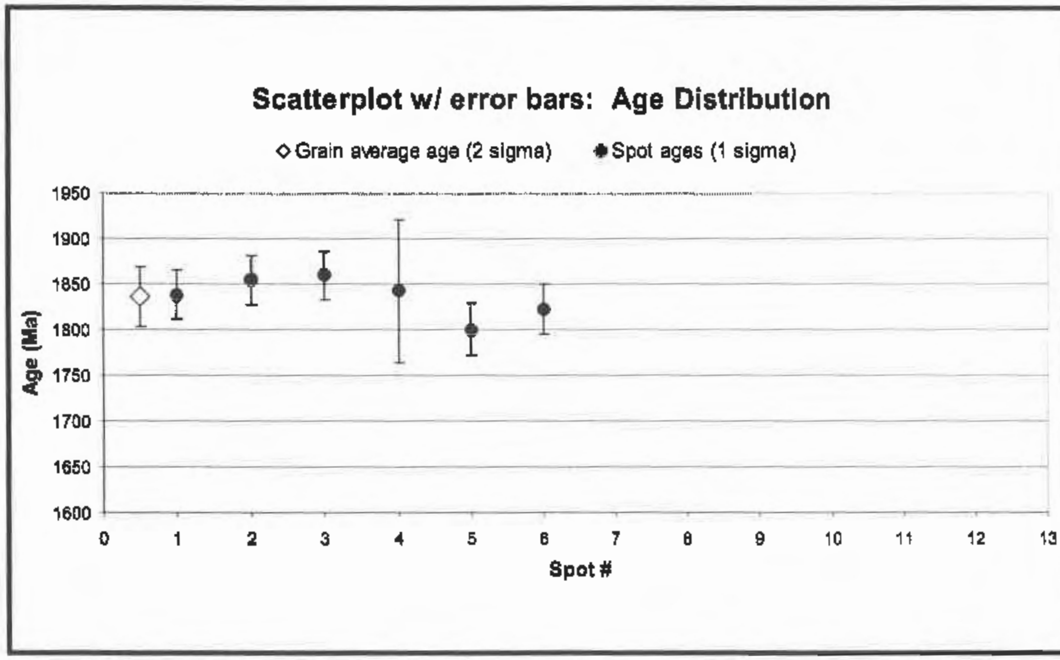

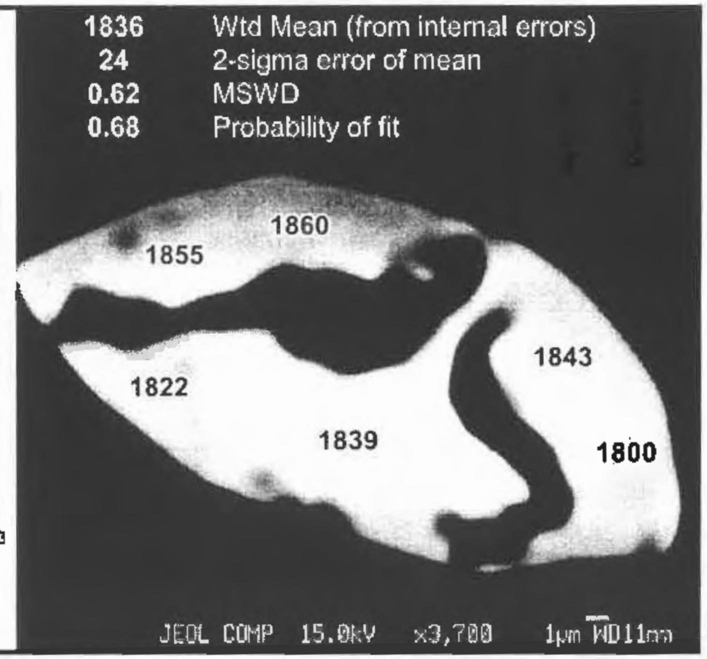

Grain #: S375-12
Chemical zone: homogeneous
Analyses#: 657-668

Acc. Voltage: 15 kV
Anal. Current: 200 nA
Peak: 600 sec.

Bkg: 300 sec.
Pb Ma / PETH Th Ma / PETJ
U Mb / PETJ Y La / TAP

Spot #	Pb uncorr. (ppm)	Pb corr. (ppm)	Pb error (%)	Th (ppm)	Th error (%)	U uncorr. (ppm)	U corr. (ppm)	U error (%)	Y (ppm)	Y error (%)	Age (Ma)	S.D. 2s (Ma)	S.D. 2s (%)
1	1989	1905.17	1.6070	15646	0.5634	1435	1292.82	6.1591	7705	0.4090	1992.0	255	12.78
2	2733	2634.70	1.2473	22470	0.4291	2024	1819.46	4.4664	8494	0.3760	1933.5	180	9.32
3	3027	2938.01	1.1520	16701	0.5360	4435	4283.23	2.1862	8170	0.3888	1929.0	98	5.08
4	5275	5142.94	0.7843	24069	0.4089	9293	9074.00	1.1947	12211	0.2760	1908.7	57	2.99
5	5866	5723.24	0.7346	26560	0.3813	10392	10150.21	1.0999	13128	0.2601	1909.3	53	2.77
6	3452	3330.34	1.0490	28332	0.3636	2826	2567.75	3.2938	10439	0.3150	1890.0	131	6.96
7	2764	2666.11	1.2359	23473	0.4154	1607	1593.25	4.9705	8315	0.3830	1945.0	200	10.28
8	5387	5251.68	0.7742	24637	0.4021	9832	9407.81	1.1630	12516	0.2704	1892.8	55	2.92

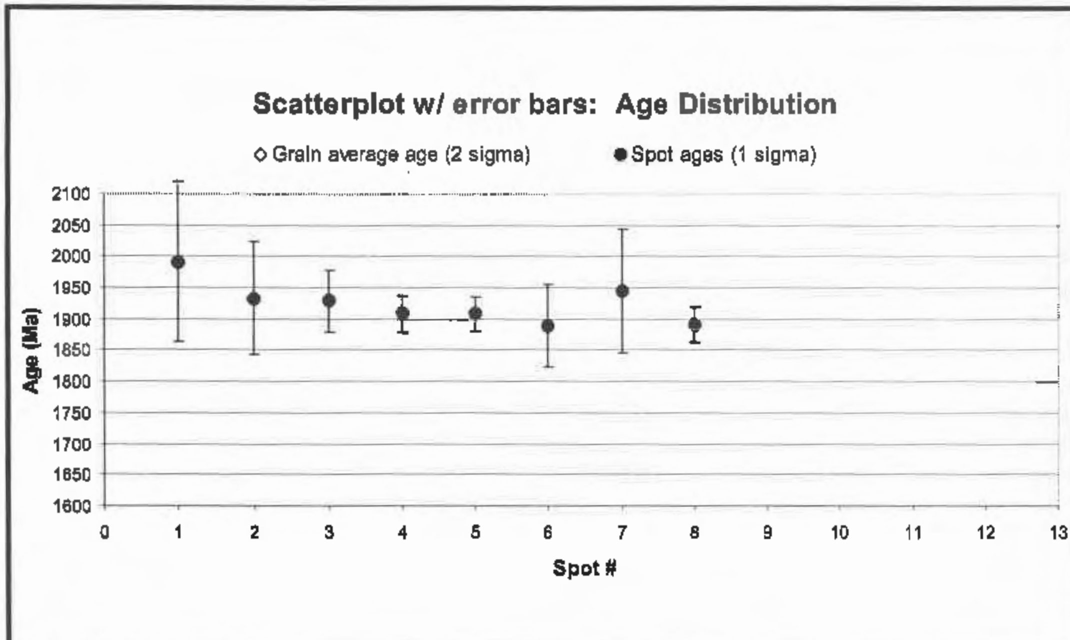

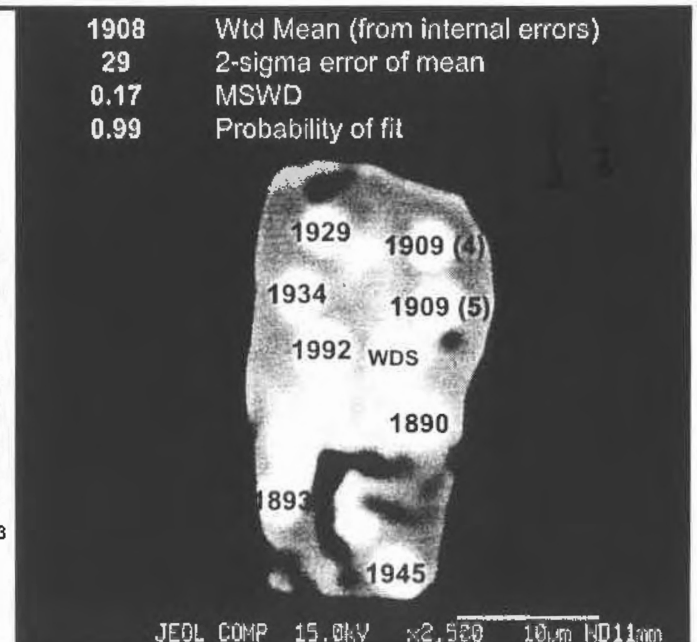

Grain #:	S383-01	Acc. Voltage:	15 kV	Bkg: 300 sec.	
Chemical zone:	core	Anal. Current:	200 nA	Pb Ma / PETH	Th Ma / PETJ
Analyses#:	472-476	Peak: 600 sec.		U Mb / PETJ	Y La / TAP

Spot #	Pb uncorr. (ppm)	Pb corr. (ppm)	Pb error (%)	Th (ppm)	Th error (%)	U uncorr. (ppm)	U corr. (ppm)	U error (%)	Y (ppm)	Y error (%)	Age (Ma)	S.D. 2s (Ma)	S.D. 2s (%)
1	5675	5500.63	0.4530	50977	0.2018	4471	4001.45	1.3437	13595	0.1935	1803.8	52	2.88
2	5510	5338.35	0.4615	49136	0.2069	4361	3908.63	1.3708	13519	0.1944	1810.0	53	2.94
3	7298	7112.18	0.3904	58968	0.1836	7459	6914.82	0.8604	13896	0.1905	1813.8	36	1.98
4	6191	6010.59	0.4300	55075	0.1919	5046	4537.17	1.2161	13768	0.1918	1804.3	47	2.62
5	5531	5361.11	0.4601	49130	0.2069	4494	4041.69	1.3350	13316	0.1969	1804.5	52	2.87

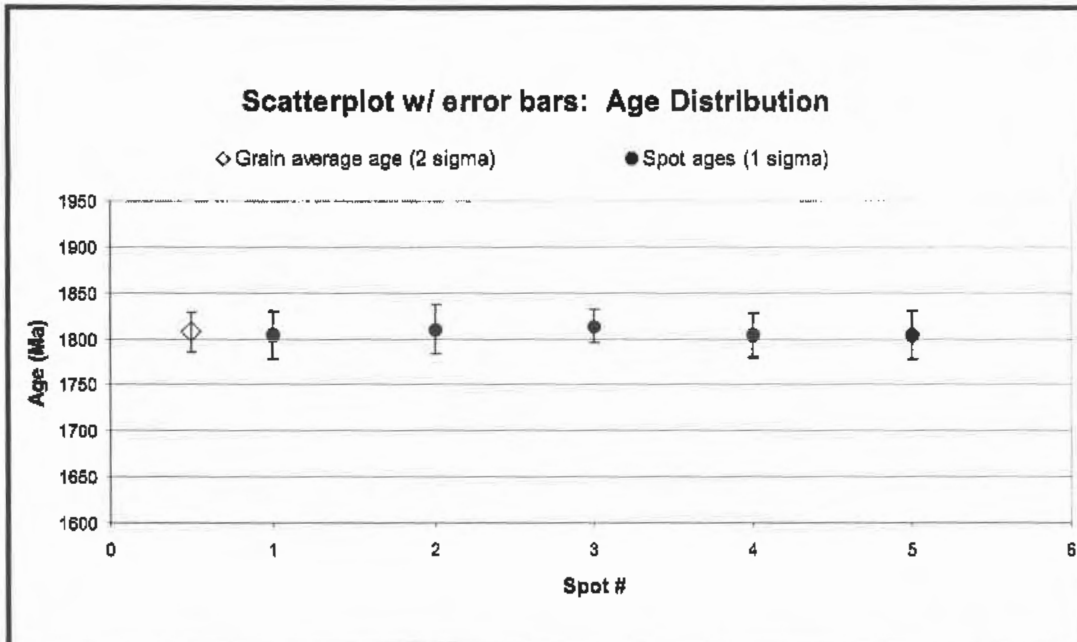

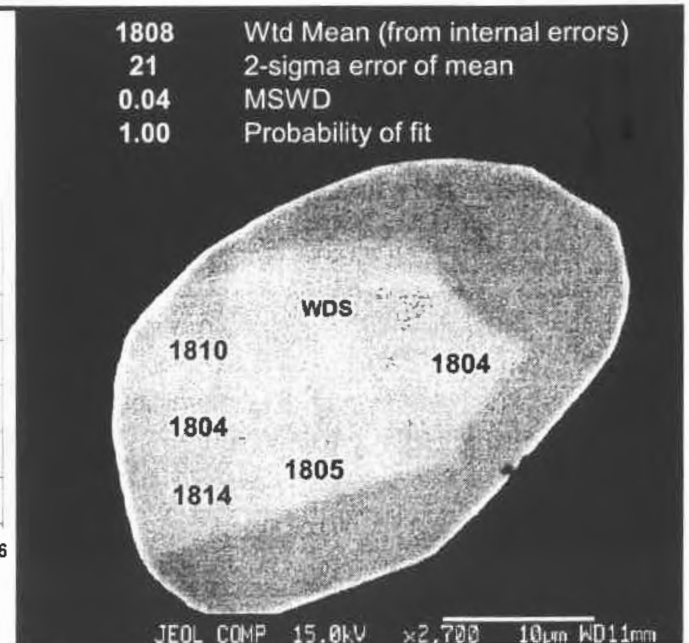

Grain #:	8383-01	Acc. Voltage: 15 kV	Bkg: 300 sec.	
Chemical zone:	rim	Anal. Current: 200 nA	Pb Ma / PETH	Th Ma / PETJ
Analyses#:	477-480	Peak: 600 sec.	U Mb / PETJ	Y La / TAP

Spot #	Pb uncorr. (ppm)	Pb corr. (ppm)	Pb error (%)	Th (ppm)	Th error (%)	U uncorr. (ppm)	U corr. (ppm)	U error (%)	Y (ppm)	Y error (%)	Age (Ma)	S.D. 2s (Ma)	S.D. 2s (%)
1	7079	6853.25	0.4044	48404	0.2107	9678	9232.69	0.7039	19758	0.1464	1793.0	30	1.70
2	6562	6345.71	0.4219	46814	0.2154	8624	8193.43	0.7681	18877	0.1517	1779.0	33	1.83
3	6498	6293.93	0.4229	45992	0.2179	8600	8176.99	0.7687	17686	0.1605	1784.2	33	1.83
4	7183	6954.39	0.4015	47835	0.2122	9859	9418.09	0.6941	20143	0.1442	1812.3	30	1.68

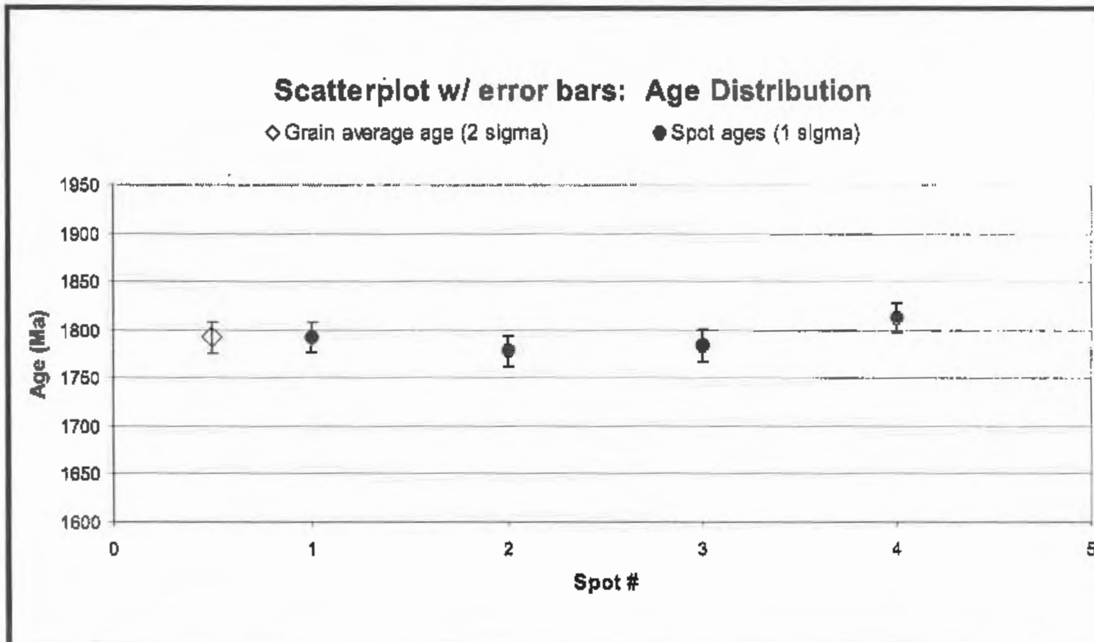

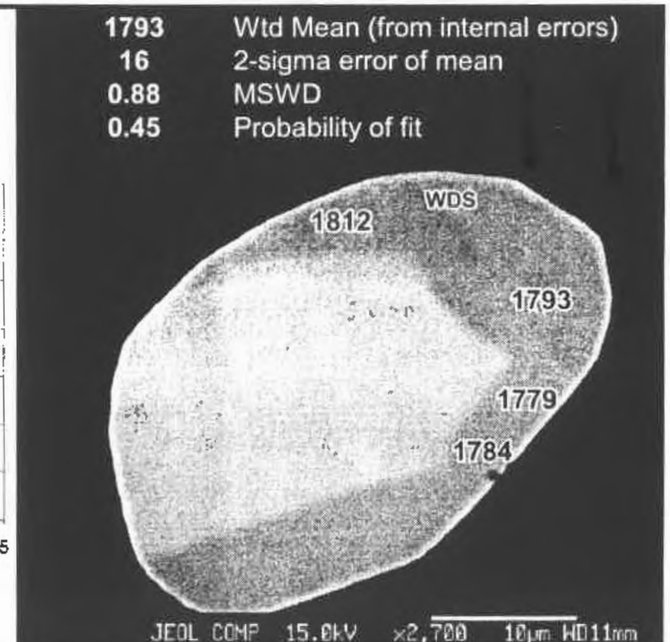

Grain #:	S363-02A		Acc. Voltage:	15 kV		Bkg(s):	300	
Chemical zone:	homogeneous		Anal. Current:	200 nA		Pb Ma / PETH	Th Ma / PETJ	
Analyses#:	620-623		Peak(s):	600		U Mb / PETJ	Y La / TAP	

Spot #	Pb uncorr. (ppm)	Pb corr. (ppm)	Pb error (%)	Th (ppm)	Th error (%)	U uncorr. (ppm)	U corr. (ppm)	U error (%)	Y (ppm)	Y error (%)	Age (Ma)	S.D. 2s (Ma)	S.D. 2s (%)
1	3776	3624.89	0.9745	30542	0.3399	3438	3158.84	3.0181	13583	0.2553	1847.5	118	6.39
2	2668	2543.43	1.2572	20867	0.4457	2560	2369.75	3.9294	11760	0.2876	1847.0	153	8.30
3	3603	3440.91	1.0103	27713	0.3638	3505	3251.95	2.9612	15213	0.2323	1861.5	117	6.31
4	2674	2551.62	1.2554	20079	0.4587	2934	2750.97	3.4651	11609	0.2909	1818.5	135	7.43

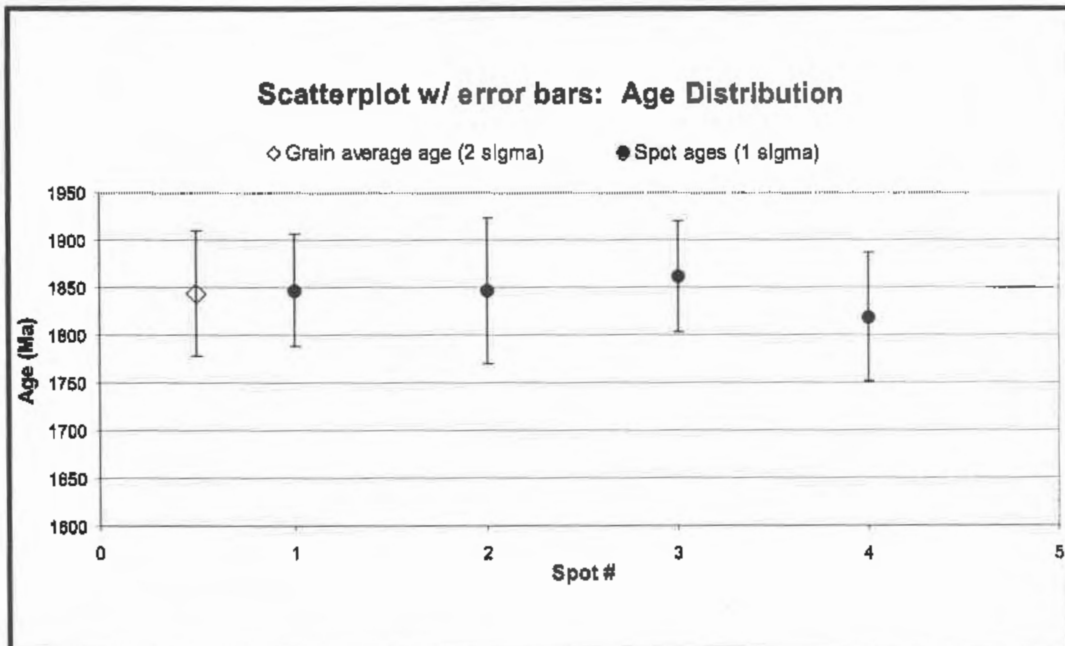

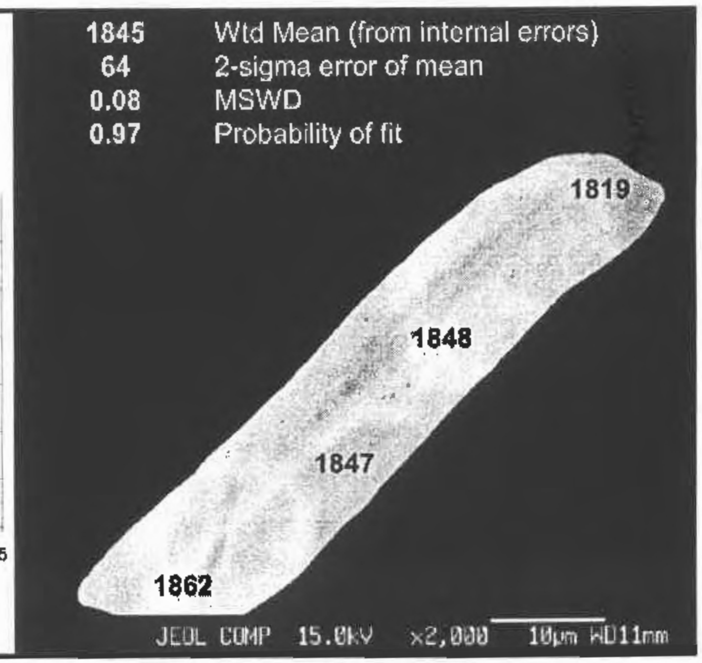

Grain #: 8383-02
Chemical zone: homogeneous
Analyses#: 463-471

Acc. Voltage: 15 kV
Anal. Current: 200 nA
Peak(s): 600

Bkg(s): 300
Pb Ma / PETH Th Ma / PETJ
U Mb / PETJ Y La / TAP

Spot #	Pb uncorr. (ppm)	Pb corr. (ppm)	Pb error (%)	Th (ppm)	Th error (%)	U uncorr. (ppm)	U corr. (ppm)	U error (%)	Y (ppm)	Y error (%)	Age (Ma)	S.D. 2s (Ma)	S.D. 2s (%)
1	3623	3483.24	0.6083	31153	0.2822	3184	2899.12	1.7533	12191	0.2108	1795.0	68	3.76
2	3310	3166.51	0.6522	25289	0.3291	3651	3420.19	1.5458	13378	0.1952	1801.5	62	3.43
3	2550	2424.41	0.7928	20014	0.3927	2489	2306.56	2.1781	11986	0.2136	1829.0	86	4.71
4	2490	2357.86	0.8097	19094	0.4074	2583	2409.03	2.1049	12885	0.2010	1815.5	83	4.59
5	3649	3498.07	0.6081	30003	0.2905	3411	3136.79	1.6492	13631	0.1924	1813.0	65	3.57
6	2990	2856.52	0.7022	24137	0.3407	2852	2631.74	1.9289	12368	0.2083	1818.0	76	4.17
7	3938	3805.85	0.5729	27673	0.3079	4854	4601.22	1.2066	11763	0.2175	1834.0	51	2.76
8	5423	5278.16	0.4632	34038	0.2656	7673	7361.63	0.8296	12415	0.2084	1852.5	37	1.99
9	6498	6317.38	0.4178	39810	0.2393	9497	9134.31	0.7064	15953	0.1699	1851.0	32	1.73

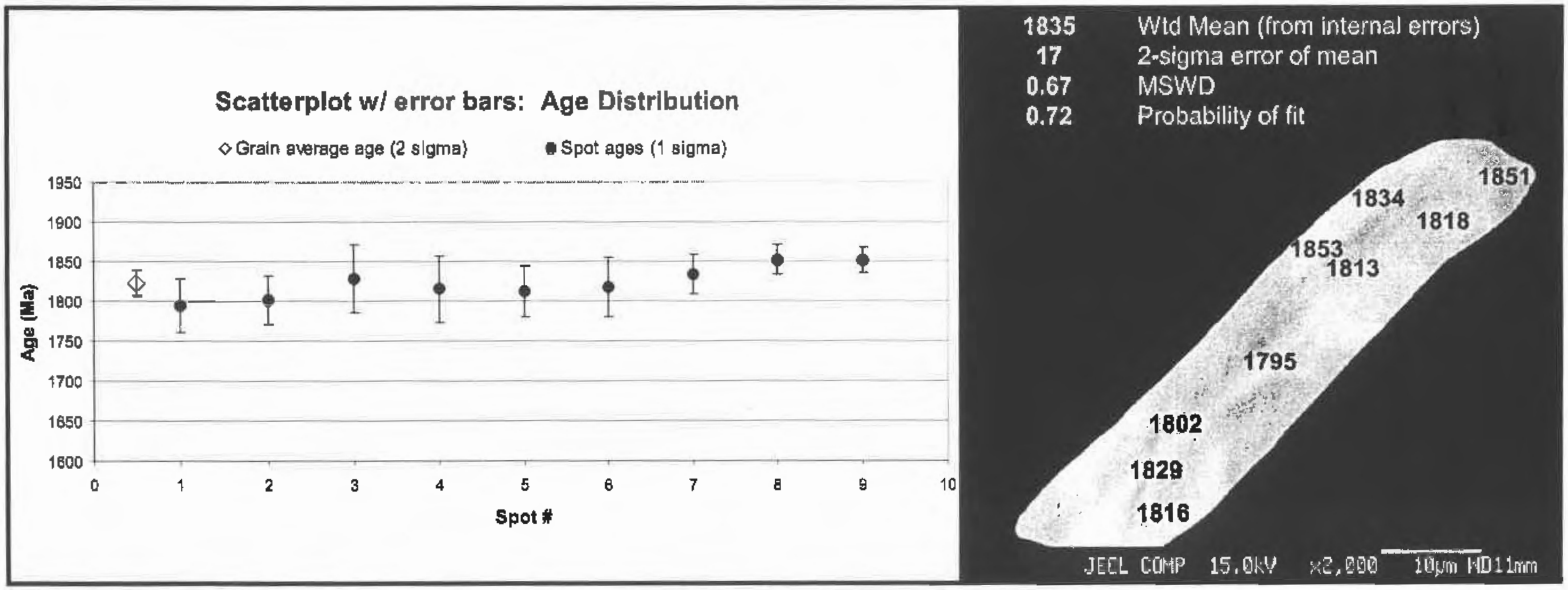

Grain #: S383-07
Chemical zone: homogeneous
Analyses#: 481-492

Acc. Voltage: 15 kV
Anal. Current: 200 nA
Peak(s): 600

Bkg: 300
Pb Ma / PETH Th Ma / PETJ
U Mb / PETJ Y La / TAP

Spot #	Pb uncorr. (ppm)	Pb corr. (ppm)	Pb error (%)	Th (ppm)	Th error (%)	U uncorr. (ppm)	U corr. (ppm)	U error (%)	Y (ppm)	Y error (%)	Age (Ma)	S.D. 2s (Ma)	S.D. 2s (%)
1	6351	6179.20	0.4205	51623	0.2008	6425	5949.58	0.9846	13225	0.1978	1810.0	40	2.20
2	3346	3220.19	0.6406	31995	0.2789	2125	1831.75	2.5773	10431	0.2403	1792.0	96	5.35
3	6716	6486.05	0.4140	44631	0.2220	9341	8931.26	0.7262	20796	0.1375	1802.5	32	1.75
4	6872	6637.43	0.4090	46359	0.2164	9195	8769.19	0.7364	21106	0.1361	1816.3	32	1.76
5	6815	6584.64	0.4106	44670	0.2219	9363	8952.88	0.5076	20838	0.1374	1824.5	26	1.41
6	7202	6973.70	0.3971	46251	0.2168	10273	9848.22	0.6766	20406	0.1397	1818.7	30	1.65
7	7098	6853.75	0.4025	46226	0.2169	9877	9452.51	0.6974	22005	0.1318	1820.0	31	1.69
8	8181	7961.19	0.3673	48377	0.2103	12537	12092.30	0.5860	16877	0.1626	1840.5	27	1.47
9	7582	7356.14	0.3554	46934	0.2147	11171	10739.86	0.6364	20044	0.1418	1828.8	29	1.57
10	8255	8063.98	0.3640	50277	0.2048	12621	12158.50	0.5838	15624	0.1730	1824.7	27	1.46
11	7317	7071.91	0.3959	46020	0.2177	10525	10102.45	0.6650	22357	0.1303	1827.4	30	1.63
12	5940	5770.78	0.4381	51090	0.2024	5182	4711.48	1.1806	12992	0.2009	1815.7	47	2.57

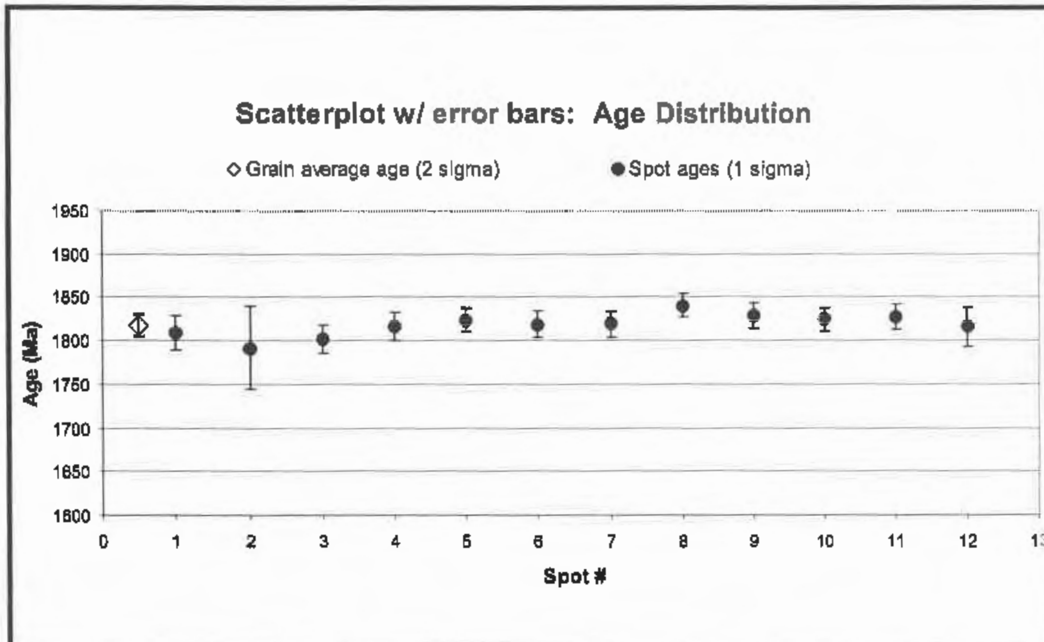

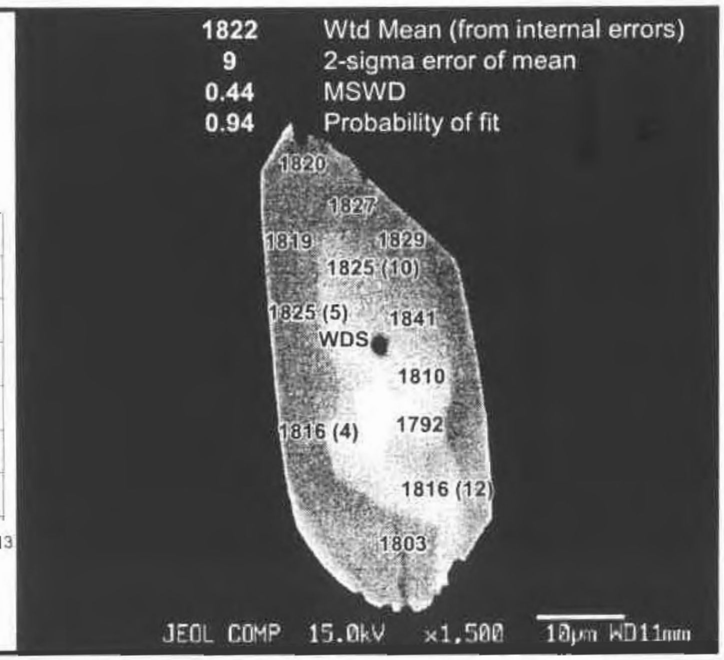

Grain #: S388-01
Chemical zone: Inner rim
Analyses#: 55-61, 66, 67

Acc. Voltage: 15 kV
Anal. Current: 200 nA
Peak: 600 sec.

Bkg: 300 sec.
Pb Ma / PETH Th Ma / PETJ
U Mb / PETJ Y La / TAP

Spot #	Pb uncorr. (ppm)	Pb corr. (ppm)	Pb error (%)	Th (ppm)	Th error (%)	U uncorr. (ppm)	U corr. (ppm)	U error (%)	Y (ppm)	Y error (%)	Age (Ma)	S.D. 2s (Ma)	S.D. 2s (%)
1 (57)	10862	10646.55	0.3153	41241	0.2155	22988	22609.38	0.3892	19505	0.1425	1835.8	21	1.13
2 (58)	11456	11236.75	0.3079	42154	0.2126	24263	23875.93	0.3779	19828	0.1408	1851.5	20	1.10
3 (59)	11625	11391.32	0.3070	44332	0.2061	24403	23995.78	0.3775	21198	0.1340	1841.8	20	1.09
4 (60)	10226	10015.76	0.3243	38161	0.2266	21737	21386.74	0.4013	19290	0.1436	1838.3	21	1.16
5 (61)	11421	11205.67	0.3081	41974	0.2132	24301	23915.60	0.3776	19404	0.1432	1847.6	20	1.10
6 (56)	10189	9975.84	0.3313	43938	0.2077	20050	19647.73	0.4292	19126	0.1452	1841.1	22	1.19
7 (66)	9455	9268.75	0.3396	35653	0.2395	19533	19207.91	0.4238	17155	0.1605	1865.0	23	1.22
8 (67)	9041	8816.26	0.3508	37197	0.2332	17691	17351.83	0.4513	21426	0.1352	1866.8	24	1.27

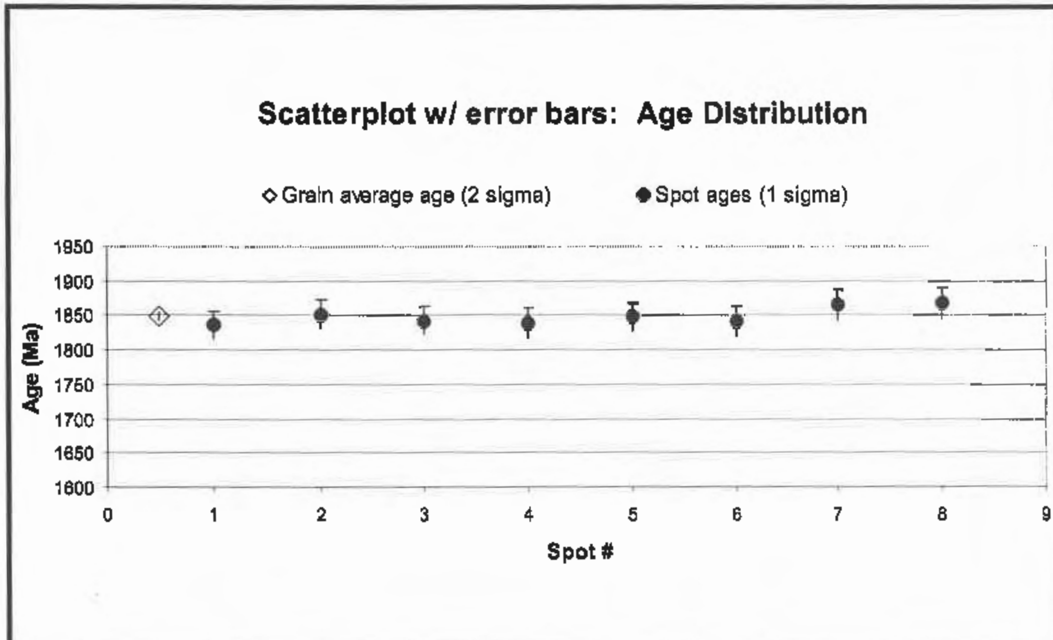

1848	Wtd Mean (from internal errors)
8	2-sigma error of mean
1.13	MSWD
0.34	Probability of fit

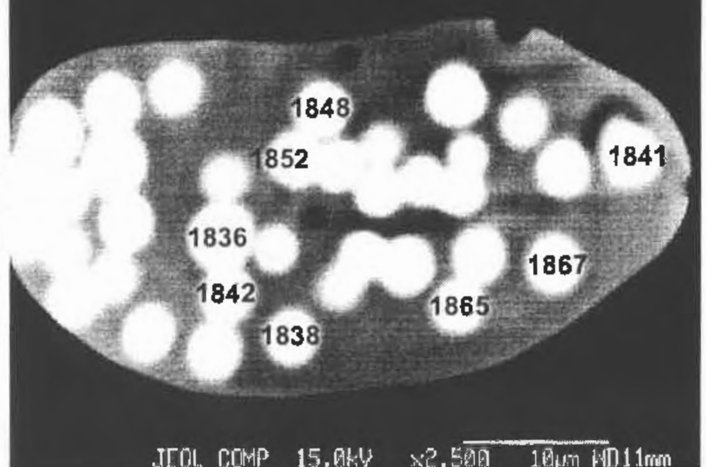

Grain #: 5388-01
Chemical zone: Outer rim + core
Analyses#: 52-55, 62-65, 523-532

Acc. Voltage: 15 kV
Anal. Current: 200 nA
Peak: 600 sec.

Bkg: 300 sec.
Pb Ma / PETH Th Ma / PETJ
U Mb / PETJ Y La / TAP

Spot #	Pb uncorr. (ppm)	Pb corr. (ppm)	Pb error (%)	Th (ppm)	Th error (%)	U uncorr. (ppm)	U corr. (ppm)	U error (%)	Y (ppm)	Y error (%)	Age (Ma)	S.D. 2σ (Ma)	S.D. 2σ (%)
1 (52)*	6541	6424.69	0.4133	36151	0.2345	11471	11140.12	0.6185	8840	0.2709	1794.6	28	1.56
2 (53)*	6973	6849.53	0.3969	37160	0.2306	12185	11844.82	0.5931	9568	0.2536	1823.6	28	1.53
3 (54)	6446	6332.59	0.4174	35760	0.2365	11169	10861.71	0.6307	8576	0.2787	1801.0	29	1.61
4 (55)*	7147	7007.22	0.3946	37327	0.2302	12760	12418.40	0.5747	11447	0.2184	1815.3	27	1.49
22 (528)	2301	2214.94	0.8590	17747	0.4456	2504	2342.61	2.3483	7762	0.3090	1809.0	92	5.09
23 (529)	2636	2535.82	0.7742	15951	0.4861	4058	3913.06	1.5135	9652	0.2561	1800.0	64	3.55
24 (530)*	4887	4762.00	0.4967	25760	0.3349	8305	8070.41	0.8309	11273	0.2251	1842.6	38	2.07
25 (531)	2168	2082.60	0.9023	17165	0.4579	2231	2074.94	2.6163	7761	0.3093	1808.5	102	5.62
26 (532)	2018	1932.24	0.9572	13399	0.5605	2699	2577.31	2.1844	8299	0.2915	1817.0	89	4.91
17 (523)	6578	6459.27	0.4161	36338	0.2620	11686	11352.40	0.6689	9121	0.2705	1783.5	30	1.68
18 (524)	6546	6427.84	0.4172	35716	0.2652	11588	11261.15	0.6726	9137	0.2701	1795.2	30	1.69
19 (525)	6556	6436.31	0.4170	38172	0.2628	11657	11325.94	0.6700	9255	0.2671	1783.2	30	1.69
20 (526)	6636	6515.15	0.4142	37364	0.2570	11612	11269.93	0.6728	9233	0.2678	1782.5	30	1.69
21 (527)*	9817	9605.45	0.3404	44753	0.2273	19249	18839.14	0.4761	16832	0.1493	1811.3	23	1.29
11 (62)*	4884	4760.11	0.4912	22626	0.3261	9051	8645.09	0.7114	9217	0.2660	1856.3	35	1.87
12 (63)	1852	1775.62	1.0171	13807	0.4710	2072	1946.57	2.5272	7147	0.3310	1822.0	101	5.54
13 (64)*	6663	6508.60	0.4091	25498	0.3007	13894	13662.00	0.5242	14753	0.1805	1842.2	27	1.49
14 (65)*	4858	4733.86	0.4951	23421	0.3186	8720	8506.86	0.7332	11234	0.2252	1854.0	35	1.90

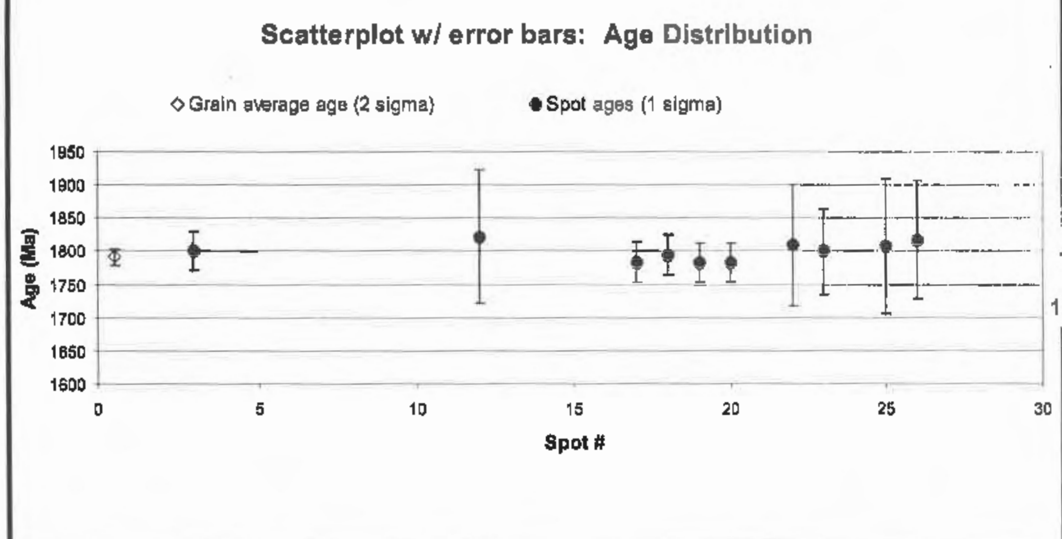

1791	Wtd Mean (from internal errors)
13	2-sigma error of mean
0.27	MSWD
0.98	Probability of fit

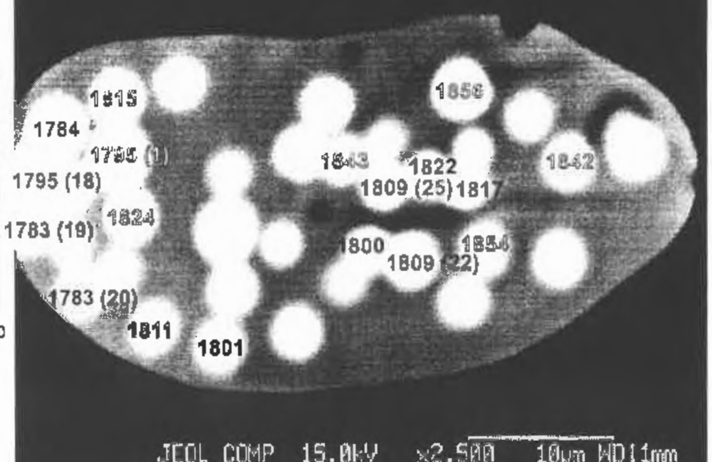

Grain #: S388-02
Chemical zone: homogeneous
Analyses#: 657-665

Acc. Voltage: 15 kV
Anal. Current: 200 nA
Peak(s): 600

Bkg(s): 300
Pb Ma / PETH Th Ma / PETJ
U Mb / PETJ Y La / TAP

Spot #	Pb uncorr. (ppm)	Pb corr. (ppm)	Pb error (%)	Th (ppm)	Th error (%)	U uncorr. (ppm)	U corr. (ppm)	U error (%)	Y (ppm)	Y error (%)	Age (Ma)	S.D. 2s (Ma)	S.D. 2s (%)
1	11439	11232.01	0.6321	40543	0.3400	25203	24831.90	0.8086	18818	0.2176	1828.2	40	2.18
2	7471	7251.28	0.7921	35392	0.3738	14101	13777.34	1.1774	20905	0.1995	1812.0	53	2.95
3	1663	1594.09	2.3221	11488	0.8910	2334	2229.39	5.3276	6527	0.5309	1750.0	206	11.76
4	6720	6549.15	0.8362	35685	0.3712	12284	11957.37	1.3008	15230	0.2572	1774.0	57	3.19
5	6090	5971.52	0.8806	36565	0.3640	10278	9942.91	1.4865	9044	0.4733	1763.5	62	3.54
6	6914	6728.74	0.8244	35368	0.3738	12642	12318.38	1.2742	16935	0.2360	1796.5	56	3.14
7	6194	6073.50	0.8726	37160	0.3599	10447	10106.23	1.4695	9200	0.3945	1764.0	62	3.50
8	2847	2760.69	1.4980	16099	0.6750	4824	4677.26	2.7561	7954	0.4454	1787.0	115	6.42
9	6631	6402.09	0.8525	31060	0.4108	12799	12515.33	1.2609	22505	0.1882	1789.6	57	3.17
10	6299	6068.92	0.8807	25400	0.4766	13207	12975.44	1.2294	23353	0.1827	1788.7	57	3.18
11	6647	6468.27	0.8428	34768	0.3782	12158	11839.89	1.3103	16258	0.2438	1781.2	57	3.22
12	6029	5822.46	0.9000	29613	0.4228	11336	11063.72	1.3786	20068	0.2056	1781.0	61	3.41
13	6321	6193.13	0.8625	37623	0.3557	10679	10332.32	1.4452	9973	0.3678	1764.0	61	3.45
14	6303	6160.34	0.8661	36769	0.3631	10631	10294.16	1.4509	11825	0.3179	1780.2	62	3.47
15	6649	6481.37	0.8412	36569	0.3718	11962	11636.24	1.3265	14870	0.2623	1783.0	58	3.24
16	6628	6464.24	0.8420	36818	0.3628	11742	11404.84	1.3452	14263	0.2714	1771.5	58	3.27

Scatterplot w/ error bars: Age Distribution

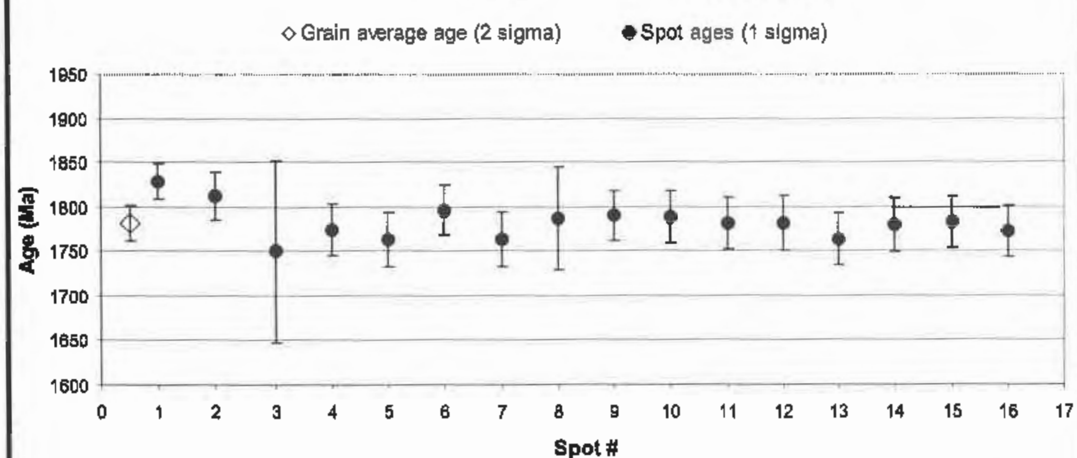

1788 Wtd Mean (from internal errors)
15 2-sigma error of mean
0.51 MSWD
0.93 Probability of fit

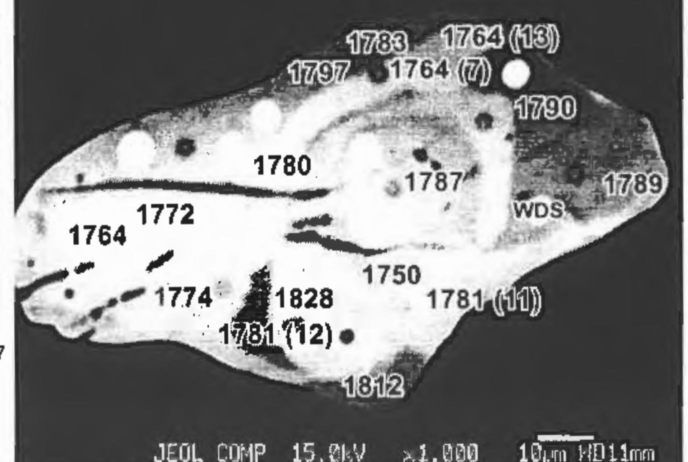

Grain #:	S388-02	Acc. Voltage:	15 kV	Bkg(s):	300		
Chemical zone:	homogeneous	Anal. Current:	200 nA	Pb Ma / PETH	Th Ma / PETJ		
Analyses#:	657-668	Peak(s):	600	U Mb / PETJ	Y La / TAP		

Spot #	Pb uncorr. (ppm)	Pb corr. (ppm)	Pb error (%)	Th (ppm)	Th error (%)	U uncorr. (ppm)	U corr. (ppm)	U error (%)	Y (ppm)	Y error (%)	Age (Ma)	S.D. 2s (Ma)	S.D. 2s (%)
1	6987	6802.26	0.4097	35468	0.2644	12910	12585.26	0.6278	16861	0.1660	1792.2	29	1.62
2	7123	6931.32	0.4060	36814	0.2574	12900	12562.13	0.6292	17479	0.1615	1796.2	29	1.61
3	1768	1689.54	1.0922	11597	0.6300	2331	2225.43	2.6580	7621	0.3238	1835.0	108	5.89
4	6047	5820.73	0.4547	31008	0.2922	10900	10616.77	0.7119	22201	0.1336	1790.5	32	1.81
5	2116	2034.60	0.9405	15608	0.4876	2494	2349.91	2.5007	7419	0.3321	1793.5	98	5.44

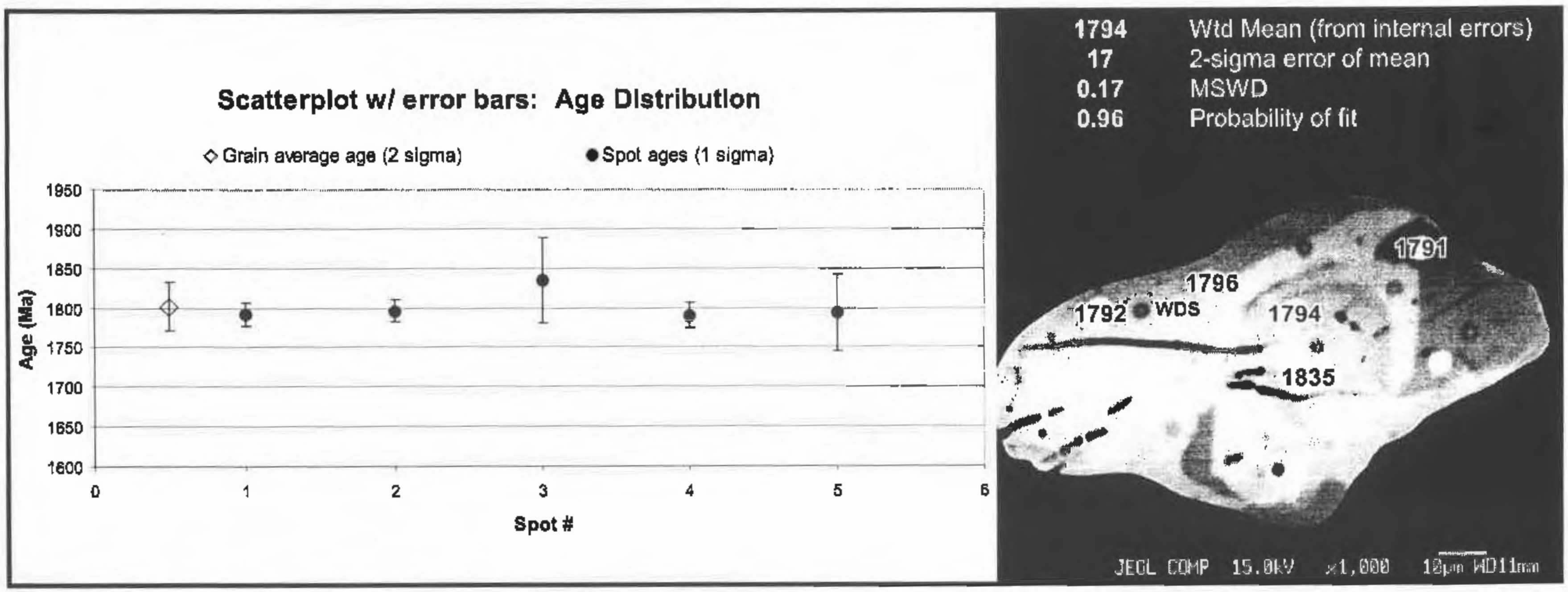

Grain #:	8388-16	Acc. Voltage:	15 kV	Bkg(s):	300
Chemical zone:	homogeneous	Anal. Current:	200 nA	Pb Ma / PETH	Th Ma / PETJ
Analyses#:	91-99	Peak(s):	600	U Mb / PETJ	Y La / TAP

Spot #	Pb uncorr. (ppm)	Pb corr. (ppm)	Pb error (%)	Th (ppm)	Th error (%)	U uncorr. (ppm)	U corr. (ppm)	U error (%)	Y (ppm)	Y error (%)	Age (Ma)	S.D. 2s (Ma)	S.D. 2s (%)
1	5192	4947.25	0.4864	41153	0.2149	5777	5399.46	1.0181	22780	0.1330	1751.8	41	2.31
2	4629	4380.50	0.5267	36608	0.2320	4963	4627.60	1.1534	23767	0.1286	1763.6	46	2.59
3	4968	4706.51	0.5044	40801	0.2163	4849	4474.79	1.1811	24717	0.1249	1773.5	46	2.62
4	5038	4764.78	0.5021	40160	0.2185	5083	4714.80	1.1333	26121	0.1197	1786.5	45	2.53
5	5181	4886.51	0.4977	38495	0.2211	5637	5275.11	1.0394	28605	0.1119	1788.7	42	2.36
6	5297	5017.47	0.4865	44544	0.2046	5038	4629.13	1.1475	26291	0.1193	1759.5	45	2.54
7	5000	4747.04	0.5006	39942	0.2192	5342	4975.71	1.0869	23658	0.1283	1760.0	43	2.45
8	4938	4686.01	0.5048	37155	0.2297	5756	5415.59	1.0176	24097	0.1273	1771.8	41	2.33
9	4964	4711.33	0.5032	36852	0.2309	6037	5699.38	0.9762	24213	0.1268	1759.7	40	2.27

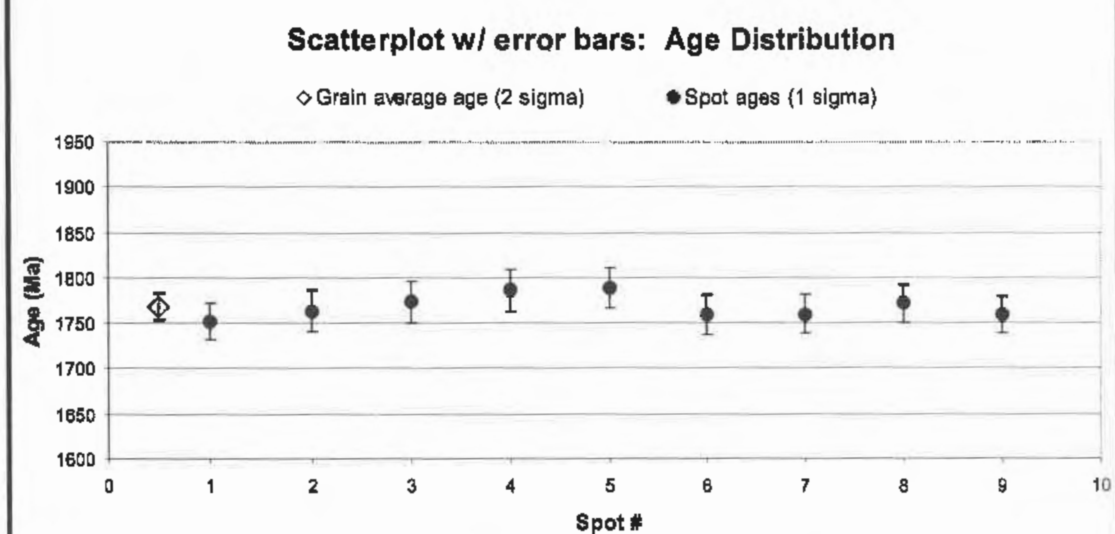

1768 Wtd Mean (from internal errors)
14 2-sigma error of mean
0.36 MSWD
0.94 Probability of fit

Grain #: S392-01
Chemical zone: homogeneous
Analyses#: 657-668

Acc. Voltage: 15 kV
Anal. Current: 200 nA
Peak(s): 600

Bkg(s): 300
Pb Ma / PETH Th Ma / PETJ
U Mb / PETJ Y La / TAP

Spot #	Pb uncorr. (ppm)	Pb corr. (ppm)	Pb error (%)	Th (ppm)	Th error (%)	U uncorr. (ppm)	U corr. (ppm)	U error (%)	Y (ppm)	Y error (%)	Age (Ma)	S.D. 2s (Ma)	S.D. 2s (%)
1	4125	3970.38	0.9793	28773	0.3663	5100	4837.17	2.0136	14231	0.2438	1832.4	83	4.55
2	4205	4053.18	0.9654	31653	0.3429	4604	4314.58	2.2020	13536	0.2542	1833.5	89	4.87
3	4032	3878.99	0.9951	31405	0.3448	4183	3895.86	2.3951	13705	0.2516	1824.5	96	5.24
4	3963	3814.27	1.0071	27114	0.3818	5043	4785.43	2.0297	13764	0.2506	1831.5	84	4.60
5	4180	4072.68	0.9624	31172	0.3459	4804	4518.83	2.1187	8440	0.3803	1832.0	86	4.71
6	4061	3866.02	0.9989	24746	0.4079	5728	5502.38	1.8201	19398	0.1899	1844.5	78	4.24
7	4227	4022.72	0.9727	28841	0.3651	5498	5253.14	1.8877	20197	0.1840	1868.0	81	4.33
8	4210	3899.86	0.9772	25503	0.3985	5971	5738.46	1.7603	21042	0.1783	1842.5	76	4.11
9	4090	3972.71	0.9787	33587	0.3288	3954	3846.56	2.5188	9283	0.3501	1819.0	99	5.45
10	4010	3853.00	0.9991	32467	0.3369	4320	4023.07	2.3305	14028	0.2468	1760.5	90	5.12
11	3988	3835.04	1.0023	28875	0.3651	4890	4626.20	2.0856	14025	0.2466	1800.0	84	4.69
12	4579	4416.42	0.9113	26831	0.3647	6857	6612.10	1.5676	15405	0.2285	1851.8	69	3.72

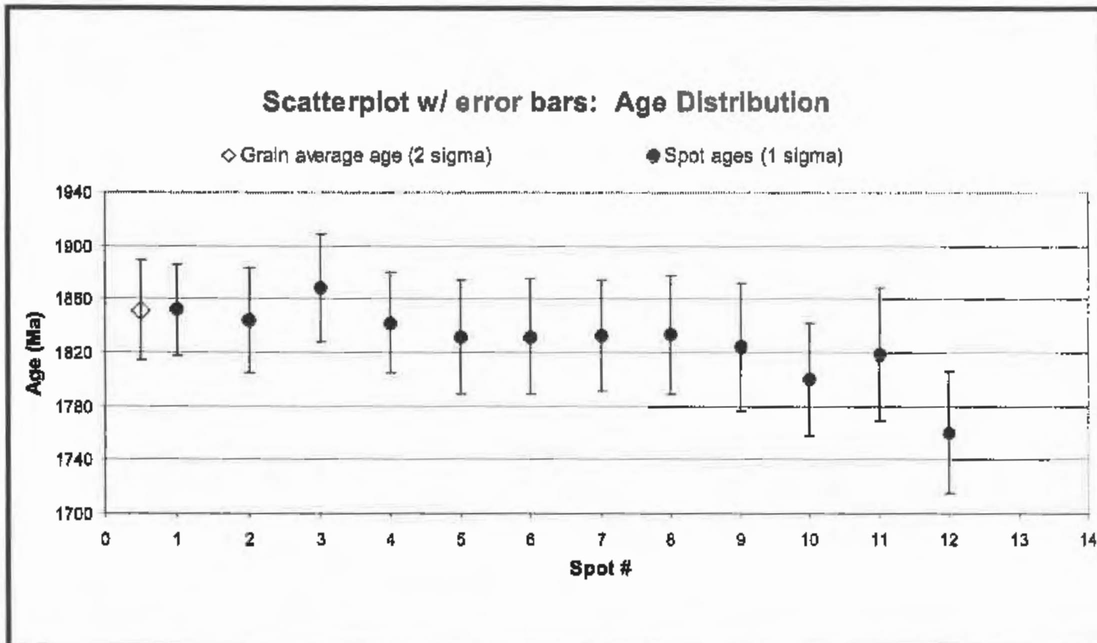

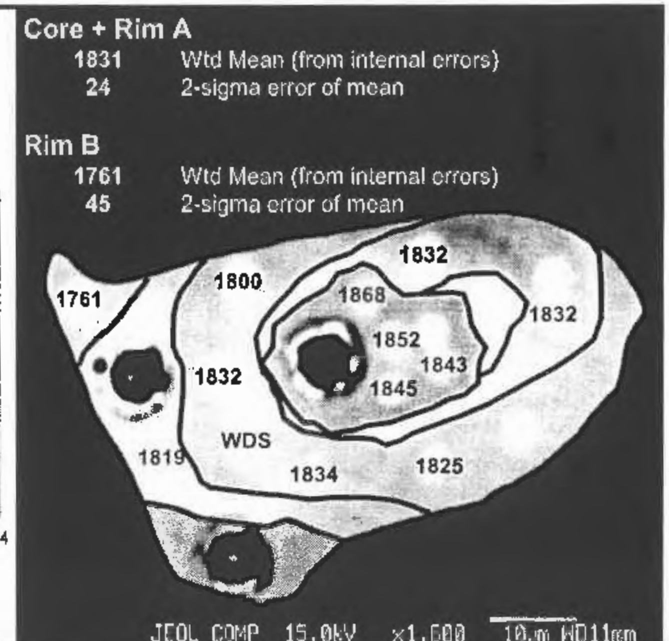

Grain #: S392-05
Chemical zone: homogeneous
Analyses#: 657-668

Acc. Voltage: 15 kV
Anal. Current: 200 nA
Peak: 600 sec.

Bkg: 300 sec.
Pb Ma / PETH Th Ma / PETJ
U Mb / PETJ Y La / TAP

Spot #	Pb uncorr. (ppm)	Pb corr. (ppm)	Pb error (%)	Th (ppm)	Th error (%)	U uncorr. (ppm)	U corr. (ppm)	U error (%)	Y (ppm)	Y error (%)	Age (Ma)	S.D. 2s (Ma)	S.D. 2s (%)
1	5508	5331.03	0.7585	31964	0.3325	7465	7172.93	1.4592	16421	0.2216	1945.8	66	3.37
2	4499	4324.18	0.8661	30241	0.3454	5295	5018.75	1.9406	16386	0.2218	1899.4	82	4.31
3	5643	5513.20	0.7413	38468	0.2926	6616	6263.54	1.6139	10112	0.3340	1915.6	69	3.61
4	4402	4295.42	0.8689	31813	0.3327	4627	4335.84	2.1779	8276	0.3974	1922.3	91	4.74
5	5307	5140.05	0.7751	34047	0.3183	6671	6369.65	1.6010	14992	0.2389	1912.0	69	3.62
6	5890	5715.35	0.7272	35432	0.3100	7929	7604.90	1.3933	15708	0.2301	1923.2.	62	3.22
7	3921	3816.46	0.9411	31835	0.3325	3654	3362.71	2.6835	8034	0.4079	1854.0	106	5.73
8	3879	3727.37	0.9552	33616	0.3208	2859	2551.45	3.3585	13266	0.2642	1861.8	131	7.02
9	4659	4610.82	0.8317	34114	0.3166	5109	4796.43	1.9981	1152	2.5656	1906.0	84	4.38

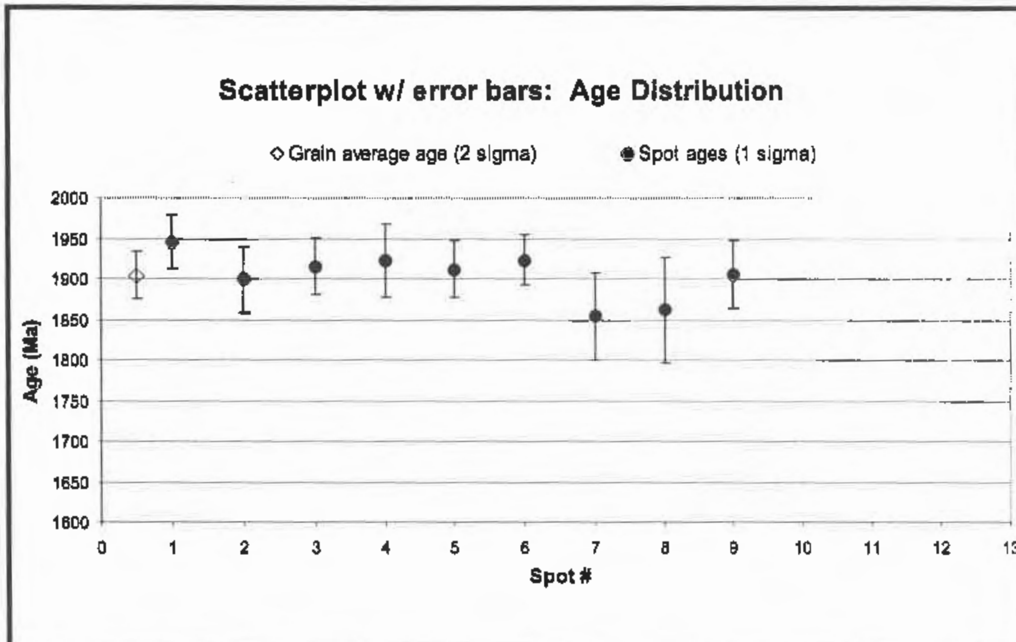

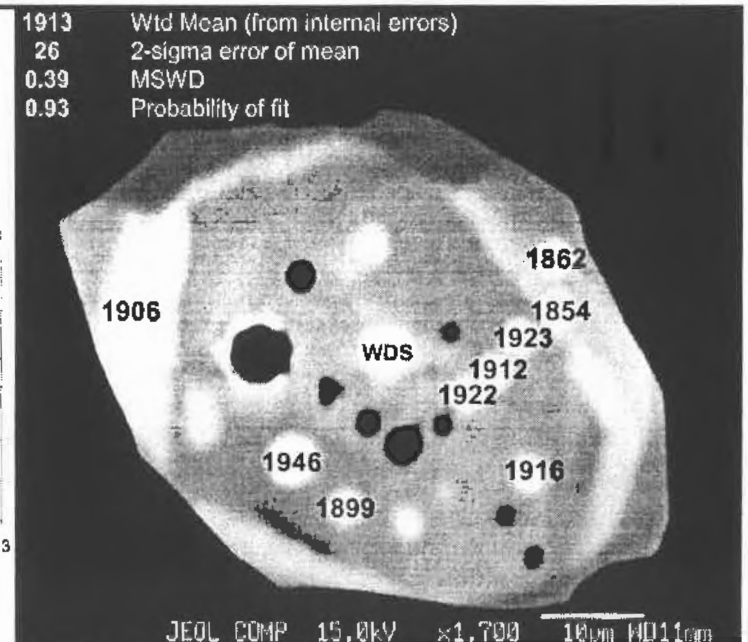

Grain #:	8392-06	Acc. Voltage:	15 kV	Bkg: 300 sec.	
Chemical zone:	homogeneous	Anal. Current:	200 nA	Pb Ma / PETH	Th Ma / PETJ
Analyses#:	657-668	Peak: 600 sec.		U Mb / PETJ	Y La / TAP

Spot #	Pb uncorr. (ppm)	Pb corr. (ppm)	Pb error (%)	Th (ppm)	Th error (%)	U uncorr. (ppm)	U corr. (ppm)	U error (%)	Y (ppm)	Y error (%)	Age (Ma)	S.D. 2s (Ma)	S.D. 2s (%)
1	7246	7083.81	0.6643	37275	0.3007	11803	11461.90	1.0234	14037	0.2509	1903.5	48	2.53
2	5871	5679.23	0.7587	36981	0.3026	7875	7536.65	1.3950	17485	0.2094	1879.5	61	3.24
3	4602	4375.28	0.8976	36704	0.3043	4185	3849.29	2.3798	21532	0.1772	1848.0	95	5.13
4	4621	4516.93	0.8759	39471	0.2887	3968	3606.05	2.4898	6981	0.4592	1841.5	98	5.32
5	4680	4594.34	0.8666	37983	0.2960	4681	4332.75	2.1492	5028	0.6194	1832.0	86	4.68
6	4249	4078.55	0.9378	33833	0.3210	4136	3826.57	2.3941	15418	0.2315	1831.0	95	5.19
7	3559	3392.58	1.0649	28641	0.3603	3584	3322.44	2.7140	15618	0.2268	1790.0	105	5.88
8	4527	4351.43	0.8981	36855	0.3029	4262	3924.66	2.3382	15621	0.2292	1825.0	92	5.05
9	4556	4371.15	0.8958	36796	0.3034	4439	4102.25	2.2551	16700	0.2170	1813.5	89	4.90
10	4484	4409.38	0.8916	39093	0.2903	3989	3630.40	2.4738	3592	0.8479	1810.3	96	5.30
11	4811	4709.23	0.8520	38490	0.2936	4959	4606.14	2.0467	6844	0.4675	1827.0	82	4.48
12	3820	3708.81	1.0016	36311	0.3052	2200	1867.31	4.2545	8222	0.3961	1847.4	162	8.77
13	3129	3030.85	1.1593	28841	0.3576	1928	1664.30	4.7927	7679	0.4202	1863.0	184	9.89

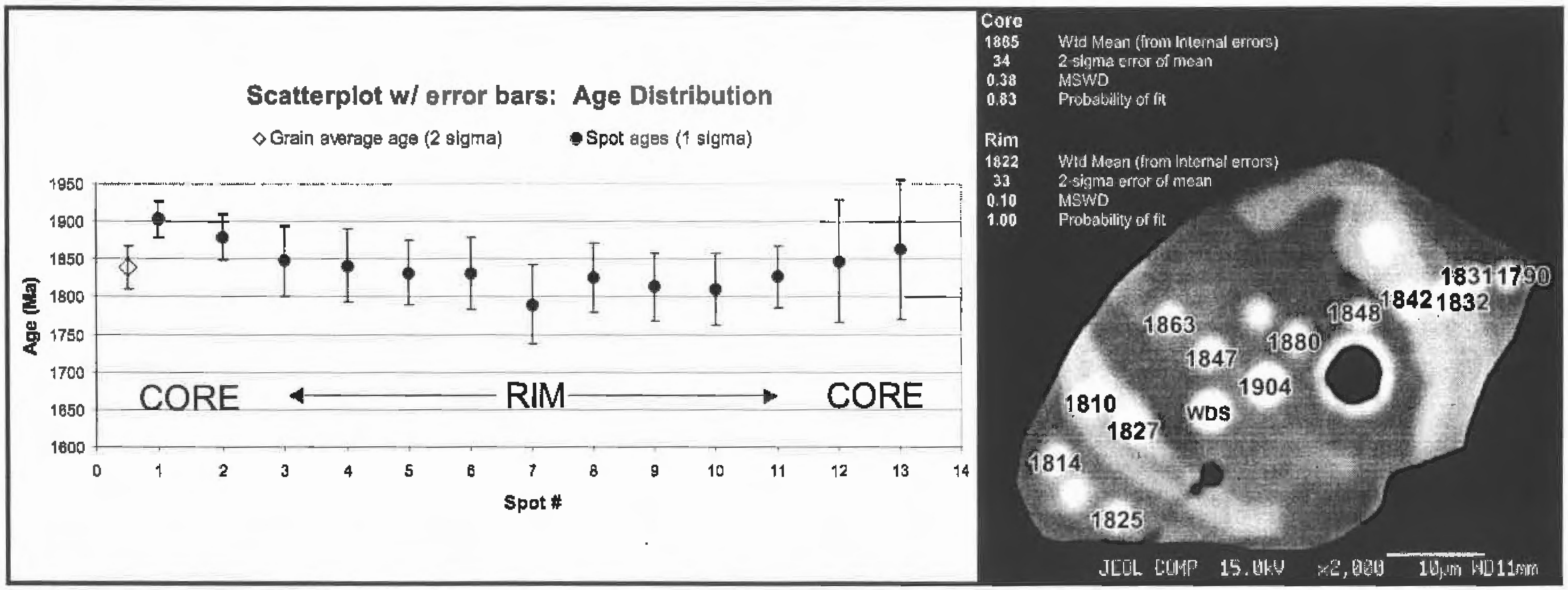

Grain #:	S392-17	Acc. Voltage:	15 kV	Bkg(s):	300
Chemical zone:	Zone 1	Anal. Current:	200 nA	Pb Ma / PETH	Th Ma / PETJ
Analyses#:	100-105	Peak(s):	600	U Mb / PETJ	Y La / TAP

Spot #	Pb uncorr. (ppm)	Pb corr. (ppm)	Pb error (%)	Th (ppm)	Th error (%)	U uncorr. (ppm)	U corr. (ppm)	U error (%)	Y (ppm)	Y error (%)	Age (Ma)	S.D. 2s (Ma)	S.D. 2s (%)
1	4757	4688.76	0.4975	39550	0.2204	4489	4125.95	1.2850	2781	0.7496	1841.6	52	2.80
2	4681	4613.59	0.5037	39011	0.2228	4343	3984.95	1.3261	2756	0.7583	1847.3	53	2.89
3	4878	4810.50	0.4905	41459	0.2143	4213	3832.21	1.3652	2444	0.8502	1859.4	55	2.95
4	4776	4705.07	0.4978	37186	0.2303	5137	4795.95	1.1471	3406	0.6228	1843.7	47	2.56
5	4969	4880.16	0.4852	39243	0.2223	5123	4762.88	1.1521	4057	0.5297	1850.4	47	2.55
6	4805	4731.21	0.4956	38996	0.2231	4773	4415.15	1.2226	3501	0.6067	1841.0	50	2.69

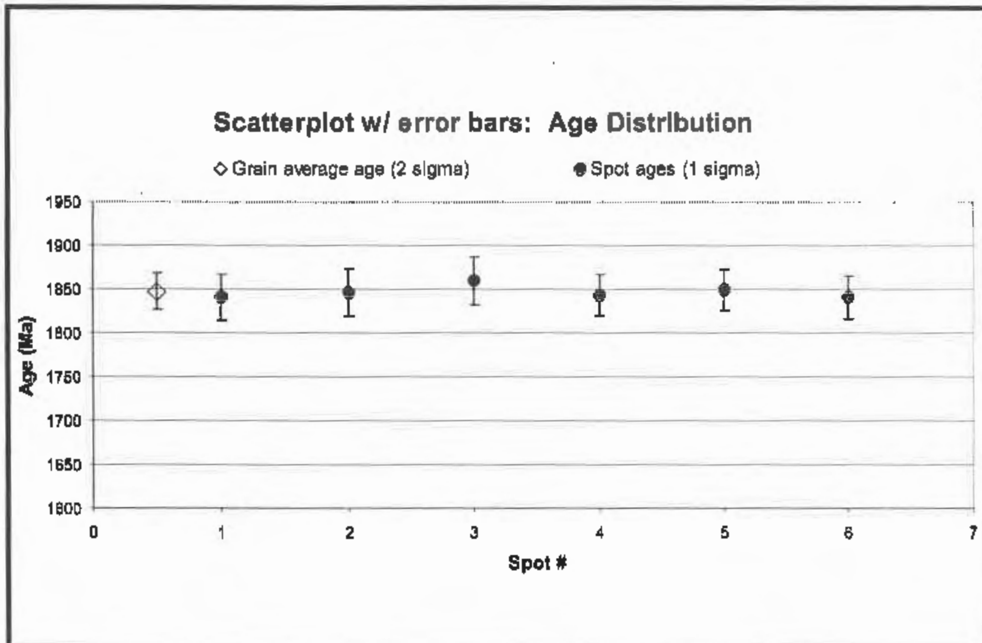

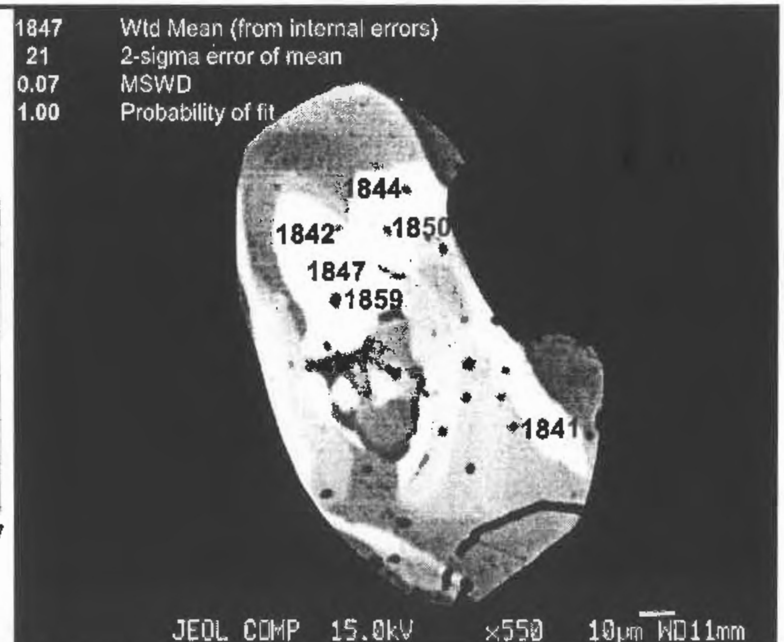

Grain #:	S392-17	Acc. Voltage:	15 kV	Bkg(s):	300
Chemical zone:	Zone 2	Anal. Current:	200 nA	Pb Ma / PETH	Th Ma / PETJ
Analyses#:	106-115	Peak(s):	600	U Mb / PETJ	Y La / TAP

Spot #	Pb uncorr. (ppm)	Pb corr. (ppm)	Pb error (%)	Th (ppm)	Th error (%)	U uncorr. (ppm)	U corr. (ppm)	U error (%)	Y (ppm)	Y error (%)	Age (Ma)	S.D. 2s (Ma)	S.D. 2s (%)
1	4487	4384.47	0.5234	32212	0.2521	5408	5112.99	1.0736	7713	0.3058	1845.2	45	2.46
2	4539	4433.73	0.5196	33155	0.2474	5367	5063.26	1.0819	7907	0.2995	1839.8	45	2.47
3	4931	4796.46	0.4949	34411	0.2419	6133	5817.79	0.9706	11125	0.2241	1845.3	42	2.25
4	4991	4847.36	0.4920	33486	0.2463	6540	6233.40	0.9200	12294	0.2061	1844.8	40	2.16
5	4874	4764.18	0.4960	36329	0.2330	5444	5110.90	1.0721	8024	0.2960	1855.0	45	2.42
6	4045	3874.29	0.5728	25871	0.2939	5228	4991.75	1.1031	16370	0.1632	1876.0	48	2.57
7	4339	4123.21	0.5529	33792	0.2453	4196	3866.85	1.3423	20518	0.1371	1842.5	54	2.96
8	4581	4418.67	0.5240	29351	0.2694	6157	5888.69	0.9645	14947	0.1757	1858.0	42	2.28
9	4667	4502.49	0.5176	29537	0.2682	6526	6255.97	0.9193	15197	0.1734	1839.8	40	2.19
10	4518	4391.59	0.5239	31773	0.2549	5564	5273.15	1.0499	10526	0.2345	1843.5	45	2.42

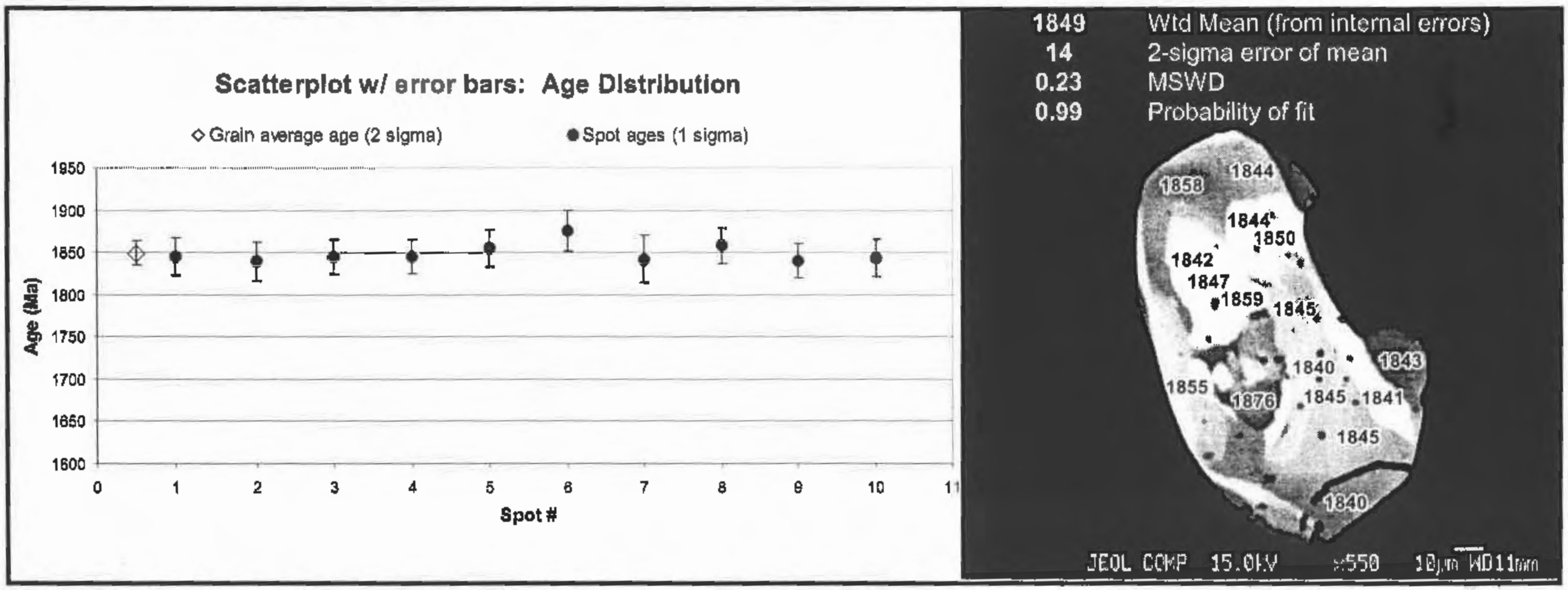

Grain #:	S392map5	Acc. Voltage:	15 kV	Bkg(s):	300
Chemical zone:	zoned	Anal. Current:	200 nA	Pb Ma / PETH	Th Ma / PETJ
Analyses#:	657-668	Peak(s):	600	U Mb / PETJ	Y La / TAP

Spot #	Pb uncorr. (ppm)	Pb corr. (ppm)	Pb error (%)	Th (ppm)	Th error (%)	U uncorr. (ppm)	U corr. (ppm)	U error (%)	Y (ppm)	Y error (%)	Age (Ma)	S.D. 2s (Ma)	S.D. 2s (%)
1	4479	4356.95	0.8792	43139	0.2701	2496	2099.42	3.6862	8533	0.3660	1842.5	140	7.60
2	3425	3323.01	1.0614	33815	0.3177	1918	1607.89	4.6865	7421	0.4131	1802.0	174	9.64
3	7019	6871.72	0.6640	35031	0.3107	11951	11630.09	0.9887	12493	0.2644	1887.2	47	2.48
4	2667	2571.54	1.2819	24994	0.3921	1764	1525.38	5.0591	7800	0.3943	1810.0	190	10.47
5	4337	4221.91	0.8982	35239	0.2926	3292	2940.97	2.8563	8362	0.3724	1849.7	111	6.02
6	4456	4280.59	0.8907	31136	0.3370	5343	5058.09	1.8612	16195	0.2133	1848.0	77	4.19
7	5161	4895.41	0.8059	29458	0.3503	8230	7960.60	1.3061	15291	0.2236	1827.3	58	3.16
8	3279	3171.86	1.0970	30716	0.3394	2150	1868.62	4.2045	8412	0.3697	1817.0	158	8.72

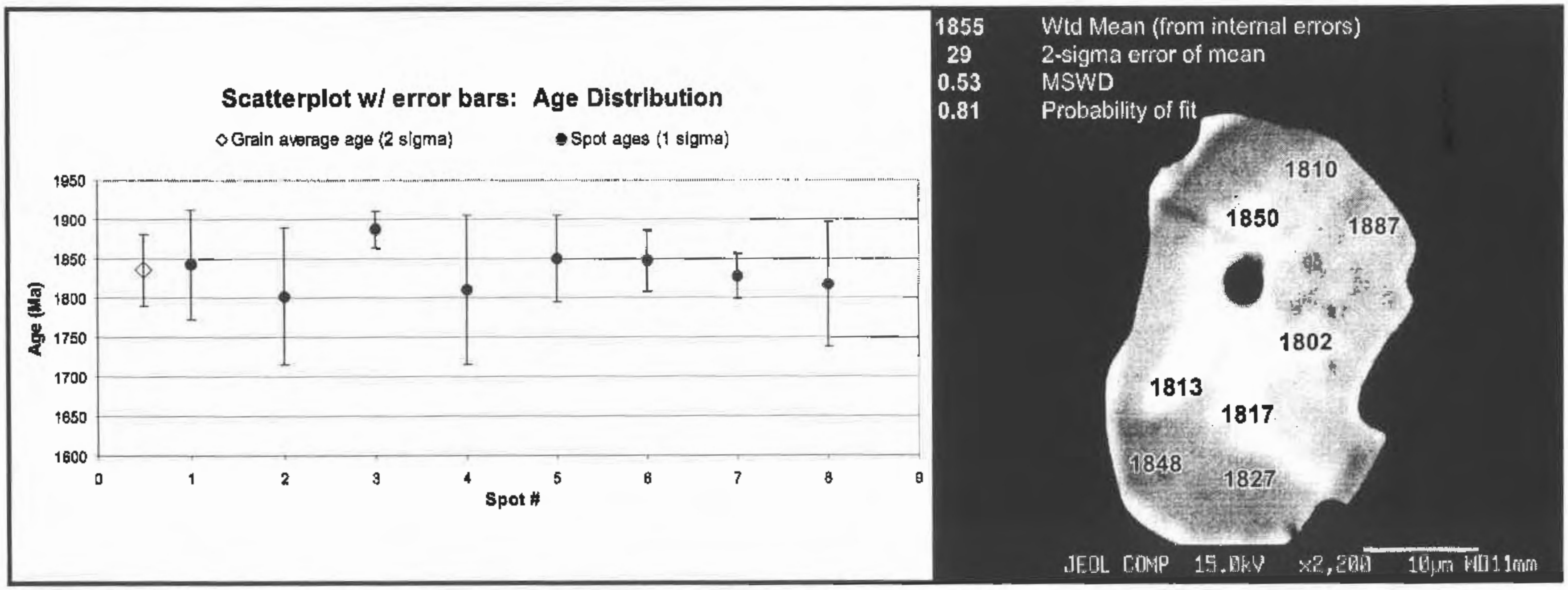

Grain #:	S397-01	Acc. Voltage:	15 kV	Bkg(s):	300
Chemical zone:	core	Anal. Current:	200 nA	Pb Ma / PETH	Th Ma / PETJ
Analyses#:	386-391	Peak(s):	600	U Mb / PETJ	Y La / TAP

Spot #	Pb uncorr. (ppm)	Pb corr. (ppm)	Pb error (%)	Th (ppm)	Th error (%)	U uncorr. (ppm)	U corr. (ppm)	U error (%)	Y (ppm)	Y error (%)	Age (Ma)	S.D. 2s (Ma)	S.D. 2s (%)
1	9883	9666.78	0.3387	56226	0.1874	14574	14056.15	0.6177	18753	0.1495	1911.9	28	1.48
2	8874	8658.23	0.3575	53241	0.1942	13480	12988.98	0.6519	17935	0.1548	1840.0	29	1.56
3	10376	10153.92	0.3305	50861	0.2002	18914	18445.49	0.5117	18967	0.1481	1835.9	24	1.31
4	8943	8728.25	0.3560	56070	0.1877	13116	12598.41	0.6676	17464	0.1583	1831.2	29	1.58
5	9510	9277.20	0.3465	51633	0.1983	15770	15294.22	0.5809	20077	0.1415	1844.7	27	1.44
6	9197	8977.17	0.3512	54246	0.1918	14266	13765.62	0.6259	18272	0.1525	1837.8	28	1.51

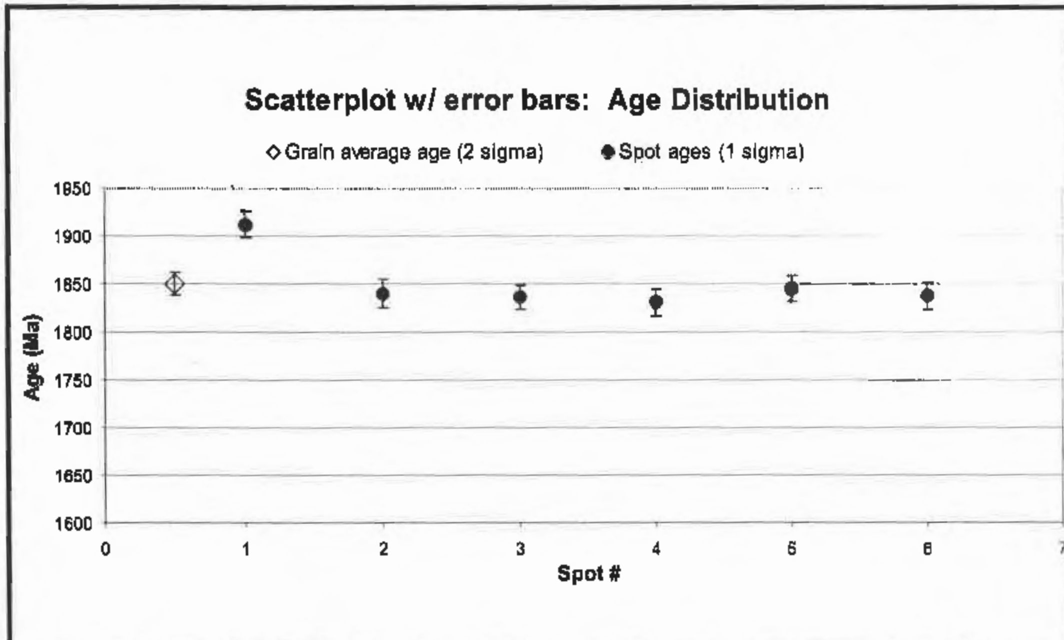

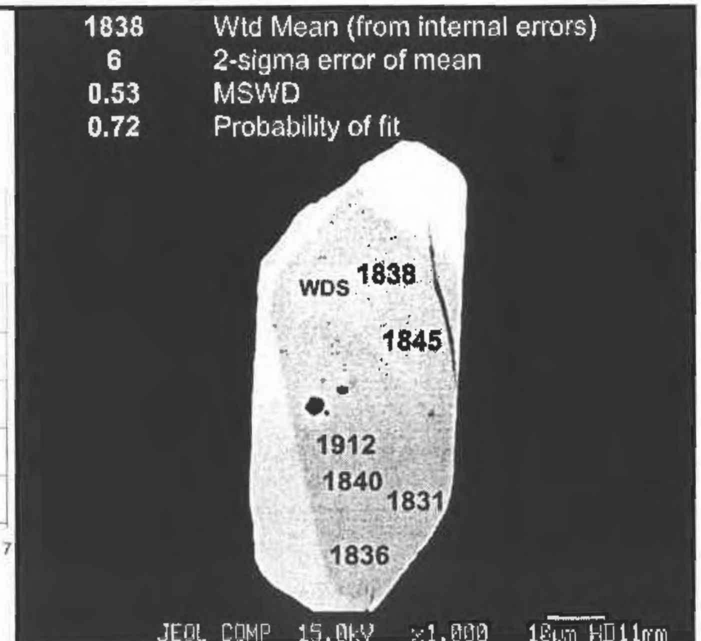

Grain #:	S397-01	Acc. Voltage:	15 kV	Bkg(s):	300
Chemical zone:	rim	Anal. Current:	200 nA	Pb Ma / PETH	Th Ma / PETJ
Analyses#:	392-396	Peak(s):	600	U Mb / PETJ	Y La / TAP

Spot #	Pb uncorr. (ppm)	Pb corr. (ppm)	Pb error (%)	Th (ppm)	Th error (%)	U uncorr. (ppm)	U corr. (ppm)	U error (%)	Y (ppm)	Y error (%)	Age (Ma)	S.D. 2s (Ma)	S.D. 2s (%)
1	8523	8329.75	0.3633	60812	0.1783	10547	9984.97	0.7481	14455	0.1822	1835.2	32	1.72
2	8335	8142.87	0.3678	60300	0.1794	10223	9665.79	0.7666	14391	0.1829	1826.7	32	1.76
3	8134	7942.64	0.3727	58974	0.1820	9935	9390.20	0.7823	14469	0.1820	1826.5	33	1.79
4	7812	7620.21	0.3812	56624	0.1869	9529	9006.27	0.8060	14816	0.1784	1825.6	34	1.84
5	7845	7653.42	0.3804	57014	0.1861	9595	9068.61	0.8023	14742	0.1792	1821.5	33	1.84

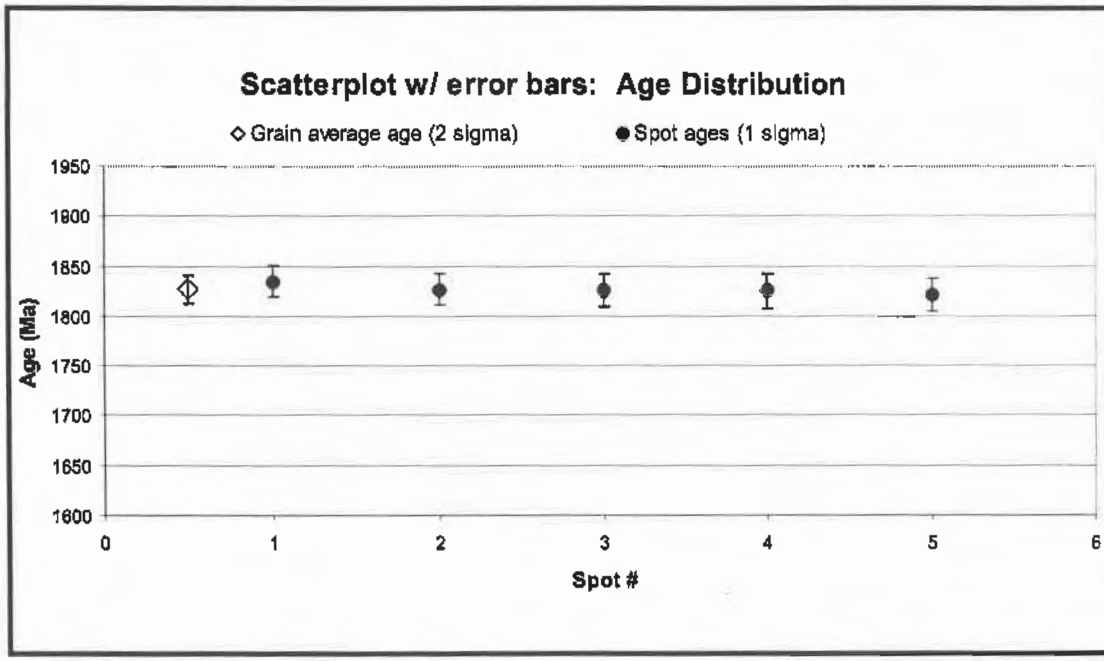

1827	Wtd Mean (from internal errors)
15	2-sigma error of mean
0.1	MSWD
0.98	Probability of fit

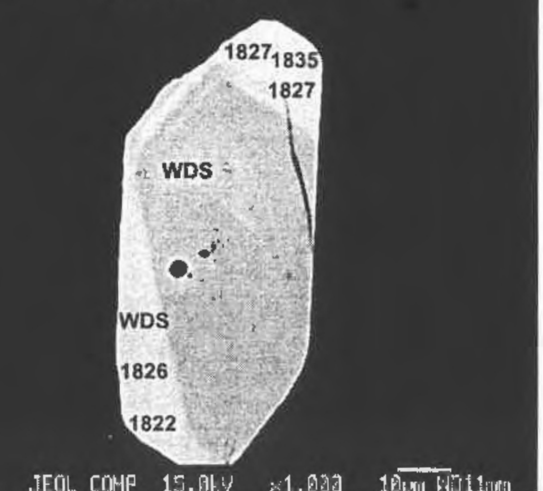

Grain #:	S397-02	Acc. Voltage:	15 kV	Bkg(s):	300
Chemical zone:	zoned	Anal. Current:	200 nA	Pb Ma / PETH	Th Ma / PETJ
Analyses#:	397-406	Peak(s):	600	U Mb / PETJ	Y La / TAP

Spot #	Pb uncorr. (ppm)	Pb corr. (ppm)	Pb error (%)	Th (ppm)	Th error (%)	U uncorr. (ppm)	U corr. (ppm)	U error (%)	Y (ppm)	Y error (%)	Age (Ma)	S.D. 2s (Ma)	S.D. 2s (%)
1	8475	8325.54	0.3627	62123	0.1757	9604	9229.06	0.7963	9265	0.2575	1859.7	34	1.81
2	8706	8545.40	0.3583	63488	0.1735	10154	9566.32	0.7771	10374	0.2341	1858.3	33	1.77
3	8243	8083.04	0.3691	68669	0.1649	7716	7079.27	0.9761	9630	0.2494	1835.2	39	2.13
4	8110	7951.09	0.3723	67204	0.1671	7646	7023.09	0.9816	9698	0.2478	1837.4	39	2.14
5	8527	8379.59	0.3615	61467	0.1770	10090	9521.24	0.7786	9113	0.2614	1863.0	33	1.77
6	8581	8430.08	0.3605	62204	0.1757	9955	9379.31	0.7875	9423	0.2540	1869.3	33	1.79
7	8515	8360.63	0.3621	62185	0.1757	9767	9191.53	0.7991	9822	0.2450	1868.0	34	1.81
8	8131	7932.09	0.3748	62503	0.1754	8641	8062.86	0.8830	14890	0.1734	1848.5	36	1.97
9	8228	8030.94	0.3721	62154	0.1760	9104	8529.15	0.8463	14495	0.1772	1844.6	35	1.90
10	8770	8590.27	0.3583	62871	0.1747	10009	9427.31	0.7856	12649	0.1983	1866.3	34	1.78

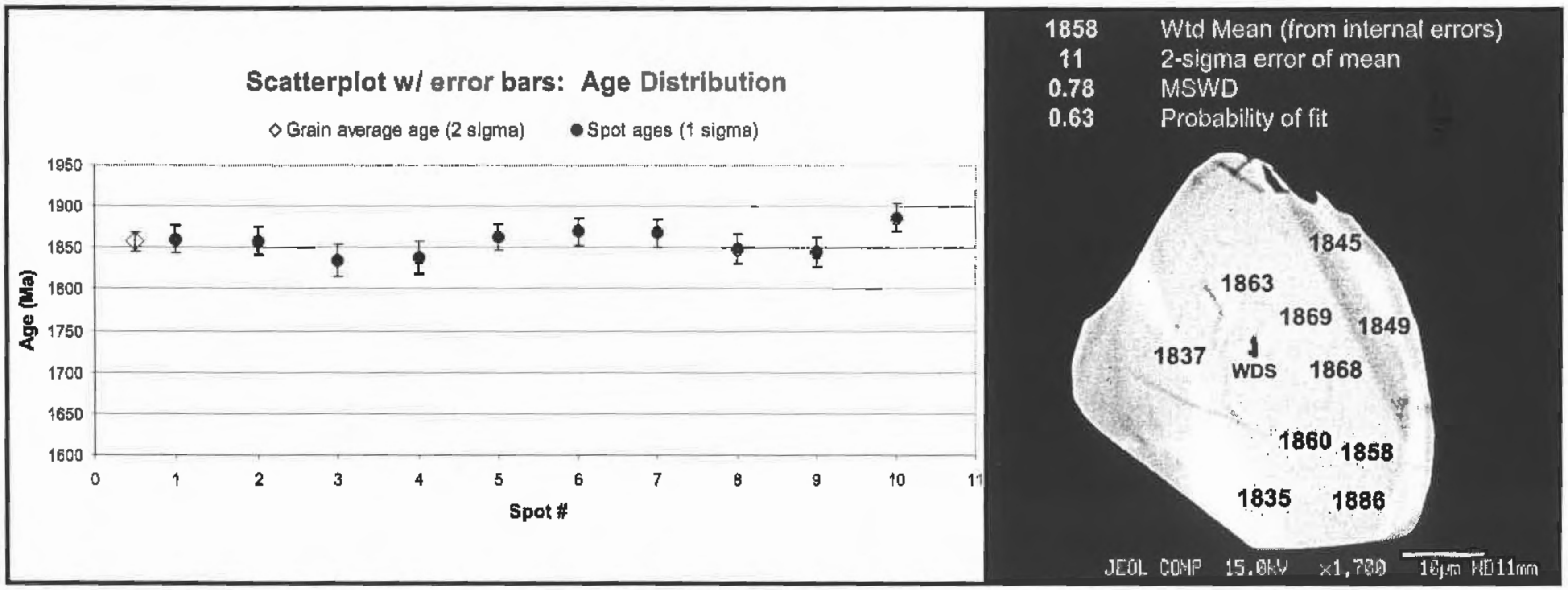

Grain #: 8401-01
Chemical zone: very zoned
Analyses#: 407-418

Acc. Voltage: 15 kV
Anal. Current: 200 nA
Peak(s): 600

Bkg(s): 300
Pb Ma / PETH Th Ma / PETJ
U Mb / PETJ Y La / TAP

Spot #	Pb uncorr. (ppm)	Pb corr. (ppm)	Pb error (%)	Th (ppm)	Th error (%)	U uncorr. (ppm)	U corr. (ppm)	U error (%)	Y (ppm)	Y error (%)	Age (Ma)	S.D. 2s (Ma)	S.D. 2s (%)
1	9801	9656.01	0.3359	80763	0.1488	10341	9588.47	0.7902	6352	0.3506	1776.7	31	1.76
2	11107	10936.40	0.3175	89233	0.1401	11995	11162.04	0.7149	8217	0.2804	1807.4	29	1.61
3	10971	10721.99	0.3239	84164	0.1456	11910	11126.52	0.7137	17851	0.1476	1841.7	30	1.62
4	9422	9193.47	0.3478	80867	0.1491	8667	7914.42	0.9124	15921	0.1613	1800.9	36	2.00
5	9575	9349.64	0.3447	67432	0.1673	12760	12155.00	0.6603	17263	0.1512	1796.4	28	1.55
6	9936	9778.07	0.3339	74037	0.1573	12077	11368.71	0.6940	8708	0.2658	1815.0	29	1.60
7	10484	10347.47	0.3252	83750	0.1458	11591	10809.93	0.7281	4991	0.4373	1804.2	30	1.65
8	10326	10161.07	0.3285	80084	0.1500	11701	10955.27	0.7186	8738	0.2658	1816.5	30	1.63
9	11169	10854.20	0.3275	74448	0.1577	15693	15002.78	0.5757	26542	0.1095	1803.0	25	1.39
10	10044	9854.68	0.3341	72093	0.1603	13131	12461.56	0.6513	12560	0.1956	1800.0	27	1.52
11	10322	10055.15	0.3355	76438	0.1548	12769	12079.22	0.6693	20852	0.1310	1792.8	28	1.55
12	10865	10553.76	0.3316	73352	0.1591	15253	14573.09	0.5863	26275	0.1102	1791.6	25	1.41